APPLIED METAL FORMING

INCLUDING FEM ANALYSIS

HENRY S. VALBERG

CAMBRIDGE

CAMBRIDGE www.cambridge.org/9780521518239

This page intentionally left blank

APPLIED METAL FORMING
Including FEM Analysis

Applied Metal Forming: Including FEM Analysis describes metal forming theory and how experimental techniques can be used to study metal forming operations with great accuracy. For each primary class of processes, such as forging, rolling, extrusion, wiredrawing, and sheet-metal forming, it explains how finite element analysis (FEA) can be applied with great precision to characterize the forming conditions and in this way optimize the processes. FEA has made it possible to build realistic FEM models of most metal forming processes, including complex three-dimensional forming operations, in which complex products are shaped by complex dies. Thus, using FEA, it is now possible to visualize any metal forming process and to study strain, stress, and other forming conditions inside the parts being manufactured as they develop throughout the process.

Henry S. Valberg is a professor in the Department of Engineering Science and Materials at the Norwegian University of Science and Technology (NTNU). He began his professional career as a metallurgist at the Royal Norwegian Air Force (LFK), and continued it at A/S Norsk Jernverk, Mo i Rana, and then as a research scientist at SINTEF, Division of Materials and Processes, before joining the Norwegian Institute of Technology (NTH) as a senior lecturer in 1984 and full professor in 1994. He was a visiting professor at Denmark's Technical University in 1997–1998. Professor Valberg's main fields of research are materials, metal forming, experimental deformation analysis, and FEA. His work covers all the main metal forming processes, including forging, rolling, extrusion, drawing, and sheet-metal forming. He is the author of more than 60 refereed journal articles and has supervised numerous graduate students. Professor Valberg is currently a research manager in a project run by three Norwegian forging companies.

Applied Metal Forming

INCLUDING FEM ANALYSIS

Henry S. Valberg
Norwegian University of Science and Technology

CAMBRIDGE
UNIVERSITY PRESS

CAMBRIDGE UNIVERSITY PRESS
Cambridge, New York, Melbourne, Madrid, Cape Town, Singapore,
São Paulo, Delhi, Dubai, Tokyo

Cambridge University Press
The Edinburgh Building, Cambridge CB2 8RU, UK

Published in the United States of America by Cambridge University Press, New York

www.cambridge.org
Information on this title: www.cambridge.org/9780521518239

© Henry Valberg 2010

This publication is in copyright. Subject to statutory exception and to the provision of relevant collective licensing agreements, no reproduction of any part may take place without the written permission of Cambridge University Press.

First published in print format 2010

ISBN-13 978-0-511-72943-0 eBook (NetLibrary)

ISBN-13 978-0-521-51823-9 Hardback

Cambridge University Press has no responsibility for the persistence or accuracy of urls for external or third-party internet websites referred to in this publication, and does not guarantee that any content on such websites is, or will remain, accurate or appropriate.

Contents

Preface *page* vii

1 **Characteristics of Metal Forming** . . . 1

2 **Important Metal Forming Processes** . . . 18

3 **FEA of Metal Forming** . . . 34

4 **Theory** . . . 53

5 **Reduction and Proportions of the Plastic Zone** . . . 77

6 **Deformations from the Velocity Field** . . . 84

7 **Technological Tests and Physical Simulation** . . . 92

8 **Flow Stress Data** . . . 115

9 **Formability and Workability** . . . 127

10 **Friction and Friction Models** . . . 139

11 **Thermal Effects** . . . 159

12 **Experimental Metal Flow Analysis** . . . 181

13 **Theoretical Methods of Analysis** . . . 204

14 **Finite Element Analysis** . . . 219

15 **FEA of Technological Tests** . . . 242

16 **Forging** . . . 268

17 **FEA of Forging** . . . 285

18 **Extrusion** 320

19 **FEA of Extrusion** 347

20 **Rolling** 365

21 **FEA of Rolling** 376

22 **Drawing of Wire, Profiles, and Tubes** 395

23 **FEA of Wiredrawing** 414

24 **Sheet-Metal Forming** 435

25 **FEA of Sheet-Metal Forming (Available at www.cambridge.org/valberg)** . . . .

Index 453

Preface

Finite element analysis (FEA) has currently been developed into an efficient, user-friendly tool for investigation of metal forming processes. At the same time, cheap, efficient computers have been developed that allow simulation of metal forming to be done by use of the finite element method (FEM), within reasonable times. This recent development is, as this book will show, about to revolutionize the art of metal forming.

This technology has made it possible to build realistic FEM models of perhaps any metal forming process, including complex three-dimensional forming operations, in which complex products are shaped by means of complex dies. Thus, by FEA, it is now possible to visualize any metal forming process on the computer screen and to study strain, stress, and other important forming conditions inside the workpiece, as they develop throughout the duration of the process. Because of this, FEA has also become an important industrial tool in connection with development and design of new metal forming processes.

However, in spite of this development, there is still need for classical theory as a tool for providing knowledge about forming. For a person to be able to utilize the new FEA technology and to evaluate the results obtained in FEA, it is required that he or she have deep insight into the theory of metal forming.

In order to establish correct FEM models, it is still required to investigate metal forming by means of experiments performed in the laboratory or on industrial equipment. Without some experimentation, it is difficult to know what information should be fed into the FEM model, and to what extent a simulation is precise. If input data to the model is wrong, the usefulness of FEA may be limited.

Throughout his career, the author of this book has done much work to develop new visioplasticity methods for the study of metal flow in metal forming. In this way, a new advanced grid pattern technique has been developed, which allows stripe patterns to be made in the interior of a workpiece and ring patterns to be added onto its surface, to be shaped later by metal forming. These techniques are useful in that they allow precise characterization of metal flow, inside and on the surface of a workpiece.

The book describes metal forming theory briefly and explains how experimental techniques can be used to study the forming conditions of metal forming operations with great accuracy. In addition, it is shown for each of the main classes of metal forming processes – forging, rolling, extrusion, wiredrawing, and sheet-metal forming – how FEA can be applied precisely to characterize forming conditions in these operations, and in this way optimize the processes.

Examples are provided throughout the book to illustrate how theory, experiments, and FEA in combination can be used to calculate and characterize the conditions in a forming process. In each chapter, a number of illustrative problems are provided. A solution manual will be provided separately.

The chapters dealing with FEA have been written so that it is not required for the reader to apply a FEM program. Simulation results are presented, and the reader will gain experience in evaluation of postprocessing data from FEM models. However, the best situation for the reader will, of course, be if he or she has access to a FEM simulation program and hence can rerun or modify some of the FEM models presented in the book.

The book is applicable on both the undergraduate and graduate levels in universities and should also be useful for the metal-former working in industry.

In addition to the book's printed content, additional materials have been made available on the Web site www.cambridge.org/valberg. A full chapter on FEA of sheet-metal is available for free review or download. Also available are color representations of many of the book figures designed to enhance the reader's understanding. In the gray-scale figures, letters have been used to indicate color distribution as follows: R = red, Y = yellow, G = green, LB = light blue, B = blue.

I would like to thank Dr. Dirk Nolte and Dr. Rama Krishna Uyyuru, who have read through the manuscript and proposed improvements. Thanks are also due to my current and former students, most of them on the master's level, who have worked with the topics covered by the book. I would also like to thank my home university (NTNU) for providing financial support for two sabbaticals. The FEA part of the book could not have been realized without this support.

Finally, I would like to express thanks to my wife, *Beate Linge*, for her patience during the time required for writing this book.

Trondheim, January 25, 2010

APPLIED METAL FORMING

1 Characteristics of Metal Forming

Metal forming is one manufacturing method among many. In order to manufacture a machine component, such as a wheel suspension arm for a car, one can choose metal forming, casting, or machining as the shaping method. These three shaping methods can be considered competing processes. The method chosen will usually be the one that provides a product, with proper function and properties, at the lowest cost. In this chapter, characteristics of these three shaping methods will be described, with special emphasis on metal forming, when used to create the intended shape of a component through plastic deformations of an initial *workpiece* of simple shape.

1.1 Definition of Metal Forming

Metal forming refers to shaping of metallic materials by means of plastic deformation. The term *plastic deformation* describes permanent shape change, in contrast to *elastic deformation*. An elastic deformation disappears when the load is removed. Many industrial materials are shaped into useful products by plastic deformation. Clay is a material that is shaped by plastic deformation before it is fired to become a final useful solid ceramic material. In addition, polymer materials are commonly shaped in melted condition by means of plastic deformation. But in this book, the treatment is confined to plastic deformation of metals.

A more comprehensive definition of metal forming is the technology used for shaping metal alloys into useful products by forming processes such as rolling, forging, extrusion, drawing, and sheet-metal forming. With this definition, the term involves many scientific disciplines, including chemistry, physics, mechanics, and general manufacturing technology.

1.2 Plastic Deformations on Micro- and Macroscopic Scales

The term *plastic deformation* can be explained if one examines a metallic material that is subjected to deformation in a specific metal forming process.

Figure 1.1 shows the frictionless compression of a cylinder between two parallel platens as either a cold- or a hot-forming process. An area element from an internal

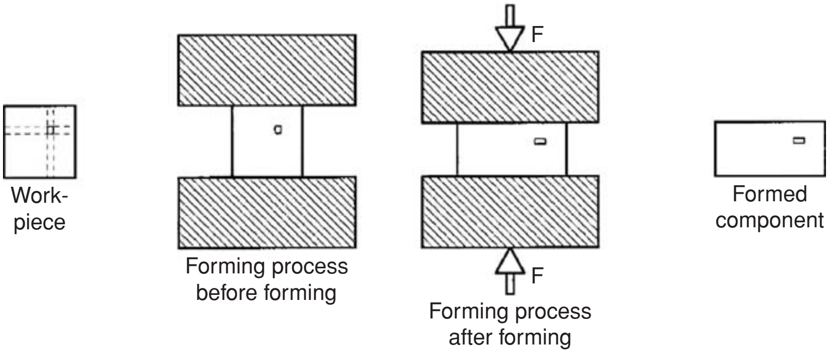

Figure 1.1. Frictionless compression of a cylinder with internal grid pattern in the horizontal midplane.

grid pattern is sketched in the axial midplane of the cylinder prior to forming. The plastic deformation of the cylinder during the test can be observed on a macro scale and quantified through the change of shape of the elements of this *grid pattern*. In Fig. 1.1 only one grid element of the pattern is shown, because all grid elements behave the same way when frictionless compression is applied. In practical cases of forming, this type of grid pattern technique is often used to map deformations inside a workpiece. As the figure illustrates, the workpiece, and the grid element inside its midsection, are compressed in the vertical direction, while they expand in the radial direction. This change of shape represents the *macroscopic deformation* of the workpiece.

In the treatment in the continuum mechanics,[1] the workpiece is considered idealized as a continuous medium, also termed a *continuum*. In such a material, the average density, for instance, will vary continuously with respect to time and position within the medium. When a volume element inside the medium is made smaller, the boundary value of this property, as the size of the element approaches zero, will then be the density in the point.

In practice a real metallic material will never be a continuum. A conventional pearlitic–ferritic C–Mn steel, for instance, will on the microscopic level be strongly inhomogeneous, as shown in Fig. 1.2(a). On examining it at sufficiently large magnification, one will see that the microstructure of the material consist of an aggregate of *ferritic* and *pearlitic* grains, with *grain boundaries* separating each grain from its neighbors. The grain boundary is known to have lower density (due to higher dislocation density) than the interior of the grain and to have mechanical properties different from those of the interior. Moreover, a pearlitic grain consists of flakes of *cementite* (Fe_3C) embedded in a matrix of ferrite. It is much harder and has much higher flow stress than a ferrite grain, which consists of pure iron with a small amount of carbon in solid solution.

If we examine a pearlite grain in more detail, we find that the flakes of cementite are extremely hard and brittle. During plastic deformation of such grains, the

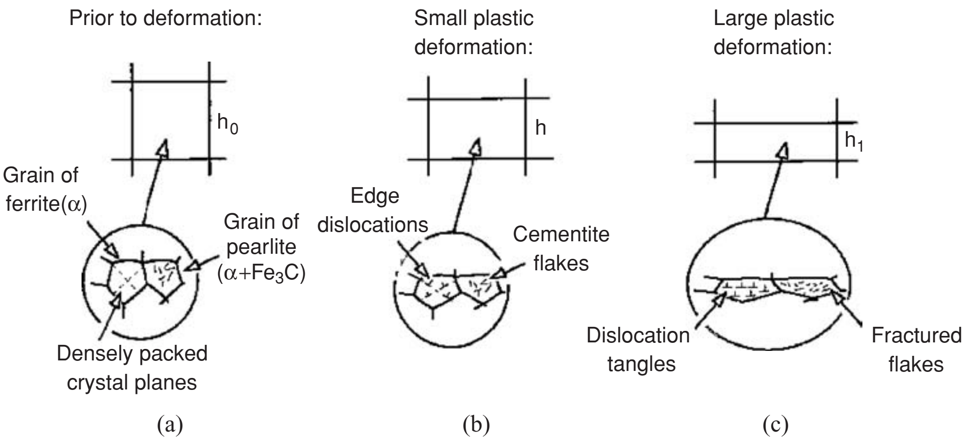

Figure 1.2. Schematic sketch showing micro-scale effects of plastic deformation in pearlitic–ferritic steel: (a) undeformed grains, (b) deformation of ferrite by dislocation movement, (c) multiplication of dislocations in ferrite and fracture of cementite flakes in pearlite.

ferrite, in which the brittle flakes are embedded, deforms severely by microscopic plastic deformation. The flakes themselves, because of their low ductility, fracture into small pieces; see Fig. 1.2(c). The reason the pearlitic grains can deform plastically without damaging the whole microstructure is the distribution of the cementite flakes as small islands in the more ductile ferrite matrix.

Cast irons, which contain much more carbon than steel (>1.7% C), sometimes can form a microstructure in which films of cementite appear as a continuous skeleton throughout the grain boundaries of the whole material. The materials in this state are very brittle and cannot be deformed plastically without fracture. If, for example, one tries to bend a component of such a material, to change its shape permanently, it will fracture before it is plasticized. This illustrates that on a micro scale a metallic material commonly consists of different phases with different mechanical properties. Moreover, most metallic materials will consist of an aggregate of crystal grains. In the grains, the atoms are packed along various crystallographic planes. The orientation of the crystal planes will be different from one grain to a neighboring grain. Because these inhomogeneities are of small size, commonly $< 100\ \mu$m, the material can, anyhow on a macroscopic level, be considered a continuum and can be well described by the theory of continuum mechanics.

When considered on a sufficiently small scale, so that atoms become visible, plastic deformation of metals is known to be caused by *dislocations*. They are generated in the metal upon plastic deformation and move through the *grains*, along the densely packed atomic planes of the microstructure, as shown in Fig. 1.2(b,c) and Fig. 1.3. New dislocations are also formed during cold forming, so that the dislocation density increases as the metal is subjected to larger strains.

However, plastic deformation in melted polymers and in clay occurs by mechanisms different from those in metals. In polymers, sliding of long polymer chains against one another is the most common mechanism of plastic deformation. In clays,

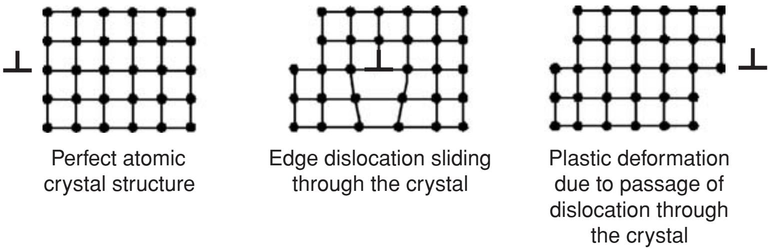
Perfect atomic crystal structure
Edge dislocation sliding through the crystal
Plastic deformation due to passage of dislocation through the crystal

Figure 1.3. Edge dislocation sliding through a perfect crystal yields plastic deformation on the atomic level.

the *deformation mechanism* is one of small flakes of the material sliding over neighboring flakes by means of thin films of water separating the flakes.

1.3 Characteristics of Metal Forming

Following are some general characteristics of metal forming processes:

- The workpiece is completely or partially subjected to plastic deformation during the forming operation; that is, it is *plasticized*.
- The plastic deformation is most commonly large.
- Little or no material is removed during the forming process.
- The microstructure of the as-cast workpiece is broken down by the plastic deformation. Therefore, the final component, or *product*, made by metal forming usually will have better mechanical properties than a similar product manufactured by casting or machining.
- During cold deformation, mechanical properties, such as the yield strength and tensile strength, will increase because of the accumulation of plastic strain in the material.

These are typical characteristics of metal forming as a manufacturing process. The first three points mentioned are illustrated by examples in Fig. 1.4. In this figure, the material that is subjected to plastic deformation is shown as a hatched area. In these examples, material removal only occurs in the closed-die forging process, where a *flash* is formed. After forming, the flash must be removed by trimming before the finished forging can be used.

1.4 Alternatives to Metal Forming

In Fig. 1.5 and in Table 1.1, common manufacturing processes, such as forging, casting, and turning, are compared when applied for production of a specific component. As shown in the figure, metal forming can result in some material loss, for instance, in closed-die forging, in which a flash forms toward the end of the forming process.

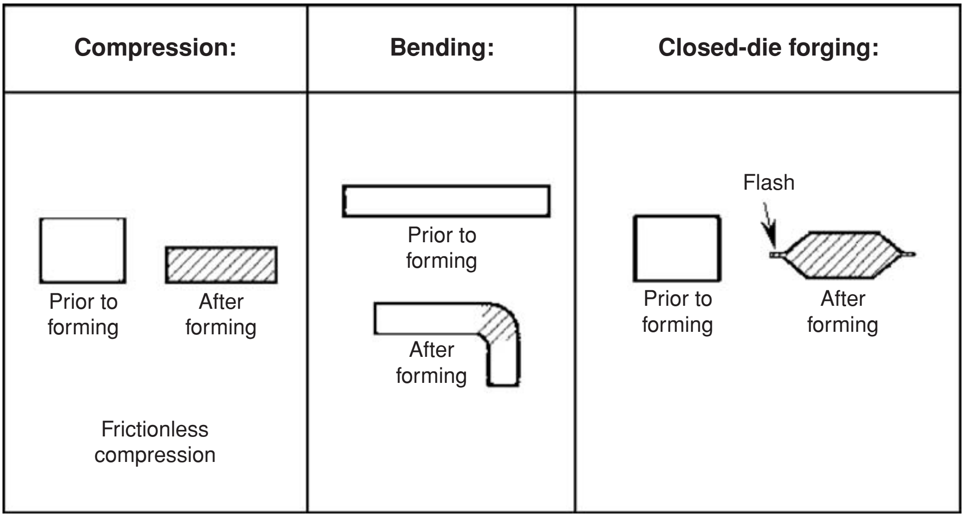

Figure 1.4. Characteristics of metal forming illustrated by different metal forming processes.

In casting, the inlet channels, consisting of *pouring cup*, *sprue*, and *runner*, represent material that is wasted. In casting, *risers* are also commonly used to feed molten metal into parts of the casting that solidify late. Without such risers, the casting would likely develop defects at these locations, such as, for instance, shrinkage cavities. The metal of a riser is commonly discarded after the casting operation and therefore represents material loss. Most commonly, however, the largest material

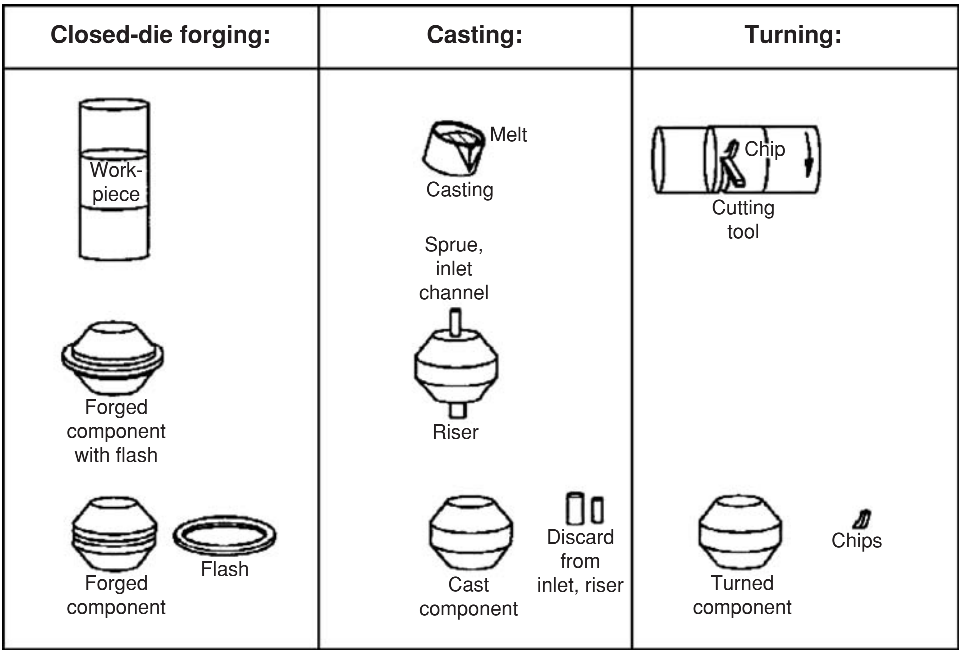

Figure 1.5. Manufacture of a massive component by means of different methods.

Table 1.1. *Advantages (+) and disadvantages (÷) of some manufacturing methods*

Property	Closed-die forging	Casting	Turning
Necessary production equipment	÷ Complex and expensive forming machine, tooling usually expensive.	+/÷ Rather cheap equipment in sand and die casting. Complex and expensive equipment in pressure casting.	+ Turning lathe is rather complex and expensive, but tooling is rather cheap.
Freedom with respect to selection of shape of formed component	÷ Little freedom: one die gives one shape.	÷ Little freedom: one sand form or mold gives one shape.	+ Large freedom: one cutting tool produces many different shapes.
Mechanical properties of finished product	+ Improved through plastic deformation.	÷ Cast microstructure; risk of porosity or other casting defects.	÷ Same as for casting, when turning cast work material.
Loss of material	+ Little (flash and machining allowance).	+ Moderate (metal in inlet channels and risers is discarded).	÷ Usually large (formation of metal chips).
Typical component	Security detail of car, such as wheel suspension.	Door handle grip of complex shape.	Machine components produced in small numbers.

loss is experienced in metal removal processes, that is, machining processes such as turning, in which a lot of metal has to be removed to obtain the final shape.

As Table 1.1 depicts, each of the three production processes discussed here has its good and bad characteristics. When it comes to production of a component in small numbers, metal forming will usually be too expensive, and the situation is the same for pressure casting because of its high tooling costs. These processes usually demand mass production to distribute the high tooling cost over many finished components. Turning, however, because of its cheap tooling and its flexibility with regard to product shape, is commonly preferred when a component is to be produced in small numbers.

If large components are to be made, or components of intricate shape, casting is usually an attractive production process. During production of long shapes with constant cross section (e.g., strips, rod, profiles, or plates), metal forming processes such as rolling, extrusion, and drawing are most commonly applied. If there are strict requirements on the quality of the product (e.g., high strength, high resistance against fatigue, or low acceptance of internal defects), then one will usually specify that the product be made by metal forming, for instance, by hot forging. During production of security components (e.g., a steering column or a heavily loaded wheel suspension in an automobile), it is usually specified that the components should be

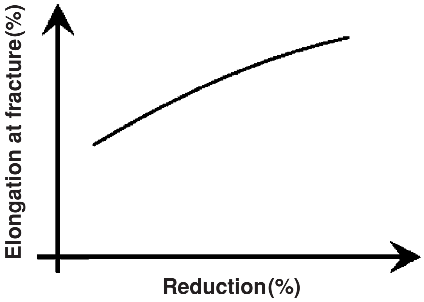

Figure 1.6. Hot working of cast metal increases its ductility because the microstructure is altered.

made by metal forming, because that ensures a component with excellent mechanical properties, such as high fatigue resistance.

If there are special demands on the finished product with regard to mechanical properties, forging may be the only acceptable manufacturing process. If not, one will in each case select the cheapest of the three mentioned candidates that gives a product of sufficient quality.

1.5 Change of Properties Due to Plastic Working

As mentioned previously, the microstructure of a casting will be broken down and refined as a result of subsequent plastic deformation. During hot forming, the working of the microstructure will improve the mechanical properties of the workpiece material, for example, by increasing its ductility; see Fig. 1.6.

If a micro-alloyed steel is hot-rolled under conditions that ensure recrystallization of the material – during or subsequent to rolling – and if the working temperature in the final passes is kept below a critical temperature (say, $< 950°\mathrm{C}$), the mechanical properties of the rolled product can be greatly improved by that thermo-mechanical treatment. The grain size of the material is then reduced during the treatment, and the resulting product will display higher yield and tensile strength, along with better ductility and toughness than in the initial cast condition. High-strength micro-alloyed steels are therefore made by means of such thermomechanical treatment.

During cold working, the mechanical strength of a metal (in terms of yield stress or ultimate tensile strength, for instance) increases with cold deformation, while the ductility decreases[2]; see Fig. 1.7. Many so-called wrought alloys are therefore used in their cold-worked and partially annealed condition. This state is characterized by a combination of rather high strength and good ductility.

The initial workpiece in metal forming, or machining, is often made by shearing or sawing off a piece of metal from a rod, a wire, or a large plate. Because these wrought products are produced by metal forming processes, such as extrusion, drawing, or rolling, they will usually have inferior properties in the short transverse direction in relation to those in the other directions, especially in the longitudinal direction. In conventional steel production, inclusions of manganese sulfide (MnS) tend to gather in planes oriented parallel to the rolling direction as illustrated in

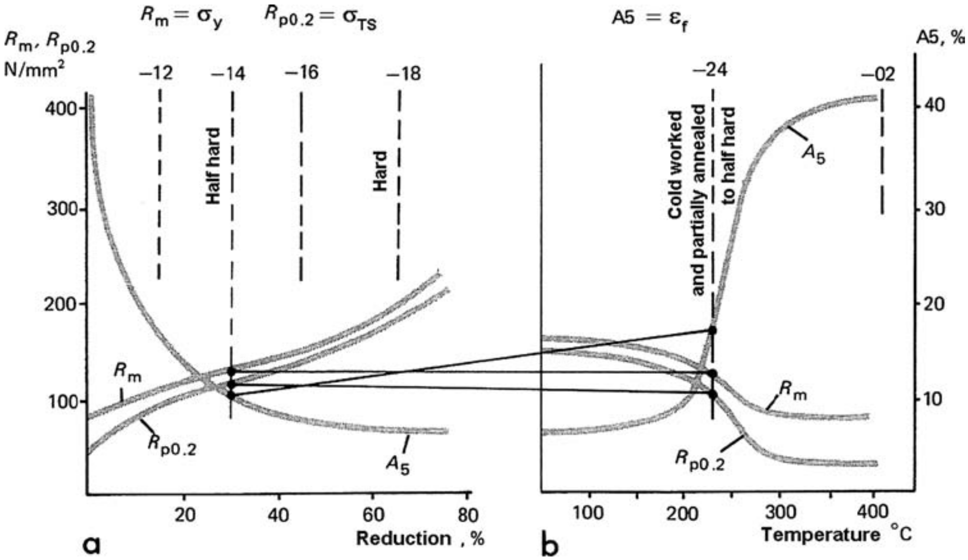

Figure 1.7. Strengthening of aluminum alloy by (a) cold working and (b) cold working followed by partial recrystallization and annealing of the aluminum alloy Al99.5. (Reproduced with due permission from SIS Förlag AB, www.sis.se.)

Fig. 1.8(a). These *enriched* planes then will have a weaker microstructure than the rest of the material. Initiation of cracks is therefore likely along these planes, and they can grow during use of the material, until a fracture occurs. The weakness of such materials in the shorter transverse direction, commonly termed the z-direction, is due to the presence of such weak planes.

If the component is made from a laminated plate like this by machining processes, the planes with inferior mechanical properties will remain unchanged and will extend through the outer surface layer of the machined component, on all faces of the component, except those running parallel to the initial surface of the plate; see Fig. 1.8(a). As already stated, the weak planes are sites for easy initiation of fatigue cracks, and the resulting product will have reduced fatigue strength.

However, if the component is made by a metal forming process like forging, the situation is quite different. If the forging schedule is optimized, all weak planes can be compressed and gathered to extend through the surface of the finished component, through the ring-shaped edge created when the flash is trimmed away.

The material on the edge is subjected to large plastic deformation during removal of the flash. Because of this, the finished forging will have better fatigue resistance than the corresponding machined component. This means that there is less risk that fatigue cracks will develop from these planes during regular use of the component. If such a forged component is macro-etched, the longitudinal direction of weak planes will become visible, because the microstructure will be fibrous along this direction[3]; see Fig. 1.8(b). In forging terminology, this layered appearance of the microstructure of forgings is termed *grain-flow*. If the forging schedule is

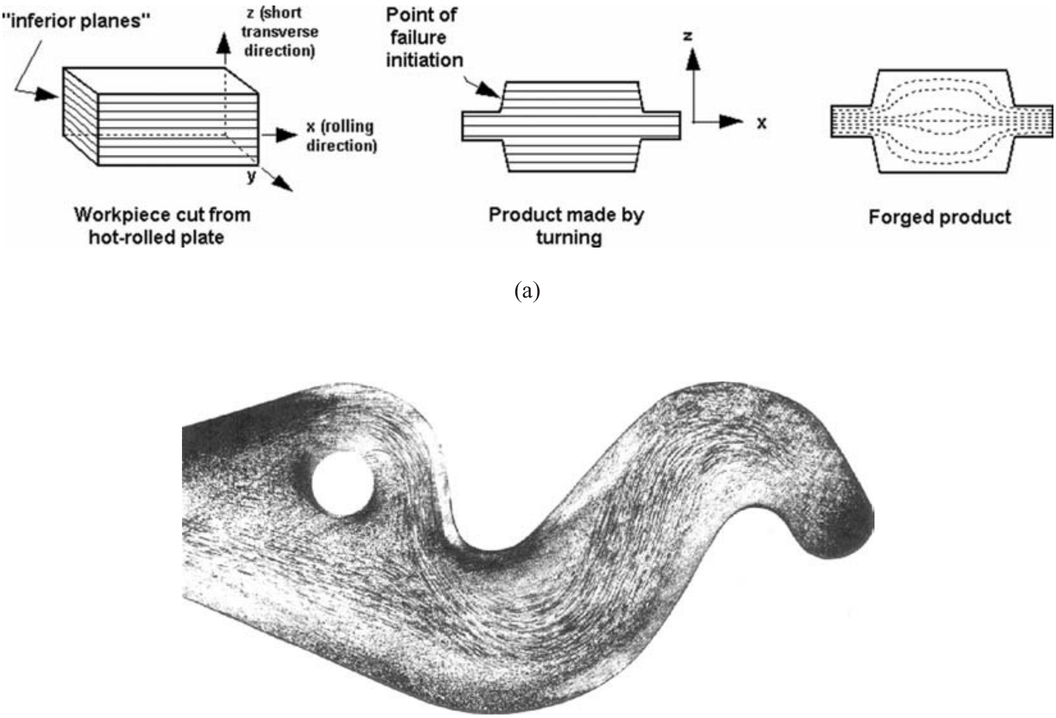
"inferior planes"
z (short transverse direction)
x (rolling direction)
y
Workpiece cut from hot-rolled plate
Point of failure initiation
z
x
Product made by turning
Forged product

(a)

(b)

Figure 1.8. (a) Inferior material planes tend to gather in the flash in forging. (b) Macro-etched hot-forged component with good grain flow. (Reproduced with permission from Teknikföretagens Branschgrupper AB, Stockholm.)

properly set up, the component will have sound grain flow and optimum mechanical properties.

1.6 Metal Forming Processes

The variety of different metal forming processes used for industrial production is large. Because of this, it is difficult to make a simple classification system that includes all existing processes while depicting each process in relation to other manufacturing methods. However, if one limits the system to the main processes, the rather simple classification system shown in Fig. 1.9 can be made. At the highest level of this system, the manufacturing processes are divided into metal forming processes, metal removal processes, joining processes, etc. One level below, the metal forming processes are divided into two subgroups: *bulk-metal forming* and *sheet-metal forming*. This division is natural in that the problems encountered in forming of a massive body are quite different from those in sheet-metal forming. While there is mainly compressive stress in bulk-metal forming, sheet-metal forming is mainly done under high tensile stress.

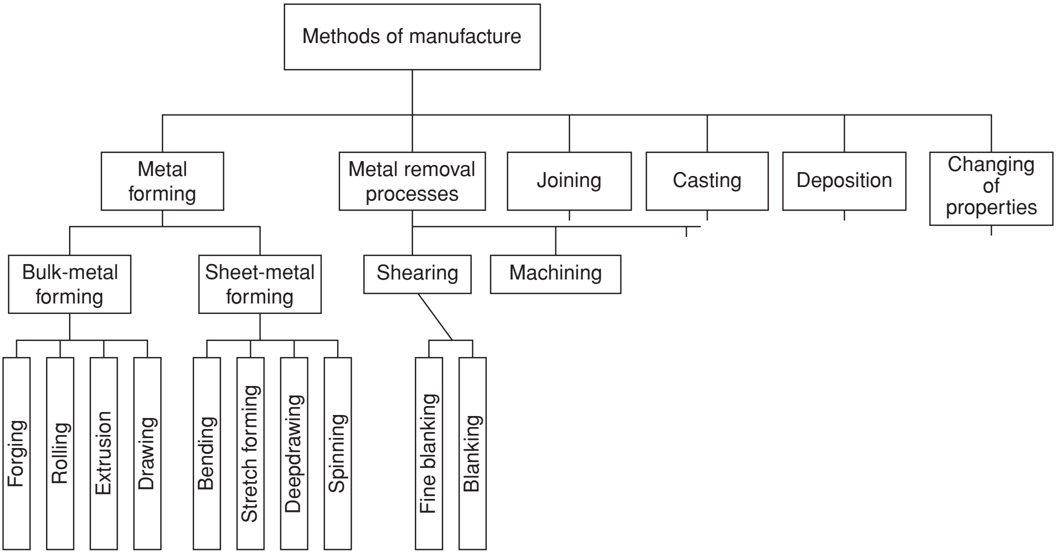

Figure 1.9. Commonly used metal forming processes classified among various manufacturing processes. Bulk-metal forming and sheet-metal forming are each divided into four subgroups.

Shearing, or cutting, is similar to metal forming in that the metal adjacent the sheared edge is subjected to plastic deformation. As a manufacturing process, shearing is often considered to be a metal removal process. At one level below, cutting is again divided into blanking, or *conventional blanking*, and *fine blanking*, according to how the shearing process is executed. Bulk-metal forming can be further divided into the four subgroups forging, rolling, extrusion, and drawing. Likewise, sheet-metal forming can be divided into bending, stretch forming, deep drawing, and spinning.

Further subdivision is also common. Forging, for instance, is divided into the two subgroups, open-die forging and closed-die forging. In the same way, extrusion can be subdivided into forward extrusion and backward extrusion.

There are similarities between the various metal forming processes. The tree structure in Fig. 1.9 can therefore be considered to be a family tree, where there are inherited similarities between the siblings at the lowest level, though at the same time there are characteristic differences. If one tries to give an overview of all metal forming processes, divided into groups and subgroups on the basis of the characteristic type of loads applied during forming, one will get a precise, but rather complex, picture. Such efforts have been carried out in the German DIN standard.[4] Because of the complexity of this system, it is not so well suited for pedagogical applications and will not be presented in full detail in this book. However, the extrusion branch of this comprehensive classification system is shown in Fig. 1.10.

At the highest level of the system, one finds metal forming as one among many other manufacturing methods. Because it is common to apply high pressure in extrusion, the process is categorized on the next level as forming under pressure. Since the

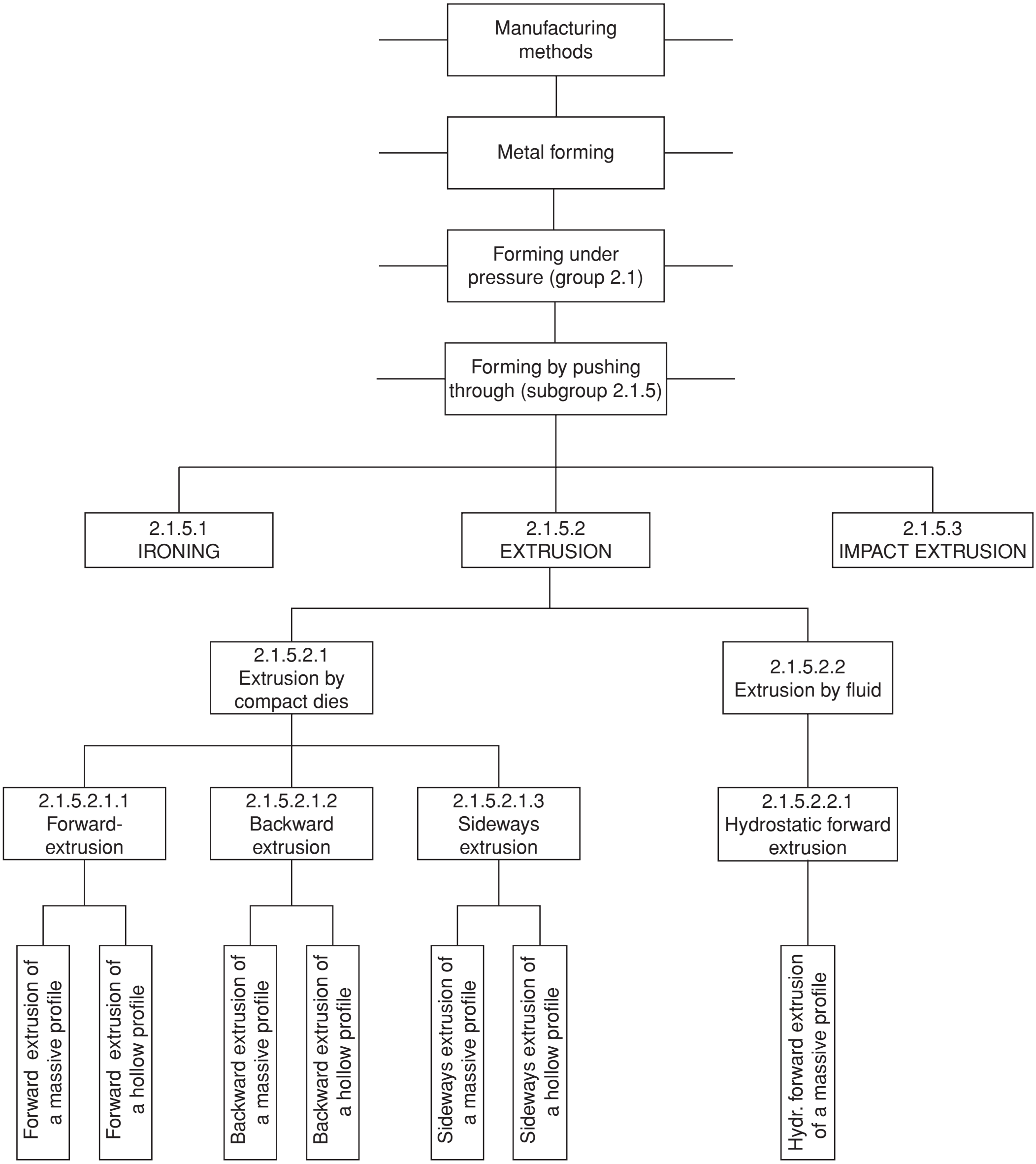
Manufacturing methods
Metal forming
Forming under pressure (group 2.1)
Forming by pushing through (subgroup 2.1.5)
2.1.5.1 IRONING
2.1.5.2 EXTRUSION
2.1.5.3 IMPACT EXTRUSION
2.1.5.2.1 Extrusion by compact dies
2.1.5.2.2 Extrusion by fluid
2.1.5.2.1.1 Forward-extrusion
2.1.5.2.1.2 Backward extrusion
2.1.5.2.1.3 Sideways extrusion
2.1.5.2.2.1 Hydrostatic forward extrusion
Forward extrusion of a massive profile
Forward extrusion of a hollow profile
Backward extrusion of a massive profile
Backward extrusion of a hollow profile
Sideways extrusion of a massive profile
Sideways extrusion of a hollow profile
Hydr. forward extrusion of a massive profile

Figure 1.10. The extrusion branch of metal forming as described in the DIN classification system.

workpiece is pushed through a *die*, the process is categorized as pushing through on a new sublevel of the system. On the next sublevel, extrusion is considered together with other processes based on pushing the workpiece through a die. Then again there are three new sublevels. First, there is a distinction between extrusion by use of compact dies and that by use of fluids to provide extrusion, as in hydrostatic extrusion. Then, the process is again subdivided into forward, backward, and sideways (transverse) extrusion. Finally, on the lowest level, there is a division between

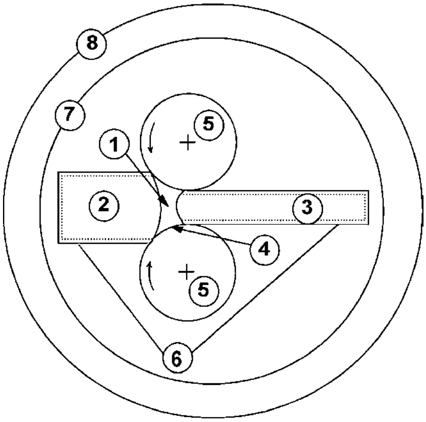

Figure 1.11. Representation of problem areas in rolling of metals.

extrusion processes, as the extruded product has a massive or a hollow cross section.

1.7 Problem Areas in the Analysis of Metal Forming

Industrial experience show that it is often convenient to split up the problems dealt with in metal forming into separate *problem areas*.[5] In this way, it is possible to analyze different aspects of a given process and eventually determine the conditions that represent the bottleneck in optimizing the actual process. Figure 1.11 shows the rolling process visualized in such a way that main problem areas to be addressed in this connection are depicted. Problems encountered during optimization of other processes can likewise be partitioned into problem areas, but then the limiting factor in that process could be within a different problem area. General problem areas to pay attention to during analysis of a given process are as follows:

1. **Plastic zone:** This zone, at a specific time step of the forming operation, encompasses the region of the workpiece in which metal is subjected to plastic deformation. As shown in Fig. 1.11, the plastic zone in a rolling process will only contain material located between the rolls, i.e., in the roll gap, at the current time step. During the course of rolling, however, new metal is fed into this plastic zone at the inlet side of the rolls. Concurrently, metal flowing through the plastic zone is fed out as a rolled product at the outlet side of the roll gap. Hence, in this forming process, plasticization occurs only locally inside the workpiece. During the course of the process, however, the plastic zone moves through the workpiece, from one end to the other, until the whole product has become worked. In closed-die forging, in contrast, the whole workpiece is inside the die from the beginning of forming, and the plastic zone extends through the whole workpiece at any instant. This situation persists until at the final stages of forging, when the flash starts to emerge from the flash gap.
2. **Workpiece at initial stage:** This term refers to material in the initial state before working, i.e., in the condition prior to plastic deformation. The state of this material, and its undeformed microstructure, are determined by the

thermomechanical treatment it has been given previously; whether it has been worked, or annealed; and whether it is cold, warm, or hot.

3. **Workpiece at final stage, i.e., the final worked product:** The final product consists of the actual material after forming, with its mechanical properties, which may have been significantly altered by plastic working of the material during the forming process. The result is either a wrought product to be processed further before use, or a finished product ready for final use after forming.
4. **Interface between workpiece and die:** When the die is pressed into the workpiece, contact is established between the surfaces of the two bodies. There can be direct contact between the workpiece and the die, but indirect contact through their oxide films is more common. Contact may eventually be established through lubricant films that partially or completely separate the two bodies. The characteristic layer(s) separating the bulk material of the two bodies from each other are commonly termed an *interface*. The surfaces that establish contact during the forming operation will have their typical initial topography, including surface roughness and oxide films that partially or completely cover the surfaces.

   The nature and the mechanical behavior of the contact interface between die and workpiece can be crucial for the stability of the metal forming process. If the lubricant film at the interface suffers breakdown during the forming operation, lumps of workpiece metal can locally pressure-weld onto the die. If this happens, the next component that is formed will be one with wrong geometry or of bad surface quality, depending on how much metal transfer there has been. With metal transfer to the die the process must be interrupted, so that the dies can be cleaned, before forming can be resumed.
5. **Dies:** As mentioned previously, the cost of making dies is usually rather high in metal forming. Therefore, to obtain sound process economy in metal forming, the dies must be made with good design and from a material that ensures a certain minimum die life. The dies should be able to shape many components without being subjected to unacceptable wear or to failure.
6. **Surface layer of the workpiece and product:** In metal forming, the surface properties of the initial workpiece are important for various reasons. One reason is that it may influence the effectiveness of the lubricant that is used. Another important aspect is that, if the surface film is abrasive, it may cause excessive die wear. Of special importance is of course the surface quality, or surface finish, of the resulting product. If the surface contains scars, or appears with a matte or dull finish, the resulting product may not satisfy the requirements of the customer and, in that case, has to be discarded.
7. **Forming machine:** For metal forming, the machines applied are most commonly complex and expensive to buy. It is obvious that the forming machines should be made so they are well suited for their specific use, so production proceeds smoothly, without unintended interruptions. If these requirements are fulfilled, high productivity can be maintained in metal forming, with sound process economy.

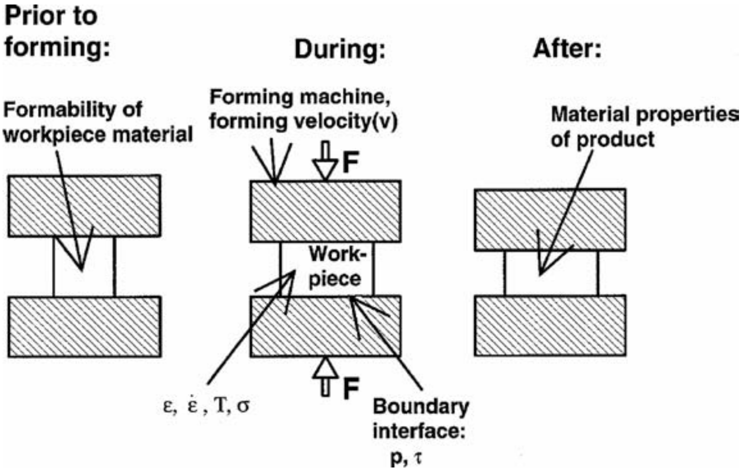
Prior to forming:
During:
After:
Formability of workpiece material
Forming machine, forming velocity(v)
F
Material properties of product
Work-piece
ε, $\dot{\varepsilon}$, T, σ
F
Boundary interface: p, τ

Figure 1.12. Important process parameters in metal forming.

8. **Company:** To obtain a good economical result as a whole, it is obvious that your company must be well organized and efficient, so that production is based on sound economic premises.

1.8 Important Process Parameters in Metal Forming

As discussed in the preceding section, it is important for the economics of any metal forming process that forming be done in the best possible way. To create conditions near to the optimum, one should preferably, in each actual process, know how the forming conditions, i.e., the *process parameters*, influence the results of the production process. This topic will be dealt with in more detail in later chapters of the book. As an introduction, some of the most important of the general process parameters in metal forming are mentioned here; see Fig. 1.12. With respect to the workpiece, it is important that it has sufficient formability to allow the intended amount of plastic deformations that is required without the material developing cracks or other defects.

Inside the plastic zone of the workpiece it is important to be able to measure and control such quantities as the strain ε, the strain rate $\dot{\varepsilon}$, the flow stress σ, and the temperature T that the material is exposed to. In the interface between the workpiece and the die, the important local parameters are the temperature T, the contact pressure p, and the shear stress τ due to friction forces transferred from the workpiece to the die.

These parameters are often influenced by the quality of the lubricant applied. The required forming load is influenced by the mentioned parameters and must not exceed the force provided by the actual forming machine. If it does, forming cannot be accomplished. As mentioned before, the mechanical properties of the final product in metal forming are also influenced by the deformation conditions during the forming operation.

If the product is to be applied in the as-formed condition, without later heat treatment, it is essential that the resulting mechanical properties should meet the requirements specified by the user of the product.

Problems

1.1. State the main assumptions made in continuum mechanics about how the material is composed when considered on the micro scale. Does this agree with our knowledge of the real microstructure of metallic materials?

1.2. Describe how particle-strengthened Al alloys are built up when considered on atomic level. How does this agree with the common assumptions made in continuum mechanics?

1.3. Describe the most typical characteristics of metal forming as a manufacturing process.

1.4. What are the names of the two manufacturing processes most commonly used instead of metal forming? Specify the main advantages and disadvantages of these classes of processes in comparison with metal forming.

1.5 Specimens made from a soft-annealed plate consisting of the aluminum alloy Al99.5 are given the following treatments:

(i) Cold-rolled from 10 mm down to 1 mm final thickness.
(ii) Cold-rolled from 10 mm down to 0.1 mm final thickness.
(iii) Treated as (ii) and then annealed at 150°C.
(iv) Treated as (ii) and then annealed at 350°C.

What mechanical properties you would expect to achieve in the final metal after these treatments?

1.6 A finite element method simulation model of cylinder compression with high friction is available as a video clip at the homepage of the book. In the simulation, the flow-net option of the software was used to visualize how an initial grid pattern inside the metal will deform during cylinder compression. Run the animation from this simulation and observe how the internal grid pattern changes as compression proceeds. On basis of your observations, describe the following:

(i) The FEM-predicted change of the outer shape of the cylinder.
(ii) The predicted deformational behavior of the grid pattern at the center of the cylinder in comparison with the behavior at the periphery of the cylinder.

1.7. Make a sketch similar to Fig. 1.11, and indicate problem areas to be analyzed in metal forming when indirect extrusion is used.

1.8. A two-dimensional FEM model was used to obtain grid pattern deformations and distribution pictures of some process parameters in a metal forming process; see Fig. 1.13. What is the name of the process? What are these

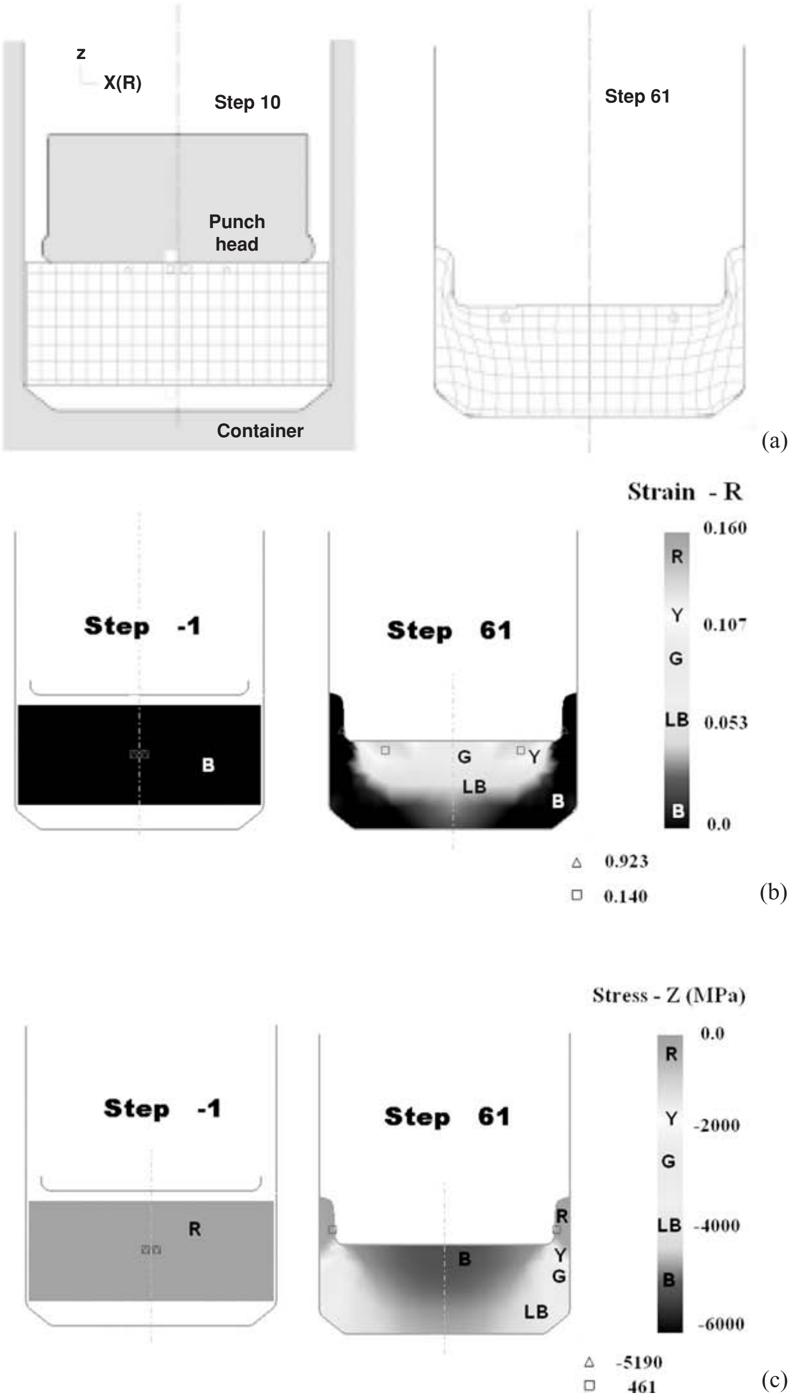

Figure 1.13. Postprocessing results from 2D FEM-model of metal forming operation.

process parameters, and what kind of information can be obtained from the pictures?

NOTES

1. http://en.wikipedia.org/wiki/Continuum_mechanics
2. "MNC Handbok nr 12, Aluminium, Konstruktions- og Materiallära," ed. 1, Dec. 1983 (in Swedish).
3. Smidesteknik, Lärobok, Smidesgruppen innom Sveriges mekanförbund, Stockholm, 1983, pp. 12–13 (in Swedish).
4. DIN 8583, "Manufacturing Processes, Compressive Methods," ed. 2003–09 (in German).
5. Lange, K.: "A system for the investigation of metal forming processes," Proc. 10th Int. M.T.D.R. Conf., Univ. of Manchester, 1969, Pergamon Press, 1970.

REFERENCES

Dieter, G. E. "Mechanical Metallurgy," McGraw-Hill, 1989.
Kalpakjian, S., and Schmid, S. R. "Manufacturing Processes for Engineering Materials," 5th ed., Prentice-Hall, 2008.
Lange, K. "Handbook of Metal Forming," McGraw-Hill, 1985.
Mielnik, E. M. "Metalworking Science and Engineering," McGraw-Hill, 1991.

2 Important Metal Forming Processes

Although there are many different metal forming processes, in this chapter only some of the most important processes will be described. A more complete overview of metal forming processes is given elsewhere.[1,2] A classification system that is useful for those who are not experienced metal formers will also be described.

2.1 Classification System for Metal Forming Processes

In Fig. 1.9, a sketch was shown in which the primary metal forming processes were organized among various common manufacturing methods. In Fig. 2.1, we have expanded the metal forming region downward, thus including the most significant metal forming processes. As seen from this figure, the processes at the lowest level of the diagram are commonly described by the name of the product created by that particular forming process.

Figure 2.1 also shows the important distinction between bulk-metal forming and sheet-metal forming. Bulk-metal forming is the shaping of bodies with concentrated mass, i.e., where the dimensions in each of the three orthogonal directions x, y, and z of the body are of similar size. Sheet-metal forming, on the other hand, is the forming of bodies with initial large extensions in two directions and small extension in the third direction, such as in a piece of sheet metal or a steel plate.

As mentioned before, sheet-metal forming is quite different from bulk-metal forming. In sheet-metal forming, a relatively thin, wide sheet is formed against a die. In this case, it is impossible to keep the workpiece inside a configuration of closed dies. In sheet-metal forming, the material is therefore most commonly subjected to tensile stresses, in contrast to bulk-metal forming, where compressive stresses dominate. Because of the presence of tensile stresses in sheet-metal forming, there are strong limitations with regard to the degree of shaping of the workpiece that is possible, without encountering problems related to material instability – for example, in terms of formation of a neck. During further forming, such a neck would tend to grow, and that would finally lead to rupture of the workpiece. Another problem in

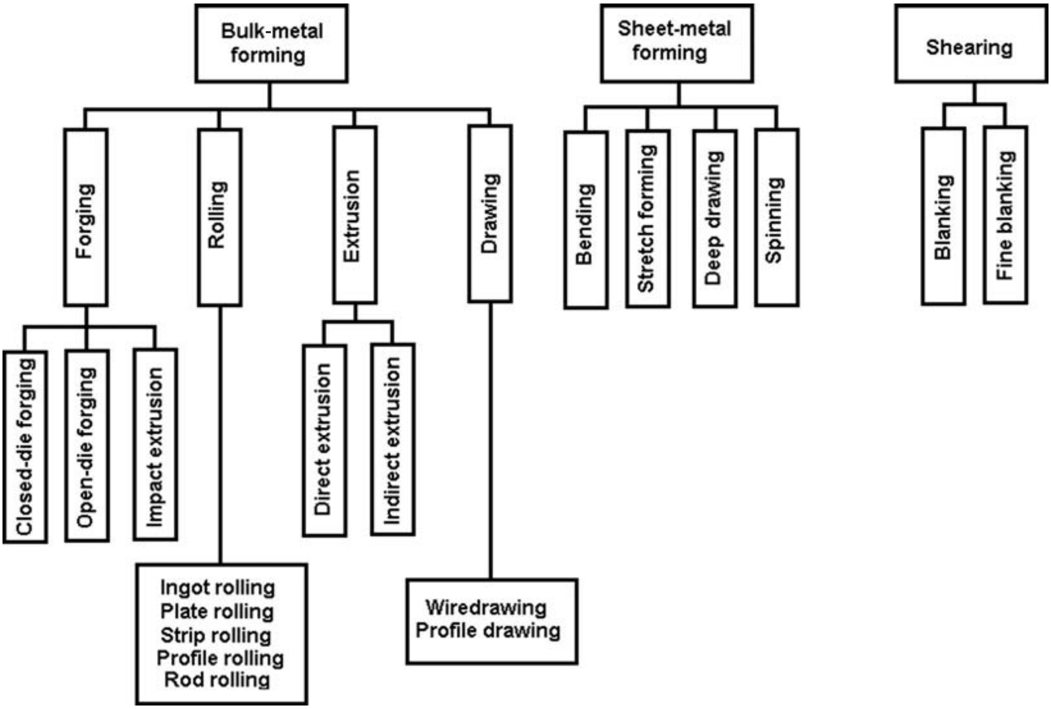

Figure 2.1. The most important metal forming processes.

sheet-metal forming is that in certain regions there is surplus material, and when there are compressive stresses in such regions, the material tends to buckle and form unacceptable wrinkles on the final shaped component.

2.2 Bulk-Metal Forming Processes

2.2.1 Open-Die Forging

This term refers to forging processes in which shaping of a metal workpiece is done by means of open dies, in contrast to the closed-die configurations used in many other forging processes. Because of the use of open dies, large parts of the workpiece will be shaped freely without intimate contact against any die. An open-die forging process, where the workpiece is formed this way in a single step, is shown in Fig. 2.2(a), (b).

Cast ingots are often so big that they cannot be forged in one single step. Instead, they are forged in a multistep process where the workpiece is moved between forging strokes, as shown in Fig. 2.2(c). Because the workpiece is big, only part of it can be forged in one blow, so after each forging step, it must be moved laterally before the next part is forged in the next blow. After a large number of forging steps, which depends on the total length of the cast *ingot*, the complete length of it has in this stepwise manner been subjected to *working*. The workpiece is then

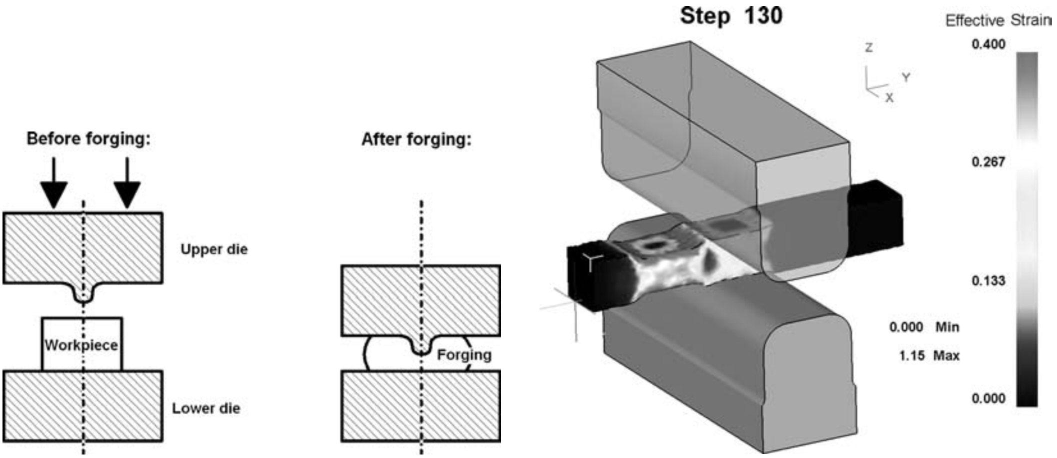

(a) (b) (c)

Figure 2.2. (a) Initial stage and (b) final stage of single-step open-die forging process. (c) Multistep open-die forging process.

commonly turned around, so that forging can be repeated on the other side of the ingot. This multistep forging process is commonly called *cogging*.

Shaping by means of forging is generally done by means of an upper (top) and a lower (bottom) die. Most commonly, the bottom die is stationary, while the top die is moved vertically downward in the forming press.

As depicted in Fig. 2.2, shaping of the workpiece in forging is in general done by squeezing it between the top and the bottom die, until the workpiece metal fills the *die cavities*, if any are present. When a certain degree of compression has been imposed on the workpiece, it will have attained a shape close to that aimed at, and the forging stroke can be stopped. The upper die is then run in reverse, and the finished forging removed from the die.

In open-die forging some of the workpiece surface is shaped without die contact, so forging processes of this type do not give an accurate final shape. It is therefore common to forge the workpiece with slightly too large dimensions in those directions where accurate geometry is required, and then machine the forged component to acquire final dimensional control.

2.2.2 Closed-Die Forging

In this forming process, the metal is shaped in a closed-die configuration as shown in Fig. 2.3. There are two variants of the forming process. If closed-die forging is done without formation of a flash, as shown in Fig. 2.3(a), the process is called flashless forging, or *precision forging*. This type of forging is also commonly referred to as *near-net shaping*. Closed-die forging is alternatively performed with a small clearance between top and bottom die toward the end of the forging stroke. Excess workpiece material is then used. In the end stages of the process, some

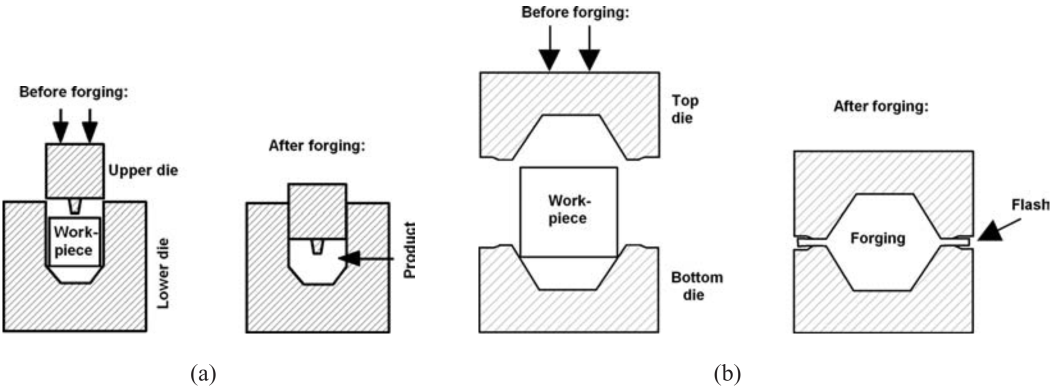

Figure 2.3. Closed-die forging (a) without flash and (b) with formation of flash.

material is squeezed through the clearance between the dies and appears as a flash.

The flash formed in closed-die forging is waste material: it is not part of the final forged component and is removed by later *trimming*, usually a shearing process. As mentioned previously in Ch. 1, the metal flow in forging, if proper, provides an advantageous grain flow, so that weak spots called *laminations* will be accumulated in the flash at the end of the forging. Because of this, closed-forged components are known to have good fatigue properties.

2.2.3 Impact Extrusion

In impact extrusion, various solid or hollow components with different geometry are made. Often components with rotational symmetry are formed this way, but also components of more complex shape. In Fig. 2.4, two typical impact extrusion processes are shown: forward impact extrusion and backward cup extrusion. In the

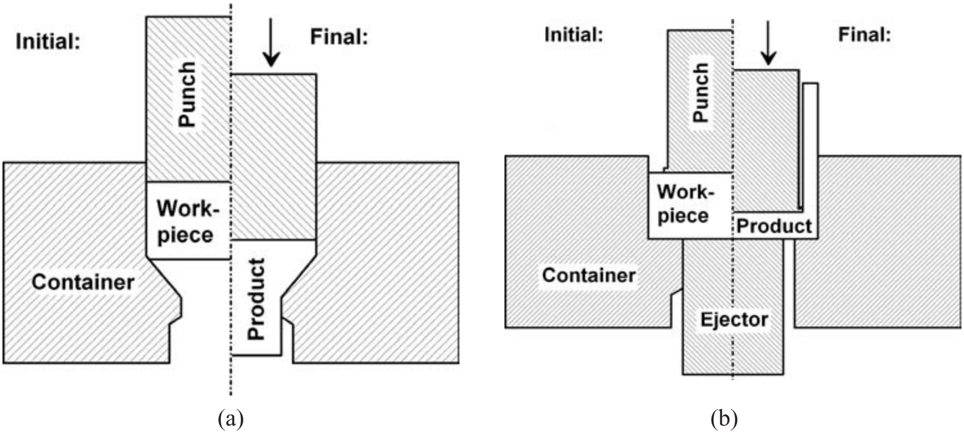

Figure 2.4. Impact extrusion processes: (a) forward extrusion and (b) backward cup extrusion.

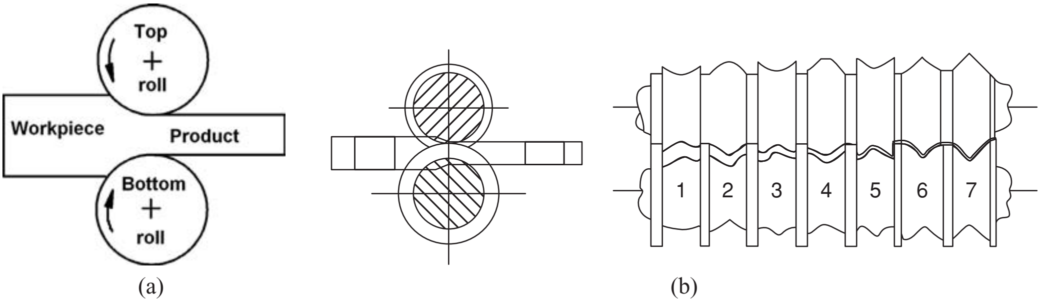

(a) (b)

Figure 2.5. Rolling: (a) flat rolling and (b) rolling schedule in section rolling.

forward extrusion process [see Fig. 2.4(a)], the workpiece moves in the same direction as the punch, whereas in the backward process [see Fig. 2.4(b)], the movement of the workpiece material is opposite to that of the punch.

2.2.4 Rolling

In rolling processes, the workpiece, for instance, a plate, is rolled between two rolls [see Fig. 2.5(a)], so that the plate is compressed in its thickness direction. As a consequence of this, the plate thickness is reduced. Because of the constancy of volume, the plate must, however, expand in the other directions: in the length direction and also to some extent in the width direction. Rolling can be divided into two types, depending on whether a flat product is rolled, or a product of more complex cross-sectional shape is worked. When flat products are rolled, the process is commonly termed *flat rolling*. When long profiles of complex cross-sectional shape are produced, the process is called profile or *section rolling*. Profiles are long beams of various cross-sectional shapes. Common rolled profiles are for instance beams with I-, H-, or L-shaped cross section.

One or two decades ago, steels were commonly cast in big ingots with square, or close to square, cross section. They were first rolled down in a *roughening* rolling mill to *semifinished* products of smaller cross section. In this way, semifinished stock like *slabs*, *blooms*, and *billets* were processed. A slab had a large rectangular cross section and was subsequently rolled down in a plate or a strip rolling mill to a plate or strip. A bloom had a large, and a billet had a smaller, square cross section. Both were processed further in shape rolling mills: the blooms were rolled into large sections, and the billets were rolled into smaller sections or into rod or wire.

Today, new casting processes have been developed, so this large production equipment has to a large extent been replaced by smaller, cheaper machines. Today slabs, blooms, and billets are most commonly made by casting in continuous casting facilities. Afterwards the slabs are rolled down to plate or strip. Plates are, as the name indicates, flat products with large length and width, whereas strips have large length but smaller width. Strip material is often coiled after rolling, because this

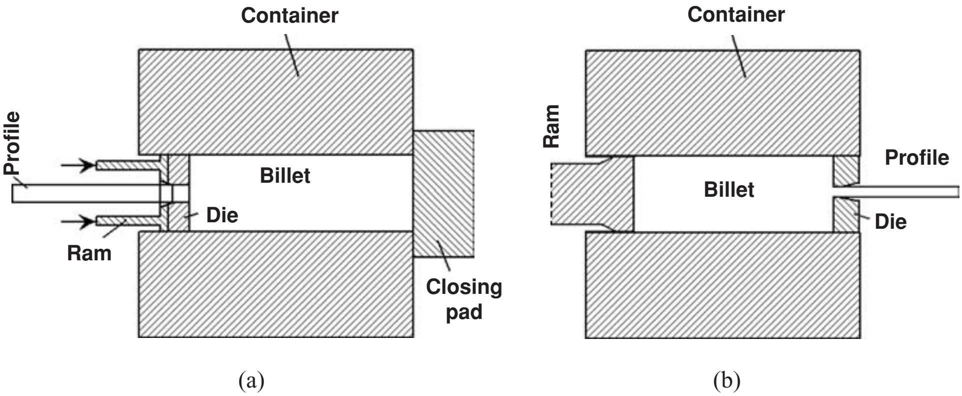

Figure 2.6. Two main extrusion methods: (a) forward extrusion and (b) backward extrusion.

provides easier handling of the product. Hot-rolled strips from coils are commonly cold-rolled down to thin flat strips to make sheet metal or foil.

Rolling of blooms and billets down to sections or profiles is done by gradual changing of the cross section from square to the final intended profile shape, as, for instance, illustrated in Fig. 2.5(b). When rolling down to rod or wire, intermediate profile shapes are also used. For instance, one can change between round and oval cross sections in a *rolling schedule* before a round shape is created in the end stage.

2.2.5 Extrusion

In extrusion processes, the metal – in the form of a cast billet – is shaped by pressing it through a die orifice of appropriate shape. When this is done, the metal flows out of the orifice in a continuous manner and appears as a long profile, with cross-sectional shape approximately the same as that of the die orifice. In extrusion the metal must first be placed inside the container, where it is pressurized. As depicted in Fig. 2.6(a), this is done by placing a die at one end of the container, and a punch or a ram at the other end of it.

Cast extrusion metal is inserted into the container as a billet. When the punch advances, the metal of the billet fills the container and is pressed against the die. With further advance of the ram, the metal starts to flow through the container and out through the die as a profile, with the same cross section as the die orifice.

When extrusion is done this way, the process is generally called *forward*, or direct, extrusion, as the metal flow is in the same direction as the ram movement. An alternative method of extrusion, less commonly used, is when the container is blocked at one end by a closing pad, and the punch is made hollow, with the die placed in front of the punch head. This process is generally termed *backward*, or indirect, extrusion, because the direction of movement of the metal is opposite that of the ram movement. The two methods of extrusion, direct and indirect, are shown schematically in Fig. 2.6.

Backward extrusion has certain advantages over forward extrusion, in that it does not require pressing the billet through the container. Because of this, the required extrusion force is lower, and in addition, there is better dimensional stability of the extruded profile – the *extrudate*. A third advantage is that the deformation of the metal flowing out through the die opening is more constant along the length of the profile than in forward extrusion, for there is almost zero predeformation of the billet in its back portion. In forward extrusion, these predeformations are bigger, especially the deformations of the peripheral layers of the billet, which is forced to slide along the container wall with the advance of the ram.

Forward extrusion, however, is the most commonly used extrusion process, because the use of backward extrusion is considerably limited in two ways. One is that the extruded profile must be taken out from the press through the ram itself. Because of this, one must use a hollow ram. This imposes considerable practical difficulties, especially when multihole dies are used to extrude many profiles concurrently, or in the extrusion of profiles with large prescribed circumference. The challenge then is to make a ram design sufficiently strong to take the large extrusion loads, because the ram must be hollow and the extrusions must be taken out through its hollow stem. Another limitation arises from the nature of metal flow in the backward extrusion process. It is a fact that the peripheral layers of the billet in backward extrusion tend to flow much more easily through the die orifice than in the forward process.

Billets are commonly produced in continuous casting processes, where *logs* of large length are made. Afterwards the logs are sheared into appropriate pieces – the billets. Because of the casting process, a billet has a peripheral cast surface layer, of less metallurgical quality than the core. For this reason, better surface quality is normally obtained in forward extrusion than in backward extrusion.

To obtain sufficient surface quality in backward extrusion, it may be necessary either to machine away the inferior surface layers of the billet before extrusion or to leave a shell of billet material in the container during extrusion. This is done by using a small clearance between the die and the container wall. Both variants of the backward extrusion technique involve additional operations in comparison with direct extrusion and hence also additional costs.

Aluminum and its alloys have low flow stress at temperatures in the range 400–500°C. Because of this, they can be hot-extruded into profiles with complex cross-sectional shape. In extrusion of copper or brass, there is less freedom regarding extrudable shapes, because the extrusion temperature required is as high as 700–1000°C. Even at these high temperatures, the flow stress of these metals is high. Because of this, the combined thermal and mechanical loads on the tooling are high. Therefore, if complex shapes are extruded on the same principles as in aluminum extrusion, the die life becomes too short to yield acceptable process economy. Hence, for copper and brasses, there are strong limitations as regards the complexity of the shape of the profiles that can be extruded with sound process

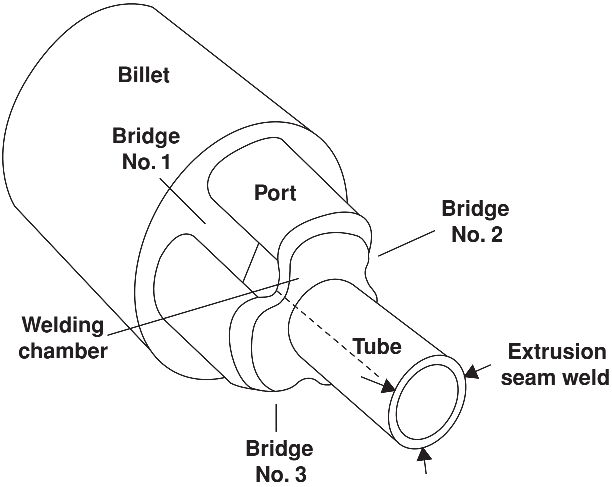

Figure 2.7. Material flow in hollow forward extrusion.

economy. For steels, the conditions in extrusion are even worse; extrusion temperatures of 1000–1200°C are required. Continuous extrusion processes applied for steel, on the same principles as for aluminum, copper, and brass, are therefore rare. Conditions are so severe that it is difficult to find die materials that will survive for a sufficiently long time. For steel materials, however, a lubricated hot-extrusion technique based on use of *glass lubrication*, which melts down ahead of the die, has been developed. With this technology, it is possible to extrude small sections with low shape complexity. Continuous hot extrusion of steel is, however, highly specialized and is not so commonly used.

Because of the good hot extrudability of aluminum and its alloys, they can even be extruded into very complex hollow profiles,[3] as for instance tubes, in a similar way to extrusion of plastics. This is done using hollow extrusion dies of high complexity. The best way to understand how this is done is to look at the metal flow in the tube extrusion process. The metal flow in this process, in which a tube is extruded by means of a porthole die with an inner mandrel and three bridges, or webs, is shown in the three-dimensional sketch in Fig. 2.7. Here only the metal of the billet, flowing through the die, and the resulting profile are shown; the complete steel dies, or tooling, which surround the metal, have been omitted to enable examining the process.

As one can see from the sketch, the billet is split in three separate metal streams when it is pushed against the bridges of the die, filling its three portholes. When the metal streams reach the bottom of the ports, they meet again in the *welding chamber*, where they are joined together into one metal stream by *pressure welding*. At this instant, the metal becomes shaped into a tube. The inner hole of the tube is formed against the mandrel placed in the middle of the die, the mandrel being carried by the bridges. The circumferential outer part of the die shapes the outside of the tube, as the metal flows through the gap between the mandrel and the outer part of the die. Since the metal flow is characterized by splitting the metal stream into separate streams, later to be joined again, the process is based

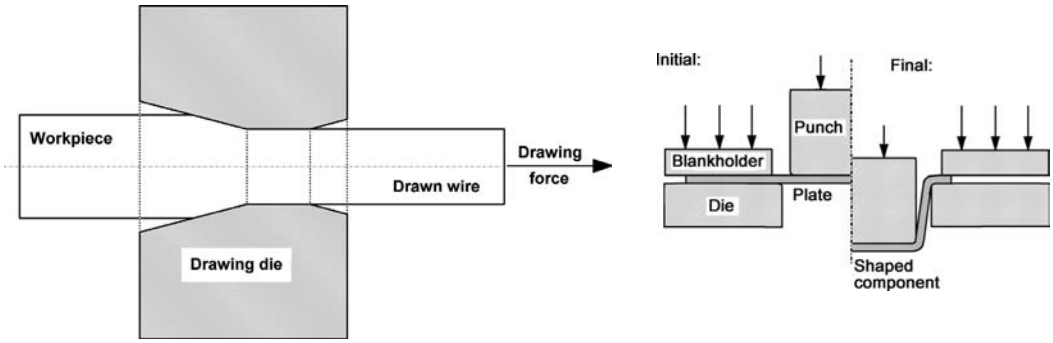

(a) (b)

Figure 2.8. (a) Wiredrawing and (b) deep drawing of sheet metal.

on pressure welding, or *extrusion welding*, as it is generally named. At the rear end of each bridge, two metal streams join by welding, and an extrusion weld is formed. The weld flows out of the die and appear as an extrusion *seam weld* in the resulting hollow profile. Hollow profiles made this way have the same number of longitudinal seam welds distributed over the cross section as the number of bridges used in the die.

2.2.6 Wiredrawing

As shown in Fig. 2.8(a), a thin rod or wire can be manufactured from a thicker initial rod or wire by pulling it through a die shaped with an inner conical die channel. To maintain stable wire dimension out of the die, the *converging channel* must be followed by a *parallel bearing*. Because of constancy of volume during forming, the length of the wire will increase correspondingly when the cross section of the wire is reduced. To be able to draw the wire through the die, a pulling force is required behind the die. Wires are drawn in long continuous lengths – most commonly from a coil of thicker wire, which originally was made in a hot-rolling process.

To avoid stopping the continuous production process, the wire from one coil is joined to the wire from the next, by pressure- or fusion-welding the ends of the two coils together. In this way, the process can be run continuously for a long time, if wire breaks do not occur.

To pull the wire through the die, it is required to use a drawing wheel, also called a *capstan*, at the back of the drawing die, to provide pulling force to the wire. When the wire has been reduced in a reduction step by one die, it is fed in a continuous movement by the capstan to the second die. This die has smaller diameter than the first die, and a second capstan is required to pull the wire. By placing as many as 20 draw cells – consisting of a die and a capstan – in sequence, wire of small diameter can be produced, in a continuous process, from initially thick wire. In drawing, it is common to use a constant reduction in each drawing step, which is usually kept below 20%. After the end of the last drawing unit, there is usually a rotating spooler in the wiredrawing machine, which accumulates the wire on a spool.

Rod and profiles can also be processed by drawing through dies. If they have a large cross section, or if there are tight dimensional requirements on the finished product, they are kept in straight lengths before and after drawing. Because of the stiffness of the die, drawing gives good dimensional stability to the finished product, i.e., there is less dimensional variation along the length of it than if the same product is made by rolling or extrusion. Drawing is therefore used as a *calibration* process in cases where final product dimensions are to be kept within narrow tolerances.

As previously shown in Fig. 1.7, cold deformation will increase the strength and the hardness of metals. Because of this, cold drawing is used to fabricate hard variants of initially soft alloys, so that the metal is strengthened by the drawing process, and a product with improved mechanical properties (increased yield strength and tensile strength) is obtained.

If a metal, or an alloy, is to be drawn through many successive dies, it is required to *soft-anneal* it at an intermediate drawing stage, because *cold working* increases the hardness of the material and reduces its ductility. In an intermediate soft-annealing process, the initial high ductility of the wire can be restored. After this, drawing can be continued further, without the risk of wire breaks or excessive die wear. By repeated sequences of drawing followed by soft annealing, wires finer than a human hair can be manufactured at a reasonable price.

2.3 Sheet-Metal Forming Processes

2.3.1 Deep Drawing

In this forming process, deep cup-shaped products, such as loaf pans and kitchen sinks, are given their shape from an initially flat sheet-metal blank. As depicted in Fig. 2.8(b), this is done by forcing a circular or rectangular upper die with rounded corners down into the sheet metal or plate. At the same time as this is done, the blank is supported at its circumference by being kept under accurately controlled pressure, between an upper *blankholder* and a bottom die. The bottom die is made with a hollow at the center, slightly bigger than the shape to be formed and with rounded edges.

In this way, the circumferential part of the specimen can be drawn gradually down, to form the walls of the product, with help of the upper die, from the region between the blankholder and the bottom die. The walls of the deep-drawn cup are mainly created by metal being pulled over the rounded corners of the bottom die. To have sufficient space between the upper die and the lower die to give room for the walls of the product, the gap between the two dies must be made slightly bigger than the thickness of the initial plate, so that there is a clearance.

In this process, it is of vital importance to maintain the right contact pressure between the blankholder and the circumferential bottom die. With too high pressure,

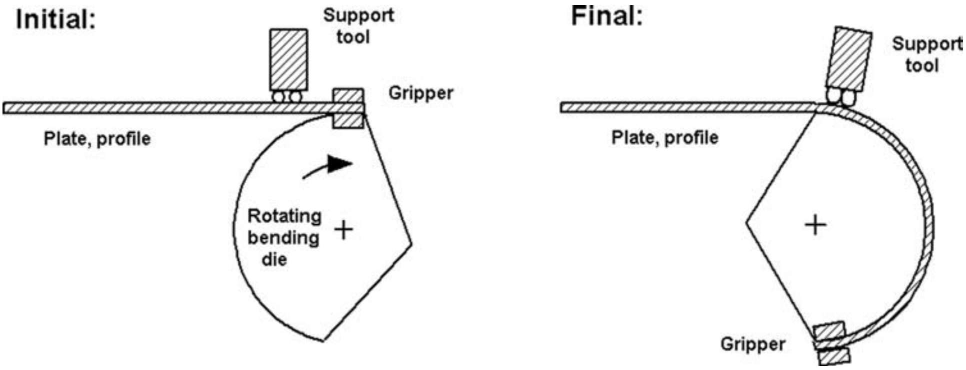

Figure 2.9. Bending: (a) initial and (b) final state.

the cup wall or the bottom section of the product will fracture. If pressure is too low, wrinkles will form in the walls of the product; hence, the product quality will be inferior. In deep drawing, one feeds material forward into the gap between the lower peripheral die and the upper die. Because of this, square or cup-shaped products, in which the wall is approximately normal to the bottom of the product, can be made. If one uses an upper die with a rounded or other shape, the bottom of the deep-drawn cup can be given this intended shape.

2.3.2 Bending

Plate or sheet-metal blanks, or even profiles, can be made to conform to a rounded die in different ways. If the specimen is bent around a curved wheel by means of a support die, as shown in Fig. 2.9, the forming process is called *bending*. If one neglects the elastic springback in such a forming operation, one can say that one reproduces the curved shape of the bending wheel in the sheet-metal blank being formed.

2.3.3 Stretch Forming

In a similar way as in bending, a sheet-metal or plate work can be formed in stretch-forming operations, as shown schematically in Fig. 2.10. Using stretch forming, one can make products with singly curved or even doubly curved shapes, as, for instance, spherical shells. Before forming, it is necessary to clamp the plate along its circumference. To make a doubly curved component, a doubly curved die, such as a punch in the form of a sphere or some other convex shape, is used. In the forming operation, the punch is forced into the workpiece, so the sheet metal is stretched over the punch head, and the die shape is reproduced on the specimen. This process can give similar products to those made by bending, but as a difference, there will be more tension in the sheet during forming. Because of this, in general there will be more thinning of the sheet in stretch forming than in

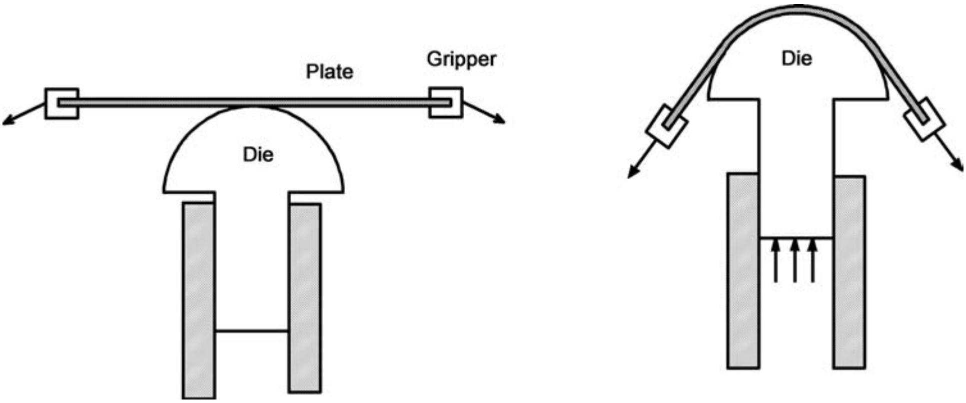

Figure 2.10. Sheet-metal forming by stretch forming.

bending. Because of tensile stresses in stretch forming, springback is reduced significantly in comparison with bending processes. The stretch-forming process is therefore attractive in cases where strict geometrical tolerances are required for the end product.

2.3.4 Spinning

By means of spinning, various thin-walled hollow products with rotational symmetry can be made from an initial flat plate, using the forming principle shown in Fig. 2.11. The plate must be fixed to the front end of a die with rotational symmetry. A configuration of symmetrically spaced pressing tools, in the form of small rotating wheels, is then pushed into the plate from the side opposite that of the die, while the workpiece is rotated (spun) around its axis. In this way, the plate is plasticized by the pressing tools, and the workpiece shape will gradually conform to the shape of the die.

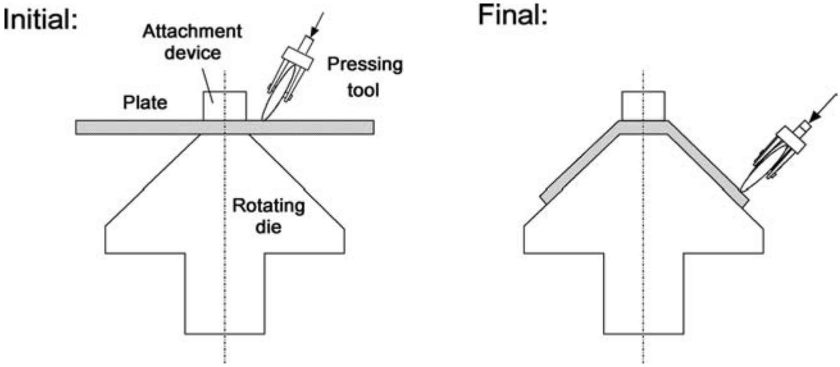

Figure 2.11. Sheet-metal forming by spinning.

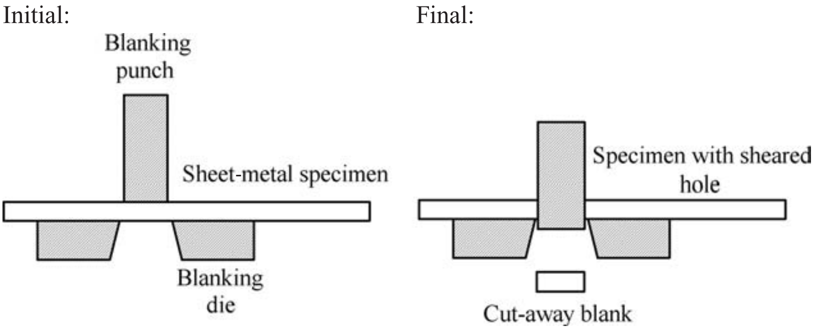

Figure 2.12. Shearing or blanking.

2.4 Shearing Processes

Shearing, or *blanking*, is commonly used as a high-production method for partitioning large sheets of plates, sheet metal, or strip into smaller pieces of given shape. Plate or sheet-metal pieces to be formed by deep drawing, stretch forming, or bending are often made by shearing from a large sheet or from a continuous strip of metal being uncoiled from a strip coil. This partitioning process is also used to remove the flash – in a *trimming* operation – from forgings made by closed-die forging.

The process is hence often considered to be a partitioning, or division, process, not a metal forming process. As shown in Fig. 1.9, it is often classified as a metal removal process. However, because the process is commonly applied in conjunction with pre- and posttreatment of workpieces and resulting products in metal forming, and because shearing can involve considerable plastic deformation of the metal being cut, it is included here as a metal forming process. The deformations in shearing that lead to the partitioning of one portion of the metal from the other are intense shear deformations, which at a certain stage of shearing create a fracture inside the section subjected to shearing.

This is a rare situation, where initiation of a crack and propagation of it into a fracture are indeed considered beneficial. In most other conditions, one aims at avoiding fracture. Fracture in shearing is desired, but in addition, it should be such that it leaves a clean cut, i.e., a fractured surface of best possible quality, with smooth surface finish, extending straight across the section of the specimen.

Shearing can generally be divided into two subtypes: conventional blanking and fine blanking. The dies and the tool configuration used in these two different types of shearing processes are shown, respectively, in the principal sketches in Fig. 2.12 and Fig. 2.13. Conventional shearing is similar to cutting with a pair of scissors, where an upper cutting edge is moved down toward a corresponding bottom edge, moving in the opposite direction. Here the sheet to be cut is placed between the two edges, and the cut is obtained by moving the upper die with its shearing edge down into the sheet, while the bottom die and shearing edge are kept stationary. In conventional shearing, the sheet often tends to lift up from the bottom die during the cutting operation, and in that case, a cut surface of less quality may result. In fine

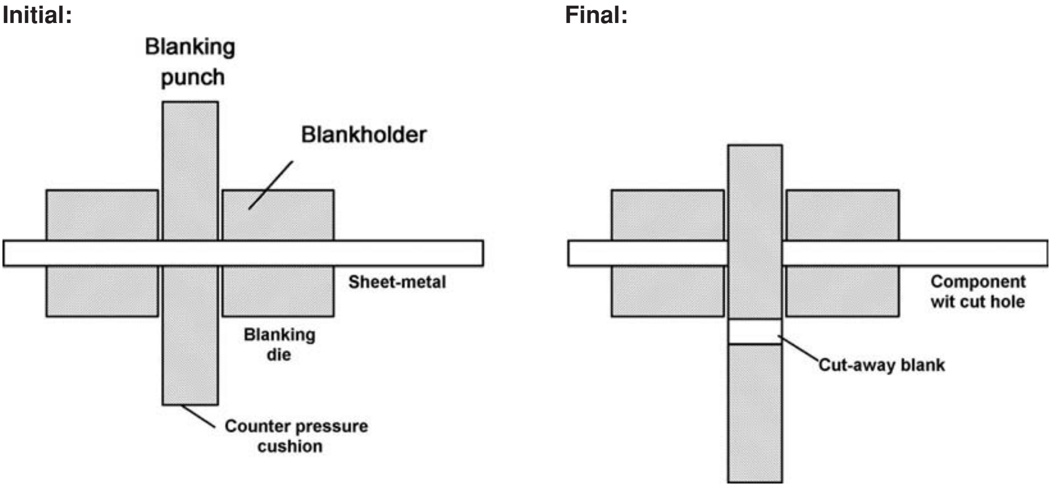

Figure 2.13. Fine blanking.

blanking, vertical movement of the sheet is avoided, for the shearing tooling is provided with a circumferential blankholder, which keeps the sheet in ideal position during the cutting action. Hence, a finer cut surface is obtained than in conventional blanking.

Problems

2.1 The following products are to be made:

(a) Five pieces of a cup-formed component with rotational symmetry from an aluminum alloy.
(b) The component specified in (a), but 10,000 pieces.
(c) An L profile of 1 m length with 10 mm wall thickness.
(d) The profile specified in (c) in a total amount corresponding to the length of 10,000 m.

Propose manufacturing methods for these products. Explain the reasons for your choice.

2.2 Mention some advantages and disadvantages of extrusion of aluminum alloys by the forward and the backward extrusion processes. Suppose that you are to put up an extrusion plant for production of aluminum rods by forging. Write down the main arguments for selection of each of these extrusion methods for this purpose.

2.3 Use one or two sentences to define and describe the metal forming processes mentioned in this chapter.

2.4 Three different FEM models are provided by means of animations that visualise the sequence of the forming operation. State the name of each of these processes. Make a description of what takes place in each process during the course of forming.

2.5 Some industrial products are shown in Fig. 2.14. What metal forming processes would you propose to use for shaping of these different products?

(a) Large stainless steel valve (of 2 m length) for a diesel engine.
(b) Beer can.
(c) Viking ship logo.
(d) Hollow cup-shaped body of Al-alloy with flange in one end.

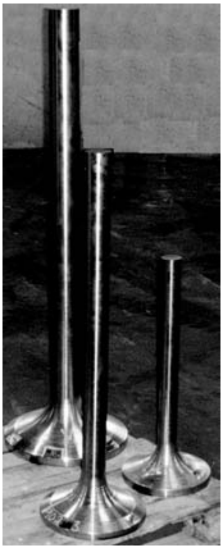

(a)

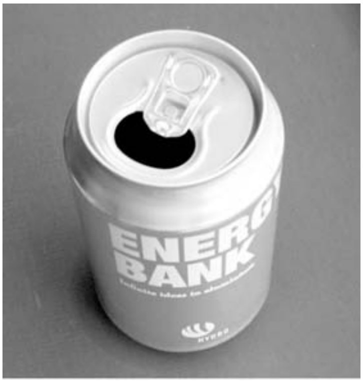

(b)

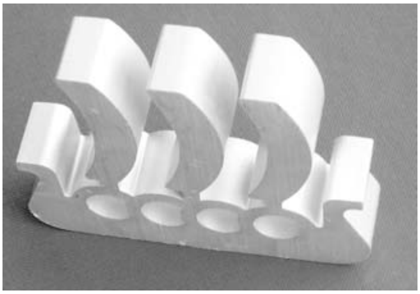

(c)

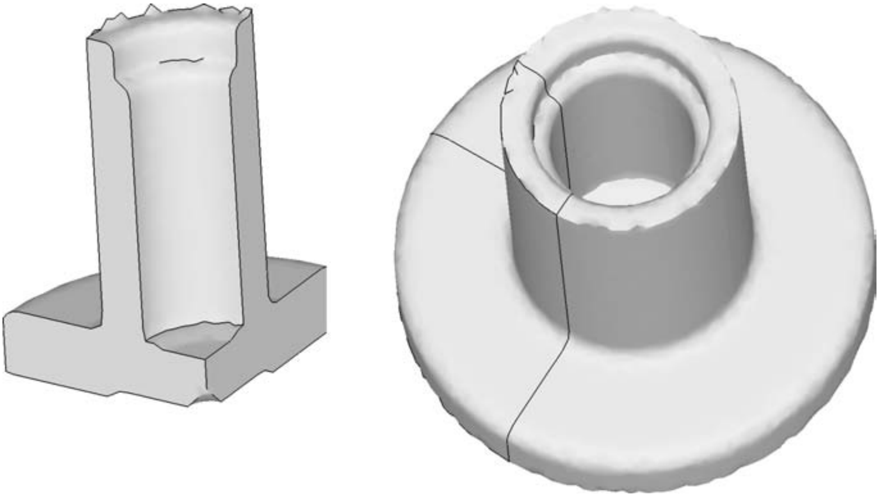

(d)

([a] is reproduced with permission from Scana Steel Stavanger AS and [b] is courtesy of T. Rønning, Alupro-N, www.alupro-n.no.)

NOTES

1. Altan, T., Oh, S.-I., and Gegel, H. L.: "Metal Forming, Fundamentals and Applications," ASM, 1983, pp. 8–36.
2. Kalpakjian, S., and Schmid, S. R.: "Manufacturing Processes for Engineering Materials," 5th ed., Prentice-Hall, 2008.
3. Valberg, H.: "Extrusion welding in aluminium extrusion," Int. J. Materials and Product Technology, Vol. 17, No. 7, 2002, pp. 497–556.

REFERENCES

"ASM Handbook, Vol. 14A, Metalworking: Bulk Forming," ASM Int., 2005.
"ASM Handbook, Vol. 14B: Metalworking: Sheet Forming," ASM Int., 2006.
Dieter, G. E.: "Mechanical Metallurgy," McGraw-Hill, 1989.
Lange, K.: "Handbook of Metal Forming," McGraw-Hill, 1985.
Mielnik, E. M.: "Metalworking Science and Engineering," McGraw-Hill, 1991.

3 FEA of Metal Forming

Finite element analysis (FEA) has been developed during the last decades as a very useful tool for analysis of metal forming processes. Progress in development of cheap and efficient computer technology, and the implementation of the finite element method (FEM) into user-friendly, window-based programs, has brought this technology forward. One can state that this development has more or less revolutionized the art of metal forming analysis.

In this chapter, it is demonstrated how 3D FEA can be applied for the analysis of a particular metal forming operation, namely, plane strain compression. To show how well such analysis describes the actual conditions in metal forming, it is used to model and to reproduce a series of experiments conducted on an aluminum alloy in the laboratory. In the experiments, an advanced *grid pattern technique* was used to characterize the real *metal flow* occurring in this deformation process.

3.1 The Plane Strain Compression Test

The *plane strain compression*[1] test is conducted as either a cold- or a hot-forming test. Although thermal effects are generally negligible in cold forming, they are important in hot forming. So to gain good accuracy, thermal effects must be included in hot-forming models. The flow stress of the workpiece material is an important parameter used in the FEM model. This parameter is very different in cold and in hot forming, as discussed in Ch. 8. Whereas flow stress is not significantly influenced by temperature in cold forming, in hot forming it depends strongly on temperature.

Schematic sketches of the test are shown in Fig. 3.1. Here (a) shows the initial stage of the test in 3D view, and (b) and (c) show a longitudinal midsection cut through the test, before and after compression, respectively. In the test, a rectangular strip, block, or slab is compressed in its midregion by two parallel platens. The ends of the specimen remain unchanged, as they reside outside the compression gap. The transverse plane in the middle of the specimen remains in the same location during the compression stroke and is therefore called the *neutral plane*. Metal on both sides of this plane flows laterally away from the neutral plane. If initially far enough away from this plane, the material will flow out of the

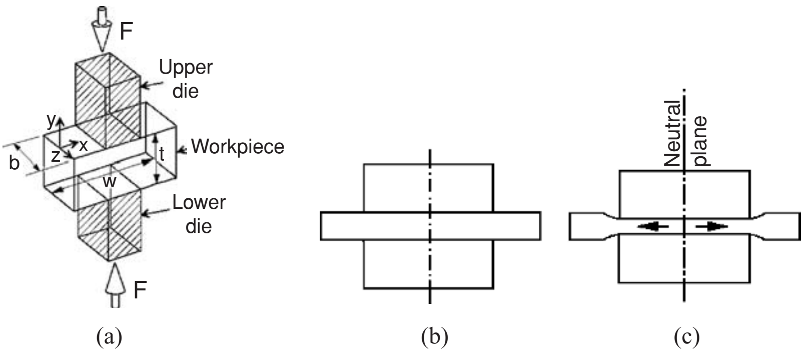

Figure 3.1. Schematic view of tool and workpiece configuration in the plane strain compression test.

compression gap. The rest of the metal remains in the gap, so after the test the specimen has been reduced in thickness, from initial thickness t_0 down to final thickness t_1. In ideal plane strain conditions, the breadth b of the specimen does not change. To achieve approximately ideal plane strain conditions, it is common to use a specimen of large breadth in relation to thickness.

To check the accuracy of a FEM model, it is of course required to perform accurate experiments, so that one knows the forming conditions exactly. Describing the actual conditions in a real metal forming process, to gain necessary input for modeling of the process, is also an important task.

Such techniques have currently been developed to an advanced level, as will be shown by use of grid pattern analysis in the continuation.[2]

When a forming process has been reproduced by FEA, it can be used for detailed studies of the mechanics of the process. To illustrate this methodology, a particular plane strain compression test, performed in a *Gleeble test machine*, is subjected to analysis in the forthcoming sections.[3] Some important general principles of the deformation mechanics in metal forming are thus demonstrated.

3.2 Experimental Investigation

A series of three experiments, each consisting of three equal parallels, were run to study plane strain compression testing in a *physical metal forming simulator*; see Fig. 7.4. The experiments were run at room temperature, and the specimens were lubricated by graphite; the workpiece material was a soft-annealed AA 6082 Al alloy. More details about the experiments are given elsewhere.[3] Since the Gleeble machine had rather low compression force, specimens of very large breadth in relation to thickness were not used, though that is generally recommended, to minimize lateral flow. Because of this, there was some metal flow in the breadth direction (b) also [see Fig. 3.1(a)], not only in the thickness (t) and the width (w) directions, as in the ideal test.

It is well known that the *aspect ratio* (eq. 5-12) in the plane strain compression test has a strong effect on the deformation conditions. So to include this effect in

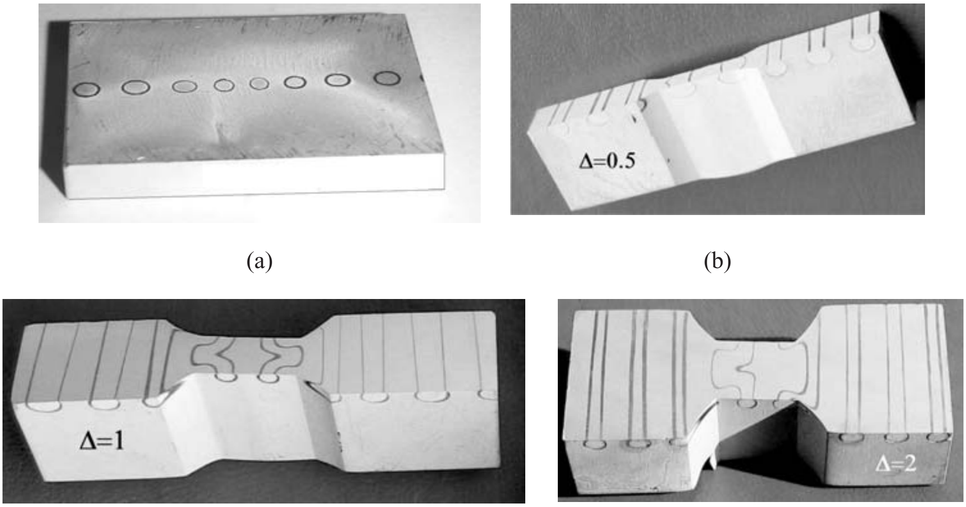

(a) (b)

(c) (d)

Figure 3.2. Specimens for plane strain compression test with surface ring pattern and internal stripe pattern. (a) Thin specimen before compression. (b) Thin specimen after compression, cut along the longitudinal section. (c,d) Same as (b), but for medium-thick and thick specimens.

the analysis, three different aspect ratios, or values of the parameter Δ (eq. 5-13), were used in the experiments; see Fig. 3.2. This was achieved by the use of three different specimen thicknesses, a thin (5 mm), a medium-thick (10 mm), and a thick specimen (20 mm). The width of the compression die, i.e., the dimension specified as w in Fig. 3.5(c), was in all experiments kept constant, equal to 10 mm. To map the deformations in the test, the specimens were made with an advanced internal grid pattern. This pattern has been tailor-made at NTNU[4] to trace metal flow inside and on surfaces of workpieces subjected to metal forming.

The specimens used in this investigation are shown in Fig. 3.2. In Fig. 3.2(a), an initial specimen is shown after the applied surface ring pattern has been revealed by etching. This surface pattern is used to trace friction in the experiment, as will be described. In Fig. 3.2(b–d), longitudinally cut midsections of the specimens are shown in etched condition after forming. Here both *surface ring patterns* and *internal stripe patterns* are visible. The internal stripe pattern is useful in that it can be applied to trace the actual deformations inside the specimen.

The Gleeble machine allowed accurate measurements of load vs. stroke during the test. Recordings from the tests are shown in Fig. 3.3(a). Throughout each experiment, the compression speed was monitored to keep the average strain rate in the compression gap constant, equal to 10 s^{-1}. This means that the compression speed was lowered during the compression stroke, being highest in the beginning. The compression speed also varied with the specimen height, so that the thickest specimen was compressed with the highest speed; see Fig. 3.3(b).

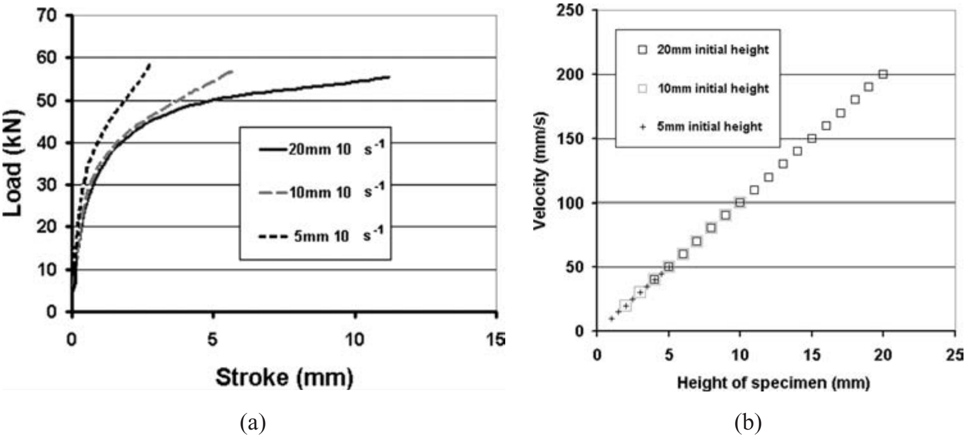

(a) (b)

Figure 3.3. (a) Load–stroke curves and (b) compression velocities in the experiments.

3.3 FEM Model and Input Data to the Model

As a cold-forming test, the process was modeled as isothermal, neglecting all eventual thermal effects. Friction was modeled as Tresca friction, and the numerical value of the friction factor m was varied in the simulations until there was good agreement between the appearance of the experimental ring pattern on the surface of the specimens and the corresponding ring pattern on the surface of the specimen in the FEM model.

This method of determination of friction – performing simulations, and then comparing results with regard to surface sliding of the specimen against the die with conditions in the experiment until there is good agreement, then accepting the obtained friction value as the one valid in the experiment – is commonly termed *inverse modeling*, or the *indirect parameter identification* (IPI), approach.

The flow stress of the material was determined by physical modeling in a cylinder compression test performed in the same Gleeble machine, using standard procedures to obtain flow stress from the load–stroke curve in the test. Two different constant compression speeds were used in cylinder compression, and it was shown that flow stress of the actual material is slightly strain-rate dependent, as depicted by the two recorded flow curves in Fig. 3.4(a).

The two flow curves were first used directly in the FEM model, but there was some deviation, with regard to both load–stroke response and metal flow in simulation, from the corresponding conditions in the experiments. Thus, the IPI approach was again used, but now the flow stress was changed, to get better correspondence between simulation and experiment. In many instances, it has been observed that the applied simulation program tends to predict the shear zones too hard, so that there is insufficient localized shearing in them. Since the shear zones often are characterized by higher strain-rates than elsewhere inside the deforming body, better agreement with the experiment can be obtained if the flow stress at the high

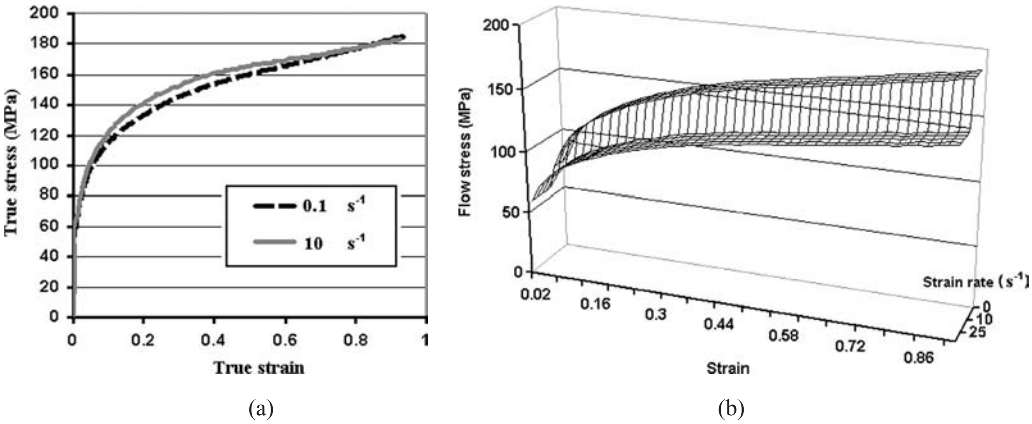

(a) (b)

Figure 3.4. (a) Flow curves obtained in cylinder compression and (b) modified flow stress with softened shear zones.

strain-rate level in the shear zone is lowered in relation to the flow stress from the cylinder compression test.

This is, of course, not a sound scientific approach but, in many instances, can be a remedy to get correct metal flow and can also explain why there are deviations between simulations and experiments. Actually, it may indicate that the *flow criterion* used in the FEM-model does not describe the constitutive behavior of the workpiece material with sufficient accuracy. With future development of improved flow criteria for various alloys, and the implementation of such data into the FEM code, better agreement can be expected between experiment and simulation, without the necessity to manipulate the flow stress input as done in the present analysis.

The FEM model for compression of the thick specimen is shown in Fig. 3.5. Here (a) shows the test in the initial stage with the upper die made invisible, (b) shows the test in the final stage with both dies present, and (c) is the same as (b) with the upper die made invisible.

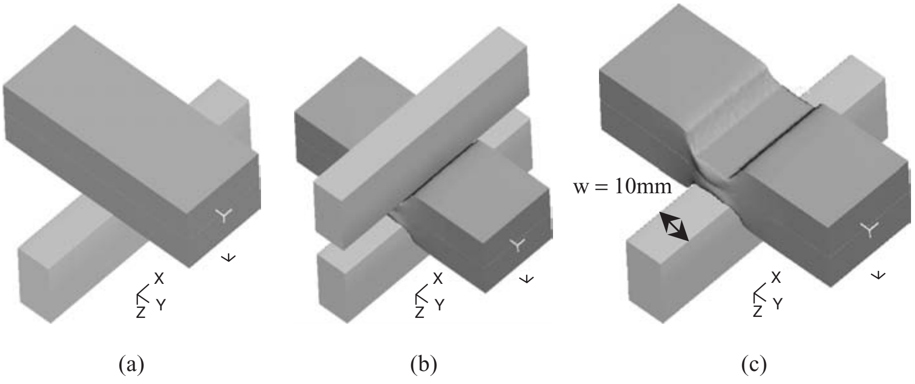

(a) (b) (c)

Figure 3.5. FEM model of the plane strain compression of the thick ($t = 20$ mm) specimen.

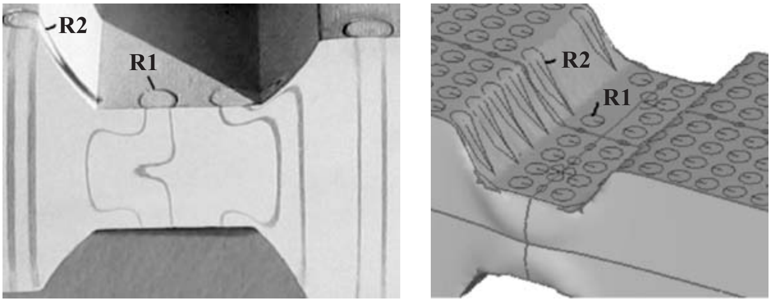

(a) (b)

Figure 3.6. A friction factor of $m = 0.35$ yielded good correspondence between (a) experimental surface ring pattern and (b) corresponding simulated pattern.

3.4 Similarity between Simulation and Experiment

As mentioned before, a ring pattern on the surface of the specimen will slide against the die in a friction-dependent way. It can therefore be used to determine the actual friction in the experiment, or eventually, a friction test must be run instead. But there could be doubts about the relevance of a friction test: whether it describes friction in this application with sufficient accuracy. The IPI approach applied to our thick plane strain compression specimen is illustrated in Fig. 3.6. For our case there was confirmed good correspondence between the two surface ring patterns, the experimental and the simulated one, when simulation was run with a friction factor of $m = 0.35$.

After the friction had been determined this way, we also checked the metal flow inside the specimen by recreating the same stripe pattern in the cross section of the simulation model, as in the experiment. With flow stress data from the cylinder compression test, there was deviation between simulated pattern and real pattern: the deformations in the shear zone were more localized in the experiment than in simulation.

The simulation showed that deformations in the process were characterized by an X-shaped *shear cross*, and that effective strain rate in the shear band was above $10\ \mathrm{s}^{-1}$; it was lower in the rest of the plastic zone [see Fig. 3.12(b)]. The flow stress of the shear cross in the simulation was therefore reduced by 20%, by introducing the flow stress relationship shown graphically in Fig. 3.4(b). Now excellent correspondence was obtained between experiment and simulation with respect to the flow pattern in the longitudinal section of the specimen, as shown by simulated stripe pattern in Fig. 3.7(b) and the corresponding experimental pattern in Fig. 3.7(a). The same good agreement was now also obtained for the two thinner specimens.[3]

Finally, the agreement between simulated and experimented load–stroke curve was checked, with the specified friction value and the modified flow stress shown in Fig. 3.4(a) as input in the simulation model. Now there was also good agreement between simulation and experiment with respect to load–stroke curves for all three specimens of different thickness depicted in Fig. 3.3(a). Since deformations, loads,

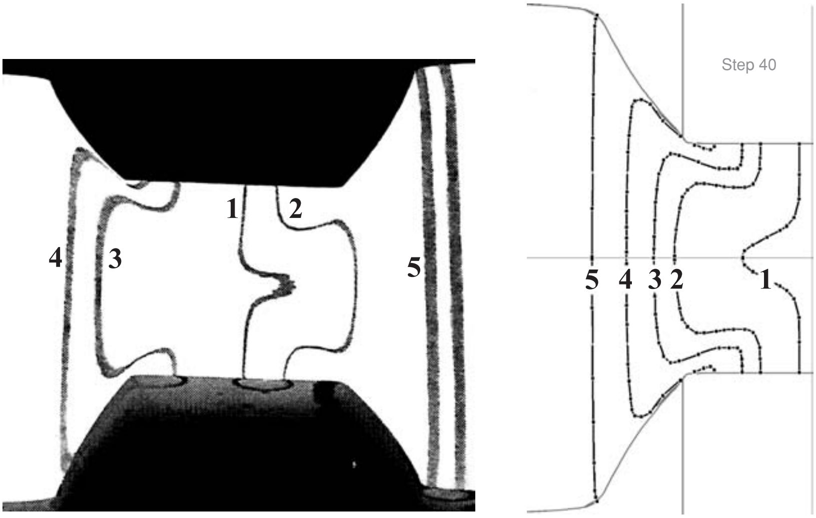

(a) (b)

Figure 3.7. Comparison between (a) experimental stripe pattern and (b) corresponding simulated pattern in midsection of thick plane strain compression test specimen.

and exterior shape of the specimen are well reproduced in the simulation, it is clear that the optimized simulation models are able to mimic the experiments accurately.

3.5 Information Deduced from the Simulation Models

With optimized FEM models that reproduce the plane strain compression test series well, it is possible to describe the forming conditions in the conducted tests in much detail. A vast number of results (postprocessing data) can be obtained from each model. The problem is to decide what is relevant information and what to use it for. In the following treatment, the focus is on the deformations imposed on the specimens in the tests and how they are influenced by the value of the parameter Δ in each experiment. In addition, the model will be used to consider the risk of cracking of the workpiece during compression, by interpretation of the calculated damage parameter.

3.5.1 Deformations in the Compression Gap

The deformation conditions in the plastic zone in a particular case of plane strain compression can be well understood by examining the deformations observed on a grid pattern in a section cut through the specimen, as visualized by the FEM-computed pattern at different stages of forming; see Fig. 3.8. Because a detailed comparison was made in Fig. 3.7 between some vertical lines in the simulated pattern, and corresponding lines in the experimental pattern, and excellent correspondence was confirmed, we know that the computed pattern indeed represents the conditions in our experiment.

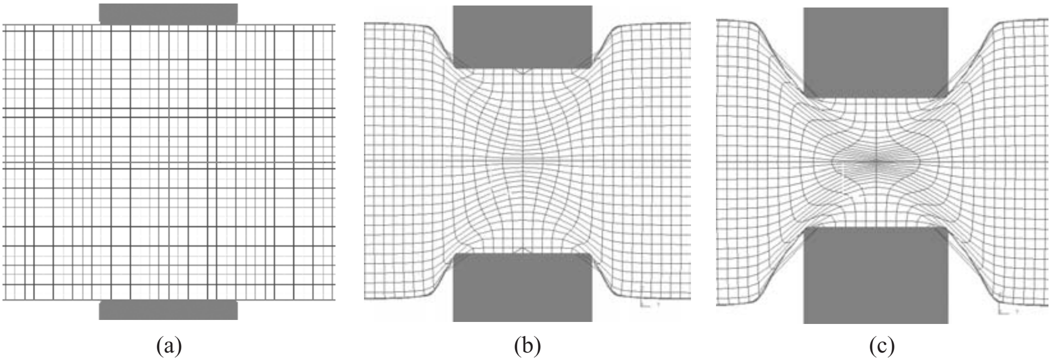

Figure 3.8. Deformations inside thick specimen ($\Delta = 2$) evaluated from deformed grid pattern: pattern at (a) initial, (b) intermediate, and (c) final stage of compression.

The deformations inside the specimen can be characterized if we look at four specially selected grid elements, those labeled 1 to 4 in Fig. 3.9, in the section we are examining. It is then easy from comparison of initial and final shapes of the elements, and their location inside the specimen, to describe the deformations in the longitudinal section of the workpiece.

Under each die, there is a triangular zone with only small plastic deformation, extending as a wedge down into the plastic zone. This region is commonly termed a *dead zone* (DZ), or sometimes also a *stagnant zone*. Grid element 1 is located inside this zone. As Fig. 3.9(b) depicts, the plastic deformation in this element is very small, i.e., the element hardly changes shape at all during the forming operation.

At the center of the specimen, between the dies, there is a *center zone* (CZ) indicated by a ring in Fig. 3.10. In this zone, there are very large plastic deformations characterized by both shear and compressive deformations, as this zone becomes squeezed between the dead zones under each die. Each dead zone residing under each punch is squeezed down into the specimen, much like two knife edges pushed against each other. Grid element 2 resides inside this center zone and is pressed flat upon compression. It is also shear-deformed on the left-hand side, while there is no shear deformation at the other side of the element, i.e., the side that coincides with the neutral line in the middle of the compression gap.

Figure 3.9. Four selected grid elements depict the deformation characteristic of the forming operation: (a) initial configuration and (b) final configuration of deformed elements.

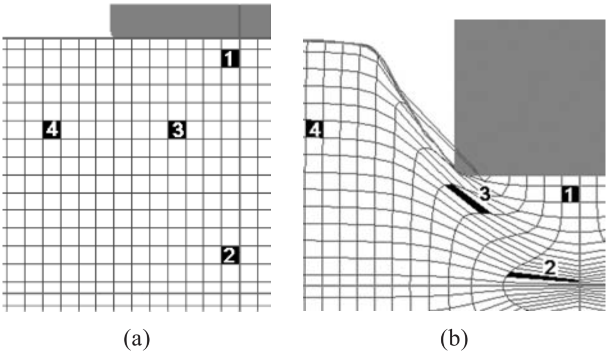

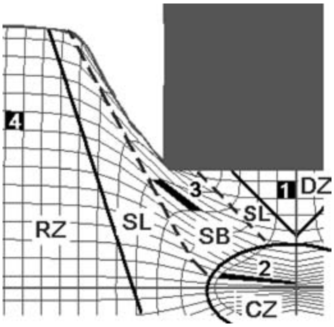

Figure 3.10. Zones of different deformations identified inside deformed grid pattern.

A layer of material in which there is shear deformation, but of rather small magnitude, can be identified in between each dead zone and the metal further away from the neutral plane. We call this layer a *layer of moderate shear* (SL) [see Fig. 3.10]. In fact, a corresponding layer also exists adjacent to the dead zone.

In between these layers, a distinctive *shear band* (SB) can be identified. During the compression stroke, this layer is greatly stretched out by shearing. The initially vertical grid lines of the pattern in this layer are subjected to ≈45° rotation, and after deformation, they appear with oblique orientation. Grid element 3 resides inside this shear band and becomes stretched out, as it takes on oblique shape due to shear.

Finally, away from the compression gap, in the region where the specimen remains unchanged in dimensions, the grid elements – as, for instance, element 4 – do not change shape at all during the compression stroke. Here there is obviously a more or less *rigid zone* (RZ) of material. To trace the exact boundary line between the rigid and the plastic zone can be difficult from observation of the deformed grid pattern only. This would require consideration of the actual deformations inside the specimens, in terms of amount of strain, in comparison with the limiting elastic strain values of the material.

Although, as we have seen, analysis of deformations in plane strain compression of the thick specimen is straightforward, it is more complex for the specimens of less thickness (the thin and the medium-thick specimens), as shown in Fig. 3.2. The FEM-computed deformed grid pattern for the thin specimen at the end of compression is shown in Fig. 3.11. From the appearance of this pattern, it is easy to identify

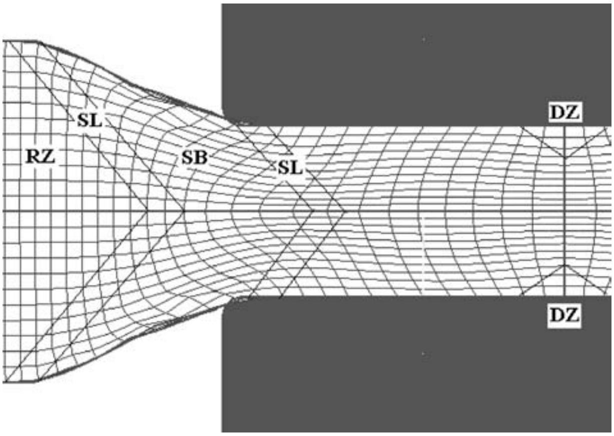

Figure 3.11. Final deformed grid pattern in plane strain compression of thin specimen ($\Delta = 0.5$).

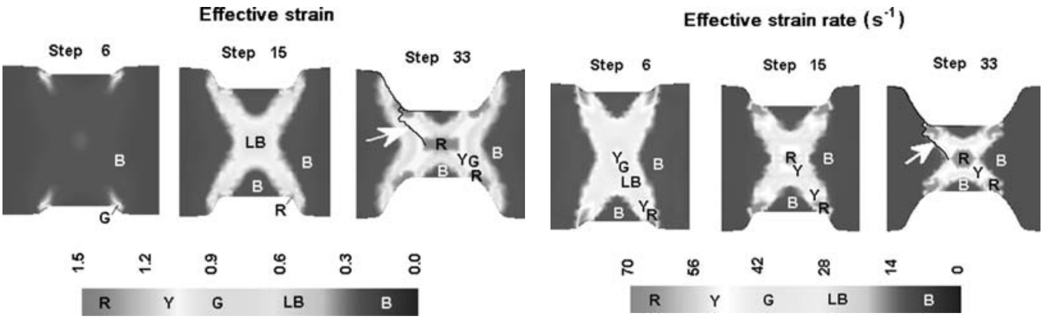

(a) (b)

Figure 3.12. Distributions of (a) effective strain and (b) effective strain-rate in the longitudinal midsection of the thick specimen at three stages of compression. R = red; Y = yellow; G = green; LB = light blue; B = blue.

a SB, and on both sides of it two SLs, and finally away from the compression gap a RZ. Moreover, inside the compression gap, a DZ can be identified, but in comparison with the corresponding zone in Fig. 3.10(b), the deformations inside the zone are much larger. The grid elements here deform a lot since they change their shape significantly. It is therefore perhaps better to term this zone the *stagnant* zone instead of the dead zone, because it resides in the middle of the specimen, with material surrounding it on all sides that deforms more.

For the rest of the material contained in the compression gap, there are considerable deformations, but the appearance of the grid pattern does not reveal any other shear bands or dead zones. To confirm the eventual existence of other shear bands or stagnant zones in the compression gap, it is therefore required to consider the strain-rate distribution in the material; see the next section.

3.5.2 Deformation History Visualized by Effective Strain and Strain-Rate Distributions

The amount of deformation inside the specimen can be determined by the simulation program by letting it compute the *effective strain* (eq. 4-38). This deformation parameter can be found at any instant of compression, in its distribution throughout the volume of the specimen, in terms of the strain at the surfaces of the specimen, or inside a section cut through the specimen. In Fig. 3.12(a), in this manner, is shown the evolution during compression of the effective strain in the longitudinal midsection of the thick plane strain compression specimen, in terms of three momentary distributions at different stages of compression.

Another important deformation parameter is the *effective strain rate* (eq. 4-39). This parameter, if shown as the distribution inside the specimen at a particular forming stage, will depict the momentary deformations per time unit at this stage, in contrast to the effective strain, which depicts the accumulated strains from the beginning of deformation until the stage examined. The effective strain-rate distribution inside the thick specimen is shown this way in Fig. 3.12(b), as computed by the FEM program, at the same stages as for the effective strain. Note the black line drawn on the specimen in Fig. 3.12(b), marked by a white arrow. This line defines the boundary between deforming and nondeforming material in the section at the end of the test. The same line is shown in Fig. 3.12(a), added to the effective strain distribution picture. As seen from this figure, there is a region on the left-hand side of the line that has been subjected to deformation but lies outside the deformation field at the end of compression. Hence these deformations must have been produced in the material in early stages of compression, after which the material has been squeezed in the lateral direction, out of the plastic zone of the specimen, and therefore has ceased to deform.

When effective strain and effective strain-rate distribution inside the specimen are considered, as shown in Fig. 3.12, and a comparison is made with Fig. 3.10, it is possible, from the distribution pictures of Fig. 3.10, also to identify the different zones DZ, SL, SZ, and RZ. From these pictures, it is in addition possible to evaluate the size of the deformations, in terms of the effective strain or effective strain rate. Both figures reveal that the shear bands form a deformation cross inside the specimen during compression. The shape of the cross changes throughout the course of compression, so that its bottom angle increases while its side angle decreases. Moreover, it is seen from the black line in Fig. 3.12 that material inside the compression gap is squeezed sideways out of the compression gap and hence moves laterally through the active shear bands. An exception, however, is material at the very center of the plastic zone. This material remains at the same location throughout the stroke, namely, at the intensely deforming center of the deformation cross. It is therefore subjected to the largest effective strain in the whole deformation gap. There are also high strains in the material adjacent to the sharp edges of the die, but here there is lateral transport of material away from the compression gap, so new, less-deformed material continuously flows into the shear band, so that the most deformed material in the band is displaced laterally out of the compression gap.

3.5.3 Influence of the Parameter Δ on the Deformations

Whereas the thick specimen had an initial value of Δ equal to 2, the value of this parameter was 1 for the specimen of medium thickness and 0.5 for the thin specimen; see Fig. 3.2.

Examination of the FEM-computed deformations of the specimen of medium thickness showed that the deformations here were similar to those of the thick specimen throughout a large part of the stroke, so that there existed one deformation cross inside the specimen. But at a certain stage of compression, there was a transition in deformation pattern, so that the single deformation cross was replaced by two crosses.

The FEM-computed deformations inside the longitudinal section of the thin specimen, in terms of effective strain and effective strain-rate values, are shown in Fig. 3.13. When the specimen is compressed down to simulation step 24, as depicted in Fig. 3.13(b), the deformations are characterized by the presence of altogether three deformation crosses. With the gray scale chosen in Fig. 3.13 – to depict

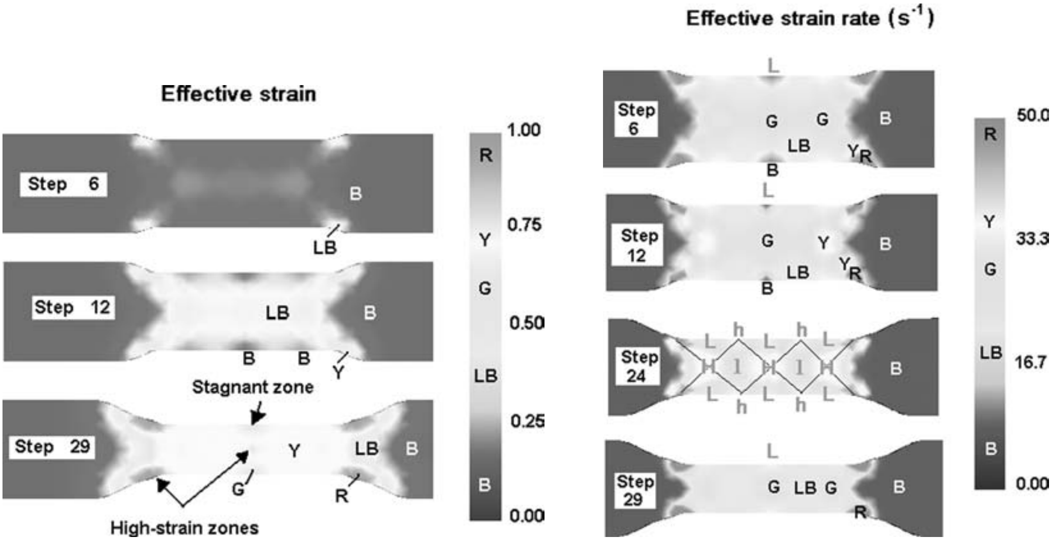

(a) (b)

Figure 3.13. (a) effective strain and (b) effective strain-rate distributions in the longitudinal midsection of the thin specimen.

different levels of effective strain rate – alternating zones of high (*H, h*) and low (*L, l*) strain rate, are clearly revealed inside the material in the compression gap. At mid-thickness of the specimen, between the crosses, one can identify stagnant zones, denoted by *l* to indicate that the strain rate there is higher than in the corresponding stagnant zones denoted by *L*, close to the surface of the specimen. Moreover, in the region between two stagnant zones, there is always *a high-strain-rate zone* (HSRZ), denoted by *h*, where strain rates are less than in a corresponding high-strain-rate zone denoted by *H*. When Fig. 3.12(b) is compared with Fig. 3.13(b), it is also seen that deformation rates in the thin specimen are distributed more evenly over the longitudinal section of the compression gap, than for the thick specimen. Because of this, the final accumulated deformations are also much more even inside the deformed part of the specimen; compare the pictures from step 33 in Fig. 3.12(a) and those from step 29 in Fig. 3.13(a). However, in the middle of the thin specimen, at both sides of it, there are two small stagnant zones that are less deformed than the rest of the material in the compression gap, with a high-strain zone located between them. In addition, highly strained regions are predicted to be present in the specimen below the edges of the dies.

The effective strain-rate distribution of the longitudinal midsection with three deformation crosses in Fig. 3.13(b) has for the sake of clarity been shown again in Fig. 3.14, with different scaling. As this figure depicts, the effective strain-rate variations within this section lie in the range ≈15 to ≈40 s^{-1}, when the high-strain-rate regions below the edges of the dies are excluded. A 3D view of the effective strain rate on the surface of and inside the thin specimen, at the end of compression, is

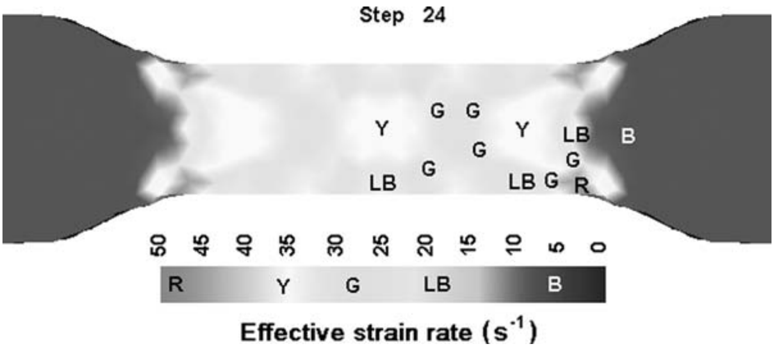

Figure 3.14. Triple deformation crosses enlarged from Fig. 3.13(b).

shown in Fig. 3.15. As this figure depicts, the effective strain-rate variation within the section of the specimen now has been reduced even further, so that the deformation rates have become rather uniform within the compression gap, if we neglect the presence of the small stagnant zones close to the die.

Figure 3.16 depicts a graph made to show when the deformation pattern of the thin plane strain compression test is changed from a single deformation cross to a double-cross configuration and finally to a triple-cross configuration. As this figure shows, transition from single to double crosses occurs when $\Delta \approx 0.7$ and from double to triple crosses when $\Delta \approx 0.4$.

The behavior described previously, with the deformation being very inhomogeneous in plane strain compression, and taking place by formation of deformation crosses, with dead or stagnant zones in between and dead zones that multiply when the parameter Δ is reduced from 2 and downward, has long been known; see the region bounded by the rectangle at the lower left in Fig. 3.17.[5] Moreover, this behavior has been utilized to create theoretical methods, such as *upper bound solutions* and the *slip-line field theory*, in order to obtain estimates of the average contact pressure in frictionless plane strain compression, see Fig. 3.17.

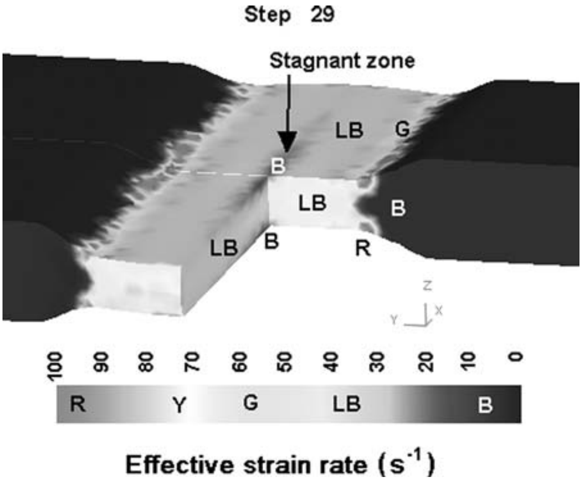

Figure 3.15. Effective strain-rate distribution inside the thin specimen at the end of compression.

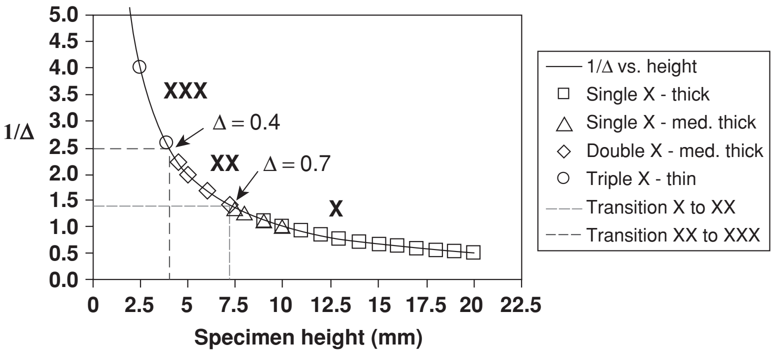

Figure 3.16. Graph depicting when single, double, or triple deformation crosses are predicted to appear in the compression gap in plane strain compression testing.

3.5.4 Damage Parameter and Edge Cracking

The distribution of the *damage parameter* in the thick specimen, as it is computed by the simulation program, is shown in Fig. 3.18(a). The damage parameter on the surface of one-half of the specimen is shown at the top and correspondingly for the whole specimen at the bottom. The damage parameter, in many instances,

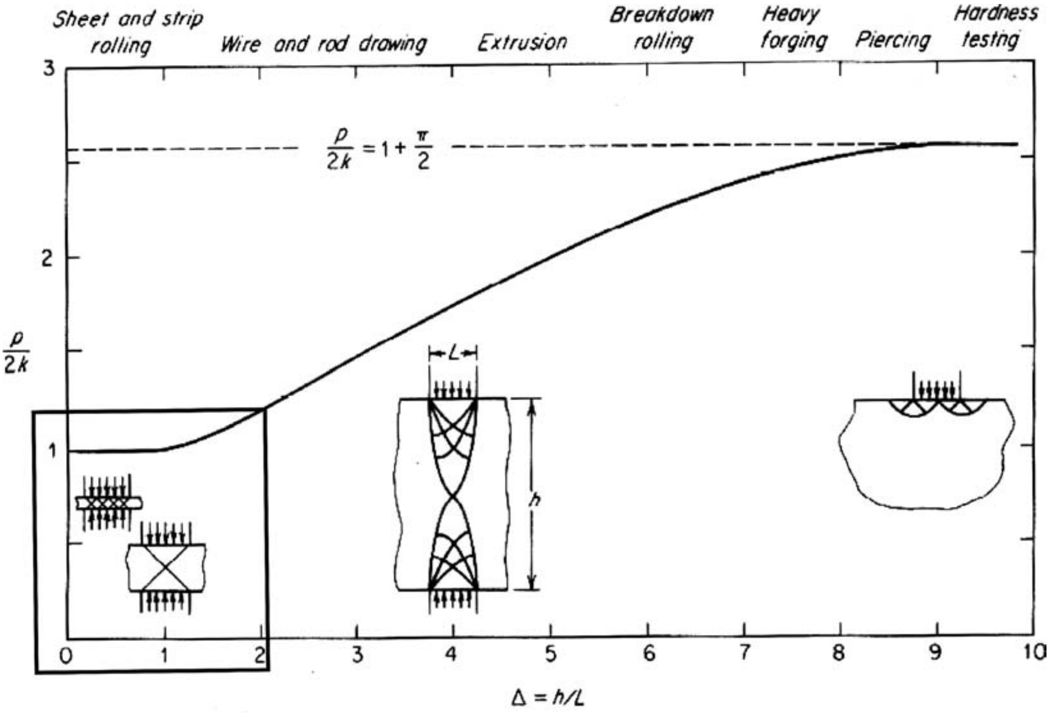

Figure 3.17. Metal flow was early realized to occur by formation of dead zones with shear bands in between. Deformation in plane strain compression for $\Delta \leq 2$ is characterized by a deformation cross, which multiplies into many crosses as Δ decreases. (BACKOFEN, DEFORMATION PROCESSING, 1st Edition, © 1972. Reprinted by permission of Pearson Education, Inc., Upper Saddle River, NJ.)

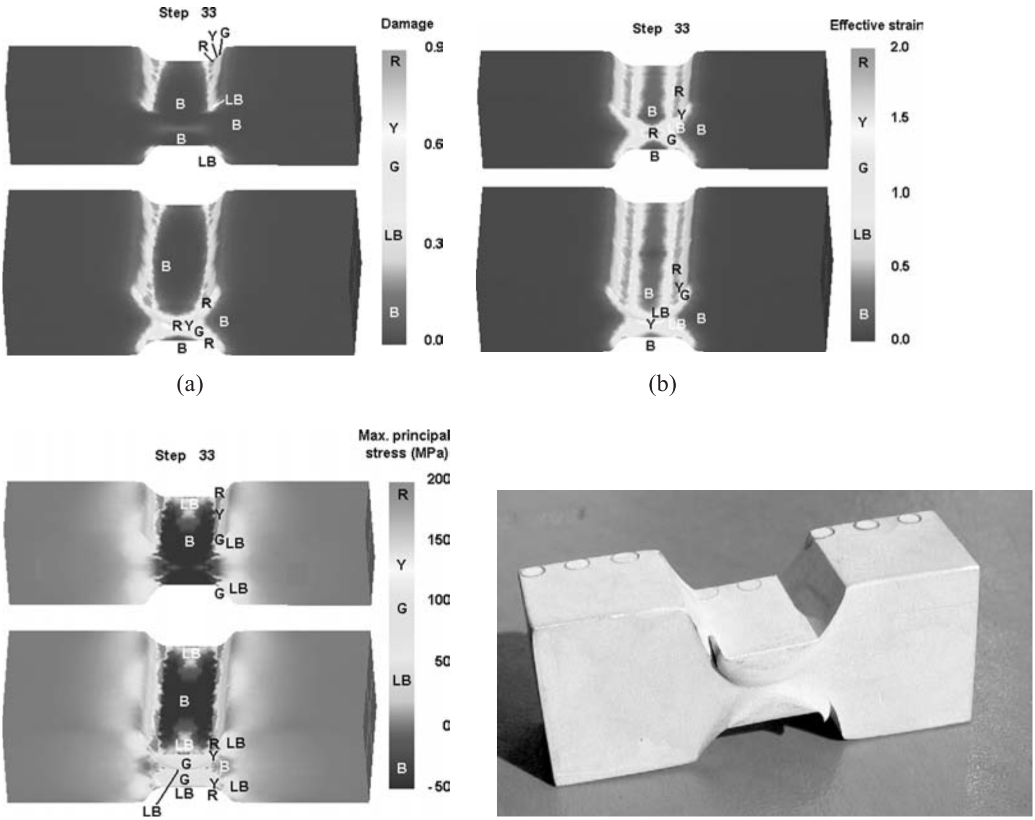

(a) (b)

(c) (d)

Figure 3.18. Distribution of (a) damage parameter, (b) effective strain, and (c) largest principal stress in thickest specimen at end of compression. (d) Edge cracking over tool edges.

predicts the risk of cracking in the workpiece due to tensile stresses; it is defined and explained in Ch. 9.

From Fig. 3.18(a), it is evident that the damage parameter has its highest value in the most intense shear band under the edge of the compression die. As shown in Fig. 3.18(d), cracks in fact developed in this location in the test specimens we compressed, so the simulation result compared with this experimental observation seems rather convincing.

In Fig. 3.18(b,c), the parameters that are incorporated in the damage parameter, namely, the effective strain and the *largest principal stress*, have been shown in the same manner as the damage parameter. As these images depict, the reason the damage parameter is low inside the specimen is because the largest principal stress is low there. There must obviously be a buildup of compressive stresses from the surface of the specimen toward the inner part of it. The outer surface layers of the specimen, however, are subjected to tensile stresses, and therefore the damage parameter is concurrently high there.

3.6 Concluding Remarks

In this chapter, it has been shown how the deformation conditions in the technological test plane strain compression can be characterized by FEA. The input to the FEM simulation was the flow stress data of the workpiece material and the friction data characterizing the shear stresses transferred through the interface between the die and the workpiece. Such data were not readily available in this case, so some tests were run to acquire them. Flow stresses were collected in a cylinder compression test. To map the sliding of the workpiece material against the die and the internal metal flow, experiments were performed in which workpieces fitted with a combined internal and surface grid pattern were used.

A FEM model was built for the process, and the experimental grid pattern was used to find the friction factor, which had a value of ≈ 0.35 in the test. The internal metal flow of the specimen then was compared with simulated flow, and some difference was found. Flow stress data were therefore slightly adjusted until the simulated metal flow became equal to the experimental flow. At this point, the simulated and the experimental load–stroke curves were compared, and excellent agreement between the two was found. Hence, the conclusion is that the conditions in the simulation models are close to those in the experiments.

The simulation was then used to study metal flow in the compression gap in the test, run for different Δ-values in the range 0.5 to 2. The analysis showed that shear band formation is pronounced in plane strain compression when $\Delta = 2$ and that two dead zones form below each die. The material at the center of the specimen is heavily deformed, as it is squeezed between the two dead zones. It was shown that the shear bands appeared with an X shape in a longitudinal section cut through the specimen, i.e., a shear cross was present in the plastic zone of the specimen. Hence, for this high Δ, the deformations inside the compression gap were extremely nonuniform. The metal in the dead zones remained almost undeformed, while the material layers in between the dead zones were subjected to large deformations.

When looking at the deformations of the specimen when $\Delta = 1$, the main pattern of deformations was similar that of the specimen with higher Δ, with a single deformation cross inside the plastic zone, but there was less inhomogeneity of deformation. The shear cross was less intense than in the thickest specimen. Instead there was more deformation in the dead zones. When the specimen had been compressed down from initially 10 mm to approximately 7.4 mm height, there was a sudden transition in deformation mode inside the material in the compression gap. Now double deformation crosses started to appear in the gap. Toward the end of compression, the deformations also became more even inside the compression gap, than before. This deformation pattern was maintained during further compression and in the beginning when the thin specimen was compressed.

When the thin specimen had been compressed from 5 mm initial thickness down to approximately 4 mm, there was a new transition in deformation mode: three deformation crosses appeared in the compression gap. Throughout further compression of the thin specimen, deformations inside the specimen became more uniform than before, i.e., the difference in strain rate from stagnant zones to shear bands decreased.

The conclusion thus seems to be that as the parameter Δ is gradually reduced from 2 to 0.25, as in the conducted experiments, the deformation mode changes twice as the number of deformation crosses multiplies, from a single cross to double crosses and finally to triple crosses. The appearance of the double and the triple deformation crosses is not readily seen when internal grid patterns are analyzed but is well visualized in the strain-rate distributions computed by the FEM simulation models.

The FEA hence documents classical findings from the literature. It was early recognized that the deformations in (for instance) plane strain compression are rather inhomogeneous, especially for high values of Δ, and that a single deformation cross would be replaced by multiple crosses[5] in the compression gap, when Δ is reduced from 1 to 0.25, as shown in Fig. 3.17.

Problems

3.1 Simulation results from cold frictionless plane strain forward extrusion are shown for a particular extrusion geometry in Fig. 3.19. Discuss how the material deforms in terms of deformation of grid elements, presence of deformation crosses, homogeneity of deformation, and non-steady-state or steady-state conditions for this forming process on the basis of the given information.

3.2 Write down a short explanation to express your understanding of the following terms used in this chapter:

(a) Metal flow
(b) FEA
(c) Physical metal forming simulator
(d) Inverse modeling
(e) Surface ring pattern
(f) Shear cross
(g) Dead zone
(h) Stagnant zone
(i) High-strain-rate zone
(j) Effective strain
(k) Effective strain-rate distribution
(l) Upper bound solution
(m) Damage parameter

3.3 Figure 9.6 shows FEM-computed distributions of some process parameters in cylinder compression.

(a) Make a 3D sketch of this metal forming test, and explain how it differs from the plane strain compression test method.
(b) Try to interpret the given simulated distributions of process parameters on the basis of deformations inside the specimen and the risk of tensile stress cracking.

3.4 In the middle of Fig. 19.1 is shown the deformed grid pattern obtained in a FEM simulation model of forward extrusion of an aluminum alloy. On the basis of this grid pattern, discuss the following relations:

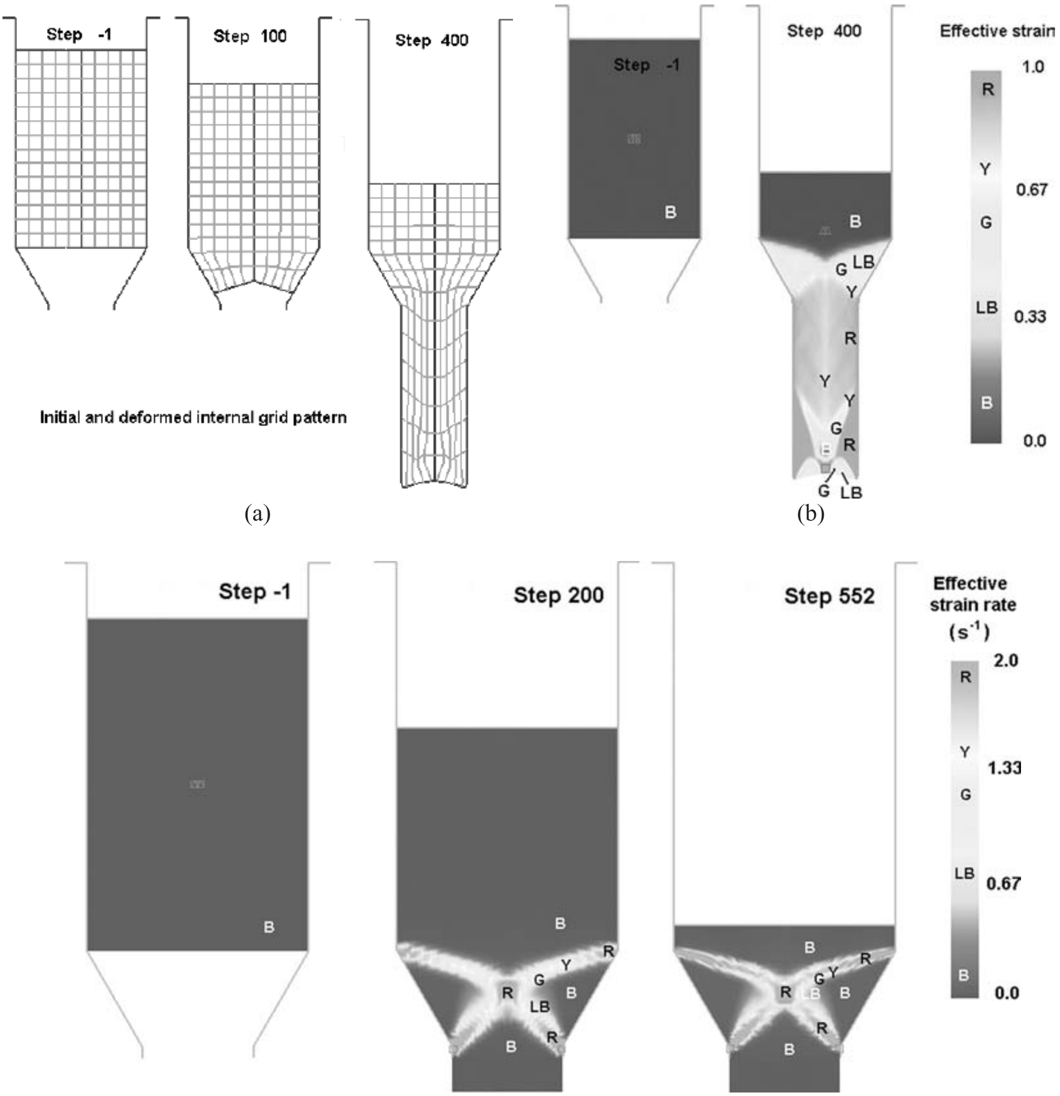

(a)

(b)

(c)

Figure 3.19. Some FEM simulation results from frictionless forward extrusion.

- (a) Appearance of the grid pattern before the start of extrusion.
- (b) Presence of different deformation zones in the extrusion metal inside the container at the instant when deformed pattern was revealed.
- (c) Predicted sliding of metal against the container wall.

NOTES

1. Uyyuru, R. K.: "Plane strain compression test as a friction-measuring test – a comprehensive review," in: Uyyuru, R. K.: "Engineering the Friction and Forming Mechanics in Cold Aluminium Forming," doctoral thesis, Norwegian Univ. of Science and Technology, Trondheim, Norway, 2003, pp. 106–124.

2. Nolte, D., and Uyyuru, R. K.: "Review and recent developments in physical modeling of metal forming," in: Nolte, D.: "Analysis of Aluminium Hot Forging," doctoral thesis, Norwegian Univ. of Science and Technology, Trondheim, Norway, 2005, pp. 89–115.
3. Valberg, H., Uyyuru, R. K., and Lefstad, M.: "Analysis of deformations in plane strain compression using advanced grid pattern technique," Proc. 9th Esaform Conf., Glasgow, 2006, pp. 891–894.
4. NTNU is an abbreviation for the Norwegian University of Science and Technology.
5. Backofen, W. A.: "Deformation Processing," Addison-Wesley, Reading, MA, 1972, p. 135.

REFERENCES

Bay, N., Wanheim, T, Danckert, J., and Nielsen, K. B.: "An appraisal of numerical and physical modelling for prediction of metal forming processes," Proc. 15th. Risø Int. Symp. on Materials Science, 1994, pp. 1–32.

Li, G., Jinn, J. T., Wu, W. T., and Oh, S. I.: "Recent development and applications of three-dimensional finite element modelling in bulk forming processes," J. Materials Processing Technology, Vol. 113, 2001, pp. 40–45.

Mielnik, E. M.: "Metalworking Science and Engineering," McGraw-Hill, New York, 1991, p. 494.

Schey, J. A.: "Introduction to Manufacturing Processes," McGraw-Hill, 1977, pp. 108–111.

Shirgaokar, M., Yadav, A., and Taylan, A.: "Simulation and optimization of metal forming processes," 19th Umformtechnisches Kolloquium Hannover, 27–28 Feb. 2008, pp. 173–186.

Wagoner, R. H., and Chenot, J.-L.: "Metal Forming Analysis," Cambridge University Press, 2001.

4 Theory

Because metal forming produces elastic and plastic deformations in the workpiece material and elastic deformations in the dies, an in-depth study of the metal forming process will require the determination of stresses and strains in the workpiece and the tooling. In addition, one needs to know some basic topics from the theory of elasticity and plasticity. In this chapter, a short introduction to this theory is therefore given. Because of the rather shallow treatment here, readers who are unfamiliar with this theory are referred to other textbooks[1–3] for a more profound study.

4.1 Stresses

During metal forming the workpiece is deformed plastically by forces transferred from the die to the workpiece. A successful forming operation requires that there be plastic deformations in the workpiece, so that it changes shape permanently and conforms to the geometry of the die, while the die remains in the elastic state. If the die material becomes plasticized, the situation is one of overloading of the tooling, and the die geometry will gradually change because of the excessive forming loads. This means that the correct geometry of the formed component no longer can be maintained, so to continue appropriate metal forming, the dies must be replaced by new dies that can work the material while remaining in the elastic state.

4.1.1 The Stress Concept

Stress is defined as force per unit of area and refers to a particular point in a material. Suppose a force $\mathrm{d}F$ is directed at an angle to a surface $\mathrm{d}A$ at a particular place inside a material. If the area is made smaller until it approaches toward zero, the area will become a point. In addition, a stress will act on this point, directed in the same direction as the force, with magnitude $\sigma = \mathrm{d}F/\mathrm{d}A$. This stress can be decomposed into two components, a *shear stress* and a *normal stress*, as expressed by:

$$\tau = \frac{\mathrm{d}F_t}{\mathrm{d}A} \tag{4-1}$$

$$\sigma_n = \frac{\mathrm{d}F_n}{\mathrm{d}A} \tag{4-2}$$

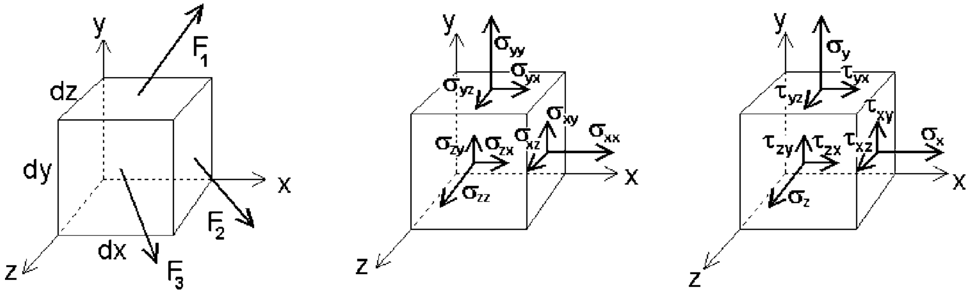

(a) (b) (c)

Figure 4.1. Homogeneous stress state. (a) Forces acting on side faces of volume element. (b, c) Stress components given with different notation.

There are two different stress definitions. If the force is divided by the *initial area* A_0 on which the stress acts, i.e., the nominal area, the stress obtained is called the *nominal stress*:

$$\sigma_{\text{nom}} = \frac{F}{A_0} \tag{4-3}$$

Instead the stress can be obtained by dividing the force by the *actual area* at any instant during deformation, i.e., A. The stress then obtained is called *true stress*, and takes account of the *change of the area* as the material is subjected to deformation:

$$\sigma = \frac{F}{A} \tag{4-4}$$

In the case of elastic deformation of a body, the area change is small, so the two stress definitions are approximately equal. In the case of plastic deformation, however, the change of the area can be large, and the true stress definition is the better one. An equation is commonly derived that relates the two stresses to each other:

$$\sigma = \sigma_{\text{nom}}(1 + e) \tag{4-5}$$

where e is nominal strain, defined in eq. 4-11.

Consider a small volume element of material with dimensions dx, dy, and dz, in force equilibrium. If these dimensions are made smaller until they approach toward zero, the element will represent a point in the material. In the general case, each boundary surface of the element will be subjected to a force that may be oriented at an angle to the normal to the surface on which they act, see Fig. 4.1. In the case of *homogeneous stress*, i.e., stress that does not change throughout the material, the force and stress components at the back face of the element will be equal to those at the front face but will have opposite signs. The force at each face of the element can be decomposed into components parallel to the direction of the main axis and components orthogonal to this direction. When the force components obtained this way are divided by the area on which they act, one obtains altogether nine stress components that act on the element; see Fig. 4.1(b) or (c).

The general stress state at a point in the material is thus described by nine *stress components*, which together make up the *stress tensor*, which in *tensor notation* is written as

$$\sigma_{ij} = \begin{bmatrix} \sigma_{xx} & \sigma_{yx} & \sigma_{zx} \\ \sigma_{xy} & \sigma_{yy} & \sigma_{zy} \\ \sigma_{xz} & \sigma_{yz} & \sigma_{zz} \end{bmatrix} \tag{4-6}$$

or

$$\sigma_{ij} = \begin{bmatrix} \sigma_{x} & \tau_{yx} & \tau_{zx} \\ \tau_{xy} & \sigma_{y} & \tau_{zy} \\ \tau_{xz} & \tau_{yz} & \sigma_{z} \end{bmatrix} \tag{4-7}$$

where i and j are iterated over x, y, and z; see Fig. 4.1(b). Given this way, two identical indices (as for instance σ_{xx}) identify a normal stress, and two different indices (as for instance σ_{xy}) identify a shear stress. An alternative notation – with stress components as shown in Fig. 4.1(c) – is the tensor given in eq. 4-7. Force equilibrium for the volume element in Fig. 4.1 requires that there be no rotation of the element around any of its axes, and this requirement is fulfilled only if $\tau_{xy} = \tau_{yx}$, etc., i.e., if $\tau_{ij} = \tau_{ji}$. Equilibrium thus reduces the number of different stress components at a material point, in the general case, from nine to six.

To be consistent when stresses are given, one has to define *positive stress*. A positive normal stress is a tensile stress; a negative normal stress is a compressive stress. Shear stress components directed as shown in Fig. 4.1(b), (c) are defined to be positive, i.e., they are positive when they point in the direction of the positive axis. If they act in the opposite direction, i.e., they point against the direction of the positive axis, they are considered negative stresses. However, on the back sides of the element (i.e., the faces of the element not visible in the figure), the conditions are opposite: positive stresses are shear stresses directed against the direction of the positive axis.

The notation used with regard to indices, when specifying the tensor in eq. 4-6 and eq. 4-7, is that the first index, i, defines the face on which the stress component acts, given by the normal to the plane, and the second index, j, defines the direction in which the stress component itself acts.

4.1.2 Principal Stresses

As just described, the general stress state is characterized by nine stress components, whereof only six components are different, because the shear stresses in the strain tensor – placed symmetrically around the normal-stress diagonal – are equal in size. For a general state of stress it can generally be shown that there always exists one orientation of the coordinate axes, and only one such orientation, for which all shear stress components vanish. A material element with this orientation will therefore only have normal stress components. The normal stress components in this particular coordinate axis system are generally termed *principal stresses* and are

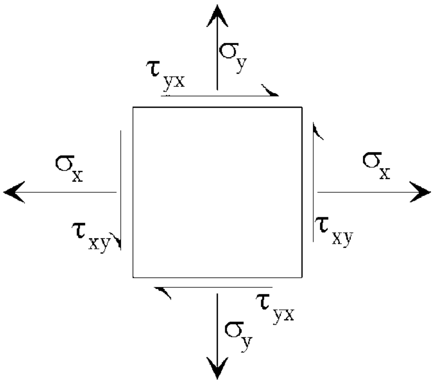

Figure 4.2. Stress components in plane stress.

denoted by the symbols σ_1, σ_2, and σ_3, where σ_1 by convention is the largest, and σ_3 the smallest principal stress.

A general stress state with six different stress components is difficult to analyze; therefore, it is common to consider the simplified case of *plane stress*, also called *biaxial stress*, where all stress components in the *xy* plane of the element in Fig. 4.1 are zero, i.e., $\sigma_z = \tau_{zy} = \tau_{zx} = 0$. For this case, it is more common to show a two-dimensional sketch of the stress state, as depicted in Fig. 4.2. In the case of plane stress, it can be shown that the principal stresses can be expressed by the equation:

$$\sigma_1, \sigma_2 = \frac{1}{2}(\sigma_x + \sigma_y)^2 \pm \frac{1}{2}\left[(\sigma_x - \sigma_y)^2 + 4\tau_{xy}^2\right]^{1/2} \tag{4-8}$$

The orientation of the planes on which principal stresses occur can be determined by the expression

$$\tan 2\phi = \frac{2\tau_{xy}}{\sigma_x - \sigma_y} \tag{4-9}$$

Hence, by these equations, the principal stresses can be determined for an arbitrary state of plane stress.

4.1.3 Maximum Shear Stress

In addition to the principal stresses, it is also of interest to determine the *maximum shear stress*, in the plane stress state, and its orientation. The plane on which this shear stress acts is oriented at an angle of 45° to the planes on which the principal stresses act. The maximum shear stress can be expressed by the equation

$$\tau_{\max} = \frac{1}{2}\left[(\sigma_x - \sigma_y)^2 + 4\tau_{xy}^2\right]^{1/2} \tag{4-10}$$

4.1.4 Stress Transformation by Mohr's Circle

If one principal stress and its orientation are known, a graphical approach, called *Mohr's circle*,[4] can be used to determine the stresses on planes orthogonal to the

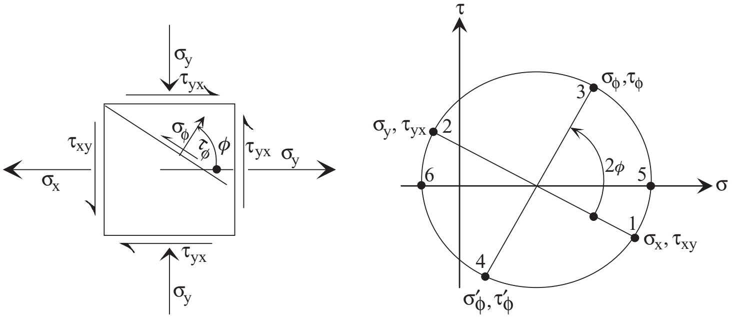

(a) (b)

Figure 4.3. (a) Stress state on the physical material element and (b) Mohr's representation of the stress state.

given direction of principal stress, for all orientations of these planes. If the known principal stress acts in the z-direction, Mohr's circle will give a graphical representation of the stresses in the xy plane, for all possible rotations of the x and y axes.

The sign convention used when Mohr's circle is drawn deviates from the standard sign convention for stresses. Normal stresses are drawn along the abscissa, with tension considered positive and compression considered negative. Shear stresses are drawn along the ordinate, with shear stress that causes clockwise (counterclockwise) rotation considered positive (negative). The angle in Mohr's circle is twice the angle in the physical plane. This definition of positive and negative shear stress is used only for drawing Mohr's stress circle; otherwise, the definition in Sec. 4.1.1 is used.

As an example, Mohr's circle for the stress state specified in Fig. 4.3(a), is shown in Fig. 4.3(b). Point 1 represents the stress components on the yz plane of the element and point 2 defines the stress components on the xz plane. Points 3 and 4 represent the stress components when the stress element has been rotated an angle ϕ with respect to its initial orientation. Finally, points 5 and 6 represent the principal stress directions in the xy plane for the given stress state. If all stress components are drawn on the same scale, they can all be read out from the diagram. Angle of rotation in the physical plane can also be determined as half the angle of rotation in Mohr's circle diagram.

EXAMPLE 4.1: PRINCIPAL STRESSES AND LARGEST SHEAR STRESS

Problem: Determine the principal stresses and their orientation, including the largest shear stress, for the stress state $\sigma_x = 10$, $\sigma_y = 5$, $\tau_{xy} = 3$, $\sigma_z = \tau_{zx} = \tau_{zy} = 0$ (in MPa).

Solution: To solve the problem, Mohr's circle is constructed for the given case; see Fig. 4.4(a). The principal stresses can be read from the graph as $\sigma_1 = 11.4$ MPa, $\sigma_2 = 3.6$ MPa, and $\sigma_3 = 0$ MPa. The orientation of the plane of the principal stresses is defined by the angle

$$\sin 2\phi = \frac{\tau_{xy}}{\frac{\sigma_1 - \sigma_2}{2}} = \frac{3}{\frac{11.4 - 3.6}{2}} = 0.769, \qquad \text{i.e.,} \quad \phi = 25.14^\circ$$

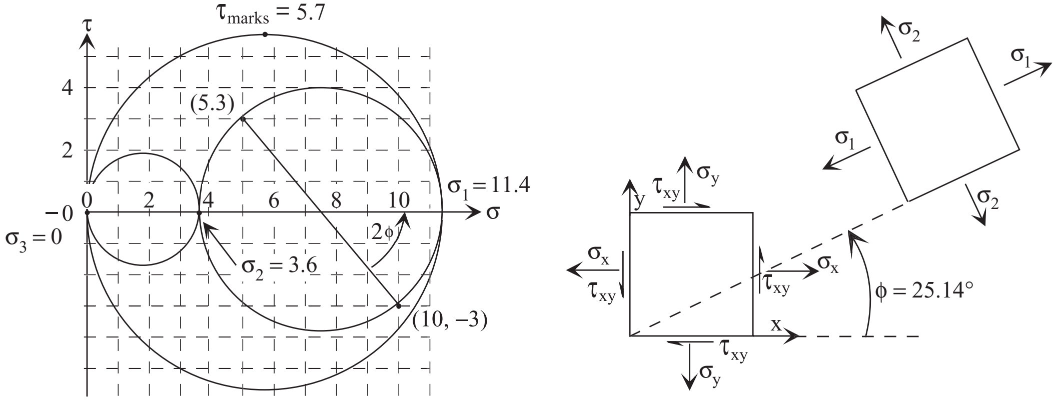

(a) (b)

Figure 4.4. (a) Mohr's circle and (b) orientation of principal stress for given case.

Hence, the orientation of the principal stresses in the *xy* plane can be shown as drawn in Fig. 4.4(b). The largest shear stress in the *xy* plane is ≈4 MPa. The maximum shear stress in this case acts in the plane oriented normal to the principal stress, σ_2. This shear stress has a value ≈5.7 MPa. All these stresses are read out from Mohr's circle in Fig. 4.4(a).

4.2 Strains

In an engineering context, the deformations are quantified in terms of strains. Analysis of metal forming operations requires familiarity with the *strain concept* and ability to compute strains. When a body deforms, the material particles that make up the body will be displaced. Strains are defined in terms of these displacements, excluding translations and rotations, which are rigid-body movements.

Consider two points *A* and *B* initially located a distance (i.e., a length) l_0 apart from each other in a solid body. Assume that the body deforms so that the distance between the points after deformation has changed to l, where $l \neq l_0$. A *nominal strain* is then defined from the change of distance between the points, by the expression

$$e = \frac{l - l_0}{l_0} = \frac{\Delta l}{l_0} \tag{4-11}$$

Alternatively, a *true strain*, also called the *natural*, or *logarithmic strain*, can be defined from the *strain increment* defined by

$$\mathrm{d}\varepsilon = \frac{\mathrm{d}l}{l} \tag{4-12}$$

By integration of this increment, the true strain is obtained as

$$\varepsilon = \int_{l_0}^{l} \mathrm{d}\varepsilon = \int_{l_0}^{l} \frac{\mathrm{d}l}{l} = \ln \frac{l}{l_0} \tag{4-13}$$

In the case of small deformations, as, for instance, elastic deformations in metals, the difference between the two strain definitions is small, i.e., nominal and true strain are approximately equal. But for large deformations, there is a significant difference between nominal and true strain; see Example 4.2.

True strains are additive, in contrast to nominal strains, which cannot be added; see Example 4.3. For a forming operation performed in successive stages, it is advantageous if true strains are used, because the total strains in the process then can be obtained as the sum of the strains in the individual stages. Another advantage is that one can compare deformations in compression and tension, because corresponding deformations in these two opposite deformation modes will have the same true strain value with the opposite sign; see Problem 4.1. Finally, when using true strains, the sum of the three normal strains in the plastically deforming object corresponds to the volume change of the object, which, for metals that exhibit volume constancy, will equal zero. To transform true strain into a corresponding nominal strain, or vice versa, the following expression can be used:

$$\varepsilon = \ln(1 + e) \tag{4-14}$$

EXAMPLE 4.2: DIFFERENCE BETWEEN NOMINAL AND TRUE STRAIN

Problem: Compute the ratio of true to nominal strain for the following true strain values:

$$e = 0.001, 0.01, 0.1, 0.5$$

Solution: True strains are computed from nominal strain values using eq. 4-14. The ratio between the two strains definitions can then be determined with the following result:

$$e = 0.001 \quad \Rightarrow \quad \frac{e}{\varepsilon} = 0.9995, \qquad e = 0.01 \quad \Rightarrow \quad \frac{e}{\varepsilon} = 0.995,$$
$$e = 0.1 \quad \Rightarrow \quad \frac{e}{\varepsilon} = 0.953, \qquad e = 0.5 \quad \Rightarrow \quad \frac{e}{\varepsilon} = 0.811$$

This shows that nominal and true strains are approximately equal for low strain values and that nominal strain is significantly larger than the true strain for large strains. So, in the case of elastic deformations, where $e \leq 0.01$, it does not make much difference whether strain is expressed as nominal or true strain.

EXAMPLE 4.3: TRUE STRAINS CAN BE ADDED

Problem: A rod with initial length $l_0 = 10$ cm is rolled down in three rolling steps. The length after each step is measured to be $l_1 = 12$ cm, $l_2 = 15$ cm, and $l_3 = 20$ cm, respectively. Compute average strains in each step and in the whole process. Apply both nominal and true strain definitions.

Solution:

	$e = \frac{l-l_0}{l_0} = \frac{\Delta l}{l_0}$,	$\varepsilon = \ln \frac{l}{l_0}$
Step 1:	$e_1 = \frac{2}{10} = 0.2$	$\varepsilon_1 = \ln \frac{l}{l_0} = \ln \frac{12}{10} = 0.18$
Step 2:	$e_2 = 0.25$	$\varepsilon_2 = 0.22$
Step 3:	$e_3 = 0.33$	$\varepsilon_3 = 0.29$
Whole process:	$e_{1-3} = 1.00$	$\varepsilon_{1-3} = 0.69$

From this, we see that $e_1 + e_2 + e_3 \neq e_{1-3}$ and $\varepsilon_1 + \varepsilon_2 + \varepsilon_3 = \varepsilon_{1-3}$. This clearly depicts that true strains are additive, i.e., they can be summed, but this is not the case for nominal strains.

4.2.1 Strains in General and in Plane Strain Compression

As described in Ch. 3, the plane strain state is characterized by straining in two of the three possible directions. Consider such a strain state where there is zero strain in the y direction; see Fig. 4.5. Assume an initial rectangular material element $ABCD$, which under the action of applied forces deforms to the final shape $A'B'C'D'$. The corner A of the element experiences a displacement given by the displacement components u and w during the deformation.

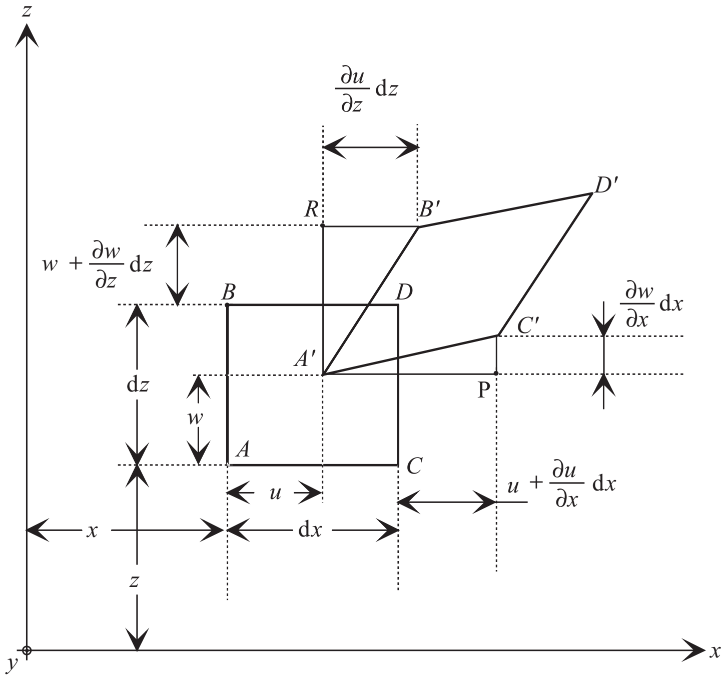
z
$\frac{\partial u}{\partial z}\,dz$
R
B'
D'
$w + \frac{\partial w}{\partial z}\,dz$
B
D
$\frac{\partial w}{\partial x}\,dx$
C'
A'
dz
P
w
A
C
$u + \frac{\partial u}{\partial x}\,dx$
u
x
dx
z
y
x

Figure 4.5. Deformation of material element in plane strain deformation.

The deformations of the body can be quantified by means of *nominal normal strains* and *shear strains*. These strains will be e_x, e_z, and $e_{xz} = e_{zx}$, of which the first is defined as follows:

$$e_x = d\varepsilon_x = \frac{A'C' - AC}{AC} = \frac{A'C'}{AC} - 1 \approx \frac{A'P}{AC} - 1 \tag{4-15}$$

Let us assume that the deformations are small, so that $A'P \approx A'C'$. As shown by eq. 4-15, this expression at the same time represents the strain increment in the case of small deformations. The normal strain can also be expressed as

$$e_x = \frac{\mathrm{d}x + (u + \frac{\partial u}{\partial x}\mathrm{d}x) - u}{\mathrm{d}x} - 1 = \frac{\partial u}{\partial x} \tag{4-16}$$

Using a corresponding approach, the other normal strain can be determined as

$$e_z = \frac{\partial w}{\partial z} \tag{4-17}$$

and the shear strain can be determined as

$$e_{xz} = e_{zx} = \frac{1}{2}\gamma_{xz} \tag{4-18}$$

where $\gamma_{xz} = \angle PA'C' + \angle RA'C'$. From Fig. 4.5, we can see that for small deformations $\angle PA'C'$ can be expressed as

$$\begin{aligned}\angle PA'C' &= \arctan\frac{PC'}{A'P'} = \arctan\frac{\frac{\partial w}{\partial x}\mathrm{d}x}{\mathrm{d}x + u + \frac{\partial u}{\partial x}\mathrm{d}x - u}\\ &= \arctan\frac{\frac{\partial w}{\partial x}}{1 + \frac{\partial u}{\partial x}} \approx \arctan\frac{\partial w}{\partial x} = \frac{\partial w}{\partial x}\end{aligned} \tag{4-19}$$

because $\partial u/\partial x \ll 1$. Correspondingly, it can be shown that $\angle RA'B' = \partial u/\partial z$. Hence, the shear strain can be expressed as

$$e_{xz} = e_{zx} = \frac{1}{2}\gamma_{xz} = \frac{1}{2}\left(\frac{\partial w}{\partial x} + \frac{\partial u}{\partial z}\right) \tag{4-20}$$

For the general three-dimensional case, there are three additional nominal strain components. Like the preceding strains, they can be determined as

$$e_y = \frac{\partial v}{\partial y} \tag{4-21}$$

$$e_{xy} = \frac{1}{2}\gamma_{xy} = \frac{1}{2}\left(\frac{\partial u}{\partial y} + \frac{\partial v}{\partial x}\right) \tag{4-22}$$

$$e_{yz} = \frac{1}{2}\gamma_{yz} = \frac{1}{2}\left(\frac{\partial v}{\partial z} + \frac{\partial w}{\partial y}\right) \tag{4-23}$$

Note that in the preceding treatment one applies two different definitions of shear strain, i.e., in one case the *engineering strain*, γ, and in the other case strain as the *tensor value*, $e = \gamma/2$.

4.2.3 Strain as a Tensor

Strains can be given in tensor notation corresponding to that for stresses. Then the shear strain must be defined by the tensor values specified in eqs. 4-16 and 4-17 and eqs. 4-20 to 4-23:

$$e_{ij} = \begin{bmatrix} e_{xx} & e_{yx} & e_{zx} \\ e_{xy} & e_{yy} & e_{xy} \\ e_{xz} & e_{yz} & e_{zz} \end{bmatrix} \tag{4-24}$$

When deformations are small, as in the case of elastic deformations, or when the strain increment $d\varepsilon$ is used, both nominal and true strains will be tensor quantities. Note that the strain tensor is analogous to the stress tensor; compare eq. 4-24 with eq. 4-6.

4.2.4 Analogy between Stress and Strain

Stresses and strains can both be expressed by similar tensors, and there are in addition a number of other similarities between them. For a strain state there is one, and only one, orientation of the coordinate system that causes shear strains to disappear, as was the case for a stress state. The strain state in which this occurs is called the principal strain state, analogous to the principal stress state, and the normal strains in this state are called *principal strains*. Moreover, the principal values of normal strains, and the orientation of the principal strain state, are determined by equations similar those for stress:

Principal strain (analog of eq. 4-8):

$$e_1, e_2 = \frac{1}{2}(e_x + e_y)^2 \pm \frac{1}{2}\left[(e_x - e_y)^2 + 4e_{xy}^2\right]^{1/2} \tag{4-25}$$

Maximum shear strain (analog of eq. 4-10):

$$e_{\max} = \frac{1}{2}\gamma_{\max} = \frac{1}{2}\left[(e_x - e_y)^2 + 4e_{xy}^2\right]^{1/2} \tag{4-26}$$

As for stresses, a Mohr's circle can be drawn for the plane strain state. This circle graphically displays the variation of strain values with orientation of the coordinate system, when rotated around its origin. In Mohr's circle, normal strains are plotted along the abscissa axis, and shear strains in terms of the tensor strain, $e = \frac{1}{2}\gamma$, along the ordinate axis. If the principal strains are known, for the case of plane strain, one can find from this circle the strain components in any arbitrary direction rotated by an angle θ relative to the plane of the principal stresses. This is done by use of the equations

$$e_x, e_y = \frac{1}{2}(e_1 + e_2) \pm \frac{1}{2}(e_1 - e_2)\cos 2\theta \tag{4-27}$$

$$\gamma_{xy} = (e_1 - e_2)\sin 2\theta \tag{4-28}$$

In the case of *isotropic materials*, the plane of principal stresses and the plane of principal strains are coincident. This means that, for a given state of stress, principal stresses and strains have the same orientation.

EXAMPLE 4.4: PRINCIPAL STRAIN STATE IN THE PARTICULAR CASE OF PLANE STRAIN

Problem: Assume that a plate of aluminum is an elastic stress where $\sigma_x = 10$, $\sigma_y = 5$, $\tau_{xy} = 3$ and where $\sigma_z = \tau_{zx} = \tau_{zy} = 0$ (in MPa). Determine the principal strains and the maximum shear strain in the *xy* plane. The following material data are given: $E = 79000$ MPa, $\nu = 0.3$, $G = \frac{E}{2(1+\nu)}$. Note that this case was analyzed in Example 4.1 to determine principal stresses.

Solution: First, we find the strain components for the given stress state by means of Hooke's law, eq. 4-56:

$$e_x = \frac{1}{E}\left[\sigma_x - \nu(\sigma_y + \sigma_z)\right] = \frac{1}{79000}\left[10 - 0.3\,(5+0)\right] = 1.1 \times 10^{-4}$$

$$e_y = \frac{1}{E}\left[\sigma_y - \nu(\sigma_x + \sigma_z)\right] = \frac{1}{79000}\left[5 - 0.3\,(10+0)\right] = 0.25 \times 10^{-4}$$

$$e_{xy} = \frac{1}{2}\gamma_{xy} = \frac{\tau_{xy}}{2G} = \frac{1+\nu}{E}\tau_{xy} = \frac{(1+0.3)}{79000}3 = 0.5 \times 10^{-4}$$

Thereafter, principal strains and largest shear strain in the *xy* plane can be determined from the Mohr's strain circle; see

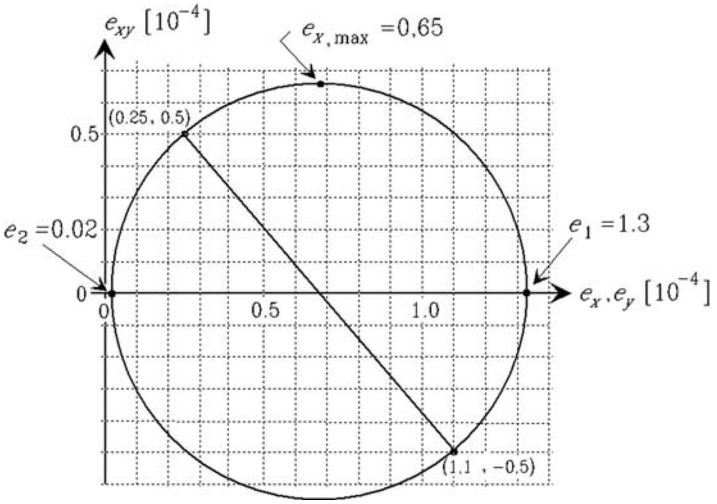

4.3 Elements of the Theory of Plasticity

4.3.1 Constancy of Volume during Plastic Deformation

It can be shown (see Problem 4.2) that, if a material maintains constant volume during plastic deformations, the volume strain must be zero, and that fact can be

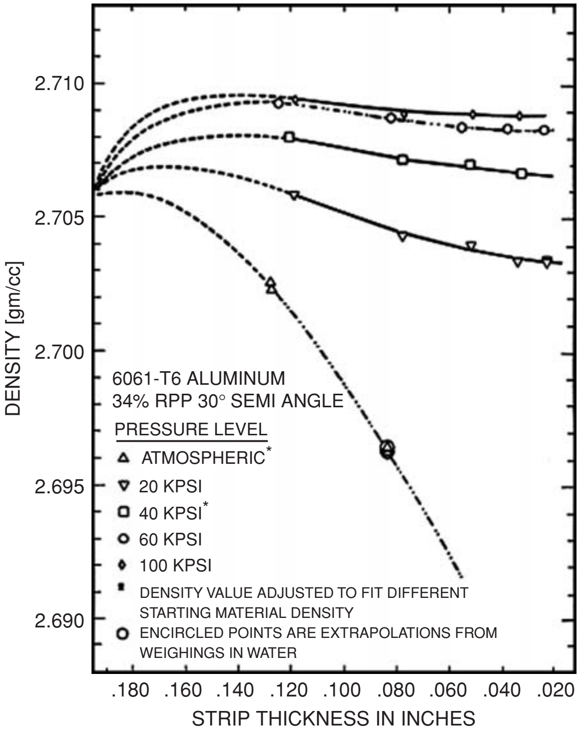

Figure 4.6. Volume change during drawing of an Al alloy. (Reprinted with permission from ASM International.)

expressed in the following way:

$$\ln\left(\frac{V}{V_0}\right) = \varepsilon_x + \varepsilon_y + \varepsilon_z = 0 \tag{4-29}$$

Experiments show that the volume of nonporous metals is maintained approximately constant when such metals are deformed plastically. However, accurate measurements show that this is only an approximation.[5] In reality, the volume of a metal increases slightly during forming under tensile stress and decreases slightly during forming under compression. The increase in volume is thought to be caused by generation and growth of pores in the metal, and the corresponding decrease by compression of pores.

In Fig. 4.6, results are shown from experiments in which density changes were measured with great accuracy in a metal during strip drawing, under various levels of hydrostatic pressure. As this figure depicts, the density of the metal investigated was reduced slightly ($<0.5\%$) in the drawing operations, but the assumption of *constancy of volume* still was approximately true.

EXAMPLE 4.5: STRAINS IN UNIAXIAL TENSION FROM VOLUME CONSTANCY

Problem: A material is subjected to a permanent plastic strain ε_x in uniaxial tension. Determine the two other axial strains, and the principal strains, in this material.

Solution: When the specimen is stretched to a strain ε_x in one direction, it will contract correspondingly in the two other axial directions, so that $\varepsilon_y = \varepsilon_z$.

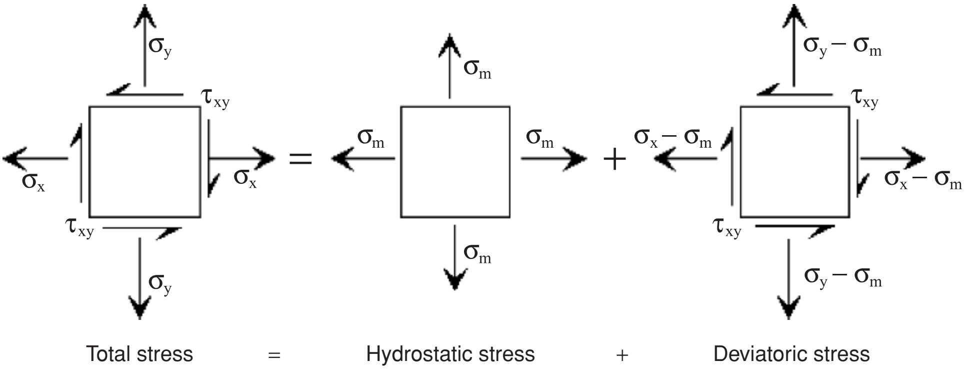

Figure 4.7. Sketch showing stress state partitioned into hydrostatic and deviatoric parts.

Because of constancy of volume, the following expression must be valid: $\varepsilon_x + \varepsilon_y + \varepsilon_z = 0 = \varepsilon_x + 2\varepsilon_y \;\Rightarrow\; \underline{\underline{\varepsilon_y = \varepsilon_z = -\frac{1}{2}\varepsilon_x}}$.

Because there are no shear deformations, these strains must concurrently be the principal strains, so that

$$\underline{\underline{\varepsilon_x = \varepsilon_1}}, \qquad \underline{\underline{\varepsilon_2 = \varepsilon_3}} = \varepsilon_y = \varepsilon_z = -\frac{1}{2}\varepsilon_x = \underline{\underline{-\frac{1}{2}\varepsilon_1}}$$

4.3.2 Hydrostatic and Deviatoric Stress and Strain

In plasticity theory, it is shown that it is convenient to split a stress state into two parts, a *deviatoric stress* and a *hydrostatic stress*. The hydrostatic stress is also often termed the *mean stress*.

By means of experiments, it has been shown that whether a body deforms plastically or not does not depend on the hydrostatic stress. Instead, the deviatoric stress represents the part of the stress state that contributes to plastic deformations. In Fig. 4.7, this relationship is illustrated schematically. The hydrostatic stress is defined as the *mean normal stress* by the following expression:

$$\sigma_m = \frac{\sigma_x + \sigma_y + \sigma_z}{3} \tag{4-30}$$

The deviatoric stress can be expressed as

$$\sigma_d = \begin{bmatrix} \sigma_x - \sigma_m & \tau_{yx} & \tau_{zx} \\ \tau_{xy} & \sigma_y - \sigma_m & \tau_{zy} \\ \tau_{xz} & \tau_{yz} & \sigma_z - \sigma_m \end{bmatrix}$$

$$= \begin{bmatrix} \dfrac{2\sigma_x - \sigma_y - \sigma_z}{3} & \tau_{yx} & \tau_{zx} \\ \tau_{xy} & \dfrac{2\sigma_y - \sigma_z - \sigma_x}{3} & \tau_{zy} \\ \tau_{xz} & \tau_{yz} & \dfrac{2\sigma_z - \sigma_x - \sigma_y}{3} \end{bmatrix} \tag{4-31}$$

In view of the analogy between stresses and strains, the strain state can also be partitioned in two parts, one part that contributes to volume change, called the *hydrostatic strain*, or *mean strain*, and another part, called the *deviatoric strain*, that causes change of shape of the strained body. Corresponding to eqs. 4-30 and 4-31, the nominal hydrostatic and the nominal deviatoric strains are given as

$$e_m = \frac{e_x + e_y + e_z}{3} \tag{4-32}$$

$$e_d = \begin{bmatrix} e_x - e_m & e_{yx} & e_{zx} \\ e_{xy} & e_y - e_m & e_{zy} \\ e_{xz} & e_{yz} & e_z - e_m \end{bmatrix} = \begin{bmatrix} \dfrac{2e_x - e_y - e_z}{3} & e_{yx} & e_{zx} \\ e_{xy} & \dfrac{e_y - e_z - e_x}{3} & e_{zy} \\ e_{xz} & e_{yz} & \dfrac{2e_z - e_x - e_y}{3} \end{bmatrix} \tag{4-33}$$

In these equations, the nominal values of the strain components are used, but alternatively they can be replaced by true strain values.

EXAMPLE 4.6: EFFECT OF INCREASED HYDROSTATIC STRESS ON PLASTIC YIELD

Problem: A stress condition characterized by the principal stresses $\sigma_1 = 80$, $\sigma_2 = 45$, $\sigma_3 = -30$ MPa does not cause plastic deformation in a particular material. What happens if this material in addition is exposed to a fluid pressure of 50 MPa?

Solution: The diameters of the Mohr's circles for the initial stress condition (see unnumbered figure), are

$$d_1 = \sigma_1 - \sigma_2 = 80 - 45 = 35, \qquad d_2 = \sigma_2 - \sigma_3 = 45 - (-30) = 75,$$
$$d_3 = \sigma_1 - \sigma_3 = 80 - (-30) = 110$$

The principal stresses for the pressurized condition are

$$\begin{aligned} \sigma_{1,\mathrm{pr}} &= \sigma_1 - 50 = 80 - 50 = 30 \\ \sigma_{2,\mathrm{pr}} &= \sigma_2 - 50 = 45 - 50 = -5 \\ \sigma_{3,\mathrm{pr}} &= \sigma_3 - 50 = -30 - 50 = -80 \end{aligned}$$

From the pressurized principal stresses, the new diameters of the Mohr's circles are determined as

$$\begin{aligned} d_{1,\mathrm{pr}} &= \sigma_{1,\mathrm{pr}} - \sigma_{2,\mathrm{pr}} = 30 - (-5) = 35 \\ d_{2,\mathrm{pr}} &= \sigma_{2,\mathrm{pr}} - \sigma_{3,\mathrm{pr}} = -5 - (-80) = 75 \\ d_{3,\mathrm{pr}} &= \sigma_{1,\mathrm{pr}} - \sigma_{3,\mathrm{pr}} = 30 - (-80) = 110 \end{aligned}$$

In the accompanying figure Mohr's circles for these two conditions are drawn. The figure depicts that adding a hydrostatic pressure only displaces the circles toward the right, so that the situation with regard to plastic yield does not change. Hence, the material will not start to yield because of the added fluid pressure.

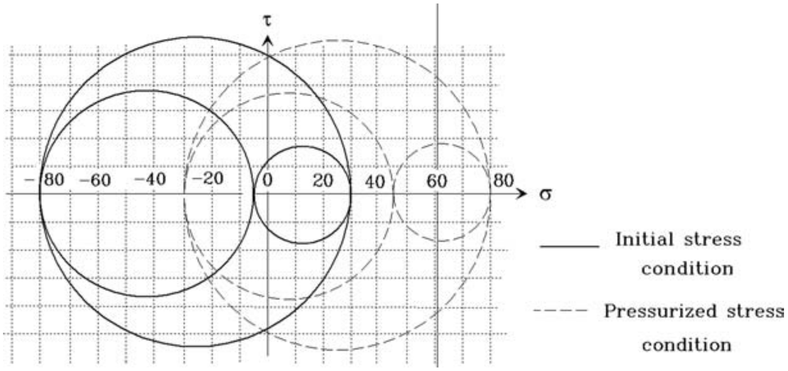

4.3.3 Strain Rate

Strain rate is the time derivative of strain. For nominal and true strains, it can be expressed by the equations

$$\dot{e} = \frac{\mathrm{d}e}{\mathrm{d}t} \tag{4-34}$$

or

$$\dot{\varepsilon} = \frac{\mathrm{d}\varepsilon}{\mathrm{d}t} \tag{4-35}$$

Like the strain, the strain rate can be expressed in tensor notation, by the equation

$$\dot{e} = \begin{bmatrix} \dot{e}_{xx} & \dot{e}_{yx} & \dot{e}_{zx} \\ \dot{e}_{xy} & \dot{e}_{yy} & \dot{e}_{zy} \\ \dot{e}_{xz} & \dot{e}_{yz} & \dot{e}_{zz} \end{bmatrix} \tag{4-36}$$

4.3.4 Effective Values of Stress, Strain, and Strain Rate

Effective, or *equivalent, values* of stress, strain, and strain rate are common terms in the theory of plasticity. These should be considered as resultant values that incorporate the total effect of all stress, strain, or strain rate components acting on a volume element of the material. It is convenient to define such effective values because then two different states of stress, strain, or strain rate can be compared by means of the effective value, instead of trying to compare all components separately. For the general state of stress, strain, or strain rate, these effective values are defined as follows:

Effective stress:

$$\bar{\sigma} = \frac{1}{\sqrt{2}}\left[(\sigma_x - \sigma_y)^2 + (\sigma_y - \sigma_z)^2 + (\sigma_z - \sigma_x)^2 + 6\left(\tau_{xy}^2 + \tau_{yz}^2 + \tau_{xz}^2\right)\right]^{1/2} \qquad (4\text{-}37)$$

Effective strain:

$$\bar{\varepsilon} = \left\{\frac{2}{3}\left[\varepsilon_x^2 + \varepsilon_y^2 + \varepsilon_z^2 + 2\left(\varepsilon_{xy}^2 + \varepsilon_{yz}^2 + \varepsilon_{zx}^2\right)\right]\right\}^{1/2} \qquad (4\text{-}38)$$

Effective strain rate:

$$\dot{\bar{\varepsilon}} = \left\{\frac{2}{3}\left[\dot{\varepsilon}_x^2 + \dot{\varepsilon}_y^2 + \dot{\varepsilon}_z^2 + 2\left(\dot{\varepsilon}_{xy}^2 + \dot{\varepsilon}_{yz}^2 + \dot{\varepsilon}_{zx}^2\right)\right]\right\}^{1/2} \qquad (4\text{-}39)$$

Often eq. 4-38 and eq. 4-39 are expressed as strain or strain-rate increments ($d\bar{\varepsilon}$, $d\dot{\bar{\varepsilon}}$), instead of strains ($\bar{\varepsilon}$, $\dot{\bar{\varepsilon}}$), to show that they evolve after the end of the initial elastic deformation. For large plastic deformations, however, elastic deformations are negligible in comparison with plastic deformations, and their contributions can be neglected.

The flow curve obtained for an arbitrary complex deformation condition, when plotted as effective stress versus effective strain, will equal the flow curve obtained in uniaxial tension.

EXAMPLE 4.7: EFFECTIVE STRAIN VALUE IN SHEETMETAL FORMING

Problem: Consider a circle with 5 mm initial diameter applied on the surface of the workpiece in a sheet-metal forming operation. After forming, the circle has deformed into an ellipse, with major and minor axes measured to be 6.5 mm and 5.5 mm, respectively. Determine the effective strain in this forming operation at the location of the circle.

Solution: The two principal strains in the plane of the plate can be calculated from the change in the diameter of the circle during the forming operation:

$$\varepsilon_1 = \ln\frac{d_{\max}}{d_0} = \ln\frac{6.5}{5} = 0.26 \quad \text{and} \quad \varepsilon_2 = \ln\frac{d_{\min}}{d_0} = \ln\frac{5.5}{5} = 0.1$$

The third principal strain, in the thickness direction of the sheet, is obtained from the following relationship, deduced on the basis of the assumption of constancy of volume:

$$\begin{gathered}\varepsilon_x + \varepsilon_y + \varepsilon_z = 0 = \varepsilon_1 + \varepsilon_2 + \varepsilon_3 = 0.26 + 0.1 + \varepsilon_3 \\ \Rightarrow \quad \varepsilon_3 = -(\varepsilon_1 + \varepsilon_2) = -0.36\end{gathered}$$

The effective strain can now be determined by use of eq. 4-38:

$$\bar{\varepsilon} = \left\{\frac{2}{3}\left[\varepsilon_{1^2} + \varepsilon_2^2 + \varepsilon_3^2\right]\right\}^{1/2} = \left\{\frac{2}{3}\left[0.26^2 + 0.1^2 + (-0.36)^2\right]\right\}^{1/2} = \underline{\underline{0.37}}$$

EXAMPLE 4.8: EFFECTIVE STRESS IN THE PLANE STRESS CASE

Problem: A state of plane stress is considered, in which the stresses are as follows: $\sigma_x = \sigma_1 = 2\sigma_2$ and $\sigma_3 = 0$. Determine the effective stress in this case.

Solution: The effective stress is determined by use of eq. 4-37:

$$\bar{\sigma} = \frac{1}{\sqrt{2}}\left[\left(\sigma_1 - \frac{\sigma_1}{2}\right)^2 + \left(\frac{\sigma_1}{2}\right)^2 + (-\sigma_1)^2\right]^{1/2} = \frac{\sqrt{3}}{2}\sigma_1$$

4.3.5 Energy Dissipation

Consider elastic stretching of a tensile test specimen up to a strain of ε_x. The energy required in this stretching operation can be expressed as

$$W = \int_0^{\varepsilon_x} \mathrm{d}W = \int_0^{\varepsilon_x} F\,\mathrm{d}l = \int_0^{\varepsilon_x} \sigma_x A\,\mathrm{d}l = V\int_0^{\varepsilon_x} \sigma_x \frac{\mathrm{d}l}{l} = V\int_0^{\varepsilon_x} \sigma_x\,\mathrm{d}\varepsilon_x \tag{4-40}$$

When the loads are removed from this specimen, this elastic energy will be released again. The *energy dissipation*, i.e., the applied energy per unit of volume of material, hence can be expressed as

$$U = \frac{W}{V} = \int_0^{\varepsilon_x} \sigma_x\,\mathrm{d}\varepsilon_x \tag{4-41}$$

In the case of elastic deformations only, this energy dissipation can alternatively be expressed as

$$U = \int_0^{\varepsilon_x} E\varepsilon_x\,\mathrm{d}\varepsilon_x = \frac{1}{2}E\varepsilon_x^2 = \frac{1}{2}\sigma_x\varepsilon_x \tag{4-42}$$

During loading of a specimen up to a general complex elastic stress state, all stress components contribute to energy consumption. Then the applied energy per unit of volume of material can be expressed as

$$U = \frac{1}{2}(\sigma_x\varepsilon_x + \sigma_y\varepsilon_y + \sigma_z\varepsilon_z + 2\tau_{xy}\varepsilon_{xy} + 2\tau_{yz}\varepsilon_{yz} + 2\tau_{zx}\varepsilon_{zx}) \tag{4-43}$$

The energy consumption per unit of volume, during uniaxial stretching of a tensile test specimen from initial plastic strain ε_a up to final strain ε_b, can be expressed as

$$U = \int_{\varepsilon_a}^{\varepsilon_b} \sigma_x\,\mathrm{d}\varepsilon_x \tag{4-44}$$

When loading upto a general stress state, all stress components contribute to energy consumption. The dissipated energy per unit of volume, then, in infinitesimal form, is

$$\mathrm{d}U = \sigma_x\,\mathrm{d}\varepsilon_x + \sigma_y\,\mathrm{d}\varepsilon_y + \sigma_z\,\mathrm{d}\varepsilon_z + 2\tau_{xy}\,\mathrm{d}\varepsilon_{xy} + 2\tau_{yz}\,\mathrm{d}\varepsilon_{yz} + 2\tau_{zx}\,\mathrm{d}\varepsilon_{zx} \tag{4-45}$$

Integration of this expression over the added plastic strain region yields the energy consumption per unit of volume due to plastic deformations. Alternatively, this energy dissipation can be expressed in terms of effective stress and strain values by

$$U = \int_{\varepsilon_a}^{\varepsilon_b} \bar{\sigma}\,\mathrm{d}\bar{\varepsilon} \tag{4-46}$$

The dissipated energy per unit of volume and unit of time, i.e., the applied power, can finally be computed by the equation

$$\mathrm{d}\dot{U} = \sigma_x\,\mathrm{d}\dot{\varepsilon}_x + \sigma_y\,\mathrm{d}\dot{\varepsilon}_y + \sigma_z\,\mathrm{d}\dot{\varepsilon}_z + 2\tau_{xy}\,\mathrm{d}\dot{\varepsilon}_{xy} + 2\tau_{yz}\,\mathrm{d}\dot{\varepsilon}_{yz} + 2\tau_{zx}\,\mathrm{d}\dot{\varepsilon}_{zx} \tag{4-47}$$

4.3.6 Yield Criteria

A body subjected to elastic stresses will return to its initial shape upon unloading. On the other hand, a body deformed plastically will change shape permanently. To initiate plastic deformation in a body loaded in uniaxial tension or compression, it is required to subject the body to a tensile or a compressive stress equal to the *flow stress* of the material. When the stress exceeds the flow stress, some permanent shape change will remain after unloading.

So for a uniaxial stress state it is easy to determine when the material will start to deform plastically. However, if the body is subjected to a complex stress state, it is no longer straightforward to predict when deformations will become plastic. To be able to predict the onset of plastic flow for stress states other than uniaxial tension, various *yield criteria* have been developed.

A *yield criterion* for a general state of stress is commonly expressed as follows:

$$f(\sigma_x, \sigma_y, \sigma_z, \tau_{xy}, \tau_{yz}, \tau_{zx}) = \text{constant} = C \tag{4-48}$$

Alternatively, it may be formulated by the use of principal stresses:

$$f(\sigma_1, \sigma_2, \sigma_3) = \text{constant} = C \tag{4-49}$$

Equations 4-48 and 4-49 state that onset of plastic yield is determined by a function that includes all stress components – or, alternatively, the principal stresses in the actual stress state. Furthermore, these equations state that the onset of plastic yield occurs when this function reaches a certain critical value C.

If we assume that the onset of plastic yield is independent of hydrostatic stress, and only is influenced by the deviatoric stress, eq. 4-49 can be modified to give the following expression:

$$f\,(\sigma_1 - \sigma_2, \sigma_2 - \sigma_3, \sigma_3 - \sigma_1) = C \tag{4-50}$$

This equation expresses that onset of plastic yield is only dependent on the diameter (i.e., the size) of Mohr's circle for the actual stress state and not the location of the circle; see Example 4.6. Two stress states with the same deviatoric stress but different hydrostatic stress will behave identically with respect to the onset of plastic yield.

There are two commonly used yield criteria for isotropic materials, namely, the *Tresca yield criterion*[6] *and the von Mises yield criterion.*[7] The Tresca yield criterion, also called the *shear stress criterion*, states that onset of plastic yield occurs when the maximum shear stress in the material reaches a critical level. From Example 4.1, we see that the maximum shear stress equals the radius of the largest Mohr's circle of the stress state, i.e.,

$$\tau_{\max} = \frac{\sigma_{\max} - \sigma_{\min}}{2} = \frac{\sigma_1 - \sigma_3}{2} = C \tag{4-51}$$

The numerical value of the constant C can either be determined by consideration of the stress state in uniaxial tension, or the stress state in pure shear. When this is done the Tresca yield criterion can be expressed as follows:

$$\tau_{\max} = \frac{\sigma_1 - \sigma_3}{2} = \frac{\sigma_0}{2} = k \tag{4-52}$$

Here σ_0 is the yield stress of the material in uniaxial tension, and k the shear flow stress of the material in pure shear.

The other yield criterion, the von Mises criterion, states that onset of plastic yield occurs when the second invariant of the deviatoric stress reaches the critical value C. This is equivalent to stating that the effective stress value (see eq. 4-37) should reach a critical value. Hence the von Mises criterion can be expressed as

$$\bar{\sigma} = \frac{1}{\sqrt{2}}\left[(\sigma_x - \sigma_y)^2 + (\sigma_y - \sigma_z)^2 + (\sigma_z - \sigma_x)^2 + 6\left(\tau_{xy}^2 + \tau_{yz}^2 + \tau_{xz}^2\right)\right]^{1/2} = C \tag{4-53}$$

Alternatively it can be expressed in terms of principal stresses:

$$\bar{\sigma} = \frac{1}{\sqrt{2}}\left[(\sigma_1 - \sigma_2)^2 + (\sigma_2 - \sigma_3)^2 + (\sigma_3 - \sigma_1)^2\right]^{1/2} = C \tag{4-54}$$

The constant C can be determined by consideration of the simple stress states of uniaxial tension and pure shear; see Example 4.9 and Example 4.10. After this, the von Mises criterion can be expressed as

$$\bar{\sigma} = \frac{1}{\sqrt{2}}\left[(\sigma_x - \sigma_y)^2 + (\sigma_y - \sigma_z)^2 + (\sigma_z - \sigma_x)^2 + 6\left(\tau_{xy}^2 + \tau_{yz}^2 + \tau_{xz}^2\right)\right]^{1/2} = \sigma_0 = k\sqrt{3} \tag{4-55}$$

Note that because the von Mises criterion is expressed in terms of the differences between the normal stress components ($\sigma_x - \sigma_y$, etc.), this criterion is independent of hydrostatic stress. Moreover, because all stress components appear inside squared expressions, it is not required to consider the sign of the stress components, i.e., whether they are positive or negative. Sometimes the von Mises criterion gives better agreement with experimental results than the Tresca criterion.

To visualize the different yield criteria, they can be plotted in a triaxial coordinate system, with the three principal stresses added along each of the three orthogonal axes; see Fig. 4.8. When presented this way, the critical conditions causing onset of plastic yield will appear as a three-dimensional surface. For stress states inside the surface, there will be elastic deformations only, but if a principal stress component

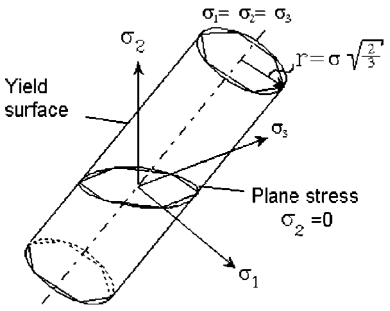

Figure 4.8. Tresca and von Mises yield criteria expressed in the three-dimensional principal stress space.

is increased so that the stress state $(\sigma_1, \sigma_2, \sigma_3)$ touches the yield surface, there will be plastic yield in the material.

In a section cut through the three-dimensional stress space, defined by $\sigma_1 = \sigma_2 = \sigma_3$, the von Mises criterion will appear as a circle with radius $\sigma_0\sqrt{\frac{2}{3}}$, whereas the Tresca yield criterion will appear as a prism: see the top portion of the yield surface shown in Fig. 4.8. Alternatively, the two criteria can be plotted in a two-dimensional graph if one principal stress is constant. Such a graph is sketched in Fig. 4.8 and in Fig. 7.13. When presented this way, the von Mises criterion appears as an ellipse, whereas the Tresca criterion appears as a polygon inside the ellipse. In Fig. 7.13, the common stress states in different technological tests are shown.

EXAMPLE 4.9: VON MISES YIELD CRITERION IN CASE OF UNIAXIAL STRESS

Problem: Determine the constant C in eq. 4-53 in the case of uniaxial tension.

Solution: In uniaxial tension, we have $\sigma_1 = \sigma_x$, $\sigma_3 = 0$. Introduced into eq. 4-53, this yields

$$\bar{\sigma} = \frac{1}{\sqrt{2}}\left[(\sigma_x)^2 + (-\sigma_x)^2\right]^{1/2} = C$$

A specimen loaded in uniaxial tension will start to yield when the axial stress reaches the flow stress of the material σ_0:

$$\frac{1}{\sqrt{2}}\left[(\sigma_x)^2 + (-\sigma_x)^2\right]^{1/2} = \sigma_x = C = \sigma_0$$

and the yield criterion becomes

$$\bar{\sigma} = \frac{1}{\sqrt{2}}\left[(\sigma_x - \sigma_y)^2 + (\sigma_y - \sigma_z)^2 + (\sigma_z - \sigma_x)^2 + 6\left(\tau_{xy}^2 + \tau_{yz}^2 + \tau_{xz}^2\right)\right]^{1/2} = \sigma_0$$

EXAMPLE 4.10: VON MISES YIELD CRITERION IN PURE SHEAR

Problem: Determine the constant C in eq. 4-53 if deformations are characterized by pure shear.

Solution: In pure shear, the stresses are $\sigma_x = \sigma_y = \sigma_z = \tau_{xz} = \tau_{yz} = 0$. In addition, we know that onset of yield is characterized by $\tau_{xy} = k$. These conditions introduced into eq. 4-53 yield

$$\bar{\sigma} = \frac{1}{\sqrt{2}}\left[6\tau_{xy}^2\right]^{1/2} = \sqrt{3}\cdot\tau_{xy} = \sqrt{3}\cdot k = C \quad \Rightarrow \quad C = \sqrt{3}\cdot k$$

4.3.7 The Flow Rule

In the case of elastic deformation, *Hooke's law* describes the relationship between stresses and strains. In the general stress state, the principal strain arising as a consequence of present stresses when determined by this law is given by the expression

$$e_1 = \frac{1}{E}\left[\sigma_1 - \nu(\sigma_2 + \sigma_3)\right] \tag{4-56}$$

and corresponding expressions for the other principal elastic strains.

In the case of plastic deformation, plastic strains are related to present stresses in a similar way. The law that describes the relationship between stresses and strains in the plastic state is commonly called the flow rule, or the *Lévy*[7]*–Mises*[8] flow rule, after the scientists who first proposed it. A common formulation of the flow rule is

$$\frac{\mathrm{d}\varepsilon_1}{\sigma_1'} = \frac{\mathrm{d}\varepsilon_2}{\sigma_2'} = \frac{\mathrm{d}\varepsilon_3}{\sigma_3'} = \mathrm{d}\lambda \tag{4-57}$$

or, alternatively,

$$\mathrm{d}\varepsilon_1 = \frac{\mathrm{d}\bar{\varepsilon}}{\bar{\sigma}}\left(\sigma_1 - \frac{1}{2}(\sigma_2 + \sigma_3)\right) \tag{4-58}$$

$$\mathrm{d}\varepsilon_2 = \frac{\mathrm{d}\bar{\varepsilon}}{\bar{\sigma}}\left(\sigma_2 - \frac{1}{2}(\sigma_3 + \sigma_1)\right) \tag{4-59}$$

$$\mathrm{d}\varepsilon_3 = \frac{\mathrm{d}\bar{\varepsilon}}{\bar{\sigma}}\left(\sigma_3 - \frac{1}{2}(\sigma_1 + \sigma_2)\right) \tag{4-60}$$

In this latter formulation, we see similarity with Hooke's law: The constant ν in Hooke's law is replaced by $\frac{1}{2}$ in the flow rule. In addition, the constant $1/E$ is replaced by the ratio $d\bar{\varepsilon}/\bar{\sigma}$, whose value changes as deformation proceeds. However, this ratio is always positive, because the effective plastic strain increment and the effective stress are always positive; see the definition of these parameters, eqs. 4-37–4-38.

EXAMPLE 4.11: LÉVY–MISES FLOW RULE USED TO COMPUTE STRESSES IN PLANE STRAIN COMPRESSION AND IN PLANE STRESS

Problem: A material with a constant flow stress σ_0 is deformed up to a permanent plastic deformation ε_x in:

(i) plane compression with $\sigma_3 = 0$,
(ii) deformation with stress characterized by $\sigma_x = \sigma_1 = 2\sigma_2$ and $\sigma_3 = 0$.

Determine the principal stresses in case (i) and the principal strains in case (ii).

Solution:

(i) Plane strain compression: In this case, the strain in the z-direction is $\varepsilon_z = \varepsilon_2 = 0$. Constancy of volume gives $\varepsilon_x = \varepsilon_3 = \varepsilon_{x,a} = -\varepsilon_y = -\varepsilon_1$. The principal stress in the x-direction is $\underline{\underline{\sigma_3 = 0}}$. When the principal strains are known, the principal stresses can be determined by means of the Lévy–Mises flow rule, eq. 4-59, as

$$\mathrm{d}\varepsilon_2 = \frac{\mathrm{d}\bar{\varepsilon}}{\bar{\sigma}}\left[\sigma_2 - \frac{1}{2}(\sigma_1 + \sigma_3)\right] = 0 \quad \Rightarrow \quad \underline{\underline{\sigma_2}} = \frac{1}{2}(\sigma_1 + \sigma_3) = \frac{1}{2}(\sigma_1 + 0) = \underline{\underline{\frac{1}{2}\sigma_1}}$$

(ii) From the given principal stresses, the principal strains can now be determined by use of the Lévy–Mises flow rule, eqs. 4-58–4-60:

$$\mathrm{d}\varepsilon_1 = \frac{\mathrm{d}\bar{\varepsilon}}{\bar{\sigma}}\left[\sigma_1 - \frac{1}{2}(\sigma_2 + \sigma_3)\right] = \frac{\mathrm{d}\bar{\varepsilon}}{\bar{\sigma}}\left[\sigma_1 - \frac{1}{2}\left(\frac{\sigma_1}{2}\right)\right] = \frac{\mathrm{d}\bar{\varepsilon}}{\bar{\sigma}} \cdot \frac{3\sigma_1}{4}$$

$$\mathrm{d}\varepsilon_2 = \frac{\mathrm{d}\bar{\varepsilon}}{\bar{\sigma}}\left[\sigma_2 - \frac{1}{2}(\sigma_1 + \sigma_3)\right] = \frac{\mathrm{d}\bar{\varepsilon}}{\bar{\sigma}}\left[\frac{\sigma_1}{2} - \frac{1}{2}(\sigma_1)\right] = 0 \quad \Rightarrow \quad \underline{\underline{\varepsilon_2 = 0, \quad \varepsilon_1 = -\varepsilon_3}}$$

$$\mathrm{d}\varepsilon_3 = \frac{\mathrm{d}\bar{\varepsilon}}{\bar{\sigma}}\left[\sigma_3 - \frac{1}{2}(\sigma_2 + \sigma_1)\right] = \frac{\mathrm{d}\bar{\varepsilon}}{\bar{\sigma}}\left[0 - \frac{1}{2}\left(\frac{\sigma_1}{2} + \sigma_1\right)\right] = \frac{\mathrm{d}\bar{\varepsilon}}{\bar{\sigma}}\left(-\frac{3\sigma_1}{4}\right)$$

Problems

4.1 A tensile test specimen with initial gauge length l_0 is stretched uniformly to a new permanent length $l = 2l_0$. A cylinder of the same height as the length of the tensile test specimen is compressed to a final height of $l = 0.5l_0$. Compute the nominal and true strains for these two opposite deformations, and comment on the result.

4.2 A rectangular slab with dimensions l_0, w_0, and t_0 is deformed to new dimensions l_1, w_1, and t_1. Determine the true volume strain in terms of $\ln(V/V_0)$, where V_0 and V denote the initial and final volumes of the slab, respectively. What does this volume strain imply for a material that is incompressible upon plastic deformations, like a metal?

4.3 A metal plate of $t = 0.9$ mm thickness has large width in relation to the thickness. It is bent to a radius of curvature of 150 mm as shown in the figure below.

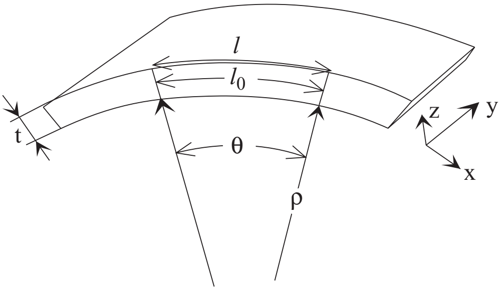

The following assumptions are made for the bend: there is a state of plane strain, deformations are elastic, and the stress in the width direction is zero. The plate is made of steel with $E = 200000$ MPa and $\nu = 0.33$. Determine the stress state on the outer side of the bend.

4.4 Consider frictionless plane strain compression under conditions of homogeneous deformation. Determine the following quantities: stress and strain tensor, principal stresses, principal strains, hydrostatic stress, deviatoric stress, effective stress, and effective strain.

4.5 A material with constant flow stress σ_0 is deformed up to a plastic strain ε_x in:

(a) uniaxial tension;
(b) plane strain compression, where $\sigma_3 = 0$.

The material is also:

(c) deformed to a plane stress state characterized by $\sigma_x = \sigma_1 = 2\sigma_2$ and $\sigma_3 = 0$.

Compute the energy dissipation per unit of volume during these deformation processes, using eqs. 4-44 and 4-46.

4.6 A thin-walled tube with closed ends is pressurized up to an internal pressure of 50 MPa. The average radius of the tube is 40 mm, and the tube is not to start yielding.

(a) Assume the tube material to have a flow stress of 280 MPa. Determine the smallest acceptable tube wall thickness based on the Tresca yield criterion.
(b) Assume the tube material to have a shear flow stress of 130 MPa. Determine the smallest acceptable tube wall thickness based on the Tresca yield criterion.

Stresses in closed tube: $\sigma_1 = pr/t$ (tangential), $\sigma_2 = pr/2t$ (axial), and $\sigma_3 \approx 0$ (radial).

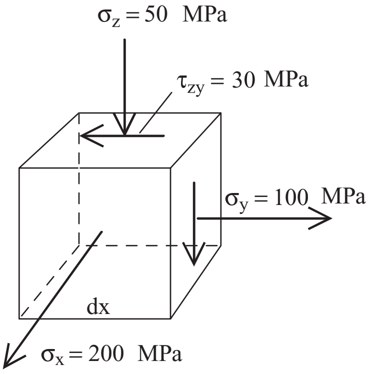

4.7 A body is loaded with the stress condition specified in the figure above.

(a) The body consists of a material with flow stress $\sigma_0 = 500$ MPa. Will the component deform plastically because of those stresses?

(b) Assume all stress components to be maintained, except for the stress in the x-direction, which is varied. Calculate the level of this stress component upon onset of yielding of the material.

4.8 Consider that a circle grid analysis has been performed on a piece of sheet metal as described in Example 4.7. Determine the stress ratio $\sigma_1/\bar{\sigma}$ during the forming operation at the location of the deforming circle. Assume that the z-axis points in the thickness direction of the plate and that there is plane stress characterized by $\sigma_z = \tau_{yz} = \tau_{zx} = 0$. Assume also the ratio $\alpha = \sigma_2/\sigma_1$ to remain constant during the test.

4.9 Show the validity of eq. 4-57, i.e., the flow rule, in the case of uniaxial tension.

4.10 The geometry of a thin-walled Al tube is characterized by a ratio $r/t = 20$, where r is the radius and t the thickness of the tube. Assume that the tube is closed at the ends and is pressurized up to the inner pressure $p = 6.9$ MPa, where it yields plastically. What will be the plastic strain in the tube in the tangential direction, i.e., along its circumference, if one neglects elastic deformations? The flow curve of the material is given by $\bar{\sigma}$ (MPa) $= 172.4(\bar{\varepsilon})^{0.25}$. The required formulas for the principal stresses are given in Problem 4.6.

NOTES

1. Hosford, W. F., and Caddell, R. M.: "Metal Forming, Mechanics and Metallurgy," Cambridge Univ. Press, 2007.
2. Dieter, G.: "Mechanical Metallurgy," McGraw-Hill, 1989.
3. Chakrabarty, J.: "Theory of Plasticity," Elsevier, 2006.
4. Mohr, O.: "Zivilingeneur," 1882, p. 113.
5. Coffin, L. F., and Rogers, H. C.: Trans. Am. Soc. Metallurgists, Vol. 60, 1967, p. 681.
6. Tresca, H.: "On the flow of solid bodies subjected to high pressures," C. R. Acad. Sci. Paris, Vol. 59, 1864, p. 754.
7. Lévy, M.: "Mémoire sur les équations génerales des mouvements intérieurs des corps solides, ductiles au-delà des limites où l'élasticité pourrait les ramener à leur premier état," C. R. Acad. Sci. Paris, Vol. 70, 1870, p. 1323.
8. Mises, R.: "Mechanik der fasten Körper im plastisch deformablen Zustand," Göttingen Nachrichten, Math. Phys. Kl., 1913, p. 582.

REFERENCES

Chakrabarty, J.: "Applied Plasticity," Springer-Verlag, 2000.
Rees, D. W. A.: "Basic Engineering Plasticity," Elsevier, 2006.

5 Reduction and Proportions of the Plastic Zone

As described in connection with eq. 4-24, the deformations imposed on a material in a general complex deformation condition can be described uniquely by the specification of the numerical values of six different strain components. An alternative simpler approach is to quantify deformations by means of the effective strain value; see eq. 4-38. This strain parameter can be considered the “resultant” strain that takes into account the effect of all different strain components.

In an industrial metal forming process, however, the conditions are complex. It is not straightforward to quantify either the different strain components or the effective strain value. To consider the total deformation imposed on a workpiece in such industrial processes, some simplified, less scientific deformation measures are therefore commonly used. Such common measures, which characterize the size of the deformations imposed on a workpiece in a forming process, are, for instance, the *area reduction*, or the *reduction ratio*. By means of the numerical value of these parameters, it is possible to compare the size of the overall deformation in different cases of forming. Some simple deformation measures applied in industry will be defined and discussed in this chapter.

5.1 Area Reduction in Stationary Metal Forming Processes

Let us first consider total deformations subjected to the workpiece in some stationary metal forming processes like stretching, drawing, extrusion, and rolling. Sketches of these processes are shown in Fig. 5.1. The workpiece has initial diameter d_0 and cross-sectional area A_0. In addition to these two parameters, a gauge length l_0 can be specified for the undeformed condition of the workpiece. Finally, there is the product $l_0 A_0$, which defines a volume of material, V_0, of the workpiece.

In the drawing process, a corresponding volume is also shown as it appears after the end of forming. The shaped product has new length, new cross section, and new diameter, denoted by symbols l_1, A_1, and d_1. Because of the constancy of volume in plastic deformation, the volume remains the same before and after forming. In plastic stretching of the specimen, this volume will deform in a similar way to that in the drawing, at least as considered from the outer shape of the specimen.

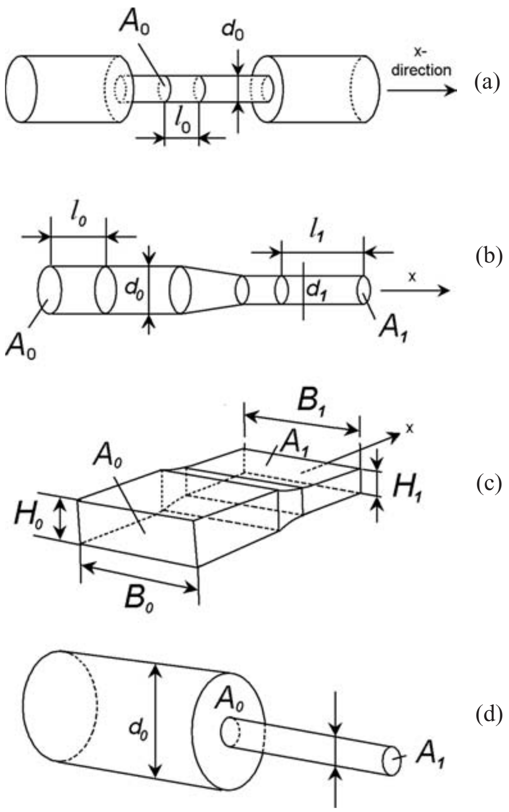

Figure 5.1. Workpiece configurations in different forming situations: (a) tensile stretching, (b) wire drawing, (c) extrusion, and (d) rolling.

In Fig. 5.1(d), a slab rolling process is shown where the initial cross-sectional area A_0 is reduced to A_1. Concurrently, also the initial cross-sectional dimensions of the slab – the thickness H_0 and width B_0 – are changed to H_1 and B_1 after rolling.

For all four stationary forming processes shown in Fig. 5.1, the *average length strain* can be computed by means of eq. 4-13 as

$$\varepsilon_x = \ln \frac{l_1}{l_0} \tag{5-1}$$

or, alternatively, as

$$\varepsilon_x = \ln \frac{l_1}{l_0} = \ln \frac{V/A_1}{V/A_0} = \ln \frac{A_0}{A_1} \tag{5-2}$$

For drawing of a round rod, it is preferably expressed as

$$\varepsilon_x = \ln \frac{l_1}{l_0} = \ln \frac{A_0}{A_1} = \ln \frac{\pi \left(\frac{d_0}{2}\right)^2}{\pi \left(\frac{d_1}{2}\right)^2} = \ln \left(\frac{d_0}{d_1}\right)^2 \tag{5-3}$$

and for rolling of a square cross section as

$$\varepsilon_x = \ln \frac{l_1}{l_0} = \ln \frac{A_0}{A_1} = \ln \frac{H_0 B_0}{H_1 B_1} \tag{5-4}$$

Another measure of the total deformation is the *degree of reduction*, specified as the *relative area reduction* quantified by the expression

$$r = \frac{A_0 - A_1}{A_0} \tag{5-5}$$

or, alternatively, the *percentage area reduction*, given as

$$r\,(\%) = \frac{A_0 - A_1}{A_0} \times 100\% \tag{5-6}$$

The reduction specified, for instance, in Fig. 1.7(a) to quantify the deformation of the material is the area reduction as defined by eq. 5-6.

As shown by the preceding equations, to determine the length strain for a circular, a square, or a rectangular section in processes like stretching, drawing, extrusion, or rolling, it is sufficient to measure the diameter, or the width and height, of the workpiece before and after forming. The same is the case when the area reduction is to be determined, for it is also determined from the initial and the final cross-sectional areas of the workpiece and the product.

Transformation from length strain to area reduction, or vice versa, is done by use of the equation (see Example 5.1):

$$r = 1 - e^{-\varepsilon_x} \tag{5-7}$$

EXAMPLE 5.1: TRANSFORMING AREA REDUCTION TO LENGTH STRAIN

Problem: Show that the expression $r = 1 - e^{-\varepsilon_x}$ can be used to calculate area reduction from length strain for the wire drawing operation shown in Fig. 5.1(b).

Solution:

$$\varepsilon_x = \ln\frac{l_1}{l_0} = \ln\frac{A_0}{A_1}$$

$$\Rightarrow \quad \underline{\underline{r}} = \frac{A_0 - A_1}{A_0} = 1 - \frac{A_1}{A_o} = 1 - e^{\ln(A_1/A_0)} = 1 - e^{-\ln(A_0/A_1)} = \underline{\underline{1 - e^{-\varepsilon_x}}}$$

5.2 The Reduction Ratio in Extrusion

In extrusion processes, very large reductions are commonly used, as shown, for instance, in Fig. 5.1(d). When area reduction is used to quantify the total deformation in the extrusion process, then the value of this deformation measure will lie close to 1, even though the extruded profiles may have rather different final cross sections. A better measure for the overall deformation, which distinguishes better between different reductions in extrusion, is the *reduction ratio* defined by

$$R = \frac{A_0}{A_1} \tag{5-8}$$

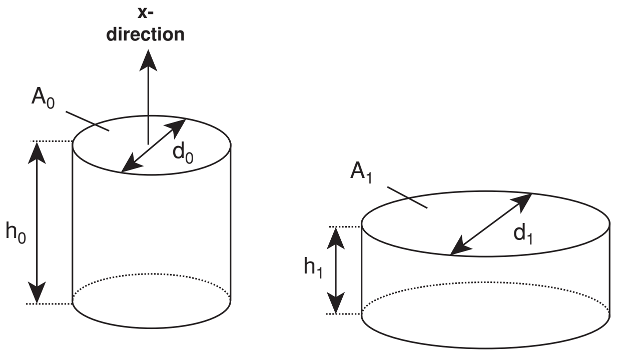

Figure 5.2. Homogeneous cylinder compression.

This reduction measure can also be transformed into area reduction, or vice versa, by use of the formula

$$R = \frac{1}{1 - r} \tag{5-9}$$

In industrial extrusion, it is quite common to apply reduction ratios in the range 20–200. This corresponds to reductions in area in the range 0.95–0.995, or 95–99.5%.

5.3 Height Reduction in Cylinder Compression

Consider the homogeneous compression test shown in Fig. 5.2. Whereas the dimension in the length direction of the specimen is called length in the tensile test, the corresponding dimension in the compression test is called height and is denoted by symbols h_0 and h_1, in Fig. 5.2, for the initial and final height, respectively. Cross-sectional areas, however, are represented by the same symbols as for the tensile test. The height strain can be determined as for the tensile test:

$$\varepsilon_x = \ln \frac{l_1}{l_0} = \ln \frac{h_1}{h_0} = \ln \frac{A_0}{A_1} \tag{5-10}$$

with height replacing length. In compression, this strain value will have a negative sign because $h_0 > h_1$. But in compression, it is quite common to redefine strain so that it becomes positive, and in that case one expresses the height strain by the formula

$$\varepsilon_{x,\mathrm{redef}} = -\varepsilon_{x,\mathrm{tension}} = -\ln \frac{h_1}{h_0} = \ln \frac{h_0}{h_1} > 0 \tag{5-11}$$

5.4 The Aspect Ratio in Cylinder Compression

Cylinder compression is described in Ch. 7 as a technological test commonly applied in metal forming. Cylinders of different slenderness can be used in this test. When the initial height-to-diameter ratio of a cylinder is increased above 2.5, problems are encountered in performing the test properly, because the cylinder tends to bulge out in one lateral direction instead of being ideally compressed in its height direction.

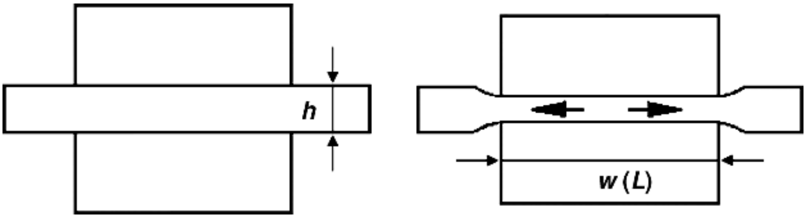

Figure 5.3. Plane strain compression.

The height-to-diameter-ratio of the cylinder is commonly used to quantify its proportions. It is sometimes also called the *aspect ratio* and expressed as

$$\mathrm{AR} = \frac{h}{D}\left(= \frac{h}{L}\right) \tag{5-12}$$

The magnitude of this ratio is important in cylinder compression, because the size of friction effects on the compression force depends on it. For acquisition of flow stress data, the aspect ratio should be made large, because friction effects on the compression load then tend to cancel out (see discussion in Sec. 15.2.6).

5.5 The Parameter Δ in Metal Forming

The parameter Δ quantifies the proportion of the plastic zone in metal forming. It is important because deformations change a lot when Δ is changed, as shown in Ch. 3. It is quantified as follows (see Fig. 5.3):

$$\Delta = \frac{h}{w}\left(= \frac{h}{L}\right) \tag{5-13}$$

As the figure depicts, this parameter coincides with the height-to-width ratio of the compression gap in compressive processes. It was early recognized that the flow field in compression depends strongly upon this parameter. This is the case also in stationary metal forming processes, such as drawing, extrusion, and rolling. In these processes, h in eq. 5-13 denotes the average height of the deformation zone. When we compare eqs. 5-12 and 5-13, we see that the aspect ratio in cylinder compression is the same as Δ.

In Fig. 3.17, the average pressure transferred from the workpiece material onto the die in frictionless plane strain compression, given as a dimensionless parameter $p/2k$, as deduced in theoretical analysis, is shown graphically versus Δ. In the same figure, the appearance of metal flow in terms of dead zones and shear crosses is sketched for various values of Δ. The figure shows that hardness testing and plane strain compression, with dies of large width in relation to workpiece thickness, represents different extreme cases of compression geometry. Whereas hardness testing is characterized by large Δ ($\Delta > 8$), the parameter Δ is small in plane strain compression when applying dies of large width ($\Delta < 1$).

We also see from Fig. 3.17 that the geometrical conditions of the plastic zone are quite different in these two extreme cases of compression. In hardness testing, the plastic zone is localized just below the indenter, i.e., it does not penetrate deep down into the workpiece material. The theoretical average die pressure in this case is therefore almost three times larger than the material's flow stress, because the material below the indenter is forced to flow laterally under the indenter to escape when the indenter penetrates down into the workpiece.

However, in plane strain compression with use of punches of the same or larger width than the height of the workpiece, the frictionless die pressure is only one-third of the pressure in hardness testing. In this case, the whole workpiece in the gap between the dies becomes plasticized, and material can easily escape from the deformation zone by lateral flow out of the gap between the two approaching dies.

Friction between die and workpiece will of course hinder lateral metal flow in plane strain compression and will contribute to higher die pressure than predicted in frictionless analysis.

Problems

5.1 In the middle of the twentieth century, before the development of continuous slab casting techniques for steels, a production line for manufacture of coiled steel sheet consisted of altogether three different rolling processes, as shown in the following figure:

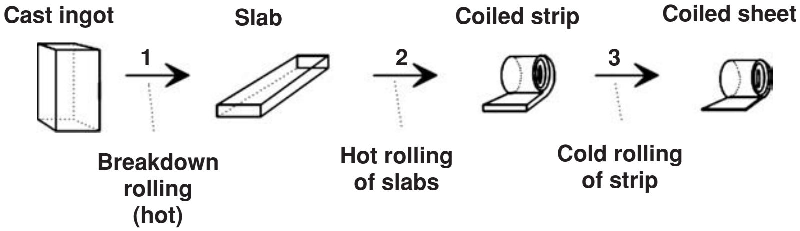

Assume that the width of the workpiece remained constant, equal to 1000 mm, during the rolling processes and that only the thickness of the workpiece was changed. The cast ingot was reduced from an initial thickness of 700 mm, in three separate rolling processes, down to the following final thicknesses for various semifinished products:

(i) 180 mm slab
(ii) 2 mm rolled strip
(iii) 0.25 mm rolled sheet metal
(a) Determine the area reduction, nominal strain, and true strain in the length direction for the rolling processes described.
(b) Check whether any of the deformation measures can be added.
(c) Consider a cast ingot of 1 m length being rolled down to strip before coiling. Calculate the final length of the resulting strip, if we assume no material waste.

Modern production technology today, however, is based on direct continuous casting of slabs, so the first of the previously used rolling processes is omitted.

(d) Compute the total area reduction and the true strain in the length direction of the material, after the introduction of recent technology.

5.2 Calculate the area reduction and the nominal and true strains in the length direction of the workpiece for the following cases:

(a) Cylinder compression characterized by $h_1 = \frac{1}{2}h_0$.
(b) Rolling step with rolling parameters $B_1 = B_0$ and $H_1 = 0.9H_0$.
(c) Extrusion characterized by $D_0 = 100$ mm and $D_1 = 10.2$ mm.
(d) Extrusion characterized by $D_0 = 100$ mm and $D_1 = 8.0$ mm.

On the basis of the computed deformations in (c) and (d), explain why it is practical to use the reduction ratio to quantify overall deformations in extrusion.

5.3 Consider the FEM-simulated indirect Al extrusion process shown in Fig. 19.12, where a 95.7-mm-diameter billet is extruded down to a final rod of 28 mm diameter. In this case, a container of 100 mm diameter was used. Calculate the reduction ratio and the average length strain in this process. Discuss the obtained results in relation to the simulated effective strain distribution in the extruded rod (see Fig. 19.12).

5.4 Consider the FEM-simulated wiredrawing process shown in Fig. 23.19, where a 3.43-mm-diameter wire was drawn down to a final dimension of 2.54 mm diameter. Calculate the reduction of area and the average length strain in this process. Discuss the obtained results in relation to the simulated effective strain distribution in the drawn wire; see Fig. 23.19(a) and (b). Calculate also the parameter Δ in this case.

6 Deformations from the Velocity Field

It may be useful to know the *velocity field*[1] for a metal forming process, as will be shown in the forthcoming sections. If the velocity field is known, a number of deformation parameters can, in principle, be deduced from it. This is realized if one considers the definitions of the different strain and strain-rate components in Sec. 4.2.1 and Sec. 4.3.3.

Let us first explain what is meant by a velocity field. The term refers to the distribution of velocities, at a given moment of forming, within a workpiece, and the evolution of them with time, from beginning to end of the forming process.

The usefulness of determining the velocity will first be shown for the simple case of homogeneous slab compression. It will be shown how a simple velocity field can be determined, which gives an adequate description of the overall deformational behavior of the slab. Then it will be shown how different strain and strain-rate components can be deduced from this velocity field. In the last problem at the end of this chapter, a complex velocity field that incorporates the effect of bulging in cylinder compression, is dealt with.

6.1 Stationary and Nonstationary Velocity Fields

Metal forming processes are commonly classified in two groups, *stationary processes* and *nonstationary processes*,[2] dependent on whether there is a constant velocity field or the field changes with time throughout the forming operation.

Rolling, drawing, and lubricated extrusion through conical dies are forming processes in which metal flow is approximately stationary; see, for instance, wiredrawing as shown in Fig. 6.1(a). In stationary processes, the material flows as a rigid body toward the die and starts to deform plastically when it approaches the plastic zone. Upon flow through the plastic zone, the material is subjected to increasing deformation, and deformation ceases as the material exits from the plastic zone, i.e., the material becomes a rigid body again. After start-up of the process, an approximately constant time-independent velocity field will exist in the plastic zone, when a constant forming speed is used. Material particles that at different times enter the

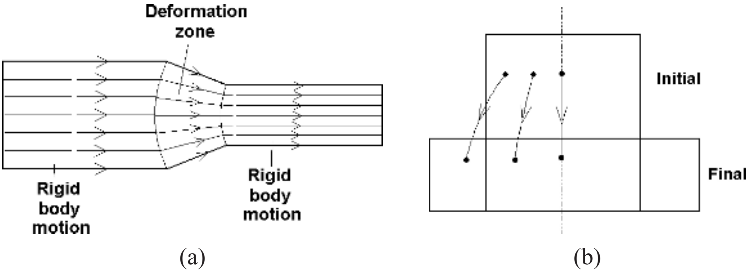

Figure 6.1. Velocity fields in different forming processes: (a) stationary field in wiredrawing and (b) nonstationary field in cylinder compression.

plastic zone at the same distance below the wire surface will follow the same particle paths – see the lines drawn in Fig. 6.1(a). They will all have the same velocity, as depicted by arrows in the figure, and will therefore be subjected to the same deformations. This velocity field will remain throughout the whole duration of the process, except at the very beginning and at the very end of it.

When the front and the tail end of the workpiece move through the die, however, conditions are not stationary. This is clearly demonstrated, for instance, in case of rolling in Fig. 21.2.

Forging represents a typical nonstationary forming process, as shown for cylinder compression in Fig. 6.1(b). In this process, the whole workpiece is subjected to deformation from the beginning of the process. During compression, the particle velocities for different material particles inside the deformation zone change continuously with time, as the material of the cylinder flows downward and spreads out laterally in the radial direction of the cylinder.

6.2 Deformations and Deformation Rates Deduced from the Velocity Field

In Sec. 4.2, the nominal strain tensor for a general state of deformation was defined. It was shown that deformations in general can be quantified by nine different strain components, in which shear strains appear in pairs of equal size, but with different sign. The strain state is therefore altogether characterized by six different; strain components see eq. 4-24. The nominal strain was also defined by setting it equal to the incremental true strain value; see eq. 4-15. The true incremental strains during deformation are therefore described by the following six strain components:

$$\varepsilon_x = \frac{\partial u_x}{\partial x} \tag{6-1}$$

$$\varepsilon_y = \frac{\partial u_y}{\partial y} \tag{6-2}$$

$$\varepsilon_z = \frac{\partial u_z}{\partial z} \tag{6-3}$$

$$\varepsilon_{xy} = \varepsilon_{yx} = \frac{1}{2}\left(\frac{\partial u_x}{\partial y} + \frac{\partial u_y}{\partial x}\right) \tag{6-4}$$

$$\varepsilon_{yz} = \varepsilon_{zy} = \frac{1}{2}\left(\frac{\partial u_y}{\partial z} + \frac{\partial u_z}{\partial y}\right) \tag{6-5}$$

$$\varepsilon_{xz} = \varepsilon_{zx} = \frac{1}{2}\left(\frac{\partial u_z}{\partial x} + \frac{\partial u_x}{\partial z}\right) \tag{6-6}$$

Here u_x, u_y, and u_z are displacement components of a material particle in the directions of the three axes x, y and z of a Cartesian coordinate system, inside the deforming body. Actually, they are the same displacements as those denoted u, v, and w in Fig. 4.5.

The velocity components[3,4] of a material particle in the same three directions can also be determined by these displacements, or more precisely the time derivatives of them, as

$$v_x = \frac{\partial u_x}{\partial t} \tag{6-7}$$

$$v_y = \frac{\partial u_y}{\partial t} \tag{6-8}$$

$$v_z = \frac{\partial u_z}{\partial t} \tag{6-9}$$

The normal strain-rate components will be

$$\dot{\varepsilon}_x = \frac{\partial \varepsilon_x}{\partial t} = \frac{\frac{\partial u_x}{\partial x}}{\partial t} = \frac{1}{\partial x}\frac{\partial u_x}{\partial t} = \frac{\partial v_x}{\partial x} \tag{6-10}$$

$$\dot{\varepsilon}_y = \frac{\partial v_y}{\partial y} \tag{6-11}$$

$$\dot{\varepsilon}_z = \frac{\partial v_z}{\partial z} \tag{6-12}$$

Correspondingly the shear strain-rate components are

$$\dot{\varepsilon}_{xy} = \dot{\varepsilon}_{yx} = \frac{1}{2}\left(\frac{\partial v_x}{\partial y} + \frac{\partial v_y}{\partial x}\right) \tag{6-13}$$

$$\dot{\varepsilon}_{yz} = \dot{\varepsilon}_{zy} = \frac{1}{2}\left(\frac{\partial v_y}{\partial z} + \frac{\partial v_z}{\partial y}\right) \tag{6-14}$$

$$\dot{\varepsilon}_{xz} = \dot{\varepsilon}_{yx} = \frac{1}{2}\left(\frac{\partial v_x}{\partial z} + \frac{\partial v_z}{\partial x}\right) \tag{6-15}$$

Thus, it is clear that if the velocity field incorporating all material particles in a particular metal forming process is uniquely known – i.e., if we know the velocity

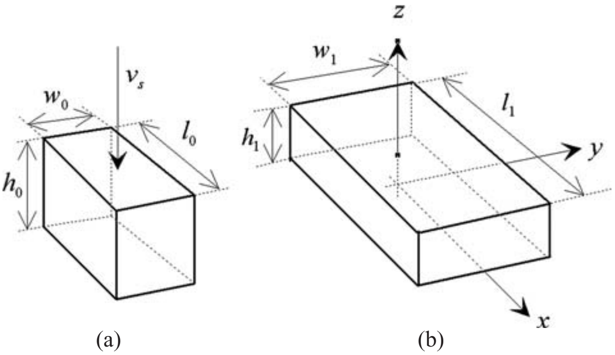

Figure 6.2. Homogeneous compression of rectangular slab: (a) initial and (b) deformed slab.

components v_x, v_y, and v_z, including their time variation through the duration of the process – then all displacements, strains, and strain-rate components can be deduced from this field by means of the preceding equations.

6.3 The Velocity Field during Homogeneous Slab Compression

In the following sections, we shall analyze the velocity field of a particular metal forming process and show that, if this field is known, the strain and strain rate can be deduced from it.[5]

Consider axial compression of the slab in the negative z-direction as sketched in Fig. 6.2(a), down to the deformed condition shown in Fig. 6.2(b), between two plane-parallel dies. Assume that the lower die remains stationary, while the upper die moves downward with constant velocity v_s. In addition, assume that there is perfect lubrication between the slab and the dies, so the process is frictionless. As the slab is compressed down in the negative z-direction, it will concurrently expand in the two lateral directions, x and y, without being affected by interfacial friction. The velocity field during the deformation process then can be expressed by the equations

$$v_x = \frac{v_s x}{2h} \tag{6-16}$$

$$v_y = \frac{v_s y}{2h} \tag{6-17}$$

$$v_z = -\frac{v_s z}{h} \tag{6-18}$$

The proposed velocity field to describe metal flow in a particular metal forming process must fulfil certain basic conditions imposed on it by the basic nature of plastic deformations, for it to be valid. These conditions are[5]:

(a) Constancy of volume, i.e., eq. 4-29 must be valid everywhere inside the deforming body.
(b) Boundary conditions of the process, i.e., the external surfaces of the workpiece must move the same way as in the real forming process.

In Example 6.1, it is shown how the velocities in eqs. 6-16 to 6-18 can be deduced. Then, in Example 6.2, it is shown that this velocity field conforms to both the preceding basic conditions (a) and (b).

From the velocity field specified in eqs. 6-16 to 6-18, the strain rates for the homogeneous slab compression process can readily be deduced by means of eqs. 6-10 to 6-12. In this way, the following expressions for the normal strain rate components are obtained:

$$\dot{\varepsilon}_x = \frac{\partial v_x}{\partial x} = \frac{\partial \left(\dfrac{v_s x}{2h} \right)}{\partial x} = \frac{v_s}{2h} \tag{6-19}$$

$$\dot{\varepsilon}_y = \frac{\partial v_y}{\partial y} = \frac{\partial \left(\dfrac{v_s y}{2h} \right)}{\partial y} = \frac{v_s}{2h} \tag{6-20}$$

$$\dot{\varepsilon}_z = \frac{\partial v_z}{\partial z} = \frac{\partial \left(\dfrac{v_s z}{h} \right)}{\partial z} = -\frac{v_s}{h} \tag{6-21}$$

Because deformations are homogeneous in the compression process, all shear strain and shear strain-rate components are equal to zero. The true strains subjected to the material in the deformation process can also be determined from the velocity field. The strain in the z-direction (see figure in Example 6.1) can be expressed as

$$\varepsilon_z = \int_0^t \dot{\varepsilon}_z \, \mathrm{d}t = \int_0^t \frac{\partial v_z}{\partial z} \mathrm{d}t = \int_0^t \frac{-v_s}{h} \mathrm{d}t \tag{6-22}$$

From this figure, it is clear that

$$h = h_0 - v_s t \quad \Rightarrow \quad \mathrm{d}h = -v_s \mathrm{d}t \quad \Rightarrow \quad \mathrm{d}t = -\frac{\mathrm{d}h}{v_s}$$

This again yields the result

$$\varepsilon_z = \int_0^t \frac{-v_s}{h} \mathrm{d}t = \int_{h_0}^{h_1} \frac{-v_s}{h} \frac{-\mathrm{d}h}{v_s} = \int_{h_0}^{h_1} \frac{\mathrm{d}h}{h} = \ln \frac{h_1}{h_0} \tag{6-23}$$

Correspondingly, the normal strain components in the x- and y-directions (see Problem 6.2) can be determined as

$$\varepsilon_x = \int_0^t \frac{v_s}{2h} \mathrm{d}t = \ln \frac{l_1}{l_0} \tag{6-24}$$

$$\varepsilon_y = \int_0^t \frac{v_s}{2h} \mathrm{d}t = \ln \frac{w_1}{w_0} \tag{6-25}$$

EXAMPLE 6.1: FINDING THE VELOCITY FIELD

Problem: Deduce the velocity field for axial compression of a rectangular slab as shown in Fig. 6.2.

Solution: Consider the velocity distribution in the z-direction of the specimen. It can be drawn graphically as illustrated in the accompanying sketch, i.e., the velocity in the z-direction is drawn so it points in a direction orthogonal to the z-axis, namely, along the x-axis. Assume a linear increase in this velocity over the height of the slab, from the minimum value in the bottom layer of the slab, adjacent the stationary lower die, up to the maximum value of $v_z = -v_s$, in the top layer of the slab, adjacent the upper die.

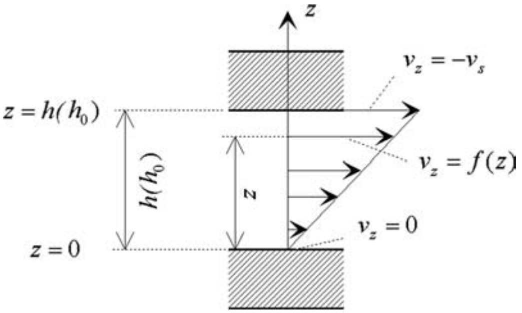

The velocity distribution in the z-direction of the slab then can be expressed as

$$\frac{v_z}{-v_s} = \frac{z}{h} \quad \Rightarrow \quad v_z = -\frac{z}{h} v_s$$

The material that flows downward with velocity v_z must spread out in the two lateral directions of the slab, x and y, because of constancy of volume during plastic deformation. Hence velocities in these two directions are reduced down to half of the velocity in the z-direction. In the positive quadrant of the coordinate system, metal flow in the x- and y-directions of the slab must be directed along the respective axes; hence, the velocity must be positive, i.e.,

$$v_y = \frac{y}{2h} v_s, \qquad v_x = \frac{x}{2h} v_s$$

EXAMPLE 6.2: VALIDITY OF VELOCITY FIELD

Problem: Show that the velocity field given by eqs. 6-16 to 6-18 satisfies the requirement of volume constancy during deformation, including the boundary conditions of the compression process.

Solution: First we check if the boundary conditions are satisfied. If we consider the initial stage of the process at the time $t = 0$, the proposed velocity field yields the following velocities:

At the origin of the coordinate system: $x = y = z = 0 \Rightarrow v_x = v_y = v_z = 0$.

On the moving surfaces of the slab (defined by $x = l_0/2$, $y = w_0/2$, and $z = h_0$):

$$v_{x,\text{surface}} = \frac{v_s l_0}{4h_0}, \quad v_{y,\text{surface}} = \frac{v_s w_0}{4h_0}, \quad \text{and} \quad v_{z,\text{surface}} = -\frac{v_s z}{h_0} = -\frac{v_s h_0}{h_0} = -v_s$$

From this we see that the boundary conditions are fulfilled.

Next we check whether the volume remains constant. The volume displaced downward per unit of time by the upper die in the beginning of the compression stroke equals $v_s w_0 l_0$. The corresponding volume per unit of time displaced in the two lateral directions is

$$2v_{x,\text{surface.}}\, h_0 w_0 + 2v_{y,\text{surface.}}\, l_0 h_0 = 2\frac{v_s l_0}{4h_0} h_0 w_0 + 2\frac{v_s w_0}{4h_0} l_0 h_0 = v_s l_0 w_0$$

Hence, constancy of volume is satisfied, for the volume displaced downward equals the sum of the flow of volume in the two lateral directions.

Problems

6.1 Show that $\varepsilon_x = (\ln l_1/l_0)$ (eq. 6-24) during frictionless axial compression of a slab (Fig. 6.2), by deducing this normal strain from the material velocity in the x-direction, i.e., $v_x = v_s x/2h$.

6.2 A rectangular slab with initial height $h_0 = 10\,\text{mm}$ is compressed axially with constant compression velocity $v_s = 5\,\text{mm s}^{-1}$. Assume frictionless conditions and homogeneous deformations. Compute the strain-rate components and effective strain rate in the slab, both initially and after time $t_1 = 0.8$ s. Compute the strain components and effective strain in the specimen at the same time.

6.3 The following velocity field[6] has been proposed for the purpose of describing flow velocities in axisymmetric upsetting of a cylinder when there is friction so that bulging occurs:

$$v_\theta = 0, \qquad v_z = -2Az(1 - \beta z^2/3), \qquad v_r = Ar(1 - \beta z^2/3)$$

Here β is a parameter representing the severity of the bulge, and A is determined from the velocity boundary condition at $z = h$ to be

$$A = \frac{V_D}{2h\left(1 - \beta h^2/3\right)}$$

(a) Determine the general strain-rate tensor for this general case.

(b) Find an expression for the effective strain-rate distribution inside the cylinder.

NOTES

1. Altan, T., Oh, S. I., and Gegel, H. L.: "Metal Forming, Fundamentals and Applications," ASM, 1983, pp. 41–44.
2. Lange, K.: "Handbook of Metal Forming," McGraw-Hill, 1991, pp. 5.2–5.3.

3. Backofen, W. A.: “Deformation Processing,” Addison-Wesley, 1972.
4. Rowe, G. W.: “Principles of Industrial Metalworking Processes,” Edward Arnold Publishers, London, 1977.
5. Johnson, W., and Mellor, P. B.: “Engineering Plasticity,” Van Nostrand Reinhold, London, 1975.
6. Lee, C. H., and Altan, T.: “Influence of flow stress and friction upon metal flow in upset forging of rings and cylinders,” ASME Trans. J. Engineering for Industry, Aug. 1972, p. 775.

7 Technological Tests and Physical Simulation

In order to model metal forming processes either by theoretical models or by FEM modeling, as already shown in Ch. 3, it is required, for instance, to know the flow stress of the metal that is formed, and the actual friction between the die and the workpiece. To obtain such data, a number of different test methods have been developed over the years, by which it is possible to bring a specimen of the actual material, usually of small size, into a plastic state, and during plastic deformation of it measure the required deformation force, concurrently as the size of deformations subjected to the specimen is measured. Tests of this kind are called *technological tests* and are commonly run on small specimens of the material, often in advanced equipment especially designed for the purpose. In this chapter, the most common technological tests for measurement of flow stress and ductility of metallic materials are discussed. The main focus will be on the tensile test and the compression test. The basic mechanics of these technological tests, and how to determine stresses and strains during the tests, will be reviewed.

7.1 Physical Simulation of Metal Forming

Some industrial metal forming processes – as for instance rolling, extrusion, and forging – are commonly run in large industrial equipment, where the possibilities of experimentation is limited. Most commonly the machinery lacks sensors to allow accurate recording of relevant process parameters. Moreover, running of full-scale experiments in big industrial equipment is expensive. If there is continuous production in the equipment, full-scale experiments will reduce the productivity of the process to be investigated.

In heavy industrial equipment, large workpieces are shaped, and each specimen therefore will have high economic value. For example, if steel slabs of 5 ton weight are rolled, it is obvious that the loss of one slab will be expensive. If the product is made with (for instance) wrong final dimensions or unacceptable mechanical properties, it may have to be scrapped. Hence, industrial experimentation is limited by its cost, though recycling of metals by remelting and casting is common practice.

Another disadvantage of full-scale experimentation is that in such equipment there are limitations on the extent to which one can apply extreme forming conditions. To fully understand the mechanics of a particular forming process, scientific experimentation sometimes requires extreme conditions. In a conventional rolling mill, for instance, there is a limit on how large reductions can be taken in each rolling stand, without overloading and damaging the equipment. If one wants to investigate the influence of large rolling passes on microstructure development in a rolled product and on the resulting mechanical properties, it is therefore preferable to run the experiments in specially designed laboratory equipment, for instance, in a *metal forming simulator*,[1] instead of performing full-scale industrial experiments. Not only is there a better chance to monitor and record actual processing conditions accurately, but the cost of the investigation is also lower.

In *physical simulation* of metal forming in the laboratory one commonly uses much smaller specimens than in the industrial process. But through accurate monitoring of the process conditions in the simulator, one can generate intended forming conditions in the test specimen, corresponding to those in the industrial process, or even more extreme conditions. In a metal forming simulator, it is thus possible to collect information regarding conditions of forming exceeding those achievable in the process itself.

7.2 Technological Tests to Mimic Metal Forming

The most common *technological tests*[2,3] used for the purpose of physical simulation of metal forming are *tensile testing*, *torsion testing*, *cylinder compression*, and *plane strain compression*; see Fig. 7.1. The deformations in cylinder compression and plane strain compression are compressive, whereas in tensile testing there is uniaxial tension and elongation of the material. Torsion testing is very different from the other test methods in that the material is twisted.

Hardness testing has a certain potential as a technological test method to mimic metal forming, as it provides small plastic deformations in the test body in a layer below the *hardness indenter*. Hardness testing can be considered a compression test in which the workpiece is much larger than the die, i.e., the indenter, which penetrates into the specimen. However, most of the workpiece remains undeformed in this test, so that it is not subjected to bulk plastification.

In hardness testing, the initial metal below the indenter is forced to escape in lateral directions away from it [see Fig. 7.2(a)], toward the surface of the specimen on each side. Because of this, protrusions appear around the indentation mark after the end of the test, in volume equal to the metal displaced by the indenter.

Hardness testing is often modeled by assuming the indenter to have an ideal butt-ended shape, like a punch with a flat-faced head. Moreover, it is common to assume plane strain conditions in the indenting process, as depicted in Fig. 7.2(b). The material flow then can be assumed to be ideal, occurring by the movement of three rigid dead zones under and on each side of the punch head.

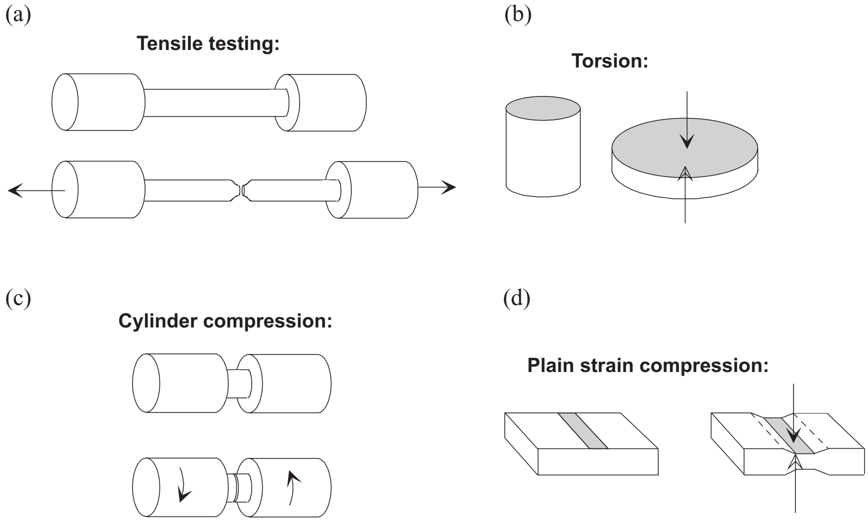

Figure 7.1. Technological test methods: (a) tensile testing, (b) torsion testing, (c) cylinder compression, and (d) plane strain compression testing.

7.2.1 Tensile Testing

Tensile testing is most commonly used as a general test for materials to determine their mechanical properties, such as yield strength, tensile strength, and fracture strain. These properties characterize the strength and ductility of a metal and are used as design parameters in connection with design and dimensioning of metallic products. But in addition, as will be focused on here, tensile testing[4] has an important role as a technological test method in metal forming. Here the most common application of it is for acquisition of the *flow curve* of a metal. A flow curve is the graphical presentation of the flow stress of the material versus the parameters that influence it, such as strain, strain rate, and temperature. In addition, the value of the *fracture strain* or the *elongation at fracture* is of interest in metal forming, in that they both by their value indicate whether the material has good *workability* or not.

In tensile testing, *instability* takes place in the specimen, so that it starts to neck, when it has been stretched to a certain level of uniform strain; see Fig. 7.1(a). When this happens, all plastic deformations occur in the short section of the specimen where there is neck growth. Concurrently, plastic deformation elsewhere in the specimen stops, so the rest of the specimen remains unchanged upon further stretching; deformations are then said to *localize* in the neck.

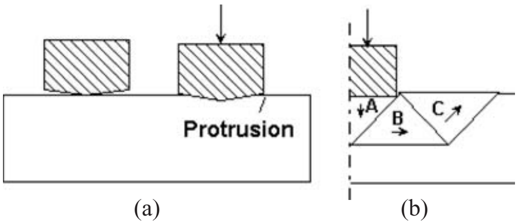

Figure 7.2. Material flow under the indenter in hardness testing: (a) macroscopic behavior and (b) idealized material flow in a common theoretical model of the test.

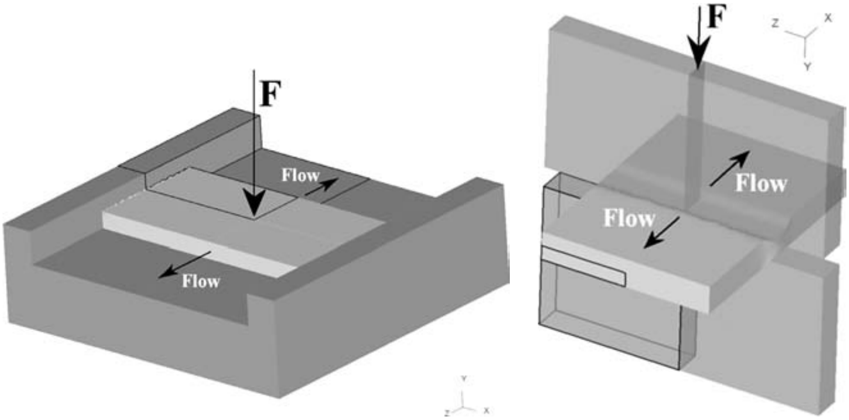

(a) (b)

Figure 7.3. Plane strain compression in the laboratory: (a) in a well-lubricated die channel and (b) by use of a large specimen.

7.2.2 Cylinder Compression

Cylinder compression as a technological test can be considered the opposite test as compared to tensile testing. In this test, it is common to apply a specimen of cylindrical shape, with initial height in the range from 1 to 2 times the diameter. Height 2.5 times the diameter is also sometimes used, but as the specimen height is increased above twice the diameter, stable compression is no longer easy to achieve, because high slender cylinders in compression will tend to buckle sideways at their midheight. If such buckling occurs, the experiment must be rerun until a proper test is obtained, to get a usable experiment.

The advantage of cylinder compression over to tensile testing is that there is commonly no instability. Because of this, the specimen can be subjected to much larger plastic deformations than in the tensile test; see Fig. 7.1(c). However, for brittle materials with low ductility compression testing is not straightforward, as the specimen can crack at an early stage of compression.

7.2.3 Plane Strain Compression

Instead of deforming a cylinder in compression, one can use a test specimen of the material with rectangular cross section, i.e., a slab, and the specimen can be compressed in a state of plane strain.[5,6] In principle, this can be realized in two different ways as shown in Fig. 7.3.[7]

One alternative is to compress the whole specimen in a channel-shaped die; see Fig. 7.3(a). There are then die walls that hinder lateral flow of the specimen in one of three axis directions. If compression is done this way in a completely frictionless state, a perfect plane strain test can be run. However, in practice it is difficult to realize frictionless conditions. Even if the best possible lubricants are applied, there will be some friction, which makes the specimen deform in a manner different from ideal plane strain. When this happens, the initially perfect rectangular cross section of the slab will not be rectangular after the test; hence, deformations will deviate from intended ones.

The simplest practical way to achieve close to plane strain conditions in compression, while the compression force is measured, is to compress a slab that only partly resides inside the compression gap; see Fig. 7.3(b). In this test, the rigid material outside the compression gap will hinder the metal inside the gap from flowing in the lateral direction. Moreover, if a specimen with large breadth w (Fig. 7.12(a)) is used, the material in the middle of the specimen will deform under conditions close to ideal plane strain.

7.2.4 Torsion

Torsion testing of metallic specimens is often used as an alternative method for acquisition of flow stress data and as an appropriate test for determination of the *ductility* of a material. The torsion test[2] is advantageous in some ways, one of them being that the test specimen can be subjected to large plastic deformations without significant shape change. However, because the specimen is twisted, the deformations will be in shear. It is an interesting test method but will not be further dealt with here, as it is considered beyond the scope of this book.

7.3 Physical Modeling of Metal Forming

Various kinds of commercial machines are available today that can impose deformation on metal specimens under controlled thermomechanical conditions corresponding to metal forming. Generally, one can call these machines *physical simulators*. Such machines are able to deform metal specimens, under controlled, monitorable conditions, to mimic the deformation conditions in almost any metal forming process. Two machines of this kind will be described here, to illustrate their working principles and to show how such machines can be used for physical simulation of metal forming.

One simulator of this kind is the *Gleeble machine*,[8] whose working principle is shown in Fig. 7.4. Gleeble machines are provided with different load capacities; for instance, one particular model can deliver a maximum force of 50 tons (0.5 MN). With this load capacity, the machine can deform workpieces of metal under specified, carefully monitored conditions. In a machine of this kind, only small workpieces can be used if high compression speeds are to be achieved. The use of small specimens greatly limits the kinds of mechanical tests the deformed specimen can be subjected to after the technological test. Relevant tests on the material after technological testing of a specimen of so small size are hardness testing and investigation of the microstructure by looking at sections cut through the material.

The Gleeble machine is built on a module principle, so that various exchangeable testing modules can be inserted to perform either tensile, compression, or torsion testing. When these tests are run on small specimens, miniature tensile test

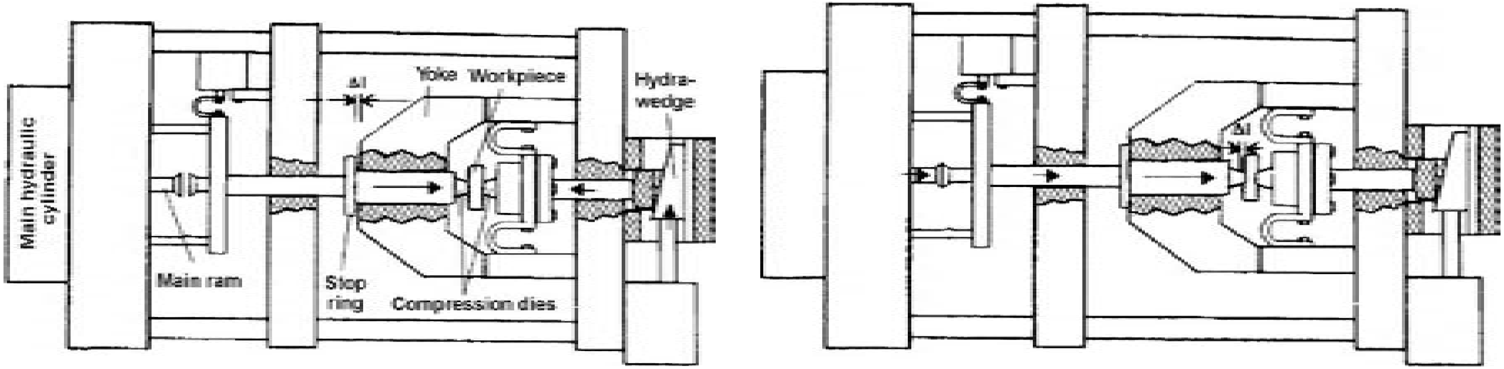

(a)

(b)

Figure 7.4. Gleeble 3500 physical metal forming simulator used in an industrial metal forming laboratory: (a) before and (b) after compression. (Courtesy Dynamic Systems, Inc.)

specimens can be obtained afterwards from the deformed specimens, to determine their mechanical properties in traditional mechanical tests. The machine is fitted with an electrical resistance heater for heating the test specimen. The machine is also equipped with a special, patented system called HydraWedge, which allows multistep compression to be performed on specimens, with specified time intervals (pause times) between steps. A sketch of a Gleeble machine is shown in Fig. 7.4.

The HydraWedge compression module[8] uses the following working principle: The adjustment of the compression height is done by a hydraulic wedge located on the right-hand side of the machine in Fig. 7.4. By positioning the wedge, a certain distance can be selected between the stop ring and the yoke. In this way, a certain compression stroke length Δl can be obtained, corresponding to the intended reduction in a particular forming step. When the stroke length has been set, pressure is provided to the main hydraulic cylinder, and the main ram is fed to the right as shown in Fig. 7.4(b). When the ram has been moved the distance Δl, the stop ring hits the yoke, and the compression movement stops. The pressure is now removed from the main cylinder and the wedge is moved forward to a new preset position, to give the wanted reduction in the second compression step. Then, by repeating a similar work cycle, a second deformation step can be obtained. In this manner, many successive blows can be given to the same workpiece, with set pause times between blows. In this simulator, it is thus possible to mimic the deformation history in most industrial *multistep forming* processes, as, for instance, a rolling process, in which the workpiece is fed in a continuous movement through many rolling passes in sequence; see Example 7.1.

A similar but bigger metal forming simulator[9] that works in compression mode is one operating in a German research institute. This simulator has a force capacity of 250 tons (2.5 MN), an acceleration of $300\,\mathrm{m\,s^{-2}}$, and a maximum ram velocity of $1.5\,\mathrm{m\,s^{-1}}$. This means that in this machine physical simulation of hot forming of steel can be done, using rather large specimen sizes. For specimens of (for instance) 70 mm thickness, compression can be done with average strain rates as high as $100\,\mathrm{s^{-1}}$. After physical simulation, the test specimen still has sufficient size for traditional mechanical testing to be conducted on the deformed part of the specimen; see Fig. 7.5. A schematic sketch of this machine is shown in Fig. 7.6.

As the sketch depicts, the specimen in this machine is heated by an induction coil placed around it. Compression is performed by the movement of the lower ram. A cooling unit is placed at the side of the machine, by which cooling at chosen rates can be provided by spraying water onto the specimen. The principles used during physical simulation of the forming conditions in a multistep rolling process in this machine are outlined in Example 7.1.

EXAMPLE 7.1: PHYSICAL SIMULATION OF MULTISTEP HOT ROLLING

Problem: The intention is to mimic an industrial hot rolling process by physical simulation. The workpiece is rolled in a continuous sequence through six successive steps. Describe a plan for conducting this simulation test using the

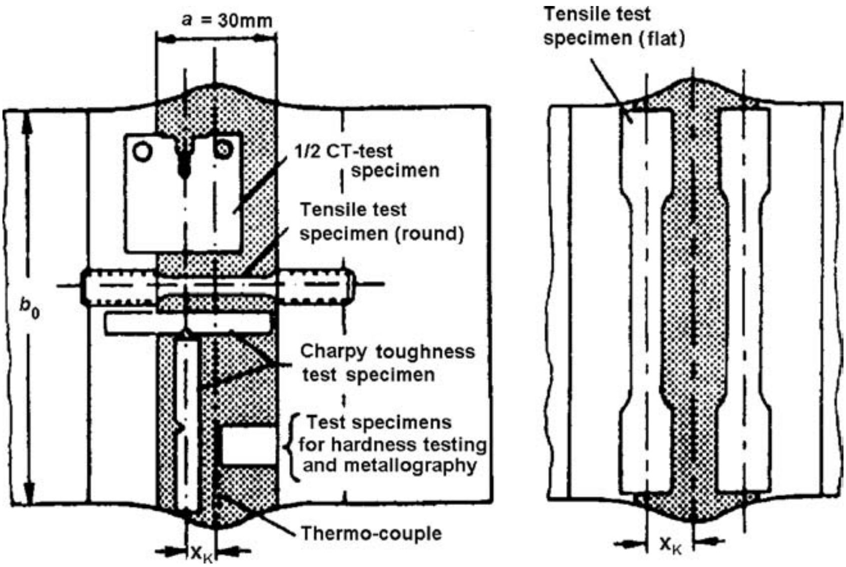
a = 30mm
1/2 CT-test specimen
Tensile test specimen (round)
b_0
Charpy toughness test specimen
Test specimens for hardness testing and metallography
Thermo-couple
x_K
Tensile test specimen (flat)
x_K

Figure 7.5. Plane strain compression specimens sufficiently large for fracture mechanics testing. (Courtesy The Max-Planck Institute für Eisenforschung, GmbH, Düsseldorf.)

big metal forming simulator just described. What useful information would you expect to deduce from the laboratory test?

Solution: My choice is to use plane strain compression as the physical simulation test method to reproduce the deformation conditions in the rolling process. It is generally claimed that deformation conditions in this laboratory test

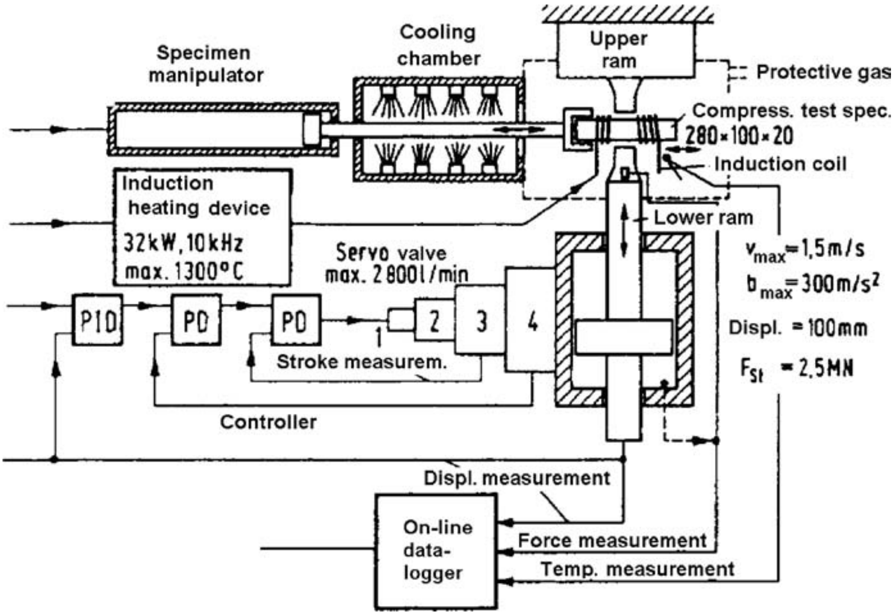

Figure 7.6. Sketch illustrating design and working procedure of big metal forming simulator. (Courtesy The Max-Planck Institute für Eisenforschung, GmbH Düsseldorf.)

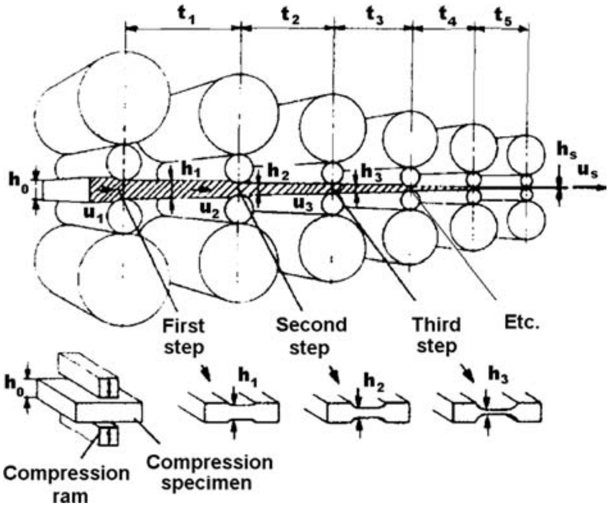

Figure 7.7. Industrial rolling process (top) and plane strain compression laboratory process to simulate it (bottom). (Courtesy The Max-Planck Institute für Eisenforschung, GmbH, Düsseldorf.)

are similar those experienced in rolling. My experimental test setup is depicted in Fig. 7.7.

The test sequence will depend on the thickness of the workpiece used in the industrial process:

1. Rolling of thin workpiece ($t < 70$ mm): Each reduction step should be simulated by a compressive stroke that produces a reduction equal to that in the rolling process; i.e., h_1, $h_2, \ldots$ should be the same in the rolling and in the compression process. The workpiece should be heated to the same temperature as in the rolling process, and compression should be done so that temperature history is as nearly as possible equal to that in the rolling process, and likewise the cooling history after rolling. The time intervals between the rolling steps, i.e., the pause times t_1, $t_2, \ldots$ should be selected equal those in the rolling process. The pause time is the time from when a cross section of the workpiece leaves the exit of one rolling stand until it reaches the inlet of the next stand. Because this is a hot rolling process, it is also important to choose the right compression speeds, so that effective strain rates during compression are as nearly equal as possible to those in rolling.
2. Rolling of workpiece with large initial thickness (for instance, $t = 210$ mm): My choice is to scale down the thickness of the workpiece threefold, i.e., to use an initial workpiece of 70 mm thickness in the plane strain compression test. Moreover, I would choose the same reductions, initial temperature, and strain rates as in the first case. Because of different scales, I would expect temperatures to drop faster in the laboratory test than in the industrial process, because of stronger cooling against dies. A larger temperature drop in the scaled-down laboratory process could eventually be compensated for by use of warmer dies in the compression experiments than in the rolling process. FEM simulation would be a good alternative for determining thermal effects.

Information to be deduced in physical simulation could include the following:

(a) The flow stress data on the workpiece material can be obtained from the measured compression force versus stroke length. To obtain accurate flow stress data, it is advantageous if one knows the friction conditions and the temperature in each compression step.

(b) The resulting microstructure of the rolled product can be estimated from the microstructure in the final compressed specimen if it is subjected to microstructural analysis. If specimens are taken out at intermediate steps of compression, the gradual development of microstructure throughout the rolling process can of course be investigated.

(c) Expected final mechanical properties of the rolled product can be estimated if appropriate test specimens are made and subjected to mechanical testing. Thermomechanical conditions throughout the compression sequence can also be varied. If the resulting microstructure and final mechanical properties of the material are characterized, one can determine an eventual optimum rolling sequence for a particular workpiece material. This optimum procedure will then be the thermomechanical treatment that provides the best mechanical properties in the finished product – for instance, highest yield strength and tensile strength together with acceptable ductility.

7.4 Basic Mechanics of Tensile Testing

Stresses and strains in a tensile test specimen can be determined as either nominal or true values. As shown in Table 7.1, the *nominal stress* is obtained when the tensile force in the test specimen is divided by the nominal cross-sectional area, i.e., the initial cross-sectional area of the specimen. *True stress* is a better stress definition and is obtained by dividing the tensile force by the true cross-sectional area of the specimen at any instant during the test. Because of the constancy of the volume of metal during plastic deformation, the area of the cross section of the tensile test specimen decreases as it is stretched. It follows from their definitions that the true stress is always larger than the nominal stress, except at small strains. At small strains, as in the case of elastic deformations, nominal and true stress values are approximately equal, because there is insignificant reduction in the cross section of the specimen.

Table 7.1. *Nominal and true stress and strain values*

	Stress	Strain
Nominal value	$\sigma_{\mathrm{nom}} = \dfrac{F}{A_0}$	$e = \dfrac{l_1 - l_0}{l_0}$
True value	$\sigma = \dfrac{F}{A}$	$\varepsilon = \ln \dfrac{l_1}{l_0}$

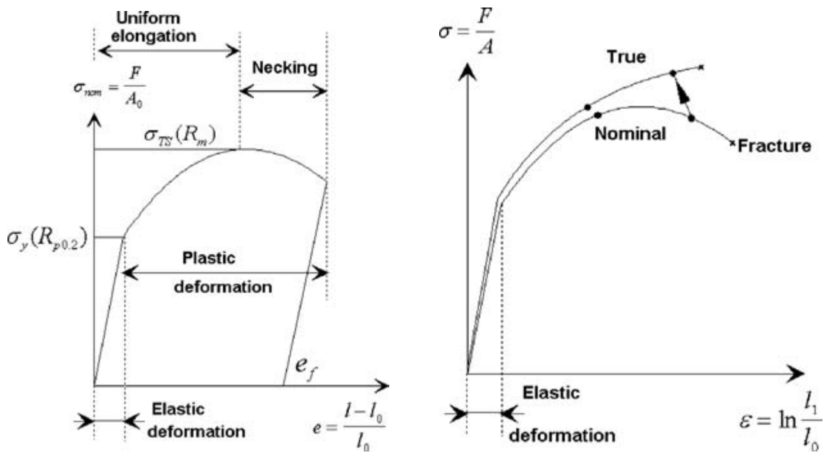

(a) (b)

Figure 7.8. The flow curve in tensile testing: (a) Nominal curve and (b) nominal and true curves in the same sketch.

As there are for stress, there are also two different definitions of strain, the *nominal* and the *true strain*, as shown in Table 7.1. The true strain is the best deformation measure and should preferably be used. Moreover, as shown in Example 4.3, true strain values can be added, whereas nominal strain values cannot. In the tensile test, the relation between stress and strain is determined by measurement of concurrent values of tensile force and length increase during the course of the test, for a chosen initial gauge length of the test specimen. From these measured data, the nominal and true stress and strain values are easily determined, and the graphical relationship between them is shown as either a nominal or a *true flow curve*; see Fig. 7.8.

As seen from the characteristic nominal flow curve in Fig. 7.8(a), the specimen will deform linear-elastically at low strain at the beginning of the test. If the specimen is unloaded while in the elastic state, the elastic deformations will disappear upon unloading. At a higher stress level, however, there is a sudden transition where deformations become plastic. In contrast to elastic deformations, the plastic deformations will remain in the specimen if it is unloaded again.

During the first part of the test, before reaching the peak value of the nominal flow curve, the specimen deforms uniformly. *Uniform deformation* means that the specimen is stretched in the length direction over its whole length, while it contracts in the radial direction. When the peak of the nominal flow curve is reached, the test specimen starts to neck locally [see Fig. 7.1(a)], and plastic deformation elsewhere in the specimen ceases. Hence, beyond the maximum of the flow curve, further plastic deformations occur only in the neck itself. Because these deformations are limited to a short length of the specimen, the deformation velocity increases considerably when necking begins, if the stretching velocity is kept constant; thus, the lateral contractions there will then be speeded up. *Neck growth* will therefore be rapid, and fracture will soon occur in the middle of the neck, shortly after initiation of the neck. Because of this, the deformations during necking are said to be unstable, and the phenomenon of necking is called an *instability*.

In Fig. 7.8(a), it is shown graphically how the mechanical properties of a metal – the *yield stress* $R_{p0,2}$, *tensile strength* R_m, and *fracture strain* e_f, and eventually the *elongation at fracture* (A_5 or A_{10}) – can be read from a nominal flow curve.

The true flow curve differs from the nominal flow curve, in that the stress increases all the time, even after the start of necking, until fracture occurs; see Fig. 7.8(b). Points have been marked on the flow curves in Fig. 7.8(b) to denote the same stage of stretching on each curve. As the arrow indicates, the true stress at a particular stage of stretching will be higher than the nominal stress at the same stage. For strains the situation is opposite: the nominal strain is larger than the corresponding true strain.

As mentioned before, the deformations localize in a small volume in the neck after the start of necking, and the strain rate in the neck starts to increase. It is therefore difficult to quantify and monitor the plastic deformations in the neck after necking has begun. Because the plastic deformation in cylinder compression is simpler to monitor, compression is often preferred as a technological test instead of tensile testing when one intends to study large deformations, corresponding those applied in rolling, forging, and other rapid metal forming processes. However, for operations as sheet-metal and plate forming, deformations must be modest, for the workpiece must not neck. This is because even a shallow neck in the specimen will represent a defect on the surface of the finished component. In sheet-metal forming, the tensile test is therefore a commonly applied technological test.

EXAMPLE 7.2: TRUE STRAIN IN TENSILE TESTING

Problem: A wire of a soft annealed material with initial diameter $d_0 = 1.2\,\text{mm}$ was stretched until fracture. Before stretching, the gauge length $l_0 = 100\,\text{mm}$ was marked on the wire. The two pieces of the wire was put together after fracture, and the new gauge length was measured to be $l_1 = 140\,\text{mm}$. The smallest diameter of the fractured wire was also measured and was determined to be $d_1 = 0.4\,\text{mm}$.

1. Determine the true uniform strain of the specimen under the assumption that the elongation of the gauge length after the start of necking is negligible in comparison with the uniform elongation before necking.
2. Determine the true strain in the smallest cross section of the neck of the wire.

Solution:

1. True uniform strain (approximate value):

$$\varepsilon_{\text{u}} = \ln\frac{l_1}{l_0} = \ln\frac{140}{100} = 0.34$$

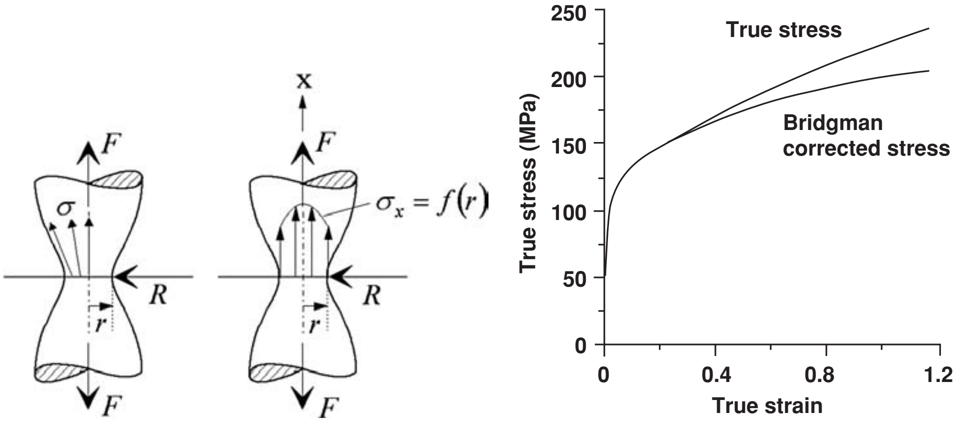

(a) (b)

Figure 7.9. (a) Triaxial stress conditions in the neck. (b) Modification of the flow curve due to the Bridgman correction.

2. True strain in the neck:

$$\varepsilon_{\text{neck}} = \ln \frac{A_0}{A_1} = \ln \frac{d_0^2}{d_1^2} = \ln \frac{1.2^2}{0.4^2} = 2.2$$

7.4.1 Instability in the Tensile Test

If a material strain-hardens in accordance with a power law, i.e., $\sigma = K\varepsilon^n$, then the true strain at which necking starts in tensile testing, ε_c, can be shown to be equal to the strain-hardening exponent:

$$\varepsilon_c = n \tag{7–1}$$

The relationship is derived in Example 7.3.

7.4.2 Bridgman Correction of the Flow Curve from a Tensile Test

After the start of necking, the plastic deformations localize in the neck, and the required force for stretching the specimen is that for deforming it in the neck. The stress state in the test specimen, which was simple uniaxial tension while deformations were uniform, changes into a *complex triaxial stress* state when necking begins. In the thin midsection of the neck, the tensile stresses will no longer act axially along the test specimen, except at the center; they will also have a radial component, as shown in Fig. 7.9(a). The stress component in the x-direction, integrated over the cross-sectional area on which it acts, gives the resulting tensile force required to stretch the specimen. After the start of necking, this axial stress component is no longer equal the effective stress in the material.

Bridgman performed a detailed theoretical analysis[10] of the stress condition in the neck. He assumed that the neck develops so that its outer surface is characterized by a radius of curvature R [see Fig. 7.9(a)], and that this radius decreases as the neck develops. He also assumed that the axial strain over the neck, which increases as the neck grows, remains constant across the neck. Under these assumptions, he derived an expression that relates the effective stress in the thinnest cross section of the neck to the *average axial stress* in the section, $\sigma = \sigma_x$:

$$\bar{\sigma} = \frac{\sigma}{\left(1 + \frac{2R}{r}\right) \cdot \ln\left(1 + \frac{r}{2R}\right)} = \frac{\sigma}{K_B} \tag{7-2}$$

The correct flow curve after the start of necking then can be determined from this equation – by dividing the measured average true axial stress in the specimen, $\sigma = F/A$, by the *Bridgman correction factor* K_B. When the correction is made, the correction factor will have the value 1 at the start of necking and will increase to a greater value (in the range 1.10 to 1.15 for soft Al alloys) at the end of the flow curve, just before the specimen starts to fracture. This value of course depends on the ductility of the material subjected to testing. Hence, when the correction is done, the stress at the end of the flow curve will be reduced by as much as 10–15%; see Fig. 7.9(b).

The parameters R and r in eq. 7-2 are the *radius of curvature of the neck* and the specimen's radius over the thinnest midsection of the neck, respectively; see Fig. 7.9(a). To perform the correction, the parameters R and r must be recorded as they vary during formation of the neck. One simple way of doing this is to stop the tensile test at three successive stages during necking of the specimen, and to measure the parameters directly from the specimen. With respect to the true strain, be aware that this parameter is determined from the smallest diameter of the specimen – i.e., the diameter in the neck, D – by use of the expression

$$\bar{\varepsilon} = \ln\left(\frac{A_0}{A}\right) = \ln\left(\frac{D_0}{D}\right)^2 = 2\ln\left(\frac{r_0}{r}\right) \tag{7-3}$$

Index 0 refers to the test specimen before stretching; symbols with no index refer to the thinnest cross section in the neck, as necking proceeds.

EXAMPLE 7.3: STRAIN AT THE START OF NECKING

Problem: Show that necking in the tensile test for a power-law material starts at a natural strain equal to the strain hardening exponent.

Solution: The tensile force in a tensile test specimen can be expressed as

$$F = \sigma A \tag{7-4}$$

Necking starts at the instant when the tensile force in the specimen reaches its highest level, i.e., the peak value. Hence,

$$\frac{\mathrm{d}F}{\mathrm{d}\varepsilon} = 0 \tag{7-5}$$

Because the natural strain in the specimen at this instant is $\varepsilon = \ln(A_0/A)$, the cross-sectional area of the specimen can be expressed by the equation

$$A = A_0 e^{-\varepsilon} \tag{7-6}$$

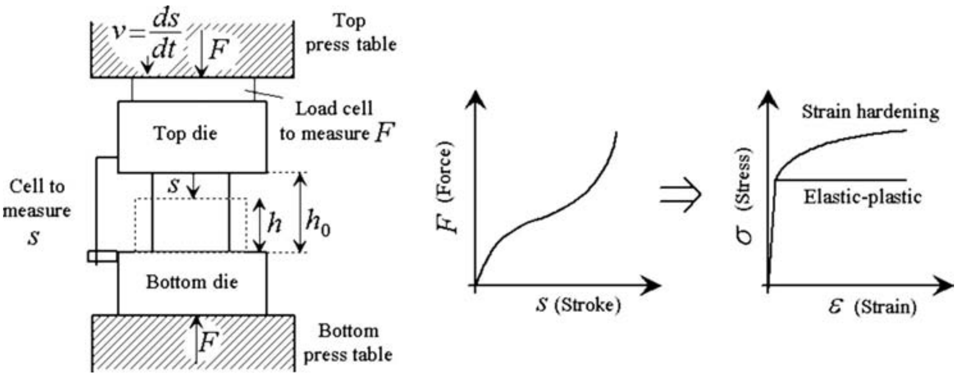

(a) (b) (c)

Figure 7.10. Compression testing: (a) experimental configuration, (b) sketch of load–stroke curve, and (c) flow curve derived from load–stroke curve.

This expression, introduced into eq. 7-4, yields $F = \sigma A = \sigma A_0 e^{-\varepsilon}$. If we differentiate this equation with respect to the true strain, we obtain

$$\begin{aligned}\frac{\mathrm{d}F}{\mathrm{d}\varepsilon} = 0 = \frac{\mathrm{d}(\sigma A_0 e^{-\varepsilon})}{\mathrm{d}\varepsilon} &= KA_0\left(\frac{\mathrm{d}\sigma}{\mathrm{d}\varepsilon}e^{-\varepsilon} + \frac{\mathrm{d}e^{-\varepsilon}}{\mathrm{d}\varepsilon}\sigma\right)\\ &= KA_0\left(\frac{\mathrm{d}\sigma}{\mathrm{d}\varepsilon}e^{-\varepsilon} - e^{-\varepsilon}\sigma\right) \quad \Rightarrow \quad \frac{\mathrm{d}\sigma}{\mathrm{d}\varepsilon} = \sigma\end{aligned}$$

Introduction of the power law $\sigma = K\varepsilon^n$ into the expression yields

$$\frac{\mathrm{d}\,(K\varepsilon^n)}{\mathrm{d}\varepsilon} = K\varepsilon^n \quad \Rightarrow \quad nK\varepsilon^{n-1} = K\varepsilon^n \quad \Rightarrow \quad \underline{\underline{\varepsilon = n}}$$

7.5 Basic Mechanics of Cylinder Compression

Cylinder compression[2,3] can be performed in a metal forming press with instrumentation to measure the load–troke history during compression. A schematic sketch of the setup in such an experiment is shown in Fig. 7.10. Compression is done by use of dies consisting of two plane-parallel platens. Most commonly the lower die is stationary, while the upper die is moved downward. During the compression stroke, the applied force F (i.e., load) is measured as a function of displacement s (i.e., stroke). The *compression velocity* at any stage is given by the time derivative of the displacement:

$$v = \frac{\mathrm{d}s}{\mathrm{d}t} \tag{7-7}$$

The relationship between displacement and height of the specimen is given by the following equations:

$$h + s = h_0 \quad \Rightarrow \quad h = h_0 - s \quad \Rightarrow \quad s = h_0 - h \tag{7–8}$$

where index 0 denotes initial value and no index the value of the parameter at a given instant during compression; see Fig. 7.10(a). The force required to compress the cylinder is measured vs. displacement, and the relationship between these two, $F = f(s)$, is the *load–stroke curve*, see Fig. 7.10(b). If frictionless compression is assumed, this data set can be transformed into the flow curve by means of eq. 7-9 and eq. 7-12.

Necessary procedures to acquire accurate flow stress data in cylinder compression are different in cold and hot forming. The flow stress in cold forming depends mainly on the strain and is approximately independent of strain rate and temperature; see Fig. 8.4(a). The applied compression speed is therefore less important when flow stress data are collected for cold forming applications.

In hot forming the situation is opposite. Strain rate and temperature are the main parameters that affect the flow stress; it is less influenced by strain [see Fig. 8.4(b)]. When flow stress data are to be collected in hot forming, the strain rate is therefore kept constant in each compression experiment, and a flow curve is recorded for the given strain rate and temperature. In this manner a family of flow curves are obtained for different constant strain rates, at different temperature levels.

7.5.1 Recording of the Flow Curve in Homogeneous Compression

Under the assumption of ideal *homogeneous deformations* in the material, the equations required to compute stress, strain, and strain rate in frictionless cylinder compression will be given. First, there is the strain (or effective strain), given as redefined positive strain (see eq. 5-11):

$$\varepsilon = \bar{\varepsilon} = \varepsilon_z = \ln \frac{h_0}{h} \tag{7–9}$$

The principle of constancy of volume is valid, as for other metal forming processes:

$$A_0 h_0 = Ah \tag{7-10}$$

The true contact area between cylinder and die platen during compression can be expressed as

$$A = A_0 \frac{h_0}{h} = A_0 \, e^{\ln(h_0/h)} = A_0 e^{\varepsilon} \tag{7-11}$$

As this equation shows, the contact area increases exponentially with increasing strain. The *flow stress* during compression can be computed from the measured compression force F by the expression

$$\sigma = \bar{\sigma} = \sigma_z = \frac{F}{A} \tag{7-12}$$

The *effective strain rate* in the cylinder can be quantified as a redefined strain rate by the equation

$$\dot{\varepsilon}_{\text{redef}} = -\dot{\varepsilon}_z = -\dot{\bar{\varepsilon}} = \frac{v_s}{h} \tag{7–13}$$

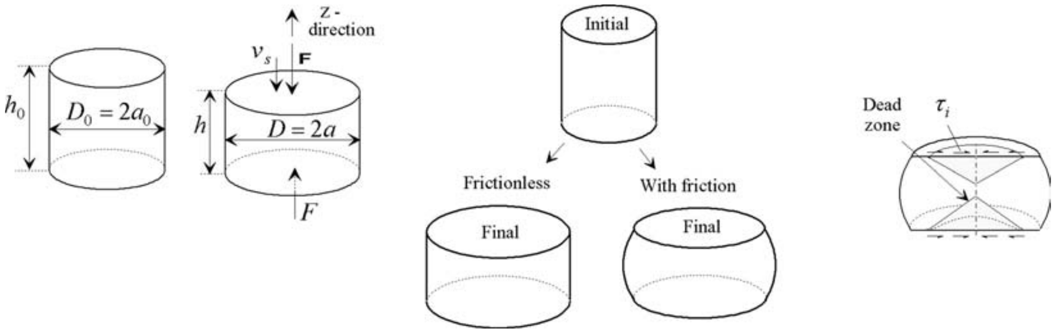

(a) (b)

Figure 7.11. Cylinder compression test: (a) frictionless homogeneous compression, (b) inhomogeneous compression with barreling, and (c) formation of dead zones in inhomogeneous compression.

This expression shows that the strain rate during compression increases if a constant upper die speed, v_s, is used in the test. The equation clearly depicts that to achieve constant strain rate in the test, it is required to reduce the compression speed throughout the stroke, i.e., to *retard compression movement* as compression proceeds. A retarded stroke that provides constant average strain rate in the compression test up to effective strain rates of 300 s^{-1} can be achieved in modern metal forming simulators in which the compression speed can be monitored freely.

7.5.2 Inhomogeneous Deformations in Cylinder Compression

The simple idealized mechanics described by the preceding equations is only valid if the cylinder deforms homogeneously. *Homogeneous* deformations are only achieved if the cylinder is compressed with approximately frictionless conditions against the compression platens. In that case, the cylinder will maintain perfect cylindrical shape during the compression test, if the material of the cylinder is isotropic. During compression the cylinder will expand in its radial direction so that the diameter increases as the height is reduced and constancy of volume will be maintained during the test; see Fig. 7.11(a).

In compression with friction between cylinder and tooling, the metal flow will be completely different. Friction stresses now will be directed against the radial, outward-sliding motion of the cylinder over the die platens, as depicted in Fig. 7.11(c). The friction shear stresses will reduce the radial outward flow of the end faces of the cylinder adjacent to the die platens. To compensate for reduced radial flow here, correspondingly, there is increased outward metal flow in the middle of the cylinder. Hence, the friction between die and tooling immediately manifests itself in the flow phenomenon called *bulging*, or *barreling* (Fig. 7.11(b)). The outer cicumferential surface, i.e., the side face, of the cylinder bulges out at mid-height of the cylinder, and the specimen develops a shape similar to a barrel. Moreover, bulging increases with increased friction throughout the compression stroke, so that the barreled shape becomes more pronounced with higher friction.

When there is bulging in cylinder compression, a conical *dead zone*, or *stagnant zone*, forms inside the cylinder, located with mirror symmetry on both sides of the horizontal midplane of the cylinder, in each end of the specimen; see Fig. 7.11(c). Material inside the dead zones is subjected to less plastic deformation than the rest of the material of the cylinder. Because the deformation varies this way within the volume of the specimen, it is said to be *nonuniform*, or *inhomogeneous*, in cylinder compression with friction. However, when frictionless cylinder compression is performed, the plastic deformation over the whole volume of the cylinder is the same, so it is then generally said to be *uniform*, or *homogeneous*.

Formulas for computation of stress and strain in cylinder compression, as presented in the preceding subsection, are valid if the compression is homogeneous and approximately valid if the friction is low. But in the case of high friction, these formulas do not accurately describe stresses and strains in cylinder compression. In the literature, it is therefore generally recommended to maintain low friction during cylinder compression, so that the preceding formulas can be used to deduce the flow curve in the test. This can be achieved, for instance, as follows:

- Use efficient lubricants to provide low friction in the compression experiment.
- Use a machined, spiral-shaped groove in each end face of the cylinder to trap and distribute lubricant over the interface during compression, to maintain low friction there.
- Perform the test stepwise, lubricating the interface between steps.
- Correct for friction effects using FEA.
- Use a high, slender, cylinder with aspect ratio 1.5 or 2, to minimize friction effects.

For a more detailed description of metal flow in cylinder compression as it appears in FEA, see Ch. 15.2. There, it is also shown how frictional effects on the load–stroke curve are reduced when the cylinder is made more slender.

7.6 Plane Strain Compression

In this technological test,[5,6] it is sometimes claimed that deformations are similar to those in rolling. The test method has therefore often been applied for physical simulation of the rolling process in the laboratory. Some semifinished industrial products are rather thin (they may have thickness $t \leq 8\,\text{mm}$), as for instance in products made of sheet metal or thin-walled extrusions. From such thin material, it is of course impossible to machine cylindrical specimens of reasonable size. Such products can, however, be tested by use of plane strain compression, and the material can then be compressed down to (for instance) 1 mm or 0.5 mm thickness.

As mentioned, plane strain compression can be performed in two different ways (see Fig. 7.3). Most commonly, the variant shown in Fig. 7.3(b) is used. The size of the specimen should then be sufficiently large so that most of it resides outside the compression gap; see Fig. 7.12. The specimen breadth in plane strain compression is in general recommended to be less than the width of the dies, i.e., $B > w$;

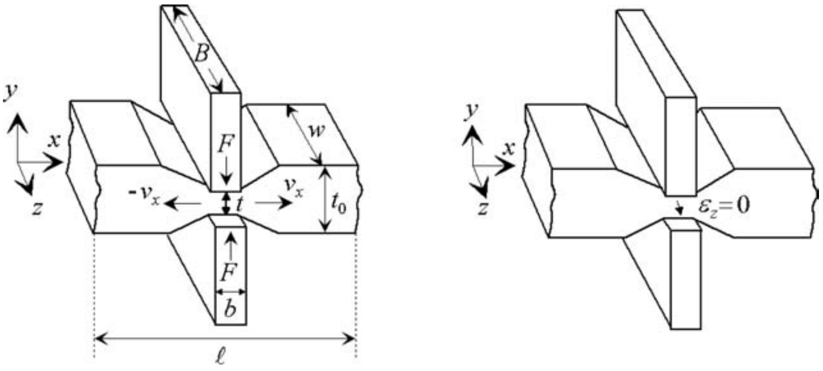

(a) (b)

Figure 7.12. Three-dimensional sketch of the plane strain compression test.

see Fig. 7.12(a). When this criterion is fulfilled, lateral spread of the specimen in the z-direction is minimized; see Fig. 7.12.

The specimen length in plane strain compression should also be considerably larger than the width of the compression die, i.e., $l \gg b$. In this case, there is sufficient rigid material outside the compression gap, on both sides of it, to reduce lateral spread in the plastic zone. When the specimen is compressed, the rigid ends at each side of the gap will flow in the x-direction, and the deformation in the compression gap will mainly consist in elongation of the specimen.

When deformations occur this way, the rigid ends of the specimen on each side of the plastic zone provide mechanical support to the material in the plastic zone, and contribute to reduced lateral flow, i.e., flow in the z-direction. In this manner, there is *plastic constraint* on the material in the gap, and significant lateral spread in the z-direction is avoided.

Reduced lateral flow in plane strain compression will also be the result if the width of the specimen, w, is made large in comparison with the thickness of the compression die, b. In the literature, it is sometimes claimed that plane strain compression can be achieved approximately if the compression geometry is selected so that $w/b > 5$.

A concluding remark is that, through selection of appropriate die and specimen geometry in the plane strain compression test, one can monitor the deformations inside the compression gap, to minimize deviations from idealized plane strain flow.

7.6.1 Basic Mechanics of Plane Strain Compression

In addition to the geometrical limitations just stated, which are required to attain approximate plane strain conditions in the test, it is also an advantage if deformations in the compression gap are maintained as homogeneous as possible. The degree of inhomogeneity in the test is mainly influenced by the thickness-to-width ratio of the compression gap, and deformations will be very inhomogeneous if this ratio is made too high. Friction effects on the compression load also depend on this ratio. Hence, to balance the conditions, to attain rather homogeneous deformations while maintaining a moderate effect of friction on compression load, it is recommended in the literature[11] to keep the thickness-to-width ratio of the specimen within the limits

$$\frac{1}{4} < \frac{t}{b} < \frac{1}{2} \tag{7-14}$$

This requirement can be fulfilled by changing to dies of less thickness b as the specimen becomes thinner during the test. In this way, one can compress a specimen down in approximately plane strain to a reduction of 90%, i.e., to a thickness strain of $\varepsilon_t = 2.3$, or a true effective strain of $\bar{\varepsilon} = 2.6$; see eq. 7-18.

Under the assumption of perfect plane strain conditions and homogeneous deformations in the compression gap, the following formulas are valid for plane strain compression:

$$\text{Average contact pressure:} \quad p = \sigma_y = \frac{F}{wb} \tag{7–15}$$

$$\text{Thickness strain:} \quad \varepsilon_y = \varepsilon_t = \ln\frac{t_0}{t} \tag{7–16}$$

$$\text{Effective stress:} \quad \bar{\sigma} = \frac{\sqrt{3}\sigma_y}{2} = 0.866\sigma_y \tag{7–17}$$

$$\text{Effective strain:} \quad \bar{\varepsilon} = \frac{2}{\sqrt{3}}\varepsilon_y = 1.155\varepsilon_y \tag{7–18}$$

For derivation of the last two expressions, see Example 7.4.

7.7 Stress States in Technological Tests

Characteristic stress states present in the different tests can be visualized[7] in a diagram as that shown in Fig. 7.13. In this diagram, all possible plane stress conditions are shown in a two-dimensional plot. This is the most common diagram in which the von Mises criterion and the Tresca criterion are visualized.

The stress states of the various technological test methods are denoted by numbers in this diagram. State 1 corresponds to the tensile test, 2 to the compression test, 4 to the plane strain compression test, and 5 to the torsion test. As shown, in the torsion test, there is *pure shear*, characterized by two equal-size principal stresses of opposite sign.

EXAMPLE 7.4: EFFECTIVE STRESS AND STRAIN IN PLANE STRAIN COMPRESSION

Problem: A material with constant flow stress is deformed to a permanent plastic strain ε_x by plane strain compression, in a test where $\sigma_3 = \sigma_z = 0$. Determine the effective compressive stress and the effective compressive strain in this test.

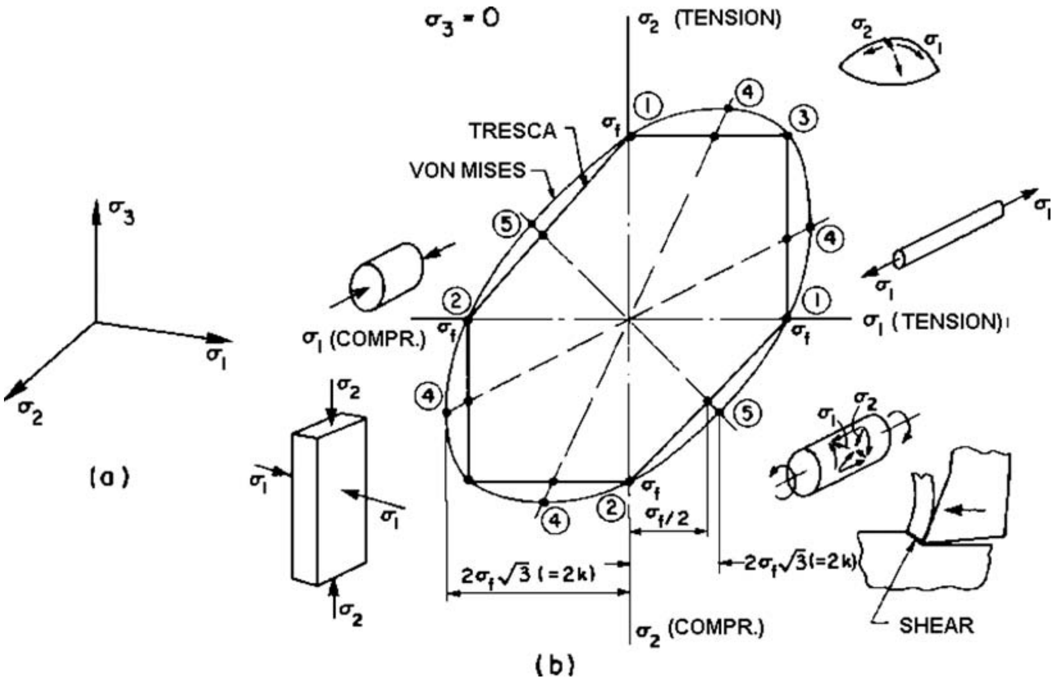

Figure 7.13. Stress states in different technological tests. (Reprinted with permission from ASM International.)

Solution: Plane strain compression is characterized by zero strain in the z-direction: $\varepsilon_z = \varepsilon_2 = 0$; see Fig. 7.12. According to the principle of constancy of volume, the two other principal strains can be determined as $\varepsilon_x = \varepsilon_3 = -\varepsilon_y = -\varepsilon_1$. When principal strains are known, the principal stresses can be determined by the flow rule:

$$\mathrm{d}\varepsilon_2 = \frac{\mathrm{d}\bar{\varepsilon}}{\bar{\sigma}}\left[\sigma_2 - \frac{1}{2}(\sigma_1 + \sigma_3)\right] = 0 \quad \Rightarrow \quad \sigma_2 = \frac{1}{2}(\sigma_1 + \sigma_3) = \frac{1}{2}\sigma_1$$

The effective stress and the effective strain can then be determined as

$$\bar{\sigma} = \frac{1}{\sqrt{2}}\left[(\sigma_x - \sigma_y)^2 + (\sigma_y - \sigma_z)^2 + (\sigma_z - \sigma_x)^2 + 6\left(\tau_{xy}^2 + \tau_{yz}^2 + \tau_{xz}^2\right)\right]^{1/2}$$

$$\bar{\varepsilon} = \left\{\frac{2}{3}\left[\varepsilon_x^2 + \varepsilon_y^2 + \varepsilon_z^2 + 2\left(\varepsilon_{xy}^2 + \varepsilon_{yz}^2 + \varepsilon_{zx}^2\right)\right]\right\}^{1/2}$$

The effective stress and the effective strain in the test then must be

$$\underline{\underline{\bar{\sigma}}} = \frac{1}{\sqrt{2}}\left[(0 - \sigma_1)^2 + \left(\sigma_1 - \frac{\sigma_1}{2}\right)^2 + \left(\frac{\sigma_1}{2} - 0\right)^2\right]^{1/2} = \frac{\sqrt{3}}{2}\sigma_1 = \underline{\underline{\frac{\sqrt{3}}{2}\sigma_y}}$$

$$\underline{\underline{\bar{\varepsilon}}} = \left[\frac{2}{3}\left(\varepsilon_y^2 + \varepsilon_y^2\right)\right] = \underline{\underline{\frac{2}{\sqrt{3}}\varepsilon_y}}$$

Problems

7.1 Measured data from a tensile test, performed on an annealed steel alloy with 0.05% C, are given in the accompanying table.

(a) Compute the unspecified parameters, and insert them into the table.

(b) Plot graphs of the flow curves obtained from the data as nominal stress vs. nominal strain, and as true stress and true Bridgman-corrected stress vs. true strain. Which flow curve do you consider the best one for the tested material?

(c) Check if the best flow curve can be fitted to the constitutive equation $\sigma = K\bar{\varepsilon}^n$. If it can, apply the data in the table to determine the exponent of strain hardening and the strength coefficient of the material.

(d) Assume a flow curve of a material to be described by the power-law expression. Show that necking then starts for $\bar{\varepsilon} = n$.

(e) Immediately after the last record in the table, the specimen fractured in the neck, so the last strain value was the true strain value at fracture. On the basis of this information, discuss to what extent the constitutive equation you have determined is able to describe the flow stress in an industrial metal forming process.

Record no.	Specimen diameter (mm)	Radius of curvature in neck, R (mm)	Load (kN)	Cross-sectional area (mm^2)	True strain ε	Nominal stress σ_n (MPa)	True stress σ (MPa)	True Bridgman-corrected stress (MPa)
1	10.03		0					
2	9.53		20.70					
3	9.06		22.65					
4	8.21		22.85					
5	7.43		21.40					
6	6.75	14.8	19.70					
7	6.08	7.9	17.85					
8	5.53	5.7	13.70					

7.2 A constant effective strain rate of $10\,\mathrm{s}^{-1}$ is to be maintained in a plane strain compression test where the initial specimen height is $h_0 = 10\,\mathrm{mm}$. Determine the necessary compression velocities in the test as the height of the specimen decreases.

7.3 Consider a cold rolling process in which the initial strip thickness is 2 mm and the final thickness 0.25 mm. A plane strain compression test is considered as a technological test to measure the flow stress of the material in the process. Specify a good procedure for the test.

NOTES

1. Ferguson, D., Chen, W., Bonesteel, T. and Vosburg, J.: “A look at physical simulation of metallurgical processes, past, present and future,” Materials Science and Engineering: A, Vol. 499, 2009, pp. 329–332.
2. Pöhlandt, K.: “Materials Testing for the Metal Forming Industry,” Springer-Verlag, 1989.
3. Dieter, G. E. (Ed.): “Workability Testing Techniques,” ASM Int., Metals Park, Ohio, 1984.
4. Davis, J. R.: “Tensile testing,” ASM Int., Metals Park, Ohio, 2004.
5. Silk, N. J., and Winden, M. R.: “Interpretation of hot plane strain compression testing of aluminium specimens,” Materials Science and Technology, Vol. 15, 1999, pp. 295–300.
6. Uyyuru, R. K.: “Plane strain compression test as a friction-measuring test – a comprehensive review,” Int. J. Forming Processes, Vol. 7, No. 3, 2004, pp. 310–319.
7. Schey, J. A.: “Tribology in Metalworking; Friction, Lubrication and Wear,” ASM Int., Metals Park, Ohio, 1983, pp. 12–13.
8. http://www.gleeble.com/
9. Storojeva, L., Ponge, D., Kaspar, R., and Raabe, D.: “Development of microstructure and texture of medium carbon steel during heavy warm deformation,” Acta Materialia, Vol. 52, 2004, pp. 2209–2220.
10. Bridgman, P. W.: “Stress distribution in the neck of a tension specimen,” Trans. Amer. Soc. Metals, Vol. 32, 1944, p. 553.
11. Dieter, G.: “Mechanical Metallurgy,” McGraw-Hill, 1989.

REFERENCE

“ASM Handbook, Vol. 8, Mechanical Testing and Evaluation,” ASM Int., Metals Park, Ohio, 2000.

8 Flow Stress Data

The flow stress of a material is indeed an important parameter in metal forming. To create a good FEM model of a forming process, for example, it is required that one be able to specify the flow stress of the workpiece material with good accuracy.

Because of this, the main processing parameters affecting the flow stress of commonly used metals and their alloys will be considered in this chapter, as regards both cold and hot forming applications. When the flow stress has been measured, so one knows how the processing parameters affect the flow stress, it is common to search for an equation that can describe the actual flow stress dependence well. When one has arrived at such an equation, one says that one has obtained a good *material model* for the material. It is also common to call the material model the *constitutive equation* for the actual metal. Commonly applied procedures to determine constitutive equations for metals will be described and material models for some commonly used metals will be reviewed in this chapter.

8.1 The Flow Stress

In Fig. 7.8(b), flow stress curves were shown as they commonly appear for a metal at room temperature. As depicted in this figure, the true flow stress often increases with increasing strain when the metal is tested at room temperature.

If we consider metals, at cold, warm, and hot forming temperatures, a number of parameters can affect flow stress, not only strain. If possible, it is useful to express the flow stress by a function, instead of using only graphs, i.e., to express the flow stress in terms of a material model or a constitutive equation for the considered material.

8.2 Constitutive Equations for Metals

There are many different metals and alloys, but in this context, I will restrict the treatment to common metals and to the more common constitutive equations.

Remember that at low strains the stress commonly has a linear relationship vs. strain, as described by Hooke's law. The stress a material is subjected to can then be

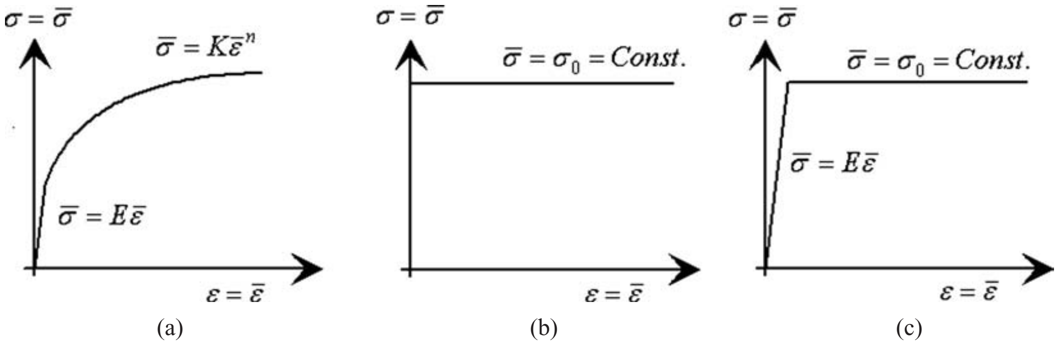

Figure 8.1. (a) Flow curve for metal. (b,c) Flow curves of ideal materials.

determined from the Young's modulus of the material, E, by the equation

$$\varepsilon_{\mathrm{el}} = \varepsilon = \frac{\sigma}{E} \tag{8-1}$$

When the stress on a material is increased beyond the level where the deformation is elastic, i.e., *the elastic limit*, the material starts to yield plastically. The material then experiences permanent deformations that remain even after unloading of the body, and the stress on the material must be derived from the flow curve of the material. In the regime of plastic flow, the steepness of the flow curve commonly decreases with increasing strain. For the more common metals at room temperature, the flow curve will have the appearance depicted in Fig. 8.1(a). Because the true stress increases with increasing true strain, it is common to say that the material *strain-hardens*. Metals deformed at room temperature are therefore most often considered elastic–plastic materials, which strain-harden upon plastic deformation.

This is true when one considers the metals most commonly used in industrial metal forming: steel, aluminum, copper, and brass. However, there are exceptions from this simplification if one considers less commonly used metals, such as lead, zinc, and tin. These metals are rather soft, and their flow stress is strain-rate-dependent even at room temperature. To simplify the theoretical treatment in mechanics, it is common to consider idealized materials like rigid–plastic or elastic–plastic materials; see Fig. 8.1(b,c). For such idealized materials, the flow stress is most commonly assumed constant, i.e., there is no strain hardening in the material.

During warm or hot forming of metals, flow stress conditions are very different from those in cold forming. The flow stress at elevated temperature is commonly dependent on a number of parameters, of which the strain rate and temperature are most important. The flow stress also depends on the microstructure of the metal, which can change during a forming operation. For an aluminum alloy containing Si, for instance, the flow stress will depend strongly on whether Si is present in the microstructure as precipitates or remains in solid solution.

As mentioned, it is common to describe the flow curve of a material by an equation that describes the influence of the main process parameters on the flow stress, i.e., by a constitutive equation. If one considers cold, warm, or hot forming of common industrial metals, the major parameters affecting the flow stress are strain, strain rate, temperature, and microstructure. The general constitutive equation[1] for

Figure 8.2. Graphical representation of the flow stress of Cu and its dependence on common forming parameters.

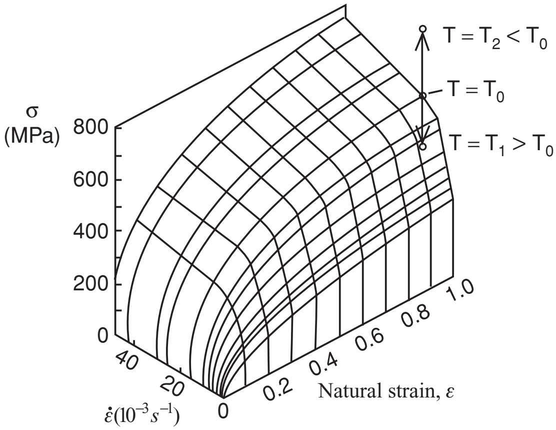

a metallic material is therefore commonly expressed by a function

$$\sigma = f(T, \bar{\varepsilon}, \dot{\bar{\varepsilon}}, S) \tag{8-2}$$

If we assume the microstructure to remain constant in the metal during forming, i.e., $S = \text{const}$, then the expression is reduced to

$$\sigma = f(T, \bar{\varepsilon}, \dot{\bar{\varepsilon}}) \tag{8-3}$$

This relationship for copper is shown in Fig. 8.2. The sketch shows that for constant temperature $T = T_0$, the flow stress varies so it forms a doubly curved surface when plotted as a function of strain and strain rate. The influence of temperature on flow stress is also shown in the figure by means of two arrows. One arrow points downwards to show that a temperature increase causes the flow stress to decrease. On the other hand, the arrow pointing upwards shows that the opposite effect occurs when the temperature is decreased.

In Fig. 8.3(a), a principal graph is shown that depicts how the flow stress of a typical Al alloy will depend on temperature. While the flow stress is rather high

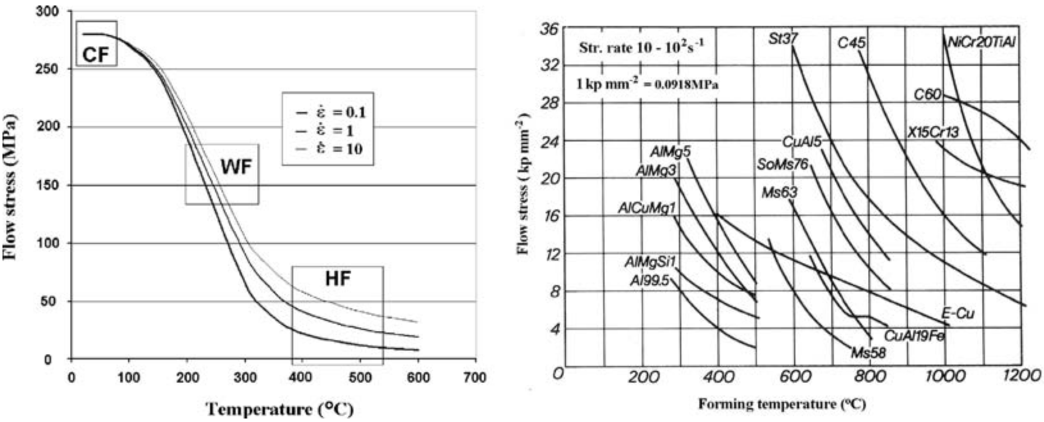

(a) (b)

Figure 8.3. Graphical representation of the temperature dependence of flow stress for some metals. (a) Typical behavior of Al-alloy at constant level of strain and (b) various alloys at commonly used hot forming temperatures (reprinted with permission from Aluminum-Verlag, Düsseldorf, Germany, www.alu-verlag.de).

and approximately independent of temperature in the cold temperature range of forming, which extends from room temperature up to ~100°C, it decreases as the temperature is raised further. In cold forming, the flow stress increases with increasing strain, i.e., the workpiece material strain hardens when it is deformed, as shown in Fig. 8.1(a). This effect, however, is not shown in Fig. 8.3(a).

If the alloy is heated up to temperatures in the range 400–500°C the flow stress is strongly reduced. This explains why it can be beneficial to apply (warm or more commonly) hot forming to metals; the flow stress can be reduced as much as five- or tenfold by changing from cold to hot forming. The reduction in the flow stress is of course accompanied with a corresponding drop in the forming load. In Fig. 8.3(a), boxes with notation have been added onto the curve; CF for cold, WF for warm, and HF for hot forming. For warm and hot forming, it has been shown in the figure that the flow stress starts to become dependent on the strain rate in the forming operation.

In Fig. 8.3(b), hot forming flow stress data for a large number of metals[2] have been shown in one diagram. As seen the hot forming temperature for an Al-alloy is much lower than those used for steels. For a steel as C45, the hot forming temperature lies in the range 900–1100°C.

For some steels, there might be jumps in the flow stress curve as the temperature changes caused by structural transformations in the metal. This is due to the allotropic behavior of these alloys, i.e., their transformation from one metallurgical phase to another upon heating or cooling. In the temperature range around 800°C, there may be a sudden increase in the flow stress with increasing temperature due to the transformation of the α-phase (i.e., ferrite with bcc crystal structure) into γ-phase (i.e., austenite with fcc crystal structure).

A function that is used often to describe the flow stress of a material and its dependence on common forming parameters is the following:

$$\bar{\sigma} = K \cdot \bar{\varepsilon}^n \cdot \dot{\bar{\varepsilon}}^m \cdot e^{\beta/T} \tag{8-4}$$

In this relationship, the symbols K, n, m, and $\beta = Q/R$ denote material-dependent constants that can determined by curve fitting from experimentally obtained flow curves; see Examples 8.1 to 8.5. The flow curves are obtained in technological tests such as those described in Ch. 7. In the German literature, this relationship is often termed the Hensel–Spittel[3] equation, in the English literature the Norton[4]–Hoff[5] equation. This constitutive equation is commonly applied to describe flow stress data for cold, warm, and hot forming. The constants in the expression are commonly named as follows: K is the *strength coefficient*, n the *strain-hardening exponent*, m the *strain-rate sensitivity*, and $\beta = Q/R$ the *temperature sensitivity*.

8.2.1 Constitutive Equations in Cold Forming

At room temperature, the flow stress of most metals is largely independent of the applied strain rate; see Fig. 8.4(a). Neither does it then depend significantly on the applied temperature, if the temperature rise is moderate. Strain, then, is the main

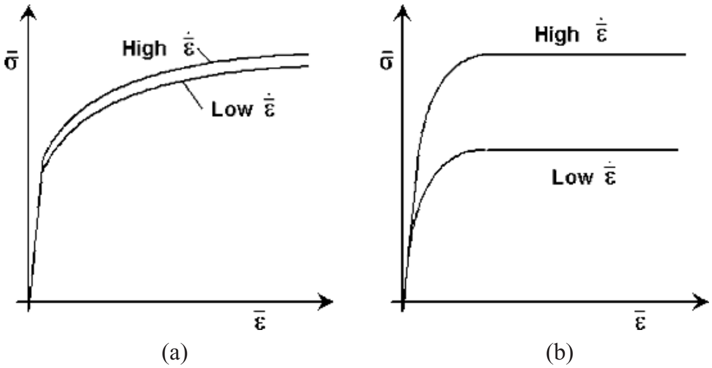

Figure 8.4. Common appearance of flow curves in (a) cold forming and (b) hot forming.

parameter that increases the flow stress, because of the effect of strain hardening. Under these circumstances, eq. 8-4 is therefore reduced to the simple expression

$$\bar{\sigma} = K \cdot \bar{\varepsilon}^n \tag{8-5}$$

because $m = 0$ and the exponential factor is equal to 1. This expression is commonly called Ludwig's law,[6] the Ramberg–Osgood[7] equation, or the power-law expression.

A number of other relationships are sometimes used to describe the flow stress in cases when the preceding equation does not fit experimental data well. They include the following three:

Swift's[8] relationship:

$$\sigma = A + K\varepsilon^n \tag{8-6}$$

Voce's[9] relationships:

$$\sigma = A - Be^{-Ce} \quad \text{or} \quad \sigma = A + D\varepsilon - Be^{-Ce} \tag{8-7}$$

Here A, B, C, and D are constants for a particular metal, and they are determined by curve fitting from experimental flow stress data.

EXAMPLE 8.1: CONSTITUTIVE EQUATION FROM FLOW CURVE

Problem: The flow curve recorded for a metal at room temperature is shown in the accompanying graph. Two data points on the curved portion of the graph were read out as $(\varepsilon_1, \sigma_1)$ and $(\varepsilon_2, \sigma_2)$. Determine the constitutive equation for this metal.

Solution: When two data points are known on the graph, curve fitting to the power law expression $\sigma = K\varepsilon^n$ can easily be done. Each coordinate set is added into the power law expression to create two equations with two unknowns, K

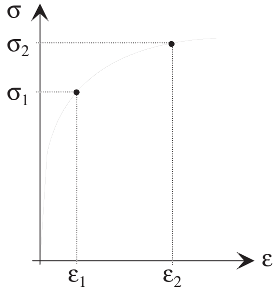

and n. Then when one equation is divided by the other, the following relationship is obtained:

$$\frac{\text{Equation 1}}{\text{Equation 2}} = \frac{\sigma_1}{\sigma_2} = \frac{K\varepsilon_1^n}{K\varepsilon_2^n} = \frac{\varepsilon_1^n}{\varepsilon_2^n} = \left(\frac{\varepsilon_1}{\varepsilon_2}\right)^n \quad \Rightarrow \quad \underline{\underline{n = \frac{\log\left(\dfrac{\sigma_1}{\sigma_2}\right)}{\log\left(\dfrac{\varepsilon_1}{\varepsilon_2}\right)}}}$$

We have now determined the strain-hardening coefficient n. The n-value is then inserted in the first equation. This way we get a new equation with one unknown, from which K, the strength coefficient, can easily be determined as

$$\underline{\underline{K = \frac{\sigma_1}{\varepsilon_1^n}}}$$

Now, to check if our data set is accurately described by this power law expression, it is recommended to make a plot of $\log\sigma$ vs. $\log\varepsilon$ for the data. A good fit has been obtained only if this plot is a straight line.

The procedure described can also be used for curve fitting of hot forming flow stress data with the expression $\sigma = C\dot{\varepsilon}^m$. Then, each co ordinate set should consist of a flow stress value and the strain-rate value for which it was determined, namely, $(\dot{\varepsilon}_1, \sigma_1)$ and $(\dot{\varepsilon}_2, \sigma_2)$. The solution then will be as in the first case, with the exception that the given strain-rate values will replace the strain values used in the first case.

Alternative solution: Make a plot of $\log\sigma = f(\log\varepsilon)$. Then read out constants K and n from the graph, as shown in the accompanying figure.

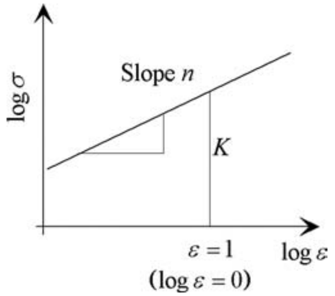

EXAMPLE 8.2: CONSTITUTIVE EQUATION FROM COLD FORMING FLOW CURVE

Problem: The flow curve of copper in cold forming was recorded at two different strain rates. The result is shown in the accompanying figure. Curve-fit the given data with the power law. The equality 1 psi $= 6.895 \times 10^{-3}$ MPa can be used to transform stress from English units to SI units.

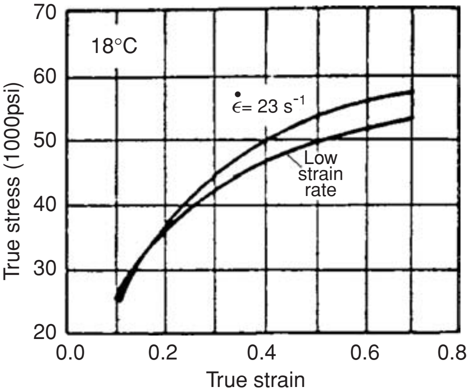

(Reprinted with permission of John Wiley & Sons, Inc., from R. Bunshah (Ed.), Techniques of Metals Research, 1968, Vol. 1, Part 3[10]).

Solution: Assume the upper flow curve to describe the flow stress data. The coordinates for two points on the upper curve are read out as follows:

Point 1 : $\bar{\sigma}_1 = 37000\,\text{psi} = 255\,\text{N}\,\text{mm}^{-2}$ for $\bar{\varepsilon}_1 = 0.2$

Point 2 : $\bar{\sigma}_2 = 56000\,\text{psi} = 386\,\text{N}\,\text{mm}^{-2}$ for $\bar{\varepsilon}_2 = 0.6$

Curve fitting with the relation: $\bar{\sigma} = K\bar{\varepsilon}^n$ is then done as in Example 8.1, with the following result:

$$\underline{\underline{n}} = \frac{\log \dfrac{\bar{\sigma}_1}{\bar{\sigma}_2}}{\log \dfrac{\bar{\varepsilon}_1}{\bar{\varepsilon}_2}} = \frac{\log \dfrac{255\ \text{MPa}}{386\ \text{MPa}}}{\log \dfrac{0.2}{0.6}} = \underline{\underline{0.377}}$$

$$\underline{\underline{K}} = \frac{\bar{\sigma}_1}{\varepsilon_1^n} = \frac{255\ \text{MPa}}{0.2^{0.377}} = \underline{\underline{468\ \text{MPa}}}$$

The flow stress for the upper curve can then be described by the expression

$$\underline{\underline{\bar{\sigma}}} = K\bar{\varepsilon}^n = \underline{\underline{468\,\text{MPa} \cdot \bar{\varepsilon}^{0,377}}}$$

From this we see that when using this relationship we make an approximation, as we neglect the strain-rate dependence of the flow stress. Instead of selecting the upper flow curve as basis data for our fit, we could have used the lower flow curve, or an average between the upper and the lower curve.

8.2.2 Constitutive Equations in Hot Forming

During forming at the intermediate temperature levels corresponding to warm forming, the flow stress is commonly dependent on strain, strain rate, and temperature as described previously by eq. 8-4. But when the temperature is increased further, up to temperatures commonly applied in hot forming, the strain-hardening effect often becomes negligible, so that the flow curves flatten out at high strain levels as shown in Fig. 8.4(b). If one neglects the low-strain region of the curves, i.e., assumes that the material is completely plasticized throughout the thickness of the workpiece in the actual forming operation, the following power law expression will give an adequate description of the flow stress at a constant temperature:

$$\bar{\sigma} = C \cdot \dot{\bar{\varepsilon}}^{m} \tag{8-8}$$

If there is significant temperature change in the material, the following relationship should preferably be used:

$$\bar{\sigma} = C \cdot \dot{\bar{\varepsilon}}^{m} \cdot e^{\beta/T} \tag{8-9}$$

An alternative expression commonly used to describe flow stress in hot forming applications is the Zener–Hollomon relationship,[11,12] which expresses the flow stress by a hyperbolic-sine function as follows:

$$\sigma = \frac{1}{\alpha} \sinh^{-1}\left[\left(\frac{\dot{\varepsilon} \cdot e^{Q/RT}}{A}\right)^{1/n}\right] \tag{8-10}$$

Absence of strain-hardening effects in a metal at high temperatures is closely connected to the onset of microstructural changes due to recovery and recrystallization taking place inside the workpiece subjected to metalworking. Whereas an ever-denser dislocation network is formed in a metal subjected to cold working, recovery and recrystallization will take place in metals subjected to hot working, so that the dislocation network formed in a forming step tends to disappear inside the metal during or after forming. In a rolling process, for instance, recovery and recrystallization can take place both during forming and in between the rolling steps. Thus strain hardening is concurrently balanced by recovery and recrystallization, so that the flow stress of the material is maintained approximately constant even though the amount of deformation increases. Because microstructure controls the flow stress through the dislocation movement, a lot of research is now being conducted to arrive at constitutive equations of metals by considering such microstructural mechanisms.[13]

EXAMPLE 8.3: CONSTITUTIVE EQUATION FROM A HOT-FORMING FLOW CURVE

Problem: The flow curves shown in the accompanying graph have been recorded for hot forming of copper at 900°C. Fit the data with the power law expression $\bar{\sigma} = C\dot{\bar{\varepsilon}}^{m}$.

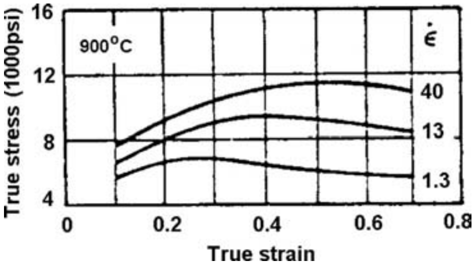

(Reprinted with permission of John Wiley & Sons, Inc., from R. Bunshah (Ed.), Techniques of Metals Research, 1968, Vol. 1, Part 3.)

Solution: To fit these data with the relationship $\bar{\sigma} = C\dot{\varepsilon}^m$, one must assume no dependence of strain rate on flow stress. This is equivalent with drawing straight lines in the diagram. The accompanying figure shows this approximation.

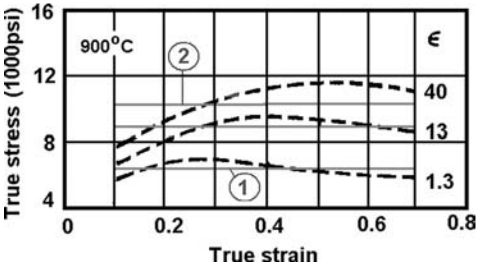

(Reprinted with permission of John Wiley & Sons, Inc., from R. Bunshah (Ed.), Techniques of Metals Research, 1968, Vol. 1, Part 3.)

The following set of data can be read from the figure:

Line 1: $\bar{\sigma}_1 = 6000\,\text{psi} = 41.4\,\text{MPa}$ for $\dot{\varepsilon}_1 = 1.3\,\text{s}^{-1}$

Line 2: $\bar{\sigma}_2 = 10000\,\text{psi} = 69.0\,\text{MPa}$ for $\dot{\varepsilon}_2 = 40.0\,\text{s}^{-1}$

Curve fitting is done as was shown in Example 8.1, with the result

$$\frac{\bar{\sigma}_1}{\bar{\sigma}_2} = \frac{C\dot{\varepsilon}_1^m}{C\dot{\varepsilon}_2^m} \quad \Rightarrow \quad \left(\frac{\dot{\varepsilon}_1}{\dot{\varepsilon}_2}\right)^m = \frac{\bar{\sigma}_1}{\bar{\sigma}_2} \quad \Rightarrow \quad m = \frac{\log\dfrac{\bar{\sigma}_1}{\bar{\sigma}_2}}{\log\dfrac{\dot{\varepsilon}_1}{\dot{\varepsilon}_2}} = \frac{\log\dfrac{41.4\,\text{MPa}}{69.0\,\text{MPa}}}{\log\dfrac{1.3}{40}} = \underline{\underline{0.149}}$$

$$\bar{\sigma}_1 = C\dot{\varepsilon}_1^m \quad \Rightarrow \quad \underline{\underline{C}} = \frac{\bar{\sigma}_1}{\dot{\varepsilon}_1^m} = \frac{41.4}{(1.3)^{0.149}}\frac{\text{MPa}}{\text{s}^{-0.149}} = \underline{\underline{40\,\text{MPa}\,\text{s}^{0.149}}}$$

Hence, the flow stress can be described approximately by the expression

$$\underline{\underline{\bar{\sigma}}} = C\dot{\varepsilon}^m = \underline{\underline{40 \cdot \dot{\varepsilon}^{0.149}\,\text{MPa}}}$$

EXAMPLE 8.4: NORTON–HOFF CONSTITUTIVE EQUATION FROM HOT-FORMING FLOW STRESS DATA

Problem: Fit the flow stress data given in the accompanying table with the Norton–Hoff constitutive equation.

T (°C)	ε	$\dot{\varepsilon}$ (s^{-1})	σ (MPa)
350	0.5	1	71
425	0.5	1	43
500	0.5	1	29
350	0.5	10	99
425	0.5	10	60
500	0.5	10	40
350	1	1	81
425	1	1	49
500	1	1	31
350	1	10	109
425	1	10	66
500	1	10	42

Solution: This problem can be solved by using an Excel spreadsheet. The data are first inserted into different columns of the spreadsheet.

If we take the natural logarithm of the constitutive equation to be used, we get the following linear expression:

$$\ln\sigma = \ln K + n\ln\varepsilon + m\ln\dot{\varepsilon} + \beta\frac{1}{T}$$

A linear regression analysis can then be done by means of the spreadsheet, based on the data in the table. An Excel spreadsheet that shows this regression analysis is available at www.cambridge.org/valberg.

The result of the regression analysis is

$$\begin{aligned}\ln\sigma &= -0.40247 + 0.136914\varepsilon + 0.136483\dot{\varepsilon} + \frac{2979.473}{T}\\ &\approx -0.402 + 0.137\varepsilon + 0.136\dot{\varepsilon} + \frac{2979.5}{T}\end{aligned}$$

Thus the following constitutive equation is obtained for the given data set:

$$\underline{\underline{\sigma = 0.669 \cdot \varepsilon^{0.137} \cdot \dot{\varepsilon}^{0.136} \cdot e^{2979.5/T}}}$$

EXAMPLE 8.5: ZENER–HOLLOMON CONSTITUTIVE EQUATION FROM HOT-FORMING FLOW STRESS DATA

Problem: Fit the flow stress data in the accompanying table with the Zener–Hollomon constitutive equation.

T (°C)	$\dot{\varepsilon}$ (s^{-1})	σ (MPa)	T (°C)	$\dot{\varepsilon}$ (s^{-1})	σ (MPa)
444.8	0.0106	23.2	529.6	0.66	32.1
485.5	0.0106	15.9	569.1	0.57	23.1
528.4	0.0095	11.6	454.1	4.76	67.9
566.9	0.0095	8.5	493.2	5.31	56.2
446.3	0.127	41.4	531.7	5.51	46.6
481.5	0.107	29.6	574.1	4.01	34.8
526.3	0.129	22.3	457.4	14.01	73.2
570.1	0.127	15.1	495.3	9.75	59.9
450.2	0.66	53.5	536.2	13.59	52.5
490.6	0.56	40.9	573.9	10.82	40.4

Solution: This problem can also be solved by use of an Excel spreadsheet.[14] The data are inserted into three columns of the spreadsheet. By use of the "Goal Seek" option under the "Tool Menu," the problem can be solved as explained in files available at www.cambridge.org/valberg. The following constants of the Zener–Hollomon relation are then obtained:

$$A = 3.34 \times 10^{10}, \qquad Q = 173114.4, \qquad \frac{1}{\alpha} = 26.582, \qquad n = 3.286$$

Problems

8.1 Determine the flow stress and its dependence upon strain for the two materials A and B, which have been tested in approximately frictionless cylinder compression at room temperature. The initial specimen geometry was characterized by $D_0 = h_0 = 30\,\text{mm}$. The specimens were first compressed down to $h_1 = 14.42\,\text{mm}$ before remachining to new cylinders characterized by $D_0' = h_0' = 14.42\,\text{mm}$. They were then compressed down to a final height of $h_1' = 6.93\,\text{mm}$. The load vs. height of the specimens was recorded at three stages of compression both for the large (L) and the small (S) cylinder, as specified in the accompanying table.

Record	Cylinder height (mm)	Cylinder radius (mm)	True strain	Material A		Material B	
				Force (kN)	Flow stress (MPa)	Force (kN)	Flow stress (MPa)
1	24.0 (L)			117.5		132.5	
2	18.0 (L)			185.2		176.6	
3	14.42 (L)			248.6		220.7	
4	11.0 (S)			38.6		32.2	
5	9.0 (S)			48.9		39.3	
6	6.93 (S)			66.2		51.0	

(a) Compute the missing data in the columns, and insert them into the table.
(b) Plot the flow stress graphically vs. true strain for the two materials.
(c) Characterize the material behavior expressed by each of the two materials.
(d) One of the materials can be fitted with a power law. Determine the strength coefficient and the strain-hardening exponent for this material.

(e) Specify the strain range for which the material model is valid.
(f) Comment upon use of the obtained flow stress data for various metal forming applications.

8.2 A cylinder is compressed between two plane parallel dies. The velocity of the upper die was kept constant at 10 mm s^{-1} while the lower die remained stationary. The initial specimen height was 30 mm, and the final height was 15 mm.

(a) Determine the effective strain and the effective strain rate applied in this test for cylinder heights of 30, 25, 20, and 15 mm.
(b) Plot a graph of the strain and the strain rate in the test as functions of the stroke.
(c) Add an abscissa axis the graph to depict the height of the specimen.
(d) Propose different means for obtaining constant strain rate in the compression test.

NOTES

1. Altan, T., Oh, S.-I., and Gegel, H. L.: "Metal Forming, Fundamentals and Applications," ASM Int., 1983, pp. 45–73.
2. Laue, K., and Stenger, H.: "Strangpressen; Verfahren – Maschinen – Werkzeuge," Aluminum-Verlag, Düsseldorf, 1976, p. 39.
3. Hensel, A., and Spittel, T.: "Arbeitsbedarf der bilsamen Formgebungsverfahren zum Aufname von Fliesskurven," VEB Deutscher Verlag für Grundstoffindustrie, Leipzig, 1978 (in German).
4. Norton, F. H.: "The Creep of Steel at High Temperature," McGraw-Hill, New York, 1929.
5. Hoff, H. J.: "Approximate analysis of structures in presence of moderately large creep deformations," Quart. Appl. Mathematics, Vol. 12, 1954, p. 49.
6. Ludwik, P.: "Elemente der Technologishen Mechanik," Springer Verlag, Berlin, 1909 (in German).
7. Ramberg, W., and Osgood, W. R., "Description of Stress–Strain Curves by Three Parameters," Technical Note no. 902, National Advisory Committee for Aeronautics, Washington, DC, 1943.
8. Swift, H. W.: J. Mechanics and Physics of Solids, Vol. 1, 1952, pp. 1–18.
9. Voce, E.: J. Institute of Metals, Vol. 74, 1948, pp. 537–562.
10. Schey, J. A.; "The more common fabrication processes," Ch. 34 in R. F. Bunshah (Ed.): "Techniques of Metals Research," Part 3; Techniques of materials preparation and handling, Interscience Publishers, 1968, p. 1429.
11. Zener, C., and Holloman, J. H., J. Appl. Physics, Vol. 15, 1944, pp. 22–32.
12. Sellars, C. M., and Tegart, W. J. M. Mem. Sci. Rev. Metallurgie, Vol. 63, 1966, p. 731.
13. Domkin, C.: "Constitutive Models Based on Dislocation Density," Doctoral thesis, Luleå Univ. of Technology, 2005.
14. Roenning, B.: "Constitutive equations for AlZnMg-, AlZnMgCr- and AlZnMgZr-alloys," Ph.D. thesis, Norwegian Univ. of Science and Technology, 1998.

REFERENCES

Altan, T., Oh, S.-I., and Gegel, H. L.: "Metal forming, fundamentals and applications," ASM Int., 1983, pp. 45–73.

Boyer, E. H. (Ed.): "Atlas of stress-strain curves," 2nd ed., ASM Int., Metals Park, Ohio, 2002.

9 Formability and Workability

In connection with the discussion of technological tests in Ch. 7, it was stated that the tensile test specimen after some degree of stretching tends to become unstable, due to the onset of necking. With further stretching, there is neck growth in the specimen, and finally a fracture is formed in the neck, so that the specimen breaks into two pieces.

When compression testing was discussed, it was stated that for ductile metals, larger strains can in general be obtained in this test than in tensile testing, because neck formation is avoided in compression. But also in the compression test there are limitations on how much the specimen can be deformed. This is because various *cracking phenomena* may occur, especially when low-ductility materials are tested.

In metal forming, it is a common problem that the material of the workpiece breaks down during forming, in a manner like that for materials subjected to technological tests. In this chapter, different phenomena that cause *material failure* during metal forming operations will be discussed, with special emphasis on failure due to necking, *tensile stress cracking*, and *shear cracking*.

9.1 Formability and Workability

Formability and *workability* are terms that refer to the property of a material with regard to its ability to be shaped in metal forming without *breakdown*[1] during the forming operation. Formability is most commonly used to describe how much a material can be formed in sheet-metal forming processes without losing its integrity, i.e., without being subjected to excessive thinning or fracture during forming. Workability, on the other hand, refers to the ability of a material to be formed in bulk-metal forming processes without breakdown of the material due to formation of cracks of any kind. Such breakdown could be caused by partial or full fracture of the material. Partial fracture can occur close to the surface or in the interior of the body subjected to forming, so that surface or internal cracks are formed. It is natural to distinguish between crack formation in sheet-metal and in bulk-metal forming, because it is quite different phenomena that cause metal breakdown in each category of process.

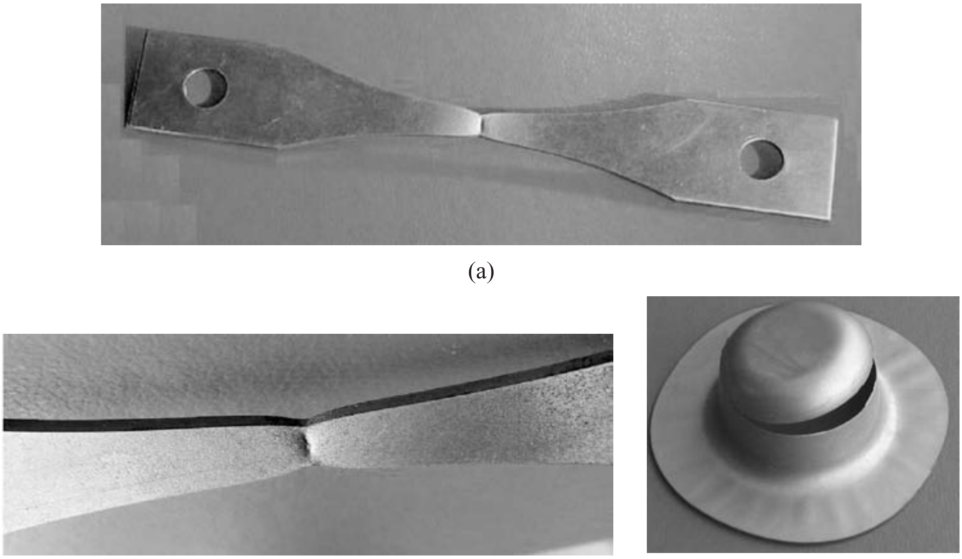

(a)

(b)

(c)

Figure 9.1 Material breakdown in steel specimens when at room temperature. (a,b) Neck in tensile testing that developed into beginning fracture. (c) Fractured deep-drawn sheet-metal cup.

Ductility is another term used in technical literature to describe to what extent a material can withstand deformations without risk of breakdown. This property is connected with the performance of a material in technological testing, as, for instance, the tensile test. Measures of ductility in this test are the elongation at fracture of a gauge length of the test specimen, and the reduction of area in the neck upon fracture. Finally, there is the term *intrinsic ductility*, used to characterize the ductility of the material subjected to testing as a property of the material itself, supposedly not influenced by the conditions in the test applied to measure ductility.

"Formability," or "workability," is sometimes erroneously used for the property *malleability*, i.e., the ease of working of a metal, which in fact refers to the flow stress of the metal (whether the material is soft or hard). This is of course an important property, because good malleability (low flow stress) will reduce the required forming loads and pressures and the size of the required metal forming machinery. However, technically considered, it is not related either to formability or to workability.

When the formability or workability of a material is exceeded, unacceptable defects, or complete fracture, will appear in the formed component. This situation is therefore unacceptable in industrial metal forming processes. Some cases of plastic deformation where the limit of ability to form has been exceeded until the material has lost its integrity are shown in Figs. 9.1 to 9.3.

Internal defects of all kinds – for instance, those due to partial cracking inside the deformed body, and other closed-surface defects – are especially dangerous. They are more difficult to detect than open surface cracks and are therefore more likely to pass quality control. If they appear in a critical construction, they can cause

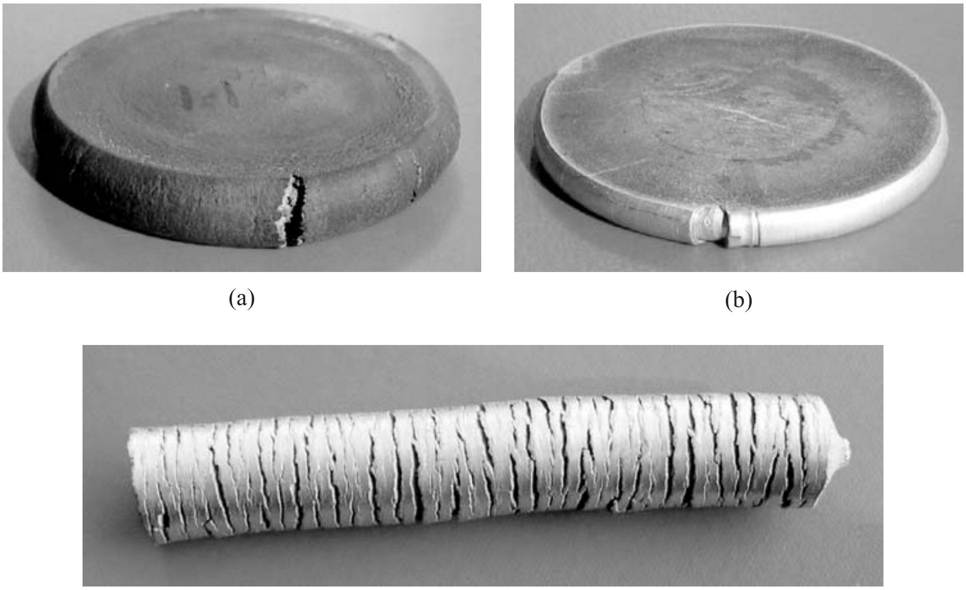

(a) (b)

(c)

Figure 9.2. Tensile stress cracks in hot cylinder compression of (a) steel and (b) aluminum alloy, and (c) in hot extrusion of metal–matrix composite rod. (Courtesy M. Lefstad, SINTEF.)

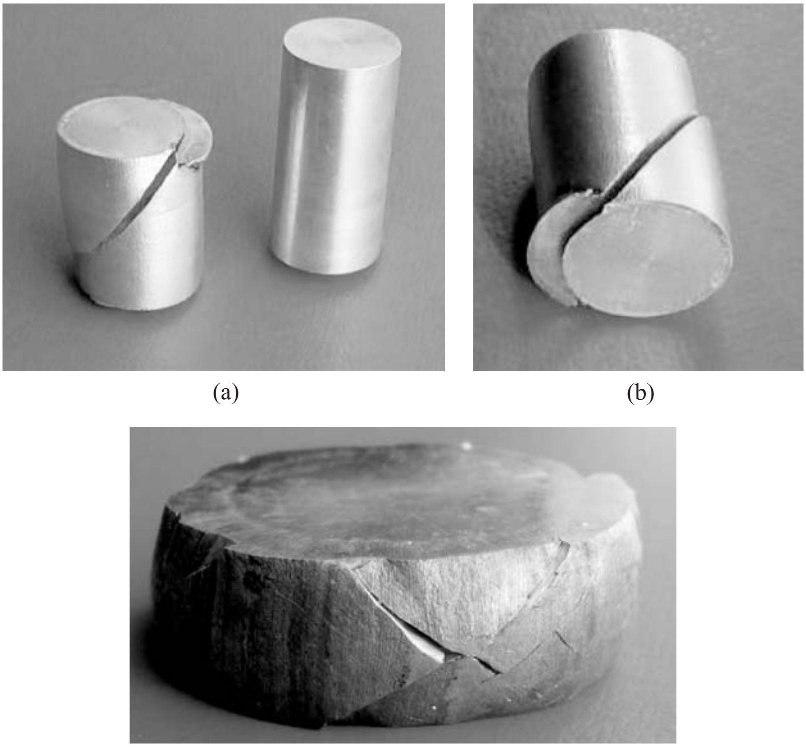

(a) (b)

(c)

Figure 9.3. Shear stress cracks formed in (a,b) cold and (c) hot cylinder compression of aluminum alloys.

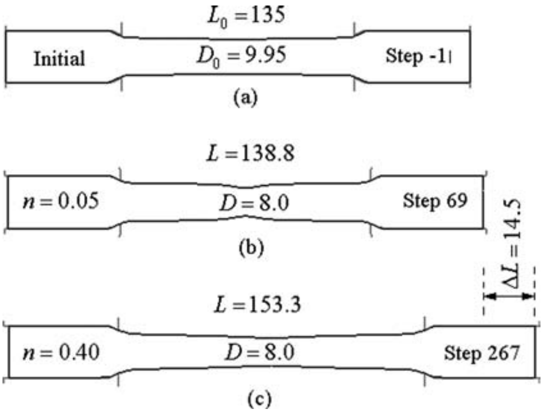

Figure 9.4. Delay of necking in tensile testing through increased strain-hardening exponent: (a) initial specimen, (b) low-n-value specimen stretched to 8 mm neck diameter, and (c) high-n-value specimen stretched to the same neck diameter as in (b).

catastrophic failure. In such cases, as, for instance, in load-carrying aircraft structures, it is therefore common practice to search for defects by nondestructive control methods, to map their eventual presence and their severity. Growth of the defects over time is regularly checked for by measurements at certain time intervals, for instance, *X-ray inspection*. When they reach *critical size*, the defects have to be repaired, or the component must be replaced by a new, safe component.

9.2 Necking as a Phenomenon Limiting Formability

Necking is most commonly the limiting phenomenon that determines how much a sheet-metal material can be formed before further forming becomes impossible, because the neck has grown and has become so severe that there is great risk that the material will fracture. Low-ductility material can, of course, fracture before the material starts to neck; however, such materials are seldom shaped by plastic deformation.

Necking occurs only when there are tensile stresses on the cross section of the specimen, which cause the specimen to elongate. To quantify formability of a specific sheet metal and to compare it with another material, so called *forming-limit diagrams* (FLDs) are recorded in special tests, performed on the material under different straining conditions until the specimens develop necking, which finally leads to fracture under each straining condition. The principle, or methodology, used when FLDs are made is described in detail in Ch. 24 and will not be discussed further here.

However, necking in tensile testing of a round test specimen will be considered, as an example, in an attempt to explain the special formability aspects and forming limitations encountered in sheet-metal forming. Finite element simulations performed for two round tensile test specimens of identical geometry, as shown in Fig. 9.4, illustrate in a straightforward manner what is the required property of a material if it is to have good formability, so that it would perform well in sheet-metal forming.

Imagine that the test specimens are made from two different materials, both which have flow stress that conforms to a power law. Assume the flow stress for both materials to be characterized by the same strength coefficient $K = 180$ MPa, but let the two materials have different strain-hardening characteristic, with strain-hardening exponents $n = 0.05$ and $n = 0.40$, respectively.

The results of stretching of the tensile test specimens of the two materials, as predicted in FEM simulation, are shown in Fig. 9.4(b) and (c), when stretched to the same chosen degree of thinning, i.e., 8 mm diameter. Because the strain in the neck now is approximately 0.44, both specimens have begun to develop necking. But at this instant, the test specimen with the higher n-value has been stretched to considerably larger total length than the lower-n-value specimen. This is because necking started later in the high-n-value material. The uniform deformation stage in the beginning of the test lasted considerably longer in this material. So in this simulation, increased deformation length of the specimen at the same degree of thinning was predicted to be 14.5 mm, caused by the increase of n from 0.05 to 0.40.

This agrees well with the conclusion in the simple analysis in Example 7.3, where it was deduced that necking starts at a uniform strain of the specimen equal to the strain-hardening exponent of the material. Hence, it is obvious that increasing the strain-hardening exponent will improve formability in cases where necking is the limiting phenomenon, because high-n-value delays the onset of necking. This is why, for instance, extruded shapes are heat-treated into the T4 condition before forming, even though this will increase the forming load. In the naturally aged T4 condition, the material has a high n-value (for instance, $n = 0.25$), and the onset of necking is delayed in comparison with the soft annealed condition of the material ($n = 0.17$). When necking starts, the material begins to thin out and cannot be stretched further, to any extent, without fracturing. In sheet-metal forming neck formation is therefore commonly characterized as an instability phenomenon.

In the preceding treatment, we considered materials for which the flow stress only depended on strain. If, in addition, the flow stress of the material depends on the strain rate and temperature, the conditions of necking becomes considerably more complex, as both strain rate and temperature will influence neck formation.

9.2.1 Diffuse and Localized Necking in Sheet-Metal Forming

In tensile testing of sheet metals, two different necking phenomena can sometimes occur in the same specimen. This is clearly demonstrated by the two fractured tensile test specimens shown in Fig. 9.5(a). Whereas the stainless steel specimen at the top exhibited both *diffuse necking* (D) and *local necking* (L), the corresponding aluminum alloy specimen at the bottom only exhibited local necking. In both cases, it is evident that fracture did occur in the thinnest section of the localized neck of the specimens. While diffuse necking took place in a rather long part of the specimen, localized necking occurred in a narrow band, inclined at an angle to the longitudinal axis of the specimen. The name diffuse is used because when the neck starts to form, it is not easy to see: it encompasses a rather long part of the specimen, and neck growth in the beginning is rather slow. In localized necking, however, the neck just occurs in a very short piece of the specimen.

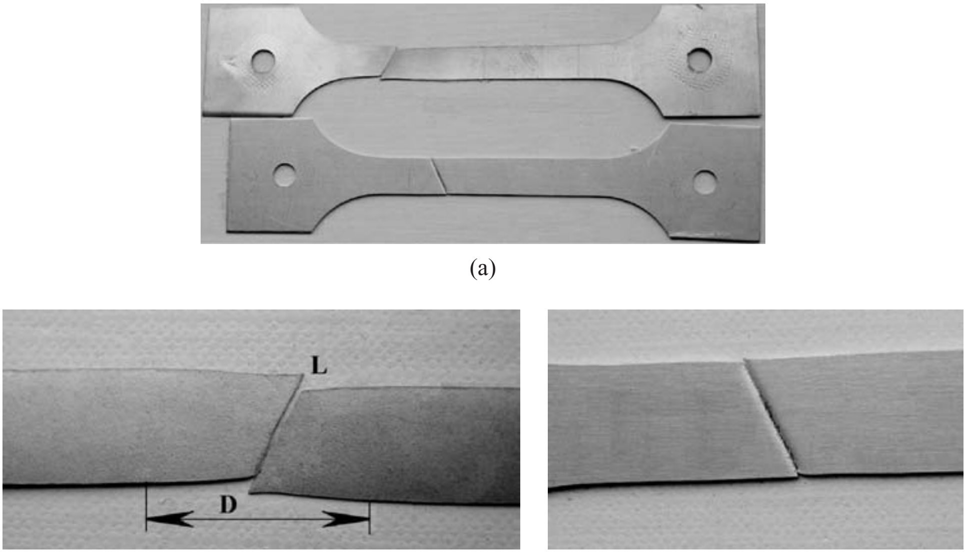

(a)

(b) (c)

Figure 9.5. (a) Examples showing diffuse and local necking in tensile testing of sheet metal. (b,c) Magnified sections showing detail of each neck.

EXAMPLE 9.1: LOCAL NECKING IN TENSILE TESTING OF SHEET METAL

Problem: Consider tensile testing of a sheet-metal specimen. Use theory to deduce an equation for the angle of inclination of a diffuse neck, ϕ (see the accompanying figure) as a function of the plastic strain ratio of the sheet metal, i.e., the anisotropy parameter $R = \varepsilon_2/\varepsilon_3 = \varepsilon_w/\varepsilon_t$, defined in eq. 24-4 in connection with description of anisotropic sheet metals.

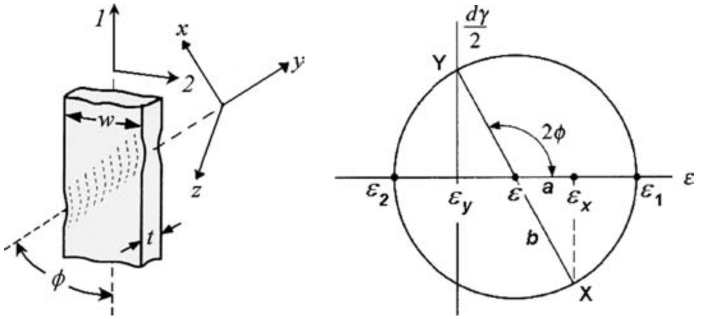

Solution: When localized necking begins, two depressions appear, each similar to a valley on each side of the specimen, as shown in the figure on the left-hand side. During growth of the neck, there is no width change of the specimen in the direction along the valley, i.e., the y-direction. This means that the specimen during formation of the neck is in plane strain, because $\varepsilon_y = 0$.

Consider plastic straining in axis directions 1 and 2 of the specimen (i.e., in the plane of the specimen) due to stretching of the specimen in its axial direction (i.e., in direction 1) up to a strain ε_1. Strains can be expressed as follows (due to volume constancy):

$$\varepsilon_1, \varepsilon_2 = -\left(\frac{R}{1+R}\right)\varepsilon_1$$

We can now draw Mohr's strain circle for this plane: see the right-hand side in the figure. The strain value at the center of the strain circle is obtained as

$$\varepsilon = \frac{\varepsilon_1 - |\varepsilon_2|}{2} = \left(\frac{1}{2\,(1+R)}\right)\varepsilon_1$$

Now, consider a new system of coordinate axes, defined by the axes x, y, and z, oriented at an angle of inclination ϕ in relation to the principal strain system. The y-axis of this new system extends along the bottom of the valley of the neck. Let us now deduce strains in the directions of the different axes in this new coordinate system.

As pointed out previously, there is zero strain in the direction along the valley, i.e., $\varepsilon_y = 0$; hence, point Y in Mohr's strain circle describes the strain in the y-direction of the material in the neck itself. The strain component in the x-direction in the neck is described by point X in Mohr's circle. The normal strains in the x- and the z-direction can be determined as

$$\varepsilon_x = \left(\frac{1}{1+R}\right)\varepsilon_1, \qquad \varepsilon_z = -\left(\frac{1}{1+R}\right)\varepsilon_1$$

Mohr's strain circle finally provides us the following expression for the angle of inclination of the local neck:

$$\cos(180^\circ - 2\phi) = \frac{a}{b} = -\cos 2\phi = \frac{1}{1+2R} \quad \Rightarrow \quad \tan\phi = \left(\frac{1+R}{R}\right)^{1/2}$$
$$\Rightarrow \phi = \arctan\left[\left(\frac{1+R}{R}\right)^{1/2}\right]$$

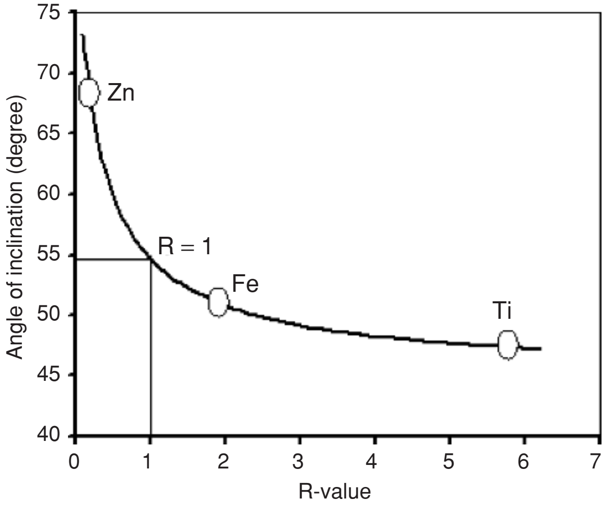

It is now straightforward to make a plot of this relationship. The figure on the previous page shows the plot, i.e., how the angle of inclination of a local neck varies with the R-value of the sheet metal subjected to tensile testing.

9.3 Tensile Stress Cracking

Three examples of tensile stress cracking were shown in Fig. 9.2. First, there was cracking in the peripheral bulge of a steel cylinder in hot compression, as shown in Fig. 9.2(a). This was for a cylinder of a low-ductility material, which cracked severely at various sites around its periphery when compressed to an average strain of approximately 0.95. Next, there was the cracked cylinder in Fig. 9.2(b), in which a single crack formed on the peripheral bulge due to a severe material defect there, while there was no cracking elsewhere in the cylinder. In this case, the cylinder was compressed to an average strain of approximately 1.5. Finally, shown in Fig. 9.2(c) was severe transverse cracking obtained in extrusion of a low-ductility material. In all three examples, cracking was due to buildup of tensile stresses in the material during the forming operation until a critical level of tensile stress and plastic deformation was reached, which then led to breakdown of the material due to fracture.

Different *failure criteria* have been proposed for prediction of the critical state in which tensile stresses cause cracking in metals subjected to plastic deformation. A commonly applied criterion is, for instance, that due to *Cockcroft* and *Latham*.[2] This criterion may be expressed in two different ways, either as

$$\int_0^{\varepsilon_f} \sigma^* \mathrm{d}\,\bar{\varepsilon} = C_1 \tag{9-1}$$

or normalized with respect to stress as

$$\int_0^{\varepsilon_f} \frac{\sigma^*}{\bar{\sigma}} \mathrm{d}\,\bar{\varepsilon} = C_1' \tag{9-2}$$

Here the parameter σ^* is the largest principal stress, $\bar{\sigma}$ is the effective stress, and $\bar{\varepsilon}$ is the effective strain at a point in the material. The *Cockcroft–Latham failure criterion*, as expressed by eq. 9-1, states that fracture occurs when the deformation energy per unit of volume of material, provided by the largest principal stress in the material, approaches the critical level C_1. It is therefore common to refer to C_1 as the *critical damage parameter*. The expression given in eq. 9–2 is normalized with respect to stress, so that materials of different softness can be compared with respect to their critical damage parameter.

FEA is an excellent tool for consideration of when tensile cracking is likely to occur in metal forming operations or in technological tests. FEM programs are able to compute the distribution of both the largest principal stress and the effective strain inside the volume of the workpiece. Moreover, the combined effect of the two is also computed by the software, in terms of the damage parameter itself, as defined by the expression on the left-hand side of eq. 9-1 or, alternatively, the damage parameter normalized with respect to stress, as given by eq. 9-2. The region inside the workpiece that attains the highest damage parameter will be the region most likely to crack. If cracking does take place in accordance with the Cockcroft–Latham criterion, a crack will form when the damage parameter reaches the critical value of C_1 (or C_1') for the actual material of the workpiece.

EXAMPLE 9.2: DAMAGE PARAMETER IN A TENSILE TEST OF A NOTCHED SPECIMEN

Problem: Consider room temperature tensile testing of a round test specimen with geometry characterized by the following parameters: diameter of specimen, 15.2 mm; diameter of notched section of specimen, 7.6 mm; radius of curvature of notch, 1.27 mm. Imagine that the test specimen consists of an Al alloy with flow stress $\sigma = K\varepsilon^n = 233\varepsilon^{0.22}$. Use FEA to consider stress and strain conditions in the specimen upon testing, both early and late during stretching. Where do you expect the specimen to develop fracture?

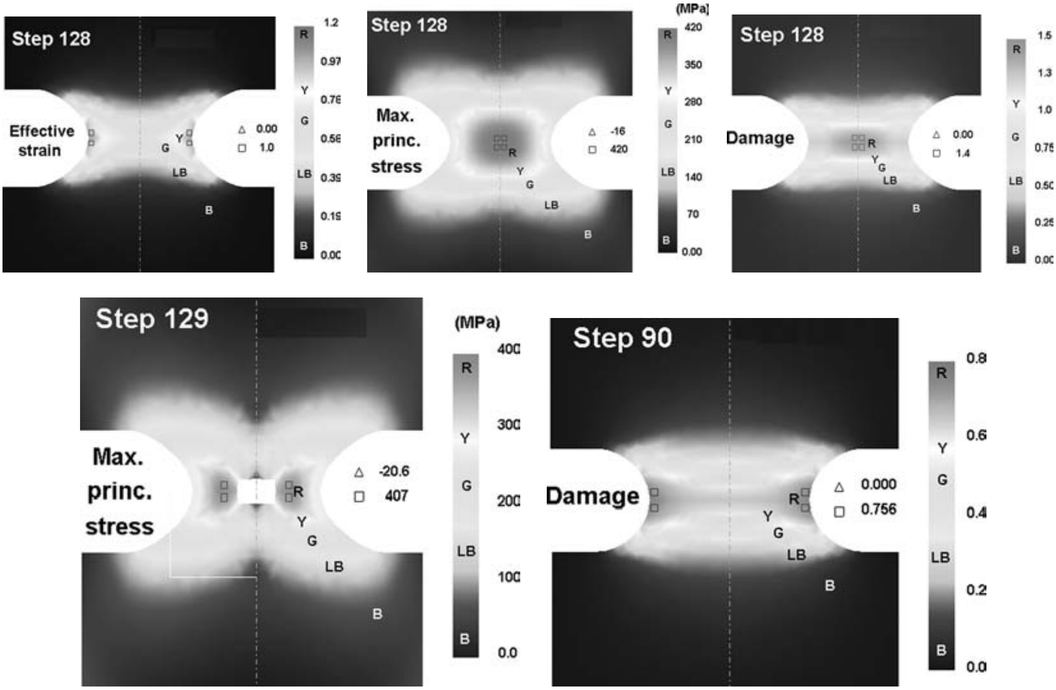

Solution: A two-dimensional FEM model of the tensile test is set up. Simulation results showing the distribution of the maximum principal stress, the effective strain, and the Cockcroft–Latham damage parameter for the notched part of the specimen, at different stages of stretching, can then be obtained from the model. These results, at a late stage during stretching (simulation step 128), are shown in the accompanying figures. It is seen that high stresses and strains are mainly localized in the notched portion of the specimen.

The effective strain, shown in the upper left picture, is highest on the surface of the specimen, just below the notch. The principal stress, which is tensile, however, is highest at the center of the notch of the specimen (upper middle picture). Finally, as shown on the upper right, the highest damage parameter during this late stage of stretching is predicted to appear right at the center of the notched part of the specimen. Hence, from the simulation results, we can conclude that late during the course of stretching, cracking due to buildup of tensile stress most likely will occur at the center of the specimen.

A simulation of crack formation in the specimen under these circumstances is shown in the figure on the lower left. The picture depicts by its principal stress distribution that, after initiation of a crack at the center of the specimen, tensile stresses remain high ahead of the crack tip. This causes further crack growth, until full fracture has been realized over the whole notched cross section.

On the lower right in the figure, the FEM-predicted distribution of the damage parameter is shown as it appears early during testing, i.e., at simulation step 90. The critical region inside the specimen as regards the damage parameter is now in the surface layer of the specimen, below the surface of the notch. These results indicate that whereas a low-ductility material in the notch would tend to develop surface cracks, a high ductility material would be most prone to fail by center cracking there.

9.3.1 Tensile Stress Cracking in Cylinder Compression

As shown in Fig. 9.2(a), cracking may occur in the bulged portion of a cylinder. For material of good ductility, this is the most likely site for crack formation.

Figure 9.6 shows results from FEM simulation of cylinder compression. The highest damage parameter is predicted to occur in the middle of the bulge. This location is therefore the most likely site for crack initiation. The high damage parameter here is caused by the high tensile stresses acting in the direction around the circumference of the cylinder, [see Fig. 9.6(b)]; the deformations at this location are not especially large [see Fig. 9.6(c)].

9.4 Shear Cracking in the Cylinder Compression Test

In Fig. 9.3(a) and (b) an example was shown where shear cracking occurred in cold cylinder compression. The material of the cylinder used in this experiment was an AA 7108 alloy in as-extruded condition. Compression testing of the material revealed that the flow curve of this material was one characterized by *strain-induced softening*; see Fig. 9.7(a).

FEA results mimicking this cylinder compression process are shown in Fig. 9.7(b). The analysis reveals the well-known fact that a deformation shear cross forms inside the cylinder when there is friction between the die and the cylinder. The largest deformations will appear in the shear cross. When the cylinder has been compressed down to a certain stage, the initial strain-hardening part of the flow curve has been exceeded for the material in the shear layer. With continued compression,

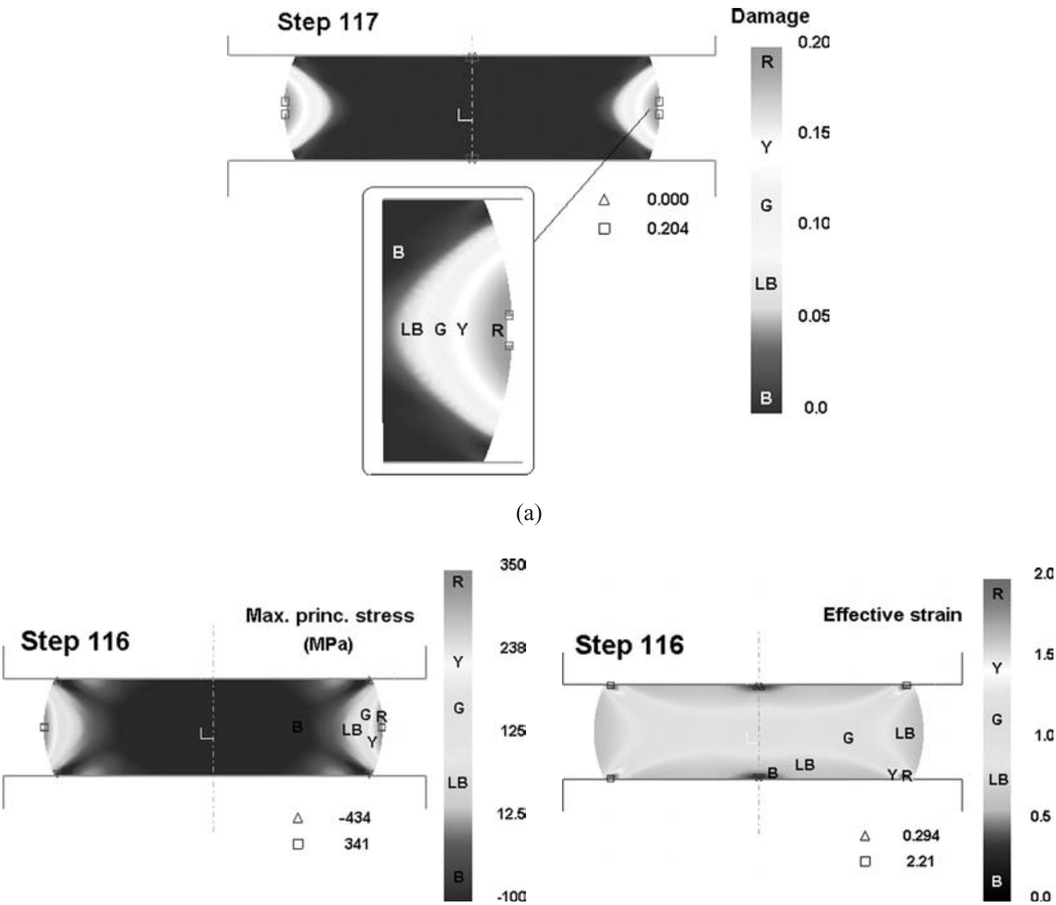

(a)

(b) (c)

Figure 9.6. FEM-simulation results showing (a) high damage parameter in the bulge of the cylinder, (b) high tensile stress over the circumference of the bulge, and (c) moderate effective strain in the bulge.

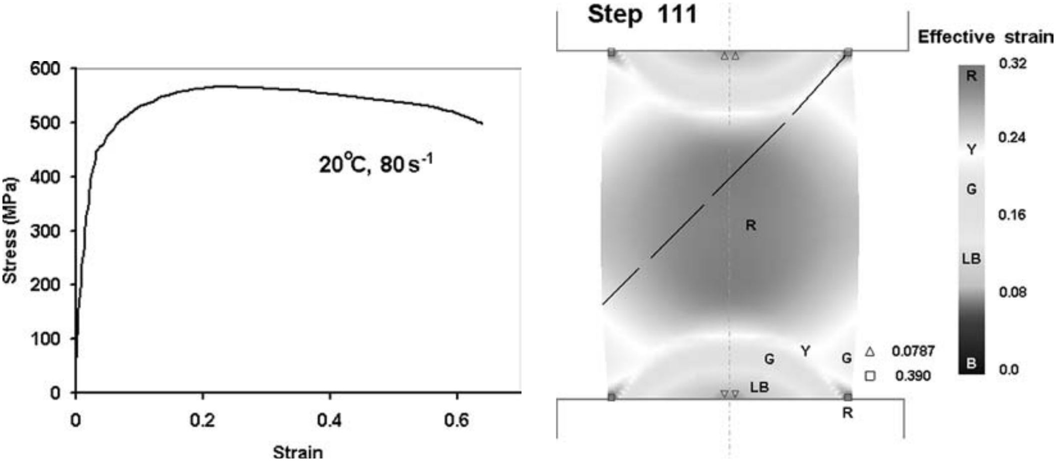

(a) (b)

Figure 9.7. (a) Flow curve for material that exhibits strain softening. (b) FEA depicting high strain at shear plane, which fails by fracture in the experiment shown in Fig. 9.3(a) and (b).

the shear layer will then experience strain-induced softening. Deformations then will tend to localize in a thin layer, as marked with the broken line in this figure. Because of strain softening, this layer will then easily become overstrained, and a shear fracture will form here.

In cylinder compression, the shear cross appears three-dimensionally with a complex shape similar to an hourglass. Even though the shear fracture is initiated somewhere along the plane of the shear cross, propagation of the fracture during further growth most commonly follows a plane path, so that a plane fracture surface is obtained. Upon cracking, a bit of the material may be detached from the rest of the cylinder; see Fig. 9.3(b).

Problem

9.1 In the accompanying figure, a FEM record of largest tensile stress vs. effective strain is shown for a material point in a tensile test specimen with a notch. The material point for which the data were attained was located in the middle of the notched part of the specimen. Estimate the Cockcroft–Latham damage parameter, eq. 9-1, for this material point for an effective strain value of 0.4 and 0.7.

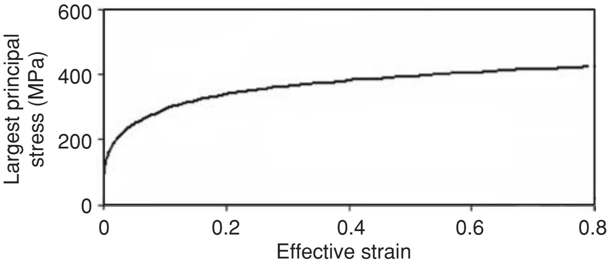

NOTES

1. Mielnik, E. M.: "Metalworking Science and Engineering," McGraw-Hill, New York, 1991, p. 494.
2. Cockcroft, M. C., and Latham, D. J.: "Ductility and workability of metals," J. Inst. of Metals, Vol. 96, 1968, pp. 33–39.

REFERENCES

Bunge, H. J., Pöhlandt, K., and Tekkaya, A. E.: "Formability of Metallic Materials: Plastic Anisotropy, Formability Testing, Forming Limits," Springer Verlag, 2000.

Dieter, G. E., Kuhn, H. A., and Semiatin, S. L.: "Handbook of Workability and Process Design," ASM Int., 2003.

Mielnik, E. M.: "Metalworking Science and Engineering," McGraw-Hill, New York, 1991.

Semiatin, S. L., and Jonas, J. J.: "Formability and Workability of Metals," ASM Int., 1984.

Wright, T. W.: "The Physics and Mathematics of Adiabatic Shear Bands," Cambridge Univ. Press, 2002.

10 Friction and Friction Models

In metal forming, friction is a crucial factor that determines whether an industrial process can be run with acceptable, economic result. In many forming applications, the actual friction conditions are not sufficiently known. In spite of much research on that important topic, there is still lack of knowledge and need for continued research.

This chapter will first explain why friction is so important in metal forming. Then the two most-applied friction models will be presented, and the characteristic of each model will be explained and discussed. Afterwards the most common lubrication mechanisms that may be present in the interface between die and workpiece will be described. Moreover, it will be explained how relevant metal forming friction data can be measured by the ring compression test. Finally, it will be shown how in situ friction measurements can be performed inside a die during the course of forming, using pins inserted into holes drilled into the tooling.

10.1 Friction Effects in Metal Forming

The friction phenomenon in metal forming is of great importance. There are various reasons for this:

- Forming loads and stresses transferred to the dies depend on friction and can be reduced by use of appropriate lubricants.
- The surface quality of the formed workpiece depends on the lubricant used. If there is lubricant breakdown during forming, the product may obtain bad surface quality (for instance, scoring).
- Wear of the dies can be reduced if lubricant films are applied, which provide reduced friction, or even full or partial separation, between the die and the workpiece during forming.

An important reason why friction in metal forming is not fully understood yet is that it is very difficult to enter into the boundary interface between the workpiece and the die, to make in situ observations of what takes place there. Most commonly it is also difficult to measure friction, because the friction shear stress transferred

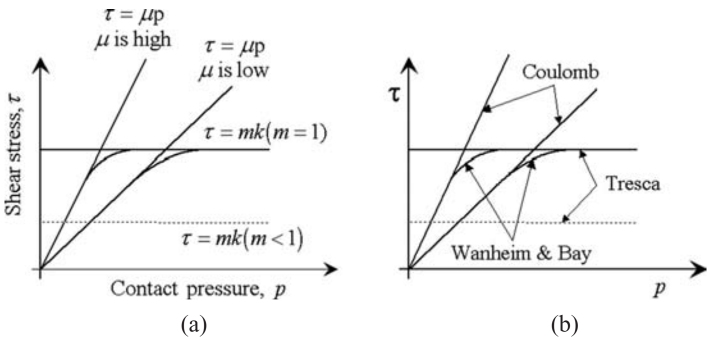

Figure 10.1. Common friction models in metal forming: (a) friction stress vs. contact pressure for different models; (b) names of the models.

through the interface is much smaller than the normal stress component (i.e., the contact pressure) transferred through the same interface.

10.2 Friction Models

In case of low contact pressure, the *Coulomb friction model* is the most appropriate model to describe friction between bodies in sliding contact. This model applies if the mean normal stress component is less than, or approximately equal to, the flow stress of the workpiece material, i.e., $\sigma_n \lesssim \sigma_0$. Low pressure like this can occur in metal forming operations like rolling, wiredrawing, and sheet-metal forming.

However, in metal forming processes like closed-die forging and extrusion, the metal is confined in between two dies, or inside a container. Under these circumstances, the contact pressure will commonly rise much higher than the flow stress of the workpiece material, sometimes many times the flow stress, i.e., $\sigma_n \gg \sigma_0$. Under high contact pressure, the Coulomb friction model may fail to describe the actual friction conditions. A friction model different from the Coulomb model is then commonly used, namely, the *Tresca friction model*. This model is often able to give a better description of the friction over the workpiece–die interface in the case of high contact pressures.

There is also a third friction model that can be used in metal forming applications. This model is often used in combination with the other two. It predicts a rounded transition between the Coulomb friction regime and that of Tresca; see Fig. 10.1(b). This model is commonly called *Wanheim and Bay's friction model*[1] after the scientists who first proposed it. It is rather complex and will not be discussed in depth here; it is beyond the scope of this book. However, in cases where part of the workpiece remains in the elastic state and the rest becomes plastic, this model will describe the friction conditions better than either of the two other models used separately.

10.2.1 The Coulomb Friction Model

The Coulomb friction model is well known from elementary physics and will be considered here for the case when a block of mass *m* is pulled over a plane surface; see

Figure 10.2. Block pulled against plane surface.

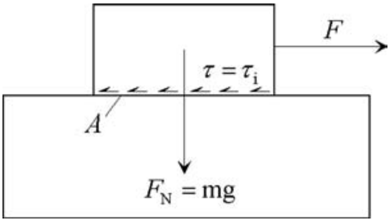

Fig. 10.2. The normal force that acts between the block and the underlying surface can be expressed by the equation

$$F_N = mg \tag{10-1}$$

where g is the acceleration of gravity. The mean pressure transferred through the boundary interface is

$$p(= -\sigma_n) = \frac{F_N}{A} \tag{10-2}$$

In this expression, the symbol σ_n denotes the average normal stress component transferred between the block and the underlying surface, and A is the area of apparent contact between the two bodies.

At low contact pressures, contact between the block and the underlying body occurs only through the highest asperity tips of the two bodies. Because of this, the real area of contact will be very small. However, the *apparent contact area* between the two bodies is the whole area of the bottom surface of the block; see Fig. 10.3. Because actual contact between the bodies is limited to their high *asperity peaks*, the local normal stress over the small areas of contact may sometimes even exceed the flow stress of the softer body. Because of this, local plastification can take place at the asperity tips, even though this would not be expected from the value of the average contact pressure.

To pull the block against the plane surface with constant velocity, a force F is required, which equals the *friction force*. Moreover, this force acts in the direction opposite to the *friction force*, so apparently the friction force tries to counteract the sliding action of the block. The force required to move the block can be expressed

Figure 10.3. Apparent and true area of contact between mating rough surfaces in low-pressure contact.

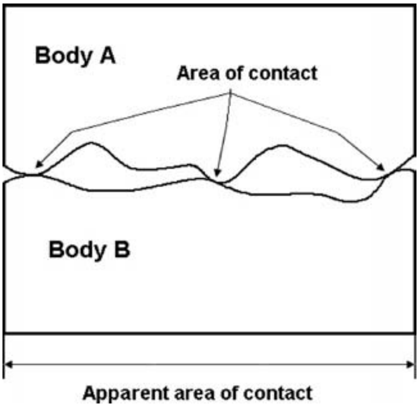

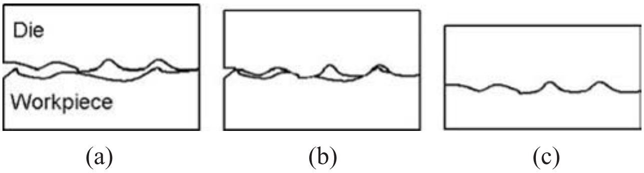

Figure 10.4. Interaction between workpiece and die at different levels of contact stress: (a) contact through asperity peaks at low pressure, (b) partial conformity between workpiece and die surface at moderate pressure, and (c) full conformity at high pressure.

in terms of the *frictional shear stress*, τ_i, as

$$F = \tau_i A \tag{10-3}$$

From eq. 10-3 it is obvious that the friction shear stress can be expressed as

$$\tau_i = \frac{F}{A} \tag{10-4}$$

The Coulomb *coefficient of friction* is then determined as the ratio between the friction force and the normal force on the block, i.e.,

$$\mu = \frac{F}{F_N} = \frac{\tau_i A}{pA} = \frac{\tau_i}{p} = \left|\frac{\tau_i}{-\sigma_n}\right| = \frac{\tau_i}{\sigma_n} \tag{10-5}$$

This expression clearly depicts that the friction coefficient is equal the ratio of the mean friction shear stress to the mean negative normal stress (which equals the mean contact pressure) at the boundary interface where sliding takes place. Alternatively, eq. 10-5 can be expressed as follows:

$$\tau = \tau_i = \mu p = \mu \left| -\sigma_n \right| = \mu \sigma_n \tag{10-6}$$

Coulomb observed that the coefficient of friction, so defined, had a constant numerical value for a specific pair of materials, as, for instance, steel sliding against a specific type of wood. It is important to note that the Coulomb friction model is strictly valid only when the mean contact pressure between the two contact bodies lies below the flow stress of the softer body.

10.2.2 The Tresca Friction Model

With higher contact pressure between die and workpiece, i.e., $\sigma_n > \sigma_0$, where σ_0 is the flow stress of the softer contact body, this body is subjected to significant plastic deformation. As stated in the beginning of Ch. 4, the metal forming die should always remain in the elastic state and should not deform plastically. If a die experiences plastic deformation, it will concurrently change shape and will be unable to provide a constant geometrical shape to the formed component. Another important condition is that if the die is plastically deformed, it will be prone to low-cycle fatigue, so its life will be unacceptably short.

High contact stresses, characterized by $\sigma_0 < \sigma_n < 3\sigma_0$, lead to extensive plastification of the high asperity peaks of the softer contact body. In this range of contact pressure, the contact surface of the softer body will be squeezed deeper and deeper into the roughness valleys and depressions of the harder contact surface, i.e., the die, as the contact pressure is increased, but without penetrating to the very bottom of the depressions; see Fig. 10.4(b). First, at sufficiently high contact pressures, namely, for $\sigma_n > 3\sigma_0$, the workpiece material will penetrate into the deepest depressions of the die surface, if there are no lubricant pockets trapped there; see Fig. 10.4(c). When such penetration occurs, intimate contact is established between the two bodies over the complete contact surface.

In practice, there is an upper limit to the increase in friction stress. It cannot exceed the shear flow stress, commonly denoted by the symbol k, of the softer contact material, i.e., the workpiece material. As soon as the friction shear stress reaches this level, the workpiece material will stick to the surface of the die, and sliding will no longer take place at the interface; instead, sliding will take place via shearing of the workpiece in a layer below its surface. This phenomenon is therefore named *subsurface sliding*.

Instead of the Coulomb friction model, it is recommended to use the Tresca model at high contact pressures. If one increases the contact pressure, for a constant value of the Coulomb friction coefficient (see Fig. 10.1), the frictional stress will also increase correspondingly, for it is proportional to the contact pressure. When the frictional shear stress has reached the shear flow stress of the workpiece material, k, the coefficient of friction must drop if the pressure is increased further. But if this happens, the Coulomb friction model will no longer be valid, for it requires the coefficient of friction to be constant. Realizing this fact, Tresca proposed a different friction model, which is able to describe the physics of the friction at an interface at high contact pressures. *Tresca's friction model* is commonly expressed the following way:

$$\tau = \tau_i = mk \tag{10-7}$$

The parameter m is called the *friction factor*, and can vary in the range $0 < m < 1$. In the case of sticking between workpiece material and the die, this factor equals 1, and the friction shear stress transferred through the interface equals the shear flow stress of the softer contact body, so that the situation agrees with the physics of the interface.

If lubricants are introduced into the interface, the friction factor will be lower than 1, and its numerical value will characterize the lubricant's performance in interaction with the die and the workpiece materials. With improved lubrication, the friction factor will decrease, and in the frictionless case, it will become zero.

The Tresca friction model, as expressed by eq. 10-7, has been plotted in Fig. 10.1 together with the graph for the Coulomb friction model. As this figure depicts, the Tresca friction model appears graphically as straight lines parallel to the pressure axis. So for a lubricant characterized by a constant friction factor, there is no pressure effect on the frictional stress. As mentioned before, the friction factor lies in the range $0 < m < 1$. Depending upon how effectively the lubricant reduces friction, the friction with the lubricant will lie between the pressure axis (which represents frictionless sliding, i.e., $m = 0$) and the line representing sticking friction (i.e., $m = 1$).

Alternatively, the Tresca friction model can be formulated in terms of the flow stress of the workpiece material instead of the shear flow stress. The expression of this friction model will then depend upon whether the von Mises or the Tresca flow criterion is applied. If the von Mises criterion is used, eq. 4-55 describes the relationship between the flow stress in uniaxial tension and the shear flow stress. The Tresca friction model then yields the following expression:

$$\tau = \tau_i = mk = \frac{m}{\sqrt{3}}\sigma_0 \qquad (10\text{-}8)$$

As can be seen from the postulates of the frictional shear stress in the two models, the shear stress is proportional to the contact pressure for Coulomb friction (see eq. 10-6), whereas for Tresca friction, it is proportional to the shear flow stress of the workpiece material (see eq. 10-8), in the interface between workpiece material and die.

10.3 Lubrication Mechanisms

Lubrication mechanisms in metal forming refer to the way lubricant, applied to the interface between die and workpiece, interacts with the two contact bodies and affects the mechanical conditions over the interface. One question that is important in this context is whether the lubricant will provide *full separation* between the two contact bodies, or there will be some extent of *direct contact* between the bodies.

There are a number of different lubrication mechanisms that may prevail in metal forming applications – dry friction, hydrodynamic lubrication, and boundary-film lubrication. They are described in the following subsections.

10.3.1 Dry Friction in Metal Forming

The term *dry friction* is commonly used to describe the friction between two bodies in sliding contact, when there is no added lubricant. Most bodies that surround us are covered with thin films of contamination on their surface. To remove these films, and to establish dry friction conditions between two bodies in contact, it is required to clean them thoroughly by means of chemical solvents, as, for instance, acetone or alcohol, which dissolve and remove contaminating layers on the surfaces. Even a cleaned metallic body, however, will in normal air atmosphere always be covered with an *oxide layer* on the surface. An oxide layer differs both in chemical composition and in physical and mechanical properties from the internal bulk metal of the body. If an oxide layer is removed from the surface of a metal, for instance, by grinding, a new oxide layer will immediately form on the virgin surface created by chemical reaction between the metal and the oxygen in the air.

So because of the high chemical reactivity between oxygen and metals, metallic surfaces in air will always have a natural oxide layer. The oxide film on the surface of a metal can be very different from one metal to another with regard to the thickness of the layer, its stability, and its ability to lubricate. On a newly created aluminum

Figure 10.5. In dry friction compression of a cylinder of Al there is (a) sticking friction; for Cu there is (b) sliding friction.

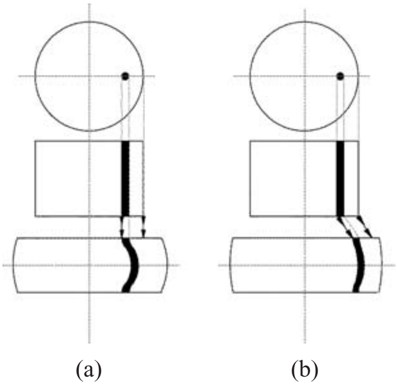

surface, for instance, a thin, adhering film of Al_2O_3 will immediately form. This film is dense and protects the underlying metal from further chemical reaction with the surrounding air. Copper, brass, and steel surfaces likewise form chemical reaction films, but these films are less dense and, therefore, less stable, so they will usually grow in thickness over time. The growth conditions of such films will be strongly influenced by the presence of water or corrosive liquids on the surface considered, as well as the temperature.

Because oxide layers normally cover metallic surfaces, the dry friction behavior of different metals may vary a lot. When a workpiece establishes contact with a die, the natural oxide films on the surfaces of both bodies will appear as films in the interface between the bodies. Dry friction contact conditions usually depend strongly on whether the films are able to lubricate the contact surface.

The difference in behavior of the end surface of a cylinder of Al and one of Cu in nonlubricated compression, i.e., in the case of dry friction, illustrates clearly (see Fig. 10.5), to what extent oxide layers can lubricate an interface. If the cylinders of the two metals are well cleaned before compression, the Al cylinder will stick completely to the die surface, whereas for the Cu cylinder there will be *sliding friction*. The different behavior can be shown by use of a stripe of marker material in the cylinder, obtained by inserting a contrast pin into the cylinder, as explained in Ch. 12. Then for the cylinder of Al, the stripe will remain in the same position on the interface before and after compression [see arrows in Fig. 10.5(a)], and hence will document *sticking friction*. In contrast, for the Cu cylinder there will be sliding friction [see arrows in Fig. 10.5(b)]. As a consequence of this, during compression the stripe will flow outward in the radial direction at the die–cylinder interface.

The difference in metal flow during dry friction compression of the two cylinders in the experiments mentioned is caused by the different properties of the oxide layers on the surfaces of the two metals. Al has a dense adherent oxide layer on the surface that does not lubricate the interface, and sliding will therefore not take place in this layer. On the other hand, Cu has a porous oxide layer of low shear strength that acts as a lubricant and reduces friction. Because of this, the material particles on the surface of the Cu cylinder will slide along the interface, instead of remaining in the same position during the compression stroke as they do for an Al cylinder.

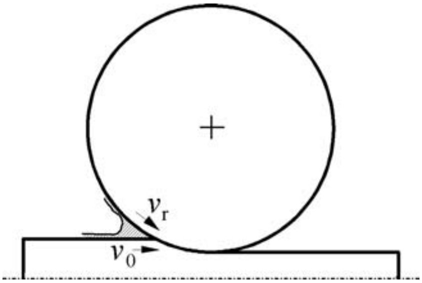

Figure 10.6. Workpiece and roll movement favor hydrodynamic lubrication in the rolling process.

10.3.2 Hydrodynamic Friction

In metal forming processes like wiredrawing and rolling, the nature of the forming process favors buildup of *hydrodynamic lubrication*. This lubrication mechanism is characterized by the formation of a thick lubricant film that completely separates the workpiece from the die. This lubricant mechanism is favored in wiredrawing or rolling processes because the workpiece then moves with high speed into the dies.

Another condition that favors hydrodynamic lubrication in these processes is that at the inlet side of the die there is a *wedge-shaped opening*, which becomes narrower as one moves deeper into the die. The lubricant is forced to flow into this wedge by the movement of the workpiece.

In wiredrawing pressure buildup is provided in the wedge by the movement of the wire alone, whereas in rolling it is provided by movement of both roll and workpiece in the direction pointing into the roll gap; see Fig. 10.6. With lubricant adhering to the workpiece surface, and with rapid movement of the workpiece into the wedge, a thick lubricant film can be realized in the interface between the workpiece and the die.

If a thick lubricant film forms, there can be complete separation between die and workpiece through the film. Even though such a thick film leads to low friction forces and almost no die wear at all, it is not considered favorable in metal forming. This is because when it occurs, the surface quality of the workpiece will be reduced in comparison with the achievable quality if thin lubricant films are used. In hydrodynamic lubrication, the metal surfaces subjected to forming develop a *matte appearance* [see Fig. 10.7(c)], with high surface roughness. This surface appearance is less attractive on the component than the *smooth, shiny surface* obtained if there is *boundary friction* over the interface during the forming operation; see Fig. 10.7(a). The high roughness of surfaces created in forming processes where the lubrication mechanism is characterized by hydrodynamic friction is commonly explained to be the effect of single grains of the microstructure of the workpiece deforming individually at its surface. This takes place because of insufficient pressure support through the lubricant film, so that individual surface grains are allowed to deform in their own way, along favorable slip planes, without conforming to deformations in neighboring grains.

In metal forming, when there is a thin boundary lubrication film in the die–workpiece interface instead of hydrodynamic lubrication, deformations will be more

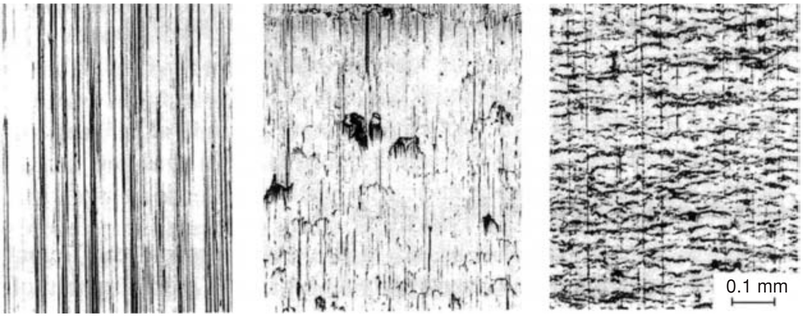

(a) (b) (c)

Figure 10.7. Surface appearance (magnified) of surfaces produced in rolling[2] processes by (a) boundary layer lubrication, (b) breakdown of lubricant film, and (c) hydrodynamic lubrication (reprinted with permission of ASM International. All rights reserved. www.asminternational.org).

evenly distributed throughout the volume of the surface grains, and a smoother, brighter surface appearance will result.

From this it is obvious that the main factor favoring formation of hydrodynamic lubrication in metal forming processes like rolling and drawing is high forming velocity. The lubricant is then forced with high speed into the wedge-shaped opening at the inlet side of the plastic zone, so that a high lubrication pressure builds up there. With increased lubricant supply into the wedge, lubricant penetration into the interface between the two contact bodies is eased, and hence lubrication will be improved. Another process parameter of great importance is the *viscosity* of the lubricant. Higher viscosity will lead to higher pressure buildup in the wedge at the inlet side of the deformation gap, where forming takes place. Because of this, lubricants with high viscosity favor the formation of hydrodynamic lubrication films.

When the lubrication mechanism is hydrodynamic, friction is low. This is because the shear stresses transferred through the interface between the two contact bodies depend on the shear properties of the lubricant film only, as there is no longer direct contact between the surface asperities of the two bodies. In the case of hydrodynamic friction, the coefficient of friction can therefore be as low as $\mu < 0.01$.

10.3.3 Boundary Film Lubrication

It is generally claimed that the most favorable lubrication condition in metal forming is *boundary film lubrication*. When this lubrication mechanism prevails, a thin – and very effective – lubricant film persists in the interface between workpiece and die. Boundary film lubrication is able to provide rather complete separation between the two contact bodies; see Fig. 10.8(a). The thickness of the lubricant film in this case is typically of the same magnitude as the average length of the chain molecules of the lubricant. In this case, relatively high stresses can be transferred across the film, and through the contact interface, without damaging the film. In boundary film lubrication, each surface grain of the microstructure of the workpiece will be forced

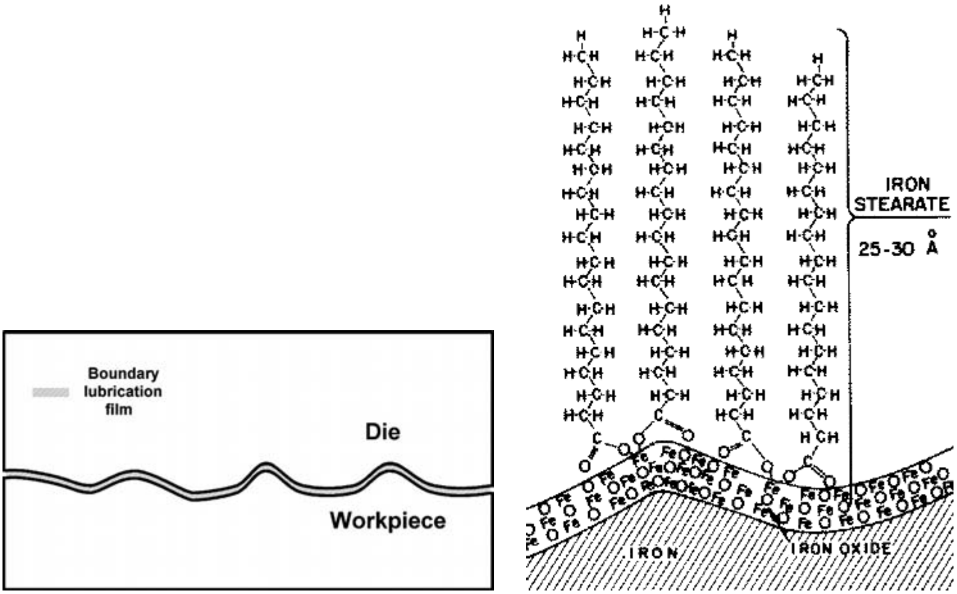

(a) (b)

Figure 10.8. Lubricant film in boundary film lubrication: (a) appearance of film and (b) lubricant molecules attached to metal surface by secondary molecular bonds.[3]

to deform as if it were in the interior of the body. Individual deformation of each surface grain, characterised by localized deformation along favorably located slip planes of the grain, will not take place as in hydrodynamic lubrication. Instead the deformations will be evenly distributed throughout the volume of the grains and in the grain boundaries. Because of this, an attractive, smooth, bright, shiny surface appearance is then obtained on the formed component. With this lubrication mechanism, the value of the Coulomb coefficient of friction will commonly lie in the range $0.01 < \mu < 0.1$.

When this kind of lubrication mechanism prevails during forming, the surface of the formed component at the end of forming will have the appearance of a fine stripelike pattern extending in the same direction along the workpiece surface as the sliding motion of the workpiece against the die during the course of forming. This surface appearance is shown magnified in Fig. 10.7(a). When looked upon by the naked eye, without magnification, this surface has, as already mentioned, a desirable shiny appearance.

Some lubricants applied in metal forming react chemically with the surface of the die or the workpiece. Because of this, they can give effective boundary lubrication films. A stearate lubricant, which is able to provide efficient *thin film lubrication* when used on steel, is shown in the sketch in Fig. 10.8(b). When this lubricant is used, secondary molecular bonds form between the stearate molecules and the iron oxide molecules present in the oxide layer covering the steel surface. Because of this rather strong chemical bonding, the lubricant film on the surface can withstand high shear stresses due to friction without being torn away from the surface. The thin film formed this way adheres firmly to the surface that it is bonded to and hence can provide efficient boundary film lubrication in metal forming.

In practical cases of metal forming, it is quite common to have boundary film lubrication combined with metallic contact at local spots on the die surface, i.e., a *mixed lubrication* mechanism. For this kind of contact, the Coulomb coefficient of friction is commonly claimed to lie in the range $\mu = 0.1–0.3$.

In some situations, there may be local breakdown of the lubricant film in spots along the boundary interface between die and workpiece. In contrast to boundary film lubrication, the workpiece surface may then obtain an unattractive, *speckled*, appearance, such as that shown in Fig. 10.7(b).

10.4 Measurement of Friction in Metal Forming

Although it is commonly straightforward to measure friction in general non-metal-forming situations encountered in everyday life, this is not the case when it comes to friction in metal forming. In metal forming, the most commonly used method of measuring friction is perhaps the *ring compression test*. This test method will therefore be described in detail.

An alternative method for measurement of friction in metal forming is by use of pins inserted into the die. A pair of holes is first drilled through the tooling, where steel pins, which consist of a material the same as or similar to the die material, are inserted into the holes. The end face of the pins must be flush with the die surface during the measurement. Each pin is fitted with a sensor at its rear end, inside the tooling. The force transferred to each pin from the workpiece material at the interface with the die can be read out by means of this sensor. In this way, the contact stress, both normal and shear, at a point on the contact surface can be obtained from primary force measurements. When the stresses have been determined, it is straightforward to compute the local friction value on the interface where the measurement was performed. Various aspects of use of pins on the die or workpiece for friction measurement will be discussed in the further treatment here.

Strip drawing[4] is a metal forming process in which the average friction on the drawing die can be determined directly from measurement of the *die splitting force* and the drawing force. It will not be treated here, being beyond the scope of this book.

10.4.1 Metal Forming Friction from Ring Compression

In metal forming, it is common to apply the ring compression test[5] to determine friction in situations where metallic bodies are subjected to plastic deformations against die surfaces. This technique was developed quite early, and in most cases, it will provide reasonable friction values for a selected material pair (workpiece and die material), either in dry friction or in interaction with a particular lubricant.

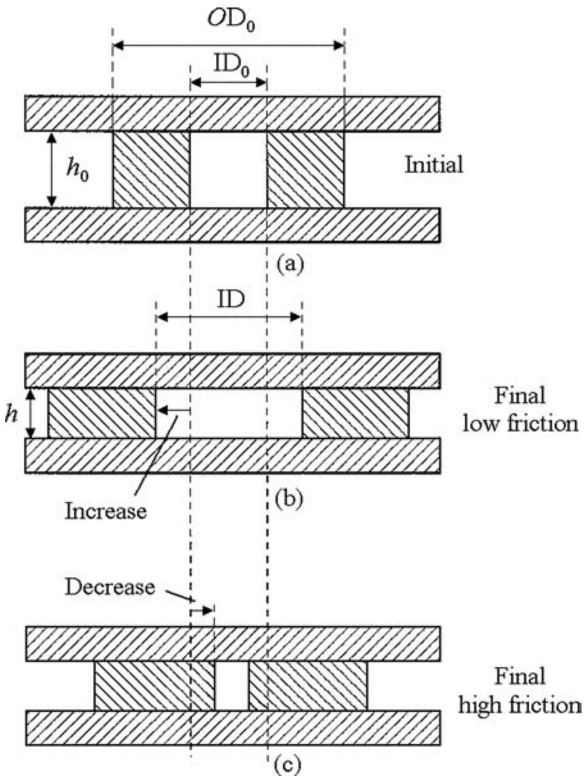

Figure 10.9. Material flow in ring compression: (a) initial ring, and compressed ring in case of (b) low and (c) high friction.

In the ring compression test, when applied for measurement of friction in metal forming, a flat ring such as that shown in Fig. 10.9(a) is applied. It is lubricated and placed between two flat dies, where it is compressed down to less height. The technique can be applied because the metal flow of the ring is highly friction-sensitive.

In the frictionless state, the ring will flow outwards in the radial direction, as if it were a solid cylinder, i.e., as if there were no hole in the middle. In this case, material flow of the ring is characterized by expansion of both the inner and the outer diameter of the ring, as depicted in Fig. 10.9(b). But as the friction between the ring and the dies is gradually increased, there will be a continuous change in the behavior, so that the outward material flow gradually becomes less. When the friction has been increased sufficiently, there will be a situation where there is no change in the inner diameter of the ring during compression. When the friction is further increased, the diameter of the hole of the ring will start to decrease during the course of compression, so that metal flow is directed opposite what it was at lower friction, i.e., the flow will be directed inward toward the center of the ring; see Fig. 10.9(c).

From this it is obvious that the shape of the final ring after compression depends on the friction. When cylinders of the same height are compressed to the same height reduction, the diameter of the hole of the ring will change continuously as

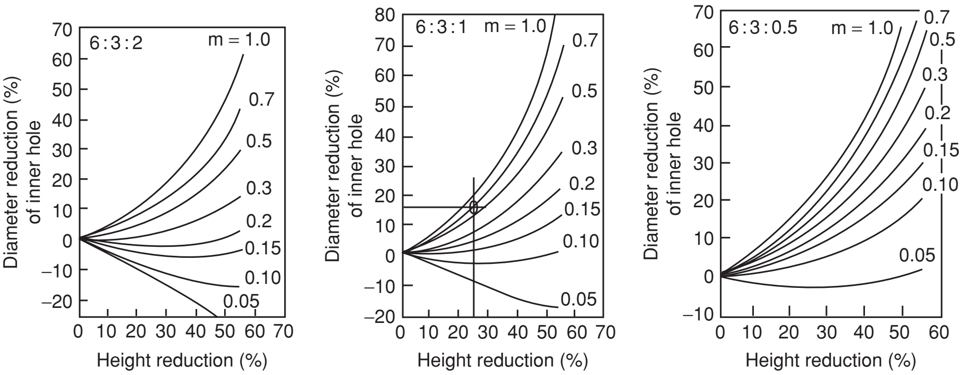

(a) (b) (c)

Figure 10.10. Diagrams for determining friction factor in ring compression for different proportions of initial rings. (Reprinted with permission of Prof. T. Altan. www.ercnsm.org.)

the friction is increased from zero to the highest possible value, which is the sticking friction.

It was realized early that friction must continuously change the inner diameter (ID) of the hole in the flat ring applied in this test, and that this diameter, therefore, can be used as a measure from which friction can be determined in ring compression. Mathematically this behavior can be expressed by

$$\mathrm{ID} = f(\mu, r) \tag{10-9}$$

$$\mathrm{ID} = f(m, r) \tag{10-10}$$

Here, the first equation refers to compression with Coulomb friction and the second equation to Tresca friction. As the equations show, the parameter height reduction r also influences the final value of the diameter of the inner hole.

A third factor that must be considered is the initial proportions of the ring, which of course can be selected differently. Commonly used proportions for rings applied for friction testing, are as follows (see Fig. 10.10):

$$\mathrm{OD}_0 : \mathrm{ID}_0 : h_0 = 6:3:2, \quad \mathrm{OD}_0 : \mathrm{ID}_0 : h_0 = 6:3:1,$$

$$\text{or} \quad \mathrm{OD}_0 : \mathrm{ID}_0 : h_0 = 6:3:0.5$$

EXAMPLE 10.1: FRICTION FROM RING COMPRESSION EXPERIMENT

Problem: A ring specimen with proportions characterized by $\mathrm{OD}_0 : \mathrm{ID}_0 : h_0 = 6:3:1$ and dimensions $\mathrm{ID}_0 = 60\,\mathrm{mm}$, $h_0 = 20\,\mathrm{mm}$, was compressed down to a final height $h = 15\,\mathrm{mm}$. After compression the diameter of the inner hole of the ring was measured as $\mathrm{ID} = 50\,\mathrm{mm}$. Determine the friction in this test, assuming that it complies with the Tresca friction model.

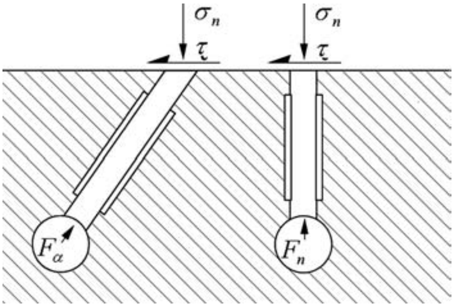

Figure 10.11. Sketch of pins that extend into the die surface for contact stress measurement on the die–workpiece interface.

Solution: The height and diameter reductions of the ring are

$$r = \frac{h_0 - h}{h_0} 100\% = \frac{(20 - 15)\,\text{mm}}{20\,\text{mm}} 100\% = 25\%$$

$$\text{ID}_{\text{red}} = \frac{\text{ID}_0 - \text{ID}}{\text{ID}_0} 100\% = \frac{(60 - 50)\,\text{mm}}{60\,\text{mm}} 100\% = 17\%$$

The point given by $r = 25\%$ and $\text{ID}_{\text{red}} = 17\%$ can then be identified as indicated by a small circle in the friction diagram in Fig. 10.10(b). This yields a friction factor $m = 0.7$, i.e., rather high friction.

10.4.2 Pin Measurement of Friction

Contact stresses in a particular location on the interface between workpiece material and die can be measured[6,7] if two pins are inserted at a particular place in the die, as shown in the schematic sketch in Fig. 10.11. It is then required to drill holes that extend from the back of the tooling through the die. The pins are inserted into the holes so that they remain flush with the die surface during the measurement. The workpiece metal should slide over the end faces of the pins as if they were an integral part of the die surface.

To measure the pressure on the pins at the die surface, force transducers are placed at the other end of the pins, to sense the force transferred axially through the pin. To measure both contact stresses, one pin must be orthogonal to the die surface and the other oriented at an angle (for instance, $\alpha = 30°$) to the surface.

The orthogonal pin is able to measure the normal stress component, σ_n, transferred to the end of the pin, and from there axially down through the pin, as the force F_n. The other pin, with inclination to the die surface, correspondingly senses the force F_α transferred down through the pin. But this force is a resultant of both the normal stress component σ_n and the shear stress component τ on the end surface of the pin.

To deduce the two stress components σ_n and τ from the measured forces F_n and F_α, it is required to establish a force balance for each pin. The force balance yields two equations, in which the stress components are the unknowns. The equations are

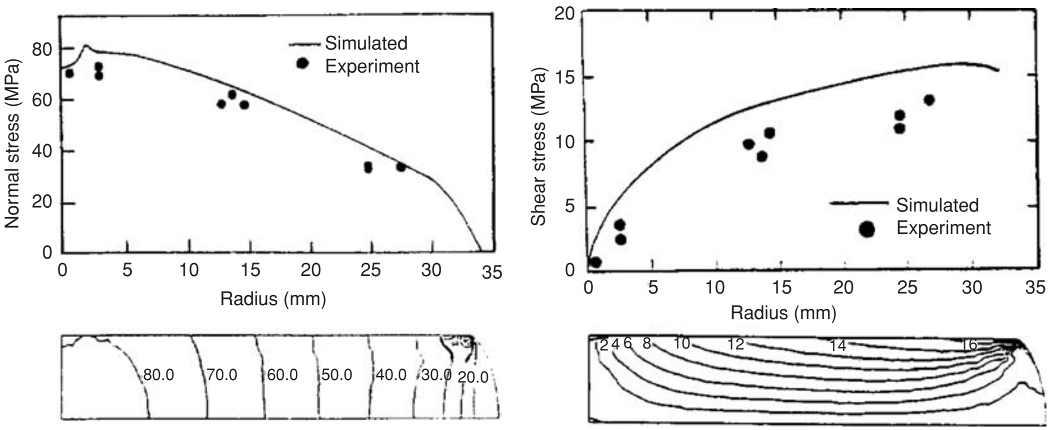

(a) (b)

Figure 10.12. Measured and computed contact stresses, (a) normal component and (b) shear component, against compression platen in hot cylinder compression.

developed in Example 10.2 and Problem 10.2. The final result of the analysis is

$$\sigma = \sigma_n = \frac{\mu F_\alpha + F_n(\tan\alpha + \mu)}{\pi r^2[\tan\alpha\ (1-\mu^2) + 2\mu]} \tag{10-11}$$

$$\tau = \tau_i = \frac{F_\alpha - F_n(1 - \mu\tan\alpha)}{\pi r^2[\tan\alpha\ (1-\mu^2) + 2\mu]} \tag{10-12}$$

Here, μ is the friction coefficient describing frictional contact between the pin and the hole wall the pin extends through, not the friction coefficient at the die–workpiece interface. When the pins are used for measurement, this way, they will be pushed against the *die bore*, because of the shear stress component at their end face, while they are being compressed elastically in their length direction.

Hence, they will slide backwards inside the bore, and the measurement will be affected by friction forces against the bore. The force that finally reaches the transducer is therefore the force acting on the end face of the pin, minus the friction force against the bore.

In a series of experiments, friction stresses were measured this way in cylinder compression. When this was done, a coefficient of friction of $\mu = 0.4$ was used for the friction between the pin and the bore.

Finally, when the stress components defined by eqs. 10-11 and 10-12 have been measured at a location on the die surface, the Coulomb friction coefficient at this spot is determined easily from the stress components, by use of eqs. 10-5.

10.5 Pins Applied in Cylinder Compression to Determine Friction

A pin arrangement consisting of two pins was used, as described, to measure the contact stresses[8] in a hot cylinder compression test performed under conditions of sticking friction, i.e., without use of lubricant. Measurement was done in three different radial positions along the die interface. The compression test was also

FEM-modeled. The finite element program was used to compute contact stresses corresponding to those measured in the experiments. The cylinders consisted of an AA 6060 alloy. Both workpiece and die temperature were kept at 500°C in the beginning of the compression test. All surfaces were cleaned before each experiment, to secure sticking friction in the test.

In Fig. 10.12, the contact stresses in this compression test are shown as they were measured. Simulated values have also been included in the diagrams as graphs. As the figure depicts, there was reasonable agreement between simulated and measured values. Because of general sources of errors in the pin measurements, it is not obvious which data set is the more correct one, the measured or the computed one.

There is better correspondence between simulated and measured data for the normal stress component than for the shear stress component. One should be aware that it is much easier to measure the normal stress with a pin than the shear stress. This is because the shear stress must be deduced from the force measurement on the inclined pin, which concurrently also senses the normal stress component, which is a number of times larger than the shear stress.

EXAMPLE 10.2: STRESS COMPONENTS FROM PIN MEASUREMENT

Problem: Consider a pin arrangement, such as that shown in Fig. 10.11, which is used to measure stress components σ_n and τ on a die–workpiece interface in a metal forming application. Establish a force balance for each pin, to compute stress components from the measured force components F_n and F_α. Assume friction between pins and die bore to be characterized by the friction coefficient μ.

Solution: Consider a pin arrangement consisting of an orthogonal and an inclined pin as shown in the accompanying figure, where force components acting on the ends of both pins are shown.

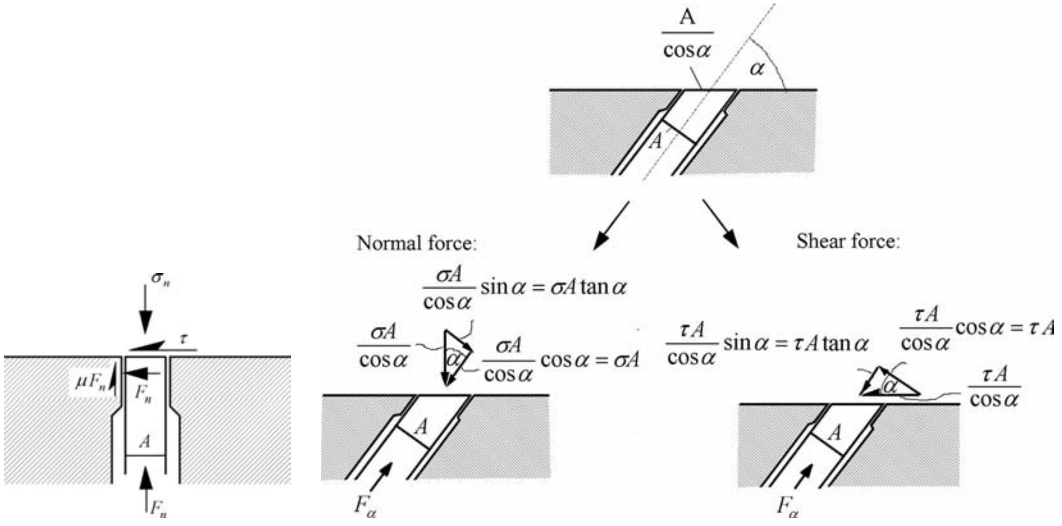
σ_n
τ
μF_n
F_n
A
F_n
$\frac{A}{\cos\alpha}$
α
A
Normal force:
$\frac{\sigma A}{\cos\alpha}\sin\alpha = \sigma A\tan\alpha$
$\frac{\sigma A}{\cos\alpha}$
α
$\frac{\sigma A}{\cos\alpha}\cos\alpha = \sigma A$
A
F_α
Shear force:
$\frac{\tau A}{\cos\alpha}\sin\alpha = \tau A\tan\alpha$
$\frac{\tau A}{\cos\alpha}\cos\alpha = \tau A$
α
$\frac{\tau A}{\cos\alpha}$
A
F_α

(a) (b)

With friction in the bore, there are friction forces counteracting the primary force components. For the orthogonally oriented pin, the normal and the friction force against the bore can be expressed as follows (see the left-hand side of the figure):

$$F_N = A\tau$$

$$F_\mu = \mu F_N = \mu A\tau$$

The force equilibrium in the axial direction of the pin can then be expressed as

$$F_n = F_N - F_\mu = A\sigma_n - \mu A\tau = A\left(\sigma_n - \mu\tau\right) \tag{10-13}$$

For the inclined pin, one correspondingly obtains the expressions

$$\begin{aligned} F_N &= \sigma_n A \tan\alpha - \tau A = A\left(\sigma_n \tan\alpha - \tau\right) \\ F_\mu &= \mu F_N = \mu A\left(\sigma_n \tan\alpha - \tau\right) \end{aligned}$$

The force equilibrium in the axial direction of this pin then yields

$$\begin{aligned} F_\alpha &= F_N - F_\mu = A\left(\sigma_n \tan\alpha - \tau\right) - \mu A\left(\sigma_n \tan\alpha - \tau\right) \\ &= A\left[\sigma_n + \tau\tan\alpha - \mu\left(\sigma_n \tan\alpha - \tau\right)\right] \end{aligned} \tag{10-14}$$

We have thus obtained two equations in which there are two unknown parameters, namely, σ_n and τ. From these equations, it is therefore straightforward to solve for the stress components, when the forces F_n and F_α are known from measurement. The result is that already given by eqs. 10-11 and 10-12.

Problems

10.1 Friction is determined in ring compression testing. The following specimen geometry is used in the test: $\text{OD}_0 = 75$ mm, $\text{ID}_0 = 37.5$ mm, and $h_0 = 12.5$ mm; see Fig. 10.9.

(a) Determine the ratio $\text{OD}_0 : \text{ID}_0 : h_0$ for the ring specimen. Three metals were tested in dry friction condition and in different lubricated conditions; see the accompanying table. In all cases, the final height of the specimen after compression was $h = 9$ mm. The final inner ring diameter was measured in each test, and results are given in the table.

(b) Determine the friction in each ring test, both as coefficient of friction and friction factor. Use the graphs in Fig. 10.10 and the one accompanying this problem to determine the friction values.

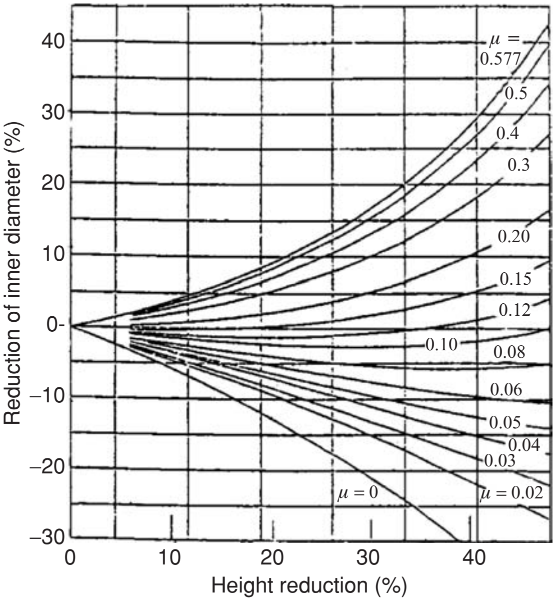

(c) Discuss the results you obtain. Try to explain the characteristic trends in the friction behavior.

Alloy	Lubrication	ID after compression (mm)	Reduction of ID (%)	μ	m
Al-alloy	Dry friction	30.8			
	Graphite–oil	38.1			
	Teflon foil	37.7			
Cu	Dry friction	33.0			
	Graphite–oil	37.2			
	Teflon foil	38.5			
Soft steel	Dry friction	33.9			
	Graphite–oil	38.4			
	Teflon foil	39.4			

10.2 Consider measurement of contact stresses by means of pins extending into the die–workpiece interface during a metal forming application:

(a) Apply the two eqs. 10-13 and 10-14 to determine the contact stresses, as well as the Coulomb coefficient of friction, at the location where the measurement is done. (The solution is eqs. 10-11 and 10-12.)

(b) At a specific location on the surface of a die, the contact stresses were measured to be $\sigma = 40\,\text{MPa}$ and $\tau = 18\,\text{MPa}$. Determine the friction coefficient at this location.

10.3 A cylinder of soft steel was compressed down to an average strain of $\bar{\varepsilon} = 1$. A thin layer of aluminum foil was used as solid lubricant between the cylinder and the die. Determine the friction factor in the compression process, under the assumption that cylinder and foil are subjected to the same deformation. The flow stress relationships at the actual temperature of compression for the steel specimen and the aluminum foil, respectively, are given as

$$\bar{\sigma} = K\bar{\varepsilon}^{n} = 715.7\,\mathrm{MPa} \cdot \bar{\varepsilon}^{0.22}$$

$$\bar{\sigma} = K\bar{\varepsilon}^{n} = 119.3\,\mathrm{MPa} \cdot \bar{\varepsilon}^{0.297}$$

10.4 In the two graphs presented here, contact stress data from pin measurements performed over the workpiece interface in ring compression are given. The data refer to different locations at the end faces of cylinders of pure Al, compressed down to a height reduction of 10%, for which the shear flow stress was determined to be $k = 8$ kpsi. Three different conditions of lubrication were investigated: dry friction, condition A; condition B, where a mixture of oleic acid in mineral oil was used as lubricant; and, finally, condition C, where Pb foil was used as a solid lubricant.

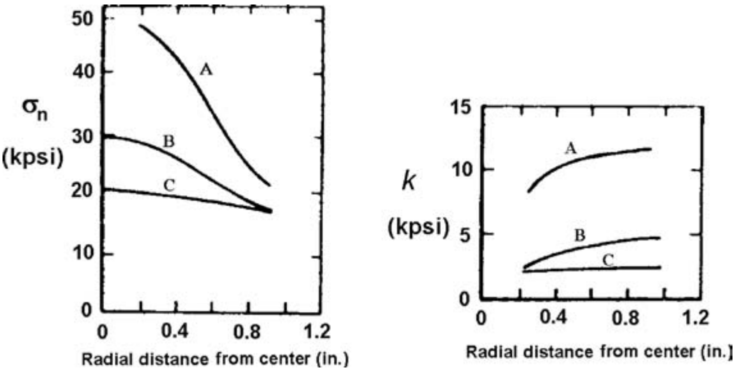

(Reprinted from Int. J. Mech. Sci., Vol. 1, van Rooyen, G. T., and Backofen, W. A., "A study of the interface friction in plastic compression," pp. 1–27, 1960 with permission from Elsevier.)

(a) Specify the general expressions for shear stress in the cases of (i) Coulomb and (ii) Tresca friction, and define the symbols used.
(b) Use the contact stress data in the figure to determine which of the two friction models will describe measured data best for each of the lubricant conditions A, B, and C.
(c) Calculate the friction factor for lubricant conditions A and B for points at distances $r = 0.3$ in. and 1.0 in. from the center of the cylinder.

NOTES

1. Wanheim, T., and Bay, N.: "A model for friction in metal forming processes," Ann. CIRP, Vol. 27, No. 1, 1976, pp. 189–193.
2. Schey, J. A.: "Tribology in Metalworking: Friction, Lubrication and Wear," ASM Int., Metals Park, Ohio, 1983, pp. 78–79.
3. Godfrey, D. in Ku, P. M. (Ed.): "Interdisciplinary approach to friction and wear," NASA Sp-181, Washington, 1968.

4. Suthcliffe, M. P. F., Lee, H. R., and Farrugia, D.: “Simulation of transfer layer formation in strip drawing of stainless steel,” Wear, Vol. 254, 2003, pp. 523–531.
5. Male, T., and Cockcroft, M. G.: “A method of the determination of the coefficient of friction of metals under conditions of bulk plastic deformation,” J. Inst. Metals, Vol. 93, 1964–65, pp. 38–46.
6. Siebel, E., and Lueg, W.: Mitt. Kaiser Wilhelm Inst. Eisenforschung, Vol. 15, 1933, p. 1.
7. van Rooyen, G. T., and Backofen, W. A.: “A study of the interface friction in plastic compression,” Int. J. Mechanical Sciences, 1960, Vol. 1, pp. 1–27.
8. Hansen, A. W., Welo, T., and Valberg, H.: “A technique for measuring stresses on the tool surface,” Proc. 4th Int. Conf. on Technology of Plasticity, Beijing, China, 1993, Vol. 1, pp. 303–308.

REFERENCES

Bay, N.: “Modelling and testing of friction in forging,” in “New Developments in Forging Technology,” Mat-Info Werkstoff-Informationsgesellschaft, Frankfurt, 2007, pp. 233–252.

Lenard, J. G. (Ed.): “Metal Forming Science and Practice,” Elsevier, 2002.

Mang, T.: “Die Schmierung in der Metallbearbeitung,” Vogel-Buchverlag, 1983.

Schey, J. A.: “Tribology in Metalworking: Friction, Lubrication and Wear,” ASM Int., Metals Park, Ohio, 1983.

11 Thermal Effects

The energy consumed in a metal forming operation, as, for instance, in a forging stroke, is mainly transformed into heat, which leads to temperature rise in the die and the workpiece. In heavy metal forming equipment, a lot of energy is supplied to the workpiece this way, and there can be substantial global and local heating effects in the workpiece material.

In many metal forming applications, there are limits on how high the temperature of the workpiece can rise before one experiences problems such as reduced or unacceptable product quality. This is, for instance, the case in aluminum extrusion, where the maximum temperature of the metal near the outlet from the die should not exceed a certain critical temperature. In this process, material defects, such as surface cracking due to hot tearing of the material, start to appear when this critical temperature is exceeded, and a usable profile can no longer be manufactured. This phenomenon is explained and discussed in this chapter.

In addition, it is shown how one can quantify different thermal effects in a metal forming process, such as *heating due to plastic deformation* inside the workpiece, and *heating due to friction* over its surface. When the workpiece has higher temperature than the dies, there is *cooling* against the dies, and the physics required to calculate the cooling is shown for a simple two-dimensional case.

It is also explained how the temperature inside the tooling and on the surface of the workpiece can be measured by use of *thermocouples*. Use of *pyrometry* to measure the surface temperature on a body is also discussed. Finally, characteristic thermal conditions in some typical nonstationary and stationary metal forming processes are described by examples.

11.1 Thermal Effects in Metal Deformation Processes

When it comes to thermal effects, *heat radiation* is in many cases neglected in metal forming applications. But, for instance, hot forming of steels is performed at temperatures as high as 1000–1200°C. At these temperatures, loss of heat due to radiation becomes significant and must be included if an accurate thermal analysis is to be done. Al and Al alloys, however, are seldom formed at higher temperature than

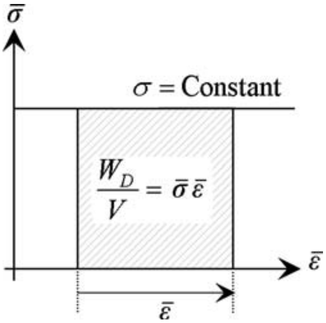

Figure 11.1. Energy consumption during deformation of ideal rigid–plastic material with constant flow stress.

550°C, and radiation effects are less significant at these low temperatures. They can therefore be neglected without much error.

If radiation effects and cooling to the surrounding air are neglected, the following equation[1,2] can be used to estimate the temperature in a workpiece during a metal forming operation:

$$T_1 = T_0 + \Delta T_D + \Delta T_F - \Delta T_T \tag{11-1}$$

Here, the following symbols are used:

- T_0 is the initial temperature of the workpiece.
- ΔT_D is the temperature increase in the workpiece due to dissipated deformation energy during forming.
- ΔT_F is the temperature increase due to friction in the interface between die and workpiece.
- ΔT_T is the temperature decrease in the workpiece because of cooling by colder dies.

11.1.1 Effects Due to Dissipated Deformation Energy

Consider an ideal rigid–plastic workpiece without strain hardening, i.e., a workpiece of an ideal material with constant flow stress $\bar{\sigma}$.

The energy added to this workpiece by deformation up to an average strain of $\bar{\varepsilon}$ (see Fig. 11.1), can be expressed as

$$W_D = \bar{\sigma}\bar{\varepsilon}V \tag{11-2}$$

Correspondingly, the amount of heat required to give the workpiece the temperature rise ΔT_D is given by

$$Q_D = cm\,\Delta T_D \tag{11-3}$$

In this equation, symbols are

c (J kg^{-1} K^{-1}), the *heat capacity* of the workpiece material;
m, the mass of the workpiece (V is the volume).

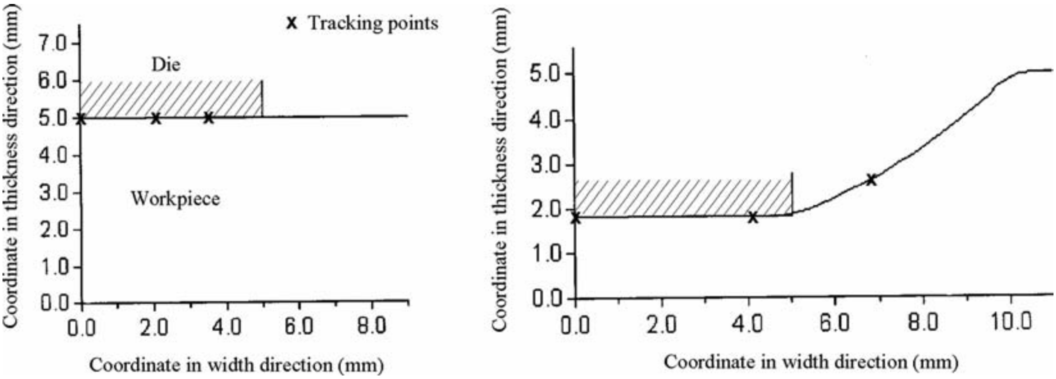

(a) (b)

Figure 11.2. Material particles on surface of workpiece sliding over die surface in plane strain compression: (a) initial and (b) final positions.

As mentioned, the largest part of the energy consumed in a metal forming operation is transformed into heat. But some energy is also stored in the microstructure of the deforming body, for instance, because of the formation of vacancies or dislocations. This energy varies from case to case but will make up approximately 5% of the total energy contribution.[3] The following equality can then be set up, where the factor β (≈ 0.95) compensates for the energy stored in the workpiece:

$$W_D \cdot \beta = Q_D \tag{11-4}$$

By the introduction of the terms given in eq. 11-2 and eq. 11-3, this equation will yield the following expression:

$$\bar{\sigma}\bar{\varepsilon}V\beta = cm\,\Delta T_D \quad \Rightarrow \quad \bar{\sigma}\bar{\varepsilon}\frac{m}{\rho}\beta = cm\,\Delta T_D$$

where ρ is the *density* of the workpiece material.

The temperature increase of the material due to deformations[2] now can be expressed as

$$\Delta T_D = \frac{\beta}{c\rho}\bar{\sigma}\bar{\varepsilon} = \frac{\beta}{c\rho}\bar{\sigma}\dot{\bar{\varepsilon}}\,\Delta t \tag{11-5}$$

The relationship $\bar{\varepsilon} = \dot{\bar{\varepsilon}}\,\Delta t$ has been introduced into the formula to include time effects.

11.1.2 Effects Due to Frictional Heating

Most commonly, the workpiece material will slide against the die with friction forces acting against the sliding movement. Because of this, there will also be energy consumed over the die–workpiece interface, which manifests itself in a temperature increase. The sliding movement, as predicted in FEM simulation of a plane-strain compression test, is shown in Fig. 11.2. In the figure, one-fourth of the compression test is shown. Initial positions on the workpiece surface are shown in

Fig. 11.2(a), and final computed positions for the same three material points are shown in Fig. 11.2(b).

In the previous chapter, it was shown that friction shear stresses commonly are present on die–workpiece interfaces. On the surface of the workpiece or the die, this shear stress will appear as a shear force. So when there is sliding movement over the interface, the energy dissipated over the interface will equal the shear force multiplied by the sliding length, i.e., the displacement along the interface. The energy dissipation in an interface due to friction therefore can be expressed as

$$W_F = \tau A s = \frac{m}{\sqrt{3}}\bar{\sigma} \cdot As = \frac{m}{\sqrt{3}}\bar{\sigma} \cdot A \cdot v\,\Delta t \tag{11-6}$$

The symbols used in this expression are

A, the apparent area of contact,
s, the sliding length,
m, the friction factor (see eqs. 10-7 and 10-8),
v, the displacement velocity, and
Δt, the time required for the displacement.

The friction-induced energy contribution is all dissipated as heat in the die and the workpiece. We can make a simplification and assume that all this heat, Q_F, is dissipated in a layer of volume V_a near the surface of the workpiece. Then we can establish the following equation:

$$Q_F = cm\,\Delta T_F = c \cdot V_a\rho \cdot \Delta T_F \tag{11-7}$$

The energy provided by the friction can now be set equal to the heat dissipated in the surface layer:

$$W_F = Q_F \quad \Rightarrow \quad c \cdot V_a\rho \cdot \Delta T_F = \frac{m}{\sqrt{3}}\bar{\sigma} Av\,\Delta t \quad \Rightarrow \quad \Delta T_F = \frac{m\bar{\sigma} Av\Delta t}{\sqrt{3} \cdot c \cdot V_a\rho} \tag{11-8}$$

We have now obtained an expression for the friction-induced temperature increase[2] in a given surface layer of the workpiece. The equation shows which main parameters of both the workpiece material and the forming process that the temperature increase will depend on.

11.1.3 Cooling Effects

In hot forming applications, it is common to use a die that is initially colder than the workpiece. In cold forming, the die and the workpiece will initially be at the same temperature, namely, the room temperature, but during the forming operation the workpiece will heat up, and heat will then start to flow from the workpiece to the colder die.

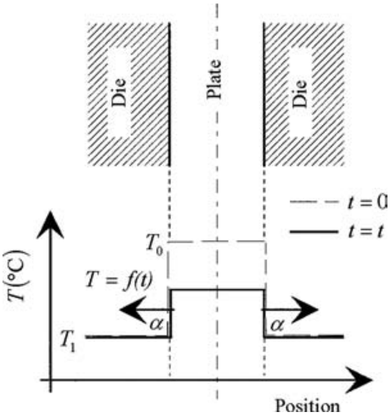

Figure 11.3. Thermal conditions in hot plate cooled by dies at both sides.

In metal forming, it is therefore often useful to estimate the cooling of the workpiece by the die to reveal what parameters affect the cooling. Let us develop an expression for the cooling effect on a hot plate, kept between two colder dies over some time, as shown in Fig. 11.3. Assume the plate and the dies to have infinite extension in the vertical direction and to be directed into the plane of the paper. Then there will be one-dimensional heat transfer. Assume also the dies to be massive and to consist of a material that conducts heat so fast that the dies remain at the same temperature in spite of the heat supply from the hotter plate. Finally, assume the thermal conductivity of the plate to be sufficiently high so that the temperature across the thickness of the plate remains constant. In that case, the heat transfer from the plate to the dies determines how fast the plate cools down.

Let us try to quantify how the temperature of the plate will decrease vs. time. Assume heat transfer through the plate–die interface to be characterized by a *coefficient of heat transfer*, α. First, we must consider the amount of heat that flows through this interface in the time interval dt at the time t:

$$\mathrm{d}Q = \alpha A\,\Delta T\,\mathrm{d}t = \alpha A\,(T - T_1)\,\mathrm{d}t \tag{11-9}$$

In this equation, A is the interfacial area between the plate and the dies considered, T_0 is the initial temperature, and T is the instantaneous temperature of the plate; see Fig. 11.3. The amount of heat transferred through the interface, alternatively, can be expressed as

$$\mathrm{d}Q = cm\,\mathrm{d}T = cV_a\rho\,\mathrm{d}T \tag{11-10}$$

because this heat is lost from the plate in the same time. In this expression, the parameters are as follows; c is the heat capacity, ρ is the density of the plate material, and V_a is the volume of the plate bounded by the area A. The two expressions for the amount of heat flowing out of the plate can be set equal:

$$\mathrm{d}Q = \alpha A\,(T - T_1)\,\mathrm{d}t = cV_a\rho\,\mathrm{d}T \tag{11-11}$$

This expression can be reorganized and integrated:

$$\int_0^t \frac{\alpha A}{c\rho V_a} \mathrm{d}t = \int_T^{T_0} \frac{\mathrm{d}T}{T - T_1} \quad \Rightarrow \quad \frac{\alpha A}{c\rho V_a} t = [\ln(T - T_1)]_T^{T_0}$$
$$= \ln(T_0 - T_1) - \ln(T - T_1) = \ln \frac{T_0 - T_1}{T - T_1}$$

[Formula of integration: $\int \mathrm{d}x/(ax + b) = (1/a)\ln(ax + b)$, where a and b are constants and $x \neq 0$]. Further development of the expression yields^2

$$\frac{T - T_1}{T_0 - T_1} = \exp\left(-\frac{\alpha A}{c\rho V_a} t\right) \quad \Rightarrow \quad T = T_1 + (T_0 - T_1)\exp\left(-\frac{\alpha t}{c\rho}\frac{A}{V_a}\right)$$

The ratio $V_a/A = h$ represents the thickness of the plate and can be added into the expression to give

$$T = f(t) = T_1 + (T_0 - T_1)\exp\left(-\frac{\alpha t}{c\rho h}\right) \tag{11-12}$$

We have now determined the temperature of the plate as function of time. As eq. 11-12 shows, the temperature is predicted to decrease exponentially with time, from the initial temperature T_0 to the die temperature T_1. This means that the temperature of the plate will drop as a *transient* down to the die temperature. How rapid the temperature drop is, and how it is influenced by various process parameters, is also revealed by the equation.

In the beginning of the chapter, the current temperature in a workpiece subjected to metal forming was denoted by T_1; see eq. 11-1. This equation now can be reformulated as follows:

$$\begin{aligned} T_1 &= T_0 + \Delta T_D + \Delta T_F - \Delta T_T = (T_0 - \Delta T_T) + \Delta T_D + \Delta T_F \\ &= T + \Delta T_D + \Delta T_F \end{aligned} \tag{11-13}$$

Here, the term T includes the cooling effect because of the use of colder dies.

11.2 Temperature Measurement

In metal forming applications, two different techniques, namely, thermocouple and pyrometer measurement, are commonly used to determine either the die or the workpiece temperature.

Steel has an approximately constant emissivity at a fixed temperature, i.e., a certain fraction of its heat is lost per time unit, due to heat radiation at this temperature. Because of this, the surface temperature of visible surfaces of a workpiece of steel can be measured with good accuracy using radiation pyrometry. A *pyrometer* is an optical device that receives radiated energy from a small area on the surface of a body and that, from the amount of received energy, computes the mean surface temperature of the area. The temperature of invisible surfaces of a workpiece, such as those inside a die, can of course not be determined by pyrometry.

In the case of closed die configurations, where the workpiece surfaces are invisible during forming, temperature measurements are most commonly made by means of thermocouples. A *thermocouple* consists of two wires of different chemical composition, which are brought into contact with each other at one end, most commonly by means of making a small *spherical weld deposit* between the two. The *weld joint* produces an electric potential in the wires, which can be measured between the other ends of the wires. This potential shows an approximately linear increase vs. the temperature of the joint. The electric potential can therefore be read out as a signal, which represents the temperature of the joint, and approximately the temperature in a small volume surrounding the joint.

Modern radiation pyrometers and thermocouples are easy to use, and allow continuous temperature measurements to be made, for instance, as a function of time, and to be recorded by data logging.

However, the oxide layers formed on the surface of a body of aluminum or an aluminum alloy at elevated temperature vary unpredictably in their emission of radiant energy, due to changes in their optical properties. So in the application of pyrometry to these metals it is not straightforward to interpret the signal from the pyrometer and relate it to the actual temperature of the surface on which the measurement is made.

Because of this, a thermocouple is the best device for measurement of the temperature in aluminum processing. However, because a thermocouple consists of a weld joint in the form of a small bead, and with wires extending from the joint, there is a limit to how rapid thermal changes the device can sense.

Because of the size of the thermocouple, it will take some time before it heats up or cools down to the actual temperature of its surroundings. This *inertia effect* is illustrated in Fig. 11.4(b) for a thermocouple covered with a mantle with insulating ceramic powder inside [see Fig. 11.4(a)]. When the thermocouple is immersed in hot water, it takes almost 2 s before the thermocouple measures the water temperature. A thermocouple with a mantle is the most robust solution, because the weld bead and the wire inside the mantle are well protected against mechanical damage, but the presence of the mantle reduces the *thermal response* of the thermocouple.

To measure the temperature of a cylinder subjected to compression, for instance, one can use two thin thermocouple wires directly welded onto the side of the cylinder, without use of any mantle, because there is enough space to keep the wires separated from each other while the voltage at the end of the wires is measured. This simple thermocouple arrangement gives a much faster thermal response than a thermocouple with a mantle.

In the literature,[5] use of specially designed thermocouples for measurement of the temperature inside a die, or near its surface, has been reported; see Fig. 11.5(a). Forging is a rapid metal forming process, and much heat is generated at the die–workpiece interface during forming, because of deformation heating and dissipation of frictional energy, as the workpiece material slides over the die surface. In order to measure the thermal conditions in the die at its surface or in the subsurface layers below, it is required to use a thermocouple with a very short response time.

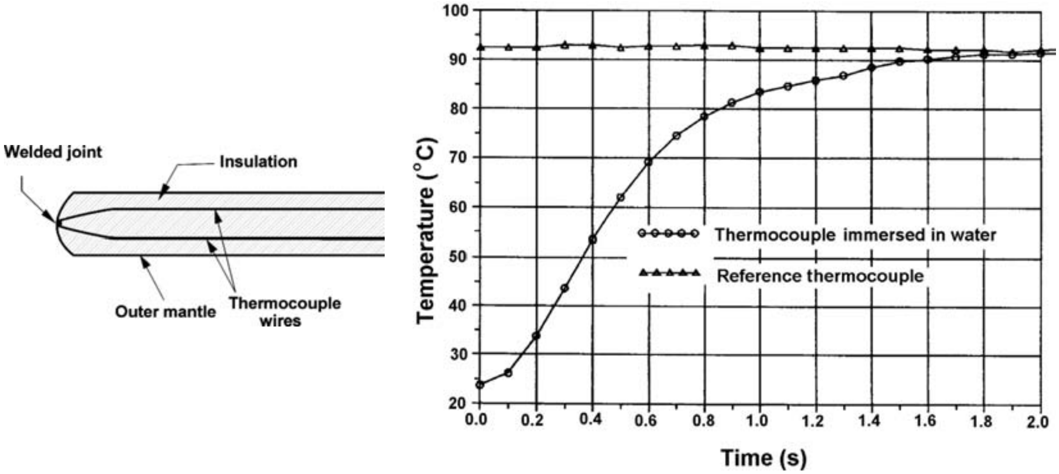

(a) (b)

Figure 11.4. (a) Thermocouple with outer mantle. (b) Thermal response of thermocouple immersed in hot water.[4] (Courtesy of Arne Småbrekke.)

In rapid metal forming processes, it is important that the volume of the welded joint of the applied thermocouple be small and positioned close to the die surface, if the actual temperature variations are to be sensed. In the special thermocouple design shown in Fig. 11.5(a), only one thermocouple wire was used, and this wire was spot-welded onto a small steel plate, which covered the hole of the thermocouple plug. The signal obtained from the thermocouple was the electromotive force

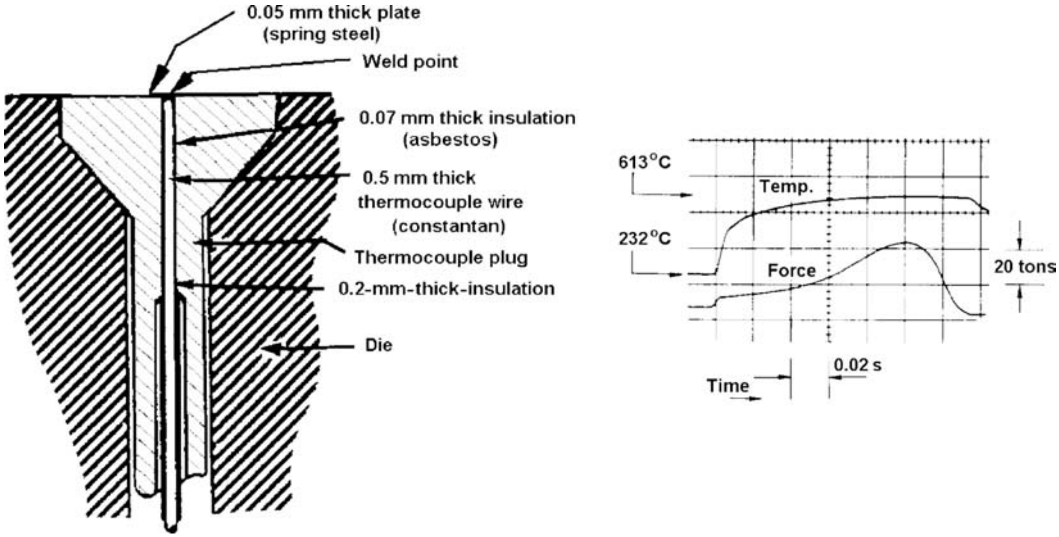
0.05 mm thick plate (spring steel)
Weld point
0.07 mm thick insulation (asbestos)
0.5 mm thick thermocouple wire (constantan)
Thermocouple plug
0.2-mm-thick-insulation
Die
613°C
232°C
Temp.
Force
20 tons
Time
0.02 s

(a) (b)

Figure 11.5.[6] (a) Short-response-time thermocouple placed close to the surface of a forging die. (b) Temperature–time recording obtained by thermocouple.

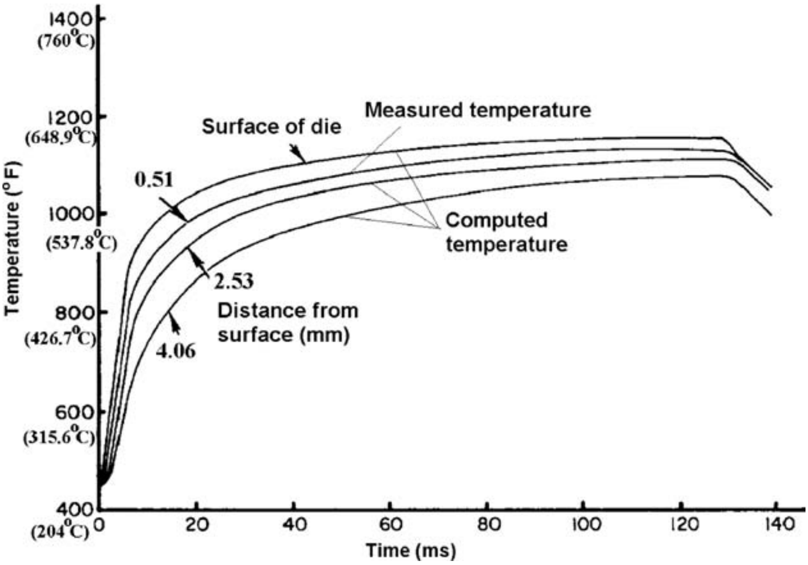

Figure 11.6. Measured temperature at various depths below the surface of a hot-forging die, including computed temperature on and below the surface.[6]

created at the junction between the thermocouple wire and this steel plate, measured as the voltage between the steel plate and the thermocouple wire.

11.3 Thermal Conditions in Nonstationary Metal Forming

The thermocouple signal in a rapid hot forging process, where the temperature was measured by the thermocouple described, in a position slightly below the die surface, is shown in Fig. 11.5(b). The forging load is shown in the same diagram, to depict the progress of forging. The measurement shows that the temperature increase at the actual point below the surface of the die was very rapid in the beginning of the forging operation, immediately after contact had been established between workpiece and die. This is because the initial workpiece temperature is much higher than the die temperature. Because of this, the die surface is subjected to a thermal shock on establishing contact with the workpiece. The figure also clearly reveals that the temperature increase later during the forging operation is less than that upon initial contact between the two bodies.

The measured temperature vs. time for the special thermocouple, when positioned 0.51 mm below the surface of the die, is shown in Fig. 11.6. In the same figure, the temperature of the surface, and at different depths below the surface of the die, is shown as computed by theory from the measured temperature. The figure reveals that there is a strong *temperature gradient* in the surface layer of the die during forging.

Theory has been well developed in order to compute one-dimensional heat flow and can easily be applied to determine thermal conditions when the die–workpiece geometry is simple, as described in connection with Fig. 11.3, for a hot plate kept

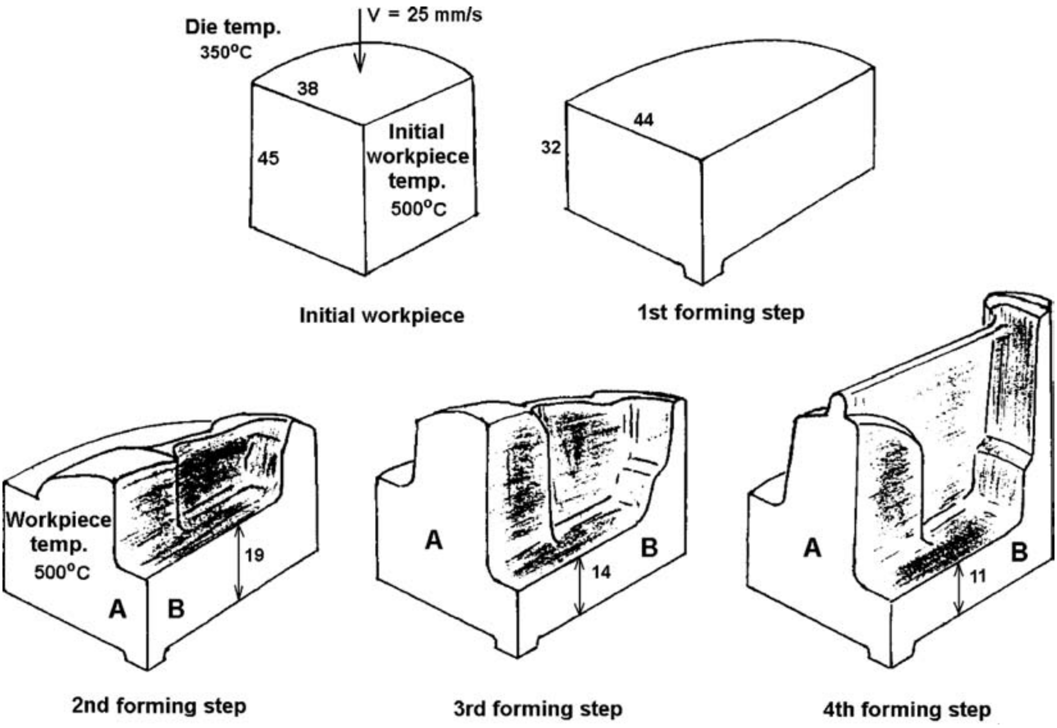

Figure 11.7. Multistep forging of piston head. Because of symmetry, only one-fourth of the specimen is shown. (Courtesy of A. W. Hansen, NTNU.)

between colder dies. But in three-dimensional cases, as in forging when using complex die and workpiece geometry, it is not straightforward to compute thermal conditions by theoretical analysis.

Today, FEA is a good alternative for the purpose of mapping the thermal conditions in metal forming operations, even in complex geometrical conditions. See the next example.

EXAMPLE 11.1: THERMAL CONDITIONS IN MULTISTEP FORGING PROCESS FROM FEM ANALYSIS

Problem: Use FEA to determine thermal conditions in a workpiece during hot forging of an AA 6060 Al alloy.

Description of forging process[6]: The sequence of steps in the forging process is shown in the sketch in Fig. 11.7. A piston head was hot-forged from an initial cylindrical workpiece in four steps. The initial workpiece was made by sectioning of a 60 mm diameter Al billet into a 45 mm long specimen.

The resulting cylinder was upset down to a height of 32 mm in the first forging step, while the diameter increased correspondingly, so the bottom die was filled with metal. In the second forging step, shaping was done at the top side of the workpiece only, as metal in continued forging was forced to flow upwards to fill the cavities of the upper die. To accomplish this filling operation, three forging steps were required. The initial temperatures of workpiece and die and the forging velocity are specified in the sketch. After each forging step, the upper die was pulled backwards and lubricated before the next blow. The component had two symmetry planes A and B; see sketch in Fig. 11.7.

Solution: Thermal conditions in the workpiece can be determined by FEA – for instance, by use of the two-dimensional version of the program FORGE®.[7] First, a FEM model of the process is built, from which thermal conditions can be computed and visualized by the program. Two different simplified models were used to obtain the results presented here. In both, the forging speed was assumed to be constant at 25 mm s^{-1}, whereas, in reality, the speed was only that high in the beginning of the process, and it decreased throughout the stroke. Another simplifying assumption made was that the final component was forged in one continuous stroke, instead of in three consecutive steps as required in the industrial process, with relubrication between steps. Because the forging in reality has three-dimensional geometry, one two-dimensional simulation model was built based on the assumption of rotational symmetry, corresponding to the axial section denoted A in Fig. 11.7. Another model was also built, based on assumption of a component with rotational symmetry corresponding to the axial section denoted B in the figure.

These finite element models were then used to determine the effect of component design on the thermal conditions, with either a thick forged rib extending around the component, corresponding to section A, or a thin forged rib, as in section B.

FEM-computed temperature distributions over the longitudinal section of these forgings are shown in Fig. 11.8(a) and (b). As this figure illustrates, the temperature in the thick rib is higher than in the thin rib, even though heat generation because of plastic deformation obviously is higher when the thin rib is forged. From this, it can be concluded that cooling effects from the dies are strong, especially when the thin section is forged. In the thick rib, cooling effects are nearly balanced by heating effects due to deformation and friction work, because the temperature drop in this case is only $\approx 10^{\circ}$C at the top of the rib at end of forging. Because we have neglected pause times and assumed higher forging speed during the stroke than in reality, the temperature decrease in the real forging must be even larger than in our simulation model. To perform the simulation, a number of thermal data, characterizing both the workpiece and the die, as well as the interface between the two, were specified in the simulation program. These data are given in Table 11.1 for the simulation reported here.

11.4 Thermal Conditions in Stationary Metal Forming Processes

When one needs to know the thermal conditions in a specific metal forming process, one can measure the temperature directly in the industrial process.

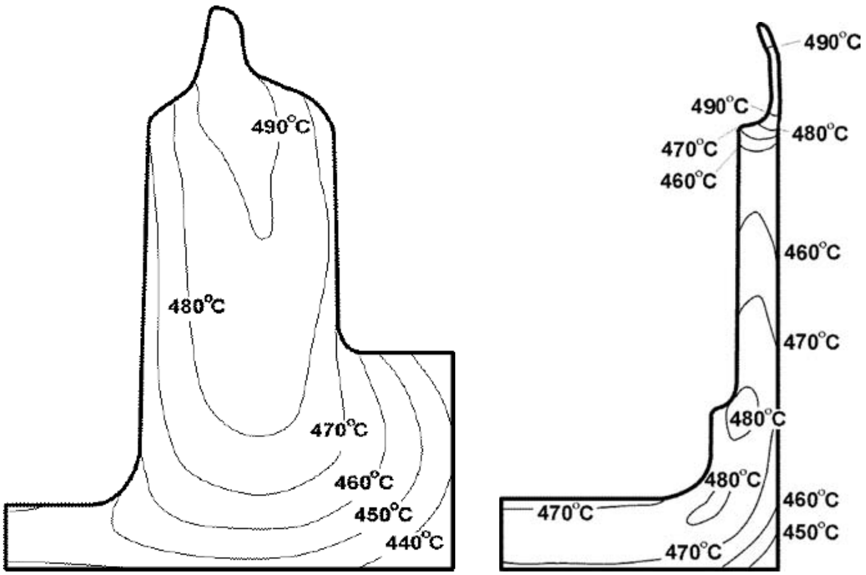

(a) (b)

Figure 11.8. Thermal conditions at end of forging for part with (a) thick rib and (b) thin rib.

Alternatively, one can try to model the process either by theory or by FEM modeling. Most accurate, however, is an approach where one combines a theoretical estimate with measured or FEM-computed thermal data. In the case of measurement, it will be practical to register the temperature only at some particular points on the die or workpiece surface, or inside the die. Theory or FEA is capable of providing temperature data throughout the entire process, both for the die and for the workpiece.

As mentioned in Ch. 6, the velocity field and the metal flow in the plastic zone in a stationary metal forming process will become stable after the start of the process, so that conditions become approximately constant over time. In a stationary process, a constant temperature field is also established in the workpiece and die when the process has been running for a sufficiently long time.

Typical FEM-predicted temperature distributions inside the die and the wire in steel wiredrawing[8] are shown in Fig. 11.9 for simulations with two different drawing

Table 11.1. *Input data used in thermally coupled simulation of forging operation*

Symbol	Value	Unit	Property
ρ_{Al}	2.70×10^{-6}	$\mathrm{kg\,mm^{-3}}$	Density of Al
k_{Al}	2.30×10^{5}	$\mathrm{kg\,mm\,s^{-3}\,K^{-1}}$	Thermal conductivity of Al
c_{Al}	1.10×10^{9}	$\mathrm{mm^{2}\,s^{-2}\,K^{-1}}$	Heat capacity of Al
$h_{\mathrm{Al-Fe}}$	1.00×10^{4}	$\mathrm{kg\,s^{-3}\,K^{-1}}$	Coefficient of Al–Fe heat transfer
ρ_{Fe}	7.80×10^{-6}	$\mathrm{kg\,mm^{-3}}$	Density of Fe
k_{Fe}	3.20×10^{4}	$\mathrm{kg\,mm\,s^{-3}\,K^{-1}}$	Thermal conductivity of Fe
c_{Fe}	0.46×10^{9}	$\mathrm{mm^{2}\,s^{-2}\,K^{-1}}$	Heat capacity of Fe
$h_{\mathrm{Al-air}}$	2.50	$\mathrm{kg\,s^{-3}\,K^{-1}}$	Coefficient of Al–air heat transfer
ξ	0.7		Emissivity of Al

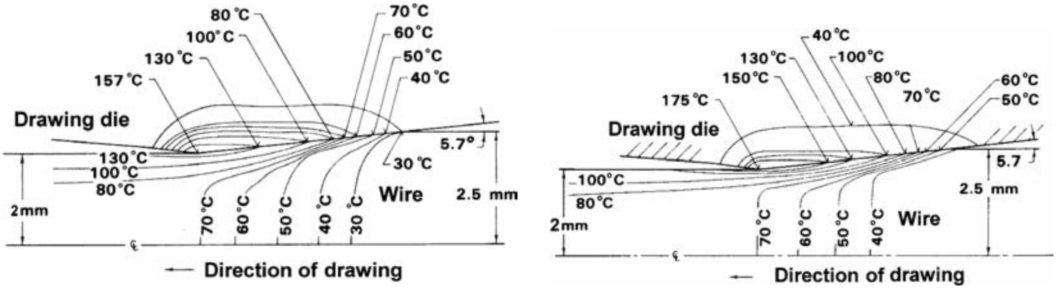

(a) (b)

Figure 11.9. Temperature distribution inside wire and die during drawing of steel wire at drawing speeds of (a) 1 ms^{-1} and (b) 2 ms^{-1}. (This figure was copied with permission from the Marcc 1970 Wire Journal publication. Copyright © WAI Inc.; all rights reserved.)

velocities, while other process variables were kept constant. As depicted in this figure, there is a temperature increase from the center toward the surface of the wire. The hottest spot is on the wire surface at the outlet side of the die, and the temperature drops from there inwards into the wire. The same is the case with the die, which becomes hottest at the surface adjacent to the point where the wire is hottest. The maximum temperature of the die seems to be higher than that of the wire. Moreover, the temperature of the die drops with increasing distance from the workpiece–die interface. The reason why the wire is hottest at the surface is mainly the temperature increase due to frictional dissipation along the workpiece–die interface but also to some extent the extra deformation heat produced in the outer surface layer of the wire because of inhomogeneous deformation there.

When Fig. 11.9(a), is compared with Fig. 11.9(b), one can see that thermal conditions in wire and die are strongly influenced by the drawing speed. When the drawing speed is doubled, the maximum temperature in the die is increased from 157°C to 175°C. The highest temperature of the wire, however, seems to drop slightly when the drawing speed is increased, but there are uncertainties about this trend. It could be that the temperature in a thin surface layer of the wire, close the outlet of the die, is higher at high than at low drawing velocity. This is possible because there is a steep thermal gradient toward the hottest spot on the wire, and this gradient is not so well described by the temperature distribution given in the figures.

The thermal conditions[9] in a die made of cermets fitted into a steel ring by thermal shrinking, used for drawing of soft steel wire, are shown in Fig. 11.10. The figure clearly depicts a strong thermal gradient extending from the surface of the die toward its interior, in the wire outlet region of the die. Note also that there is cooling at the inlet side of the die, where the cold incoming wire establishes initial contact with the die.

11.5 Thermal Effects in Hot Extrusion of Aluminum

Hot extrusion of aluminum is an important metal forming process in the author's home country, for a large fraction of the aluminum produced in the Norwegian aluminum plants is worked by extrusion into aluminum profiles abroad, before the

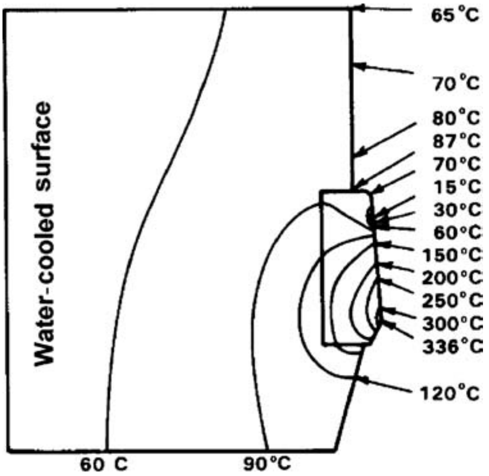

Drawing conditions:

$D_0 = 2.9$ mm
$D_1 = 2.6$ mm
$v = 7.11\ \mathrm{ms}^{-1}$

Figure 11.10. Temperature distribution inside the die during drawing of soft steel wire. (Reprinted with permission of Maney Publishing; www.maney.co.uk/journals/irs, www.ingentaconnect.com/content/maney/ias.)

metal is sold as semifinished products. In the extrusion process, the temperature is important and must be kept within certain limits in order to produce profiles with acceptable mechanical properties and without surface defects. Because of this, thermal conditions during hot extrusion have been investigated thoroughly. In a doctoral thesis,[10] techniques have been developed for measurement of the local maximum temperature at the hottest spot on the bearing channel in extrusion dies.

Characteristic temperature distributions in the billet and in the die can be computed by means of FEA of the extrusion process. A typical temperature distribution[2] determined this way is shown in Fig. 11.11. As the figure depicts, there is a hot spot at the die exit. The hot spot occurs because more heat is generated in the outer layer of the billet material at this location than elsewhere. This is due to localized shear deformations taking place there and to frictional energy dissipated at the interface between the workpiece and the die as the workpiece material slides over the die edge into the bearing channel of the die. Because it is common

Extrusion conditions:
Ram speed: 1.89 m/min
Billet diameter: 71.1 mm
Billet length: 142 mm
Ram disl.: 94 mm
Cont./billet temp.: 440°C

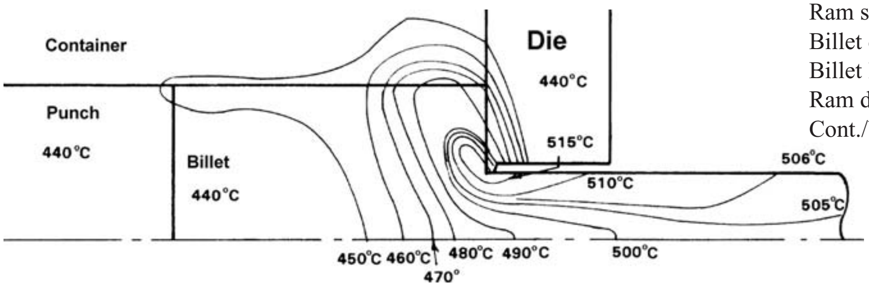

Figure 11.11. Computed temperature distribution in axisymmetric extrusion of AA 5052 Al alloy[11] (reduction ratio 5). (Reprinted with permission of Prof. Taylan Altan. www.ercnsm.org.)

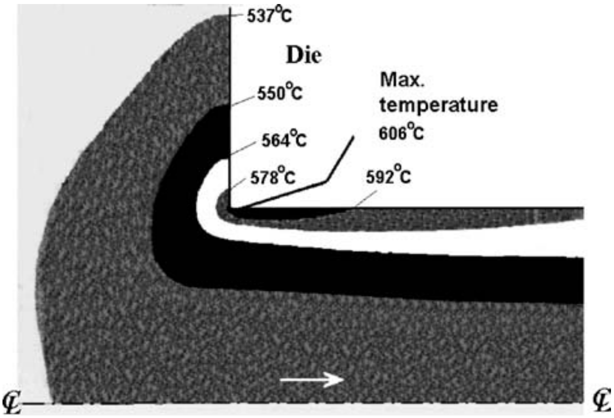

Extrusion conditions:
Alloy: AA 6082
Billet diameter: 100 mm
Rod diameter: 10 mm
Billet temperature: 500°C
Container temperature: 430°C
Ram velocity: 16 mm/s
Die land length: 0.5 mm
(Parallel bearing)

Figure 11.12. Hot spot predicted close to the die edge at outlet from extrusion die in FEM simulation. (Courtesy of M. Lefstad, SINTEF.)

to extrude Al without use of lubricants, friction is high in this region as are shear stresses imposed by the die on the workpiece.

In Fig. 11.12, a detail of the temperature distribution over the die edge and in the bearing channel is shown as it was computed in a FEA of axisymmetric Al extrusion.[12] The figure shows that the hottest spot is predicted to be inside the bearing channel just behind the edge of the die. The result of the simulation, of course, depends on how the boundary conditions are defined over the die–workpiece interface in the FEM model.

FEM simulation is able to give a more or less accurate prediction of real conditions at the boundary interface, depending on how well the real physics is described in the FEM model. It is therefore also important to measure the thermal conditions at this location. A methodology[10,13] for measurement of the temperature in the hottest region of the die in Al extrusion was therefore established, in the case of use of a robust thermocouple with outer mantle, as shown in Fig. 11.4(a). The thermocouple is mounted in a bore drilled into the die, from one side, to appear on the surface of it, adjacent to the hottest spot of the metal stream, flowing over

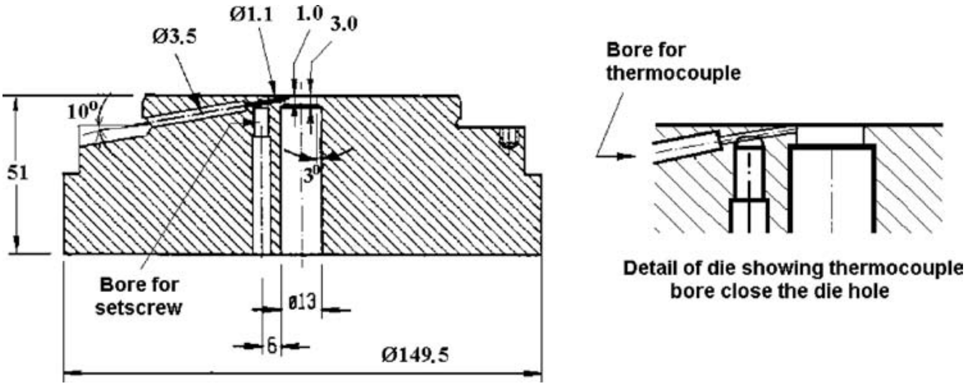

Figure 11.13. Side view of extrusion die with bore for insertion of thermocouple (dimensions in millimeters). (Courtesy of M. Lefstad, SINTEF.)

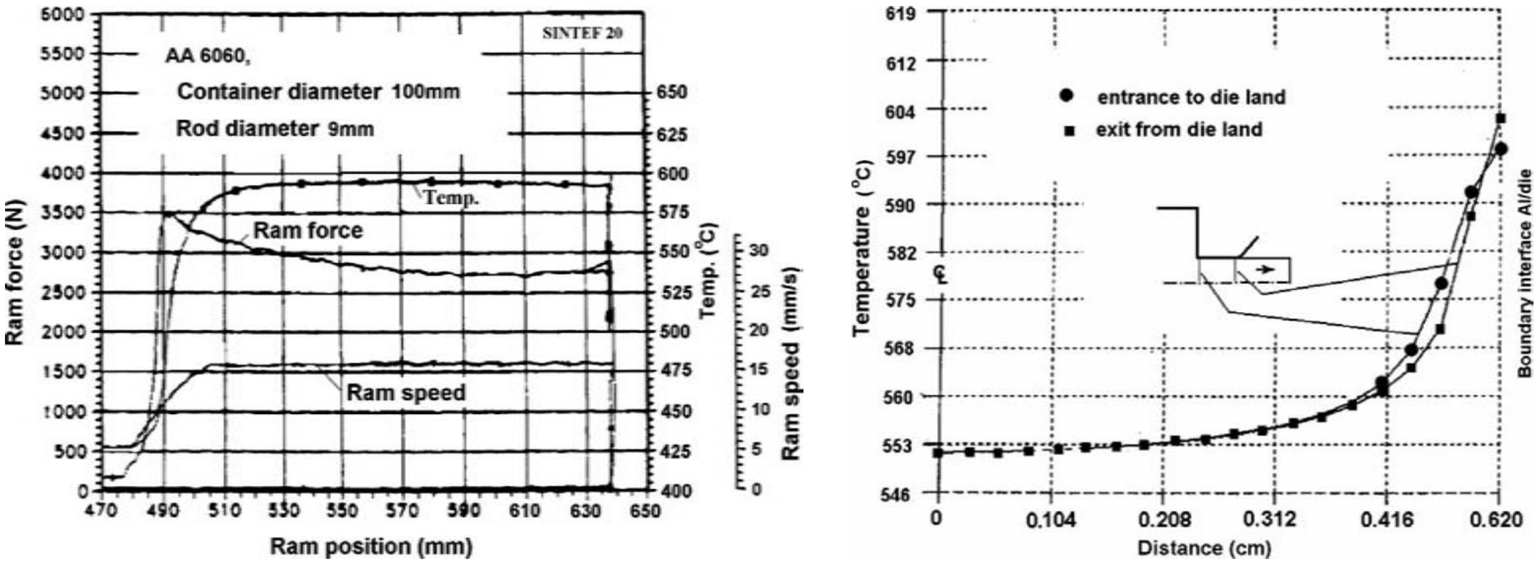

(a)

(b)

Figure 11.14. (a) Common data recording in laboratory extrusion experiment. (b) FEM-simulated temperature gradient across metal stream in the bearing channel in Al extrusion. (Courtesy of M. Lefstad, SINTEF.)

the die edge or through the bearing channel; see Fig. 11.13. By preparation of different holes, various measurement locations were reached along the die–workpiece boundary. The thermocouple was inserted into the bore from the side of the die so that it appeared with the weld point flush with the die surface or extending slightly above it; see Fig. 11.16. After the thermocouple had been inserted this way, it was fastened by a setscrew from the side. A thermocouple that extends above the surface of the die will plow a shallow groove into the extrusion as it flows past the bearing, and this groove will appear on the surface of the final extrusion.

With many thermocouples in different locations over the workpiece–tooling interface, temperature data for a number of points can be obtained concurrently over the deforming body. In addition to temperature, a number of other parameters preferably should be measured and recorded continuously vs. ram displacement, during the extrusion cycle. The required force and the ram displacement are such parameters. When the ram displacement is recorded vs. time, the time derivative of this parameter, i.e., the extrusion speed in terms of the ram speed, is also known. With one thermocouple positioned at the hottest spot of the die exit, the typical data set, as shown in Fig. 11.14(a), was obtained in a particular extrusion experiment.

In industrial extrusion it is quite common to keep the extrusion speed constant throughout the press cycle. This speed is usually low, so that it typically takes a minute to extrude one billet. When extruding in a small laboratory press, the duration of the extrusion stroke can be one-half or one-third of that in industrial extrusion, where large billet sizes are usual. Because extrusion is approximately a stationary process, there is a temperature increase in the beginning of the process, but after a while, the temperature becomes stable, and it remains nearly constant throughout most of the press cycle; see Fig. 11.14(a). Note that the process data shown in Fig. 11.14(a) were recorded in laboratory extrusion using a billet without taper. (For an explanation of taper, see Sec. 18.6). The thermal response of a thermocouple with a mantle is therefore rapid enough for the purpose of recording the main thermal effects in extrusion, if one does not need to record the steep temperature rise in the beginning of the cycle with great accuracy. In that case, it is required to use thermocouples with shorter response time.

The rapid temperature increase in the beginning of an extrusion experiment is due to the flow of hot extrusion metal into the die and due to deformation and frictional heating effects in the extrusion process when the metal starts to flow through the die, as already explained in the previous sections. When steady-state conditions are reached after a while, the temperature curve flattens out. The measured temperature in a particular location on the die then will depend on the positioning of the weld bead of the thermocouple, i.e., whether it *plows* into the metal stream or *appears flush* with the surface of the metal stream. Measurement of the true surface temperature of an extrusion is difficult because of the steep thermal gradient extending from the surface down into the stream.

The temperature gradient through a cross section of the extrusion metal flowing through a bearing channel is easily determined in FEM simulation. Such data are shown in Fig. 11.14(b). As depicted here, the temperature drop through the

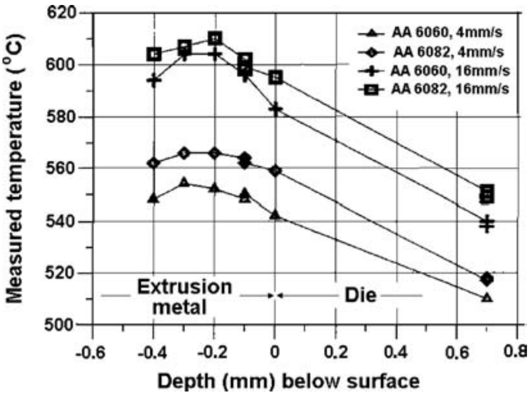

Figure 11.15. Temperature at and below surface of extrusion, obtained by thermocouple measurements. (Reprinted with permission of M. Lefstad, SINTEF.)

outer surface layer was predicted to be as high as 50°C, and varied slightly from the entrance to the exit of the bearing channel. In this case, the thickness of the hot layer was approximately 2 mm. In the steel die, there was of course a corresponding temperature gradient, determined by the heat generated in the extrusion process, as well as the initial temperature difference between extrusion metal and the die. The thermal properties of the boundary interface between the workpiece and the die, and of the die material, will also influence this temperature gradient.

11.5.1 Surface Temperature of the Metal in an Extrusion Die

The measured temperature at and slightly below the profile surface[10] inside an extrusion die is shown in Fig. 11.15. The measurement was performed with a thermocouple covered with a mantle, placed in a bore of the die, in accordance with the principles just outlined. Results for one alloy and extrusion speed were obtained by running many identical extrusion experiments, in which only the thermocouple location was changed from one to the next experiment, by displacement of the thermocouple in the radial direction inside the bore. As the figure depicts, the *highest temperature* was measured when the thermocouple tip extended 0.2 mm out from the bore, so it plowed a 0.2 mm deep groove into the surface of the resulting profile.

Measured temperatures in Fig. 11.15 are presented for two different alloys extruded at two different velocities. The figure demonstrates the temperature measurements that can be made this way. However, it is uncertain to what extent they reveal the real surface temperature of the extrusion at the bearing. This is because the measurement is done at a spot where there is a steep temperature gradient from the core into the surface of the extrusion, and because there may be local thermal effects, for instance due to friction, when the metal stream flows past the thermocouple tip.

To determine the real surface temperature of the metal stream inside the die in this case, a special *indirect measurement method* was developed.[10] The principle of the method is sketched in Fig. 11.16. It is based on the observation that the alloy Al–1.2%Si contains particles of Si that will melt when the temperature rises above their melting point, 577°C. Concurrently with melting, the *particle morphology*

Figure 11.16. Thermocouple tip plowing into the metal stream inside a die bearing[14]. (Reprinted with permission of M. Lefstad, SINTEF.)

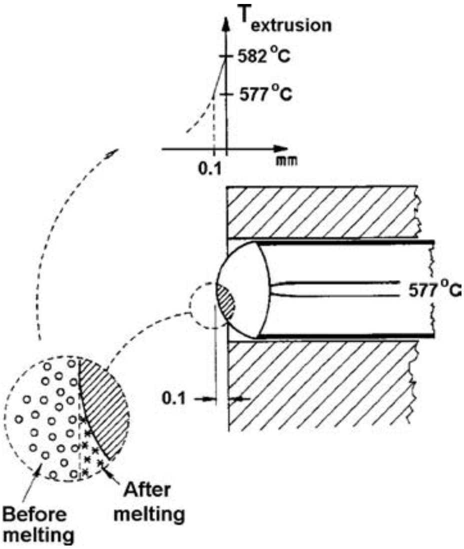

also changes, as shown in Fig. 11.17. Before melting, the particle has an *massive angular appearance*, as shown in Fig. 11.17(a), whereas after melting and resolidification, it has been modified to a *branched eutectic aggregate* of small particles; see Fig. 11.17(b). It is therefore easy, by this technique, after the end of extrusion, to determine with good accuracy the thickness of the surface layer of the extrusion that has exceeded the temperature 577°C. This is done simply by measuring the thickness of the layer of the extrusion in which the particle morphology has been modified.

In the sketch in Fig. 11.16, a situation is shown in which the thermocouple plows a groove of a certain depth into the extrusion, and where the surface layer containing

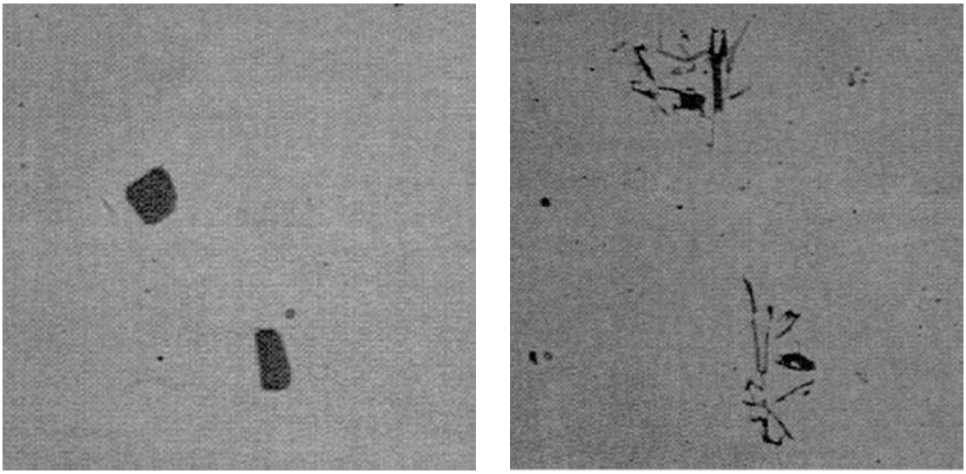
(a) (b)

Figure 11.17. Morphology of Si particles in Al–1.2%Si alloy (a) before and (b) after exceeding 577°C. (Reprinted with permission of M. Lefstad, SINTEF.)

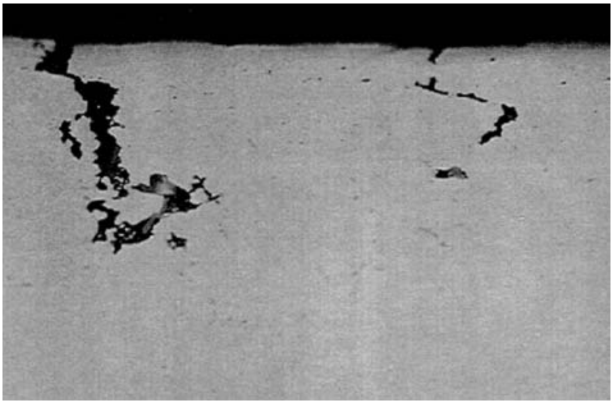

Figure 11.18. Surface cracks formed at extrudate surface in extrusion[14] (~500×). (Reprinted with permission of M. Lefstad, SINTEF.)

modified particles is of the same thickness as the depth of the groove. In this case, one knows that the temperature at the tip of the thermocouple is indeed 577°C, and hence the thermocouple should have measured this temperature if the measurement was correct.

This Al–Si alloy[10] was extruded while increasing the extrusion speed stepwise to increase the surface temperature of the extrusion metal inside the bearing of the die. In the experimental series, the depth of the surface layer that had exceeded the melting temperature of the Si particles, 577°C, was also measured. The results are shown in terms of the graph in Fig. 11.16. As this figure reveals, when the thermocouple used extended 0.1 mm out of the thermocouple bore and scratched a 0.1 mm deep groove into the surface of the extrusion, the thermocouple measured a temperature approximately equal to the real temperature at the same depth.

11.5.2 Surface Cracking in Aluminium Extrusions

In addition to accurate temperature measurements for the Al–Si alloy, work was conducted to study thermal conditions on the surface of the extrusion,[9] at *the hottest spot in the die*, at the instant when surface cracks start to form on the surface of the extrusion; see Fig. 11.18. The investigation showed, as depicted in Fig. 11.19, that surface cracking began to appear when the first Si particles at the surface of the extrusion started changing their morphology due to melting, i.e., at a real surface temperature of the extrusion equal to 577°C. However, at this instant the temperature measured by the thermocouple was only 572°C. Hence, the thermocouple positioned with its tip at a depth of 0.1 mm below the surface of the extrusion will measure a temperature approximately 5°C below the real surface temperature of the extrusion.

Hence the investigation confirms that the mechanism that causes surface cracking in the Al–1.2%Si alloy is one of *melting of Si particles* in the alloy. Hence, the occurrence of this phenomenon must be connected with the very outer surface layer of the extrusion reaching the critical temperature 577°C. The melting of the particles obviously must result in pronounced loss of ductility in the very outer surface

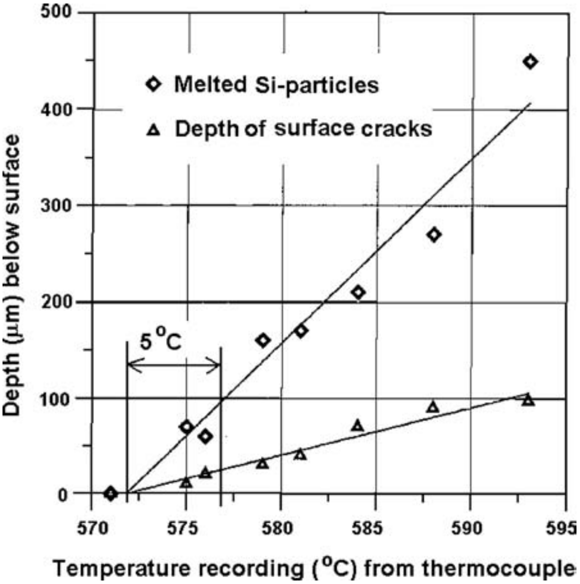

Figure 11.19. Depth of cracks and melted Si particles below extrudate surface vs. measured surface temperature of hottest spot of metal. (Reprinted with permission of M. Lefstad, SINTEF.)

layer of the profile. Because it is concurrently subjected to tensile stresses, it will start to develop cracks.

Similar investigations[9] were conducted for the commercial extrusion alloys AlMgSi1 (AA 6082) and AlMgSi0.5 (AA 6060). Onset of cracking at the surface of the extrusion, for both these alloys, was also shown to appear when the highest surface temperature increased above the critical temperature at which eutectic particles in the alloys start to melt.

Problems

11.1 Compare the temperature rise when cylindrical specimens of Al and Ti are compressed down to an average deformation corresponding to the strain $\bar{\varepsilon} = 1$. Assume frictionless conditions and short contact time against compression dies, so that cooling effects from the dies can be neglected. Required data for the two metals are specified in the accompanying table.

Metal	$\bar{\sigma}$ (MPa)	$\bar{\varepsilon}$	ρ (Mg m^{-3})	c (J kg^{-1} K^{-1})
Al	200	1	2.69	900
Ti	400	1	4.5	512.6

NOTES

1. Altan, T., and Gerds, A. F.: "Temperature effects in closed-die forging," Technical Report No. C70–30.1, ASM Int., 1970.
2. Altan, T., Oh, S.-I., and Gegel, H. L.: "Metal Forming, Fundamentals and Applications," ASM Int., 1983, pp. 89–99.

3. Farren, W. S., and Taylor, G. I.: “The heat developed during plastic extrusion of metals,” Proc. R. Soc. Ser. A, Vol. 107, 1925, pp. 422–451.
4. Småbrekke, A.: “Verification of simulation results from FORGE2,” Master thesis, NTNU, 1992 (in Norwegian).
5. Vigor, C. W., and Hornaday, J. R.: “A thermocouple for measurements of temperature transients in forging dies,” in “Temperature, Its Measurement and Control,” Vol. 3, Part 2, Reinhold, New York, 1961, p. 625.
6. Valberg, H., Svinning, T., and Welo, T.: “Material Flow during Forging of a Piston,” Memo 200760.20, SINTEF (1992).
7. Welo, T.: “Simulation of Full-Scale Piston Forging using FORGE2,” Memo 200760.30, SINTEF (1992).
8. Altan, T.: “Heat generation and temperatures in wire and rod drawing,” Wire J., March 1970, p. 54.
9. Ranger, A. E.: “An electrical analogue for estimating die temperature during metal forming,” J. Iron and Steel Inst., Vol. 185, 1957, pp. 383–388.
10. Lefstad, M.: “Metallurgical speed limitations during the extrusion of AlMgSi-alloys,” Dr. Sci. thesis, Department of Physics, UNIT/AVH (1993).
11. T. Altan, Lee, C. H., and Akgerman. N.: “Approximately calculation of velocity and temperature distributions in axisymmetric extrusion and drawing,” in Proc. first North American metalworking research conference, Mc. Master University, Hamilton, Ontario, Canada, 1973, pp. 107–127.
12. Lefstad, M.: “Simulation of Some of the Experiments Utilising ALMA,” Memo 200677, SINTEF (1993).
13. Lefstad, M.: “Experiments Performed in Dec. 1992,” Memo 200677, SINTEF (1993).
14. Lefstad, M., and Reiso, O.: “Temperature measurements in extrusion dies,” Materials Science Forum, Vols. 217–222. 1996, pp. 409–414.

REFERENCES

Altan, T., Oh, S.-I., and Gegel, H. L.: “Metal Forming, Fundamentals and Applications,” ASM Int. (1983).

Lefstad, M.: “Metallurgical Speed Limitations during the Extrusion of AlMgSi-alloys,” Dr. Sci. thesis, Department of Physics, UNIT/AVH (1993).

12 Experimental Metal Flow Analysis

In this chapter, the principles of metal flow analysis will be discussed, with particular emphasis on use of stripe or line patterns, made of contrast material, to map metal flow in hot aluminum extrusion. Emphasis will also be on use of ring patterns on the surface of workpieces to trace friction-dependent metal flow against die surfaces.

12.1 Grid Pattern Techniques Used to Trace Metal Flow

Grid pattern analysis was developed as a tool for understanding different metal flow phenomena encountered in metal forming processes. In the beginning, it was common to use *model materials*,[1] such as Plasticine or clays, to imitate metal flow. These model materials have deformation characteristics similar to metals, and thus can be used to reproduce the real metal flow conditions with good similarity, when chosen appropriately. Such materials require only low loads in forming, and therefore their flow could be studied visually through glass plates in order to determine the main factors affecting metal flow. Grid patterns were also added on the surface of the model materials, or to their interior, to study material flow, as for metals.

Typical flow-related defects were observed to occur on various occasions; for instance, *pipe formation* can appear in the rear end of an extrusion. That some of these defects are related to the nature of the metal flow in the process was discovered through the use of grid pattern techniques. To prevent the formation of such defects, the engineer needs to thoroughly understand the nature of metal flow and, in addition, know how metal flow is influenced by the material and the processing conditions.

12.1.1 The Scratched Grid Pattern Technique

A common technique for experimental investigation of metal flow is use of the *scratched*, or inscribed, *grid pattern*.[2] When this technique is applied, the initial workpiece to be investigated is split in two halves along an axial symmetry plane.

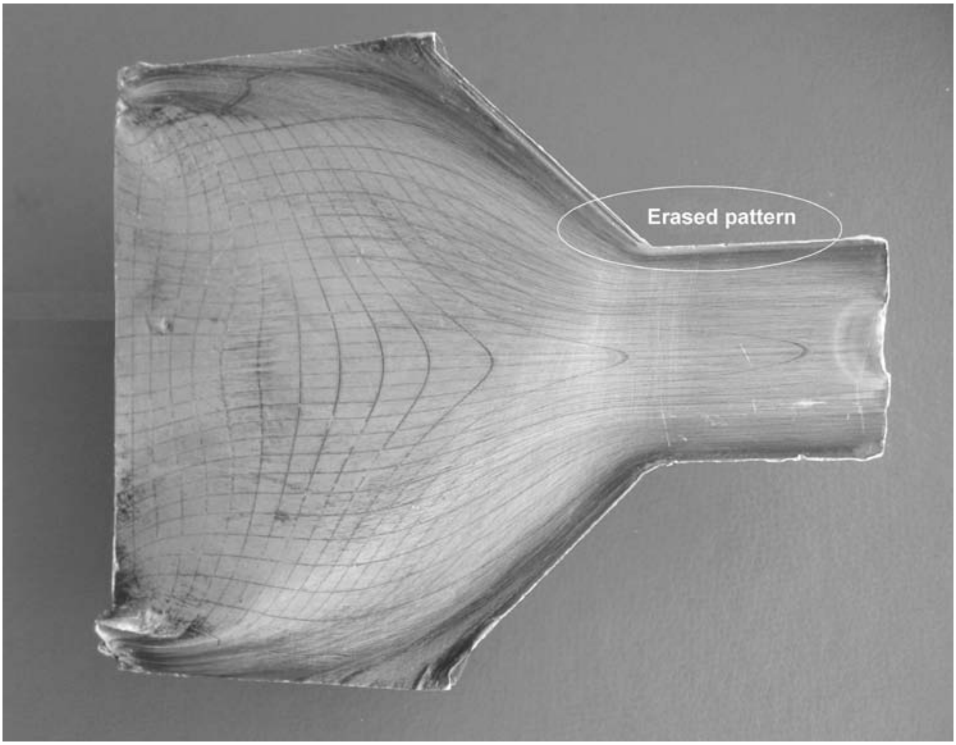

Figure 12.1. Conventional grid pattern technique applied in forward extrusion[3] through conical die. Photo of the grid pattern after partial extrusion of the billet. (Courtesy of J. O. Løland, jol@fac.no.)

One of the halves of the workpiece is fitted with a grid pattern, made by scratching lines or shallow grooves onto the plane cut surface. The grooves extend as straight lines over the sectioned surface. Usually two sets of lines with constant spacing are made, one set extending in one direction, and another identical set orthogonal to the first. In this way, a *grid pattern* made up of *square area elements* is obtained.

The halves of the workpiece are then put together. To avoid welding across the sectioned plane during forming, it is common to add a *parting agent* in between the two halves. After partial or complete forming of the reassembled workpiece, the halves are split apart again. The gridded half reveals a visual picture of the deformation of the specimen during the partial forming step until forming was interrupted. By comparing initial and final patterns, information regarding the nature of the metal flow and deformations is deduced. Deformations are visually estimated from the distorted shape of the area elements, both type and size of deformation: whether elements have been compressed or stretched with or without shear deformation.

Figure 12.1 shows a deformed grid pattern obtained this way by means of the scratched grid pattern technique in forward aluminum extrusion[3] conducted through a conical die.

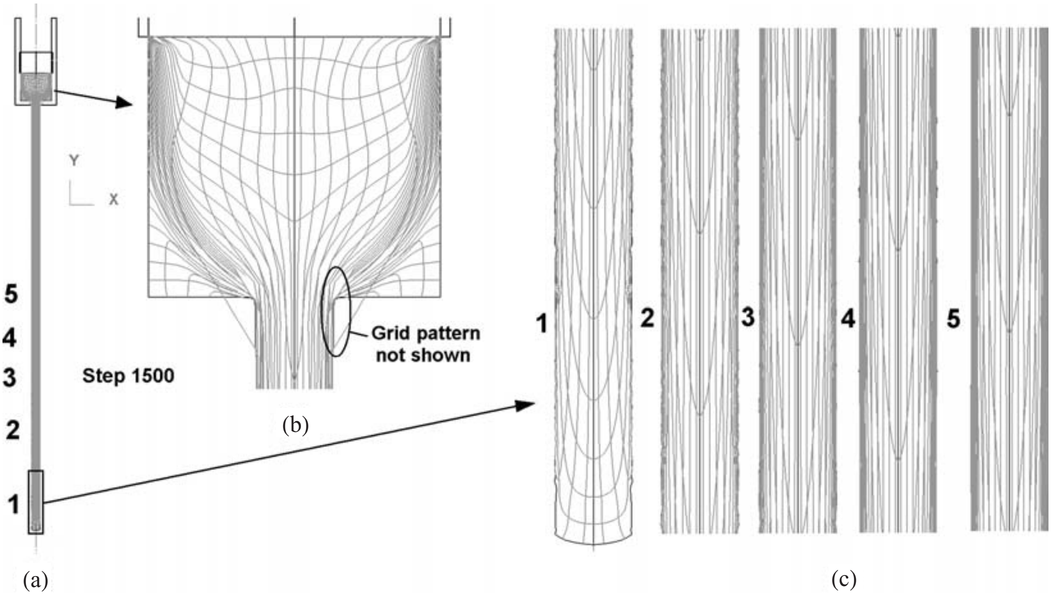

Figure 12.2. Grid pattern analysis in FEM–simulation of forward extrusion; (a) the whole grid pattern and the grid pattern inside; (b) the deformed billet; and (c) the extruded rod.

Another corresponding deformed grid pattern made by FEA is shown in Fig. 12.2. Fig. 12.2(a) shows both the remaining billet after partial extrusion and the extruded rod with the deformed grid pattern. In addition is shown a magnified picture of the deformed billet (Fig. 12.2b) and a number of magnified sections of the extruded rod (Fig. 12.2c).

As Fig. 12.2(b) clearly depicts, a *dead zone* is present in the billet, in the corner between the die and the container. In this zone, the metal is not subjected to significant plastic deformation upon extrusion, i.e., there is no significant distortion in the area elements located there. However, the metal in the middle of the billet has started to flow through the die orifice and has been subjected to large deformation.

One can also see that, during extrusion, there is plastic deformation in the grid pattern at the rear end of the billet, which is adjacent to the ram head. Deformations here, however, are not large and the grid lines are easily identified. But in the shear zone between the dead zone and the inner parts of the billet, deformations are large. In this region, especially near to the die aperture, the simulation program is therefore not fully able to show the presence of the grid lines. When scratched grid patterns are used one will observe the same behavior in heavily deformed regions inside the split billet and close to the surface of the rod, namely, that the grid lines have disappeared; see Fig. 12.1. Then they are missing because they have become erased by the large plastic deformation.

The deformed grid pattern in the rod in an extrusion simulation is shown in Fig. 12.2(c). It appears in a similar manner as when the experimental scratched pattern technique is used. The grid pattern in the front end of the rod is clearly visible, but farther away from the end, the grid pattern becomes very dense so each individual grid line is not readily visible.

Conclusion is that when the scratched pattern technique is applied the technique starts to fail because the grid pattern becomes erased in regions where there are heavy deformations, as in the shear zones in the billet and in the subsurface layers of the extruded rod.

Another drawback of scratched grid patterns that should be mentioned is that they are not well suited for analysis of sliding along the die–workpiece interfaces, because they cannot be detected precisely when they extend into an interface. Because of this, such patterns do not reveal the nature of metal flow along die–workpiece interfaces with sufficient accuracy.

12.1.2 Grid Patterns Made from Contrast Pins

A modified grid pattern technique, based on introduction of a *stripe pattern* of contrast material pins into the initial billet,[4,5] is often a better option than use of scratched grid patterns. After partial extrusion such stripe pattens can be revealed and depicts the nature of metal flow, at each stage of forming, better than scratched patterns do. The advantage of such patterns over scratched ones is that they do not get erased – not even in heavily deformed regions as the *shear zones* – and hence deformations can be investigated even there. A disadvantage is that workpieces with internal stripe patterns are expensive to produce and to apply. But they can be tailor-made even inside industrial-sized workpieces, and very accurate experiments can therefore be performed to study metal flow, on the industrial and the laboratory scale.

Internal stripe patterns, which also can be termed *intrinsic grid patterns*, have been used with great success in deformation analysis of extrusion of aluminum.[5] The pins are inserted into holes drilled into a longitudinal symmetry plane of the initial workpiece. Inserts of contrast alloys have been applied for a long time for studies of metal flow, though not in the same systematic manner as in this new variant of the technique, to create a complete grid pattern inside the workpiece.

When an intrinsic pattern like this is made for an AlMgSi1-alloy (AA 6082) to be hot-formed, the alloy AlCu1.8 is an appropriate contrast alloy to be used as pin material. Not only will this alloy have approximately the same flow stress as the matrix alloy, so that both will flow the same way, but, because of the Cu content of the contrast alloy, it will turn black when etched in caustic soda or in Tucker's etchant, while the base alloy retains its bright Al color after treatment. This aggregate of contrast pins, after partial or complete forming, appears as a clear pattern in the plane inside the workpiece where they are present. The workpiece is a massive body during forming, and afterwards it must be sectioned along the plane containing the pattern. The cut section is then carefully ground until it coincides with the midplane of all the pins, whereupon the pattern is "exposed" to make it visible by the etching treatment. For the alloy AlMgSi0.5, the contrast alloy AlCu1.2 is used as marker material. Similar patterns can also be made for other metals than aluminum, though here the focus is on applications in aluminum forming.

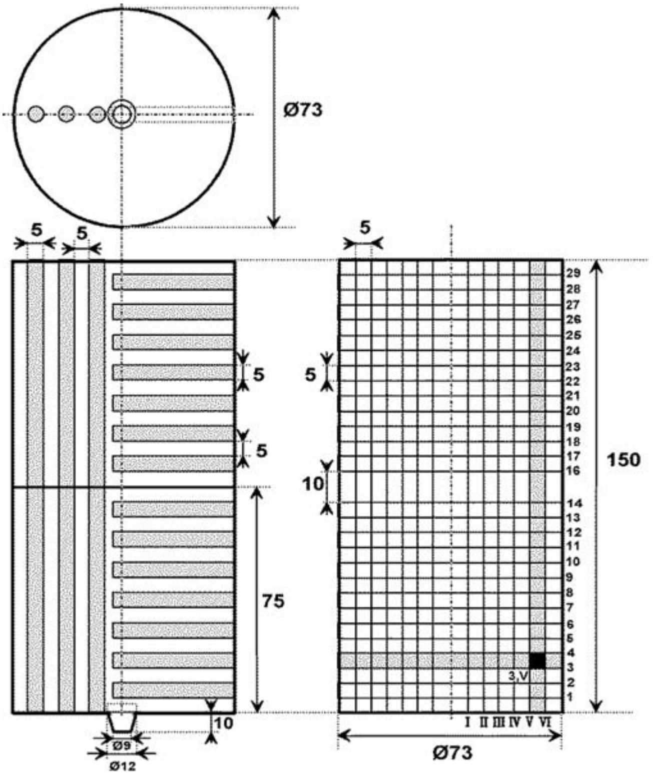

(a) (b)

Figure 12.3. Extrusion billet with (a) internal contrast pins and (b) resulting internal stripe pattern.

Figure 12.3(a) depicts how an extrusion billet is provided with internal contrast pins. Axially oriented pins are placed in one-half of the billet and radial pins in the other half. The pattern is made by drilling out holes in appropriate planes; then pins consisting of the indicator alloy are put into the holes. Each pin is upset inside its hole by a light hammer blow at the end, until it expands and fills the hole. In this way one prevents the pin from falling out during later handling of the billet.

Figure 12.3(b) shows that a complete grid pattern can be made this way, inside a longitudinal section of an extrusion billet. Each pin defines, by means of its boundaries with the surrounding matrix material, two parallel grid lines with spacing equal to the diameter of the pin. If 3 axial pins and 14 radial pins of 5 mm diameter are used, a pattern with 5 mm spacing, as that shown in Fig. 12.3(b), is obtained inside the billet. An exception is the two lines in the midle of the billet that are spaced 10 mm apart.

To get the axial pins accurately placed, it is required to split the billet at its midlength, so it consists of two halves. This is because it is very difficult to drill holes with good accuracy through the whole length of a long billet, because a long drill will tend to bend out sideways due to its elasticity.

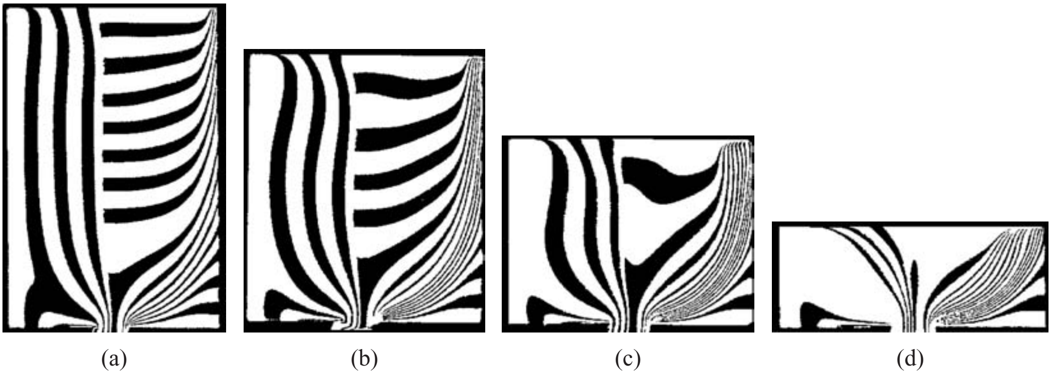

Figure 12.4. Stripe patterns of contrast pins in partially extruded billets: (a) stage 1 – 113.7 mm billet length; (b) stage 2 – 85.3 mm length; (c) stage 3 – 56.8 mm length; (d) stage 4 – 28.4 mm length.

The pattern inside the billet is a pattern with stripes extending in the radial and the axial direction of the billet, on each side of the axis. Placing the axial and radial pins on each side of the axis of the billet is advantageous because it eases identification of the stripes when there are large deformations (as in the extruded rod). But in cases of axial symmetry, the metal flow on each side of the midline is almost identical, so a grid pattern can be made from the stripe pattern by rotating the radial stripes 180° around the axis, and then superposing them on top of the axial ones; see Fig. 12.3(b). In this way, radial and axial stripes can be coupled together after the stripe pattern has been revealed. This procedure was used on the stripe pattern shown in Fig. 12.4(b) to create Fig. 12.5(a).

A notation is defined so that different lines of the pattern can be identified uniquely. The individual axially oriented lines are numbered I, II, etc., up to line VI, which is the line closest to the billet periphery, 5 mm away from the billet surface. Radial lines are numbered 1, 2, etc., up to line 29, which is at a distance $5\,\text{mm} \times 29 = 145\,\text{mm}$ from the front end of the billet and 5 mm from its rear end. Radial line 15 is absent from the pattern.

When this notation is used, each *square element* can also be specified uniquely. The black element in Fig. 12.3(a) is denoted by (3–4, V–VI). The crossing point between a particular radial and an axial line is the corner of an element, and this point identifies a material particle in the workpiece. The point defined, for instance, as the lower left-hand corner of the black element in Fig. 12.3(a) can thus be specified by the notation 3,V.

To reveal the hidden pattern after an experiment, the workpiece is cut close to the gridded midplane, and then one slowly grinds away metal from the cut surface. If grinding is stopped at the right instant, one can exactly expose the midplane and reveal a clear deformed grid pattern. The section billet must be etched properly until all stripes become clearly visible. Figure 12.4 depicts *perfect patterns* obtained this way for a particular aluminum extrusion process, at four stages of the

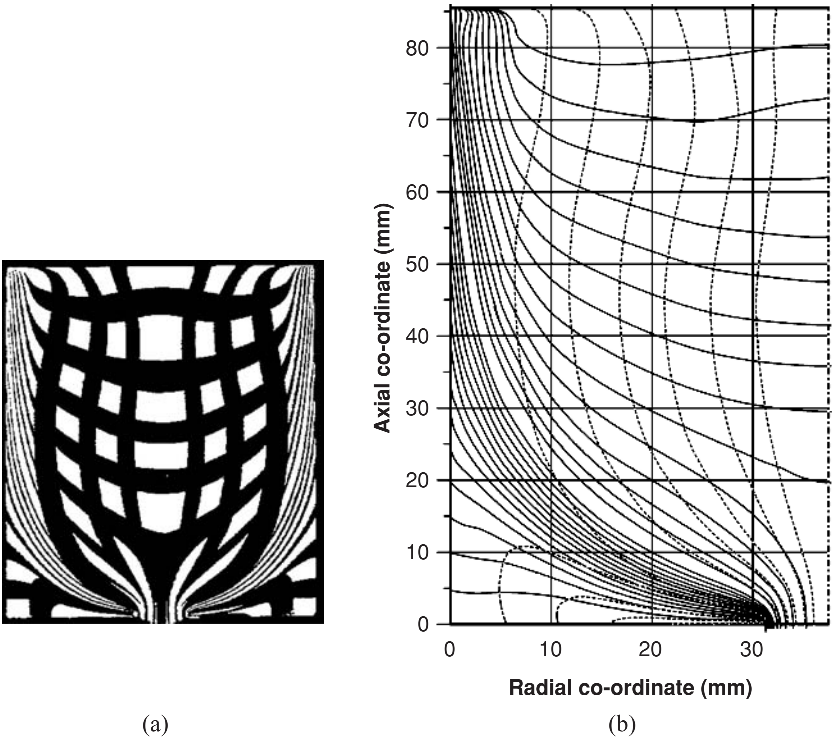

Figure 12.5. Modification of the stripe pattern in Fig. 12.4(b): (a) transverse and longitudinal stripes added together and (b) graphical reproduction of grid pattern.

process. These patterns reveal the conditions of metal flow in this experiment. A rod with 12 mm diameter was extruded in this case, by use of a laboratory extrusion container with 75 mm diameter. This yielded an extrusion ratio as high as $R = 40$.

As Fig. 12.4 shows, the stripe pattern[6] is clearly visible over the whole longitudinal section of the partially extruded billets, except in some regions close to the die opening, where the grinding was too deep, so the pattern was removed. In spite of this, the patterns are among the most perfect deformed grid patterns so far obtained in aluminum extrusion.

Figure 12.5(a) depicts the stripe pattern after combination (described earlier) of the stripes on both sides of the symmetry plane. Figure 12.5(b) shows a more elaborate version of the grid pattern, made by measurement of axial and radial coordinates for various points on each grid line, from which a graphical plot of the pattern was made.

12.2 The Deformed Grid Pattern Inside the Rod

The appearance of the grid pattern inside the extruded rod[4,7] can also be recorded accurately when the new contrast pin technique is used for metal flow analysis.

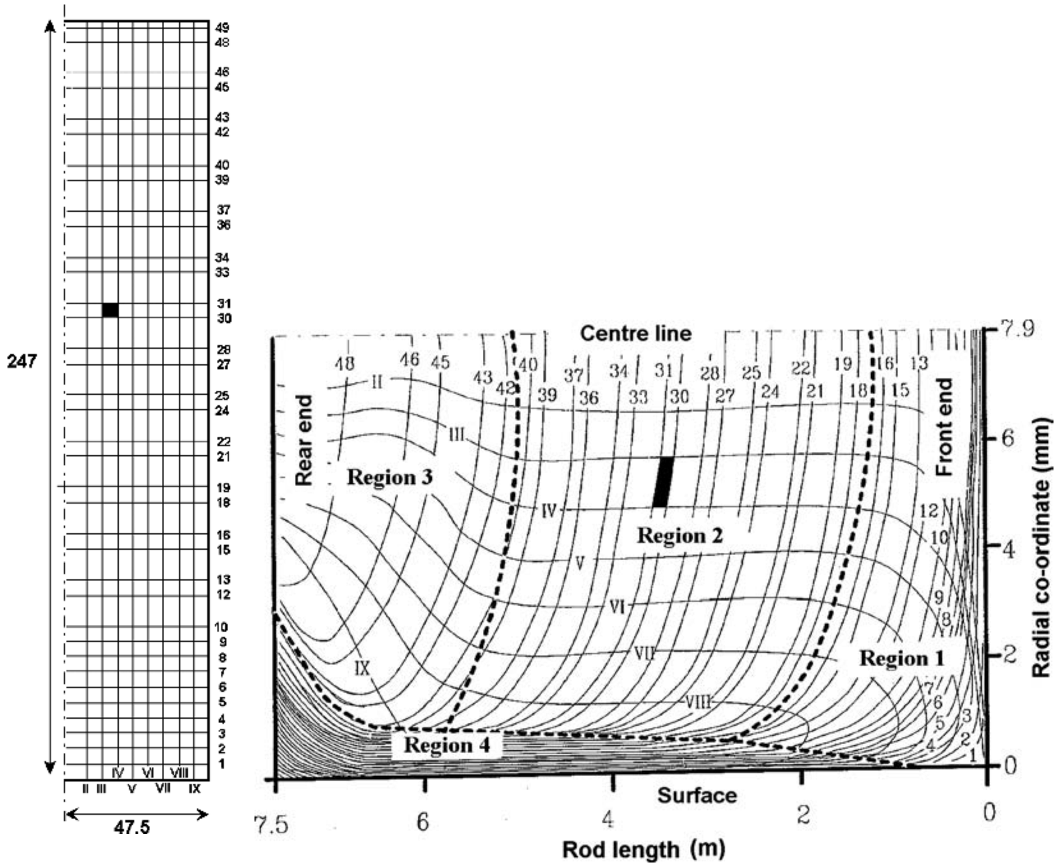

(a) (b)

Figure 12.6. Appearance of grid pattern inside (a) initial billet and (b) extruded rod. Dimensions in millimeters.

To obtain the final deformed grid pattern inside the extrusion requires much work. First, cross sections must be cut at certain distances along the extruded rod. Then,for each section, the grid pattern must be quantified by means of measurement in an optical microscope. To be measured is the distance between the surface of the rod and each pin, i.e., the depth below the surface of the rod of each side of each pin. Resulting measured data for many cross sections cut through the extrusion are then combined into a graphical plot. In the graph, the depth of each grid line below the surface of the extrusion is plotted vs. rod length, as the line extends through the rod. Once measured data have been obtained, the graph is easily made using an appropriate computer program. An example of a deformed grid pattern inside the extruded rod, obtained this way in a particular experiment, is shown in Fig. 12.6(b).

The notation already specified for the initial grid pattern in the billet is useful also for the deformed grid pattern inside the rod. It reveals the final positions of all grid elements, which then can be considered in relation to their initial positions

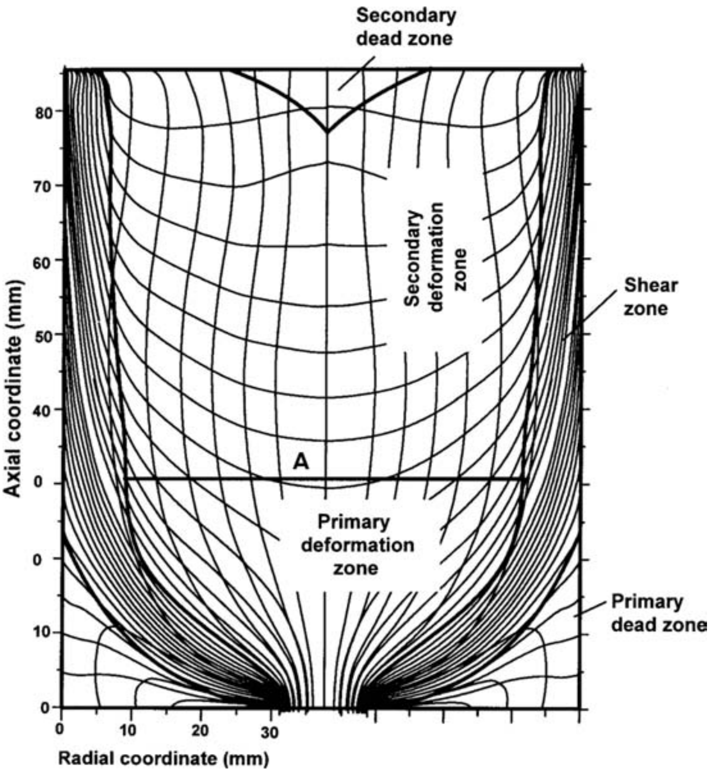

Figure 12.7. Partial extruded billet with deformed internal grid pattern. The deformed volume is partitioned into zones of different deformation characteristics.

in the unextruded billet. Consider for instance the element denoted (30–31, III–IV), which has been painted black in Fig. 12.6. The initial location of this element is easily detected as shown in Fig. 12.6(a), and the final location in the deformed state; see Fig. 12.6(b).

Important information regarding metal flow, useful for understanding the mechanics of the extrusion process, can be deduced from the initial grid pattern as compared with the partially extruded and the final grid pattern. Some important information collected this way is discussed in the following sections.

12.3 Metal Flow Inside the Billet in Unlubricated Al Extrusion

In Fig. 12.4 and Fig. 12.5, it was shown how a stripe pattern inside a partially extruded billet can be transformed into a grid pattern made up of orthogonal crossing lines; see Fig. 12.5(b). In Fig. 12.7, another version of this pattern is presented. Here additional lines have been added on top of the pattern to partition the longitudinal section of the billet into regions, in which the material deforms differently during the course of extrusion. This sketch eases understanding of the nature of metal flow in extrusion processes. Figure 12.7 applies for extrusion of soft aluminum alloys, i.e., alloys that flow in accordance with *flow type* B1; see Fig. 12.8(b). In this case, the interior metal of the billet can be partitioned into three

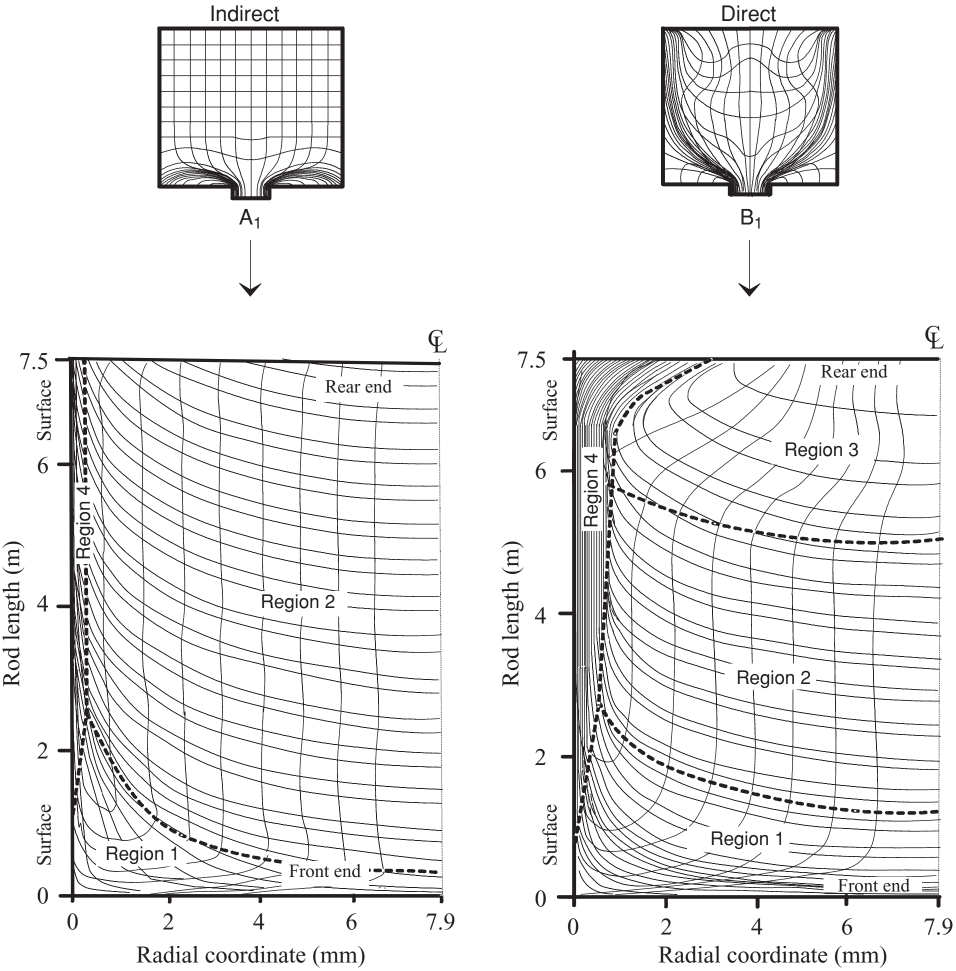

(a) (b)

Figure 12.8. Partially extruded billet with deformed grid pattern (at top). Half longitudinal section of rod (at bottom) depicting regions of different deformations: (a) indirect and (b) direct extrusion.

different regions, or *zones*: the dead zone and the primary and secondary deformation zones.

First, there is the metal in the conical, or funnel-shaped, region located ahead of the die and the die orifice. Metal in this zone is subjected to very large deformation as it is forced toward the die orifice and takes the shape of the die opening. This region is therefore called the *primary deformation zone* in general extrusion terminology; see Fig. 12.7.

In the middle of the billet, behind the primary deformation zone, plastic deformation is much smaller, and this region is therefore often termed the *secondary deformation zone*. The deformed grid pattern here depicts that in this zone there are two different kinds of deformation. Adjacent to the primary deformation zone, a number of adjacent transverse grid lines have the same characteristic convex shape. Behind this region, however, the deformation is somewhat different. Here two or three transverse lines close to the rear end of the billet have a double convex shape. This is because the material here encompasses the *secondary dead zone* on the billet axis, adjacent to the ram head. Depending on the alloy extruded, this dead zone will be more or less well developed. It is termed secondary to distinguish it from the primary dead zone located ahead of the die.

The metal of the secondary deformation zone gradually flows into the primary deformation zone. The deformation imposed on the metal while in the secondary deformation zone can therefore be termed *predeformation*, in that additional larger deformation will occur when this material, later during extrusion, flows through the primary deformation zone.

In the peripheral region of the billet, two other zones can be identified, and they deform differently from those in the interior of the billet. First, there is the *shear zone*. Because of sticking friction between billet and container wall in unlubricated hot extrusion of Al, the surface layers of the billet will be *retained against* the container wall. The core of the billet, however, is pushed forward by the advancing ram, and a shear zone forms between the core material, which flows forward, and the peripheral surface layer of the billet, which sticks to the container wall. In extrusion, this shear zone appears as a heavily deformed layer inside the billet extending down along the container wall. The layer of shear deformed material, due to the presence of this zone, gradually grows in thickness throughout the course of extrusion. Toward the die orifice, this layer bends inwards as a *truncated* conical layer, located in between the primary dead zone and the primary deformation zone.

Finally, ahead of the die, the billet material located in the corner region between the die and the container wall is situated off from the main stream flowing through the die orifice, and is therefore subjected only to minor plastic deformations. This material is therefore commonly termed the *primary dead zone*, but sometimes also the *elastic zone*. The former term is better, because small plastic deformations do occur in this zone.

Figure 12.7 represents the metal flow in an intermediate stage of the extrusion process. The metal, which at this instant resides in the shear zone and in the secondary deformation zone, sooner or later during continued extrusion will be squeezed into the primary deformation zone. It then either flows through the primary deformation zone, out into the rod, or is accumulated in the discard at end of extrusion.

When the ram has reached the horizontal line marked A in Fig. 12.7, the secondary deformation zone no longer is present. With even further advancement of the ram, as in industrial Al extrusion, only a thin slice of metal will be left as a discard inside the container, ahead of the die, at the end of extrusion. When the ram starts to penetrate into the primary deformation zone, the flow pattern completely changes its nature. Material that prior to this instant resided in the primary dead zone will now start to deform plastically, and some of this material will also flow out into the extrudate.

12.4 The Deformation Distribution Inside the Rod

Because the deformation inside the billet is uneven, as described, it is reasonable to suppose that resulting deformation in the extruded rod must also be uneven. The deformed grid pattern as it appears inside the rod [see Fig. 12.6(b)] shows that this is true. Note that the rod in Fig. 12.6 was extruded from a longer billet than that shown earlier in Figs. 12.3 to 12.5. The grid pattern inside the rod, when presented as a graph, is intentionally plotted with different units along the length axis and the radial axis. As Fig. 12.2 depicts, the rod in extrusion is very long compared to its radius, especially in large-reduction extrusion. The grid pattern, if shown to scale for the whole length of the rod, would therefore require many pictures, each showing just (say) 1 m of the rod. If the extruded rod has 7.5 m length altogether, as in the experiment shown in Fig. 12.6, many pages would then be required to visualize the full pattern. When the pattern is reproduced after measurement, it is therefore better to shrink the length axis and expand the radial axis, because the radius of the rod is so small. Then the grid pattern of the whole rod can be shown in one single graph. But, when this is done, the shape of the area elements will become distorted because of the changed scaling, and will no longer represent the true deformations. Nevertheless, the shape of the elements still will reveal where there are homogeneous or inhomogeneous deformations, and where there are large or small deformations. From the appearance of the deformed grid pattern in extrusion [see Fig. 12.6(b)], the section of the rod can be partitioned into five regions subjected to different deformations.[8] This can be done both in direct and in indirect extrusion, and it can be shown that the deformations are very different in direct and in indirect extrusion.

Three of these regions, regions 1 to 3, are in the core of the rod, whereas region 4 makes up the surface layer. Finally, region 5 is material contained in the discard left unextruded at end of extrusion. If forward and backward extrusion are considered, the following conditions apply for the two, on the basis of interpretation of deformed grid patterns in the extruded rod (see Fig. 12.8):

12.4.1 Non-steady-state Start-up Region, Region 1

The front region of the extruded rod consists of material in the primary deformation zone, ahead of the die, at start of extrusion. Because it is initially close to the die hole, it is only subjected to minor plastic deformation upon flow through the die hole, and appears largely undeformed in the final rod.

Material in the primary deformation zone, initially located farther behind, however, will flow a small distance inside the primary deformation zone before it reaches the die exit, and will therefore be subjected to larger deformation. Finally, there is the material initially at the rear end of the primary deformation zone. It flows all the way through the primary deformation zone and will be subjected to larger deformation. Hence, the initial material contained in the primary deformation zone will form a start-up region in the rod, in which deformation increases gradually along the length of the rod. The front end will be subjected to nearly zero deformation, and then there will be increasing deformation, building up to large values at the other end of the start-up region of the rod. Moreover, the size of these deformations will increase if the reduction ratio in the process is increased.

Forward extrusion yields a primary deformation zone of greater thickness than backward extrusion. The non-steady-state start-up region, region 1, as depicted in Fig. 12.8, therefore is present in a larger part of the rod in direct than in indirect extrusion.

12.4.2 Steady-state Region, Region 2

The material in the core of the billet, initially located behind the primary deformation zone, is subjected to small predeformation as it flows toward the primary deformation zone. Later, it is subjected to additional large deformation during flow through the primary deformation zone. The same applies to the rest of the material initially in the secondary deformation zone.

Because of this, there is a region in the rod that experiences almost steady-state deformation. This region is denoted as region 2 in Fig. 12.8, and occurs directly behind region 1. The deformation in this region is approximately constant along the length of the rod, but increases from the center toward the surface, as it also does in regions 1 and 3. In indirect extrusion this steady-state region extends deep into the rod, whereas in direct extrusion a second well-developed non-steady-state region, region 3, appears toward the rear end of the rod.

12.4.3 Non-steady-state Back End Region, Region 3

Both in direct and in indirect extrusion there is a non-steady-state region behind the steady-state region of the rod, in which the deformation increases over that experienced in the steady-state region; see Fig. 12.8.

In direct extrusion, the increased deformation experienced by material in the rear end of the rod is due to two different phenomena. First, there is the *scraping action* of the ram against the container wall during the course of extrusion. The retained peripheral layer of the billet being scraped off by the ram head is forced to flow inward in the radial direction, in the rear end of the billet. Because of this, the rear billet end is strongly *predeformed* prior to its entry into the primary deformation zone. The deformation at the rear end of the billet is therefore the sum of the scraping predeformation and later deformation during flow through the primary deformation zone.

The other phenomenon occurs when the ram approaches the die, for it then starts to push out the dead zone ahead of the die. Prior to this, the dead zone remains largely stationary adjacent to the die. When the ram head approaches the dead zones, they start to deform, and dead zone material flows in the radial direction inward into the billet, causing further radial compression of the core of the billet.

Both flow phenomena occur concurrently in the end phase of extrusion, so the radial compression of the rear billet end is due to their combined effects.

In indirect extrusion, the non-steady-state deformation region does not occur unless the billet is extruded almost completely. The deformed indirect extrusion grid pattern, shown in Fig. 12.8, was obtained in an extrusion experiment that was terminated before the final non-steady-state flow at the rear end of the billet started to appear.

Toward the end of indirect extrusion, the height of the remaining metal in the container becomes less than the corresponding height of the primary plastic zone in the steady-state regime. Hence, also in indirect extrusion, the metal flow changes completely toward the end of the process.

12.4.4 Non-steady-state Outer Surface Layer, Region 4

In both processes, direct and indirect extrusion, the outer surface layer of the rod is formed by outflow of the shear zone developing inside the deforming billet during extrusion. This layer, termed region 4, is quite different in direct and indirect extrusion; see Fig. 12.8. The difference is easy to understand, when one considers the difference of the shear zones in the deforming billet in the two processes.

In direct extrusion, the shear zone extends in a curved shape from the die exit, along the dead zone and the container wall. Even material at the rear end of the billet, scraped off from the container wall by the advancing ram, is included in the shear zone. In indirect extrusion, however, the shear zone only develops adjacent to the die, for there is no relative motion between billet and container wall. The amount of material contained in the shear zone is therefore considerably less in indirect extrusion than in direct extrusion. Because of this, the peripheral layers of the extrusion formed from the shear zone must be much thicker in direct extrusion than in indirect extrusion. Furthermore, in direct extrusion the peripheral shear layer increases in thickness along the length of the extrusion, whereas in indirect extrusion the thickness of this layer remains approximately constant along the length of the extrusion. Finally, in direct extrusion there is a pronounced increase in thickness of this layer at the rear end of the extrusion, where the peripheral billet layer, scraped off by the advancing ram, starts to appear inside the extrusion, but this is not the case in indirect extrusion. This is obvious in that the scraping action does not take place at all in indirect extrusion.

12.4.5 The Discard, Region 5

In industrial extrusion, a small discard is left unextruded in the container when the process is terminated, because it contains material of lesser quality. Both in direct and in indirect extrusion, subsurface material from the billet is accumulated in the billet discard during the course of extrusion. Because this is waste material, it is of less interest to describe its deformations, though this can be done by considering the deformed grid pattern inside the discard after end of extrusion; see, for instance, Fig. 12.4(d).

12.4.6 Concluding Remarks

Because of different metal flow, the deformation distribution inside the extrusion is very different in the direct and the indirect extrusion process. The non-steady-state region occurring in direct extrusion, at the rear end of the rod, does not appear in indirect extrusion, unless the billet is completely extruded. In indirect extrusion, the steady-state region extends far into the rear end of the extrusion. The non-steady-state surface layer of the extrusion, formed from the shear zone, is quite different in direct and indirect extrusion. In direct extrusion, the thickness of this layer increases approximately linearly along the length of the rod. In direct extrusion, toward the tail end of the rod, this layer increases greatly in thickness when the peripheral layers of the billet starts to flow out into the rod, toward the end of the extrusion stroke. In indirect extrusion this non-steady-state surface layer is thin and has nearly constant thickness along the length of the rod.

12.5 The Origin of the Outer Surface Layer of the Rod

In connection with the discussion of Fig. 12.6(a), it was shown how an area element of the grid pattern can be defined by grid lines that bound the element. On this basis, a notation was also defined by which such an element can be identified. The final location in the extruded rod of an area element can also easily be described by this notation; see Fig. 12.6(b). Hence, by means of this methodology,[7] it is straightforward to identify the particular elements located in a 500-μm-thick surface layer of the rod, as shown in Fig. 12.9(a), and to find their initial positions in the billet before the extrusion process; see Fig. 12.9(b).

The initial billet material that flows through the die and forms the outer surface layer of the rod in direct extrusion can be identified this way, as depicted in Fig. 12.9(b). As shown in this figure, it will consist of a curved slice of material, similar to a half-moon, adjacent to the primary dead zone of the billet. Taking into account the full rotational symmetry of the process, this slice appears with shape like a teacup, in the front end of the billet.

12.6 The Emptying Diagram in Extrusion

If a partially extruded billet with internal grid pattern is considered concurrently with the initial pattern, it is easy to identify the part of the billet material that has flown into the rod and distinguish it from the material still remaining inside the container. In Fig. 12.10(a), area elements in the grid pattern that have not yet flowed out of the die orifice have been identified, colored black, and labeled with letters a, b, c, etc. The same grid elements can be identified in the initial longitudinal section of the billet also, as they existed there before extrusion; see Fig. 12.10(b).

Grid elements that are about to flow out of the die orifice can be detected correspondingly; see Fig. 12.10(a). They can also be traced back to their initial location, as shown in Fig. 12.10(b), where they have been marked by hatching. If we now

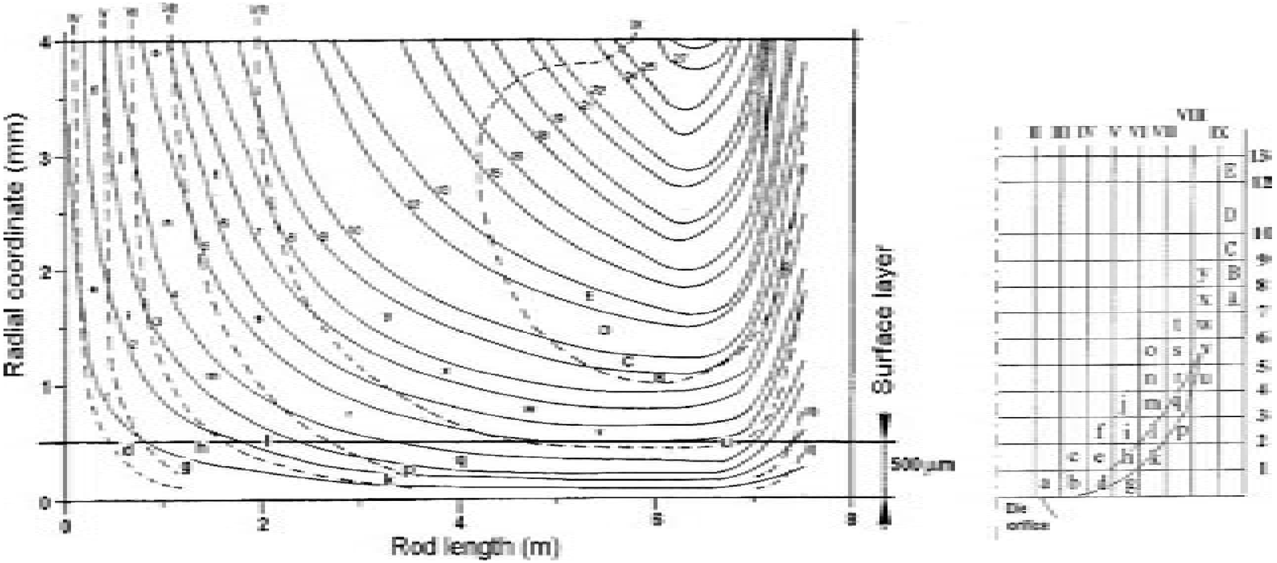

(a)

(b)

Figure 12.9. (a) Deformed grid pattern in surface layer of rod. (b) Surface layer of rod traced back to initial location in billet before extrusion.

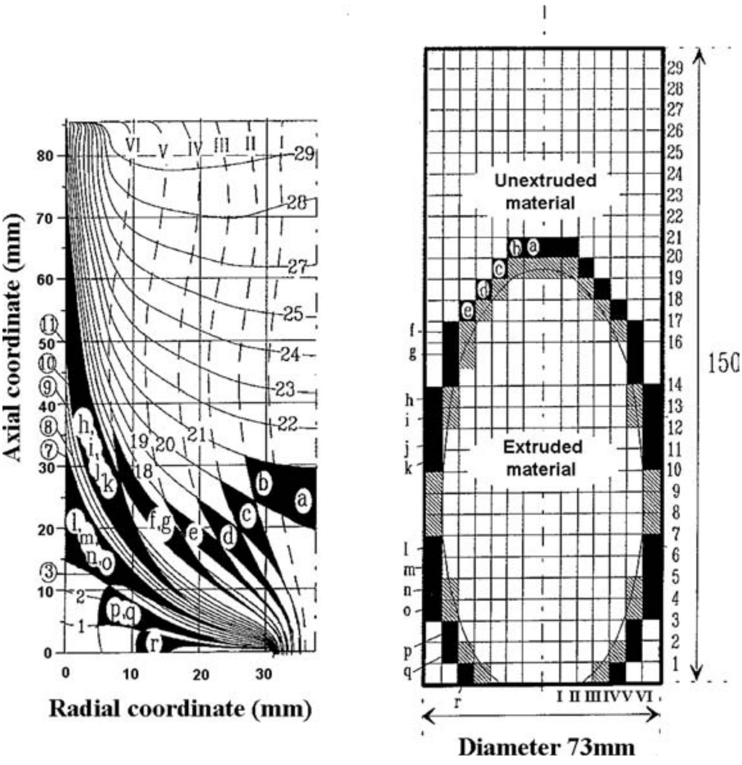

(a) (b)

Figure 12.10. Principle used for identification of transverse emptying line in emptying diagram.

draw a continuous line through the grid elements that appear in the die opening at the moment when extrusion was stopped, we obtain a balloon-shaped ring inside the section of the initial billet. This line can be termed a *transverse emptying line* (T-line). The name refers to the fact that, at one instant, material along this line is flowing out of (is emptied through) the die orifice, to become a straight transverse line in the final rod.

The T-line represents the parting line between billet material that had and that had not flowed out of the die hole when extrusion was stopped. The material inside the balloon has flowed into the rod, while the material outside it is still inside the container.

If transverse grid lines are laid out this way, with constant spacing, on top of the deformed grid pattern in the rod, as, for instance, in the pattern shown in Fig. 12.6(b), these lines can, of course, be traced back correspondingly to their positions in the initial billet. When this is done systematically for all transverse lines, an emptying diagram containing emptying T-lines is obtained for the whole extrusion process; see Fig. 12.11(b).

The emptying diagram with T-lines clearly illustrates the sequence in which the material inside the initial billet flows through the die hole. It also depicts how the peripheral layer of the billet is retained close to the container wall during extrusion,

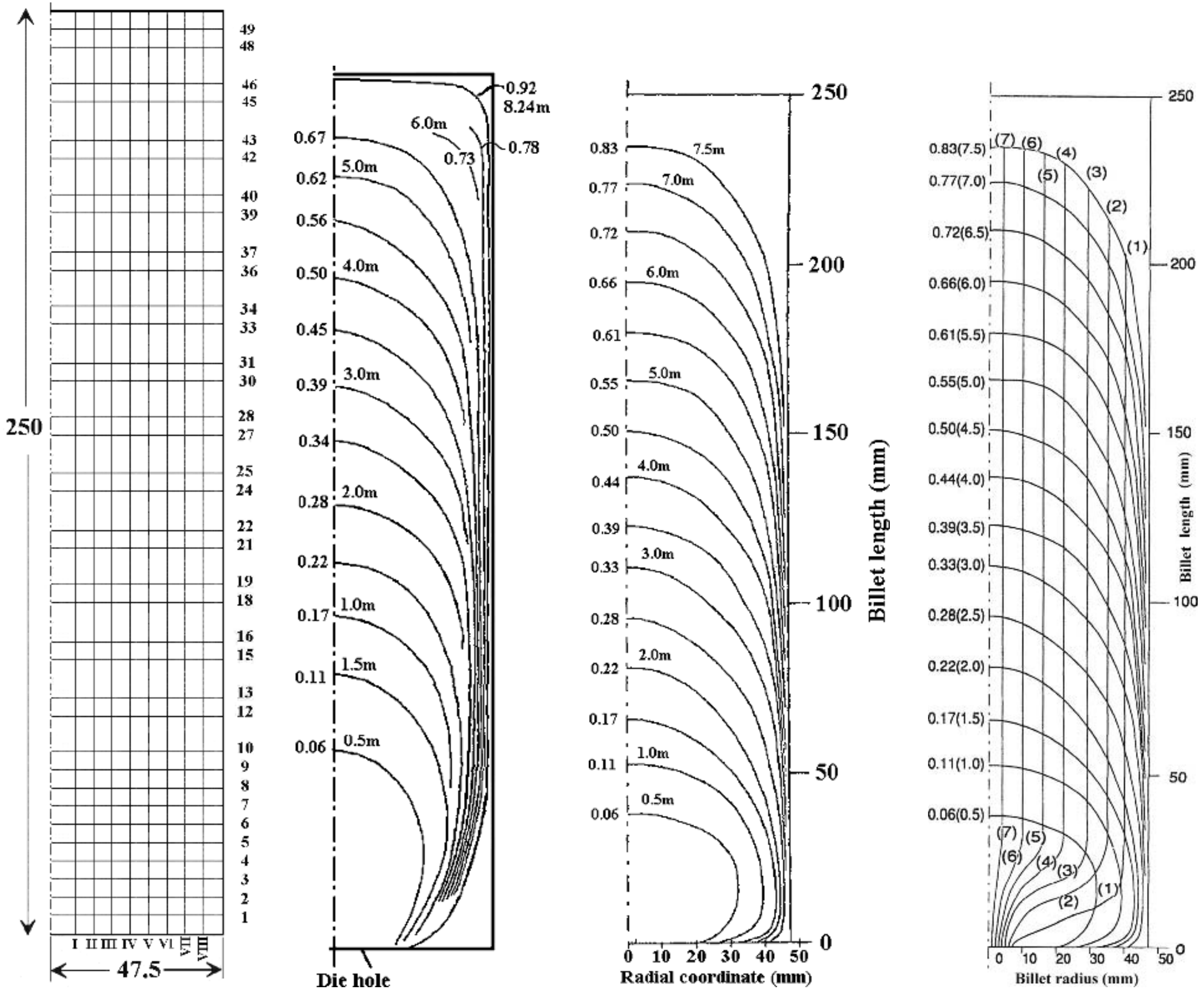

(a) (b) (c) (d)

Figure 12.11. (a) Initial grid pattern. T-line emptying diagram for (b) forward and (c) backward extrusion. (d) Backward extrusion emptying diagram with L-lines also included.

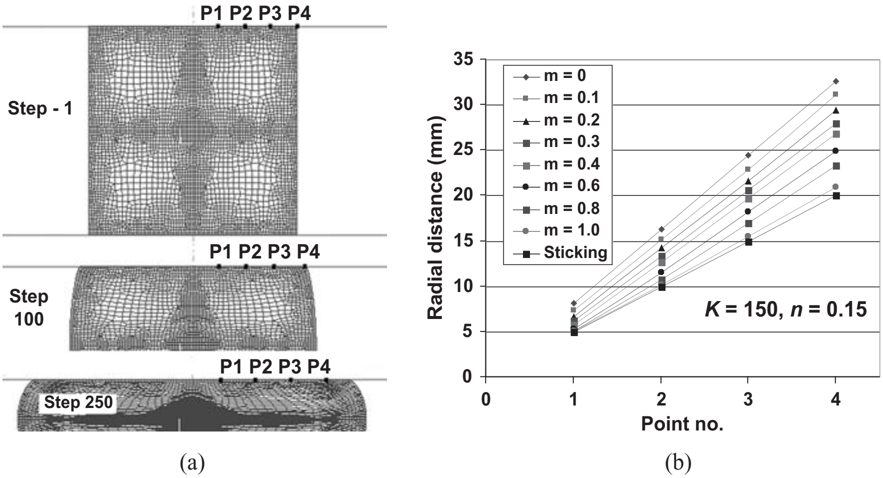

Figure 12.12. (a) Sliding movement of marker points over the end face of a cylinder in compression, $m = 0.65$. (b) Graphical presentation of friction dependence.

due to sticking friction on this wall. Because of this, the outer layer of the billet also accumulates in the billet discard during extrusion.

The T-line emptying diagram obtained in forward extrusion of the gridded billet in 12.11(a) is shown in Fig. 12.11(b). A corresponding diagram for indirect extrusion is shown in Fig. 12.11(c). Comparison of the two diagrams reveals that in backward extrusion, there is a much stronger tendency for the peripheral layer of the billet to flow out into the rod than in forward extrusion.

Using a corresponding principle, *longitudinal* (L) *emptying lines* can also be made. A full *emptying diagram*[7] can finally be obtained by merging of T and L lines. Figure 12.11(d) shows an emptying diagram for indirect extrusion where both T and L emptying lines are shown.

12.7 Surface Ring Patterns to Trace Friction

In connection with Fig. 3.6, it was shown how an experimental surface ring pattern can be used for the purpose of determining friction in a metal forming operation. Friction between die and workpiece was in this connection determined by inverse modeling. The pattern was used to trace the movement and the stretching of the outer surface layer of the workpiece against the die, in order to find the numerical value of the friction factor by means of a FEM model of the actual forming operation.

In addition, such rings can be applied on surfaces that deform plastically to trace large surface deformations. The methodology can be applied in any laboratory, or in industrial metal forming applications, but requires that an accurate FEM model of the forming process be available. In the following paragraphs, the use of this technique for determining friction in cylinder compression will be outlined.

First, let us consider the friction dependence of the flow of the end face of a cylinder compressed between plane-parallel platens. In Fig. 12.12(a), it is shown

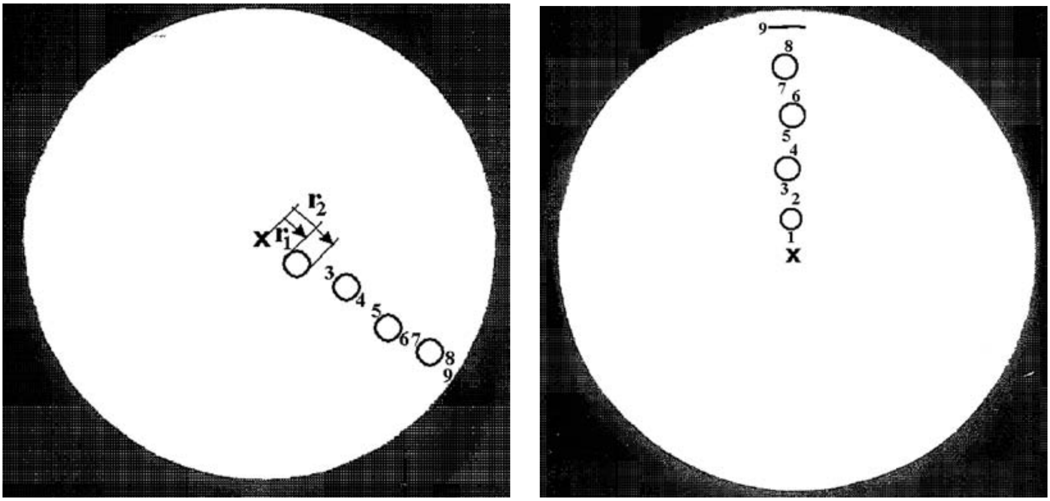

(a) (b)

Figure 12.13. Surface ring pattern in cylinder compression applied to determine friction: (a) initial ring pattern and (b) ring pattern after compression.

how a FEM model of cylinder compression predicts this sliding action and how sliding depends on the value of the friction factor characterizing the conditions of the die–cylinder interface. The sliding motion was determined by using the point tracking option of the software, by considering four points marked on the end face of the initial cylinder. When there is sliding friction, these points will slide radially along the die surface away from their initial location, as compression proceeds. Simulation results in terms of final radial positions of the points, along the die–workpiece interface, for different levels of friction factor, are shown in Fig. 12.12(b). The results were obtained for a particular power-law strain-hardening material, compressed down to a given height, at room temperature.

As the figure demonstrates, there is no sliding when full sticking friction is specified in the simulation model. But for $m = 1$, the FEM model predicts some sliding against the dies. Furthermore, when the friction factor is reduced stepwise from 1 to 0, there is a gradual increase in the sliding lengths. This shows that marker points on the end face of a cylinder can be used for inverse analysis of friction in cylinder compression experiments, if one can determine the location of the same points at the end of compression.

The end face of a real Al-cylinder with such a ring pattern is shown in Fig. 12.13. The cylinder in Fig. 12.13(a) shows the initial ring pattern before compression, and Fig. 12.13(b) shows the corresponding pattern after compression in a particular die set with use of a particular lubricant. On the end face of the cylinder, it is straightforward to measure radial distances, r_1, r_2, etc., for two points on each ring; see Fig. 12.13(a). When the initial and final radial distances have been measured, the sliding behavior of the cylinder is easily quantified from these data. Then to visualize the sliding movement obtained in the experiments, the graph shown in Fig. 12.14 can be made.

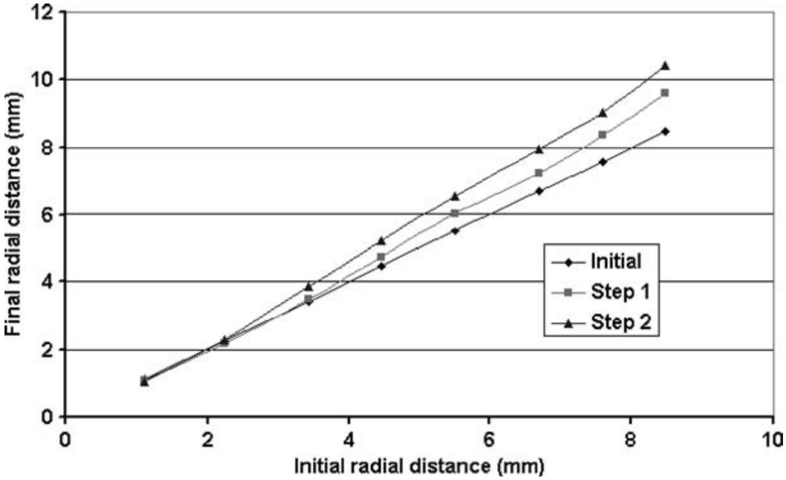

Figure 12.14. Graph of experimental sliding movement of rings over die–workpiece interface.

If the experiment then is reproduced in a simulation model, and corresponding data are recorded in this model for different values of the friction until the same sliding behavior is obtained in simulation and experiment, one can deduce a friction value valid for the experiment from the simulation. Application of this procedure is rather time consuming, but yields a rather accurate friction value if the simulation model is good. Alternatively, as in connection with Fig. 3.6, a direct comparison of the appearance of the surface rings in simulation and experiment can be done more easily, but with less precision.

Problems

12.1 Consider the experimental grid pattern shown in Fig. 12.15. One T-line has been drawn on top of the grid pattern in Fig. 12.15(b) and has been labeled 40″. In Fig. 12.15(a) the deformed grid pattern inside the partially extruded billet is shown. Draw first a sketch of the initial grid pattern near the die in this experiment (to be figured out from Fig. 12.15(a)). Add notation to the grid pattern as defined in Figs. 12.1 and 12.2. Construct the emptying T-line 40″ in the initial grid pattern on the basis of Fig. 12.15(b).

12.2 Consider the initial grid pattern in the billet and the final pattern in the rod shown in Fig. 12.6. Draw a T-line across the pattern inside the rod at distance 4 m from the front end of the rod, and an L-line at distance 6 mm from the surface of the rod. Trace these two lines back into the initial grid pattern of the billet (Fig. 12.6(a)) as they must have appeared before the start of extrusion. Compare the obtained results with the emptying diagram shown in Fig. 12.11(b).

12.3 A surface ring technique was applied on the end face of an initial cylinder with dimensions $D_0 = 20\,\text{mm}$ and $h_0 = 20\,\text{mm}$, for determining friction. Compression

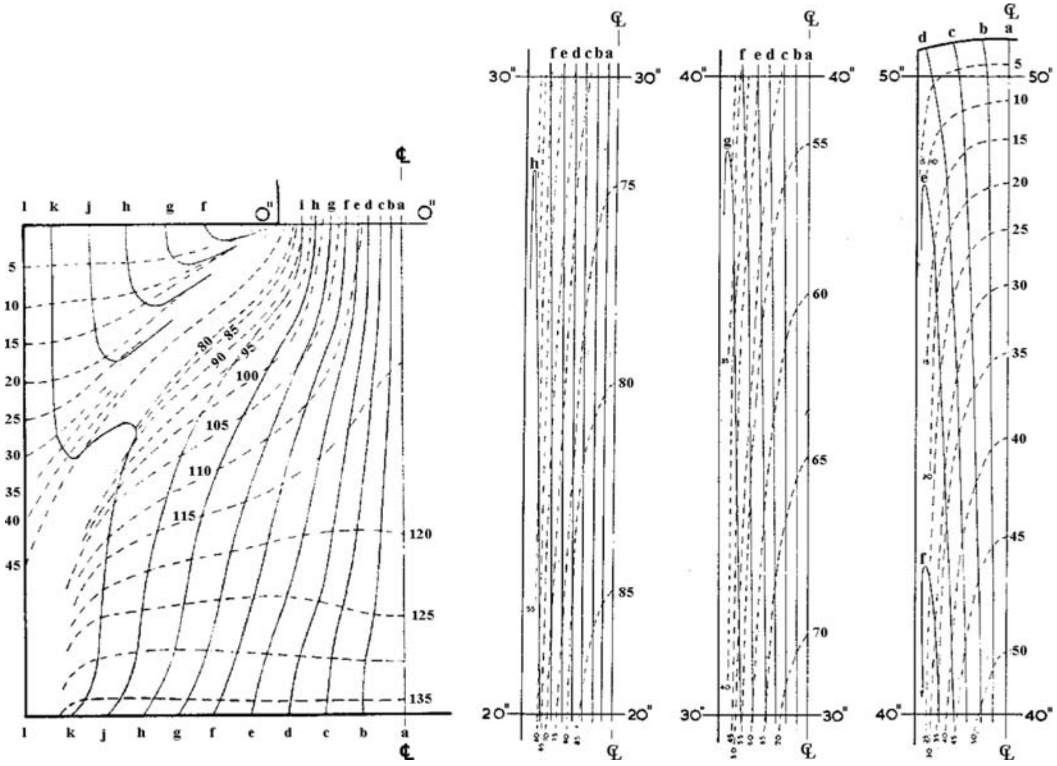

(a) (b)

Figure 12.15. Deformed grid pattern in aluminium extrusion from early literature[2].

was done at room temperature with lubricated parallel die platens. Radial distances to points on the rings in the end face of the cylinder were measured initially and at two partial stages of compression, characterized by cylinder heights $h_1 = 10\,\text{mm}$, $h_2 = 6\,\text{mm}$. FEM simulations corresponding to the experiment were performed for different values of the friction coefficient. The cylinder material was modeled by the expression $\sigma = 200\varepsilon^{0.2}$. Data are given in the first accompanying table for the experiment, and in the second table for the simulation. Use the data to make a diagram corresponding to Fig. 12.14 for the compression test. Add simulation results to the diagram. Then find the actual coefficient of friction in the experiment.

	Radial distances (mm)							
Stage	r_1	r_2	r_3	r_4	r_5	r_6	r_7	r_8
Initial	1.12	2.23	3.42	4.47	5.51	6.70	7.59	8.48
Step 1	1.14	2.31	3.65	4.91	6.22	7.72	8.85	9.96
Step 2	1.15	2.39	4.02	5.68	7.43	9.46	10.93	12.32

		Radial distances (mm)							
Stage	μ	r_1	r_2	r_3	r_4	r_5	r_6	r_7	r_8
Initial		1	2	3	4	5	6	7	8.5
Step 1	0	1.41	2.82	4.23	5.64	7.05	8.46	9.87	12.03
Step 2	0	1.81	3.64	5.45	7.27	9.09	10.91	12.72	15.53
Step 1	0.1	1.07	2.22	3.45	4.77	6.12	7.46	8.78	10.75
Step 2	0.1	1.08	2.36	3.98	5.76	7.57	9.34	11.07	13.49
Step 1	0.2	1.01	2.03	3.09	4.22	5.41	6.61	7.83	9.66
Step 2	0.2	1.01	2.08	3.33	4.73	6.24	7.79	9.41	11.81
Step 1	0.3	1.00	2.01	3.05	4.14	5.29	6.46	7.64	9.41
Step 2	0.3	1.01	2.06	3.24	4.57	5.99	7.48	9.02	11.33

NOTES

1. Valberg, H.: "Physical simulation of metal extrusion by means of model materials," Proc. 4th Int. Al Extrusion Technology Sem., Vol. 2, Chicago (1988), pp. 321–327.
2. Forrest, G., and Gunn, K.: "Problems associated with the production and use of wrought aluminium alloys," J. R. Aeronautical Soc., Vol. 60, 1956, pp. 635–658.
3. Loeland, J. O.: "Simulation with wax applied to forming processes for metals," PhD-thesis, NTH, 1985, Part 2, Ch. IX, p. 24.
4. Valberg, H.: "Metal flow in the direct axisymmetric extrusion of aluminium," J. Material Processing Technology, Vol. 31, 1992, pp. 39–55.
5. Valberg, H.: "Experimental techniques to characterize large plastic deformations in un-lubricated hot aluminium extrusion," Key Engineering Materials, Vol. 367, 2008, pp. 17–24.
6. Valberg, H., and Malvik, T.: "An experimental investigation of the material flow inside the bearing channel in aluminium extrusion," Int. J. Material Production Technology, Vol. 9, No. 4/5/6, 1994, pp. 428–463.
7. Valberg, H., and Loeken, T. M.: "Formation of the outer surface layers of the profile in direct and indirect extrusion," Proc. 5th Int. Aluminum Extrusion Technology Sem., Chicago, 1992, Vol. 2, pp. 529–550.
8. Valberg, H.: "A modified classification system for metal flow adapted to unlubricated hot extrusion of aluminum and aluminum alloys," Proc. 6th Int. Aluminum Extrusion Technology Sem., Chicago, 1996, Vol. 2, pp. 95–100.

REFERENCES

Dürrschnabel, W.: "Der Materialfluss beim Strangpressen von NE-Metallen," Teile 1–3, Metall, Vol. 22, 1968, pp. 426–437, 995–998, 1215–1219 (in German).

Forrest, G., and Gunn, K.: "Problems associated with the production and use of wrought aluminium alloys," J. R. Aeronautical. Soc., Vol. 60, 1956, pp. 635–658.

Valberg, H.: "Metal flow in the direct axisymmetric extrusion of aluminium," J. Mat. Proc. Tech., Vol. 31, 1992, pp. 39–55.

Valberg, H.: "Experimental techniques to characterize large plastic deformations in unlubricated hot aluminium extrusion," Key Engineering Materials, Vol. 367, 2008, pp. 17–24.

13 Theoretical Methods of Analysis

It is important – as shown in the preceding chapters – to be able to predict the deformations and the metal flow in metal forming with sufficient accuracy. The importance of knowing such factors as the pressure against the die and the required forming load was early recognized by the metal former. Much work was therefore done to develop theoretical models that could be used to predict these parameters, so that they could be estimated with sufficient accuracy before a new process was set up. The theoretical models established for this purpose showed that the forming load depended on such factors as die geometry and friction, for instance, and in hot forming also on the forming speed. With the development of theoretical methods, it also became possible to calculate the effect of each factor on the forming load.

There are a number of theoretical methods that can be used for analyzing metal forming processes; see Table 13.1.[1] In the following sections, they will be described, except for the *slip line field* and the *finite difference* methods, which have been described elsewhere.[2] The information that can be obtained by the different methods is specified in Table 13.1. Additional written material that describes the application of the slip line theory for analysis of metal forming and compares it with corresponding analysis by FEA is available at www.cambridge.org/valberg.

13.1 The Uniform Energy Method

The *uniform energy method* is the simplest method. It is sometimes also called the *ideal work method* because it considers ideal frictionless homogeneous deformation of the workpiece. It is based on setting up an energy balance, where the energy used in the forming operation is calculated, neglecting the effects of friction and inhomogeneous deformation. In Ch. 18.11.1, eq. 18-3, it is shown, for instance, how the required force in axisymmetric extrusion can be partitioned into four parts. The second part is denoted by the symbol F_{dh}, and is the force required if the material deforms homogeneously in the extrusion process. In Ch. 18.11.3, this second part is determined by means of the slab method; see eq. 18-17.

By use of the uniform energy method, we can obtain F_{dh} in a much simpler way. Consider a round billet being reduced by extrusion from initial cross section A_0 to

Table 13.1. *Theoretical methods of analysis used in metal forming*

	Analysis results			
Method	Velocity field	Stress field	Temperature field	Stresses on tooling
Uniform energy				x
Slab		x		x
Upper-bound	x			x
Slip line field	x	x		x
Finite element	x	x	x	x
Finite difference	x	x	x	x

a rod of final cross section A_1. The deformation energy required to transform this billet into a rod can be computed by use of either eq. 4-44 or eq. 4-46 in Ch. 4. Use of the latter yields

$$W = VU = V\int_{\varepsilon_a}^{\varepsilon_b} \bar{\sigma}\,\mathrm{d}\bar{\varepsilon} = V\bar{\sigma}\int_{\varepsilon_a}^{\varepsilon_b} \mathrm{d}\bar{\varepsilon} = V\bar{\sigma}(\varepsilon_a - \varepsilon_a)$$

$$V\bar{\sigma}\,(\varepsilon_a - \varepsilon_a) = A_0 l\bar{\sigma}\bar{\varepsilon} = A_0 l\bar{\sigma}\cdot\ln\left(\frac{A_0}{A_1}\right) = F_{\mathrm{dh}} l$$

We have now obtained the same result as that found by the slab method (eq. 18-17), i.e.,

$$F_{\mathrm{dh}} = \pi r_0^2\bar{\sigma}\ln\frac{A_0}{A_1} = A_0\bar{\sigma}\ln\frac{A_0}{A_1} \tag{13-1}$$

13.2 The Slab Method

This method will be described by demonstrating the use of it in the case of plane strain compression. Consider such compression with overhanging flat die platens; see the sketch in Fig. 13.1. The *slab method*[3–6] is based on setting up a force balance for a small slab element inside the deformation zone of the workpiece. The equations obtained this way are thereafter developed further, until an expression for the stress distribution inside the workpiece is obtained. The distribution of contact pressure over the die–workpiece interface is then estimated, and from this is obtained the force required by the die to compress the object.

13.2.1 The Slab Method in Plane Strain Compression with Tresca Friction

Consider the compression process shown in Fig. 13.1(a), where there is no metal flow in the direction normal to the plane of the paper. A longitudinal half section of the specimen has been redrawn in Fig. 13.1(b). A slab element inside the half section has also been indicated, and stress components on the element are shown.

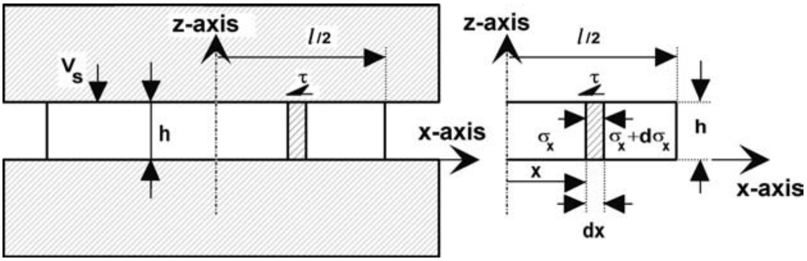

(a) (b)

Figure 13.1. Plane strain compression: (a) test setup and (b) half specimen with internal slab element.

Because of the plane strain conditions, there is no metal flow in the y-direction of the specimen, so the relation $v_y = 0 \Rightarrow \varepsilon_y = 0$ is valid. To apply the slab method in this case, a number of simplifying assumptions must be made. Assume the principal stresses to be oriented along the axes of the specimen, so that $\sigma_x = \sigma_3$, $\sigma_y = \sigma_2$, and $\sigma_z = \sigma_1$. By use of the Levy–Mises flow rule, previously given as eqs. 4-58 to 4-60, one principal stress can be expressed by the other two principal stresses by the equation:

$$\begin{aligned}
\varepsilon_1 &= \frac{\mathrm{d}\bar{\varepsilon}}{\bar{\sigma}}\left(\sigma_1 - \frac{1}{2}(\sigma_2 + \sigma_3)\right)\\
\varepsilon_2 &= \frac{\mathrm{d}\bar{\varepsilon}}{\bar{\sigma}}\left(\sigma_2 - \frac{1}{2}(\sigma_3 + \sigma_1)\right) = 0 \quad \Rightarrow \quad \sigma_2 = \frac{\sigma_1 + \sigma_3}{2}\\
\varepsilon_3 &= \frac{\mathrm{d}\bar{\varepsilon}}{\bar{\sigma}}\left(\sigma_3 - \frac{1}{2}(\sigma_1 + \sigma_2)\right)
\end{aligned}$$

This relationship, introduced into the von Mises flow criterion (left-hand side of eq. 4-54), yields the result

$$\begin{aligned}
\bar{\sigma} &= \frac{1}{\sqrt{2}}[(\sigma_3 - \sigma_2)^2 + (\sigma_2 - \sigma_1)^2 + (\sigma_1 - \sigma_3)^2]^{1/2}\\
&= \frac{1}{\sqrt{2}}\left[\left(\sigma_3 - \frac{\sigma_1 + \sigma_3}{2}\right)^2 + \left(\frac{\sigma_1 + \sigma_3}{2} - \sigma_1\right)^2 + (\sigma_1 - \sigma_3)^2\right]^{1/2}\\
&= \frac{1}{\sqrt{2}}\left[\frac{3}{2}(\sigma_3 - \sigma_1)^2\right]^{1/2} = \pm\frac{\sqrt{3}}{2}(\sigma_3 - \sigma_1)
\end{aligned}$$

$$\sigma_1 - \sigma_3 = \sigma_z - \sigma_x = \frac{2}{\sqrt{3}}\bar{\sigma} \tag{13-2}$$

In this way, we now have established an expression that connects the stress in the z-direction of the specimen to the stress in the x-direction, if the flow stress $\bar{\sigma}$ of the workpiece material is known. To be able to determine the stress in the z-direction of the specimen, σ_z, which at the same time is the contact stress between the specimen and the die, it is required to establish an additional equation between the two principal stresses σ_z and σ_x. This equation is obtained by considering force balance for the hatched slab element shown in Fig. 13.1(b). The whole specimen, and the slab element considered, are assumed to have dimension equal to unity in the direction orthogonal to the paper plane, i.e., in the y-direction.

Consider the specimen when it has been compressed down to a thickness h from initial thickness h_0. Assume the stress in the x-direction to increase by the amount $\mathrm{d}\sigma_x$ from the initial position x to a new position the incremental distance $\mathrm{d}x$ further to the right. Then the following force balance can be established for the slab element:

$$\sum F_x = \sigma_x h \cdot 1 - (\sigma_x + \mathrm{d}\sigma_x)\, h \cdot 1 - 2\tau\, \mathrm{d}x \cdot 1 = 0$$

The force contribution $2\tau\,\mathrm{d}x \cdot 1$ is the friction force created because the slab element slides laterally away from the neutral plane of the specimen during the stroke of compression. From the force equilibrium, the following differential equation is obtained:

$$\int \mathrm{d}\sigma_x = \int -\frac{2\tau}{h}\mathrm{d}x$$

After integration this expression yields

$$\sigma_x = -\frac{2\tau}{h}x + C \tag{13-3}$$

The constant C is determined by considering known boundary conditions. At the edge of the specimen, i.e., for $x = l/2$, the stress in the x-direction must be $\sigma_x = 0$, because a surface without tool contact is stress-free in the direction orthogonal to the surface. Introduction of this relationship into eq. 13-3 gives the following integration constant:

$$0 = -\frac{2\tau}{h}\frac{l}{2} + C \quad \Rightarrow \quad C = \frac{\tau}{h}l$$

The constant C is now eliminated from eq. 13-3, with the following result:

$$\sigma_x = -\frac{2\tau}{h}x + \frac{\tau l}{h} \tag{13-4}$$

It is now straightforward to express the stress component σ_z in term of known process parameters, by combining of the two equations 13-2 and 13-4:

$$\sigma_z = \sigma_x + \frac{2}{\sqrt{3}}\bar{\sigma} = -\frac{2\tau}{h}x + \frac{\tau l}{h} + \frac{2}{\sqrt{3}}\bar{\sigma} = \frac{2\tau}{h}\left(\frac{l}{2} - x\right) + \frac{2}{\sqrt{3}}\bar{\sigma} \tag{13-5}$$

If we assume Tresca friction, the expression $\tau = m\bar{\sigma}/\sqrt{3}$ (see eq. 10-8) can be introduced to give the equation

$$\sigma_z = \frac{2m\bar{\sigma}}{\sqrt{3} \cdot h}\left(\frac{l}{2} - x\right) + \frac{2}{\sqrt{3}}\bar{\sigma} \tag{13-6}$$

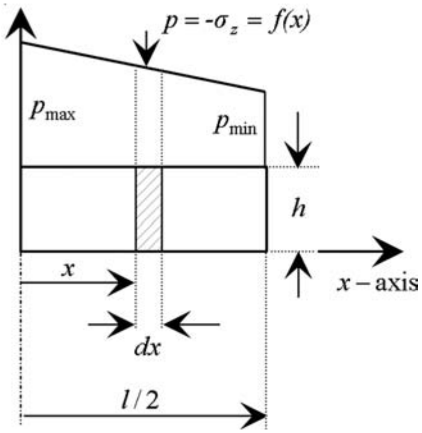

Figure 13.2. Pressure distribution over end face of specimen in plane strain compression, predicted by the slab method for Tresca friction.

By use of the slab method and a number of simplifying assumptions, an expression has now been determined for the stress distribution in the z-direction of the workpiece. The stress appears as positive even though this stress in reality is a compressive stress and should be negative. This is due to the assumption made that the stress component along the x-axis inside the specimen increases with increasing distance from the neutral plane of the specimen. To adjust for this, we can change sign in eq. 13-6 (or repeat the analysis applying a negative sign to dσ_x). In this way, the following final expression is arrived at:

$$\sigma_z = -\frac{2m\bar{\sigma}}{\sqrt{3}\cdot h}\left(\frac{l}{2} - x\right) - \frac{2}{\sqrt{3}}\bar{\sigma} \tag{13-7}$$

The obtained equation yields the normal stress distribution over the interface between the specimen and the compression die, i.e., the *friction hill*. This is also the negative pressure distribution over this contact surface; see eq. 10-2. Hence an expression has been found for the pressure distribution as a function of the friction factor, the flow stress of the workpiece material, and the specimen geometry, the last expressed in terms of the parameters h and l.

This equation, developed under the specified assumptions, predicts, as shown in Fig. 13.2, a linear pressure distribution over the end face of the specimen, where the highest pressure occurs in the middle of the specimen, and the lowest pressure at the edge. The maximum and minimum pressure can be expressed as follows:

$$\begin{aligned} p_{\text{max}} &= -\sigma_z^{x=0} = \frac{2}{\sqrt{3}}\bar{\sigma}\left(\frac{ml}{2h} + 1\right) \\ p_{\text{min}} &= -\sigma_z^{x=l/2} = \frac{2}{\sqrt{3}}\bar{\sigma} \end{aligned} \tag{13-8}$$

13.2.1.1 The Plane Strain Compression Force from the Slab Method

When the pressure distribution over the contact surface of the specimen is known, it is straightforward to find the required compressive load. This is done by integrating the pressure distribution over the surface that the pressure acts on. The force against a small slab element of breadth $\mathrm{d}x$ (Fig. 13.2) can be expressed as

$$\mathrm{d}F = -\sigma_z(x)\cdot \mathrm{d}x \cdot 1$$

The force against the whole contact surface is obtained by integrating this expression over the whole surface:

$$\begin{aligned} F &= 2\int_0^{l/2} -\sigma_z(x)\,\mathrm{d}x = 2\int_0^{l/2}\left[\frac{2m\bar{\sigma}}{\sqrt{3}h}\left(\frac{l}{2}-x\right)+\frac{2}{\sqrt{3}}\bar{\sigma}\mathrm{d}\right]x\,\mathrm{d}x \\ &= \left[\frac{2m\bar{\sigma}}{h\sqrt{3}}\left(\frac{l}{2}x-\frac{1}{2}x^2\right)+\frac{2}{\sqrt{3}}\bar{\sigma}x\right]_0^{1/2} = \frac{2\bar{\sigma}}{\sqrt{3}}\left(\frac{ml^2}{4h}+l\right) \end{aligned} \tag{13-9}$$

One should here note that the expression is valid for a workpiece of unit breadth, for instance 1 mm, in the direction into the plane of the paper. Hence, when the equation is used for a specimen of breadth b, the expression must be multiplied by b.

13.2.2 The Slab Method in Cylinder Compression with Tresca Friction

To apply the slab method in this case, one needs to know the velocity field of the deformation process. How this field is determined is shown in Example 13.1, under the assumption of homogeneous deformation. In this case, the cylinder does not develop a barrel shape during compression; see Fig. 7.11(a).

From the velocity field, the strain-rate field can also be deduced; see Example 13.2. Because homogeneous deformation is assumed, all shear strain-rate components equal zero. When principal strain rates (and strains) have been deduced, the principal strains are introduced into the Levy–Mises flow rule. The expression obtained then, when combined with the von Mises flow criterion, yields a relationship between two of the principal stresses inside the cylinder, namely, $\sigma_1 - \sigma_2 = \bar{\sigma}$; see Example 13.3. At this point, it is required to apply the slab method to establish a second relationship between the same two principal stresses. After this, both of the unknown principal stresses can be determined by solving the two equations; see the text after the two following examples.

EXAMPLE 13.1: THE VELOCITY FIELD IN CYLINDER COMPRESSION

Problem: Determine the velocity field in cylinder compression.

Solution: The velocity field in homogeneous compression of a slab was determined in Ch. 6, and the result was given in terms of three velocity components. Axisymmetric compression can easiest be analyzed by considering the process in a cylindrical coordinate system; see the accompanying figure. The velocities

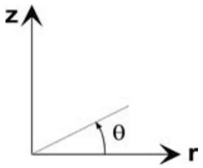

in the radial and in the axial direction, v_r and v_z, can then be expressed correspondingly as velocity components v_x and v_z in eqs. 6.16–6.18:

$$\underline{\underline{v_r = \frac{v_s r}{2h}}}, \qquad \underline{\underline{v_z = -\frac{v_s z}{h}}}$$

The third velocity component is that in the tangential direction. Because there is no material flow in this direction, this velocity must be zero:

$$\underline{\underline{v_\theta = 0}}$$

EXAMPLE 13.2: STRAIN RATES IN CYLINDER COMPRESSION

Problem: Determine the strain-rate field in cylinder compression.

Solution: The normal strain-rate components in the radial and the axial direction are determined easily by use of eqs. 6-10 to 6-12, i.e., by differentiating the velocity components already specified in Example 13.1:

$$\dot{\varepsilon}_r = \frac{\mathrm{d}v_r}{\mathrm{d}r} = \frac{\mathrm{d}}{\mathrm{d}r}\left(\frac{v_s r}{2h}\right) = \frac{v_s}{2h}, \qquad \dot{\varepsilon}_z = \frac{\mathrm{d}v_z}{\mathrm{d}z} = \frac{\mathrm{d}}{\mathrm{d}z}\left(-\frac{v_s z}{h}\right) = -\frac{v_s}{h}$$

The strain rate in the tangential direction can be determined by considering the expansion of the peripheral surface layer of a cylinder being compressed in the axial direction. The radius r of the cylinder will increase an infinitesimal amount dr during compression. Hence the peripheral surface of the cylinder will be subjected to the circumferential strain

$$\varepsilon_\theta = \frac{2\pi(r + \mathrm{d}r) - 2\pi r}{2\pi r} = \frac{\mathrm{d}r}{r}$$

The corresponding strain rate is

$$\dot{\varepsilon}_\theta = \frac{\mathrm{d}\varepsilon_\theta}{\mathrm{d}t} = \frac{1}{r}\frac{\mathrm{d}r}{\mathrm{d}t} = \frac{v_r}{r}$$

Constancy of volume ($\dot{\varepsilon}_r + \dot{\varepsilon}_z + \dot{\varepsilon}_\theta = 0$) yields the following alternative expression for the tangential strain rate:

$$\dot{\varepsilon}_\theta = \frac{v_s}{2h}$$

EXAMPLE 13.3: PRINCIPAL STRESSES IN CYLINDER COMPRESSION

Problem: Show that the relationship $\sigma_1 - \sigma_2 = \sigma_z - \sigma_r = \bar{\sigma}$ is valid in cylinder compression.

Solution: Assume that the principal stresses in the compression test coincide with the direction of the axis of the applied coordinate system, i.e., that principal stresses act in the r, z, and the θ directions, so that $\sigma_r = \sigma_2$, $\sigma_z = \sigma_1$, $\sigma_\theta = \sigma_3$.

As shown in Example 13.2, the strain rates in the two directions r and θ must be equal: $\dot{\varepsilon}_r = \dot{\varepsilon}_\theta$. The Levy–Mises flow rule, eqs. 4-58 to 4-60, then yields

$$\varepsilon_r = \frac{\mathrm{d}\bar{\varepsilon}}{\bar{\sigma}}\left(\sigma_r - \frac{1}{2}(\sigma_z + \sigma_\theta)\right) = \frac{\mathrm{d}\,\bar{\varepsilon}}{\bar{\sigma}}\left(\sigma_2 - \frac{1}{2}(\sigma_1 + \sigma_3)\right) = \varepsilon_\theta$$

$$\varepsilon_\theta = \frac{\mathrm{d}\bar{\varepsilon}}{\bar{\sigma}}\left(\sigma_\theta - \frac{1}{2}(\sigma_r + \sigma_z)\right) = \frac{\mathrm{d}\bar{\varepsilon}}{\bar{\sigma}}\left(\sigma_3 - \frac{1}{2}(\sigma_2 + \sigma_1)\right)$$

From this, we can conclude

$$\sigma_r - \frac{1}{2}(\sigma_z + \sigma_\theta) = \sigma_\theta - \frac{1}{2}(\sigma_r + \sigma_z) \quad \Rightarrow \quad \underline{\underline{\sigma_r = \sigma_\theta}}$$

In addition, the von Mises flow criterion, eqs. 4-53 to 4-55, yields the following relationship:

$$\begin{aligned}
\underline{\underline{\bar{\sigma}}} &= \frac{1}{\sqrt{2}}[(\sigma_1 - \sigma_2)^2 + (\sigma_2 - \sigma_3)^2 + (\sigma_3 - \sigma_1)^2]^{1/2} \\
&= \frac{1}{\sqrt{2}}[(\sigma_z - \sigma_r)^2 + (\sigma_r - \sigma_\theta)^2 + (\sigma_\theta - \sigma_z)^2]^{1/2} \\
&= \frac{1}{\sqrt{2}}[(\sigma_z - \sigma_r)^2 + (\sigma_r - \sigma_z)^2]^{1/2} = \sigma_z - \sigma_r = \underline{\underline{\sigma_1 - \sigma_2}} \qquad (13\text{-}10)
\end{aligned}$$

Once eq. 13-10 has been developed, it is straightforward to find an expression for the stress in the axial direction of the cylinder, if we can establish a second equation connecting σ_x to σ_r. This is achieved by means of the slab method. Force equilibrium is established for an imaginary slab element, as shown in Fig. 13.3. The force balance yields the result

$$\begin{aligned}
\sum F_r &= \sigma_r r h\,\mathrm{d}\theta - (\sigma_r + \mathrm{d}\sigma_r)(r + dr)\,h\,\mathrm{d}\theta \\
&\quad + 2\sigma_\theta h\,\mathrm{d}r \cdot \sin\left(\frac{\mathrm{d}\theta}{2}\right) - 2\tau r\,\mathrm{d}r\,\mathrm{d}\theta = 0
\end{aligned}$$

If the angle $\mathrm{d}\theta$ of the slice is small, the approximation $\sin(\mathrm{d}\theta/2) \approx \mathrm{d}\theta/2$ is valid. Upon expansion of the preceding expression, assume the product of two increments (for example, $\mathrm{d}\sigma_r\,\mathrm{d}\theta$ to be approximated to zero). Then the following expression is obtained:

$$-\sigma_r - \frac{\mathrm{d}\sigma_r}{\mathrm{d}r} r + \sigma_\theta - \frac{2\tau}{h} r = 0$$

Substitution of $\sigma_r = \sigma_\theta$ from Example 13.3, into this equation yields

$$\frac{\mathrm{d}\sigma_r}{\mathrm{d}r} = -\frac{2\tau}{h} \quad \Rightarrow \quad \mathrm{d}\sigma_r = -\frac{2\tau}{h}\mathrm{d}r$$

Integration of the differential equation yields

$$\sigma_r = -\int \frac{2\tau}{h}\mathrm{d}r = -\frac{2\tau}{h} r + C$$

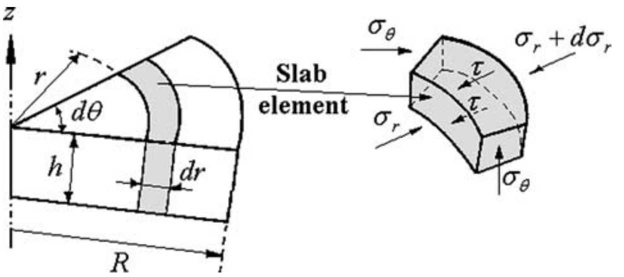

Figure 13.3. (a) Slab element inside a slice of a cylinder. (b) Stress components on slab element.

The constant C can be determined by considering the boundary conditions. The radial stress component must equal zero at the free peripheral surface of the cylinder, i.e., $\sigma_r^{r=R} = 0$. The value of the constant then must be $C = (2\tau/h)R$.

The radial stress now can be expressed as

$$\sigma_r = -\frac{2\tau}{h}r + \frac{2\tau}{h}R = \frac{2\tau}{h}(R - r)$$

Introduction of the expression $\sigma_z - \sigma_r = \bar{\sigma}$ from Example 13.3 now gives us the stress in the axial direction:

$$\sigma_z = \bar{\sigma} + \sigma_r = \bar{\sigma} + \frac{2\tau}{h}(R - r) \tag{13-11}$$

This stress equals the contact pressure against the compression platen. If one defines tensile stress as positive, one must change the sign, because in cylinder compression, there is compressive stress in the axial direction of the cylinder:

$$-p = \sigma_z = -\bar{\sigma} + \frac{2\tau}{h}(r - R) \tag{13-12}$$

This equation corresponds to eq. 13-5, which was developed correspondingly in the case of plane strain compression. Hence, a linear increase in contact pressure from the edge to the center of the specimen is also predicted in cylinder compression, as in plane strain.

The required force can be determined by integrating the contact pressure over the end face of the cylinder:

$$\begin{aligned} F &= \int_0^R p \cdot 2\pi r \, \mathrm{d}r = \int_0^R \left(\bar{\sigma} + \frac{2\tau}{h}(R - r)\right) 2\pi r \, \mathrm{d}r \\ &= 2\pi \left[\frac{1}{2}\bar{\sigma} R^2 + \frac{2\tau}{h}\left(\frac{1}{2}R^2 - \frac{R^3}{3}\right)\right] = \pi \bar{\sigma} R^2 \left(1 + \frac{2mR}{3\sqrt{3} \cdot h}\right) \end{aligned} \tag{13-13}$$

13.3 The Slab Method in Cylinder Compression with Coulomb Friction

When the slab method is applied to analysis of cylinder compression, a Coulomb friction model can alternatively be applied, instead of Tresca friction. Then the friction shear stress over the die–workpiece interface will depend on the contact pressure. Use of the method then provides more complex equations, but the final pressure distribution obtained, commonly termed the friction hill, is similar to that

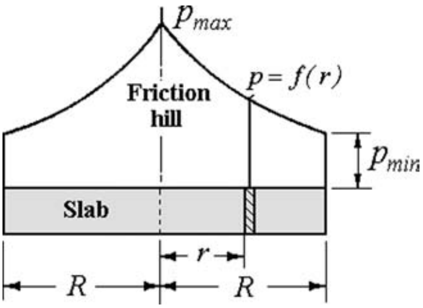

Figure 13.4. Friction hill in cylinder compression for Coulomb friction.

already shown in Fig. 13.2 for Coulomb friction. Whereas Tresca friction predicts a linear distribution of pressure from center to edge of the cylinder, Coulomb friction predicts an exponential distribution; see Fig. 13.4.

The equations[7] obtained for pressure and required load, by means of the slab method in case of Coulomb friction, are those specified in Table 13.2.

13.4 The Upper Bound Method

The *upper bound method*[8] is based on the computation of the energy consumption in the process, obtained from the flow field in the actual forming process. In case the flow field is not known well, a probable flow field is proposed, and then an analysis is performed for this field.

When the energy is known, forming parameters such as the forming load and die pressure can be determined from it. If different velocity fields are tried, the best will be the one that provides the lowest energy consumption.

If the assumed velocity field differs from the real velocity field, the computed energy will exceed the real energy consumption. Hence, when the upper bound method is applied, one gets estimates of the forming load and the pressure that are either larger than or, in the best case, equal to the real load and the real pressure. This is why the solution is termed an upper bound.

When the upper bound method is applied, the following formula,[1,9,10] is commonly used to calculate the power consumption in a particular metal forming process:

$$\dot{W}_T = F \cdot v_s = \dot{W}_D + \dot{W}_S + \dot{W}_F = \int_V \bar{\sigma}\dot{\bar{\varepsilon}}\,\mathrm{d}V + \int_A k\,|\Delta v|\,\mathrm{d}A + \int_A \tau_i v_i\,\mathrm{d}A \tag{13-14}$$

Table 13.2. *Equations deduced by the slab method for cylinder compression with Coulomb friction*

Contact pressure	Compressive force
$\sigma_z = \bar{\sigma} \cdot e^{(2\mu/h)(R-r)}$	$F = \frac{\pi\bar{\sigma}}{2}\left(\frac{h}{\mu}\right)^2\left[e^{2\mu R/h} - \frac{2\mu R}{h} - 1\right]$

Here the applied power appears as the product of the forming load, F, and the velocity of the forming die, or punch, v_s. As the equation depicts, the power consumption is split into the three parts:

$\dot{W}_D$ is the power required to deform the workpiece homogeneously.

$\dot{W}_S$ is the power required to shear-deform the workpiece. Shear deformation occurs if some or all of the workpiece material flows through a **velocity discontinuity** during the course of forming.

$\dot{W}_F$ is the power consumed due to frictional sliding of workpiece material over the interface between die and workpiece.

Let us now consider these three terms. The deformation energy in the case of homogeneous deformation was expressed in eq. 11-2 as $W_D = \bar{\sigma}\bar{\varepsilon}V$. Hence, the power consumption in an infinitesimal volume of the workpiece due to homogeneous deformation is $\mathrm{d}\dot{W}_D = \mathrm{d}W_D/\mathrm{d}t = \bar{\sigma} \cdot \dot{\bar{\varepsilon}}\,\mathrm{d}V$. As eq. 13-14 depicts, the total energy consumption is obtained by integrating this expression over the whole volume of the workpiece.

The energy consumption because of sliding friction against the die is determined as the product between the force $\mathrm{d}F$ acting across the boundary interface and the sliding distance s of the workpiece material against the die. The power is obtained by dividing the energy by the time increment during which sliding takes place, i.e., $\mathrm{d}t$:

$$\mathrm{d}\dot{W}_F = \frac{\mathrm{d}F \cdot s}{\mathrm{d}t} = \frac{\tau_i \cdot \mathrm{d}A \cdot s}{\mathrm{d}t} = \tau_i \cdot v_i\,\mathrm{d}A \qquad (13\text{-}15)$$

The symbols are

τ_i, shear stress transferred from workpiece to die surface
v_i, sliding velocity of workpiece material against the die
$\mathrm{d}A$, infinitesimal area of boundary surface

As shown by eq. 13-14, the total power consumption due to friction effects is finally determined by integrating eq. 13-15 over the whole interface between workpiece and die.

The power due to flow of workpiece material through a velocity discontinuity requires a somewhat more complex treatment.[11] Consider a plastic material that flows in a direction specified by the velocity vector $\vec{v}_a$; see Fig. 13.5(a). When the material approaches the boundary line Γ, it changes its direction of flow, so that upon further flow, it has a new velocity $\vec{v}_b$. In this case it is common to call the line Γ a *velocity discontinuity line.*

Let us first assume plane strain conditions, i.e., there are no velocity components in the direction perpendicular to the plane of the paper. In addition, consider a layer of material of depth equal to unity, in that direction. The line Γ then represents the division line between two regions, in which there is rigid-body movement, and hence no plastic deformation. At the instant when the material flows past Γ, the material is, however, subjected to plastic shear deformations, as depicted in Fig. 13.5.

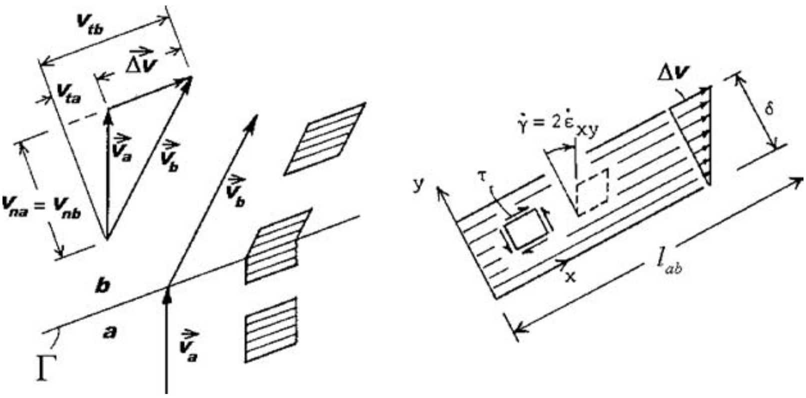

(a) (b)

Figure 13.5. Material flow through velocity discontinuity: (a) velocity components and shear deformations upon passage across discontinuity line, and (b) parallel material flow across thin layer.[11] (Reprinted with permission of Tapir.)

The analysis can also be performed with an eventual continuous deformation in the two zones, *a* and *b*, on each side of the discontinuity line, but then the effect of these deformations must be superposed on the solution given here. It is obvious that the material flow in the case shown in Fig. 13.5(a) is characterized by a change in flow direction at the instant when the material flows past the line Γ.

It can also be said that a tangential velocity component, $\Delta\vec{v}$, is added to the velocity $\vec{v}_a$ during passage of material across the discontinuity line, while the normal velocity component is maintained. Mathematically, this is expressed as

$$\vec{v}_a + \Delta\vec{v} = \vec{v}_b$$

As shown in Fig. 13.5(a), this implies that the two velocity vectors $\vec{v}_a$ and $\vec{v}_b$ can be specified with their velocity components normal to and parallel to the discontinuity line Γ, in the following way:

$$v_{na} = v_{nb}, \qquad v_{tb} = v_{ta} + \Delta v \tag{13-16}$$

The relative velocity difference between the two zones *a* and *b* can be considered as the result of a parallel material stream over an infinitely small breadth δ; see Fig. 13.5(b). Then by means of eq. 4-47, we can compute the power consumption associated with shear deformation across the velocity discontinuity line as

$$\begin{aligned}\dot{W} &= \frac{\mathrm{d}W}{\mathrm{d}t} = \frac{\mathrm{d}U \cdot V}{\mathrm{d}t} \\ &= V(\sigma_x\dot{\varepsilon}_x + \sigma_y\dot{\varepsilon}_y + \sigma_z\dot{\varepsilon}_z + 2\tau_{xy}\dot{\varepsilon}_{xy} + 2\tau_{yz}\dot{\varepsilon}_{yz} + 2\tau_{zx}\dot{\varepsilon}_{zx})\end{aligned}$$

Because all strain components except ε_{xy} are equal to zero, the expression simplifies to

$$\dot{W} = \dot{W}_s = V \cdot \tau_{xy} \cdot 2\dot{\varepsilon}_{xy},$$

where $2\dot{\varepsilon}_{xy} = \dot{\gamma}_{xy}$; see eq. 4-22 and Fig. 13.5(b). The power consumption per unit of discontinuity surface thus can be expressed as

$$\dot{W}_s^A = \int_V \mathrm{d}W_s = \int_V 2\tau_{xy}\dot{\varepsilon}_{xy}\,\mathrm{d}V = k\int_0^{\delta} 2\dot{\varepsilon}_{xy}\cdot 1\cdot \mathrm{d}y\cdot l_{ab} = kl_{ab}$$
$$\int_0^{\delta}\dot{\gamma}_{xy}\,\mathrm{d}y = kl_{ab}\int_0^{\delta}\frac{\partial v_x}{\partial y}\,\mathrm{d}y = kl_{ab}\,\Delta v$$

For a velocity discontinuity of area $\mathrm{d}A$, the power consumption can therefore be expressed as

$$\dot{W}_s = \int_A k\,\Delta v\cdot l_{ab}\cdot 1 = \int_A k\,|\Delta\vec{v}|\cdot \mathrm{d}A \qquad (13\text{-}17)$$

Here the new symbols are

k, the shear flow stress of the material ($k = \bar{\sigma}/\sqrt{3}$ by the von Mises flow criterion)
$\Delta\vec{v}$, the vectorial velocity change over the velocity discontinuity

13.4.1 Cylinder Compression Analyzed by the Upper Bound Method

We shall now apply this method to axisymmetric cylinder compression to determine an expression for the required compressive force. The different force components in eq. 13-14 are determined as follows:

$$\dot{W}_D = \int_V \bar{\sigma}\dot{\bar{\varepsilon}}\,\mathrm{d}V = \pi R^2 h\cdot\bar{\sigma}\cdot\frac{v_D}{h} = \pi R^2\bar{\sigma}v_D$$
$$\dot{W}_S = 0 \qquad \text{(there is no velocity discontinuity)}$$
$$\dot{W}_F = 2\int_A \tau_i v_i\,\mathrm{d}A = 2\int_A \frac{m\bar{\sigma}}{\sqrt{3}}\cdot\frac{v_s r}{2h}\cdot 2\pi r\,\mathrm{d}r = 2\frac{m\bar{\sigma}v_s 2\pi}{2\sqrt{3}\cdot h}\int_0^R r^2\,\mathrm{d}r$$
$$= \frac{2m\bar{\sigma}v_s\pi R^3}{3\sqrt{3}\cdot h}$$

Summing the three parts gives the following result:

$$\dot{W}_T = F\cdot v_s = \dot{W}_D + \dot{W}_S + \dot{W}_F$$
$$= \int_V \bar{\sigma}\dot{\bar{\varepsilon}}\,\mathrm{d}V + 0 + \int_A \tau_i v_i\,\mathrm{d}A = \pi R^2\bar{\sigma}v_s + \frac{2\pi m}{3}\frac{\bar{\sigma}}{\sqrt{3}}\frac{v_s R^3}{h}$$

Rearranging the equation yields the force

$$F = \frac{\dot{W}_T}{v_s} = \pi R^2\bar{\sigma}\left(1 + \frac{2mR}{3\sqrt{3}\cdot h}\right) \qquad (13\text{-}18)$$

Comparison of this expression with the result obtained by means of the slab method (eq. 13-13) shows that both methods yield the same result.

Problems

13.1 Assume homogeneous deformation during compression of a cylindrical specimen. Use the slab method to develop an expression for the pressure distribution over the end face of the specimen in the case of Coulomb friction. Assume the material of the cylinder to be of rigid–plastic *type with constant flow stress* $\bar{\sigma}$.

13.2

(a) Determine the compression force and the average contact pressure in axisymmetric cylinder compression in the case of Coulomb friction. The pressure distribution is that given in Table 13.2.

(b) Use the slab method to determine the stress distribution over the end face of a cylinder, in the situation corresponding to that specified in Problem 13.1, but now for the case of Tresca friction.

(c) Show by means of graphs how the pressure varies over the end face of a cylinder subjected to axisymmetric compression in the cases of Coulomb and Tresca friction.

13.3 Consider the case of axisymmetric backward extrusion shown in the accompanying figure.

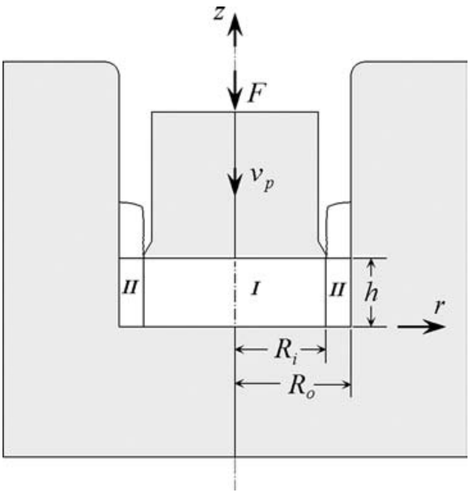

Assume the plastic zone in this case to consist of two parts, the cylindrical region denoted as I and the ringlike region II. Assume that the following velocity fields are descriptive for the metal flow in the two regions:

Region I:

$$v_{r,I} = \frac{v_p}{2h} r, \qquad v_{z,I} = -\frac{v_p}{h} z$$

Region II:

$$v_{r,I} = \frac{v_p}{2h} \frac{R_i^2}{R_0^2 - R_i^2} \left(\frac{R_0^2}{r} - r \right), \qquad v_{z,I} = \frac{v_p}{h} \frac{R_i^2}{R_0^2 - R_i^2} z$$

Use the upper bound method to find a formula for the required punch load in this case.

NOTES

1. Altan, T., Oh, S.-I, and Gegel, H. L.: "Metal Forming: Fundamentals and Applications," ASM Int. 1983, pp. 131–142.
2. Hosford, W. H., and Caddell, R. M.: "Metal Forming, Mechanics And Metallurgy," 3rd ed., Cambridge Univ. Press, 2007.
3. Siebel, E.: "Forces and material flow in plastic deformation" (in German), Stahl u. Eisen, Vol. 45, 1925, pp. 1563–1566.
4. von Karman, T.: "Contribution to the theory of rolling" (in German), Z. Angewandte Mathematik u. Mechanik, Vol. 5, 1925, pp. 139–141.
5. Sachs, G.: "On the theory of the tension test" (in German), Z. Angewandte Mathematik u. Mechanik, Vol. 7, 1927, pp. 235–236.
6. Siebel, E., and Pomp, A.: "On the further development of the compression test" (in German), Mitt. Kaiser-Wilhelm Inst. Eisenforschung, Vol. 10, 1928, pp. 55–62.
7. Dieter, G. E.: "Mechanical Metallurgy," McGraw-Hill, 1989.
8. Prager, W., and Hodge, P. G.: "Theory of Perfectly Plastic Solids," Wiley, New York, 1941.
9. Steck, E.: "Load determination in metal forming by use of the upper bound theorem" (in German), Werkstattstechnik, Vol. 57, 1967, pp. 273–279.
10. Avitzur, B: "Metal Forming: Processes and Analysis," McGraw-Hill, New York, 1968.
11. Hellan, K.: "Theory of Plasticity," Tapir, 1972, pp. 82–84 (in Norwegian).

REFERENCES

Altan, T., Oh, S.-I., and Gegel, H. L.: "Metal Forming, Fundamentals and Applications," ASM Int. 1983, pp. 131–142.
Dieter, G. E.: "Mechanical Metallurgy," McGraw-Hill, 1989.
Lange, K.: "Handbook of Metal Forming," McGraw-Hill, 1985.

14 Finite Element Analysis

Lately, the most important advancement in metal forming analysis has been the development and application of finite element analysis (FEA), i.e., use of the computerized finite element method (FEM). Recent progress in FEA, together with increasingly powerful computers, has permitted increased use of such numerical modeling. Hence, today it is possible to FEM-simulate the metal forming processes at various design stages.

When a FEM model has been made for a particular forming application, the load requirement, velocity, strain rate, strain and stress fields, etc., can easily be obtained for the considered process. Therefore, the current trend is toward increased application of FEA for process simulation and optimization. For practical applications, the modeling techniques must, of course, describe experimental observations quantitatively with sufficient accuracy.

After an introduction to modeling techniques in general in metal forming, this chapter will focus on the application of FEM modeling as a practical tool to investigate the process conditions in forming operations. An overview of some commonly applied FEM codes will be given. Afterwards, it will be shown how the two- and three-dimensional versions of the DEFORM$^{\text{TM}}$ FEM program can be used to FEM-model metal forming.

Some examples will be presented where the DEFORM FEM code is used for deformation analysis in practical metal forming cases like plane strain compression and cylinder compression. Finally, a case will be presented where the complex conditions in extrusion welding are investigated by means of FEA. There is work being done to create corresponding models using QFORM. The DEFORM and QFORM models will be available at www.cambridge.org/valberg.

14.1 Modeling Techniques in Metal Forming

There are three primary goals in performing an engineering analysis of metal forming. First, the analysis aims at reduced efforts of trial and error in tool and process design. Second, the analysis approach is useful in order to design the desired part for ease of manufacture. Finally, there may be problems in the process that need to be solved. The analysis approach commonly lowers tooling and equipment costs, provides improved tooling modifications, and helps in understanding the process. It may lead to faster production of quality products at minimum cost, including reduced material waste and shortened lead times.

In early metal forming technology, the design of a forming process, and predictions of material flow and forming loads, depended mainly upon the experience and the intuition of the metal former. Sometimes this led to costly trial-and-error experimentation in the design of new forming operations. To be able to reach the goal faster and with less effort, and to increase the understanding of the mechanics of metal forming operations, modeling techniques have been developed over the years.

Modeling techniques[1] can be said to cover all methods used to determine process parameters without conducting the actual forming process itself. They are used to refine existing process techniques or to investigate new techniques. Important process parameters in metal forming are, for example, force–stroke diagrams, energy requirements, deformation characteristics and material flow, and the distribution of stress, strain, and strain rate inside the deforming body. Modeling techniques are commonly either physical or numerical techniques.

Physical modeling techniques involve the use of experiments applying model materials or tailored materials or experiments on special metal forming processes. Physical modeling includes experiments on special test specimens used in metal forming; see Ch. 3. Material flow and strain distribution studies can, for instance, as described in Ch. 12, be conducted over a cross section of a test workpiece in forming, for instance, by placing patterns on its surface or at preferred cross sections.

Numerical modeling techniques, on the other hand, analyze a process numerically with the help of mathematics. Numerical computation results are commonly validated by comparison with measured data, such as the shape change or the required forming load. Physical and numerical modeling of metal forming processes help understand the processes better, for optimization purposes.

Many numerical methods have been developed to analyze metal forming. Classical methods like the slab, the upper and the lower bound, and the slip-line field methods (see Ch. 13), are all numerical methods. They are still useful for predicting approximate optimum process variables, such as forming loads, overall geometry changes of the workpiece, and qualitative modes of material flow. Hence, these methods still provide useful information and understanding about the mechanics of metal forming.

14.2 FEM Analysis

The first effort to develop the FEM date back to work done in 1941–1942.[2] The method was further developed in the following decades and was provided with a mathematical foundation in 1973.[3] FEM is a numerical technique for finding approximate solutions of partial differential equations and integral equations. The method was first applied in structural mechanics and is usually based on an energy principle such as that of virtual work or minimum total potential energy. FEA is today generally used for prediction of stresses and displacements in mechanical objects and systems, and in other applications. The ability to model a structural system in three dimensions can provide an accurate analysis for almost any structure. Three-dimensional models in general can be produced using common computer-aided design (CAD) packages. FEA allows entire designs to be constructed, refined, and optimized before parts are manufactured. FEA has significantly improved the standard of engineering design and the methodology of the design process in many industrial applications. It has substantially reduced the time required to get products from concept level to production line.

14.3 FEM Analysis in Metal Forming

In this book, the focus is on the use of FEA in metal forming applications. This new analysis tool has made it possible to analyze a chosen process on the computer rather than using trial and error in the forming machine. Process simulation using FEA has yielded considerable cost and quality improvements in the industry. FEM simulation has become a practical and efficient tool for prediction of performance in industrial forming operations before dies are manufactured. Today, FEA is an extremely effective tool for research and also in industrial applications.

FEM programs can predict large deformations and thermally influenced material flow in metal forming. Thus, they can provide detailed information about the forming mechanics. FEM simulation of metal forming is highly complex and computation intensive. This is due to extreme nonlinearities because of large strains, plastic flow of anisotropic materials, with interfacial friction between irregular-shaped surfaces under changing contact. Because of this, it is difficult to obtain analytical solutions to such problems for quantitative evaluation of temperature, stress, and strain distributions, within the deforming body. It is therefore common to use the FEM for this purpose.

14.3.1 FEM Modeling Approach

In FEM modeling,[1] the workpiece is represented by a collection of subdomains called *finite elements*; see Fig. 14.1. The elements are bounded by sets of *nodes*. They define localized mass and stiffness properties of the model. Equations of equilibrium, in conjunction with applicable physical considerations such as compatibility and constitutive relations, are applied to each element to construct a system of equations. The system is then solved to find unknown values using advanced numerical techniques. FEA is an approximate method, and its accuracy can be improved by increasing the number of elements used.

The path to solution of a FEM problem can be partitioned into five steps: (1) defining the elements, (2) establishing the equations for the elements, (3) finding the elements' properties, (4) assembling those element properties to obtain system equations, and finally, (5) solving the system equations using appropriate numerical techniques.

Important issues in the development of FEM codes are the choice of deformation description and solution procedure, selection of type of flow formulation,

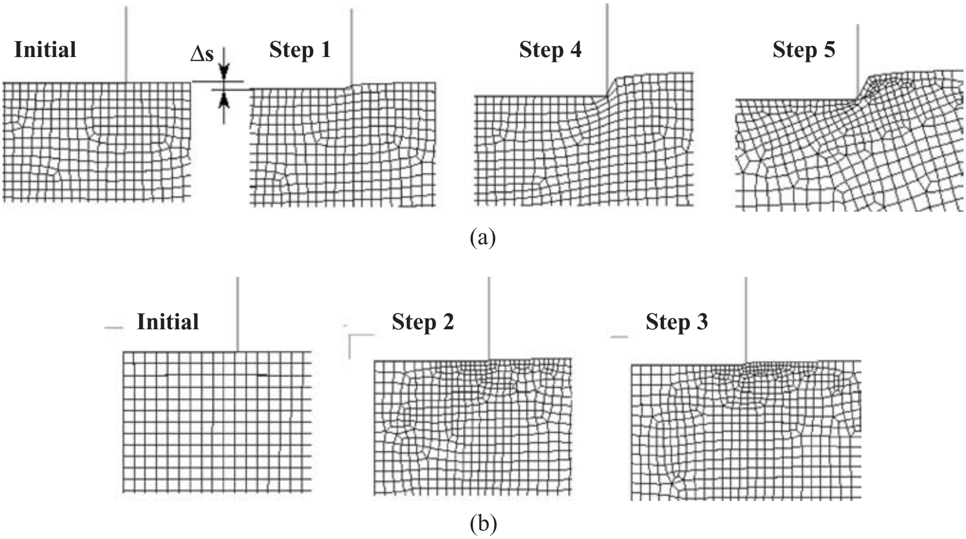

Figure 14.1. Deformation of the finite element mesh over the die edge in plane strain compression: (a) Remeshing at each fifth step. (b) Remeshing at each step yields a fine, harmonic mesh at the die edge.

application of material models, and remeshing. There are two modes of description of the deformations in continuous media, the Lagrangian and the Eulerian. The *Lagrangian description* employs the coordinates of a material point in the undeformed state as independent variables. The *Eulerian description* employs the coordinates of a material point in the deformed state. Because of this, the finite element mesh in the Eulerian system is spatially fixed, whereas in the Lagrangian system it moves with the material.

The solution procedure is either explicit or implicit. The *implicit* procedure uses an automatic incrementation strategy to solve a large system of equations. It requires a lot of storage and CPU time but has certain advantages, dependent on type of analysis. In *explicit* codes, it is easier to complete the solution. Because they have fewer control parameters, explicit codes are easy to use for optimization of the solution. There are cases in which the explicit method is superior, and cases where the reverse is true.

The *implicit method* is reasonably effective and can be faster than the *explicit method* in smaller problems and in some other applications. For more complex analysis with large, refined meshes, the explicit method is much more effective.

The material model is an important part of the FEM algorithm. Proper functions describing the constitutive behavior of the actual material must be used. In analysis of metal forming, plastic strains usually outweigh elastic strains, and the idealization of rigid–plastic or rigid–viscoplastic material behavior is commonly acceptable. In this case, the analysis is according to the *flow formulation*, based on the Levy–Mises flow rule; see eqs. 4-57 or 4-59 to 4-60. If elasticity cannot be neglected, the material model is formulated according to the *solid formulation*, i.e., the material is considered an elastic–plastic or elastic–viscoplastic solid. The solid formulations are based on the use of *Prandtl–Reuss equations* for elastic–plastic materials. Commonly the solid formulation is less time efficient than the rigid–plastic models, i.e., the flow formulation. This is due to the greater complexity of the latter, requiring smaller step sizes.

A difficulty in FEA when applied in metal forming is due to the evolution of the mesh. The finite elements sometimes become so distorted that large errors arise during computation. To overcome such difficulties, the mesh must periodically be regenerated, i.e., *remeshed*. Modern FEM codes provide the possibility for *automatic remeshing*, i.e., generation of a new mesh, and transfer of information from old to new mesh through interpolation.

There are two different approaches to remeshing. One is called *adaptive remeshing* and allows simulation of large deformations without any intervention by the user. The other approach is *static remeshing*. Although less automatic, the latter avoids excessive errors that may occur in adaptive remeshing. Adaptive remeshing also leads to heavier calculations.

Figure 14.1 shows the evolution of the FEM mesh flowing past the sharp edge of a plane strain compression die, in a DEFORM-2D FEM model of the process. During the FEM mesh evolution, in the case shown in Fig. 14.1(a), the parameters that triggered remeshing were not selected so that remeshing occurred so often. In the second case, shown in Fig. 14.1(b), however, a better result was obtained, because remeshing was done at each simulation step. In addition, the simulation step lengths were reduced. In processes where the metal deforms severely or flows past die edges, it is thus necessary to remesh often if material flow is to be well described in the FEM model. But frequent remeshing also leads to heavier FEM-models and should not be used unless required.

14.3.2 Commercial Codes for FEM Modeling of Metal Forming

There are a number of commercial FEM codes available, which have been tailor-made for bulk-metal forming applications. Such codes are, for instance, DEFORM^{TM}, FORGE^{TM}, SUPER-FORGE^{TM}, and Q-FORM^{TM}. Other general commercial codes, such as ANSYS^{TM} and ABAQUS^{TM}, can also be used successfully for this purpose. Internet links to software houses are given in the reference list at the end of the chapter. The author of this book has used the DEFORM code successfully since 1997.

In sheet-metal forming, FEM codes based on shell elements are most commonly used for FEA. Commercial codes of this category are, for instance, LS-Dyna^{TM} and Pam-Stamp^{TM}.

14.4 The Deform Code

In this book, the author mainly uses the DEFORM code for FEM modeling. There are different variants of this FEM code, but the main focus here will be on the use of the two-dimensional and the three-dimensional version of the code for metal forming applications.

The DEFORM-2D variant of the program allows simulation of axisymmetric or plane strain cases of metal forming. It is user-friendly, and its computational time is usually short, because of the simplicity of 2D as compared to 3D simulation. DEFORM-3D, on the other hand, is a powerful process simulation system, designed to analyze the three-dimensional flow of complex metal forming processes.

The DEFORM software has proved to be accurate and robust in industrial application. The automatic mesh generator produces an optimized mesh system with local element size dependent on the process to be analyzed. This facilitates the enhanced resolution of part features, while maintaining good control of the overall problem size and computing requirements. A user-defined local mesh density provides users flexible control to meet their requirements. The software provides sophisticated analysis capabilities, and the graphical user interface is intuitive and easy to learn. It also provides utilities for manipulating 3D geometry.

The FEM approaches used in the DEFORM code are described in detail in the Appendix available on this book's Web site www.cambridge.org/valberg.

14.5 Performing the FEM Analysis

The work required to perform the FEA is done in three consecutive phases. The first phase is called *preprocessing*, the second *simulation*, and finally there is the *postprocessing* phase.

During preprocessing the geometrical shapes of the bodies incorporated in the FEM model are constructed, using a CAD program. This can be in 1D, 2D, or 3D form, modeled by lines, shapes, or surfaces, respectively. The primary objective of the model is to replicate the important parameters and the features of the real problem to model it with sufficient accuracy. The geometry files are then exported to the FEM program to establish the FEM model. This includes defining the model, by adding an FEM mesh to bodies present in the model and assigning environmental conditions, or *boundary conditions*, to the model.

When the model has been created, the simulation or the analysis is performed. In this step, the FEM solver computes the solutions of the FEM model and stores the computed data. The computation procedure involves applied forces, including properties of the elements, and on this basis produces a model solution. The analysis determines resulting effects, such as deformations, strains, and stresses, caused by the applied loads (for instance, force or pressure).

Finally, there is the postprocessing phase in which computed data are processed to be visualized in an appropriate manner, to fully display the implications of the analysis. *Graphical* tools allow the *results of the analysis* to be interpreted.

14.5.1 Axisymmetric vs. Plane Strain 2D Model

When building a 2D model, there are two different options: it can either be an axisymmetric or a plane strain model. Such 2D models in FEM modeling are most

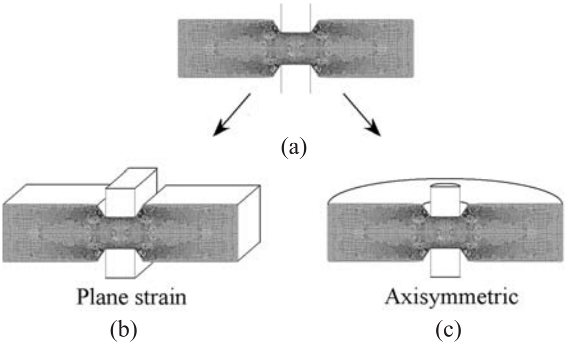

Figure 14.2. Even though plane strain compression and axisymmetric compression are visualized the same way in DEFORM-2D, they are completely different forming processes.

commonly visualized by showing a cross section of the model. In Fig. 14.2, a case is shown in which a punch compresses the midregion of a flat workpiece.

As shown in Fig. 14.2(a), visualization is the same in the plane strain and in the axisymmetric case, even though the metal forming operation that is simulated is totally different in the two cases; see Fig. 14.2(b,c). The plane strain model corresponds to traditional plane strain compression; the axisymmetric model is significantly different, in that it models the penetration of two round punches into a round plate.

EXAMPLE 14.1: 2D ISOTHERMAL FEM MODEL

Problem: How would you build a FEM model of the plane strain compression process in the Deform-2D software? The model should mimic forming of an Al alloy at room temperature. Discuss the approach of modeling with respect to

- reduced model size due to process symmetry
- an isothermal – or eventually thermally coupled – FEM model
- a stepwise simulation procedure

Solution: Because the 2D FEM program contains a geometrical modeling unit, the required die and workpiece geometry can easily be built in the preprocessor. When this is done, a longitudinal cross section of the model is visualized on the computer screen, as shown in Fig. 14.3(a).

Because of symmetric conditions, it is not required to build the full model of the compression test. With symmetry around both the x- and the y-axis, it is sufficient to create one-fourth of the longitudinal cross section of the specimen and the upper die; see Fig. 14.3(a,b). Then by applying the mirroring option of the FEM program, a full view of the process can be shown in the postprocessor; see Fig. 14.3(c,d). In real life, the workpiece will, of course, also have extension in the depth direction, i.e., into the plane of the page. To visualize the depth of the process, the 3D sketch of the simulation model shown in Fig. 14.3(e) was made.

Because the purpose is model forming of an aluminum alloy at room temperature, it is sufficient to apply an isothermal model, i.e., to neglect thermal

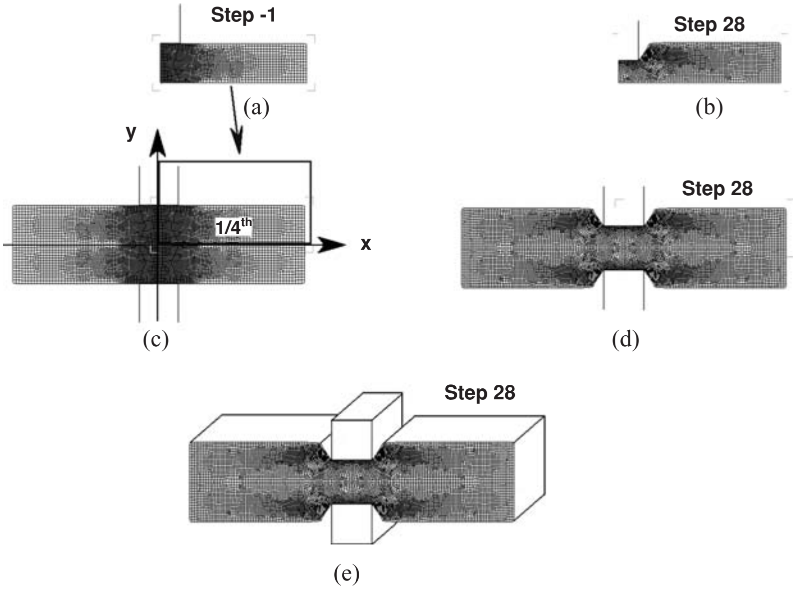

Figure 14.3. 2D FEM model of plane strain compression: one-fourth of the process at (a) initial stage and (b) final stage. (c,d) Full model after mirroring. (e) Schematic 3D view of model.

effects in the process. Then it is not required to apply a FEM mesh on the die. The surfaces of the tooling can be modeled simply by lines; see Fig. 14.3.

The simulation model imitates the forming process in a stepwise manner. A compression velocity must be specified for the die. A step length must be specified for each simulation step also. Displacement steps are specified as either length or time increments. A total number of displacement steps for the whole simulation is also specified.

14.5.2 Isothermal vs. Thermally Coupled FEM Models

In cold metal forming processes, conducted at room temperature, thermal effects are moderate and can often be neglected, as explained in the beginning of Ch. 3. Then it is sufficient to build an *isothermal model* of the actual process. As was shown in Fig. 14.3, the die then can be represented in a simplified manner, by specifying only the bounding lines of its surface. It is not required to apply a FEM mesh to the die.

However, in hot metal forming operations, thermal effects are of great importance, and accurate models can only be made if thermal effects are included. In a *thermally coupled simulation*, the heat generation inside the deforming workpiece and heat exchange to the surroundings (dies and atmosphere) are computed. It is then required to apply a FEM mesh to the die.

A room temperature FEM model of plane strain compression of an Al alloy, which includes thermal effects, is shown in Fig. 14.4. As depicted in this figure, a strong temperature increase is predicted inside the workpiece in this forming operation. But because the flow stress is not much affected by heating of the workpiece material up to a temperature of (say) 100°C, temperature effects on loads and stresses are modest and can be neglected without much error.

However, if an accurate analysis is required, thermal effects should also be included in cold-forming applications. This is especially important if the forming is rapid and if there are large deformations in the specimen, because there will then be larger local temperature rise.

In plane strain compression of an aluminum alloy, as Fig. 14.4 depicts, heat effects are predicted to be largest in the shear cross formed in the material, inside the compression gap, as well as in the material flowing over the sharp edge of the die. Heat transfer to the die, however, is predicted to be rather modest.

One should be aware that industrial forming is usually done repeatedly, so the tooling heats up gradually, from room temperature in the beginning of the process, to a stable elevated temperature after a number of pieces have been shaped.

14.5.3 Material Behavior

In many metal forming applications, one can consider the die as rigid and the workpiece material as rigid–plastic, and this approximation will suffice to get models that mimic the real processes with good accuracy. For instance, the FEM model used to model plane strain compression and to compute thermal conditions, in connection with simulation results shown in Fig. 14.4, was based on this material description. But in other applications, it may be required to apply other material descriptions. The DEFORM software has, for example, the capability of choosing different material behavior – rigid, plastic, elastic, elastic–plastic, or porous.

In case of forming sheet metal by bending, the workpiece will be subjected to *elastic springback* when the bending load is released, as shown in Fig. 24.4(a). The springback is caused by elastic stresses present in the thin elastically bent midlayer of the sheet. These elastic stresses can be said to counteract the bending process, and they cause the specimen to bend back when the load is removed. Hence to model the phenomenon of springback, it is required to describe the full elastic–plastic behavior of the bending specimen. The application of this type of material description is dealt with in more depth in Ch. 25 available at www.cambridge.org/valberg.

14.5.4 Material Models

To be able to perform a simulation, it is necessary to specify to the FEM program the flow curve of the workpiece material being used. Different material models were dealt with in the treatment in Ch. 8. FEM codes have options by which one can specify, in a simple manner, a particular material model, as, for instance, by choosing a power-law material and then typing in the actual K and n values for the selected material.

If the workpiece material is characterized by flow stress data that do not agree well with common applied material models, there is commonly the possibility to

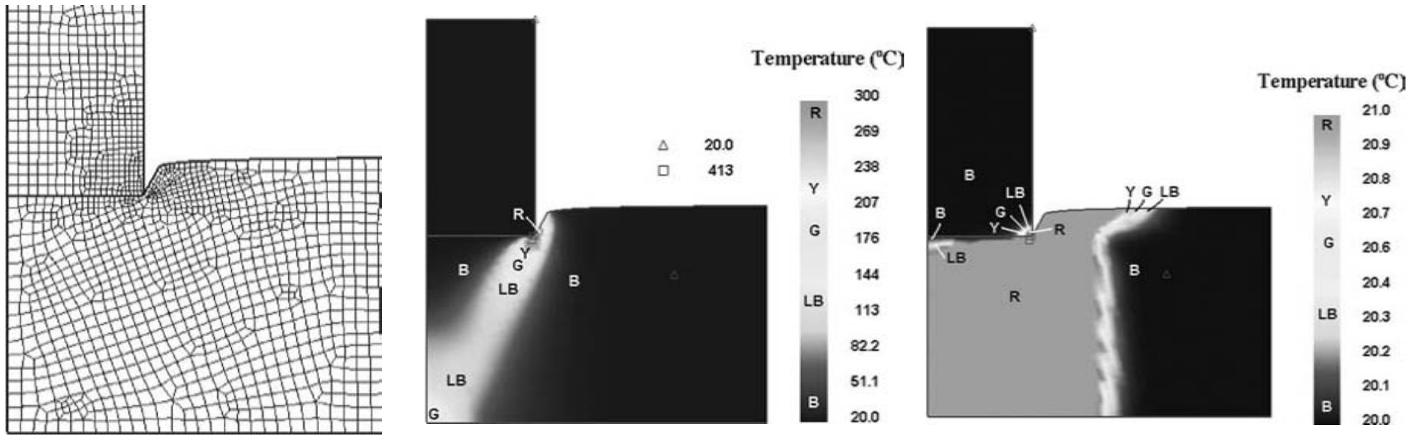

(a) (b) (c)

Figure 14.4. Temperature rise predicted in plane strain compression of Al alloy: (a) FEM mesh; (b,c) computed heating effects shown with different temperature scales.

specify the function $\sigma = f(\varepsilon, \dot{\varepsilon}, T)$ in terms of the flow curves themselves, whereupon the FEM program performs interpolation between given data. A plot of given values can also be provided by the program, and this plot in principle corresponds to the graph shown Fig. 8.2.

14.5.5 Friction Models

Commonly applied friction models in metal forming were discussed in Ch. 10. Tailor-made FEM programs for metal forming have the option to choose either the Tresca or the Coulomb friction model and then to specify a numerical value of the friction parameter, i.e., the value of m or μ. Different friction values can also commonly be specified for different dies, and even on different parts of the surface of one particular die.

14.5.6 Obtaining Postprocessing Results

When the FEM model has been made by means of the preprocessor, and simulation has been run by the FEM engine, the results are stored by the program. The postprocessor allows these data to be analyzed by the user. Most commonly, one wants to view *graphical representations* of the results, as, for instance, the temperature *distribution*, as shown in Fig. 14.4. The postprocessor has options by which data can be represented this way in a simple manner. Alternatively, data can be taken out as numerical values for users to make their own graphs. In that case, simulation results, together with corresponding experimental or theoretical results, can be plotted in the same diagram; see, for instance, Fig. 10.12 and Fig. 15.1(a). A large number of different simulation data are then available. In Fig. 14.5, this is shown by means of the postprocessor's selection menu in the current version of DEFORM-3D.

14.6 FEM Model of Cylinder Compression

In Ch. 13.2, theory based on the slab method was used to obtain the pressure distribution between the compression platen and the cylinder. In the case of Tresca friction, this pressure distribution is shown in Fig. 13.2, and the equation for this distribution is given by eq. 13.7.

Let us now compare such slab method predictions regarding the pressure distribution with corresponding predictions obtained when using FEA. Consider two different cylinder geometries with two different aspect ratios. In addition, consider a low and a high level of Tresca friction, as specified in Table 14.1. Assume the cylinder to be of ideal rigid–plastic material with a constant flow stress of 200 MPa.

The two FEM models built in this connection are shown in Fig. 14.6, where one-fourth of the FEM mesh has been mirrored three times to show the full longitudinal section of the cylinder.

Results as regards the FEM-simulated pressure distribution, and the corresponding pressure prediction from the slab method, are shown in Fig. 14.7. This is the pressure immediately after the start of compression.

Table 14.1. *Cylinder compression data*

Cylinder no.	Initial radius (mm)	Initial height (mm)	Aspect ratio	Tresca friction factor
1	10	5	0.5	0.1
2	10	5	0.5	0.4
3	10	2	0.2	0.1
4	10	2	0.2	0.4

As Fig. 14.7 depicts, the slab method predicts a pressure at the edge of the cylinder that is always equal to the flow stress, whereas simulation predicts higher pressure there. As shown later in connection with Fig. 15.13, the increased pressure at the edge of the cylinder in the simulation model is due to the presence of a

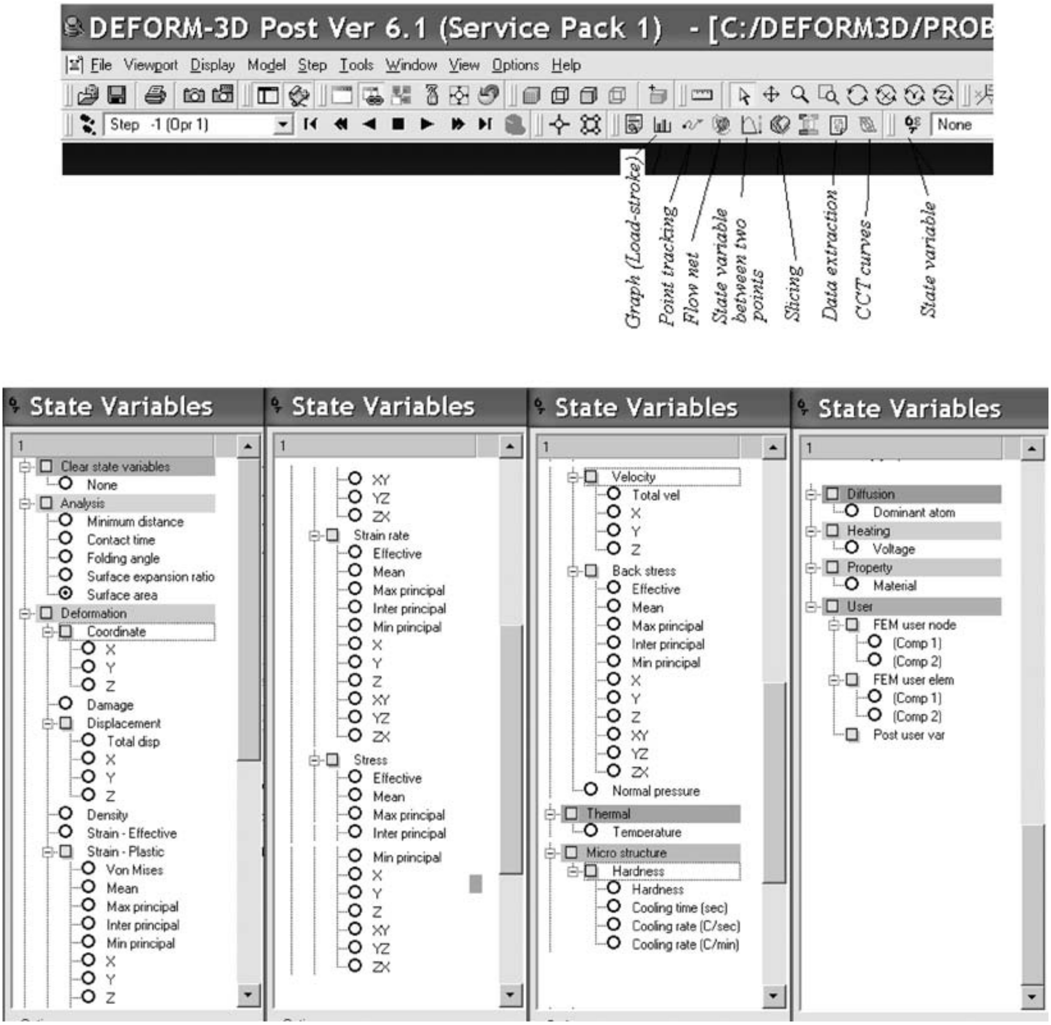

Figure 14.5. Postprocessing results that can be obtained in version 6.1 of DEFORM-3D.

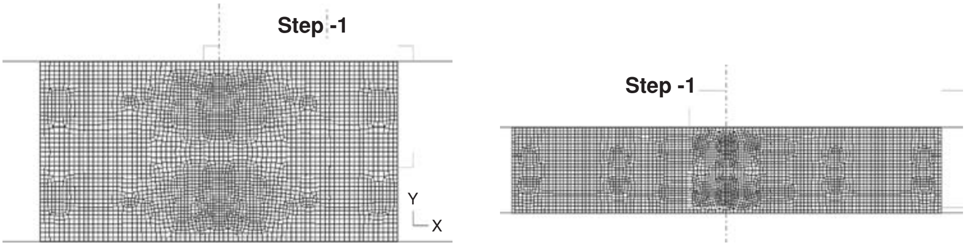

(a) (b)

Figure 14.6. Isothermal FEM model of cylinder compression: FEM mesh for (a) aspect ratio 0.5 and (b) aspect ratio 0.2.

complex mode of deformation at this edge. When the slab method is used, however, ideal homogeneous deformation is assumed, i.e., an initial slab element remains perfectly rectangular after deformation.

Toward the center of the cylinder, the slab method predicts significantly increased pressure in terms of a straight-line friction hill. Moreover, change in the process parameters, such as increased friction or decreased aspect ratio, increases the contact pressure in the center.

In the case of low friction ($m = 0.1$), the simulation model also predicts linear pressure buildup toward the center of the specimen. But for the high-friction simulation ($m = 0.4$), there is first increased pressure from the edge toward the center, but then in the midregion of the cylinder, there is predicted a strong pressure drop.

The high pressure toward the center of the cylinder is always predicted much less by the FEM model than by the slab method. The difference also becomes more pronounced when the aspect ratio is decreased from 0.5 to 0.2. The reason for the difference in predictions seems to be as follows: The slab method is based on both the assumption of idealized homogeneous deformations in the specimen, and that the principal stresses are directed either in the compression

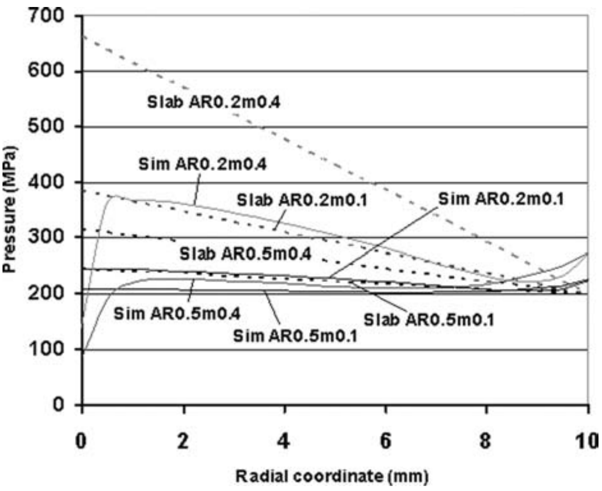

Figure 14.7. Comparison of predicted pressure distributions in cylinder compression for slab method and DEFORM-2D simulation model.

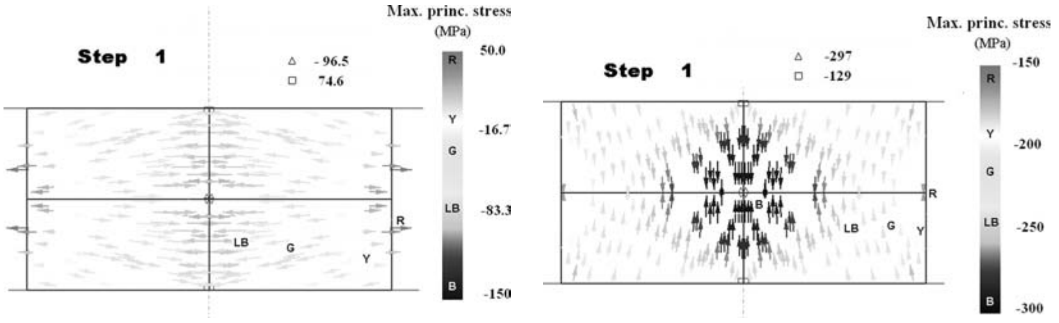

(a) (b)

Figure 14.8. Vector plot of largest and smallest principal stress components as predicted by FEM simulation in cylinder compression for AR = 0.5, $m = 0.4$.

direction or orthogonally to this direction; the FEM does not assume such idealized conditions.

Simulation results are shown in Figs. 14.8–Fig. 14.10 for cylinders with aspect ratios 0.5 and 0.2, respectively, compressed with the friction factor $m = 0.4$. The figures show that the assumption regarding the direction of principal stresses is wrong. Neither is the assumption of homogeneous deformations correct, for – as shown in Fig. 14.10 for $m = 0.4$ – a characteristic dead zone will appear at the center of the specimen, as previously explained in connection with Fig. 7.11. The presence of this dead zone seems, as shown by the pressure distributions in the graph of Fig. 14.7(c), to be the reason simulation predicts a pressure drop toward the center of the specimen. In the effective strain rate distributions shown in Fig. 14.10, the dead zones are visible.

To conclude, the FEA of cylinder compression predicts the pressure buildup from the edge toward the center of the cylinder to be considerably less than in a corresponding slab method analysis. Besides this, pressure buildup depends on the

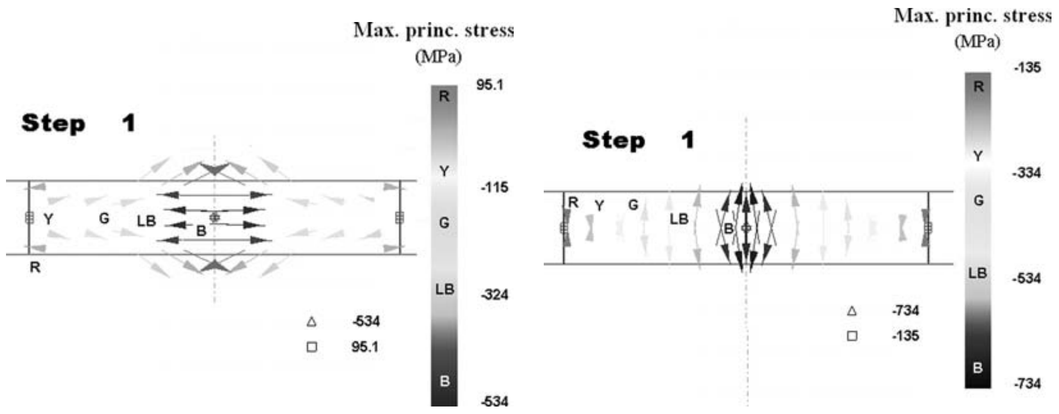

(a) (b)

Figure 14.9. Vector plot of largest and smallest principal stress components, as predicted by FEM simulation in cylinder compression for AR = 0.2, $m = 0.4$.

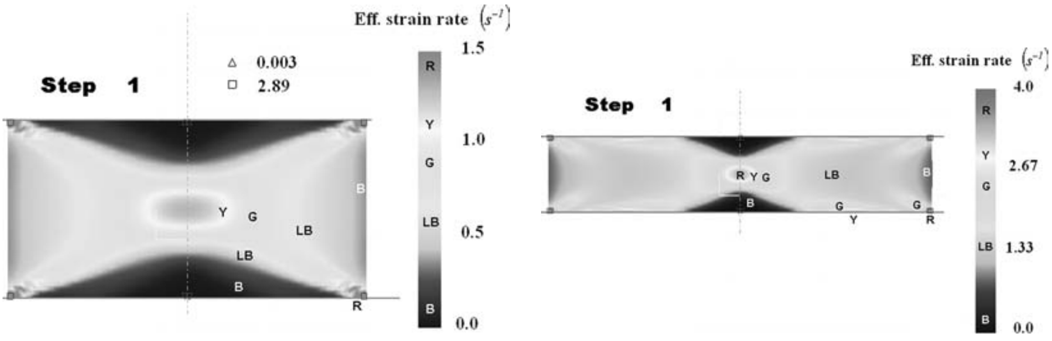

(a) (b)

Figure 14.10. Effective strain-rate distribution inside cylinders of different aspect ratio in compression as predicted in FEA with $m = 0.4$: (a) AR = 0.5 and (b) AR = 0.2.

proportions of the cylinder (the aspect ratio). Although the pressure buildup is modest when the aspect ratio is 0.5 or larger, there is a significant pressure effect when the aspect ratio is decreased to 0.2 or lower.

14.7 FEM Model of Extrusion Welding

It is often recommendable in metal forming to use 2D in combination with 3D FEM models to gain knowledge about the mechanics of a forming process. Use of this analysis strategy will now be shown in the case of *extrusion welding*. The main advantage of the 2D model is that it requires less computation time than the 3D model. The 3D model of a forming operation may require a great deal of CPU time.

A simple tool configuration for study of the mechanics of hot extrusion welding has been applied in the author's laboratory. A 3D and a 2D DEFORM model of the process were also built. Figure 14.11 shows pictures from the 3D FEM model. As depicted, the model consisted of one-fourth of the extrusion process. Because of symmetry, this was sufficient. The full process can be shown by the simulation program by use of the mirroring option. The extrusion material was a commonly used AA 6082 alloy.

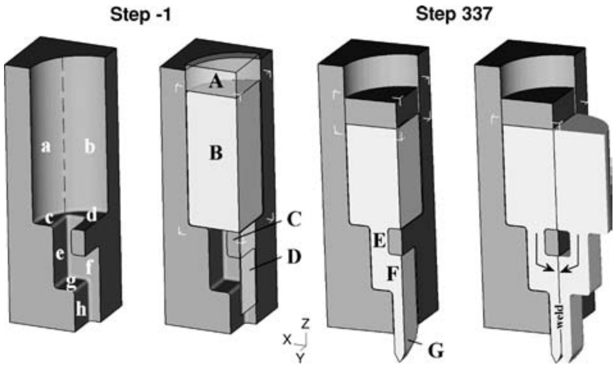

(a) (b) (c) (d)

Figure 14.11. Tool configuration and metal flow in idealized extrusion welding: (a) model of tooling, (b) initial state before extrusion, (c) model after the profile has been created, and (d) mirrored version of (c) showing half the full geometry.

As shown in Fig. 14.11(a), a simplified tool arrangement was applied in the FEM model. The extrusion die, the die bridge, and the container were modeled as one piece, though in reality they consisted of three different tool elements. Figure 14.11(b) shows the initial situation before extrusion is performed in the tooling. The billet (B) is then located inside the container, and the ram head (A) is in a position where it touches the back end of the billet. To get correct simulated metal flow behind the die bridge (C), a virtual frictionless die (D) was modeled here. Figure 14.11(c) shows the process at a partial extrusion stage, when the metal has filled the porthole (E) and the welding chamber (F) of the die. At this instant, a short extrudate (G) has emerged behind the die.

To show how extrusion welding occurs, one can apply the mirroring option to visualize half the extrusion process, as shown in Fig. 14.11(d). Here one can see that one metal stream, flowing through one porthole channel of the die, encounters another metal stream flowing through the other porthole channel, so that the two streams join on the rear end of the die bridge. A bridge with a butt-ended shape is shown in the model, but in reality, it is more common to use a bridge with a pointed back end.

Pressure builds up between the two metal streams when they encounter each other in the weld chamber. Because of this, a pressure weld is formed over the symmetry plane when they meet; see Fig. 14.11(d).

Extrusion welding is used in the industry to create *hollow extrusions*, as, for instance, tubes[4]; see the explanation in connection with Fig. 2.7. From an industrial viewpoint, the extrusion process depicted in Fig. 14.11 has no relevance, for the final extruded profile can be obtained much more simply by use of a standard flat-faced die with a rectangular hole. However, this idealized extrusion process is useful for research purposes, in that it represents the simplest way by which an extrusion weld can be made. In addition, the process is close to plane strain extrusion.

To obtain ideal plane strain extrusion in this die, some tool surfaces need to be fully lubricated, namely, surfaces b–f and part of surface d; see Fig. 14.11(a). Concurrently, one must maintain high friction on other surfaces: a, c, e, g, and part of h. Use of a container with a square hole and a billet with square cross section would also be required. To lubricate some surfaces, but not all of them, is extremely difficult in practice. Lubricants applied tend to spread out when extrusion is performed. Because of this, it is instead recommended to run the experiment without lubrication and use the 3D FEM model of the process to map 3D effects present in the experiment. In this way, one can map errors introduced when assuming the process to be ideal 2D.

Figure 14.12 shows predicted effective strain rates in the 3D FEM version of this extrusion process. In this simulation model, the friction between the billet material and the ram head was specified to be $m = 1$, while friction between the billet material and the rest of the tooling was set equal to $m = 0.5$. Figure 14.12 depicts the metal flow under these conditions, during the sequence consisting of filling the die completely with metal, and afterwards when a short extrusion is obtained behind the die.

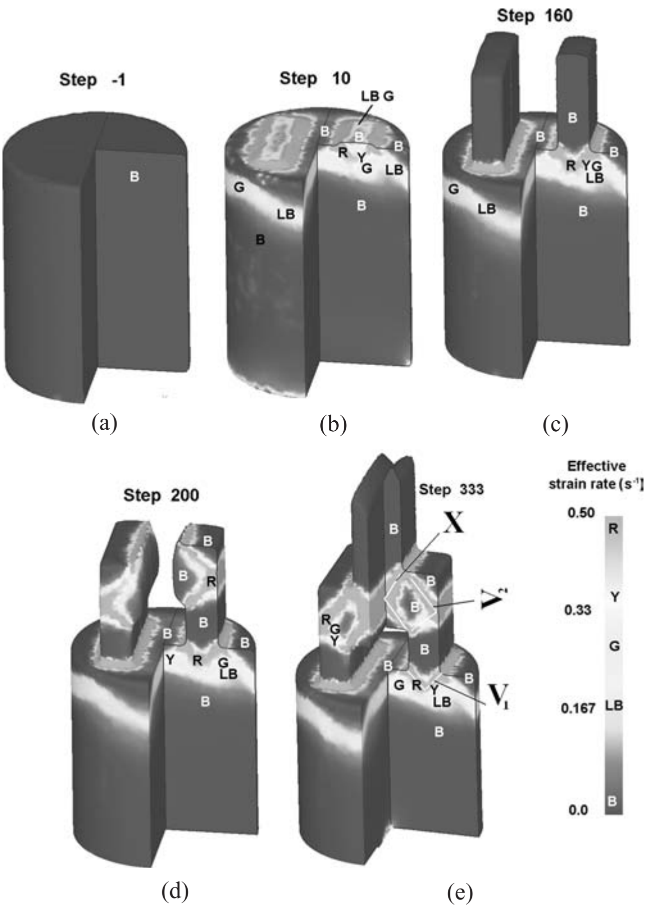

Figure 14.12. Metal flow in idealized extrusion welding visualized by effective strain-rate distribution computed by FEM model.

The first part of the extrusion process corresponds to *two-hole extrusion* of two rectangular sections; see Fig. 14.12(a–c). During this stage, the material deforms in the primary deformation zone ahead of the flat-faced die, with highest intensity of deformation in a V-shaped shear band (v_1) above each hole. In addition, dead zones appear in front of the die bridge and in the corner between the die and the container. As Fig. 14.12(d) shows, when the two rectangular sections flowing forward inside the porthole channel reach the flat bottom face of the die, there is a change in the mode of deformation. A new V-shaped shear band (v_1) now appears inside the material in the porthole channel, as the material starts to flow laterally into the weld chamber; see Fig. 14.12(d). The metal streams from each porthole now encounter each other and join into one metal stream, which flows out through the exit of the die, where it appears as the final extrusion; see Fig. 14.12(e). The two previously mentioned shear bands are maintained, but now an additional deformation cross (X) appears in the material in the middle of the weld chamber of the die.

As shown in Fig. 14.13, the material flow in the die is very complex. Inside the container volume, there is flow parallel to the container wall toward the die.

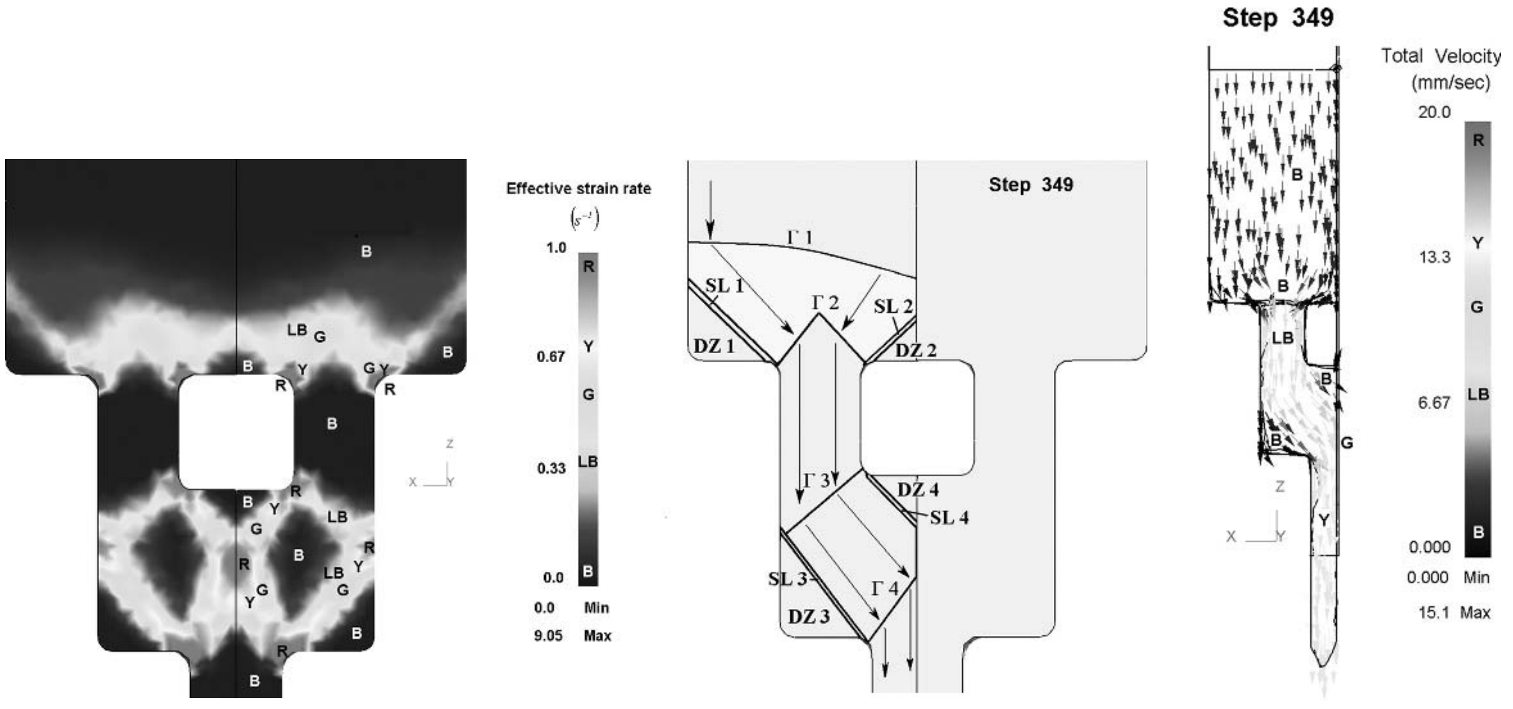

(a) (b) (c)

Figure 14.13. Material flow in extrusion welding predicted in 3D simulation model: (a) effective strain-rate distribution, (b) flow field, and (c) velocity field.

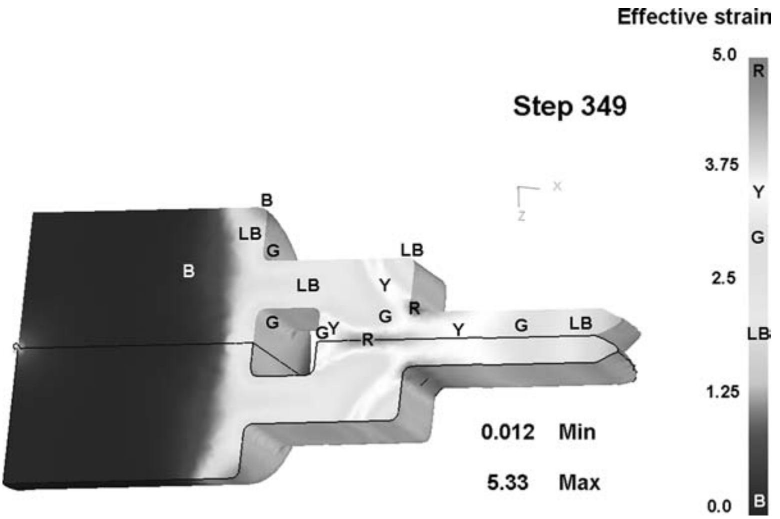

Figure 14.14. Deformations in the pressure welding zone from the 3D model.

Then, ahead of each porthole channel, a primary deformation zone appears. In an idealized model, particle paths in this zone are commonly assumed to be straight lines, as drawn in Fig. 14.13(b), with a velocity discontinuity line at the entrance into the primary deformation zone (Γ1). But as shown in Fig. 14.13(c), in the simulation model the streamlines are predicted to have curvature. Inside the porthole channel the metal flow is mainly a rigid-body movement, with a V-shaped velocity discontinuity (Γ2) at the entrance to the channel, and a velocity discontinuity line (Γ3) at its outlet.

In the space behind the die bridge, there is another zone of mainly rigid-body movement, bounded by a new velocity discontinuity line (Γ4). Behind this line the final extrusion moves vertically downward as a rigid body. Altogether four dead zones are predicted in the die, as shown in Fig. 14.13(b). In this figure, they are denoted DZ 1–4. Inside the dead zones, the flow velocity is very low compared to that in the interior of the metal streams; hence, there are pronounced shear bands in the boundary layers between the dead zones and the main metal stream. In Fig. 14.13(b) these shear bands have been indicated by double lines.

As shown in Figs. 14.12 to 14.14, the 3D simulation was ended after extrusion of a short piece of metal. This was due to the large computation time needed to run the simulation. The 2D simulation model, however, requires considerably less CPU time, and was run until all the billet material had been completely squeezed out of the container.

An experiment[5] was run in which metal flow was investigated by means of the grid pattern technique described in Sec. 12.1.2. Figure 14.15(c) shows the resulting deformed stripe pattern obtained in this experiment. The same pattern was created in the 2D simulation model,[6] to check whether there is good agreement between experimental and simulated metal flow. The initial grid pattern is shown in Fig. 14.15(a). The deformed grid pattern obtained in simulation, at approximately

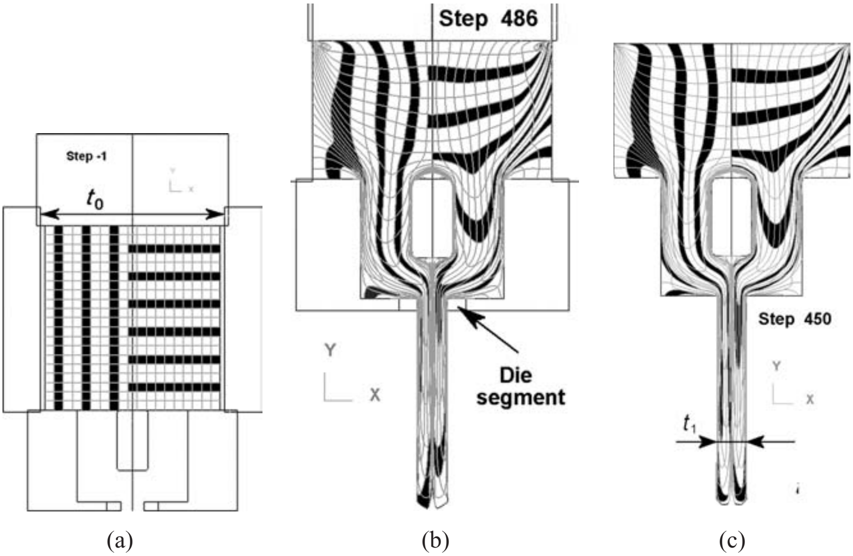

Figure 14.15. Comparison of 2D simulation model and experiment: (a) FEM model with initial grid pattern, (b) simulated grid pattern after partial extrusion, and (c) experimental grid pattern.

the same stage of extrusion as in the experiment, is shown in Fig. 14.15(b). When the two patterns are compared, one can see that there is good agreement between them. Thus, it seems convincing that metal flow in the 2D simulation model is close to the real flow in the experiment.

Because of long computation time, the 3D simulation model was stopped early, and it only reveals the deformations in the start-up phase of the process; see Fig. 14.14. However, the two-dimensional FEM model of the extrusion welding process was used to determine the deformations obtained in the material in the whole extrusion process.

A question of interest is how uniform are the predicted deformations over the cross section and the length of the profile. The results of this analysis are shown in Fig. 14.16 and Fig. 14.17. As Fig. 14.16 depicts, the deformation in terms of effective strain increases over the length of the extrusion, from the front end to the back end, and there is also increasing deformation in the material contained inside the cavities of the die throughout the course of extrusion.

To quantify the deformation gradient over the thickness of the extrusion behind the outlet of the die, as predicted by the 2D model, a row of points were added across the thickness of the extrusion, as shown in Fig. 14.17(b). Then the predicted effective strains across the profile in this location were obtained by means of the point-tracking option of the software at different simulation steps, where step 1600 represents complete extrusion of the billet material, and step 200 is the step when the extrusion has started coming out of the die. The resulting data were used to make an overlay plot as shown in Fig. 14.17(a).

As this figure depicts, there is a large increase in deformation from the front end to the rear end of the profile. In the front end, the effective strains are in the

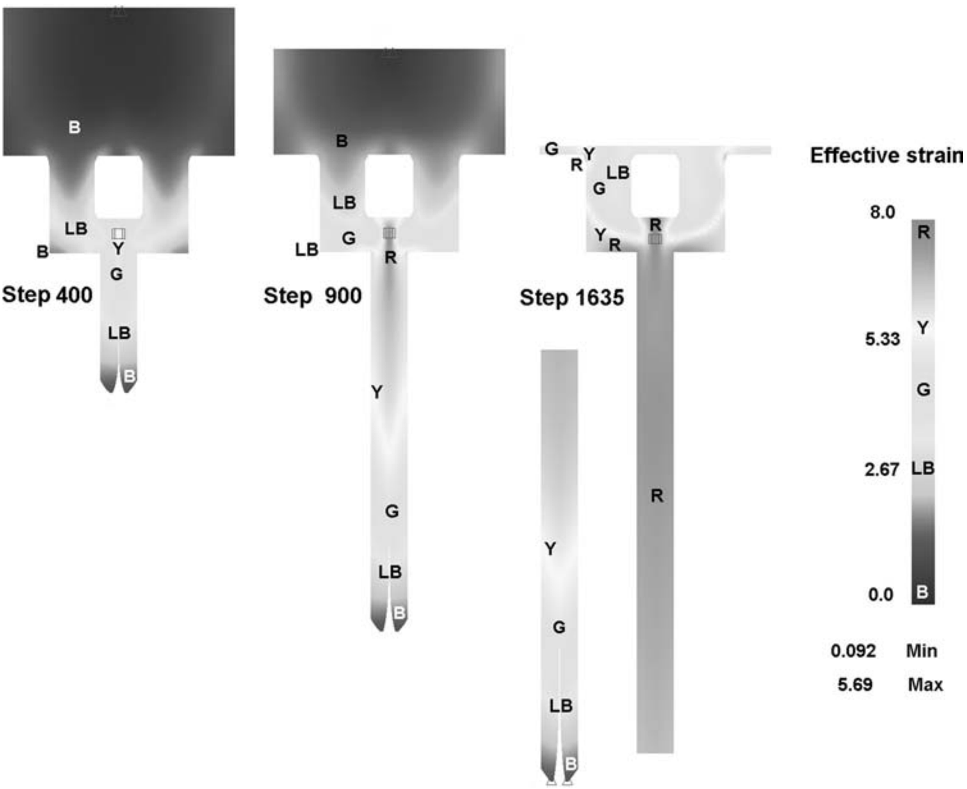

Figure 14.16. Effective strain distribution from 2D model.

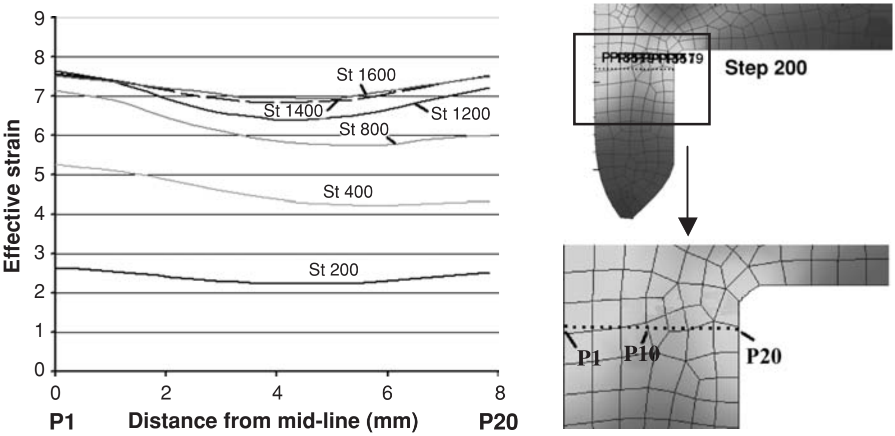

(a) (b)

Figure 14.17. (a) Graph showing predicted effective strain distribution across extrusion at different sections. (b) Location of points used to obtain graph at each simulation stage.

range 2–3; toward the back end of the profile, they are 7–8. Also, the deformations are predicted to be much more uniform over the thickness of the profile than over its length. The largest deformations in the extrusion are predicted for material flowing from the extrusion weld zone into the midlayer of the extrusion, and correspondingly for material flowing out into the outer surface layer of the extrusion. In the layers in between, the deformations are slightly less. An approximate ideal effective strain value in the case of complete homogeneous deformation can be computed by the formula

$$\bar{\varepsilon}_{ideal} = \ln(t_0/t_1) = \ln(100/12.4) = 2.1.$$

Concluding remarks are that deformations are indeed very nonuniform within the resulting extrusion. The front end of the billet flows into the portholes of the empty die without significant deformation, but it deforms much more during flow through the welding chamber out into the extrusion. Hence the effective strain imposed on this material approximately equals the ideal homogeneous deformation value. Material inside the billet, further behind, however, is subjected to larger shear deformations, so that the effective strain values in the rear end of the extrusion are 4–5 times higher than the ideal value.

Problems

14.1 Extrusion welding experiment reproduced in a 2D Simulation Model.

Experimental data: Measured data are available (see homepage of book) from extrusion welding experiments performed in a 2D laboratory extrusion tooling. Data available are the ram load and temperature on the tooling vs. stroke length. In addition, a deformed grid pattern has been recorded at a particular stage of extrusion.

Simulation model: A DEFORM-2D simulation model of the process corresponding to the experiment is available as a keyword file.

Work to be done: Create a new DEFORM-2D model and name it ExtrWeld. Import the keyword file into the preprocessor. Then create a database and run the simulation.

Open the preprocessor, and study how the model has been built. Give a description of the model based on the following keywords: modeling of tooling, axisymmetric or plane strain model, type of workpiece and die objects, friction model/value used, constitutive material model of workpiece material, initial thermal condition of billet, and tooling.

Open the postprocessor, and use it to gain the following simulation data: distributions of effective strain and effective strain rate in the material upon deformation. Use different scaling to depict areas of low and high strain rate. Explain where there are dead zones, deformation crosses, and shear bands. Comment on where inside the extruding material and the rod the largest deformations are.

Use the simulation model to perform a grid pattern analysis corresponding to the experimental analysis. Run the simulation model to a stage of extrusion corresponding to the experiment. Paint black stripes onto simulated pattern to make a pattern corresponding to the experimental one. Comment upon the similarity between experiment and simulation.

Find grid elements about to flow, respectively, out of the container and out of the die exit, at the instant when the deformed grid pattern is recorded. Trace these elements back to their initial positions inside the unextruded billet. This should be done both manually and by use of the software. Insert a grid pattern into the extrusion at end of simulation. Run the simulations backwards to obtain emptying diagrams consisting of T and L lines for the extrusion process.

Report: Report the results obtained in your analysis. Discuss them and present conclusions.

NOTES

1. Uyyuru, R. K.: "Engineering the Friction and Forming Mechanics in Cold Aluminium Forming – Use of Modelling Techniques," Ph.D. thesis, Norwegian Univ. of Science and Technology (NTNU), 2003, pp. 29–42.
2. http://en.wikipedia.org/wiki/Finite_element_method.
3. Strang, G., and Fix, G.: "An Analysis of he Finite Element Method," Prentice-Hall, 1973.
4. Jo, H. H., Lee, S. K., Jung, C. S., and Kim, B. M.: "A non-steady state FE analysis of Al tubes hot extrusion by a porthole die," J. Material Processing Technology Vol. 173, 2006, pp. 223–231.
5. Welo, T, Smaabrekke, A., and Valberg, H.: "Two-dimensional simulation of porthole extrusion," Aluminium, Vol. 71, No. 1, 1995, pp. 90–94.
6. Valberg, H., Abbas, Y., and Moe, P. T.: "The mechanics of two-dimensional aluminium extrusion welding investigated by FEA with experiment," Proc. 9th Int. Conf. Technology of Plasticity, Gyeongju, Korea, 2008.

REFERENCES

Dixit, P. M., and Dixit, U. S.: "Modeling of Metal Forming and Machining Processes: By Finite Element and Soft Computing Methods," Springer-Verlag, 2008.

Kobayashi, S.: "Metal Forming and the Finite Element Method," Oxford Univ. Press, New York, 1989.

Nee, A. Y. C., Ong, S. K., and Wang, Y. G.: "Computer Applications in Near Net-Shape Operations," Springer-Verlag, 1999.

Uyyuru, R. K.: "Engineering the Friction and Forming Mechanics in Cold Aluminium Forming – Use of Modelling Techniques," Ph.D. thesis, Norwegian Univ. of Science and Technology (NTNU), 2003, pp. 29–42.

http://www.deform.com/.

http://www.transvalor.com/forge.php.

http://www.mscsoftware.com/products/superforge_support.cfm?PI=28&Q=396&Z=404&Y=420.

http://www.qform3d.com/en/2.html.

http://www.ansys.com/products/default.asp.

http://www.simulia.com/products/unified_fea.html.

http://www.ls-dyna.com/.

http://www.esi-group.com/products/metal-forming.

15 FEA of Technological Tests

Use of FEM analysis for the study of the mechanics of some important technological test methods will be treated in this chapter. Detailed knowledge of the deforming conditions in such tests is crucial when they are to be used to collect precise material data, such as, for example, flow stress data for a particular alloy.

Tensile testing of round specimens is first considered. FEA predicts nonuniform deformation across the thinnest neck in the specimen, and experimental grid pattern analysis confirms this; the largest deformation occurs at the center of the neck. Thus, in reality one assumption in Bridgman's correction analysis fails. Because of this, for metals exhibiting strain hardening, it can be shown that in tensile testing it is appropriate to perform a larger correction of the flow stress than that proposed by Bridgman.

Cylinder compression testing is then subjected to an in-depth analysis. First, it is shown how experimental grid pattern analysis, supported by inverse FEM modeling, can be used for finding an approximate friction value in the compression test. Thereafter, FEA is used to map internal deformations inside cylinders being compressed with friction, so that overfolding of the side of the cylinder occurs.

After this, the friction effects on the compression load are investigated using FEA. It is shown that friction effects are reduced as the cylinder height is increased. Thus, it can be recommended to use high, slender cylinders in this test (specimens with aspect ratio in the range 1.5–2) when flow stress data are to be collected.

Finally, the deformational behavior of the specimen in shearing is investigated with help of FEA, supported by use of experimental grid pattern techniques. This shows the interesting potential of this method, as a test that creates very high strain and strain rates in the material and at the same time allows flow stress data to be deduced from the load–stroke curve obtained in the test.

15.1 Tensile Testing

The mechanics of the tensile test and use of it to acquire the flow curve of a material were thoroughly discussed in Ch. 7. It is commonly observed that the flow curves obtained in tensile and in compressive testing may differ. After the onset of necking

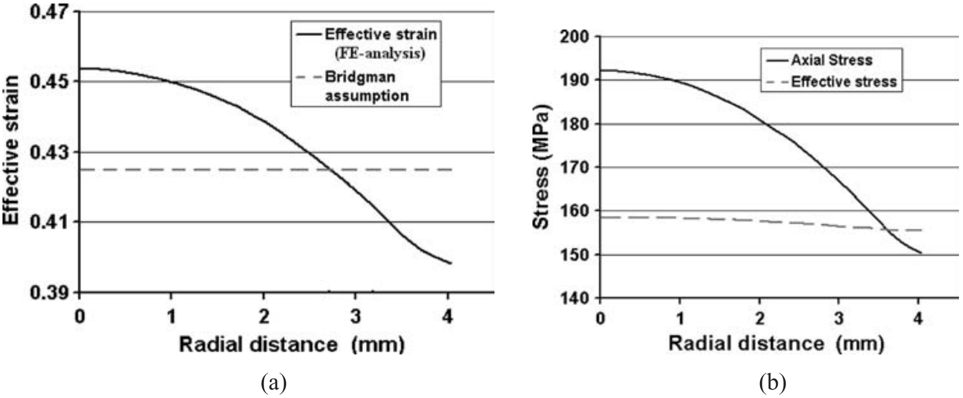

(a) (b)

Figure 15.1. (a) Strain distributions over cross section of neck for soft-annealed aluminum alloy. (b) Stress distributions across neck as predicted in simulation.

in the tensile test specimen, it is common practice to perform a Bridgman correction on the flow stress obtained, as explained in connection with Fig. 7.9. The theoretical analysis performed by Bridgman, which led to the correction procedure, was based on certain simplifying assumptions. If some of the assumptions are wrong, then the analysis is not necessarily accurate.

15.1.1 Bridgman's Analysis of Tensile Testing

When Bridgman performed his well-known theoretical analysis[1] of the stress conditions in the neck during the tensile test, he made some idealized assumptions. One was that the strain distribution over the cross section of the neck is even (given by eq. 7-3). Figure 15.1(a) shows that FEA of tensile testing does not support this assumption. Instead, the effective strain at the center of the specimen is predicted to be larger than the effective strain closer to the surface of the neck. In Fig. 15.1(b), the axial stress and the effective stress distribution are also given as they are predicted in FEM simulation. As this graph depicts, both these stress parameters have higher values at the center of the neck than close to the surface of the neck, a condition that also agrees with results from Bridgman's theoretical analysis.

Another assumption made by Bridgman was that the largest principal stress adjacent the surface of the specimen, in the narrowest part of the neck, is directed parallel to the specimen surface. For a small subsurface material element in the neck, this means that this stress is directed slightly outward in relation to the length axis of the test specimen, as shown in Fig. 15.2 and Fig. 15.3. Figure 15.2 shows that predictions in a FEM model agree well with regard to this assumption.

Because Bridgman's analysis assumes constant straining across the neck, whereas FEM analysis predicts increasing strains from the surface to the center of the neck, a stronger buildup of the axial stress peak at the center of the neck than that predicted by the theoretical analysis is expected. Hence FEA shows that a stronger

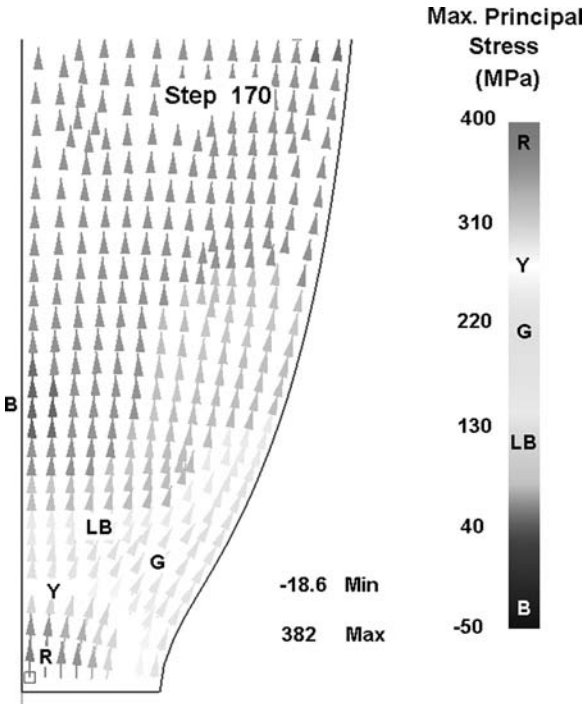

Figure 15.2. Largest principal stress the neck shown by vector plot from 2D FEM simulation.

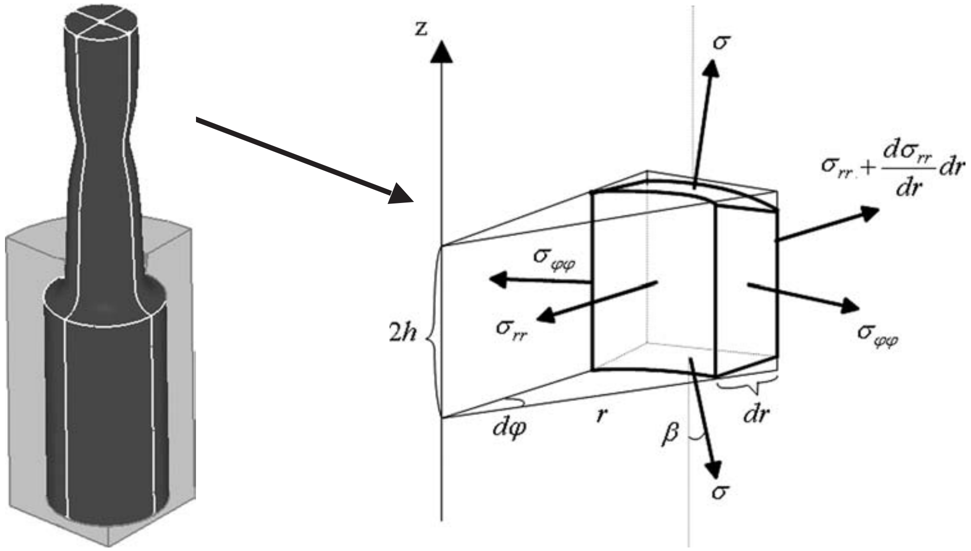
Z
σ
$\sigma_{rr} + \frac{d\sigma_{rr}}{dr}dr$
$\sigma_{\varphi\varphi}$
σ_{rr}
$2h$
$\sigma_{\varphi\varphi}$
$d\varphi$
r
β
dr
σ

(a) (b)

Figure 15.3. Largest principal stress σ on subsurface material element in the neck is directed outward with respect to the axial direction. (a) View of necked specimen from FEA. (b) Stress components on material element adjacent to the specimen surface in the middle of the neck. Courtesy Sigurd Støren, NTNU.

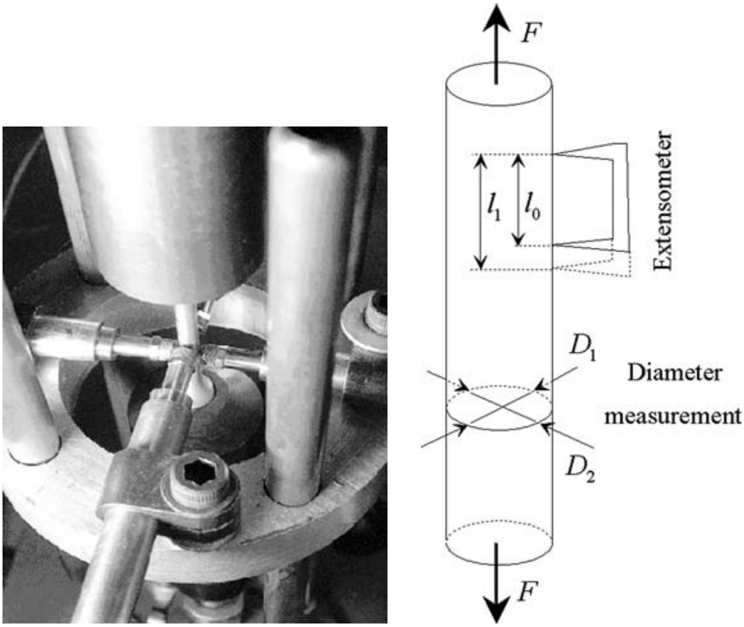

(a) (b)

Figure 15.4. Experimental techniques to measure deformation in tensile testing. (a) Diameter measured by means of inductive transducers. (b) Schematic sketch showing length and diameter measurement.

downward correction of the flow stress than the Bridgman correction is reasonable. How to perform this FEA correction is explained in the next section.

15.1.2 Corrected Tensile-Test Flow Curve Deduced by FEA

An alternative approach by which one can obtain a corrected flow curve in tensile testing is by means of FEA. To obtain the Bridgman-corrected flow stress after the start of necking, it is necessary, during the test, to measure the smallest diameter of the specimen (namely, the diameter at the bottom of the neck), as well as the radius of curvature there; see Fig. 7.9(a).

One way to record this smallest diameter is by the use of four crossing spring-loaded measuring pins connected to inductive transducers. By such equipment, it is possible to measure the displacement of each pin as the test specimen contracts during stretching. The displacements of a pair of pins can then be subtracted from the initial diameter to obtain the current diameter. The measuring principle is shown in Fig. 15.4.

The tensile load is also measured in a tensile test. One can therefore obtain a record of the load vs. the smallest diameter of the specimen. This relationship will appear graphically as shown in Fig. 15.5. If the tensile load is calculated from the primary flow stress or from the Bridgman-corrected flow stress, and the obtained

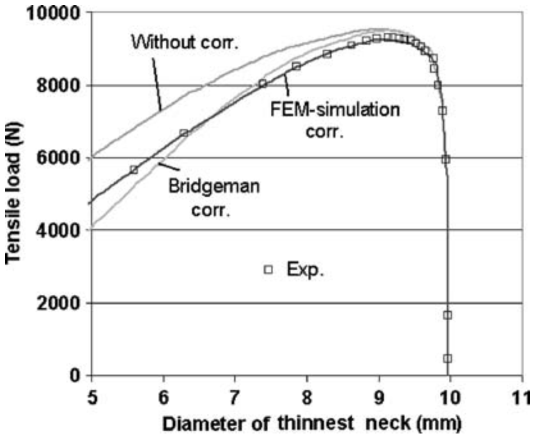

Figure 15.5. Reproduction of experiment by FEA so that simulated load–diameter curve becomes identical to corresponding experimental curve.

load values are plotted on the same diagram, one can see that there is disagreement with the experimental data after the neck has appeared in the specimen.

The experiment can be reproduced in FEA. If then the flow stress input in the simulation model is varied until good agreement is obtained between simulated and experimental data, a FEM-corrected flow curve has then been deduced. This method, when applied to find the flow curve, is called *inverse analysis*, or *inverse modeling*. Use of it to find the flow curve of a metal was explained previously in connection with the discussion of Fig. 3.4. Figure 15.6 shows the result with regard to a flow curve obtained this way by inverse analysis in tensile testing of a soft-annealed Al alloy. The FEM-based corrected flow curve shown in the figure lies significantly below the corresponding Bridgman-corrected curve, which is again significantly below the primary uncorrected flow stress curve.

15.1.3 Experimental Validation of Nonuniform Deformation in the Neck

There could of course be doubt whether there is inhomogeneous deformation over the diameter of the neck in round test specimens as predicted in the FEA

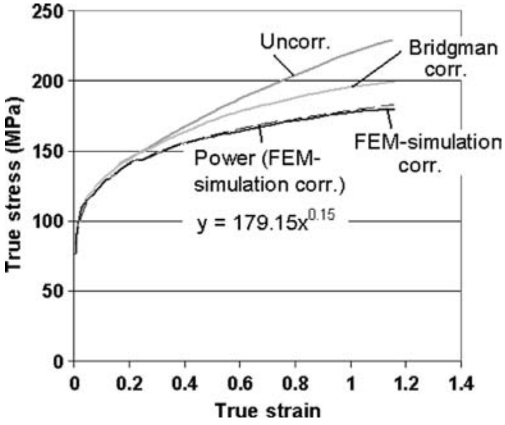

Figure 15.6. Optimum flow curve achieved by means of inverse analysis using FEA.

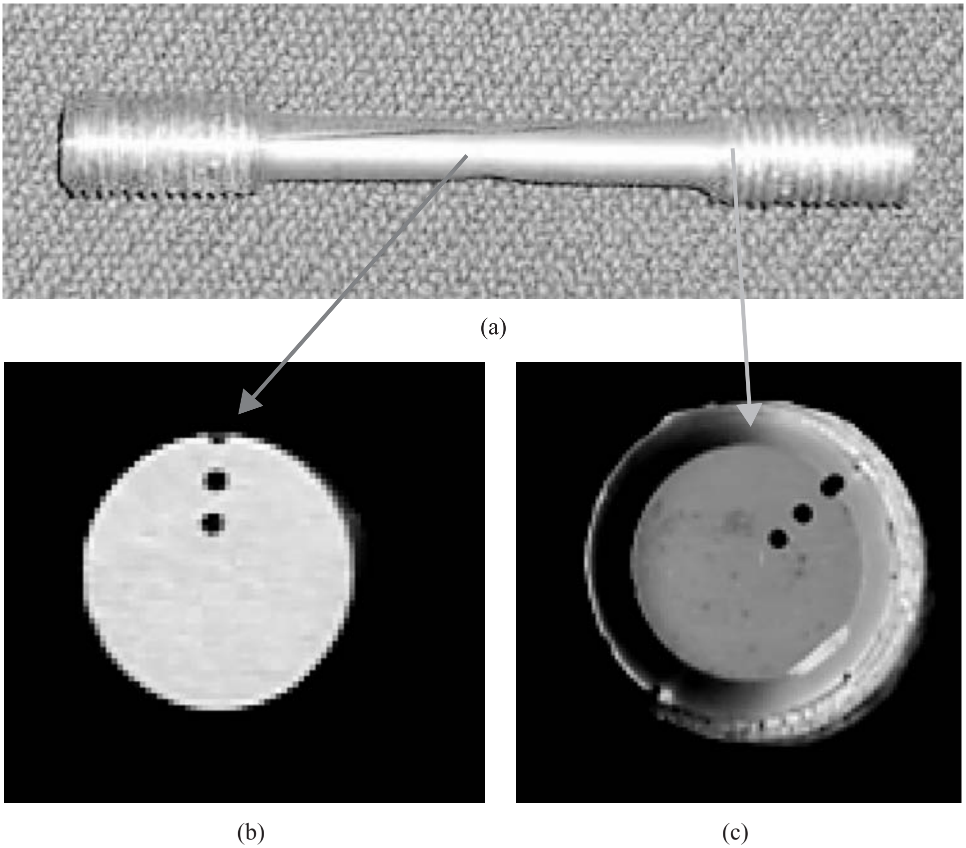

Figure 15.7. Use of visioplastic technique to determine deformations in the neck: (a) necked specimen. Cross sections near (b) the neck, (c) the head of the specimen. The internal indicator pins have been revealed by sectioning and etching.

of tensile testing. This has been checked and confirmed experimentally by use of internal contrast pins inside test specimens, as shown in Fig. 15.7 and Fig. 15.8.

Figure 15.7 shows such a specimen with internal contrast pattern after tensile testing. Two different cross sections were cut through the specimen after the test. A comparison was then made between the initial ring pattern, which remained unchanged inside the head of the specimen, and the corresponding deformed pattern close the middle of the neck. Depths below the specimen surface of each pin, and the pin diameters, were measured in the experiment. Then the optimized FEM model was run, and corresponding patterns were made in the simulation model. This method showed that there is good correspondence between the simulation and experimental results. The experiment hence proves that there are larger deformations at the center than in the subsurface layers of the neck. The predictions in the simulation model have thus been validated.

The photograph in Fig. 15.8 (a) shows the experimental appearance of the pins in a cross section close to the middle of the neck of the test specimen. Figure 15.8(b) and (c) show corresponding simulation results. One can see that there is good

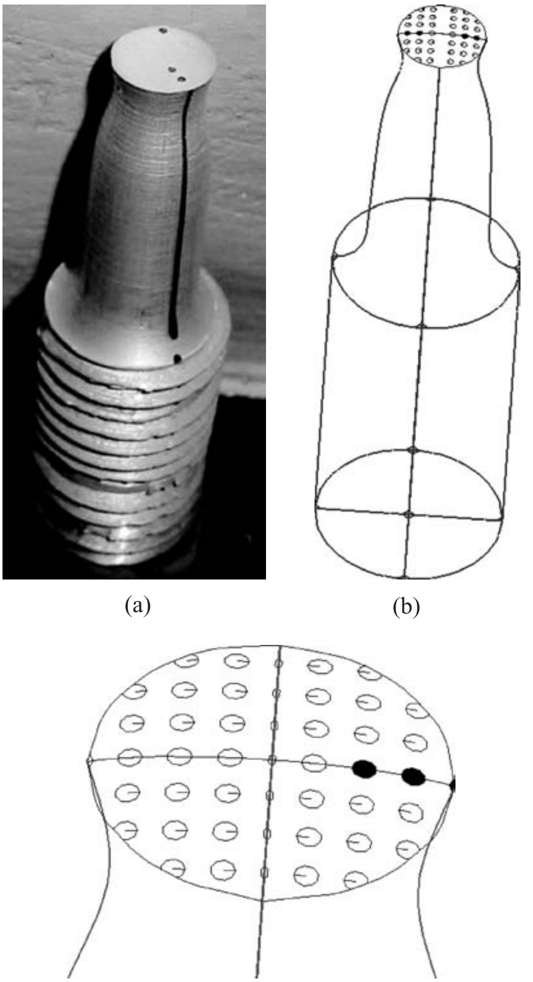

(a) (b)

(c)

Figure 15.8. Corresponding internal ring patterns in experiment and in FEM simulation: (a) sample from experiment with internal contrast pins, (b) corresponding surface ring pattern as in experiment, reproduced in FEA, and (c) detail of (b).

agreement between the appearance of the deformed marker rings in simulation and in experiment. This result was also confirmed quantitatively in the analysis performed.

15.2 Cylinder Compression

The basic mechanics of the frictionless cylinder compression test, and the use of this test to acquire the flow curve of a material, were discussed in Ch. 7. It was also mentioned that the friction between the die and the cylinder would cause barreling of the compressed cylinder, as both ends of the cylinder would expand less in the radial direction than would the middle of it. As a consequence of the bulging, the deformations of the cylinder would become inhomogeneous, and conical dead zones would appear in each end of a cylinder, below each compression platen, as shown in Fig. 7.11(c). Additionally, in connection with Fig. 12.12 it was shown that

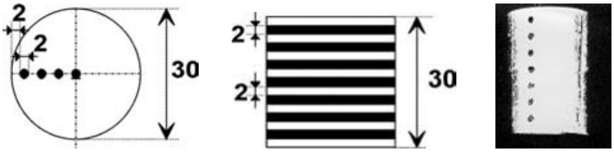

(a) (b) (c)

Figure 15.9. Internal grid pattern made by inserting marker pins into cylinders with initial aspect ratio 1: (a) view of specimen with inserted axial pins from the top, (b) longitudinal section through specimen with radially oriented pins, and (c) photograph of specimen shown in (b).

friction between cylinder and compression platen during the compression stroke can be mapped by inverse analysis based on FEM simulation with the use of marker points (small circles) placed on the end face of the cylinder. Finally, in connection with Fig. 14.7, it was shown that the friction hill effect (increased pressure from edge to midpoint of the surface of contact against the compression platen) is predicted to be much higher in theoretical analysis using the slab method than in FEA.

In the forthcoming sections, FEM simulation combined with grid pattern experiments will be used to further explain the deformational behavior of cylinders compressed between plane-parallel platens for differing friction conditions at the die–workpiece interface.

15.2.1 Compression Experiment with Internal Grid Pattern

Cylinders with internal grid patterns were made using the experimental technique previously described in Ch. 12. The geometrical conditions of the initial pattern are shown in the sketch in Fig. 15.9, where dimensions are specified also. As the figure depicts, the pattern was placed in the axial midplane of the cylinders. The pattern was obtained by drilling axially and radially oriented holes into the cylinders, whereupon pins of marker material with similar flow stress as the matrix material were inserted into the holes. The marker material had chemical composition different from the matrix material, so the pattern could be made visible by sectioning of the cylinders, followed by grinding and chemical etching.

For each lubricant condition, two cylinders were compressed, one with radially and another with axially oriented pins. Compression was done at room temperature, and the final compressed heights of the cylinders were 12 mm. The material of the cylinders was the Al alloy AA 6082 in the soft-annealed condition. A compression velocity of 5 mm/s was used in the experiments.

Deformed grid patterns after the compression test are shown in Fig. 15.10. As this figure shows, there is significant difference in metal flow inside the cylinder when it is compressed with lubricant (a graphite–oil mixture) added between cylinder and compression platens, and when it is compressed in dry friction mode, after cleaning of contact surfaces by a chemical solvent. This difference will be discussed in the next subsection in connection with reproduction of the metal flow in FEM simulation.

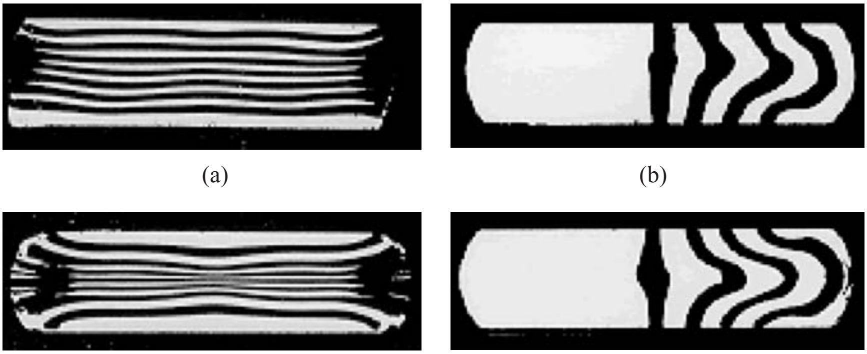

(a) (b)

(c) (d)

Figure 15.10. Deformed grid pattern after compression to final aspect ratio 0.25: (a,b) graphite–oil lubrication; (c,d) unlubricated.

15.2.2 Reproduction of the Cylinder Compression Experiments in FEM Simulation

An isothermal 2D FEM model was created with the same workpiece and die geometry as in the experiments. As explained in Example 14.1, it is sufficient to model one-fourth of the cross section of the specimen. The mirroring option of the FEM program can then be used to visualize the full cross section as shown at the initial stage of the process in Fig. 15.11(a).

The deforming object was modeled as ideally rigid–plastic with flow stress given by a power law (eq. 8-5) with values of constants specified as $K = 197.6$ MPa and $n = 0.178$. The dies were assumed rigid. Friction was modeled as Coulomb friction. Simulations were performed with different values of the coefficient of

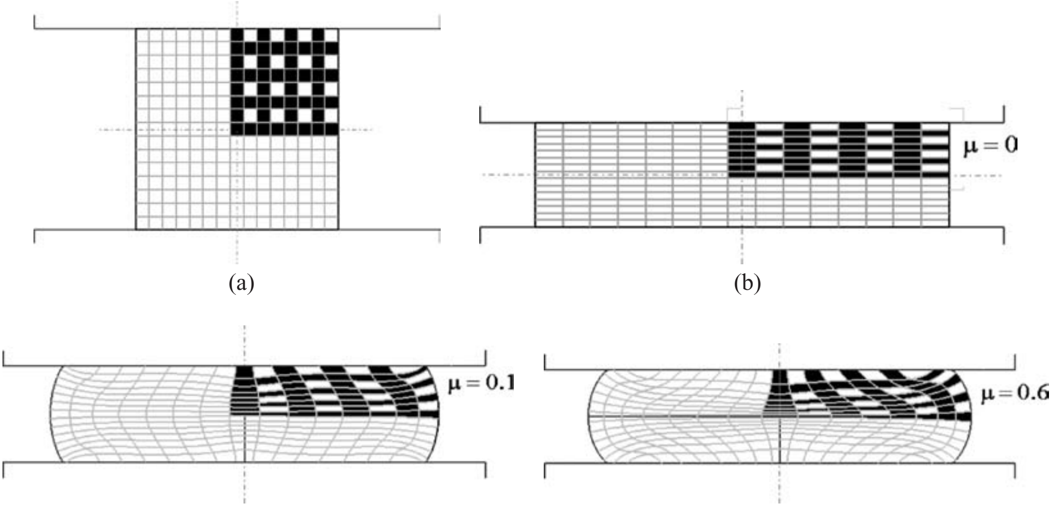

(a) (b)

(c) (d)

Figure 15.11. Deformed grid patterns obtained in FEM simulation: (a) initial pattern; (b–d) deformed pattern for different coefficients of friction.

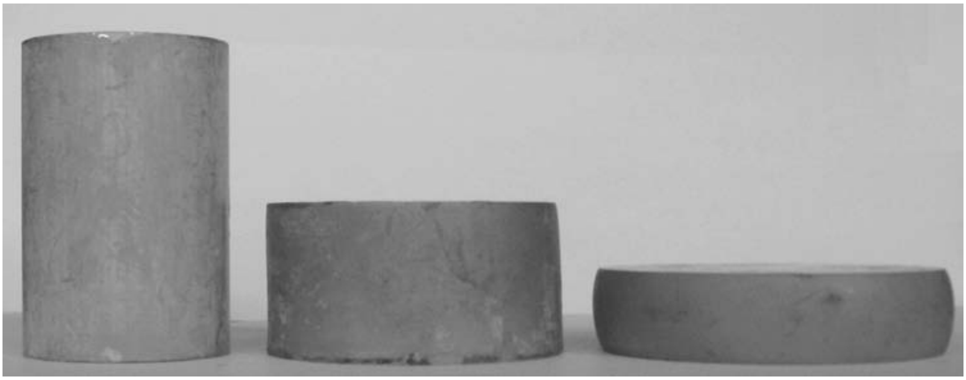

Figure 15.12. Close to homogeneous compression of cylinder in well-lubricated experiment.

friction until the deformed grid patterns obtained in the simulations corresponded reasonably well to those recorded in the experiments. A simulation with idealized frictionless conditions was also run.

The simulation results in terms of the deformed grid patterns for three different friction conditions are shown in Fig. 15.11. In this figure (a) shows the same initial grid pattern as that used in the experiments, and (b), (c), and (d) show final deformed simulated patterns for Coulomb coefficients of friction set equal to 0, 0.1, and 0.6, respectively.

If one now compares the different experimental and simulated grid patterns in Fig. 15.10 and Fig. 15.11, one can see that a friction coefficient of $\mu \approx 0.1$ reproduces the deformed pattern obtained in the lubricated experiment well, but the deformed grid pattern of the dry friction experiment is better described in the simulation where $\mu \approx 0.6$. Hence, as explained in Ch. 3, we have now, by inverse modeling from FEM simulation, approximately determined the friction conditions in the experiments.

15.2.3 Homogeneous Deformation in Cylinder Compression

Special attention should be paid to the deformed grid pattern obtained in the simulated frictionless case of cylinder compression; see Fig. 15.11(b). The deformations of all grid elements are seen to be equal, i.e., all elements in the cross section of the specimen have the same shape after the end of the deformation. Hence the strains over the whole specimen equal the idealized strains in the specimen, given by

$$\varepsilon_r = \varepsilon_\theta = \ln \frac{D_1}{D_0}, \qquad \varepsilon_e = \varepsilon_z = \ln \frac{h_1}{h_0}$$

Close to frictionless compression with approximately homogeneous deformation can, for instance, be realized in cold compression of aluminum cylinders, by using lubrication with a conversion coating. Then, as shown in Fig. 15.12, a cylinder can be compressed in the height direction down to large strains with only a minor degree of bulging; hence deformations inside the cylinder must be approximately homogeneous.

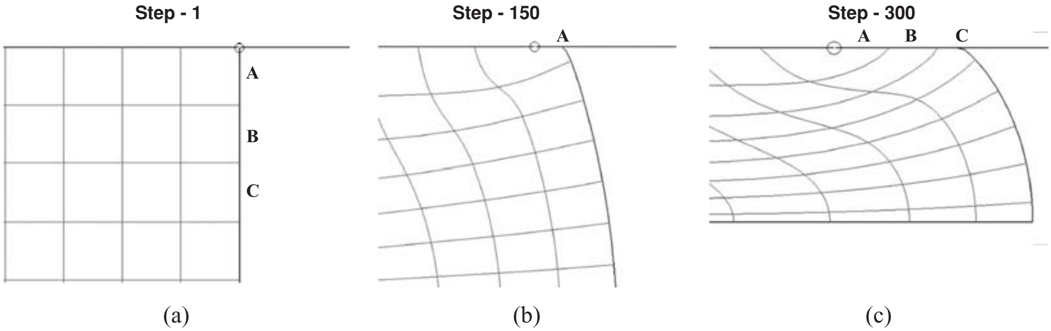

Figure 15.13. Point tracking to follow material flow of initial corner of cylinder (shown by small circle).

15.2.4 Material Flow in the Corner of the Bulging Cylinder

In cylinder compression, a special deformation phenomenon takes place at the corner edge of the cylinder when there is friction against the compression platens. The phenomenon can easily be visualized by FEM simulation, by use of the point-tracking option of the program. Note that the simulation discussed here is the same as the one used to obtain the simulated deformed grid pattern shown in Fig. 15.11(d).

The initial corner of the cylinder can be marked as a material point, whereupon the instantaneous location of this point during compression can be computed and visualized, as shown in Fig. 15.13, where it is indicated by a small circle. In Fig. 15.13(a), the initial location of this corner point is shown. As Fig. 15.13(b) and Fig. 15.13(c) show, this point will not remain on the corner edge of the specimen during compression. Instead, the initially free side face of the cylinder will start to fold over and establish contact against the upper die platen. Because of this, the initial corner point will appear in contact with the upper die platen, at increasing distance from the instantaneous corner edge of the cylinder, as compression proceeds.

Correspondingly, the line segment A, initially on the side of the cylinder, will gradually establish contact with the compression platen during the course of compression. This is due to the phenomenon of overfolding. It proceeds until the whole segment is in contact with the platen. Later during compression, additional line segments, such as B and C, will be folded over in the same way; see Fig. 15.13(c).

The material at the edge of the cylinder will attain large shear deformations during the course of overfolding. This is shown in the FEM simulation picture shown in Fig. 15.14(a). Deformation in this corner region, after some compression (for instance, at step 150), is predicted to be much larger than elsewhere inside the cylinder. The effective strain at the edge is predicted to exceed 0.83, whereas on the axis of the cylinder, adjacent to the compression platen, it is less than 0.17. In the very middle of the dead zone below the die platen it is even lower, close to zero.

Obviously, there is a ring-shaped region of material, adjacent to the current corner of the cylinder, that deforms severely in shear because of overfolding. Because

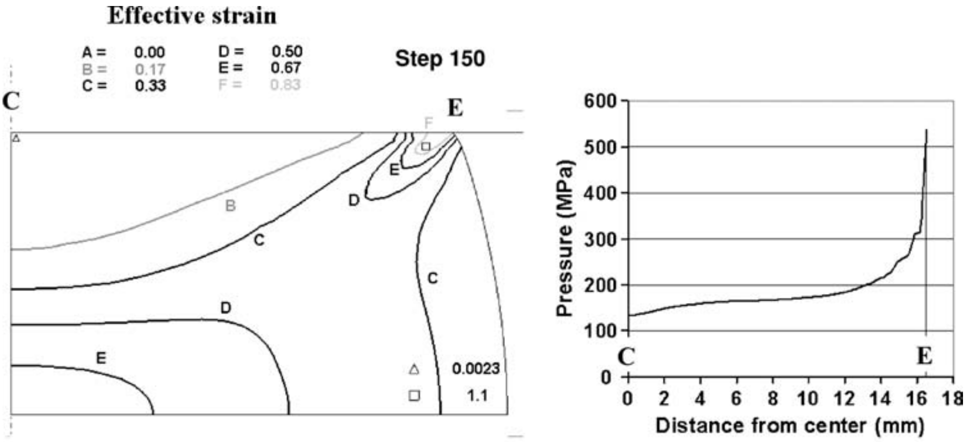

(a) (b)

Figure 15.14. (a) Largest deformation close to cylinder edge due to local overfolding of material. (b) Maximum contact pressure predicted at edge of cylinder.

of strain hardening, this ring becomes harder as compression proceeds. This seems to be the main reason why the simulation model predicts the maximum contact pressure to occur at the current edge of the cylinder in simulation step 150, as shown in Fig. 15.14(b). In addition, the deformations in this region are of complex triaxial character, and this could also contribute to increased contact pressure.

15.2.5 Material Flow Inside the Cylinder

In Ch. 3, it was shown that the deformation in plane strain compression is very uneven over the cross section of the workpiece (inhomogeneous deformation). Moreover, it was shown that shear-band formation occurs in this process and that alternating regions of high and low strain rate are present in the plastic zone. Nonuniformity of deformation was especially evident when the parameter Δ was high. As Δ was reduced from 2 to 1, and then further to 0.5, the deformations became gradually more uniform.

In the following treatment, it will be discussed how FEA predicts the deformations to be in cylinder compression in comparison with plane strain compression.

Predictions of the nature of the deformations inside a cylinder with initial aspect ratio 1, compressed under hot forging of an aluminum alloy, when friction is characterized by $m = 0.2$, will now be considered. The 3D version of DEFORM was used to obtain these results.[2] Figure 15.15 shows the effective strain distribution in the cylinder obtained in this case, and Fig. 15.16 shows the distribution of effective strain rate.

Comparison of Fig. 15.15 with Fig. 3.12(a) and Fig. 3.13(a) shows that even though the geometrical conditions are different in plane strain and cylinder compression, there are similarities with regard to the pattern of straining conditions. In both cases, a deformation cross occurs at an early stage of compression, so that

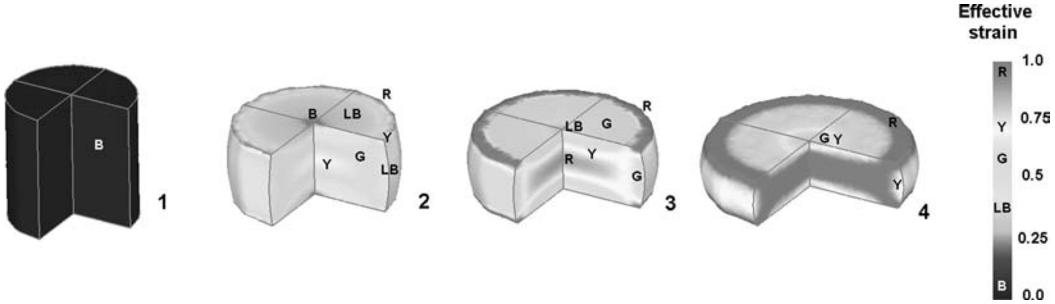

Figure 15.15. FEM-predicted distribution of effective strain in hot compression of Al cylinder.

the largest deformations in the cross section of the cylinder occur in an X configuration. Maximum strain inside the cross is at the center and on the edge of the cylinder. In the middle of the cylinder, adjacent to each die platen, regions of less-deformed material appear as stagnant zones. The unevenness of deformations increases throughout the course of compression, and in the last simulated stage of compression, the effective strain in the most-strained regions is more than double the strain in the stagnant zones.

The differences regarding predicted strain-rate distribution in cylinder compression and in plane strain compression are seen by comparison of Fig. 15.16 with Fig. 3.12(b) and Fig. 3.13(b). In both cases, when the specimen has been reduced sufficiently in height, the pattern of deformation changes. At this stage of compression a set of three deformation crosses becomes visible in the cross section of the cylinder. But because of the rotational symmetry, the deformation cross at each side of the middle cross is in fact the same cross, as it extends in a three-dimensional manner around the periphery of the cylinder. In plane strain compression the situation is different, in that the deformation crosses extend in the depth direction of the specimen, so that each cross always is separate.

Another difference is that in plane strain compression, one deformation cross multiplies into two crosses, and then again into three crosses, as compression proceeds; see Fig. 3.16. In cylinder compression, the intermediate state with two deformation crosses in the cross section of the cylinder does not occur. Instead there is a direct transfer from two [as in Fig. 15.16(a)] to three present crosses [as in Fig. 15.16(b)] during late compression.

15.2.6 Minimizing the Effect of Friction on the Load–Stroke Curve in Cylinder Compression

It was pointed out in Ch. 7 (see Fig. 7.11) that friction effects in cylinder compression increase the required compression load and hence contribute to an overestimation of the measured flow stress in the compression test, if no friction correction is done. In Fig. 14.7, it was shown that the increase in contact pressure toward the center of the interface between the cylinder and the die platen depended strongly on the

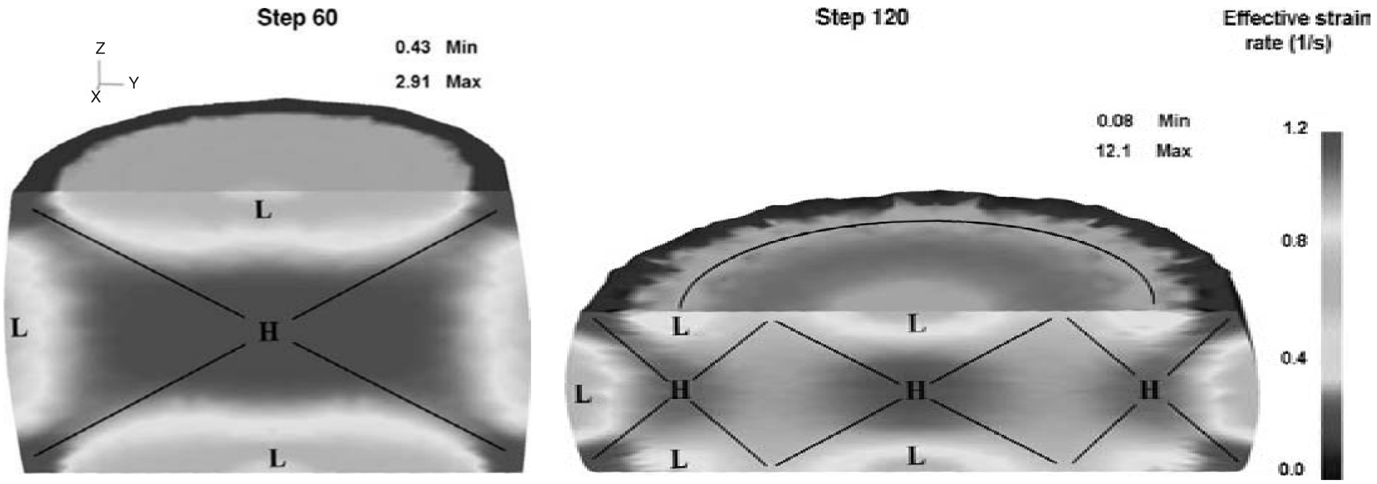

(a) (b)

Figure 15.16. Hot compression of Al cylinder: FEM-predicted distributions of effective strain rate in (a) early and (b) late stage of compression.

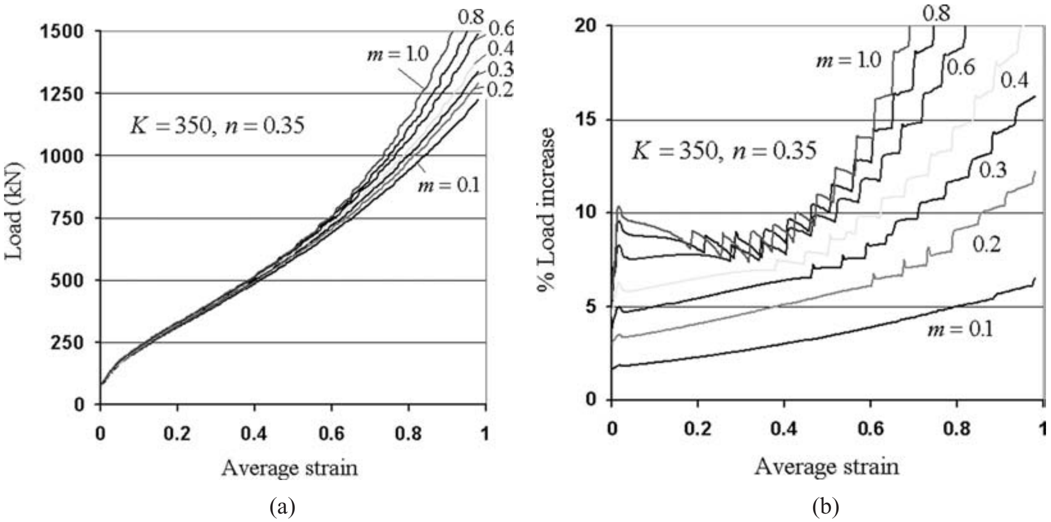

Figure 15.17. AR = 1 and $\sigma = 350\varepsilon^{0.35}$: (a) Load–stroke curves for different m-values from simulation and (b) percentage load increase over frictionless compression.

aspect ratio of the applied cylinder. The question is then: does there exist an optimum cylinder proportion in compression, which minimizes the frictional overestimate of flow stress? In order to investigate this anticipation, a study[3] was performed on materials with flow stress of the power law strain-hardening type.

A large number of simulations were run, using cylinders with aspect ratios AR = 0.5, 0.75, ..., 2. For each aspect ratio, different values of the strength coefficient and strain-hardening exponent, K and n, were used in the models to describe different material behavior. In the analysis, the strength coefficient was varied stepwise: $K = 150, 200, \ldots, 350$. For each K-value, the strain-hardening exponent was varied correspondingly: $n = 0.1, 0.15, \ldots 0.35$. Finally, for each aspect ratio and material model, the friction factor was varied stepwise: $m = 0, 0.2, \ldots, 1.0$.

For each aspect ratio and material, a number of load–stroke curves were thus obtained from the simulations; see, for example, Fig. 15.17(a) for AR = 1, $K = 350$, and $n = 0.35$. The strain value on the ordinate axis here is the redefined average strain as determined from the cylinder height; see eq. 5–11. When the simulated load–stroke curves had been obtained this way, it was straightforward to compute the percentage load increase for each friction value with respect to the frictionless state. Graphs depicting this increase are shown in Fig. 15.17(b) for AR = 1 and the same material as in Fig. 15.17(a).

As seen from Fig. 15.17(b), unless the friction factor is kept below $m = 0.2$, the load increase over the frictionless state, from the start of compression, exceeds 5%, and so does the flow stress increase. This means that errors in the flow curve due to friction will be of significant magnitude. But, as seen from the graphs, this error can be kept below 5%, if the average effective strain value 0.4 is not exceeded for $m = 0.2$ and the average effective strain value 0.8 is not exceeded for $m = 0.1$ when the test is conducted.

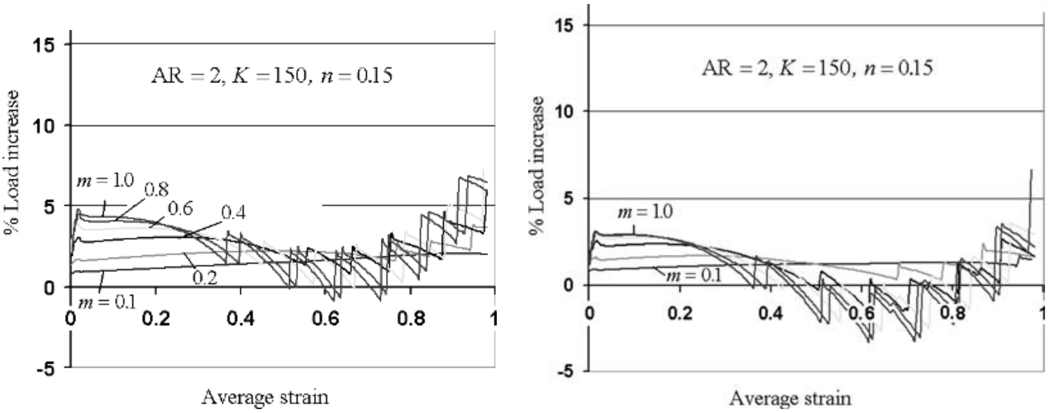

(a) (b)

Figure 15.18. AR = 2; percentage load increase in comparison with frictionless compression for material models: (a) $\sigma = 350\varepsilon^{0.35}$, (b) $\sigma = 150\varepsilon^{0.15}$.

In Fig. 15.18 is shown the load increase corresponding to that in Fig. 15.17(b), but for cylinders with higher aspect ratio, AR = 2. As these figures show, FEM-predicted frictional effects are strongly decreased when AR is increased from 1 to 2. For compression down to average strain values of 1, the load change due to friction throughout the stroke now does not exceed ±5%, whatever the friction is.

We may conclude that if flow stress data are acquired by means of cylinder compression, then high, slender cylinders with aspect ratio in the range 1.5–2 should preferably be used. Friction effects on the load–stroke curve then tend to cancel out; they generally lie below ±5%. Unless very accurate flow stress data are required, one can therefore skip the friction correction.

15.3 Partial Shearing as a Technological Test in Metal Forming

Shear tests are commonly applied in polymer processing for measurement of the rheological behavior of polymer melts; in metal forming, less attention has been paid to this method as a technological test. One interesting aspect of the shearing, or blanking, process is that it produces fracture in the material, and hence can be applied for fracture mechanics testing. Equipment for axisymmetric shearing has therefore been implemented in the author's laboratory to accommodate investigations of the basic mechanics of the shearing operation.

The midsection of one-half of a partially sheared specimen from such a test conducted in this equipment is shown in Fig. 15.19(a). A partial cut is obtained by stopping the movement of the punch and reversing it, before it penetrates down to the hole of the die. Separation of the blank from the flange of the specimen is then avoided, and one can check whether fracture has appeared in the shear zone.

In this chapter, it is shown by means of FEA, supported by experiments, that such analysis is a powerful tool to investigate the mechanics of processes that have not been sufficiently well understood yet. An axisymmetric 2D FEM model of such

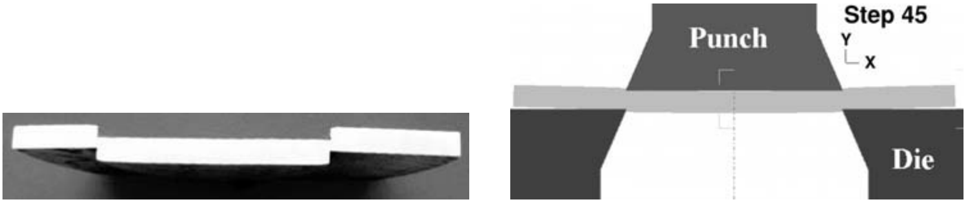

(a) (b)

Figure 15.19. (a) Specimen obtained after partial shearing; (b) FEM model of partial shearing.

an idealized shearing process, well suited for application as a technological test for acquisition of flow stress data, is shown in Fig. 15.19(a). In Fig. 15.20 are shown details of the tooling and workpiece configuration in the model.

Both the punch and die were modeled with sharp edges, $\alpha = \beta < 90^\circ$. With this tool, configuration contact is avoided between workpiece material and the nonhorizontal tool surfaces, i.e., the ones denoted a and b in Fig. 15.20(a), unlike what will occur if the die angles are 90°. Without contact here, the punch force will be that required for cutting of the material, and there will be no increase in force due to friction between tooling and workpiece.

The punch force is readily measured vs. punch stroke, and the recording can be applied to deduce the flow stress of the material. With die–workpiece contact on the nonhorizontal surfaces, correction for frictional effects is required.

As shown in the simulation picture in Fig. 15.20(b), the flange, as well as the slug in the middle of the specimen, will tilt during the course of shearing if no counterforces are applied to avoid rotation. To maintain idealized shearing conditions in the test, one should therefore consider mechanical support on the specimen at these locations, to eliminate specimen rotation. As mentioned in connection with Fig. 2.13, this is done in fine blanking by use of counter-dies below the slug and above the flange. In the experiments conducted in the author's laboratory, mechanical support was applied to the flange by means of clamps, to minimize tilting of the specimen outside the blanking area.

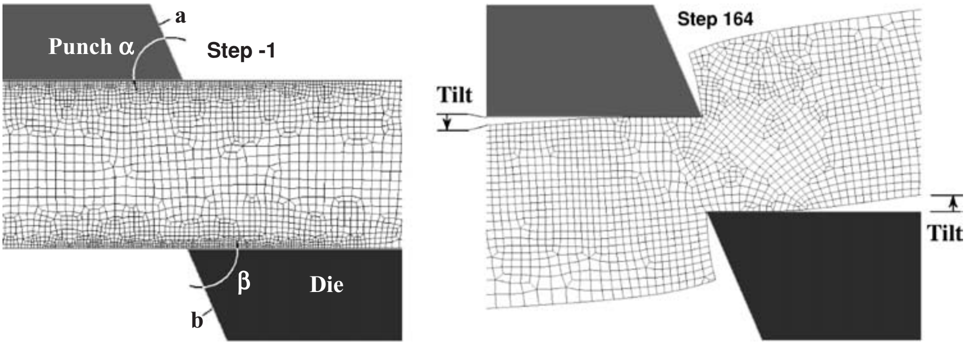

(a) (b)

Figure 15.20. Section showing shearing edges and region subjected to localized shear deformations: (a) initial and (b) after partial shearing.

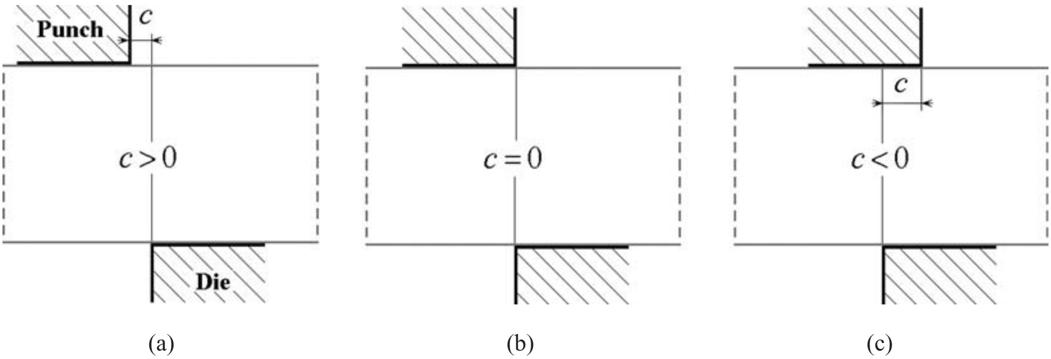

Figure 15.21. The clearance in shearing is either (a) positive, (b) nil, or (c) negative.

15.3.1 Deformations in the Shear Zone

The punch used in shearing can have a diameter equal to or less than that of the die hole. If it is less, there is positive clearance between punch and die; see the sketch in Fig. 15.21(a). If it is equal, there is no clearance; see Fig. 15.21(b). In partial shearing, negative clearance can also be applied; see Fig. 15.21(c). In industrial applications, it is generally stated that clearance values are 4–12% of the blank thickness. With increased ductility of the materials, the clearance is usually decreased.[4]

To check how well FEM simulation predicts the real deformation behavior in the most-deformed layer in the shearing process, an experimental study was conducted on an aluminum alloy strip at room temperature. The strip was made by extrusion and contained an internal pattern of grid stripes, running approximately parallel to one surface of the specimen.[5] In the experiment, a punch with diameter slightly less than the diameter of the die hole was applied. The punch was placed off center in relation to the die hole, so the clearance varied over the circumference of the specimen, from maximum (positive) value on one side to minimum (negative) value on the other side of the punch. In addition, the specimen was made with initial slope, i.e., thickness varying over the length, to produce a degree of shearing that varied over the circumference of the punch. Shearing was conducted in a mechanical press where the punch velocity varied throughout the stroke; see Fig. 15.22(c). The velocity was highest in the beginning and then decreased to zero at the instant when the partial cut had been obtained and the punch was pulled back.

The best grid pattern obtained in the experiment was at the location where the specimen was thickest. The clearance here was negative, and the deformed pattern in this location is shown in Fig. 15.22(a) as it appeared after sectioning, grinding, and etching.

An axisymmetric 2D simulation model was then made to try to reproduce the shearing conditions in the experiment. The FEM model was an isothermal model corresponding to the section investigated in the 3D experiment. The tooling was chosen rigid and the workpiece rigid–plastic, with flow stress conforming to a power law. The friction between workpiece and tooling was specified as Coulomb friction with $\mu = 0.2$. This should be close the experimental conditions, because lubrication

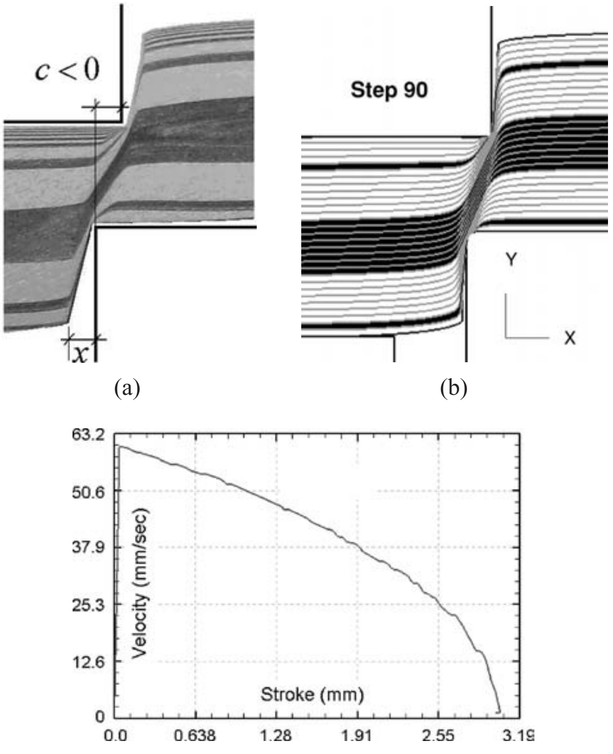

(a) (b)

(c)

Figure 15.22. Magnified section of shear zone in case of negative clearance: (a) experiment and (b) FEM simulation. (c) Velocity profile of punch in the experiment.

with MoS_2 paste was used in the experiment. Shearing edges were modeled slightly rounded at the edge. The angles α and β in Fig. 15.20(a) were 90° in the simulation, as in the experiment.

A stripe pattern corresponding to the experimental one was created in the initial specimen. The final computed appearance of the pattern is shown in Fig. 15.22(b). As seen, the simulated net deformations as revealed in distortions of contrast stripes are close in simulation and experiment. One exception is that the experimental blank is displaced by a larger distance x in the left-hand direction than in the simulation. This may be due to a 3D effect in the experiment that cannot be reproduced in the 2D model. In spite of this, the conclusion is that the FEM model mimics the main features of deformations in the experimental shear zone with good accuracy.

Inspired by the fact that the simulation model was close to the real shearing process, two additional simulations were run. Zero clearance and positive clearance of the same size as the negative clearance in the experiment were used in the new simulations. The die was kept the same as in the first model, but the punch diameter was decreased to change the clearance. Resulting deformed grid patterns in the new simulations, and effective strain-rate distributions in the sheared layer, are shown Fig. 15.23.

From this figure, one can see that the most heavily sheared layer extended in the thickness direction across the specimen in the case of zero clearance. But when

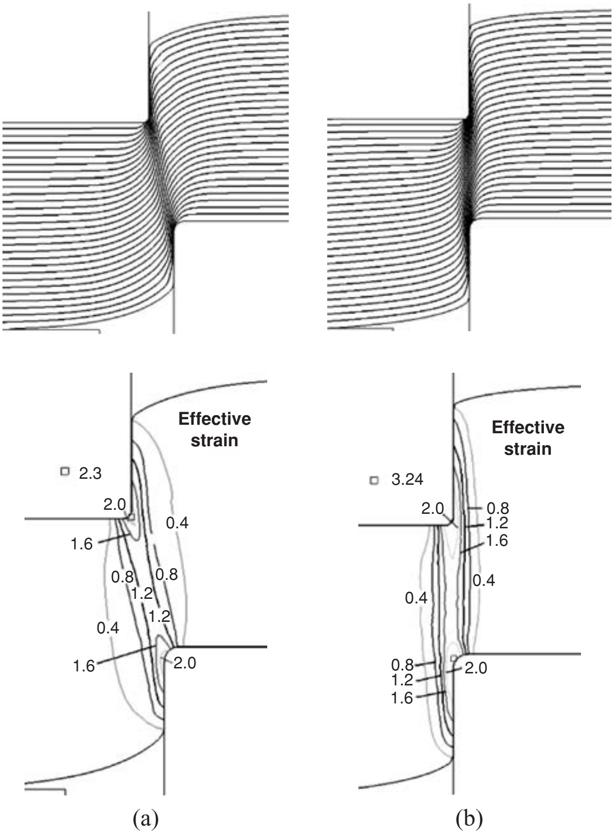

Figure 15.23. FEM-predicted grid patterns (at top) and deformations (at bottom): (a) positive clearance and (b) zero clearance.

the clearance was positive, it occurred at an oblique angle. In addition, the effective strain in the most intense shear layer was higher for zero clearance than it was for the positive clearance.

The zero-clearance simulation that provided highest deformation intensity in the shear zone was now investigated in more depth, using the point-tracking option in the simulation program. It was of interest to see whether there is metal flow out of the most intense shear layer, and what are the values of effective strains and strain rates in this layer, throughout the course of the shearing operation. The plots in Fig. 15.24 were made to show this.

This figure shows the effective strain distribution in the shear zone at four different steps during partial punching. Each distribution has been denoted by the simulation step at which it was captured. Let us first consider step 80, being the end stage when the punch has reach its bottom position and is about to travel in reverse. The effective strain reaches it highest value at this instant, of course. The contour line $F = 1.88$ is rather representative for the strains in the middle of the shear zone at this instant; strains are higher adjacent to the shear edges.

A row of 16 points was placed along a straight line, across the most heavily sheared layer, in this final step of shearing. In Fig. 15.24, this line is visible as a row of small black squares. These are the points that were used when point tracking

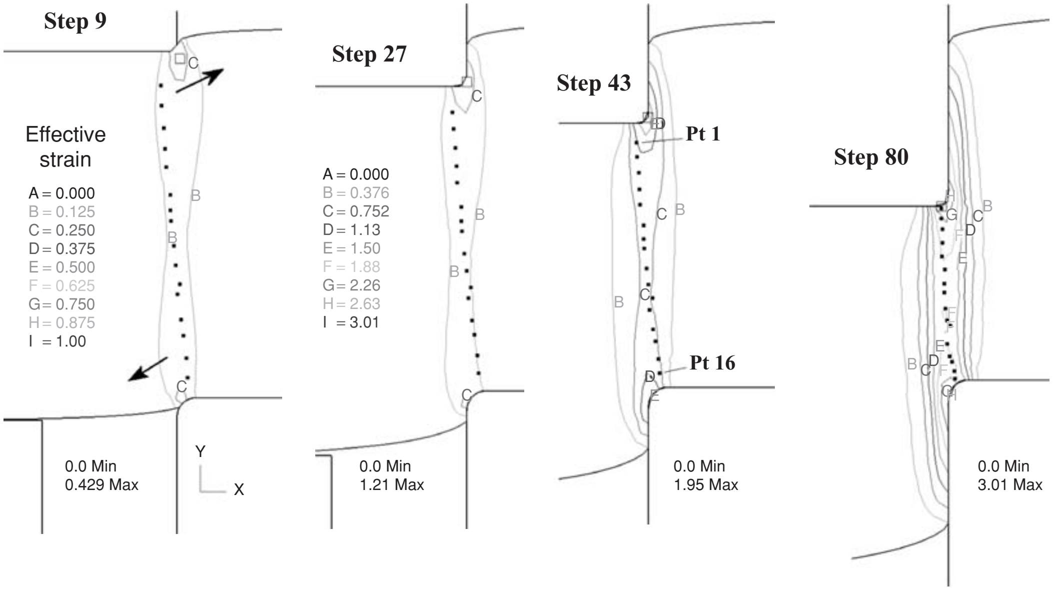

Figure 15.24 FEM-predicted effective strain distributions in shear zone when clearance is zero.

was done. Their locations at three earlier stages, as predicted in the simulation, are apparent in each picture, at step 43, step 27, and step 9, in Fig. 15.24.

As one can see, the FEM prediction is that the points will remain approximately on a straight line during the course of the punching process. But if one looks at the earliest simulation step shown in the figure, step 9, one can see that the points occur along a curved line, with a slight S-shape. This shows that the simulation predicts some lateral flow of the material in the shear layer over the die edges during the course of shearing, as depicted by the two arrows in Fig. 15.24, but the amount of flow in these directions is modest. The conclusion is that shearing occurs in approximately the same layer during the whole shearing operation. In this layer, the strains therefore accumulate and get higher as shearing proceeds.

To determine straining conditions in the shear zone during the course of the shearing process, the point-tracking option in the software was used to obtain the time history of a row of ten points across the most intense shear layer. The results are depicted in Fig. 15.25 as graphs of the point-tracking data. In this figure, (a) shows the effective strain and (b) the effective strain rate for each of the ten material points across the shear layer, throughout the course of shearing.

The two graphs in Fig. 15.25 show that the straining conditions across the heavily sheared layer in the shear zone, between punch edge and die edge, do not vary much across the layer. Effective strain values in the range 1.5–2 are obtained in this layer when the partial cut has been conducted, i.e., when approximately two-thirds of the cross section of the specimen has been sheared off. There are very high strain rates in this layer, and predicted effective strain-rate values lie in the range 20–50 s^{-1}

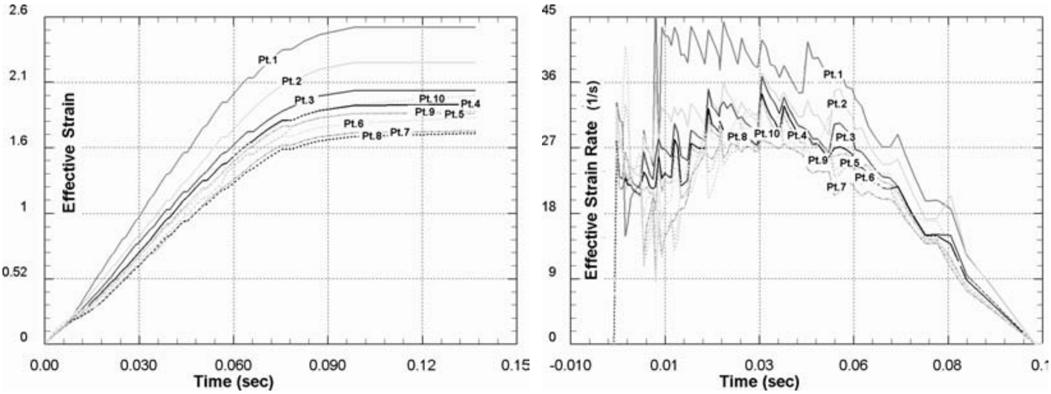

(a) (b)

Figure 15.25 FEM-predicted point tracking data: effective (a) strain and (b) strain rate.

throughout the largest part of the punch stroke, before they drop toward zero in the end stage of the shearing operation.

To conclude, because the shearing deformations are confined to a thin layer of material in the specimen, the strain rates here attain very high values, even though the punching velocity is not especially high. For the same reason, there are severe plastic deformations here, and for ductile materials high effective strain values (3 or more) can readily be achieved in the material. The load on the punch arises from this intensely sheared layer and is coupled to the flow stress there. There is some unevenness in the deformations across the shear layer, so that the layers near the edge tend to accumulate more strain than the midregion of the shear layer. But by change of tooling geometry (for instance, by modifying the sharpness of the shearing edges), this unevenness could probably be decreased.

15.3.2 Flow Stress of Ductile Power Law Materials from Shearing Tests

In the preceding subsection, it was shown that shearing is a promising technological test method because an intense shear layer forms in the test specimen. In this layer, very high strain rates are produced, and resulting deformations can become very large for ductile materials. In addition, the force required to create the plastic shear layer is transferred to the punch and can be measured in a straightforward way. As a simplification, one can say that the shear test is capable of bringing a thin layer of material up to high strain rates and high strains, and at the same time the energy input into this layer can be recorded.

How should then this test preferably be implemented for acquisition of flow stress data[6] on a particular workpiece material? To map this, a series of FEM simulations were conducted. In room temperature forming of metals, the flow stress of metals often conforms to a power law. Our analysis has therefore been limited to power law materials.

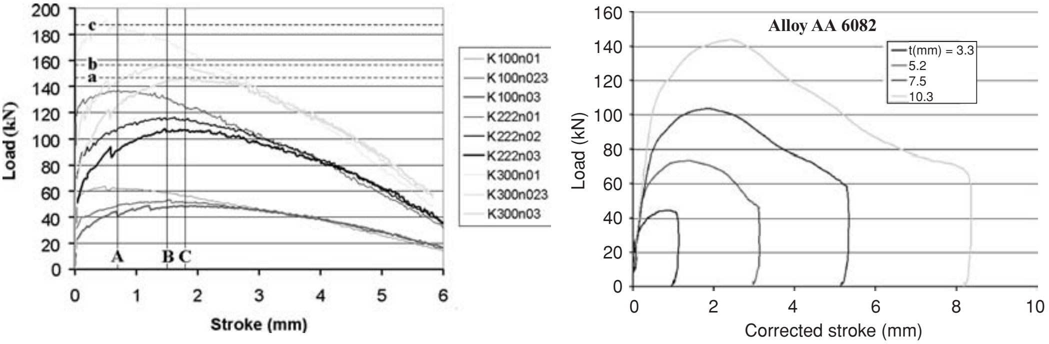

(a) (b)

Figure 15.26 (a) Load–stroke curves for different values of strength coefficient and strain hardening exponent. Here K = 100n01 means $K = 100$, $n = 0.1$, etc. (b) Load–stroke curves recorded in experiment.

A number of identical shearing simulations were run for different power law materials, to see how the predicted load–stroke curve in shearing would depend on the material parameters K and n, i.e., the strength coefficient and the strain-hardening exponent of the material. All shearing parameters were kept constant in the simulations except for K and n. These constants were varied systematically as shown by the legend in Fig. 15.26(a). The following shearing conditions were selected and kept constant in the analysis: sheet plastic, dies rigid, $t = 6.5\,\text{mm}$, $R_{\text{blank}} = 67.5\,\text{mm}$, $R_{\text{punch}} = 33\,\text{mm}$, $R_{\text{die}} = 33.13\,\text{mm}$, $v = 130\,\text{mm/s}$, $\mu = 0.6$.

Different load–stroke graphs obtained in the simulations, for different values of the material parameters K and n, were plotted in one diagram, i.e., they were shown as a family of curves; see Fig. 15.26(a). As seen from the graphs, initially they rise steeply with increasing punch movement up to a maximum, and then there is a drop in load as the punch penetrates further and the remaining cross section gets smaller.

When we consider the curves, we see that the peak value of a curve, marked by lines A, B, and C in Fig. 15.26(a), always appears at the same stroke length for one particular value of n, no matter what is the K-value. Hence, for a power law material the simulation results indicate that the stroke length at the peak value in the graph is only related to n and is independent of K.

Another observation is that when the n-value is decreased for a particular K-value, the peak value of the load–stroke graph does increase; see the dashed lines marked a, b, c in Fig. 15.26(a) for the material with $K = 300$. Hence, when considering a constant value of K, there is a shift in the level of the peak value toward higher punch load for decreasing n.

Based on these two observations, the graph shown in Fig. 15.27(a) was made by means of the simulated data. This is a graph from which one can obtain the strain-hardening exponent, if one knows the stroke length at the peak value in the shearing process for a particular unknown power law material. In addition, the material must be present in such shapes that specimens can be prepared from it with the same

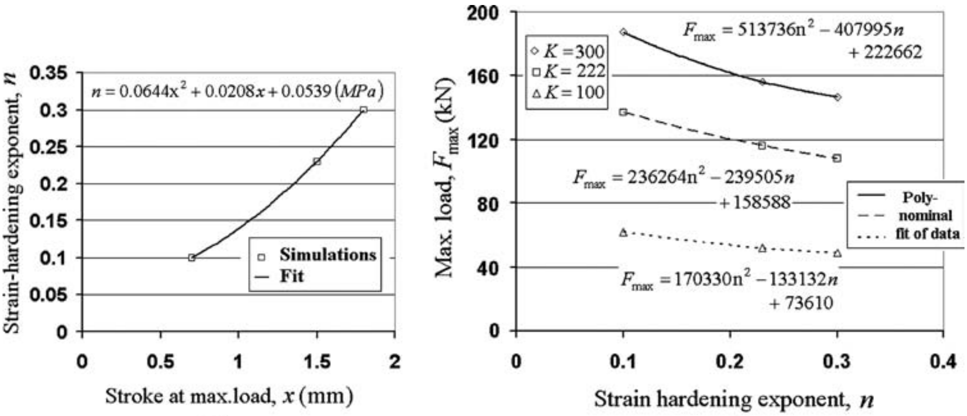

(a) (b)

Figure 15.27 Graphs obtained from simulation to deduce (a) n-value and (b) K-value in shear testing.

thickness as the specimen used in the FEA. In a corresponding way, the curve shown in Fig. 15.27(b) was made from the simulation data. This graph is used to determine the K-value of the material after the n-value has been determined from the first graph. Hence, we have arrived at a possible procedure for obtaining the flow stress relationship for a power law strain-hardening material, by simple means – from a measured load–stroke curve, in a partial shearing test.

Experimentally recorded load–stroke curves for specimens of different thickness made from one material are shown in Fig. 15.26(b).

The proposed test is a cheap and rapid one for testing sheet or plate materials. Flat pieces can be tested quickly without cumbersome and expensive preparation of specimens. Data treatment, when the procedure is applied for determination of the K and n values of power law materials, is also easy and rapid. Future work on this topic will be conducted in our laboratory to map the accuracy of the technique proposed and to study thermal and strain-rate effects in the test. It is obvious that the relations found in this preliminary FEA might be better founded by means of theoretical analysis. Such work will therefore be welcomed.

Problems

15.1 ACQUISITION OF FLOW STRESS DATA FOR AN ALLOY BY TENSILE TESTING AND CYLINDER COMPRESSION AT ROOM TEMPERATURE

Material: Tensile test and compression test specimens were made from a cast and homogenized AA 6082 aluminum alloy billet. The specimens were soft-annealed by heating to a temperature of 420°C in a furnace. The specimens were kept at this temperature for an hour and were then cooled slowly to 250°C in the furnace. After this, the specimens were cooled further to room temperature in air.

Tensile testing: The test was run in a conventional tensile test machine, with a crosshead speed of 10 mm/s. The initial diameter of the specimen was 9.98 mm, and the change in diameter was recorded vs. tensile force. Recorded data are available in a spreadsheet called Test Data.

Compression testing: Tests were run in a Gleeble machine at constant strain rates of 1 and 10 1/s, respectively. Compression force vs. stroke was recorded. Primary data from the tests are available in the Excel spreadsheet called Test Data. The initial cylinder had a diameter of 10 mm and a height of 20 mm.

FEM simulation: An optimized FEM simulation model of the tensile test is available. In the model, the flow stress has been chosen so that it provides approximately the same load–diameter curve as in the experiment.

Work to be done by each student group (consisting of two members):

1. Create your own FEM model of tensile testing on the basis of a tutorial provided. The material model to be used is $\sigma = 197.6\varepsilon^{0.178}$. Run the simulation. Then use the DEFORM-2D postprocessor to obtain the various stress components across the radius of the neck. This is to be done in a late simulation step after necking has become clearly visible, but before the specimen thins down too much in the neck. Plot all stress components and the effective stress across the neck in the same diagram. Make a corresponding plot of the effective strain distribution across the neck. Comment on whether deformations are predicted to be uniform over the neck. Discuss what data are of importance when one wants to obtain the optimum flow curve from a tensile test experiment.
2. An optimized FEM model with flow stress data, corresponding to the tensile test run in the laboratory, is available as a keyword file Tens Test Opt. Make your own FEM model on the basis of this file. Then use the model to achieve the simulated force vs. diameter diagram. Check to what extent the model reproduces the load–diameter response as it was determined in the experiment.
3. Obtain the flow stress data used in the optimized FEM model, and compare them with the flow stress data obtained directly from the experiments.
4. Use the optimized FEM model to determine strain-rate conditions in the thinnest portion of the tensile test specimen during the test.
5. On the basis of the obtained results, discuss the constitutive behavior of the applied material. Is there reasonable agreement between the flow stress obtained in tensile testing and the corresponding flow stress obtained in compression testing?
6. Write a report on your work (one report for each group consisting of two students).

NOTES

1. Bridgman, P. W.: “Stress distribution in the neck of a tension specimen,” Trans. Amer. Soc. Metals, Vol. 32, 1944, p. 553.
2. Mjoen, H. R.: “Analysis of Hot Closed-Die Forging of a Commercial Al Alloy” (in Norwegian), M.Sc. thesis, Norwegian Univ. of Science and Technology (NTNU), 2002.

3. Jesnes, G.: "FEM-analysis of compression test," unpublished work, Internal report, IPM, NTNU, June 2005.
4. Vaz, M., and Bressan, J. D.: "A computational approach to blanking processes," J. Material Processing Technology, Vol. 125–126, 2002, pp. 206–212.
5. Khan, Y. A., Ganesan, S. M., Valberg, H., Moe, P. T., and Hansen, A. W.: "Deformation conditions in conventional shearing dependent on geometrical condition of tooling," Proc. 11th Int. Esaform Conf. on Material Forming, Lyon, France, 2008.
6. Ganesan, S. M., Khan, Y. A., Valberg, H., Moe, P. T., and Hansen, A. W.: "Shearing applied as test method for acquisition of flow stress data at high strains and strain rates," Proc. 11th Int. Esaform Conf. on Material Forming, Lyon, France, 2008.

REFERENCES

Davis, J. R.: "Tensile Testing," ASM Int., Metals Park, Ohio, 2004.
Pöhlandt, K.: "Materials Testing for the Metal Forming Industry," Springer-Verlag, 1989.
Wright, T. W.: "The Physics and Mathematics of Adiabatic Shear Bands," Cambridge Univ. Press, 2002.

16 Forging

The classification system for metal forming processes shown in Fig. 2.1 partitions the forging processes into three different groups: open-die forging, closed-die forging, and impact extrusion. In reality, open-die forging consists of a number of different subprocesses, in each of which considerable parts of the workpiece are formed freely, without full contact with the dies; see, for instance, cogging, as shown in Fig. 2.2(c). Closed-die forging, on the other hand, refers to forging between dies, where at the end of forging, either the entire workpiece is confined in a closed space between the dies, or an amount of excess material is used, which flows out of the flash gap; see Fig. 2.3(b). When flash is formed, the process is most commonly called closed-die forging. When there is no flash, the process is called precision forging, flashless forging, or zero-loss forging. Impact extrusion, such as forward and backward cup extrusion, is also described in Ch. 2; see Fig. 2.4. Both are commonly classified as forging processes. In addition, many more exotic forging processes have been developed over the years.

In this chapter, some practical aspects of importance in closed-die forging processes will be considered. First, the concept of *forgeability* will be discussed. Then the implications of this concept for forging practice will be dealt with, such as selection of forging temperature and possible shapes of forgings. A common classification system for forged components will also be presented. After this, commonly used design principles in multistep forging processes will be discussed. The characteristics of the load–stroke curve in closed-die forging will be described, and the causes of characteristic flow-related forging defects, such as laps (folds), commonly present in forging will be discussed. Finally, common flash gap designs applied in closed-die forging will be considered.

16.1 Forgeability

In forging, the metal is pressed into the die cavity, and should completely fill the cavity a short while before forging is ended, so that a forged component of acceptable quality is achieved. For some metals, such *cavity filling* is achieved much more easily than for others. Hence, the ability of a metal to easily fill the empty space inside the forging die is an important aspect of *forgeability*. Other aspects, as already explained in Ch. 9, are the malleability and the workability of the workpiece material.

In practical forging the required load to forge the component is of great importance. Alloys that have high flow stress at the forging temperature, of course, require higher forging load than soft alloys do. Alloys that can be forged with low forging load are commonly said to have good *malleability*. The contact pressure between workpiece material and die is proportional to the required load, so the greater the load, the higher is the contact pressure. If the die pressure exceeds a critical level, the forging die will become overloaded. Then the die can become plasticized, it can fracture, or there can be excessive wear on the die surfaces.

Another important factor in forging is the ability of the workpiece material to withstand large deformations upon flow into the die cavity, without developing cracks. If so, the material is said to have good *workability*. Workability is commonly closely related to the ductility of the metal.

For a workpiece material of given workability, the risk of cracking during forging can be reduced if the sequence of the forming operation is optimized to provide the highest possible hydrostatic pressure during the steps of forming. The workability of a particular alloy can vary with temperature. The forging temperature should preferably lie within an interval where workability is good. The austenitic steel X10CrNiTi189, for instance, has best ductility when it is forged at a temperature close to 1200°C. For this material there is a risk of cracking if the forging temperature drops far below or rises high above this temperature; see Example 16.1.

EXAMPLE 16.1: OPTIMUM FORGING TEMPERATURE

The flow stress of an alloy to be hot-formed can be measured by, for instance, cylinder compression performed at different temperatures while the strain rate is maintained constant, as described in Ch. 7 and Ch. 8. Testing performed this way will yield a curve of flow stress vs. temperature for the alloy, as, for instance, that shown in the sketch drawn at the top of Fig. 16.1. If the ductility is also determined, for instance, by torsion testing, the ductility vs. temperature curve for the alloy can also obtained; see the bottom sketch in the same figure. When both curves are shown together, as in Fig. 16.1, one can see that there may exist an *optimum temperature* interval, ΔT_{opt}, within which the alloy has both good ductility and good malleability, the latter term reflecting that the flow stress of the alloy is low or moderate. This temperature interval should then preferably be used in forging, for one then will avoid cracking in the forging, and also the forging load will be low.

Low ductility and/or low workability can for many alloys occur if the material is forged at a high temperature, close to the melting point of the alloy. This can, for instance, be due to the presence of low-temperature-melting intermetallic phases at the boundary of the grains of the material, which can make an alloy unsuited for forging. Such constituents tend to melt when the temperature rises above a critical level; see the discussion of this phenomenon in conjunction with

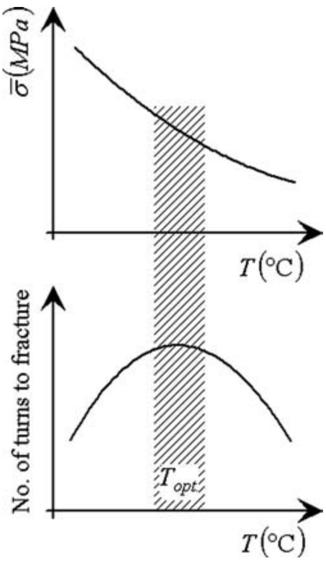

Figure 16.1. Optimum temperature range for working of alloy in hot forging.

Fig. 11.19. If a material is subjected to high tensile stresses while local pockets of metal are molten, it is easy to understand that cracks are likely to form.

EXAMPLE 16.2: FORGEABILITY OF DIFFERENT METALS

In Fig. 16.2, cross sections of two forgings that were hot-forged down to different final rib-wall thicknesses are shown. The component with the thinnest rib and web, shown on the left-hand side, represents the *critical geometry* for the forging of a particular Al alloy, whereas the thicker-walled forging on the right-hand side is the critical shape for the forging of a Ni-base superalloy. The term *critical* here means that thinner sections cannot be achieved in forging without excessive cost, so that mass production of the component by forging becomes uneconomic. The figure thus illustrates clearly an important practical aspect of forgeability in connection with forging of metals.

Because of their softness and high ductility, most Al alloys allow forging of thin ribs and thin webs to be conducted without particular problems, whereas the same thin parts cannot be achieved economically with a superalloy. Because of the high forging temperature required for superalloys, and their higher flow stress than that of Al, the same thin-walled sections cannot be realized in forging them with acceptable lifetime of the dies.

As may be understood from the discussion in the preceding examples, forgeability, as experienced in practical forging, is a complex property. In fact, it includes many properties, among them the ability of the workpiece material to fill narrow die cavities, as well as its ductility and workability, i.e., its ability to be deformed to large strains without tendency of crack formation. Finally, the malleability (softness or hardness) of the material at forging temperature, i.e., its flow stress, is also important, as this parameter influences the die pressure and forming loads required.

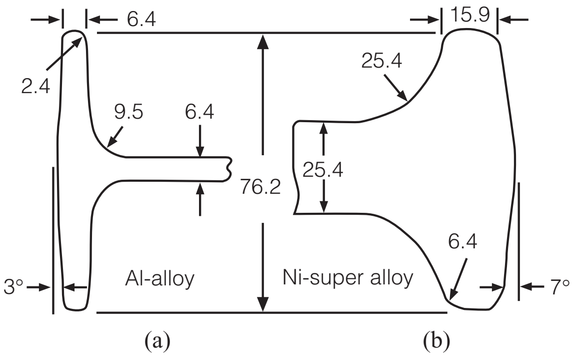

Figure 16.2. Rib-web sections[1] in forging (dimensions in millimeters). (Reprinted with permission from Alvin M. Sabroff, Metalworking Consultant Group, LLC, www.metalgroup.com.)

Because of the differences in forgeability for different materials, the design possibilities of forged components are also different for different metals, as is shown in Fig. 16.2.

Because forgeability of an alloy is closely connected with material properties like the ductility and the flow stress of the workpiece material, it is important to apply technological tests such as tensile testing, cylinder compression, and torsion, as described in Ch. 7 and Ch. 8, to quantify these properties for materials to be forged. As was shown in Ch. 9, the risk of cracking of materials can also be checked in technological tests, to assess their workability. Thus the forgeability of different alloys can be characterized in technological tests, in order to be able to select materials that will perform satisfactorily in a particular case.

Another important factor in forging is selection and application of adequate lubricants, to reduce the required loads and the die wear. It is important that the lubricant gives sufficiently low and stable friction during the forging operation. In addition, the lubricant should minimize the metallic contact between workpiece and die, to prevent workpiece material from welding onto the die. Another important property of a hot-forging lubricant is that it should reduce heat transfer from workpiece to die, so that excessive cooling of the workpiece does not take place. Hot forging is commonly conducted with die temperatures considerably lower than that of the workpiece. It is important that the workpiece remain hot and the die remain at its intended temperature when forging is conducted. Last, but not least, the lubricant should be environment-friendly, harming neither the shop nor the external environment.

16.2 Classification of Forged Shapes

Components produced by forging may have more or less complex geometrical shape. It is generally more difficult – and more expensive – to forge components with complex than with simple geometry. Because of this, it was early considered useful to establish a classification system to try to systematize the shapes of all possible forgings; see Fig. 16.4.

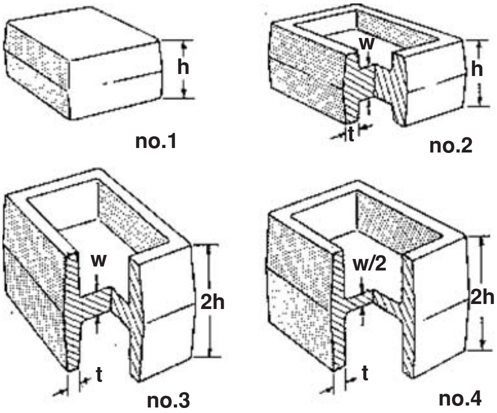

Figure 16.3. Forgings with web and rib, the latter extending around the periphery of the component. Forging becomes increasingly difficult as rib and web thicknesses decrease.[1] (Reprinted with permission from Alvin M. Sabroff, Metalworking Consultant Group, LLC, www.metalgroup.com.)

Before explaining and discussing this classification system, let us first look at the four different forgings shown in Fig. 16.3, and consider the difficulties connected with forging of these shapes.[1]

Although forging 1 has a simple slab shape and is simple to forge, the three other components have a web, which decreases in thickness from forging 2 to 4. In addition, these forgings have ribs, which extend around the circumference of the web. The ribs of the components decrease in thickness from forging 2 to 4. Both because of the increased height of the ribs and the decreased thickness of the web, it gets more and more *difficult to forge* the shapes as one goes from forging 2 to 4.

One main reason for this, which has already been discussed in Example 16.1, is that it is difficult to provide metal flow into narrow die cavities, such as the cavities providing a thin rib in forging. The other main reason is that it is difficult to forge a thin web. This is because increasingly higher pressures and forging loads are required to forge the web as its thickness decreases. This is realized by considering eq. 13-13, which expresses the required forging load in disc forging between plane-parallel platens. Here the second term inside the final parenthesis, $2mR/(3\sqrt{3} \cdot h)$, is inversely proportional to the disc thickness h. Because of this, the forging load rises strongly as discs are forged thinner.

Thus the required forging load increases in the sequence from component 2 to 4. As a consequence, especially in hot forging of steels, die wear also increases. Hence, there is a limit to how thin a web can be made in forging, if the process is to be economic.

In Fig., 16.4, a *classification system* is presented for shapes of forgings.[2] By means of this system, the degree of complexity of the shape of a forging can be considered. The complexity of shape is characterized by a three-digit number xyz. The components to be produced by forging are considered to consist of a base with or without extensions from it. In the two first columns on the left-hand side of Fig. 16.4, reading from the top down, the complexity of the basic shape is specified by means of digits xy as follows:

$x = 1$ denotes compact cylindrical and spherical bodies.
$x = 2$ denotes disc-shaped bodies.

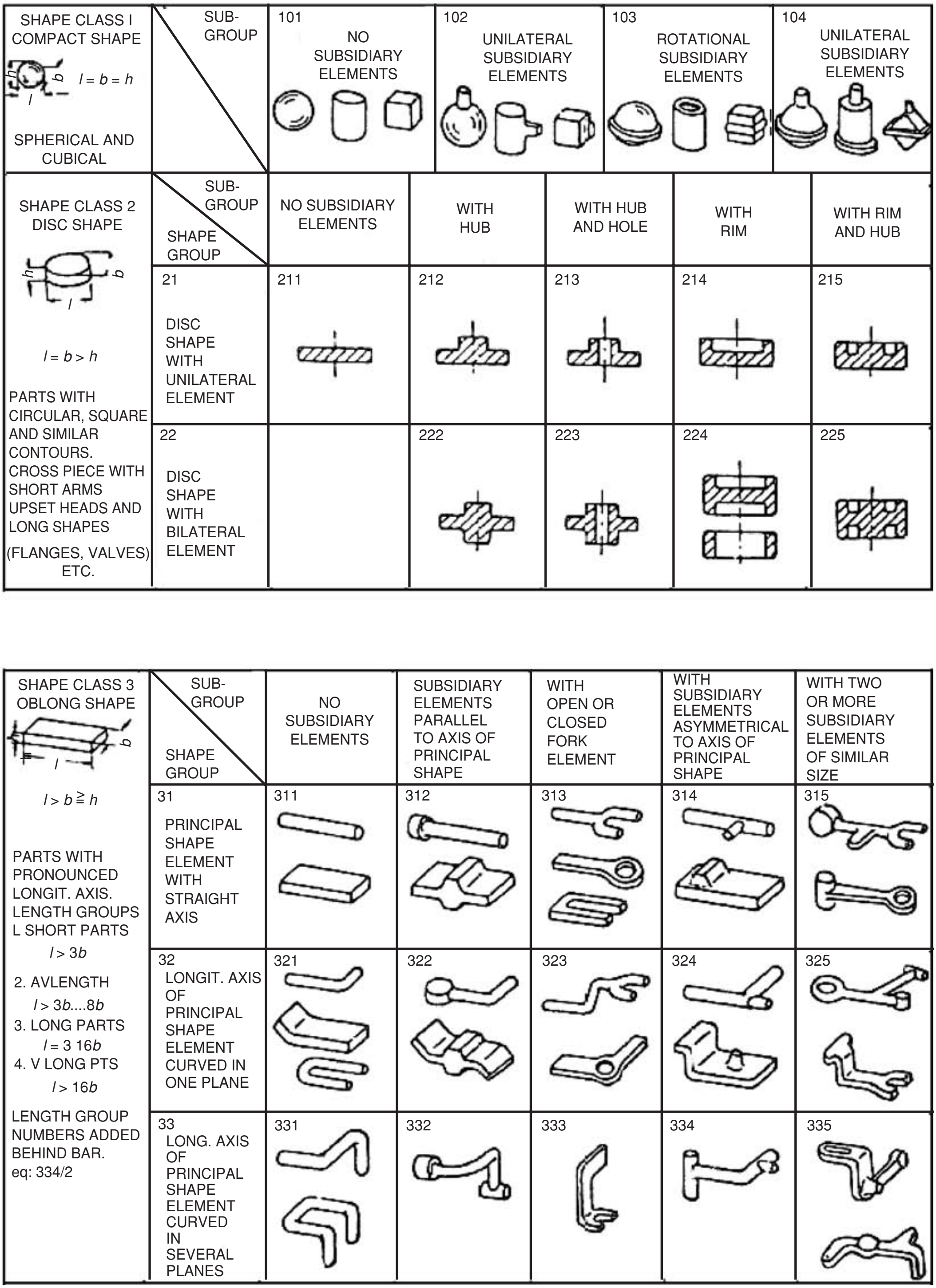

SHAPE CLASS I COMPACT SHAPE $l = b = h$ SPHERICAL AND CUBICAL	SUB-GROUP	101 NO SUBSIDIARY ELEMENTS	102 UNILATERAL SUBSIDIARY ELEMENTS	103 ROTATIONAL SUBSIDIARY ELEMENTS	104 UNILATERAL SUBSIDIARY ELEMENTS

SHAPE CLASS 2 DISC SHAPE	SUB-GROUP SHAPE GROUP	NO SUBSIDIARY ELEMENTS	WITH HUB	WITH HUB AND HOLE	WITH RIM	WITH RIM AND HUB
$l = b > h$ PARTS WITH CIRCULAR, SQUARE AND SIMILAR CONTOURS. CROSS PIECE WITH SHORT ARMS UPSET HEADS AND LONG SHAPES (FLANGES, VALVES) ETC.	21 DISC SHAPE WITH UNILATERAL ELEMENT	211	212	213	214	215
	22 DISC SHAPE WITH BILATERAL ELEMENT		222	223	224	225

SHAPE CLASS 3 OBLONG SHAPE	SUB-GROUP SHAPE GROUP	NO SUBSIDIARY ELEMENTS	SUBSIDIARY ELEMENTS PARALLEL TO AXIS OF PRINCIPAL SHAPE	WITH OPEN OR CLOSED FORK ELEMENT	WITH SUBSIDIARY ELEMENTS ASYMMETRICAL TO AXIS OF PRINCIPAL SHAPE	WITH TWO OR MORE SUBSIDIARY ELEMENTS OF SIMILAR SIZE
$l > b \geqq h$ PARTS WITH PRONOUNCED LONGIT. AXIS. LENGTH GROUPS L SHORT PARTS $l > 3b$	31 PRINCIPAL SHAPE ELEMENT WITH STRAIGHT AXIS	311	312	313	314	315
2. AVLENGTH $l > 3b....8b$ 3. LONG PARTS $l = 3\ 16b$ 4. V LONG PTS $l > 16b$	32 LONGIT. AXIS OF PRINCIPAL SHAPE ELEMENT CURVED IN ONE PLANE	321	322	323	324	325
LENGTH GROUP NUMBERS ADDED BEHIND BAR. eq: 334/2	33 LONG. AXIS OF PRINCIPAL SHAPE ELEMENT CURVED IN SEVERAL PLANES	331	332	333	334	335

Figure 16.4. Classification system[2] for shapes of forgings. (Reprinted with kind permission of Springer Science + Business Media.)

$xy = 21$ denotes extension from the basic shape in one direction.
$xy = 22$ denotes extensions in two directions.
$x = 3$ denotes oblong shapes.
$xy = 31$ denotes a straight body without bend.
$xy = 32$ denotes an oblong body bent in one plane.
$xy = 33$ denotes an oblong body bent in many planes.

The digit z is added according to horizontal position in the figure, from left to right. Along this axis subgroups of components are specified with increasing z from $z = 1$ to $z = 5$, depending on whether the basic body has extensions:

$z = 1$ denotes no extension.
$z = 2$ denotes one extension in one direction from the basic shape.
$z = 3$ denotes an extension with rotational symmetry.
$z = 4$ denotes extensions in different directions.

The complexity of the forging thus will increase as any of the three digits x, y, and z increases and so commonly does the difficulty of forming, if a component is to be made by forging.

16.3 Design of Forging Series in Closed-Die Forging

To produce a forging of high complexity in closed-die forging, it is necessary to forge the workpiece in a number of successive stages, so that the initial simple workpiece shape is gradually transformed into more complex shapes, until in the last stage the final shape of the component is obtained. In forging terminology, early steps of forging are called *preforming steps*, and the last step, which provides the final shape, is called the *finishing step*, which is obtained in the *finishing die*.

The purpose of the preforming steps of a forging sequence is to distribute material gradually to those parts of the body that require much material, i.e., to regions where the forging has thick cross section. In steel forging, it is quite common to design the forging series in a manner so that after the preforming steps, the preformed shape will be close to the end shape of the forging. Then a rather small shape change and movement of mass are required in the finishing stroke.

When forging series are designed this way, the last forging step requires the lowest possible forging load and least possible metal flow. Because of this, wear on the finishing dies will also be a minimum. Because the forging is given final shape in the finishing step, it is much more important to attain precise component shape here than in the preforming steps, where larger variation in specimen geometry is tolerated because the shape is preliminary and is modified again in the next forging step.

The most common *forging stock* for steels consists of hot-rolled bars or rods. In forging of aluminum and aluminum alloys, however, extruded rod is the main forging stock. In the case of small forgings, the workpiece can be made from wire of appropriate dimension. Hot-rolled plate can also be used as forging stock. The semifinished bar, rod, wire, or plate is partitioned into pieces of appropriate length by sawing or shearing to obtain workpieces for subsequent use in forging.

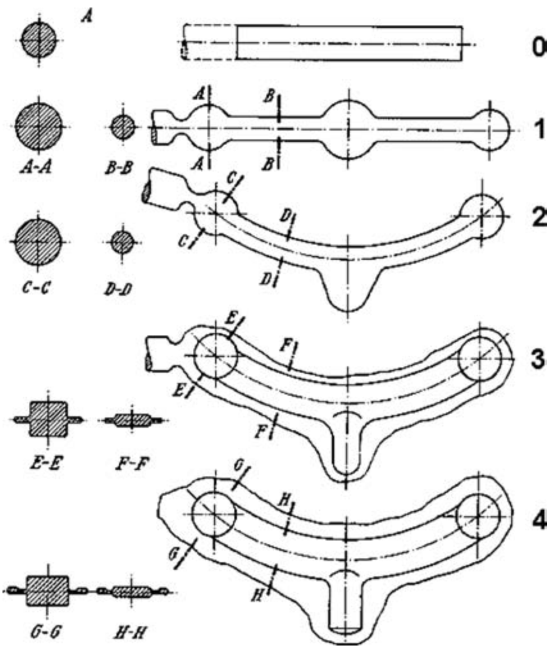

Figure 16.5. Forging sequence for production of a rather complex elongated forging. (Reprinted with permission from © Carl Hanser Verlag, München.)

A typical *forging sequence*[3] for a specific forged component is shown in the sketch in Fig. 16.5. This component is shaped in four steps. The first step is performed as a *roll forging* operation, in which the metal is redistributed over the length of the rod, so that it is accumulated in three locations. Initially, it was evenly distributed over the length of the piece cut from the rod.

Roll forging is a high-yield metal forming process that allows metal easily to be accumulated as lumps over the length of rod, while the base rod is reduced in thickness. In the case shown in Fig. 16.5, the metal is gathered in three locations along the rod: one lump at each end and a big lump approximately in the middle. The reason metal must be gathered at these locations is that the final forging is to have thick cross sections there.

The roll forging is done in a rolling stand, in which the roll geometry varies over the periphery of the roll, so that the roll gap varies in shape, corresponding to shape 1 shown in Fig. 16.5, as the rolls rotate one turn. Because the rolls rotate and only shape a short length of the rod at a time, there is less friction in the length direction of the workpiece than in other kinds of forging. Because of this, the roll forging process is able to move the mass of the rod lengthwise along the rod to a larger extent, than in other forging processes. For this reason, roll forging is considered advantageous, in many cases, in early preforming steps of forging sequences.

In the forging series shown in Fig. 16.5, the second forming step is bending, because the final forging has curvature. In the third forming step, the workpiece is forged to a shape close to the final shape. At that time preforming is finished, and what then remains is the finishing step. When one compares the shape of the workpiece in steps 3 and 4, one can see that the shape in the last preforming step is quite close to that of the final forging. The difference is primarily that the component has less width and larger height before than after final forging.

There are certain basic rules, or *guidelines*, that should be followed when closed-die forging sequences are designed. The most important guidelines are[3,4]

1. Achieve complete filling of die cavities in the final forging step without formation of any defects in the forged component.
2. Forge the component in the fewest possible steps with the smallest possible waste of material in flash.
3. Select the design so that metal is correctly distributed over the length of the workpiece at the last preforming step, before the finishing step.
4. Design the last preforming step to minimize wear in the finishing step. This is especially important in hot forging of steel.
5. Design the forging series so that material flow is good throughout, to provide optimum grain flow in the final forging; see Fig. 1.8. This will secure the best possible mechanical properties in the final forging.

In the forging of aluminum alloys, the forging temperature is rather low, as, for instance, 400°C, in contrast with of 1100°C as commonly applied when forging steels. Besides, aluminum alloys have low flow stress at the forging temperature compared to steel. Because of this, die wear is a much bigger problem when steel is forged, than when aluminum is. Therefore, if the forging sequence shown in Fig. 16.5 is to be used for an aluminum alloy, the last preforming step (step 3), can be skipped. Hence, for aluminum, the final component can be forged directly from the preformed shape (step 2). Reducing of the number of forging steps in the process is of course beneficial for the economy of the forging process.

16.4 Optimizing Steel Forging

There are certain rules – or *design principles* – in connection with design of the last forming step in steel forging. If the last preformed shape is given optimum geometry, the forging conditions in the last step will be favorable, and the life of the final die can be maximized. Some general considerations will be discussed here, in connection with forging of the component shown in Fig. 16.6(a). When designing an optimum preform for a particular finishing step, geometrical characteristics of the final forging with respect to the mass distribution over its length must be determined, including the amount of flash material, which is required in addition on the preform shape in closed-die forging; see Fig. 16.6(b–d).

From the final component, the distribution of the cross-sectional area, q_E, over the length of the component can be computed and presented graphically; see Fig. 16.6(b). This area distribution is proportional to the corresponding *mass distribution*. On top of the graph, the distribution of the cross-sectional area of the flash, q_G, can be added, as the flash is expected to appear. The sum of the two, i.e., the cross-sectional area distribution of component, including flash, represents the total distribution of cross-sectional area aimed at in the last preformed shape. When this distribution has been determined, the resulting cross-sectional area is recalculated as either rectangular or circular area, depending on whether stock of round or square section is to be applied. The obtained cross section now represents a well-suited

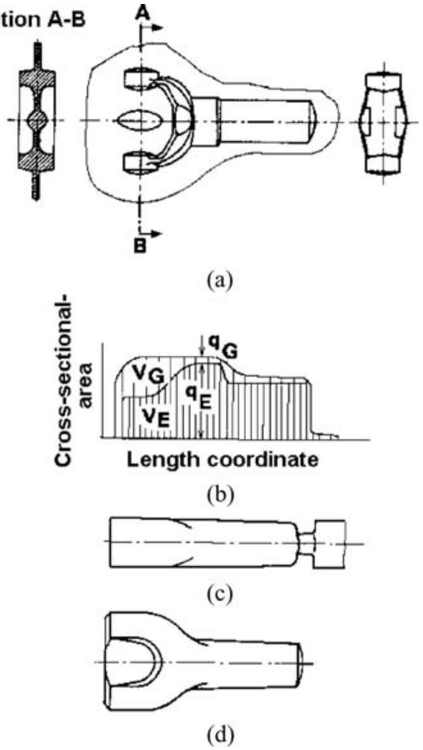

Figure 16.6. Optimum design[3] of final forging step. (Reprinted with permission from © Carl Hanser Verlag, München.)

workpiece geometry to be formed in the last preforming step; see Fig. 16.6(c,d). Design rules that apply for the last preform are to specify as follows:

6. Concave radii on the preform that are larger than the corresponding die radii of the finishing tool.
7. Dimensions in the forging direction of the preform that are larger than the corresponding dimensions of the finished forging.

In Fig. 16.7, some possible forging sequences[7] for steel forgings of H-shaped cross section are shown. The figure clearly illustrates how the forging process becomes increasingly complex and requires additional forging steps, especially when the rib height is increased. Although one forging step is sufficient when the rib height is small, three steps are required when the rib height is increased by a factor of 3, if the rib thickness concurrently is maintained constant. For the component with highest rib, the figure also demonstrates use of design principles 6 and 7 just specified.

16.5 Die Filling and the Load–Stroke Curve

A characteristic *load–stroke curve* is shown in Fig. 16.8(d) as it appears when recorded in a forging step in closed-die forging. Different stages of filling of workpiece material into the die are shown in Fig. 16.8(a–c). As Fig. 16.8(d) depicts, there is just a moderate increase in the forging load in the first part of the stroke, when there is still much unfilled space in the die cavity. Later, however, when the lateral flow reaches the flash gap [see Fig. 16.8(b)], there is a steep

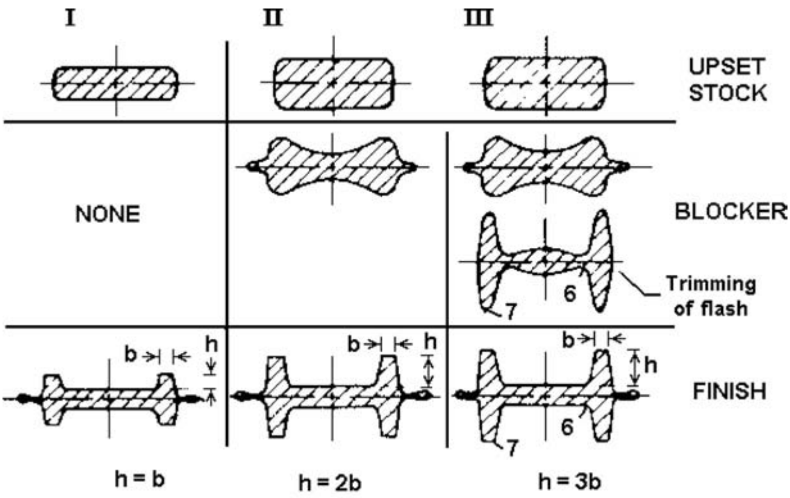

Figure 16.7. Forging series for axisymmetric components with H-shaped cross section. (Reprinted with kind permission of Springer Science + Business Media.)

increase in the forging load, because lateral flow in the die is now restricted, while concurrently metal flow in the direction opposite to the die movement is augmented; see Fig. 16.8(b). As forging proceeds, the flash gap gets narrower and metal flow into the die cavity is therefore speeded up, until the die cavity becomes completely filled with workpiece material. At this instant [see Fig. 16.8(c)], metal flow is in one direction only, namely, out of the flash gap, because

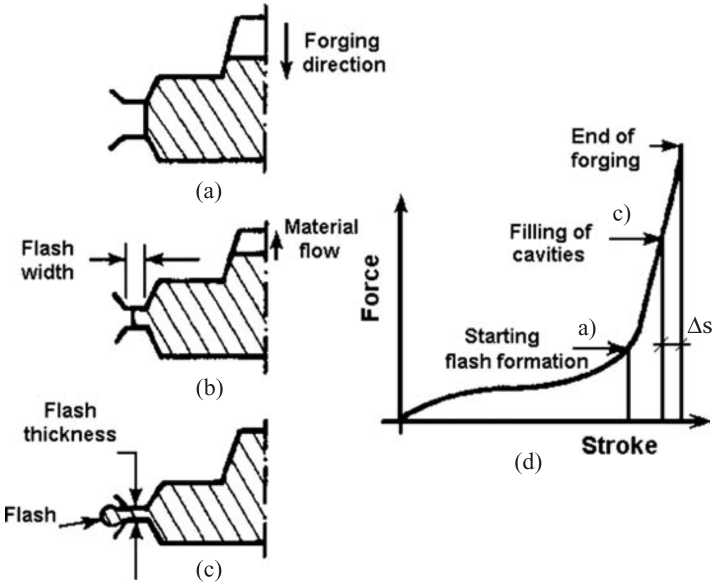

Figure 16.8. The forging load depends on the degree of filling of the die cavity.[4] (a–c) Stages of filling of the die impression. (d) Measured load–stroke curve. (Reprinted with permission of ASM International. All rights reserved. www.asminternational.org.)

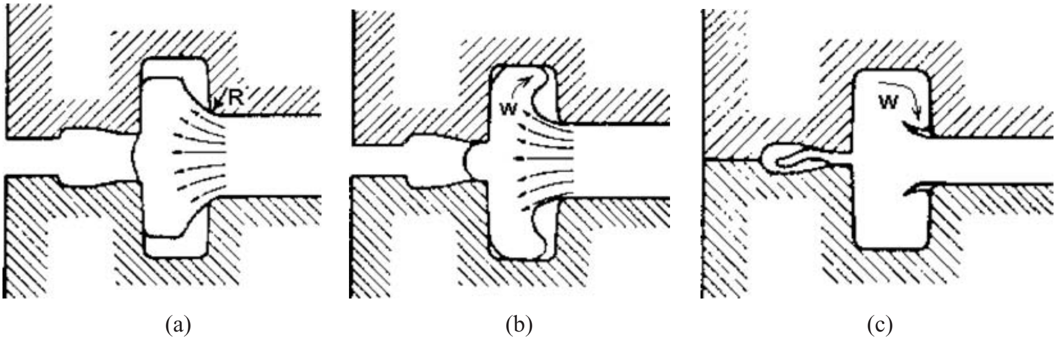

Figure 16.9. Whirl type of metal flow creating over folding,[5] a lap-type defect, in forging. (Reprinted with permission of Prof. Taylan Altan. www.ercnsm.org.)

the die cavity is completely full. Therefore, at this stage of forging the load–stroke curve rises steeply.

In an optimized closed-die forging process, forging should stop shortly after the die cavity has been filled, i.e., the duration of forging after the die is full and thus the stroke length Δs in Fig. 16.8 should be as short as possible. If the component dimensions in the height direction are correct at this moment, the forging has been obtained with minimum energy consumption and minimum mechanical loads on the dies. Concurrently, there has been produced a minimum amount of flash. In closed-die forging some excess material is applied intentionally to make sure that there is complete filling of the die cavity as forging proceeds. It is usually difficult to reduce the amount of flash below 5% of the total amount of workpiece material used. This is because of variation over time in forging conditions, so that the required amount of material may be higher during part of the production time. Industrial forging processes are more or less optimized with regard to material waste if the flash makes up 5–15% of the material usage. If it exceeds 15%, there is generally a potential to reduce the amount of excess material significantly, through improvement in the process to provide better total process economy.

16.6 Folding Defects in Forging

Characteristic flow-related defects called *laps*, or *folds*, are sometimes created during the forging operation, if conditions are not optimized sufficiently to provide sound metal flow. This kind of defect forms under certain circumstances during inflow of material into a die cavity, and when present it is detrimental to the integrity of the forging.

Metal flow that could create *overfolding* is illustrated in the example[5] shown in Fig. 16.9. If the material flow occurs as a *whirl* (w), for instance, overfolding will occur during filling of the rib cavity of the die. This can, for instance, happen if the fillet radius R between the web and the rib cavity is too small. The whirl then causes material to flow into the cavity in such a manner that the initial surface of the workpiece is folded on top of itself in the final forging.

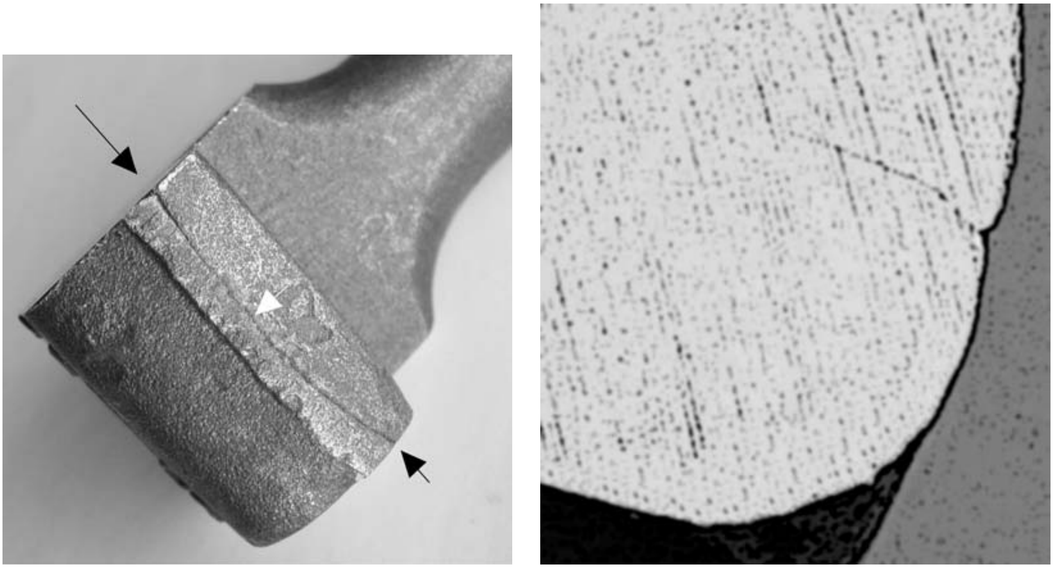
(a) (b)

Figure 16.10. Forging defect: lap formed on forged component (40×).

Toward the end of the forging operation, high pressure is created inside the die, and the fold can then close completely, forming a *shut lap*. When this happens, it is difficult to detect the defect by visual inspection of the final forging. If a metallographic section is cut through the fold, however, it will become visible, especially if the sample is properly etched. The defect can then, for instance, appear as shown in Fig. 16.10. Because the surface of the workpiece is covered with an adhering layer of oxide, the surfaces compressed against each other do not weld completely. The fold will therefore appear like a closed crack in the material; see Fig. 16.10(b). The occurrence of such defects, in most cases, is totally unacceptable, and they must therefore be avoided. If forgings contain this kind of defect, there is great risk that they will fracture during use. They are therefore commonly sorted out and discarded.

Most commonly, the formation of lap defects in forging can be eliminated by modifying the process conditions somewhat. The defect shown in Fig. 16.9, for instance, can be eliminated by change of the die geometry, namely, by making the radius of curvature R of the die larger. The metal flow then will change and the whirl will not appear; instead, the metal will bulge out like a balloon, and will fill the rib cavity without lap formation.

16.7 Flash Gap Geometry

The geometrical shape of the *flash gap* is important for the success of the forging process. Most commonly it is shaped as a parallel channel of constant width w, but with thickness (height) t decreasing continuously throughout the forging stroke, down to a minimum height when forging stops. At this instant, the die is pulled in return. A schematic sketch of a die with flash gap is shown in Fig. 16.11. The flash gap height is normally specified by its value at the moment when forging is ended,

Figure 16.11. Parameters that characterize the flash gap geometry.

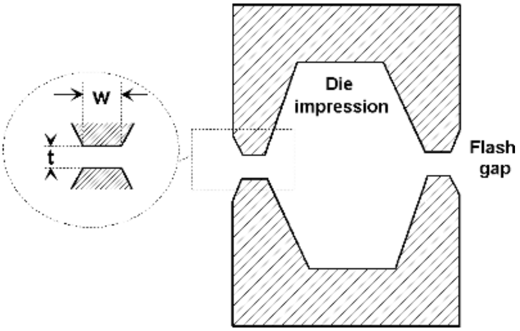

i.e., its smallest value. The flash gap geometry is often characterized by specifying the value of the ratio w/t, i.e., the *width-to-thickness ratio* of the gap. This ratio affects the forging result, as depicted in Fig. 16.12 for a particular forging process.

If forging is done with a ratio w/t as low as say 2.5, the workpiece material will flow easily through the flash gap, and the amount of excess material will be as large as ≈30% of the total required to fill the die cavity. But concurrently, the forming load, and hence also the stresses on the die, will be low; see Fig. 16.13. When the ratio is increased, the flash gap gradually gets narrower. This change causes the required forging load to increase, but concurrently, the required amount of excess material is reduced. This contributes positively to the process economy, in that the total material usage is reduced.

But as Fig. 16.13 depicts, the energy consumption will increase due to this change and so do stresses on the tooling. For a particular forging die, as the figure also depicts, there is minimum energy consumption at a certain value of the width-to-thickness ratio of the flash gap.

In industrial forging of steel, it is common to use a value of w/t for the flash gap in the range 2–5; see Fig. 16.14. Commonly, this ratio is decreased with increasing

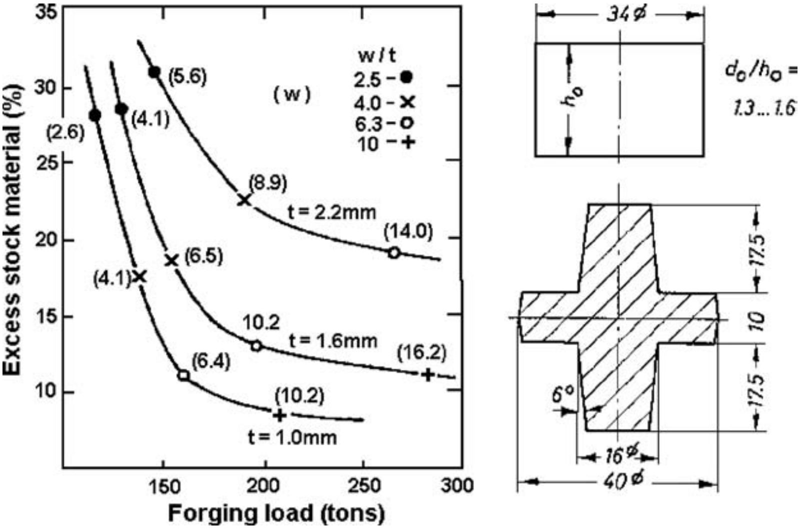

Figure 16.12. Amount of excess material in forging[6] is related to flash gap geometry. (Reprinted with permission from Dr. Kaspar Vieregge.)

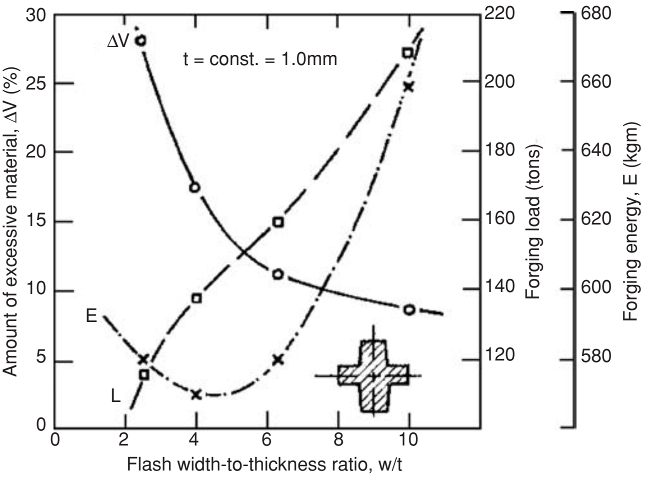

Figure 16.13. Conditions in forging are strongly dependent on flash gap geometry.[6] (Reprinted with permission from Dr. Kaspar Vieregge.)

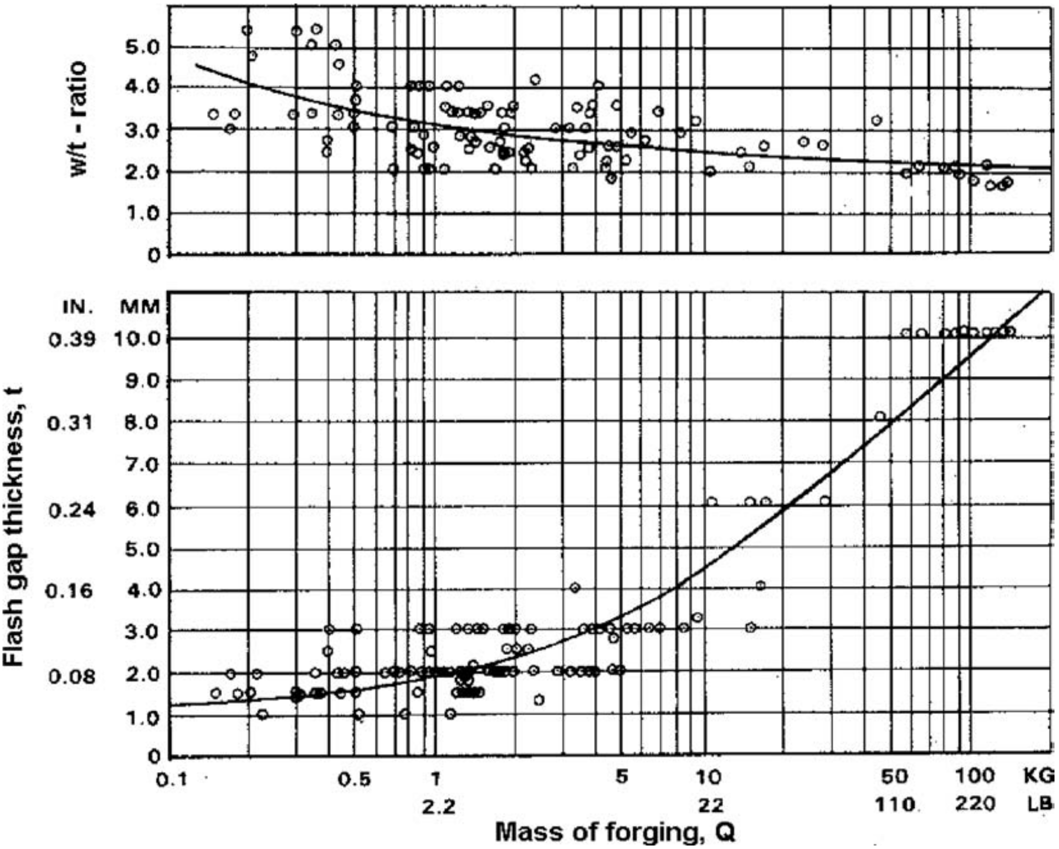

Figure 16.14. Flash gap parameters commonly used in industrial steel forging.[7] (Reprinted with permission of Prof. Taylan Altan. www.ercnsm.org.)

weight of the forging. When the width-to-thickness ratio of the flash gap exceeds 5, the stresses on the die become large. Concurrently, the die lifetime is significantly reduced, so in industrial forging, such high ratios are not commonly used.

Problems

16.1 Commonly used forging processes are divided in two subgroups.

(a) Mention the name of each subgroup. Describe the main differences between them.
(b) Sketch a typical load–stroke curve as it is measured in forging. Partition the curve into separate regions in which different flow phenomena take place inside the die cavity. Describe briefly what characterizes metal flow in each region.
(c) What characterizes the state of plane strain deformation? Explain to what extent it can be realized in a laboratory process and in industrial forging.
(d) Describe what is meant by the term *axisymmetric deformation*.

In compression of metal between two plane-parallel dies, the necessary forming load and the friction hill (i.e., the pressure distribution) depend on the nature of the compression process, i.e., whether it is axisymmetric or is in plane strain.

(e) Specify the expressions for forming load and pressure distribution for each kind of compression process, as they are determined by the slab method. Compare the expressions for each of the deformation processes. What is the difference between the two?

16.2 In technological literature, good workability of a workpiece material sometimes is claimed to require the following:

(i) The material should have low deformation resistance.
(ii) The material should deform plastically without formation of internal or surface cracks.

Comment on the goodness of the formability definition used in this case. Try to give a better definition.

NOTES

1. Sabroff, A. M., Boulger, F. W., and Henning, H. H.: "Forging Materials and Practices," Reinholdt, New York, 1968.
2. Spies, K.: "Preforming in Forging and the Preparation of Reducer Rolling," doctoral thesis, Technical University Hannover, 1959.
3. Haller, H. W.: "Handbook of Forging" (in German), Carl Hanser Verlag, München, 1971.
4. Altan, T., Oh, S.-I., and Gegel, H. L. (Eds.): "Metal Forming, Fundamentals and Applications," ASM Int., 1983, pp. 143–170.
5. Subramanian, T. L., Akgerman, K., and Altan, T.: "Application of computer-aided design and manufacturing to precision isothermal forging of titanium alloys," Batelle's

Columbus Laboratories, Final report AML-TR-77-108, Vols. I, II and III. Air Force Materials Lab., July, 1977.

6. Vieregge, K.: “Ein Beitrag zur Gestaltung des Gratspaltes beim Gesenkschmieden,” Dissertation, Technical University of Hannover, 1969 (in German).
7. Lange, K., and Meyer-Nolkemper, H.: “Closed-Die Forging” (in German), Springer-Verlag, Berlin, 1977.

REFERENCES

Altan, T., Oh, S.-I., and Gegel, H. L. (Eds.): “Metal Forming, Fundamentals and Applications,” ASM Int., 1983, pp. 143–170.

Altan, T., Ngaile, G., and Shen, G.: “Cold and Hot Forging: Fundamentals and Applications,” ASM Int., Materials Park, Ohio, 2004.

Altan, T.: “Hot forging: Trends and applications,” fourth Precision Forging Workshop, Plymouth, Michigan, 2008.

Byrer, T., Semiatin, S. L., and Vollmer, D. C.: “Forging Handbook,” ASM Int., Metals Park, Ohio, 1985, pp. 112–114.

17 FEA of Forging

In this chapter, two rather different cases of forging will be considered, the first one being cold *backward cup extrusion*, and the second one, *hot closed-die forging*. During FEA, a large number of analysis results can be achieved when realistic models of the forming operations have been made. These two cases demonstrate some important results achieved this way.

17.1 Cold Forging by Backward Cup Extrusion

As explained in Sec. 2.2.3, *hollow cups* of metal are commonly manufactured from cylindrical workpieces, called *slugs*, by use of backward cup extrusion. Even though this process is called extrusion, it is often classified as a forging process and will be so considered in the following.

Let us now analyze the backward cup extrusion process visualized in the FEM model in Fig. 17.1. Only one half of the workpiece and the dies was modeled, because there is rotational symmetry around the y-axis. The mirroring option of the program, however, was used to visualize the full longitudinal cross section of the forming process as shown in Fig. 17.1. In this figure, (a) shows the initial die and workpiece configuration, (b) shows an intermediate stage of forming, and (c) shows the final thick-bottomed cup at the end of forming.

The FEM model mimics an industrial cold-forging process, where a *soft-annealed* slug of the alloy AA 6082 was given the cup shape shown in Fig. 17.1(c). The tooling consisted of a moving punch and a stationary container. In the model shown in Fig. 17.1, the tooling has, for reasons of simplicity, been modeled by lines only. This can be done if the process is described by an isothermal FEM model. Because thermal effects are neglected then, it is not required to mesh the tooling. As Fig. 17.1(a) depicts, the slug is pressed downward by the moving punch head in the beginning of the forming process and flows down to fill the bottom cavity of the container. In this way, the slug conforms to the shape of the container. When the bottom cavity has been filled, the metal starts to flow in the opposite direction over the punch head, out into the gap between the punch and the container, and the wall of the cup is formed as shown in Fig. 17.1(b).

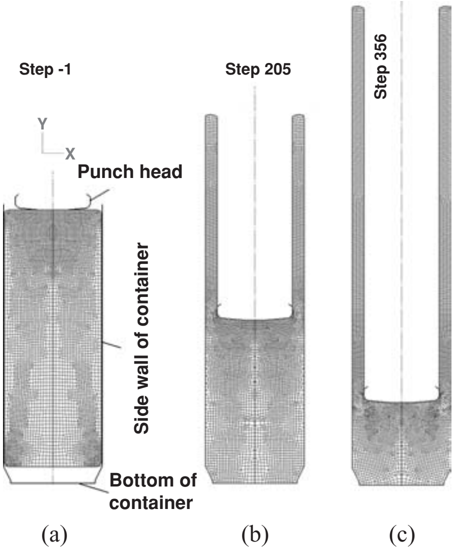

Isothermal

Axisymmetric

Flow stress:
$\sigma = 97.2\varepsilon^{0.152}$ & $\varepsilon^{0.015}$

Rigid dies

Plastic slug

Punch velocity: $1 mms^{-1}$

Friction factor: $m = 0.1$

Figure 17.1. FEM model to mimic backward cup extrusion: (a) starting step, (b) intermediate step, and (c) end step.

Some *simulation results* obtained by this model are shown in the forthcoming subsections to demonstrate the usefulness of FEA for getting knowledge of the mechanics of forging processes.

17.1.1 Deformation History of a Workpiece from the Effective Strain Rate

In Fig. 17.2 are shown some pictures, obtained from the FEM model, of the predicted *effective strain-rate distribution* in the workpiece during the forming operation.

Figure 17.2(a) shows this distribution at an early stage of forming, when the main material flow is directed downward into the bottom cavity of the container. The effective strain rate is now predicted to be low in the bottom half of the workpiece, which moves downward at this instant. However, in the top portion of the workpiece, there is significant metal flow under the punch head, where a *cone-shaped dead zone* of low effective strain rate occurs and penetrates down into the workpiece together with the punch head. A distinctive shear zone with high effective strain rate forms in the layer below the dead zone. It appears like an arrowhead pointing downward into the slug. In Fig. 17.2(a), this shear zone has been marked by a hatched black line on one half of the figure.

Figure 17.2(b) correspondingly shows the situation when the bottom cavity of the container has just become filled with workpiece material. Now there is a change in deformation pattern in the region under the punch head.

A plastic zone with effective strain rate >0.05 appears in the layer at the top of the workpiece. To see what happens inside this plastic zone, it is required to set the strain-rate scale differently. The resulting strain-rate distributions for two different

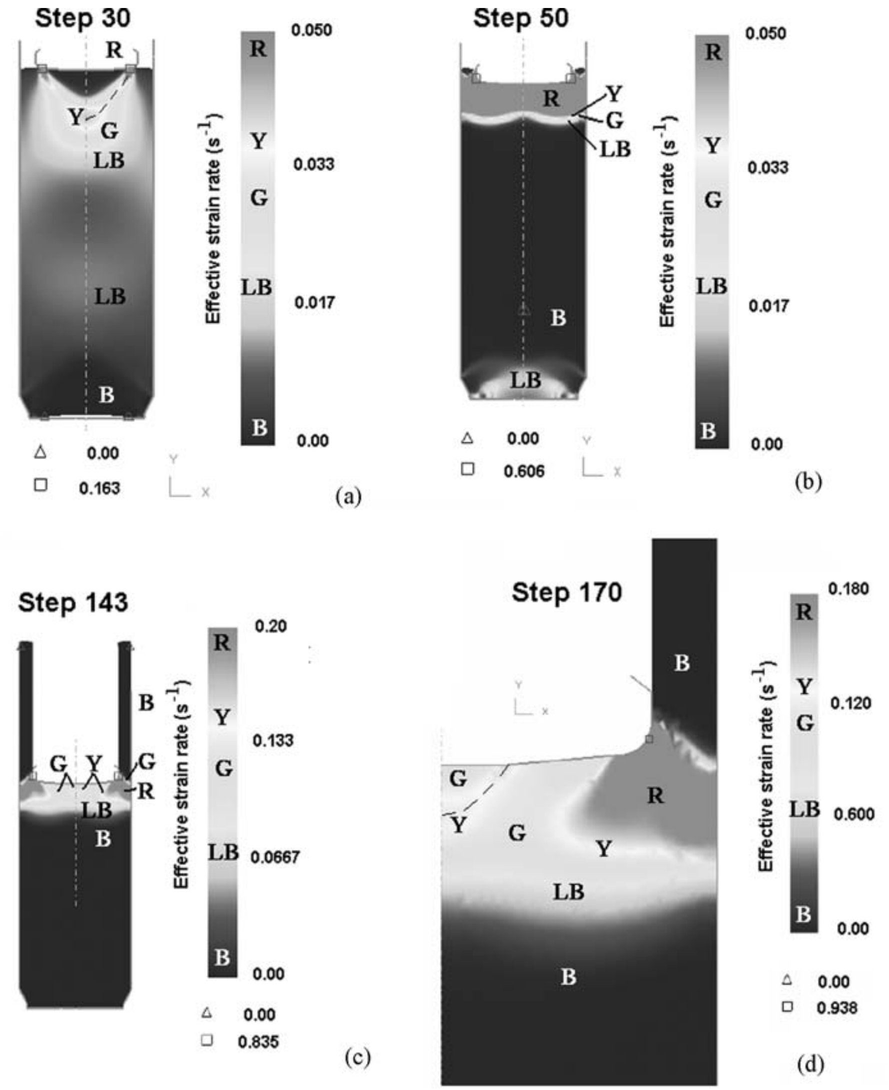

Figure 17.2. Computed effective strain-rate distribution inside the workpiece in backward cup extrusion at (a–c) different stages of forging and (c,d) different scalings to show parameter variation.

scales are shown in Fig. 17.2(c) and (d), respectively. From Fig. 17.2(d), it is seen that the effective strain rate is particularly high in the region where the material of the slug flows over the edge of the punch head. At this location, the slug material leaves the plastic zone and flows out through the gap between the container and the punch head. Upon leaving this gap, it ceases to deform, having been transformed into the wall of the cup. The cup wall appears as a rigid body, and its height increases as forming proceeds. Further behind, inside the plastic zone, strain rates are lower, except in a small *arrowhead-shaped region* close to the axis of the slug. Here there is a cone-shaped layer with local high strain rate, i.e., a *shear zone*, as indicated by the black dashed line in Fig. 17.2(d).

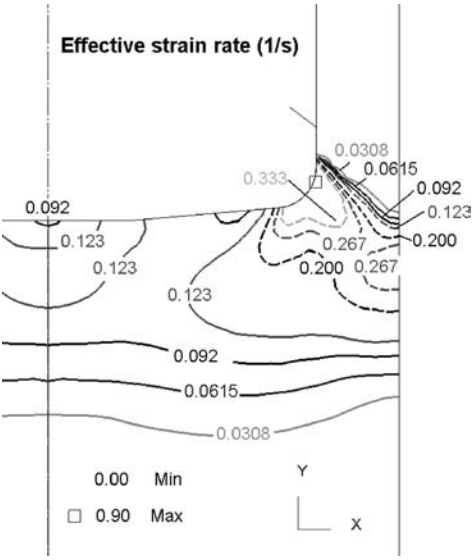

Figure 17.3. Effective strain-rate distribution inside workpiece as predicted in backward cup extrusion.

An alternative is to show the strain-rate distribution by contour lines; see Fig. 17.3. When it is presented this way, one can see that the highest effective strain rate is predicted in the region where the material slides over the punch edge. In the cup wall, there is zero strain rate, because there, there is rigid-body movement only, and no plastic deformation.

17.1.2 Deformations in the Final Cup Visualized by the Effective Strain Distribution

The *effective strain distribution* inside the final cup after forming is shown in Fig. 17.4. Figure 17.4(a) shows the whole cup; Fig. 17.4(b) and (c) show sections of the cup near the edge of the punch head and in the gap between punch and container. One can see from this figure that there are very nonuniform deformations in the cup. There are especially high effective strains in a layer below the punch head. As will be shown in the next section, there is lateral material flow here, so that slug material flows radially outwards over the punch head. When the material leaves the edge of the punch, it ceases to deform, as it becomes the inner layer of the cup wall. Because this layer is first strongly compressed in front of the punch, and afterwards shear-deformed upon flow over the edge of the punch, it experiences large total plastic deformations. The strain value therefore increases along the cup wall, from the top toward the bottom of the cup, where maximum effective strain is predicted to exceed a value of 5 at the instant when forming of the cup is finished. The material that flows out through the gap between the punch head and container into the outer layer of the cup wall, however, is considerably less strained: the effective strain here does not exceed 1.5. Another observation is that material in the top of the cup wall and material remaining in the base of the cup are subjected only to minute effective

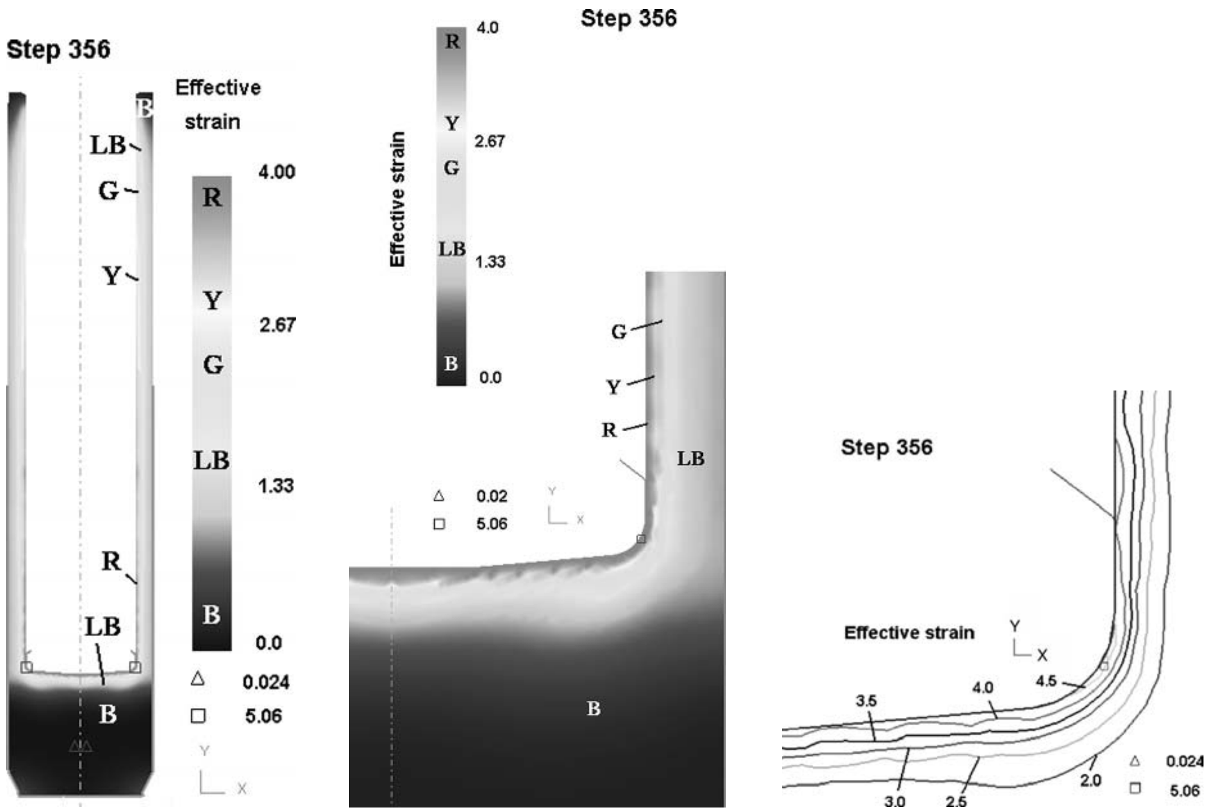

(a) (b) (c)

Figure 17.4. FEM-predicted effective strain-rate distribution inside the final cup in backward extrusion: (a) whole cup; (b,c) detail at the bottom corner of the cup.

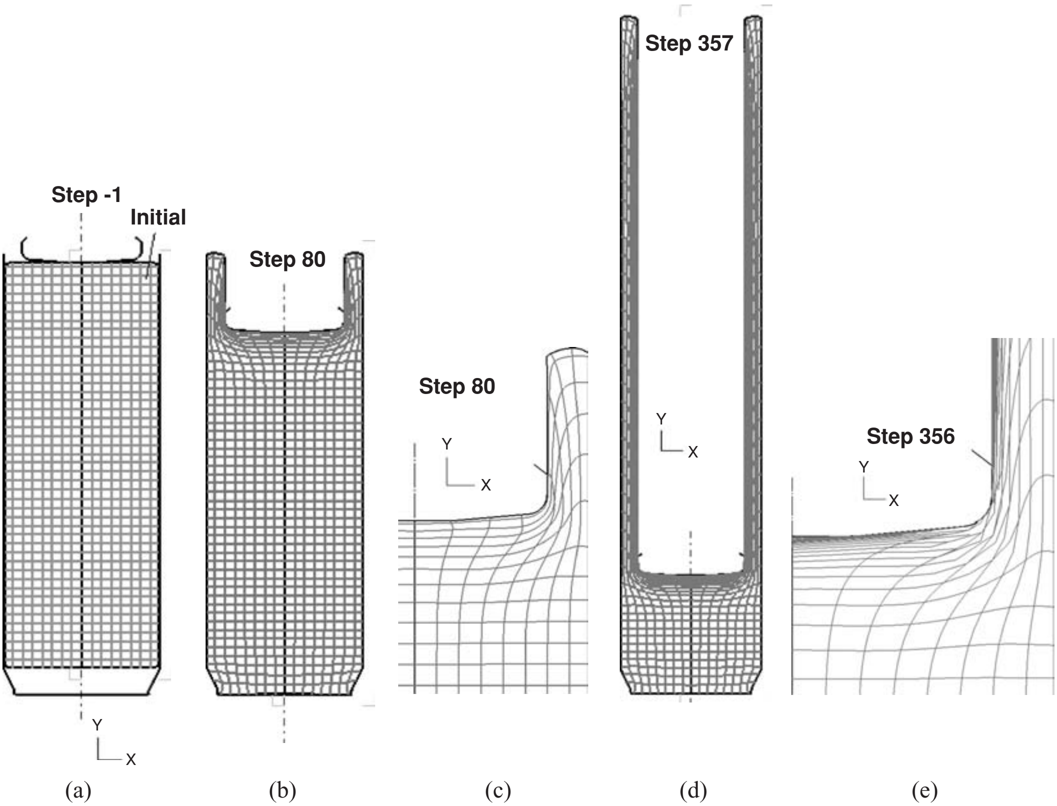

Figure 17.5. Deformed internal grid pattern; (a) initial pattern, (b) pattern at early stage of forming, and (c) detail of (b). Deformed grid pattern of final cup: (d) whole cup and (e) detail of (d).

strains. This clearly depicts that deformations are indeed very inhomogeneous in this forming operation.

17.1.3 Deformations from the Deformed Grid Pattern

As explained in Ch. 3 and Ch. 12, the deformations imposed on a workpiece in metal forming can be visualized by means of an internal grid pattern on the midsection of the workpiece. Such grid patterns can also be made in simulation. It is therefore possible to use experimental grid patterns to validate whether the simulated metal flow corresponds to the real metal flow.

In Fig. 17.5, a grid pattern is shown as it is predicted to occur in FEA at three different stages of the backward cup extrusion process. Figure 17.5(a) shows the initial pattern; Fig. 17.5(b) and (c) show the corresponding pattern in an early forming step, step 80. The detail of the pattern given in Fig. 17.5(c) shows that at an early stage of forming it is still straightforward to see the deformed pattern at the edge of the punch head. But because of remeshing of the FEM mesh close to the punch edge during simulation, this is not necessarily the case at a later stage of forming. Because there is very large deformation of the material flowing over the punch edge, the

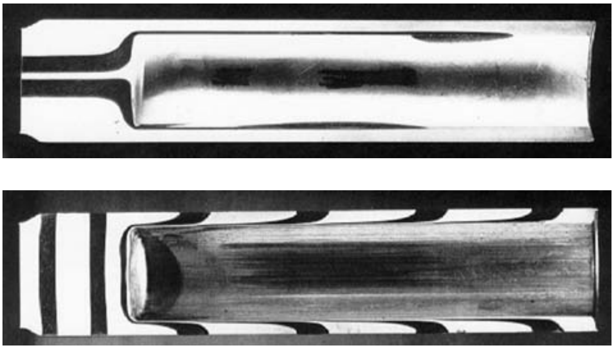

Figure 17.6. Deformed experimental internal stripe pattern in final cup. Top: longitudinal lines; bottom: transverse lines (courtesy Steertec Raufoss AS, www.willielbe.de).

software is not able to keep track of the grid pattern in this heavily deformed region during late stages of forming. This is, for instance, the case for the simulated grid pattern shown in Fig. 17.5(d), which represents the end stage of the process. This can clearly be seen in the magnified detail of the final pattern shown in Fig. 17.5(e).

However, experimental stripe patterns based on inserted contrast pins do not have this drawback. The deformed experimental grid pattern is indeed revealed even in the most heavily deformed regions, as previously explained in Ch. 12. Figure 17.6 shows corresponding stripe patterns obtained in an experimental study of the backward cup extrusion process, being analyzed here by the FEM model. When this pattern is compared with the simulated pattern shown in Fig. 17.5(e), one can see that there is close similarity between the two patterns. This documents that metal flow during the cup extrusion process is well reproduced in the simulation model.

In Fig. 17.7, the partially deformed grid pattern previously shown in Fig. 17.5(c) is shown again with numbers assigned to some grid elements in order to discuss the deformations occurring in the forming process.

As shown in Fig. 17.5(a), the initial grid pattern is made up of square grid elements of side 5 mm. The deformed grid element labeled 1 in Fig. 17.7 is still in the base of the cup at the stage of forming examined here and has only been subjected to minor plastic deformation during the upsetting stage of the forming process.

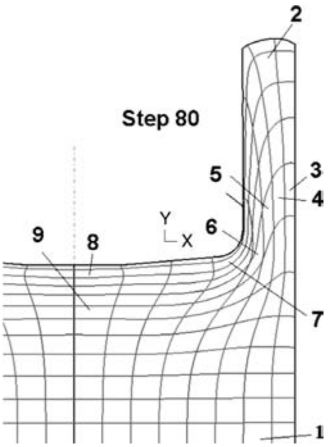

Figure 17.7. Deformations inferred from deformed grid pattern.

Another grid element that has experienced small deformations is element 2, which has left the plastic zone and resides in its final deformed state at the top of the cup wall. Hence, observations of deformations from the shape of the grid elements agree well with the previously discussed observations of deformations in terms of effective strain distributions; see the preceding subsection.

Consider grid elements 3–6, all initially located on the same transverse grid stripe. Elements 3–5 are about to leave the gap between the punch edge and the container and have more or less obtained final shape. We can see that whereas element 3 has been subjected to only minor shear deformations, the shear deformations are considerably larger in element 4, and especially in element 5. On the other hand, the grid element 6 is still inside the plastic zone and has up to now been subjected to a lot of shear. From the shape of this element, it is obvious that shear deformations for it is larger than for the previously mentioned grid elements located closer to the cup wall.The grid element that has been subjected to the largest deformations, both with regard to radial stretching and shearing, is the element labeled 7 in the figure. This element, which initially was located ahead of the punch nose, has stretched out in the radial direction during its outward radial movement. Moreover, it has experienced rotational movement during its flow over the edge of the punch nose, while becoming more and more shear-deformed, on its way out of the gap between the punch nose and the container wall.

Consider also grid elements 8 and 9. On the left side, these elements coincide with the vertical axis of the slug, and thus with the symmetry plane. Here, the elements still maintain rectangular shape; hence, there is no shear deformation. On the right-hand side of the elements, however, there are shear deformations, i.e., the elements have an oblique shape on that side. But the shear deformations are in opposite directions for elements 8 and 9. While element 8 has flowed less in the radial direction at its top, the situation is opposite for element 9.

It is seen that both grid elements 8 and 9 have been subjected to large total deformations. From the shape of the elements, it is not straightforward to say which element has the larger deformation. But Fig. 17.4(b) shows that the simulation program computes the effective strain to be largest adjacent to the edge of the punch, i.e., at the location of grid element 8.

17.1.4 Material Flow in the Plastic Zone from the Velocity Field

In Fig. 17.8 are shown various representations of the velocity field in the backward cup extrusion process at a late stage of forming, as obtained from the simulation model. Here (a) shows the distribution of the flow velocities for material particles inside the specimen by means of a grayscale; (b) shows the velocities indicated by vectors. In Fig. 17.8(c), the point-tracking option of the simulation program has been used to show the travel distance of various material particles during a short time step, in various locations adjacent to the punch head. Because this distance is proportional to the velocity of the particles, this picture also depicts the velocity field. In all the diagrams, the punch is assumed stationary, and the velocities are those experienced by material particles of the workpiece as they flow past the punch.

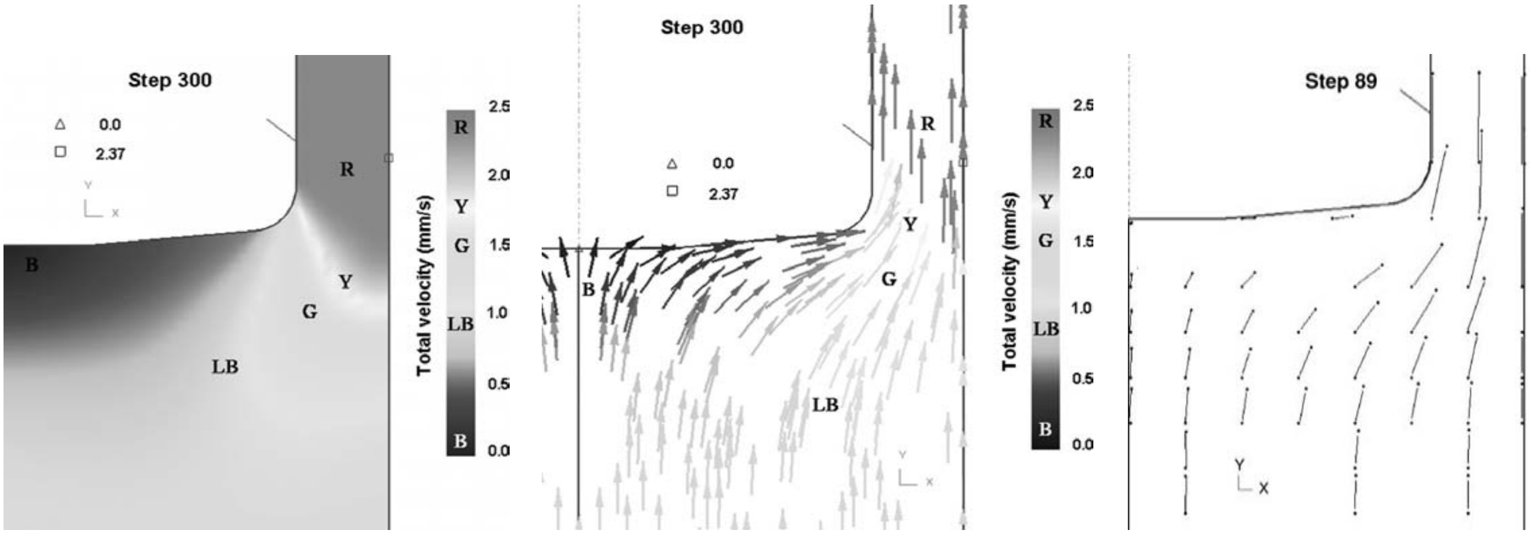

(a) (b) (c)

Figure 17.8. Flow velocities in the plastic zone.

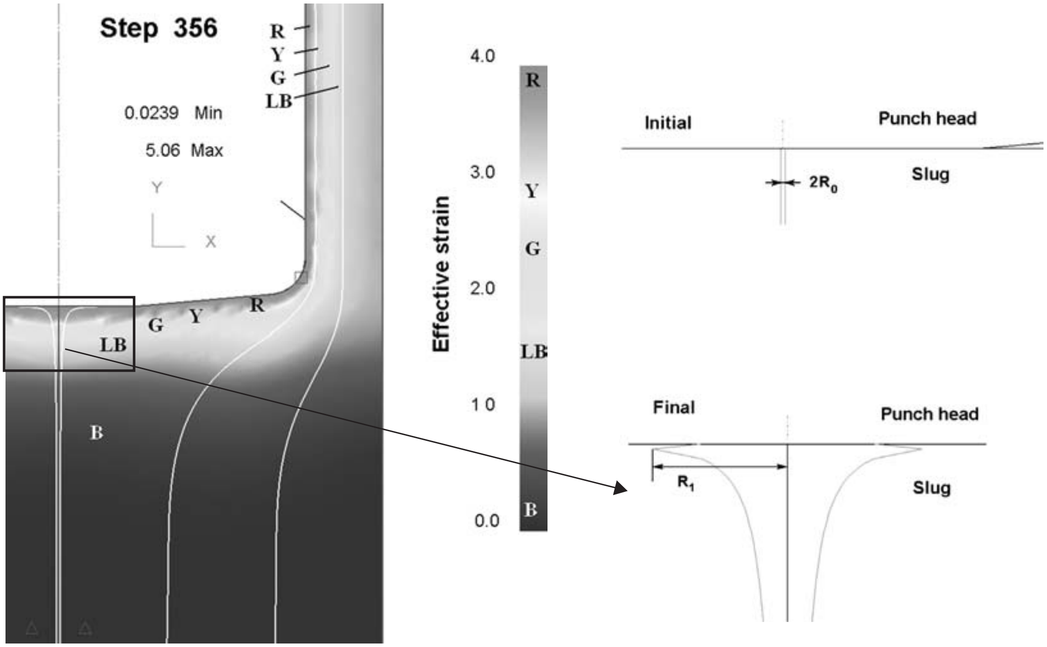

(a) (b)

Figure 17.9. Longitudinal lines of the grid pattern depict large deformation in the layer below the punch head.

Note that the slug material close to the centerline, adjacent to the punch nose, moves in a direction toward the punch, while the rest of the material takes a smooth, laterally rounded path toward the gap between the punch and the container. Material flow along the punch head at the oblique outer part of the punch is predicted to be approximately parallel to the punch surface.

Although the material velocities in the slug are low in the region below the punch head, velocities similar to the punch velocity are predicted in the rest of the slug and in a large part of the plastic zone. The upward-directed velocity in the cup wall is increased by a factor of ≈2.5 over the velocity inside the slug material.

17.1.5 Deformation in the Material Layer Adjacent to the Punch Nose

In Fig. 17.9, it is shown how the simulation model predicts the deformation behavior of the thin axial center portion of the slug initially under the punch nose. This initial cylindrical volume remains in the middle of the slug during the forming operation but becomes severely stretched out in the radial direction adjacent to the punch nose as it is pressed between the punch and the forward-flowing slug material. Because there is rotational symmetry, the situation is in reality that an initial axial cylinder of small radius becomes compressed axially into the shape of a lily. If one considers the widest section of this layer at the end stage of cup extrusion (see Fig. 17.9), the simulation program predicts that the initial cylinder of radius $R_0 =$ 0.1 mm will increase to the new radius $R_1 =$ 2.1 mm at the location where the radial expansion is largest. A simple approximate calculation of the effective strain thus yields the following result for the widest section of the lily:

$$\varepsilon = \ln \frac{A_1}{A_0} = \ln \frac{\pi R_1^2}{\pi R_0^2} = \ln \frac{2.1^2}{0.1^2} = 6.1$$

This value can be compared with the corresponding maximum effective strain value computed by the simulation model. As shown in Fig. 17.4, the maximum effective strain value predicted by the simulation model is 5.06. This strain is predicted to occur in the subsurface layer of the cup, adjacent to the edge of the punch head, at the end of forming, and it is denoted by a small square in Fig. 17.9. This shows that it is not straightforward by FEA to compute the net deformation in the heavily deforming subsurface layer of the workpiece, located in front of the punch nose during forming. The reason for this is that there are in reality large *gradients of deformation* in this layer.

17.1.6 Emptying Diagram

Emptying diagrams were made by the simulation model for the backward cup extrusion process and are shown in Fig. 17.10. They correspond to the emptying diagrams that were made manually on the basis of deformed experimental grid patterns obtained in the forward extrusion processes; see Ch. 12.

An emptying diagram is easily obtained by means of the FEM model. The simulation is run to the end stage of forming, as shown in Fig. 17.10(a) and (c); then a "grid pattern" consisting of one single transverse (T) line is added into the section of the workpiece, as shown by line A–A in Fig. 17.10(a).

This *T-line* then represents the boundary line between the material in the cup wall and the material in the base of the cup after the end of extrusion. The simulation model was run backwards to the initial state to show where material particles along this line were placed at the start of forming; see Fig. 17.10(b). Because the FEM program remeshes the FEM grid many times during the course of simulation, the simulation program is not able to keep track of those material points that flow close to the punch edge when the backward point tracking is done. Because of this, only part of the line gets tracked back to the initial location in the slug.

Because we know from the discussion in connection with Fig. 17.9 that the middle of the slug remains unextruded (i.e., inside the base of the final cup), one can manually extrapolate the transverse emptying line upwards toward the punch head. This was done by drawing the thin black lines shown in Fig. 17.10(b). From the resulting figure, the location of the slug material that forms the cup wall can be identified and distinguished from the material that forms the base.

A pattern consisting of multiple horizontal lines has correspondingly been added to the section of the final component in Fig. 17.10(c). Figure 17.10(d) shows the resulting emptying diagram when all these lines are traced back to the initial state. From this diagram, we can now clearly see from where inside the slug the top slice of the cup wall, the slice below the top slice, etc., originate.

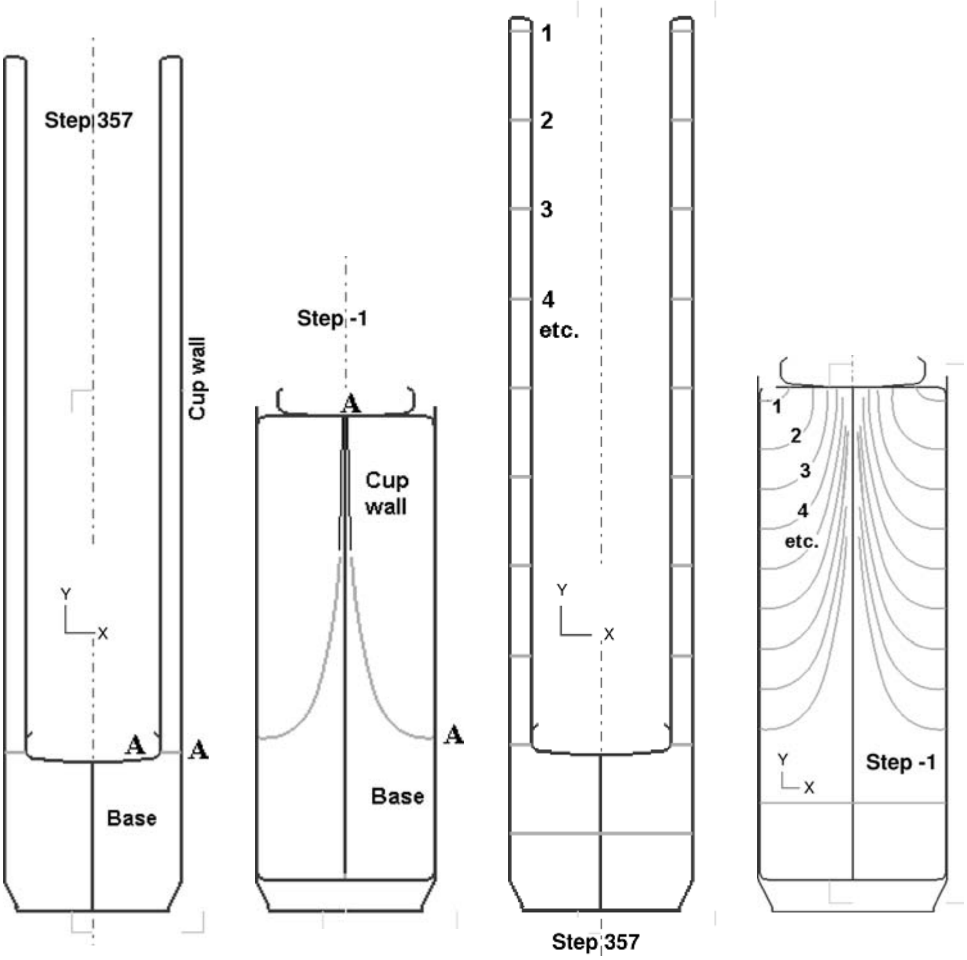

(a) (b) (c) (d)

Figure 17.10. Emptying diagrams for backward cup extrusion: (a) single T-line at the end stage, (b) single T-line traced back to the initial stage, (c) multiple T-lines at the end stage, and (d) multiple T-lines at the initial stage.

17.1.7 Effect of Friction on Punch Load

To study whether the required punch load in backward cup extrusion depends on the friction, three different simulations were run, in which friction between the slug and the tooling was assumed to conform to the Tresca friction model, eq. 10-7. In the simulations, the friction factor between container and slug was always set equal to $m = 0.1$. Three different friction conditions represented by $m = 0.1$, $m = 0.3$, and $m = 1.0$, however, were specified for the interface between the slug and the punch head. The resulting load–stroke curves obtained for these three different frictional conditions are shown in Fig. 17.11. In this analysis, process conditions other than friction were assumed constant, equal to those specified in Fig. 17.1. As Fig. 17.11 shows, the prediction in this case is that the required punch load will increase with

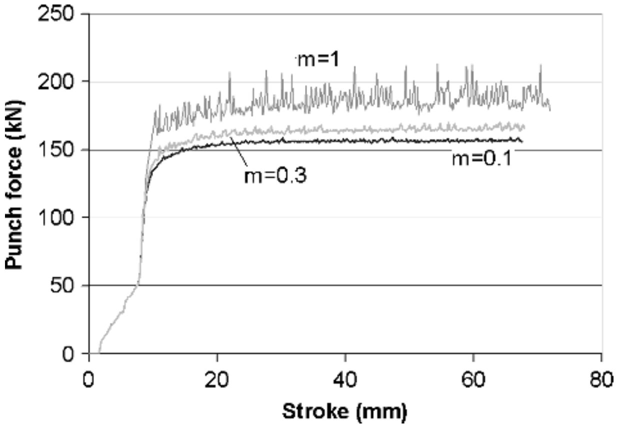

Figure 17.11. FEM simulation predicts that the punch load will increase with increasing friction in backward cup extrusion.

increasing friction, by approximately 25%, when the friction factor is increased from 0.1 up to 1.0.

17.1.8 Expansion of the End Surface of the Cup upon Punch Penetration

An experimental procedure has been developed[1,2] by which it is possible to quantify the area expansion occurring on the slug surface when being penetrated by the punch head during backward cup extrusion. The procedure is outlined in the sketch in Fig. 17.12. The flow of different areas of this surface can be followed during the forming operation by adding either a ring or a point pattern, denoted in Fig. 17.12

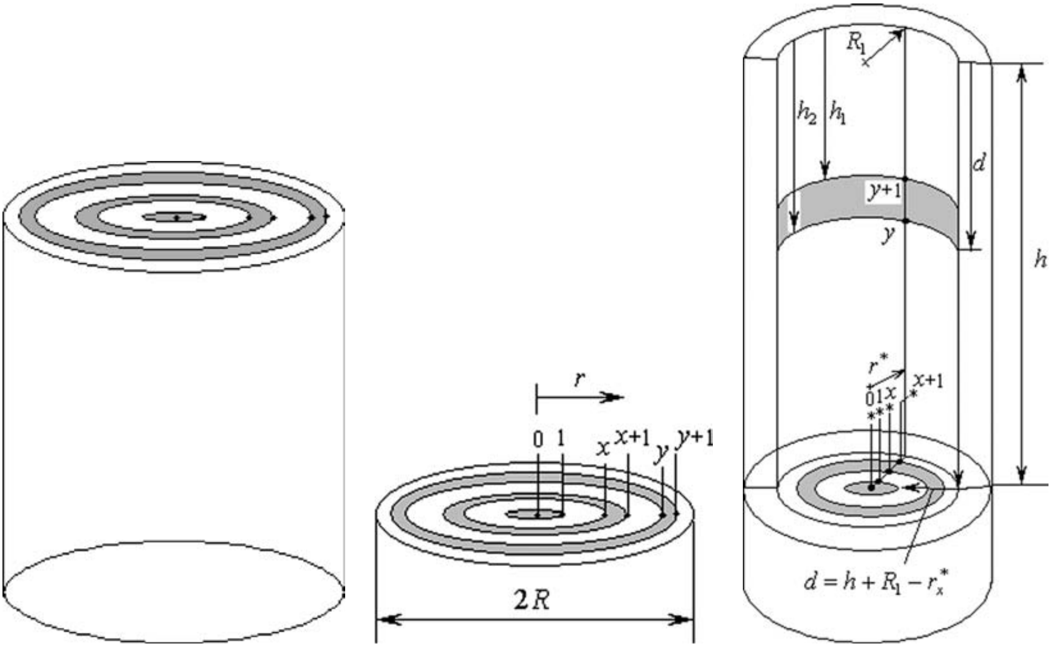

Figure 17.12. Expansion of the end face of the slug into the inner cup surface in backward cup extrusion.

as P0, P1, …, Px, P$x+1$, …, Py, P$y+1$, along a specific radial line on the end surface of the slug, which during later forming is deformed by the punch head. In this end face, assume the initial radial distances from the center point to the points P1, P2, etc. – i.e., r_1, r_2, etc. – to be known. The points must also be visible on the surface inside the cup after forming. Those closest to the center of the surface will flow radially outward from the center to new positions r_1^*, r_2^*, etc., during forming, but will remain ahead of the punch nose. Points sufficiently far from the center of the cup, however, will appear on the inside of the wall of the cup after forming. Assume this inside wall to have radius R_1. The final distances from the top of the cup to the points are measured out as h_x, h_{x+1}, etc. When these distances are known, it is straightforward, as shown in Example 17.1, to compute the surface expansion for different parts of the slug surface, and to make a plot of the distribution of surface expansion that has taken place on the inside surface of the cup during forming.

EXAMPLE 17.1: EXPANSION OF THE AREA FORMING THE INSIDE SURFACE OF THE CUP

Problem: Assume initial and final distances between points to be known as just described. Write down the required formulas to compute the surface expansion of the central circle and the ring-shaped areas between two adjacent rings on the initial end-face of the specimen. Calculate the folded-out distance of each ring area as measured from the top of the cup after forming.

Solution: Different formulas will result, depending on whether one consider the area of the central ring or the areas between rings positioned farther away from the center of the slug and depending on whether the final rings appear on the bottom surface or on the inside surface of the cup wall:

Ring in the middle of the end face of the slug:

$$\text{Area expansion: } X = \frac{\pi r_1^2}{\pi r_1^{*2}};$$

$$\text{Folded-out distance from top of cup: } d = h + R_1 - \frac{r_1^*}{2}$$

Ring remaining in the bottom surface of the cup:

$$\text{Area expansion: } X = \frac{\pi \left(r_{x+1}^{*2} - r_x^{*2}\right)}{\pi \left(r_{x+1}^2 - r_x^2\right)};$$

$$\text{Folded-out distance: } d = h + R_1 - \frac{r_x^* + r_{x+1}^*}{2}$$

Ring on the surface of the inner cup wall:

$$\text{Area expansion: } X = \frac{2\pi R_1 (d_y - d_{y+1})}{\pi \left(r_{y+1}^2 - r_y^2\right)};$$

$$\text{Distance from top of cup: } d = d_{y+1} + \frac{d_y - d_{y+1}}{2}$$

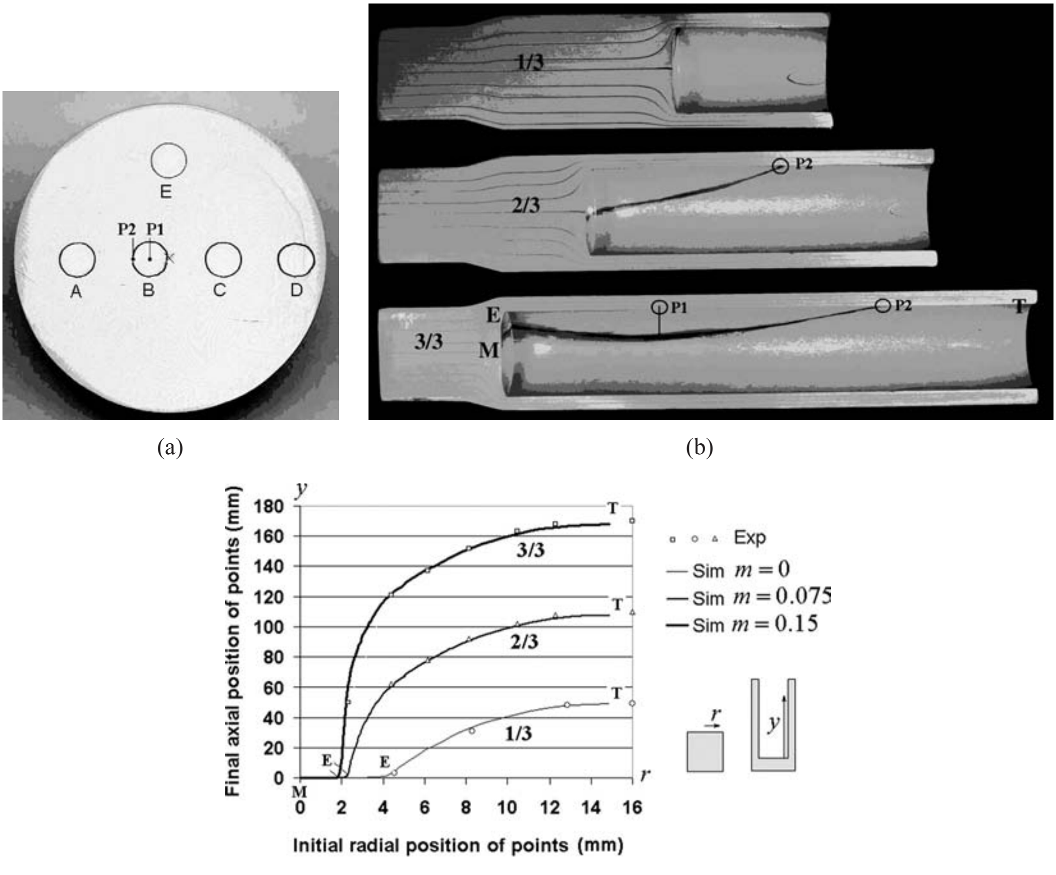

(a) (b)

(c)

Figure 17.13. Experimental metal flow of the end face of the slug reproduced in FEM analysis: (a) initial ring pattern on the end face of the slug, (b) deformed ring pattern inside the cups, and (c) graphical representation of the appearance of marker points in experiment and simulation for appropriate friction values.

17.1.9 Inverse Modeling to Deduce the Friction at the Punch–Slug Interface

It is possible by measurements, as has been shown, to characterize and quantify the outflow of various parts of the initial end face of the slug over the head of the punch during backward cup extrusion. Early investigations[1,2] showed that this outflow depends on the friction between the punch and the slug. If the outflow is mapped in an experiment and reproduced in FEA, it can be used to find the friction by inverse analysis.

Use of the experimental surface ring pattern technique for finding the interfacial friction was described in detail in Sec. 12.7. This technique has also been applied for this purpose for the case of backward cup extrusion.

The initial experimental ring pattern[3] applied on the end face of the slug is shown in Fig. 17.13(a). The center of this surface is shown by a cross, and two points, which can identified from the small circle close to the center of the slug, are denoted

P1 and P2. The pattern of the small circles inside the cup at three different stages of forming is shown in Fig. 17.13(b). The points P1 and P2 as they appear after forming are easily identified. The other marker circles – the closest (C), the middle (A), and the farthest (D) away from the center of the slug – define additional points on this surface, which can be applied for surface expansion analysis.

When the initial and final distances defined by all the small circles on the surface to be analyzed have been measured, the best way of depicting the results is as shown in Fig. 17.13(c). There, graphs are shown of the final axial distance of the points from the bottom of the cup, vs. the initial radial distance of the same points from the center of the slug surface.

The same kind of graphs can also be made by FEM simulation of the process. In the simulation, the friction between the punch head and the slug surface is varied. For a specific value of friction, one can find good agreement between experimental flow and corresponding simulated flow of the surface points. When that is achieved, one knows that the simulation mimics the experiment well with respect to the nature of the metal flow over the punch nose. Figure 17.13 depicts such results obtained in our analysis. In this figure, data are shown that depict the experimental behavior at three different stages of forming. In addition, results obtained from simulations are shown, which mimic the experimental behavior well. As one can see from the graphs, there was good agreement between experiment and simulation at the end of the first third of the operation when the friction factor in the simulation was set equal to zero. For the second cup, extruded up to the second third, the frictionless simulation was applied for the first third of the forming operation, and then a value $m = 0.075$ was applied for the rest of the stroke. This yielded good agreement between simulation and experiment for forming up to this stage. Finally, for the last third, stage, a friction factor $m = 0.15$ had to be used in the simulation.

In this manner, by measurement of the stretching of the point pattern of the slug over the punch head during outflow of it over the edge of the punch into the inner cup wall, and by reproduction of it in FEM simulation, we have found that friction increases over the punch head during the extrusion process.

One should perhaps mention what kind of lubricant was applied in the cup extrusion experiment considered here, which provided frictionless conditions from the beginning of forming, with later increase in friction up to $m = 0.15$, because of the extension and the thinning of the lubricant film during the course of forming. The lubricant was actually a conversion coating, which consisted of a calcium aluminate film applied to the slug before forming. Soap was also used on top of the coating. Conversion coatings are considered solid lubricants, because they adhere strongly as a solid layer on top of workpiece surfaces. They also have the ability to expand greatly during forming together with the surface they cover, and they can provide low friction.

When the friction has been determined, it is easy by means of the FEM model to determine the stretching (*expansion*) of the end surface of the slug as it flows over the punch head to finally appear as the inside surface of the cup. A number of points were added on this surface, and by means of point tracking, their final positions

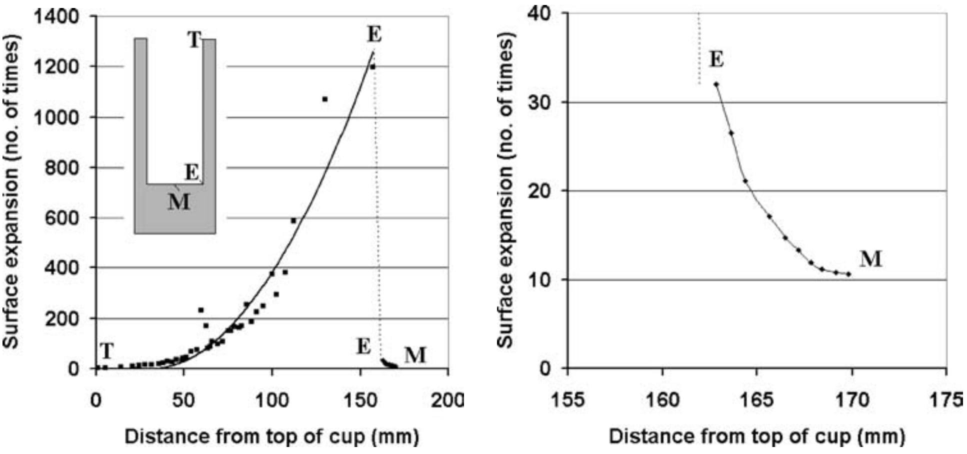

(a) (b)

Figure 17.14. Surface expansion of the end face of the slug into (a) the whole inside surface of the cup and (b) the inner bottom surface of the cup.

were found. The formulas specified in Example 17.1 were used to calculate surface expansion vs. distance from the top of the cup. The obtained results are shown in Fig. 17.14.

Figure 17.14 shows the surface expansion results for the final shape of the cup. As the figure depicts, there is little expansion of the surface close to the top of the cup, but down along the cup wall, the expansion increases, until maximum expansion is attained at the inner bottom corner of the cup. The expansion here is predicted to be as high as ~1000 times in surface area increase. At the inner bottom surface of the cup, the expansion is considerably less, with minimum expansion ~10 times in the middle of the cup and ≈35 times adjacent to the bottom corner of the cup.

This shows that the surface of the slug expands greatly when it flows over the edge of the punch head, as the surface expansion over the edge increases from 35 up to 1000 times, i.e., the increase here is ≈30-fold. The increase in friction from $m = 0$ to $m = 0.15$ determined at the punch head during the course of forming, however, seems to be caused by the extension of the lubricant film against the punch nose to yield a surface increase in the range of 10–35 times.

What we have shown now is that one can determine the friction for the slug surface sliding over the punch head, by an inverse analysis approach. This is done by using a ring pattern on the slug surface in the experiment and running corresponding FEM simulations of the forming process, until the extension and sliding of the slug surface over the punch head has become equal in simulation and in the experiment. This way, the friction at the punch head has been determined, without altering the conditions here as we most likely would have done by use of other friction measuring methods. Because of this, in future applications, this methodology has the potential to provide much deeper insight into many frictional phenomena encountered in metal forming applications.

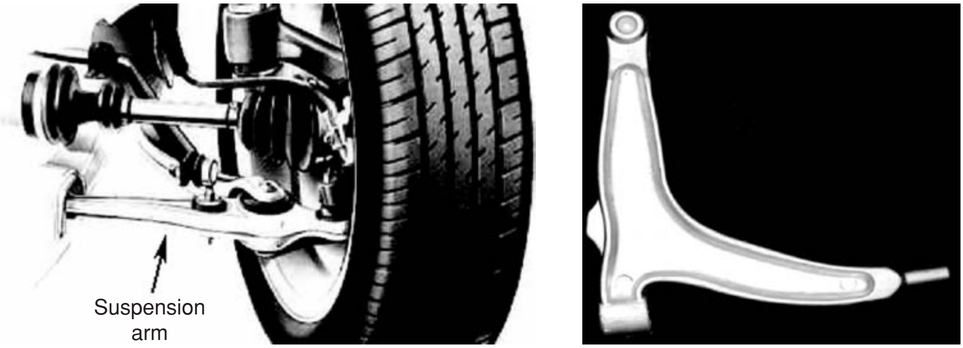

(a) (b)

Figure 17.15. Wheel suspension arms made by closed-die hot forging of an aluminum alloy: (a) wheel suspension arm used in an early Saab model and (b) current GM wheel suspension arm. (Courtesy of Raufoss Technology, www.raufossneuman.com.)

17.2 Hot Closed-Die Forging

As described in Sec. 2.2, industrial hot forging of metals is often done with use of excess workpiece material by so-called closed-die forging. Toward the end of the process, excess material is then allowed to flow through a narrow flash gap formed between the two approaching dies after the die impression has been filled with workpiece material. The excess material finally appears in the flash, at the circumference of the component. It is cut away in a trimming operation after forging to obtain the final shape of the forging. Typical components manufactured by closed-die forging are, for instance, security components such as the wheel suspension arms used in cars. Use of such components is shown in Fig. 17.15(a).

To study the mechanics of closed-die hot forging of a straight rib-shaped component of an aluminum alloy, made from an initial round extruded rod as forging stock, the process shown in Fig. 17.16 was implemented in the laboratory. In the following treatment, it will be shown how this process can be subjected to an in-depth study, by combined experiment and FEM analysis, to map different phenomena that influence the final forging result.

17.2.1 Material Flow from FEA and Forging Experiment

It is not straightforward experimentally to investigate the nature of metal flow inside a die used in closed-die forging, and to see how the material fills the die cavities, because the dies are not transparent. In FEA, however, the dies are imaginary and can easily be made transparent, or they can be removed. Metal flow can then be visualized as it occurs inside the die during the course of the forging stroke.

A parameter that characterizes the filling of workpiece material into the die cavities and that can be calculated by the FEM program is the distribution of the *minimum distance* over the surface of the deforming workpiece. This parameter quantifies to what extent there is predicted die contact over the currently existing

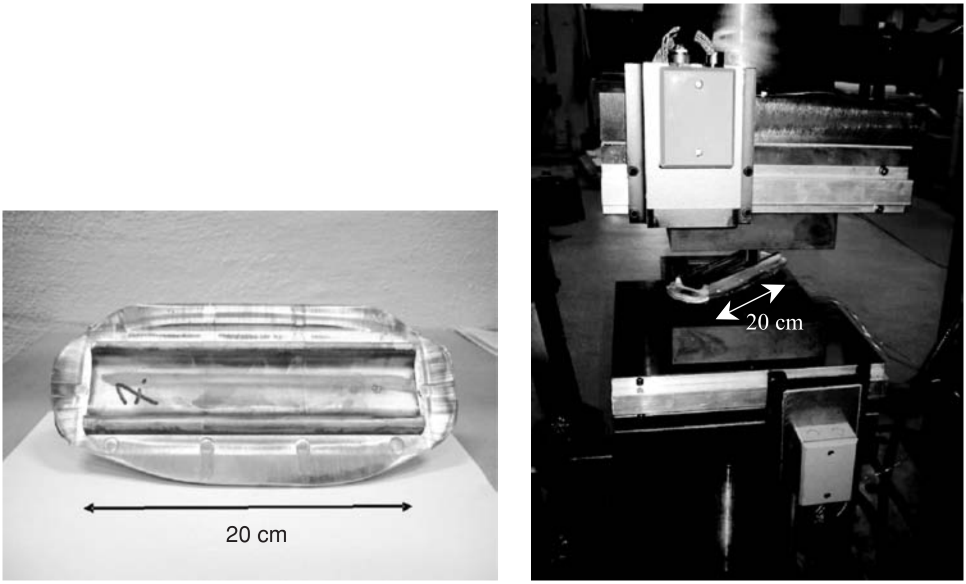

(a) (b)

Figure 17.16. Laboratory hot-forging process subjected to analysis: (a) forged component; (b) final forging shown inside forging die assembly. (Courtesy of Martin Lefstad, SINTEF.)

surfaces of the workpiece during the course of filling of material into the die. In regions where there is full contact, this parameter will have zero value. The parameter is shown in Fig. 17.17(a) as it was determined in FEM simulation for the special laboratory forging process considered here, by means of the distribution pictures captured from the simulation, showing one-fourth of the actual forging process. Pictures illustrating the die-filling sequence have been numbered from 1 to 6 in Fig. 17.17(a). Two load–stroke curves from the simulations, one representing the frictionless state, and the other the maximum-friction situation (i.e., $m = 1$), are shown in Fig. 17.17(b). As seen, there is a stepwise increase in load throughout the forging stroke, and each step is related to a transition in the nature of metal flow in the forging dies. The same four steps are predicted to occur both in the frictionless and in the high-friction case. Hence, the forging sequence can be partitioned into the following stages, dependent on the nature of the metal flow:

Stage I: As shown by picture 1 in Fig. 17.17(a), the contact between the die and the workpiece in the early forging process appears along a thin stripelike area denoted A–A, at the top and bottom of the workpiece. This is obvious, because the round workpiece, cut from a rod, has the same initial length as the die cavity and is laid down to rest on the flat middle surface of the die, before forging is started. What occurs in the continuation of forging, however, is not so obvious. Pictures 1 and 2 show that in the beginning of the forging process the workpiece is side-pressed between the two flat areas in the middle of the tooling. Deformation causes the load first to rise steeply from zero and then

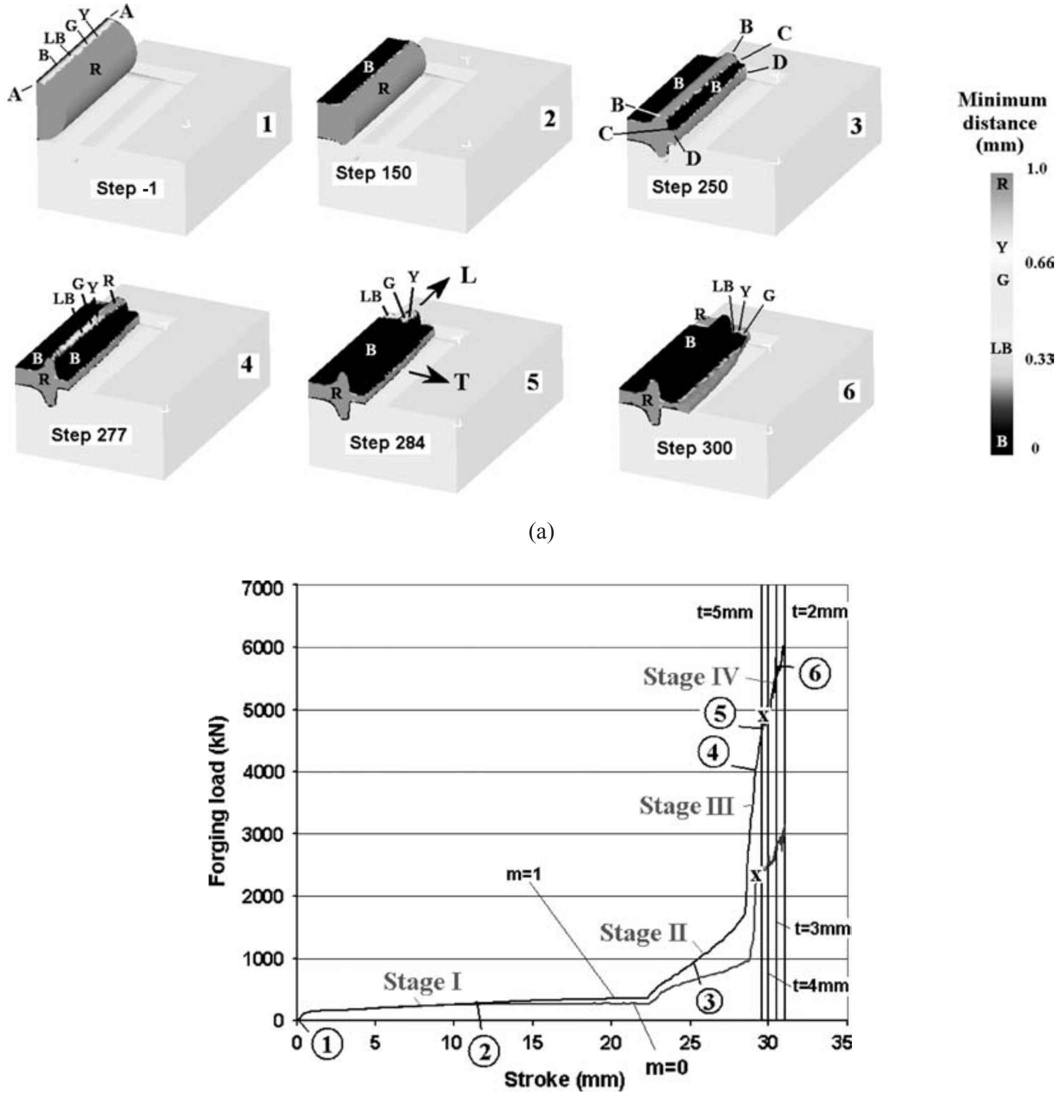

(a)

(b)

Figure 17.17. Because of change in (a) the metal flow into the die impression, the (b) load–stroke curve rises in a stepwise manner.

to be maintained approximately constant throughout more than half of the whole stroke of the forging process. Picture 2 in Fig. 17.17(a) shows that the metal flow, after some time, is altered. However, this change does not significantly affect the forging load. After the change in metal flow, there is flow laterally and downward into the die cavities, in addition to the side pressing of the workpiece.

Stage II: This stage is characterized by a sudden steep rise in the forging load. This occurs when the flow front of workpiece material reaches the outer die edge, at the entrance to the flash gap. When this occurs, contact is established along a thin stripelike area, marked C–C in picture 3. This contact area gradually grows in size as forging continues. When contact is established, there is a second change in metal flow, as one front starts to flow in the direction into the die cavity, marked B–B in the figure, while the other front flows into the flash gap, marked D–D.

Stage III: After a while, there is a new change in the appearance of the load–stroke curve. Now it starts to rise even more steeply than in stage II. This represents the start of stage III of forging; see Fig. 17.17(a). FEA shows that at the onset of this stage, the deepest recessions of the die have been completely filled with workpiece material. Complete filling first occurs in the middle of the die, and from there, it spreads out in both lateral directions inside the deepest cavity of the die, as shown in pictures 4 and 5. The stroke length from start of filling of the deepest recession of the die cavity until complete filling has been obtained is short. The stage at which complete filling has been achieved has been indicated by x on the load–stroke curves shown in Fig. 17.17(b).

Stage IV: At the end of stage III, when the die has become completely filled with workpiece material, there must, of course, again be a transition in metal flow. Because the volume of the workpiece material remains constant, the only possibility for material to escape now from the space inside the die is by outflow through the flash gap. Forging must of course continue until the specimen has obtained the right final height dimensions, i.e., the right dimensions in the direction of forging. It is therefore to be recommended that this stage should be as short as possible to minimize material and energy waste in the process. At the same time, however, the amount of excess material should always be sufficient to provide complete filling of the die impression, throughout the duration of forging. Because of this, it is common practice in closed-die forging to use some excess material and to forge out a flash.

FEM simulation shows the presence of the stages I to IV in the load–stroke curve, independent of the friction applied in the analysis. Moreover, the transition between the stages takes place at approximately the same stroke length, independent of the applied friction value. However, the last space to fill up in the die cavity is slightly away from the end of the die in the frictionless case; see Fig. 17.18(a). With higher friction, the space at the end of the die is the last to become filled up; see Fig. 17.18(b).

17.2.2 Simulation Model to Reproduce the Closed-Die Forging Process

Before presenting more results from the considered forging process, it is perhaps a good idea now to describe in more detail the FEM models that were created to reproduce the experiments. At the same time, the forging parameters will be specified.

The model consisted of one-eighth of the whole laboratory process; see Fig. 17.19(a). The fully mirrored model is shown in Fig. 17.19(b). The FEM meshes

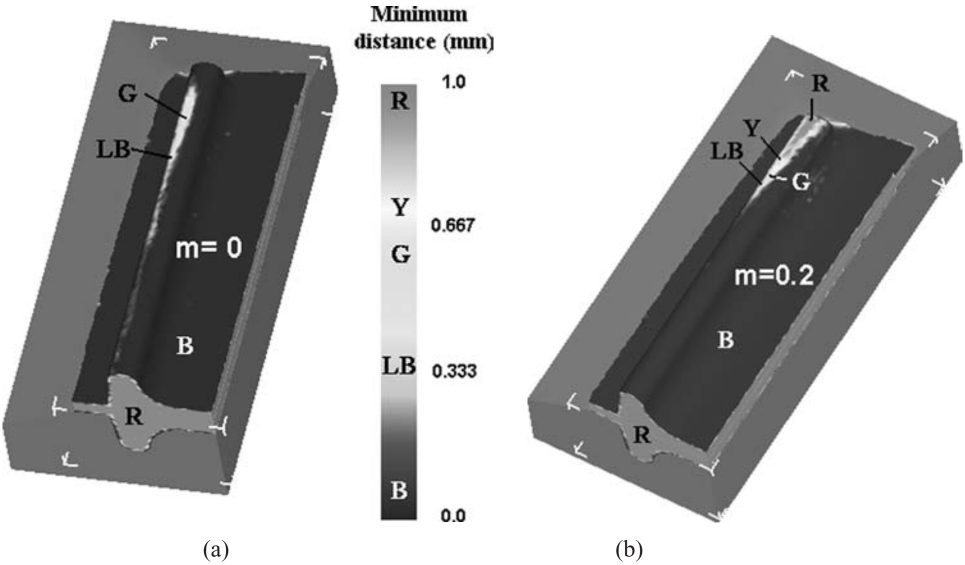

Figure 17.18. The last space in the die cavity to be filled up is predicted to be different in simulation for (a) frictionless forging and (b) forging with $m \geq 0.2$.

applied on the workpiece and the die are also shown in this figure. The die temperature was 450°C, and the workpiece temperature was 500°C. The model was non-isothermal. The workpiece was specified to be a plastic body and the die a rigid body. The workpiece material was the AA 6082 alloy. A material model based on a Zener–Hollomon constitutive relation was used. The constants applied in this model were obtained from experimental flow stress curves acquired in cylinder compression by use of the principles outlined in Example 8.5. The standard workpiece used was a piece cut from an extruded rod with 200 mm length and 38 mm diameter. Other optimal preforms were also applied as described in the forthcoming subsections.

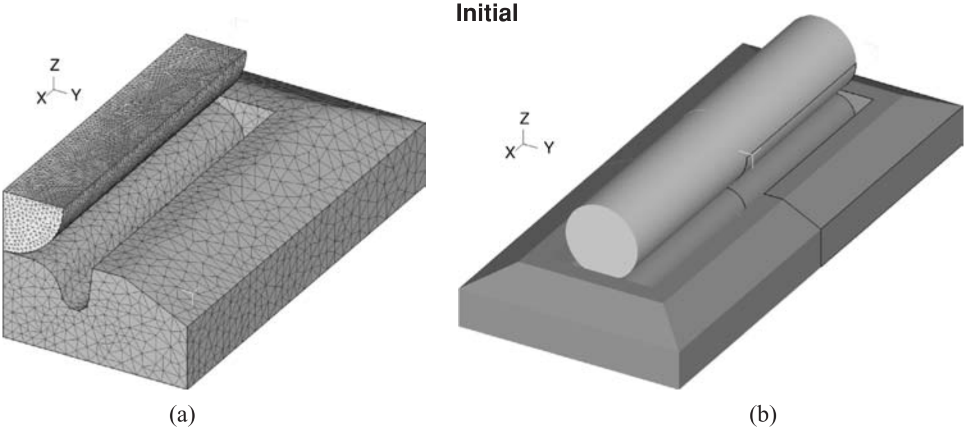

Figure 17.19. (a) FEM model consisted of one-eighth of the forging process. (b) Full view of workpiece and lower die after mirroring.

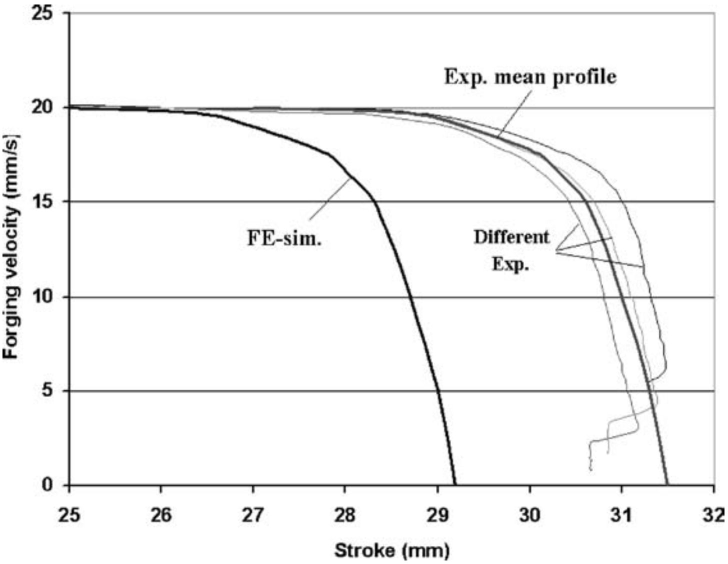

Figure 17.20. Measurements showed a drop in forging velocity toward the end of forging. This velocity profile was applied in the simulation when comparing it with experiments.

The friction was described as Tresca shear friction, and the friction factor was varied stepwise from the frictionless to the full friction state. Two different forging velocity conditions were used. A constant velocity of 20 mm s^{-1} was applied through the whole forging stroke in a number of simulations, where the purpose was to see how friction influences the forging result. To compare the simulation with experimental results, the forging velocity measured in the experiment was used. This velocity was equal to 20 mm s^{-1}, except for the end phase of the stroke, where it dropped smoothly to zero; see Fig. 17.20. When the measured stroke lengths were compared with corresponding simulated data, it was found that for lengths >28 mm this parameter was not recorded correctly in the experiments. Thus, to arrive at more accurate stroke lengths, in the last part of the forging stroke a manual correction of this parameter was performed. As shown in Fig. 17.20, the correction caused the end transient of the velocity profile to be displaced toward lower stroke values than in the measurement.

17.2.3 Friction Effects on the Forging Load and the Flash Shape

In a research project run in collaboration with the Norwegian forging industry, the focus was on frictional effects in hot closed-die forging of aluminum. FEA was therefore performed by students to mimic the process analyzed here, namely, the laboratory forging process shown in Fig. 17.16. Simulations were run with the previously described FEM model for different values of the friction factor, as already stated.

Predicted load–stroke curves, for different friction conditions, are shown graphically in Fig. 17.21. Note that load–stroke predictions are for experimental forging with velocity of 20 mm s^{-1} in the case of movement of the upper die only, or half

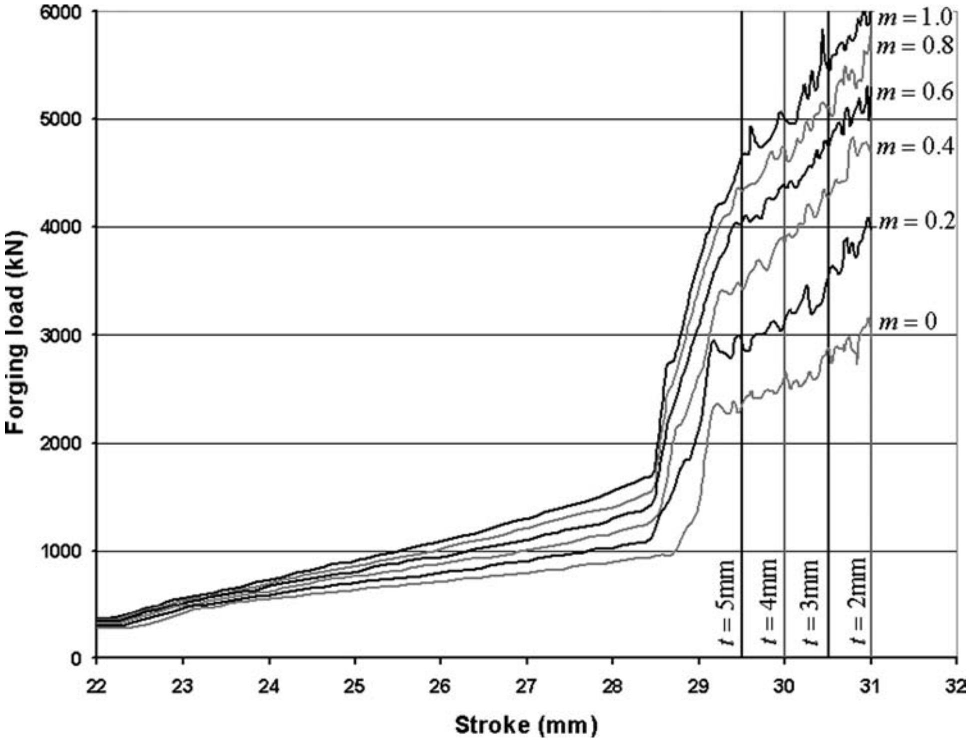

Figure 17.21. The load–stroke curve is raised when friction is increased or when flash thickness is reduced.

this value when both dies are moved, as in the FEM model. Stroke levels that provide different flash thicknesses to the final forging are also indicated in the figure by vertical lines. From the figure, the effect of friction and final flash thickness on required forging load can be assessed for the forging operation.

Two different friction-dependent characteristics were predicted in the simulations. When the friction was increased, there was always a load increase. In addition, the shape of the forged flash was changed systematically when the friction was increased in the range $0 < m < 0.6$.

As the graphs in Fig. 17.21 show, there is predicted a great potential for reducing the required maximum forging load, toward the end of the forging process, through reduced friction. Frictionless forging requires approximately half the forging load necessary in the high-friction case, represented by $m = 1$. In addition, increasing the final thickness of the flash in steps of 1 mm causes the maximum load to decrease by more than 500 kN per step for the high-friction case; see the curve marked $m = 0.8$. With the initial standard workpiece geometry applied in our analysis, a final flash thickness of 5 mm can be applied, and there is still complete filling of the die impression. However, increasing the flash thickness above this value is not an option, for forging would then lead to incomplete filling of the die impression.

The FEM-predicted effect of friction on the shape of the flash of the forging is shown in Fig. 17.22(a). The outer contour of the forged flash is predicted to be

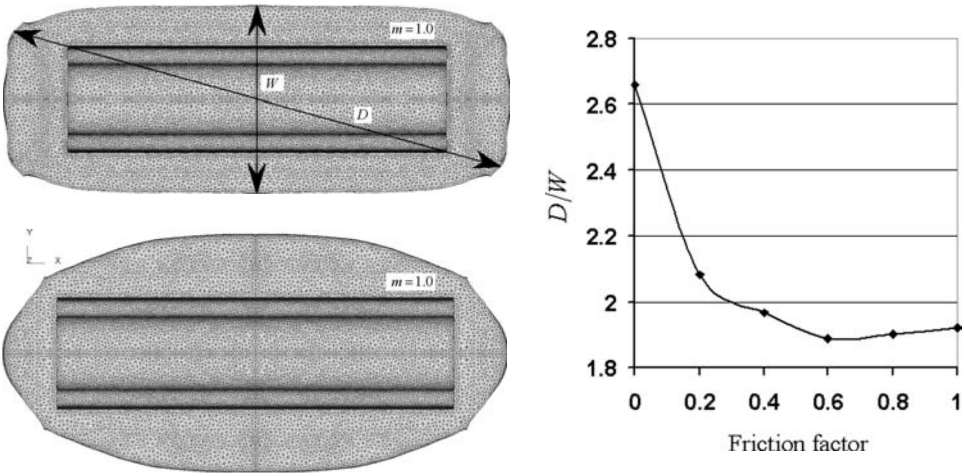

(a) (b)

Figure 17.22. Rounder flash contour is predicted as result of increased friction in simulation: (a) flash shape viewed from top side and (b) diagonal-to-width ratio vs. friction factor.

almost rectangular for frictionless forging. But when the friction between the die and the workpiece increases, the contour is gradually altered to a rounder shape. This change is predicted for friction values in the range $0 < m < 0.6$. Hence various geometrical parameters can be measured from the final flash, which are related to the friction factor – for instance, the largest width (W) and the diagonal (D) of the flash contour.

In Fig. 17.22(b) a graph obtained from the simulations is presented. It shows the FEM-predicted dependence of the diagonal-to-width ratio of the flash on the friction factor. The possibility of determining the friction from the shape of the flash contour in hot forging of Al alloys is thus limited to cases where $m < 0.6$.

17.2.4 Reliability of the Predicted Forging Load

An attempt was made to check how well the FEM-predicted forging load agrees with the corresponding measured load as obtained in the laboratory process. The results of the analysis are shown in Fig. 17.23, where the measured and the simulated load–stroke curves are shown in the same diagram.

The simulation used here was one in which the friction factor was set equal to 0.8. In addition, the experimental forging velocity profile, with decreasing velocity toward the end of the stroke (see Fig. 17.20), was applied. As Fig. 17.23 shows, there is quite good agreement between the simulated and the experimental load–stroke curve in this case. Eventual better agreement can probably be obtained but would require more accurate measurement of the stroke lengths during the forging experiment, and more work on fine tuning of the FEM model to the experiment. As long as the experiment is inaccurate, it is not worthwhile to try to obtain better agreement.

Hence, our attempt to find how well the real load–stroke curve in forging is predicted in FEA comes out satisfactory. The analysis also demonstrates that it is

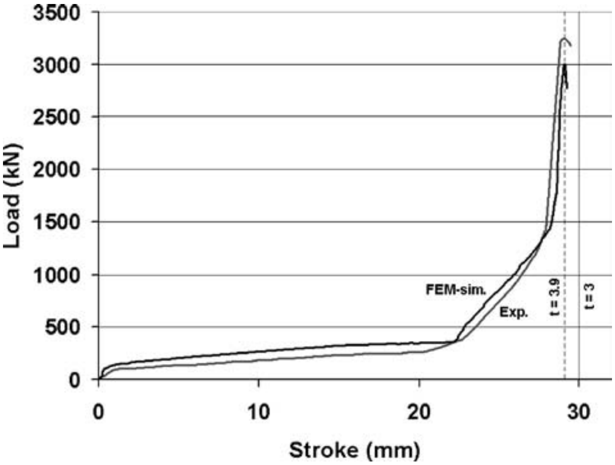

Figure 17.23. Comparison of simulated and experimental load–stroke curves.

crucial to set the forging parameters in the FEA accurately, equal to those in the experiment. It is also of great importance to know the applied forging speed profile toward the end of the forging stroke, for it determines the peak value of the forging load at the end of the load–stroke curve. Another important factor is the friction in the forging operation. A third factor is the assumed flow stress of the workpiece material, which should be that of the actual workpiece material used. A reliable prediction of the forging load in FEM-simulation hence requires that all input data to the FEM model be correct. In our analysis, this would require acquisition of new flow stress data for the specific workpiece material used, because we used data obtained from a different forging stock of the same alloy, which may differ somewhat from the actual workpiece material.

A final remark is that the experimental forging load was well predicted in our analysis when a friction factor of $m = 0.8$ was used. Hence, in this lubricated hot-forging process, conducted on the Al alloy, the friction was high. And a friction factor m in the range 0.7–0.85 would characterize the friction conditions in the process adequately.

17.2.5 Strain-Rate and Strain Predictions in the Analysis

By means of inverse analysis, we have now arrived at a value of the friction factor that reproduces the forging experiment with reasonable accuracy. In the forthcoming sections, this FEM model will be applied to consider the deformation conditions in this rib-forging process. Captured distribution pictures from the model, showing effective strain rates and effective strains inside the workpiece during the forging stroke, are presented in Fig. 17.24 and Fig. 17.25.

Figure 17.24 shows that the strain-rate conditions vary a lot inside the workpiece when it is forged into final shape. Simulation steps 10 and 135 represent stage I of forging, while the specimen is still subjected to side pressing. The strain-rate distribution is then characterized by a deformation cross as in plane strain compression;

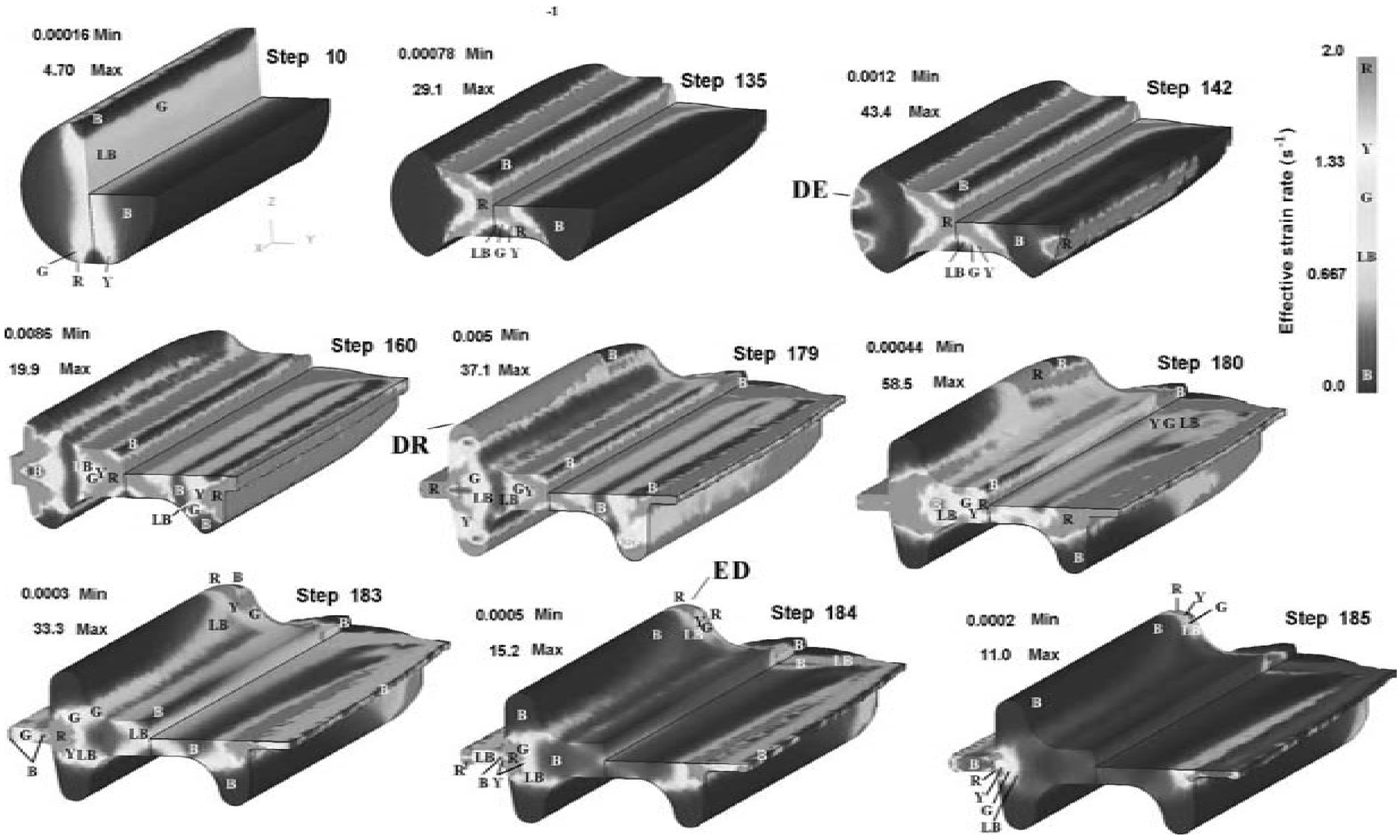

Figure 17.24. Effective strain-rate distributions inside the workpiece during forging as obtained in FEM simulation.

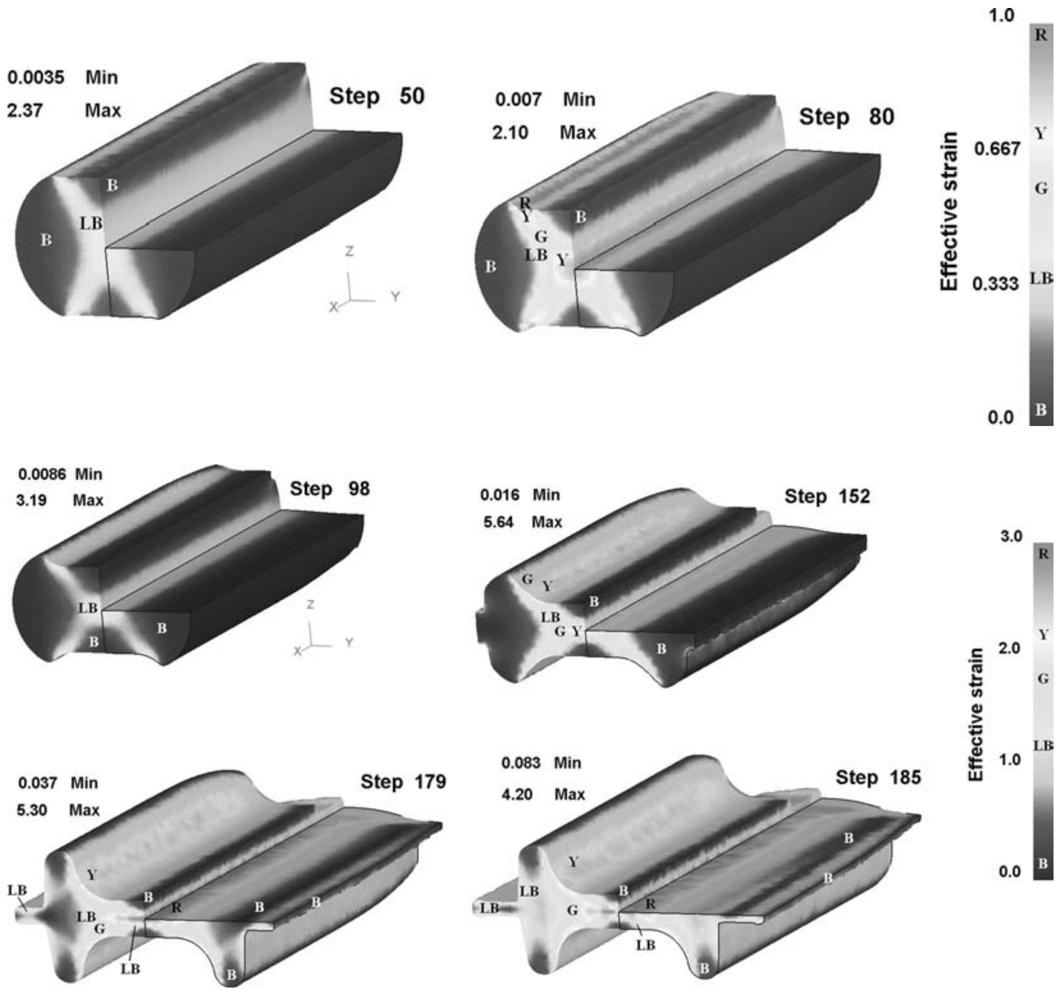

Figure 17.25. Effective strain distributions inside the workpiece during forging as obtained in the FEM model.

see Sec. 3.5.2. But later, in stage II of the process, the strain rate suddenly starts to increase locally as the flow front hits the die edge at the entrance to the flash gap, i.e., in the region marked DE in simulation step 142 in Fig. 17.24.

As forging continues, there is a distinct change in the deformation pattern: see the strain-rate distributions obtained in steps 160, 179, and 180. Now, the initially single flow front is split into two new fronts, one flowing through the flash gap, and the other one moving up into the deepest recession of the die. During this part of the forging stroke, the deformation cross in the middle of the specimen is maintained as before, but in addition, shear planes with high strain rate appear in front of the flash gap, and there is also high strain rate in the layer of material inside the flash gap. Steps 179, 180, and 183 represent the situation when the top ridges of the ribs are created, i.e., when the deepest recess of the die cavity, marked DR in Fig. 17.24, fills up completely with metal. We can see that now there is high strain rate in the

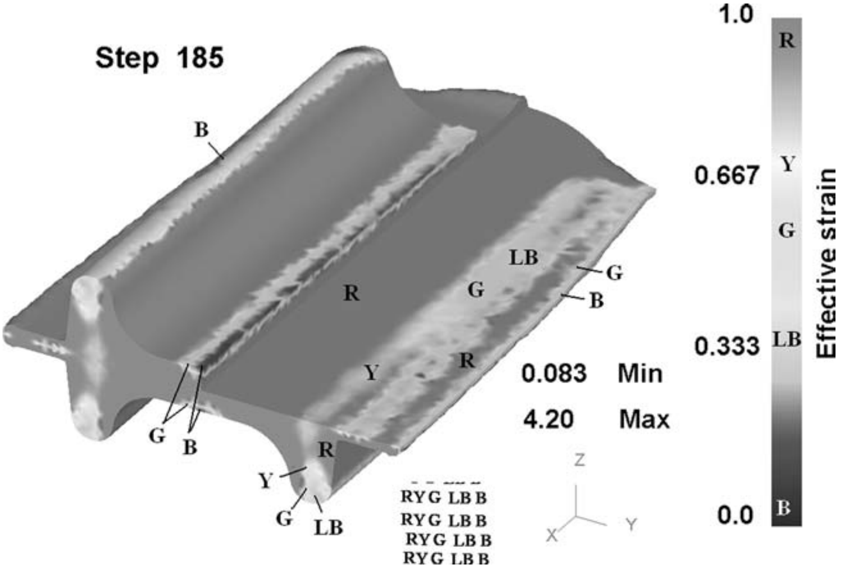

Figure 17.26. Strain distribution picture from simulation, showing the presence of material subjected to low strains.

bottom layer inside the cavity, as the flow front expands and approaches contact with the die surface there.

Then, when the cavity has been filled in the middle of the die, there are high strain rates at the end of the die, marked ED in Fig. 17.24, as the last empty space there starts to fill up. Finally, steps 183, 184, and 185 show the situation when the die cavity has been completely filled with workpiece material, with the exception of a small pocket at the end of the rib top, which is difficult to fill completely. This is close to the end of the forging stroke, and the forging velocity has started to drop gradually toward zero. The central deformation cross now has become almost invisible due to the reduced strain rate, but adjacent to the flash gap, there are still shear bands, in which rather high strain rates are maintained.

As shown in Fig. 17.24, the strain rates inside the forging mainly lie in the range $\dot{\varepsilon}_e < 2\ \mathrm{s}^{-1}$. It is not straightforward to see the highest predicted strain rates in the flash gap in this figure because of the scaling selected. But when checked more carefully in the postprocessor, they were confirmed to be $\dot{\varepsilon}_e \leq 15\ \mathrm{s}^{-1}$.

The effective strain distribution in the workpiece during filling of the die cavity, as predicted by the FEM model, is visualized in Fig. 17.25. The largest strains are seen to occur in places where a high strain rate is maintained over some time, as, for instance, in the middle of the flange of the forging. A deformation cross remains here during the whole course of forging and produces local effective strains as high as ≈ 3 in the middle of the flange. On the other hand, there are two regions where the material mainly remains in stagnant zones during the whole forging stroke, and the accumulated deformations therefore become small. One such region is the top portion of each rib, and another is the surface layer in the middle of the flange. In Fig. 17.26, the effective strain distribution inside the final forged component is

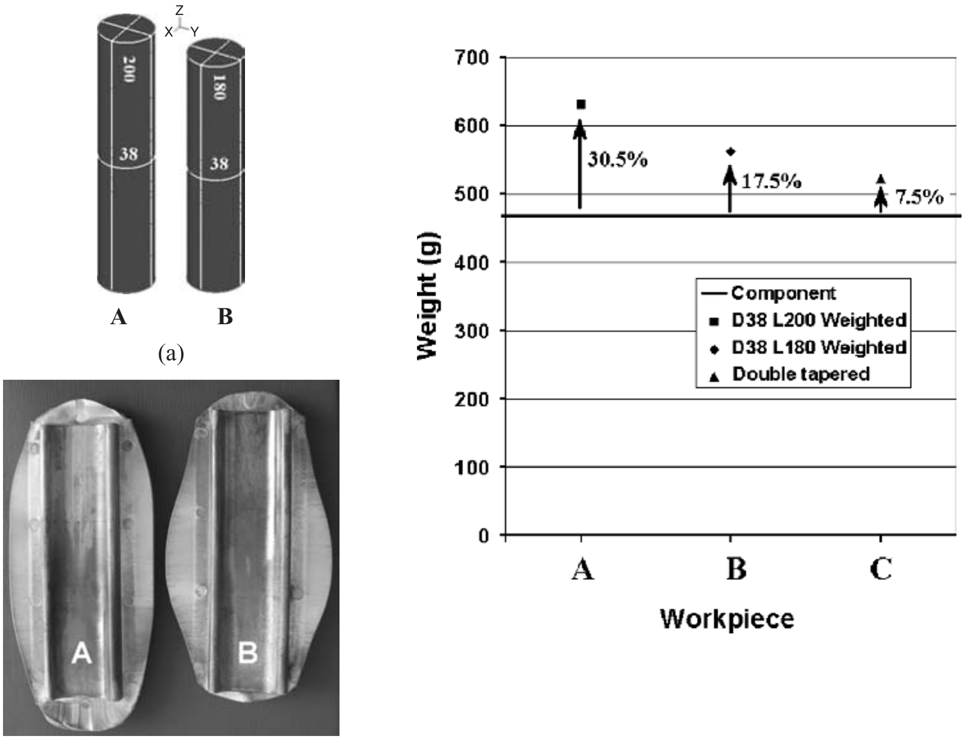

(a) (b) (c)

Figure 17.27. Optimizing the preform shape: (a) alternative preforms A and B, (b) forgings made in experiment, and (c) reduced material loss through improved preform shape.

shown again with different scaling. This figure reveals the extension of the less-deformed material at the rib top of the forging and shows that this material is predicted to be subjected to effective strains <0.5.

To conclude, the FEM model predicts very nonuniform deformation in the material in the rib-forging process and that the lowest strain is in the material in each of the four rib tops and in the surface layer at each side of the middle of the flange.

17.2.6 Optimizing the Preform Shape to Minimize the Material Loss

The closed-die forging process considered is one that produces a rather large amount of flash and can be optimized with respect to material loss. Let us look at some alternative improvements in the forging operation. In Fig. 17.27(a), two workpiece geometries that were used in the laboratory experiments are shown. One is the standard workpiece geometry: an extruded rod of 38 mm diameter, cut to 200 mm length, denoted by A in the figure. The other is an optimized workpiece with the same diameter but with a reduced length of 180 mm, denoted by B in the figure. Both were forged the same way, and the forging result is shown in Fig. 17.27(b)

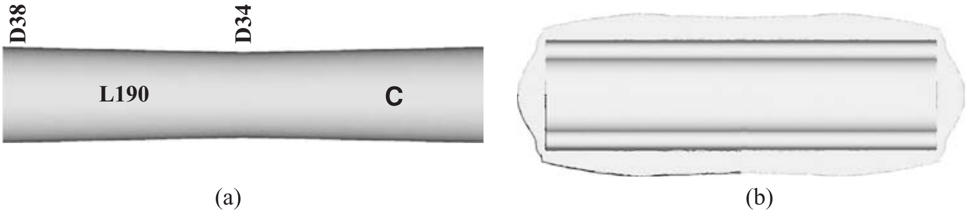

Figure 17.28. Reducing the material loss through further optimization by FEA: (a) optimized double-tapered workpiece and (b) forging with small amount of flash.

with photographs of the final forgings. The material loss due to formation of flash was determined by weight in both cases. The obtained results are shown in the diagram in Fig. 17.27(c). As the figure depicts, reducing the length of the workpiece by 20 mm contributed to a reduction in material loss, because of the formation of less flash, from ≈30% to 17%. But as Fig. 17.27(b) shows, there is still much flash present in the middle of the forging, so it is obviously possible to reduce material loss further.

An attempt was therefore made to use FEM simulation to further optimize the preform shape. The results of this analysis are shown in Fig. 17.28. A third preform shape was considered with length 190 mm and double-tapered shape, i.e., the middle diameter was reduced to 34 mm while the diameter at each end of the specimen was maintained equal to 38 mm. It is obvious that this altered preform shape, denoted as C here, will produce less flash in the middle of the forging than the preform B.

The initial workpiece and the final forging in this case, with flash profile as predicted in simulation for a final flash thickness of 1.8 mm, are shown in Fig. 17.28. As seen from the graph in Fig. 17.27(c), the total amount of material loss with this optimized preform has been reduced to 7.5%. Moreover, as shown in Fig. 17.28(b), very little flash, with approximately constant width, is obtained around the periphery of the final forging, so that further optimization of the shape will not provide significant improvement.

17.2.7 Improvements Due to the Optimum Preform

When we have arrived at an approximately optimum preform shape in the considered rib-forging process with use of FEA, we can apply our FEM models to look at the improvements the new preform shape would give, in relation to the standard forging process. Figure 17.29 shows the predicted load–stroke curve for the optimized preform in comparison with the corresponding curve for the standard preform. As seen for the optimum preform, the forging load is predicted to be lower throughout most of the forging operation. But the maximum load obtained toward the end of forging is not significantly altered.

Another observation is that onset of deformation stages II and III in the forging process when using the optimized preform has been displaced to higher stroke lengths than in the standard case. Hence, some empty space is maintained in the die

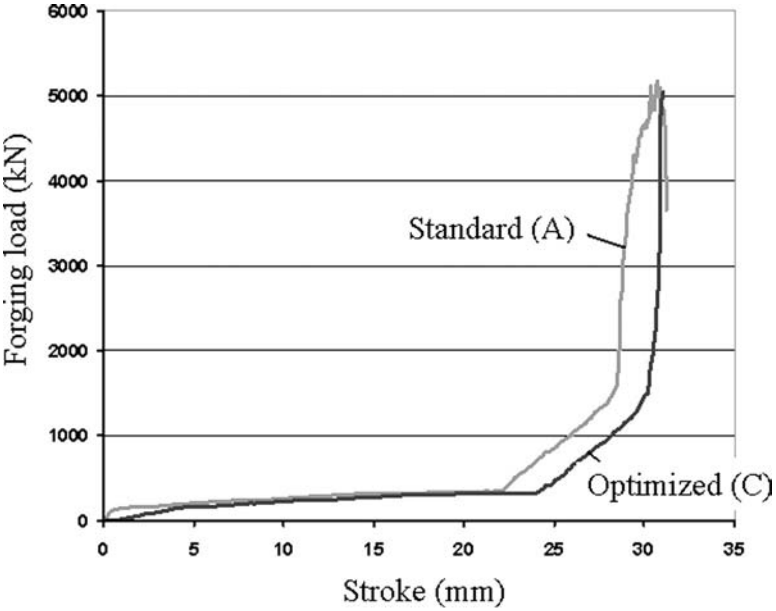

Figure 17.29. Change in load–stroke curve when using optimum preform.

cavities to a much later stage of forging. This has a distinct effect on the required energy consumption during the forging stroke, for the area under the load–stroke curve is proportional to the energy used. As one can see, this area is significantly reduced when changing to the better preform.

What, then, with regard to tribological conditions in the process – for instance, the stretching of the workpiece surface and the contact pressure against the die? Both these conditions can be determined easily by means of the software, as distribution pictures of the actual parameter over the surface of the final forging; see Fig. 17.30.

As this figure shows, there is no significant difference between the way the surface of the workpiece is stretched out when the standard and when the optimized preform is used, if one considers the contact surface between the workpiece material and the die at the end of forging. But if one considers the resulting flash, conditions are very different in the two cases. The insignificant difference in area expansion of the surface of the workpieces inside the die in the two cases stems from the fact that friction is high in the forging process. Hence, after the flow front has established contact with the die surface, the sliding movement along the die surface is small.

The contact pressure against the die equals the contact pressure against the forging. This pressure distribution is shown in Fig. 17.30(c) for the optimum shape of the preform. A maximum pressure of ≈400 MPa is predicted in the middle of the flange of the component. It is obvious that the pressure is highest there, for it is the place inside the die that is farthest away from the flash gap. The maximum pressure occurs at the instant when the load approaches its peak value.

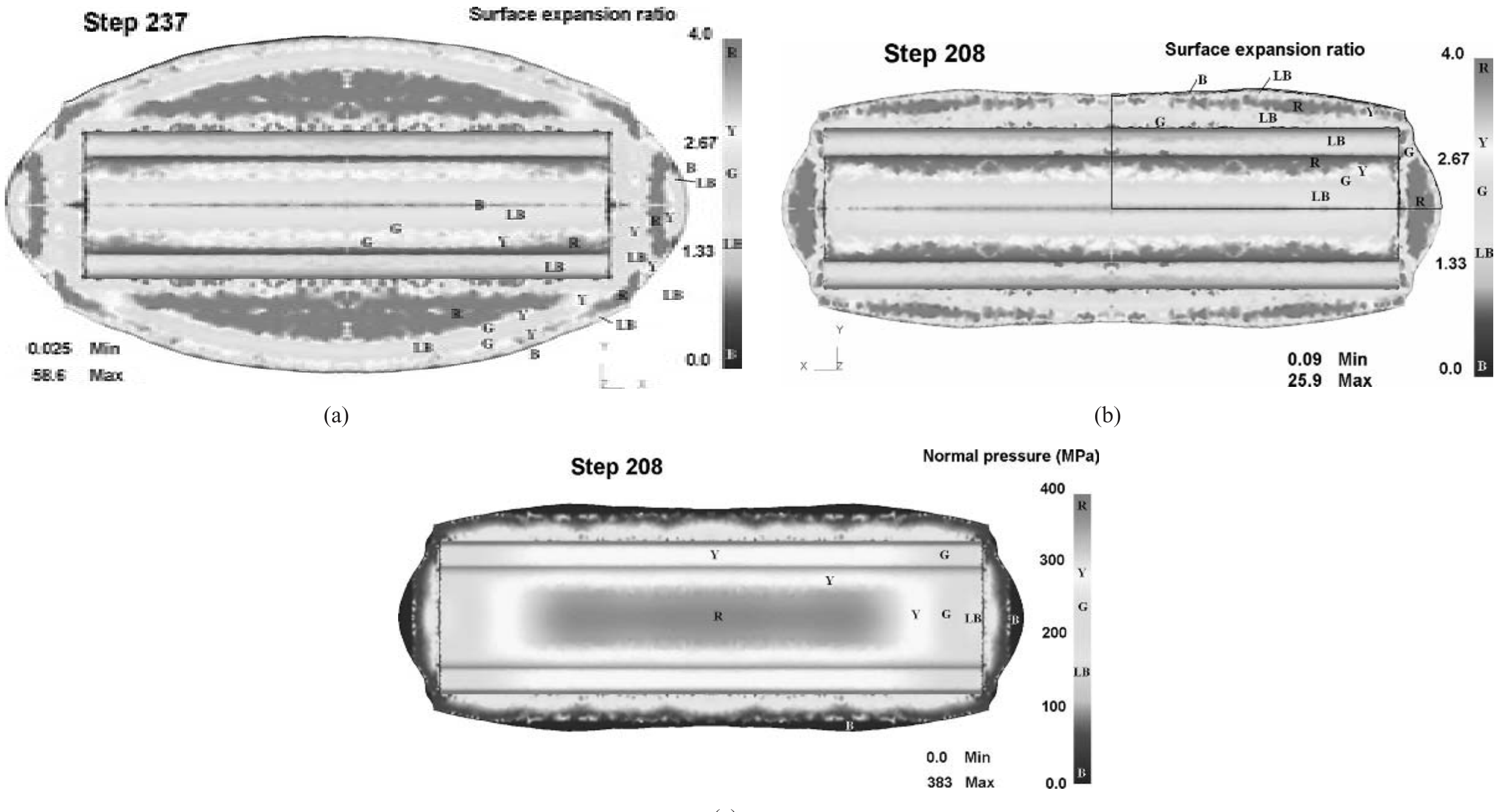

(a)

(b)

(c)

Figure 17.30. The surface-area expansion ratio predicted in the simulation model for (a) standard and (b) optimized preform shape. (c) Predicted contact pressure at maximum load.

Problems

17.1 FEM-computed temperatures at the end stage of hot forging of the standard preform shape as well as the optimized shape, considered in this chapter, is presented in the accompanying figures.

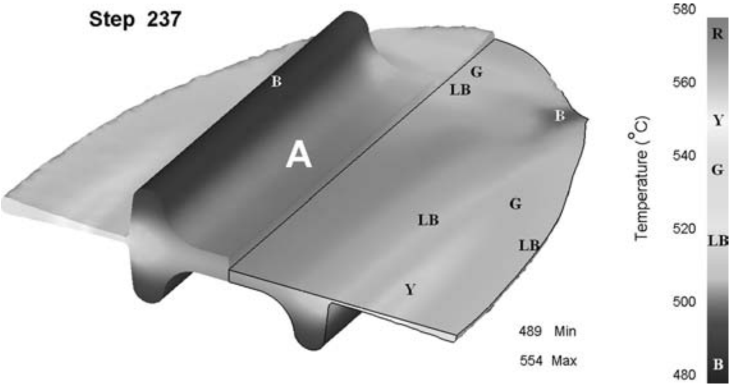

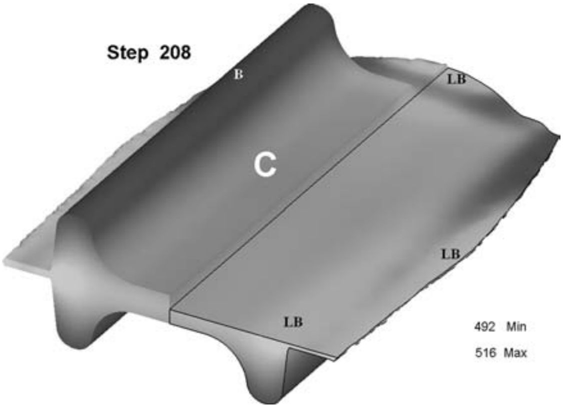

(a) Describe in your own words what characterizes the shape of each of the preforms called A, B, and C in this chapter.
(b) Determine the volume of each of the preforms.
(c) Determine the mass of each preform. Assume the density of the Al alloy to be 2.7 $\mathrm{Mg\,m^{-3}}$.
(d) Calculate the improvement in yield when preform A is replaced by preform C.
(e) Discuss the effect on the surface temperature and the internal temperature of the forging when changing from preform A to C. This is to be done on the basis of the simulated temperature distributions given in the accompanying figure, obtained at the end stage of the forging process.
(f) Try to figure out why the observed temperature differences appear.
(g) To what extent do you think the observed temperature differences will influence the required maximum forging load for forging with preforms A and C?

NOTES

1. Production Engineering Association (U.K.), PERA report No. 102.
2. Benani, B., and Bay, N.: "Limits of lubrication in backward can extrusion: Analysis by finite-element method and physical modeling experiments," J. Materials Processing Technology, Vol. 61, 1996, pp. 275–286.
3. Uyyuru, R., and Valberg, H.: "Physical and numerical analysis of metal flow over the punch head in backward cup extrusion of aluminium," J. Materials Processing Technology, Vol. 172, 2006, pp. 312–318.

REFERENCES

Nolte, D.: "Analysis of Aluminium Hot Forging," Ph.D. thesis, Norwegian University of Science and Technology (NTNU), 2004.

Uyyuru, R. K.: "Engineering the Friction and Forming Mechanics in Cold Aluminium Forming – Use of Modelling Techniques," Ph.D. thesis, Norwegian University of Science and Technology (NTNU), 2003.

Wey, E.: "New developments in FE simulation of industrial forging processes," 19th Int. Forging Congr., Chicago, 2008.

18 Extrusion

As previously described in Ch. 2, extrusion is done by placing a piece of metal of good formability, called a billet, in a hardened steel container. In direct extrusion, a ram is then pushed from the back end of the container, so the billet is forced against a die placed at the other end of the container. The die has a hole in its middle, and as the billet is pushed forward, the front part of it starts to flow into the hole, and then out into the space at the exit side of the hole. Here it appears as a continuous extrusion with cross section approximately that of the hole. The longitudinal shape obtained in this process is generally called an *extruded profile*, or an *extrudate*. This metal forming technique is hence used to manufacture products with constant cross-sectional shape along their length, either as massive or hollow profiles, or as rod, tube, wire, or strip.

Because the flow stress is reduced when metals are heated, and workability also most commonly increases, extrusion is usually conducted as hot forming. Extrusion can either be done as forward (direct) or backward (indirect) extrusion; see Ch. 2.2.5. In forward extrusion, the material is pushed through the container and the die by means of the ram, whereas in backward extrusion, the die is placed in front of the hollow ram, whereafter the die is pushed into the billet. The billet material remains stationary inside the container then until it is approached by the moving die; the billet then starts to flow through the die, i.e., in the reverse direction of the ram movement and must therefore be taken out through the ram, which must be hollow.

In this chapter, some practical aspects of industrial extrusion will first be described. It is important to be able to predict the required extrusion force, because that force is very large and sets a limit to how fast the extrusion process can be conducted without exceeding the maximum available force in the press. In the last part of this chapter, theory will therefore be used to develop an expression for the required extrusion force. The expression is useful in that it shows how the required force is influenced by different extrusion parameters.

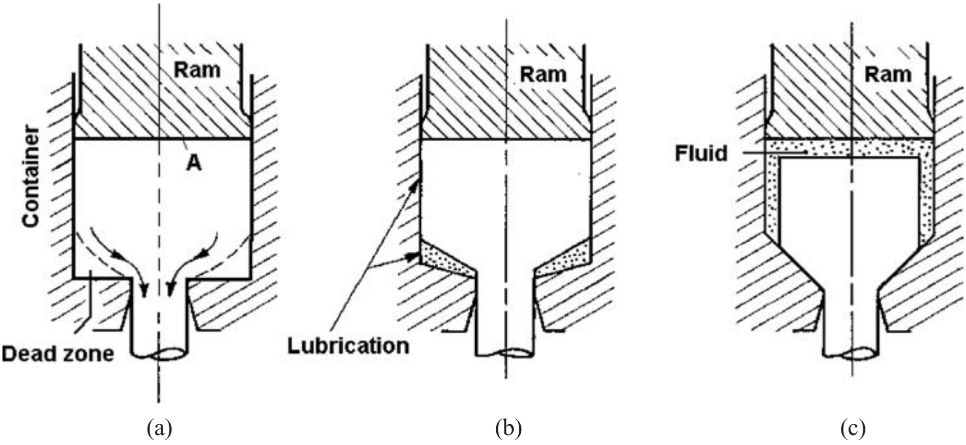

Figure 18.1. Forward extrusion with different lubrication practices: (a) unlubricated, (b) lubricated, and (c) hydrostatic. (Reprinted with permission of ASM International. All rights reserved. www.asminternational.org.)

18.1 Forward Extrusion Processes

Forward extrusion processes are commonly partitioned into three different groups,[1] according to the use of lubrication practice; see the schematic sketch in Fig. 18.1.

In extrusion of aluminum and aluminum alloys, it is most common to apply *unlubricated extrusion*, i.e., to avoid the use of lubricant, both on the surface of the die and on the container wall. But because the billet is forced with high pressure against the ram, the billet material tends to pressure-weld onto the ram head, at the location marked A in Fig. 18.1(a), if no lubrication is used there. A *pressure pad* in the form of a small tool disc is therefore sometimes inserted between the ram head and the billet. To ease removal of the pressure pad from the *extrusion residue* after the end of extrusion, the rear surface of the billet is therefore commonly lightly lubricated, for instance, by directing an acetylene flame against it. In this way, a thin layer of soot is deposited onto this surface, before insertion of the billet into the container. Alternatively, boron nitride can be used as the lubricant. It is white powder and is applied to the back face of the billet before it is loaded into the container. After lubrication of the rear of the billet, removal of the metal discard from the pressure pad is easy, and the process runs smoothly, in contrast to what happens if no lubrication is used.

However, it is always important to avoid use of excessive lubrication in unlubricated extrusion. If the lubricant should penetrate to the peripheral cylinder surface of the billet, quality problems can be experienced. The peripheral surface of the billet then may start to slide against the container wall and tend to flow into the interior of the billet. This will most commonly occur in a location just in front of the primary dead zone. Later during extrusion, however, it will flow from there into the subsurface layers of the extrudate. If this occurs, there will be unacceptable or reduced profile quality. Unwelded internal layers may then appear under the surface of the extruded product; this defect is commonly termed *subsurface lamination*.

In unlubricated hot extrusion, flat-faced dies are most commonly used; see Fig. 18.1(a). Without lubrication, as mentioned in Ch. 12, there will be high friction between the workpiece and the die and container. With such conditions, a primary dead zone will form inside the billet volume during extrusion, in the corner between the die and the container. In unlubricated extrusion, the peripheral surface layer of the billet then will tend to accumulate inside the container during the course of extrusion and will not flow out into the extrudate. This is advantageous in that the peripheral layer usually has lower metallurgical quality than the rest of the billet. It often contains intermetallic inclusions, which – if they appear on the surface of the profile – can yield extrusions with bad surface quality.

A less common extrusion process is *lubricated extrusion* [see Fig. 18.1(b)], in which conical, wedge-shaped dies are used. Dead zones will not form in lubricated extrusion; instead, the outer surface layer of the billet will slide over the die surface and will flow out into the extrusion, where it will form the outer surface layer of the extrusion. The characteristic shear zone formed inside the billet in unlubricated extrusion will not be present the same way in lubricated extrusion.

Material flow in unlubricated extrusion is characterized by the formation of a *primary* and a *secondary deformation zone*, which make up the volume of the extruding billet; see Fig. 12.7. In lubricated extrusion, however, the secondary deformation zone will be absent, or at least not well developed. Because of this difference in metal flow, the resulting extrusion in lubricated extrusion has much more homogeneous deformations than in unlubricated extrusion.

In both processes, the billet metal, which initially filled the volume ahead of the die hole, will be subjected to less deformation than metal farther behind. This material will only move through part of the primary deformation zone during extrusion. Because of this, the very front end of the rod will only be subjected to small deformation, because this metal is near the die hole when extrusion begins. After the initial volume of the primary deformation zone has flowed out, the deformation of the rest of the rod will be much more uniform over the length of the extrusion than before. It is common to cut away and discard a short length of the front end of the extrusion.

In *hydrostatic extrusion*, the pressure is transferred from the die onto the billet through a fluid, which fills the space between the billet and the ram head; see Fig. 18.1(c). During this extrusion process, the fluid will also act as a lubricant and will be squeezed under high pressure into the interface between the billet and the die. Because of this, there will be efficient lubrication in this extrusion process.

Lubricated and (especially) hydrostatic extrusion are much more complex processes to run than unlubricated extrusion and are mainly used for low-ductility materials, which tend to crack in conventional unlubricated extrusion.

18.2 Hot Unlubricated Extrusion of Aluminum Alloys

As mentioned, Al and Al alloys are usually extruded by means of unlubricated hot extrusion. Both forward and backward extrusion are used for this purpose.

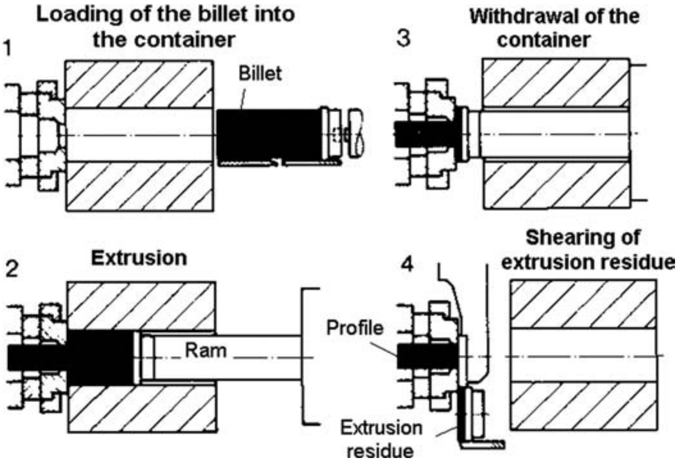
1
Loading of the billet into the container
Billet
3
Withdrawal of the container
2
Extrusion
Ram
4
Shearing of extrusion residue
Profile
Extrusion residue

Figure 18.2. Work sequence in forward extrusion.[2] (Reprinted with permission of Aluminium-Verlag, Düsseldorf, Germany, www.alu-verlag.de.)

The work sequence[2] in the forward extrusion press is shown in Fig. 18.2. In the first extrusion stage, the billet is loaded into the container bore. For this to be possible, the billet must have a diameter slightly less than the diameter of the container, i.e., there must initially be a clearance between the billet and the container wall. In the second stage of extrusion, after loading of the billet into the container, the ram is moved forward so that it is pushed against the billet. Now the billet starts to expand in the radial direction until it fills the container bore. This part of the extrusion process is commonly called *upsetting*. To obtain a sound defect-free product, the upsetting must be performed correctly. If the conditions are wrong, air pockets can be trapped inside the metal.

The radial expansion should preferably start from the front end of the billet adjacent to the die, and then spread continuously backwards toward the rear end of the billet. Then the initial air in the gap between the billet and the container wall will tend to accumulate at the rear end of the billet. From here this air can escape backwards past the ram head, without becoming trapped inside the metal.

If air is trapped in the layer between the billet and the container, it will tend to flow out with the metal through the die hole, and will appear inside the extrusion. Because of high pressure required in extrusion, the air will be highly pressurized. If it flows out and appears below a subsurface layer of the billet, it may blow up bubble-like defects, called *blisters*, on the surface of the extruded profile. The bubbles may even become punctured if expansion is sufficiently large when they leave the die exit. Scanning electron microscope images of such blisters on the surface of an extruded profile are shown in Fig. 18.3.

In the third stage of the extrusion process, the billet is extruded but not completely. Instead, some metal is left in front of the die at end of the press. This disc of metal is called the *discard* or the *extrusion residue*. During extrusion, the peripheral layers of the billet tend to accumulate inside the container, while the interior material flows out and forms the profile. The outer layers of the billet are of lesser

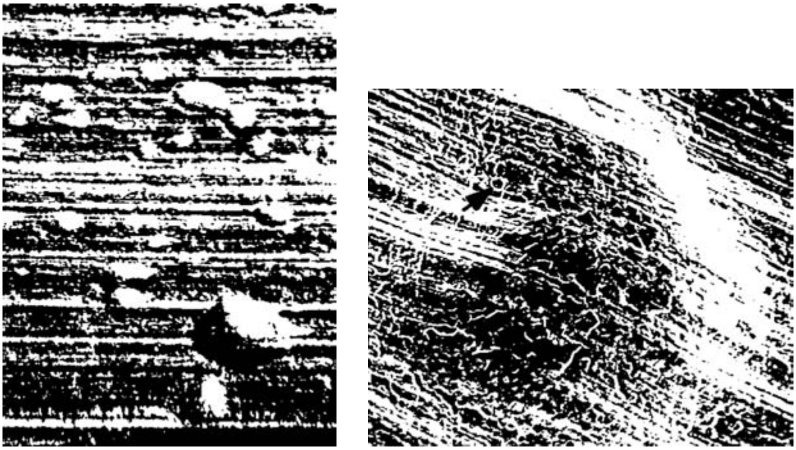
(a) (b)

Figure 18.3. Blisters on the surface of an extruded profile. (a) Many blisters. (b) Magnified image of blister with puncture hole.

metallurgical quality than the rest of the billet, so gathering them in the discard inside the billet is beneficial. The thin slice of metal left unextruded, i.e., the discard, is removed from the die, together with the pressure pad, after the extrusion stroke, in a separate shearing operation (stage 4 in Fig. 18.2), before loading of the next billet. To remove the discard, the container is withdrawn, and a knifelike tool is moved sideways along the flat surface of the die to cut away the discard.

18.3 Forward vs. Backward Extrusion

In principle there are many advantages connected to the use of the backward (indirect) rather than the forward (direct) extrusion process, such as, for example, lower extrusion load and more even deformation over the length of the extrudate. But backward extrusion has the important drawback that the extrusions must be taken out through the hallow ram stem. Because of this, forward is the most preferred extrusion process.

Another disadvantage of backward as compared with forward extrusion is that in the former the material in the outer layers of the billet tends to, to a large extent, flow out through the die. Because of the phenomenon of *inverse segregation* during casting, the outer layer of the billet will contain more contamination than the rest of it. Just below the surface of the billet there will be, for instance, a high content of *eutectic phases*. If the subsurface layers of the billet flow out into the outer surface of the extrusion, that may result in quality problems because of formation of surface defects on the profile. It is therefore common to machine away the outer layers of the cast billet, or to remove them in a separate *scalping operation*, before the billet is extruded in the indirect process. This operation will of course increase the cost and reduce the profitability in comparison with direct extrusion.

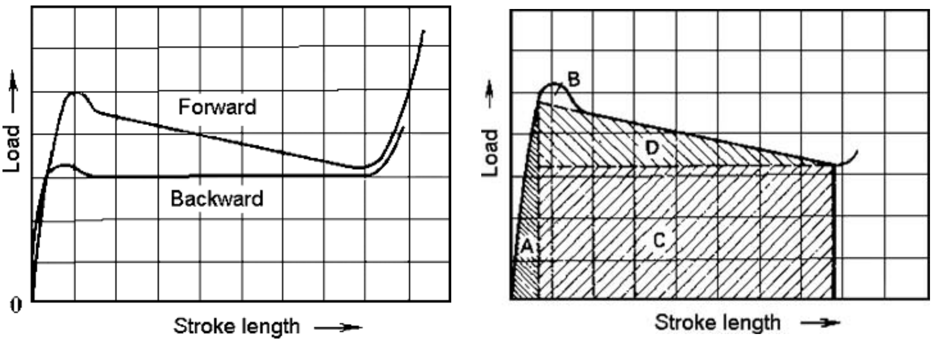

(a) (b)

Figure 18.4. (a) Comparison of the load–stroke curves in forward and backward extrusion. (b) Partition of the energy consumption into four parts. (Reprinted with permission of Aluminium-Verlag, Düsseldorf, Germany, www.alu-verlag.de.)

Another advantage of backward extrusion is that the required press force will not vary significantly during the course of extrusion, as it does in forward extrusion. A characteristic load–stroke curve recorded in direct aluminum extrusion was shown in Fig. 11.14(a). In Fig. 18.4, two load–stroke curves are shown as they appear in forward and backward extrusion.[2] As this figure reveals, the required load in direct extrusion is highest in the beginning of the process, while the billet still is long. This is because of the part of the force that is required to push the billet forward against the container wall. This part is proportional to the billet length at any instant during extrusion, and hence decreases as extrusion proceeds. Because of this, the total extrusion force decreases almost linearly throughout the press stroke, from beginning to end of extrusion, as does the billet length.

The area below the load–stroke curve in extrusion equals the required energy consumption during the process. For direct extrusion, it can be partitioned into four parts [see Fig. 18.4(b)], according to what the energy is required for:

A: Energy necessary to upset the billet into the container.
B: Energy used to initiate plastic deformation in the billet.
C: Deformation energy required to press the billet through the primary deformation zone.
D: Energy required to move the billet along the container wall.

After upsetting, the billet remains stationary inside the container in backward extrusion. Hence, no energy is spent in order to press the billet through the container; nor is any heat developed because of this. Under equal extrusion conditions, the temperature increase in the metal upon flow through the die is therefore less in backward than in forward extrusion. The is especially true as regards the surface temperature of the extrusion at the outlet side of the die. Because of this, it is possible in backward extrusion to use higher extrusion speeds than in forward extrusion and still get a sound product, without surface cracking; see the description in connection with Fig. 11.18 and Fig. 11.19.

In spite of all the mentioned advantages of backward extrusion, it is the forward extrusion process that has gained the most widespread use. The primary reason for this is that it is difficult, in backward extrusion, to take the extruded profile out through the hollow stem construction, especially when many profiles are extruded concurrently, as is done in multihole extrusion. Backward extrusion is therefore rather seldom applied in industry, and when used, it is primarily for extrusion of profiles of simple shape.

18.4 Classification of Metal Flow in Extrusion

Material flow in metal extrusion can be quite complex and can differ considerably for different metals. It was therefore early considered useful to establish a *classification system* describing the different types of flow observed. Even for a specific metal alloy, the metal flow can vary if the friction over the boundary interface between the billet and the die or container is altered, for instance, by use of lubrication. Furthermore, characteristic flow-related extrusion defects occurring in metal extrusion can be explained and understood on the basis of different types of flow patterns.

The most commonly used classification system today – the one proposed by Pearson and Parkins[3] and by Dürrschnabel[4] – refers to extrusion through flat-faced dies. This classification system divides metal flow in axisymmetric extrusion into four different classes, flow patterns S, A, B, and C. Use of grid patterns for metal flow analysis has already been explained in Ch. 12.

Metal flow in unlubricated hot extrusion of aluminum or aluminum alloys through flat-faced dies does not correspond well to any of the flow patterns originally proposed. Therefore, a *modified classification system* has also been proposed, with particular adaptation to aluminum extrusion[5]; see Fig. 18.5. In this system, two new intermediate *flow patterns A_1 and B_1* are added. In the new system, metal flow in indirect extrusion conforms to flow pattern A_1, and metal flow in direct extrusion conforms to flow pattern B_1.

If a metal flows in accordance with flow pattern B, in its natural unlubricated condition, a continuous change in metal flow in the direction B → A → S can occur for this material, if friction at the interface between the billet and the die, including that at the container wall, is gradually reduced by the introduction of lubricants of increasing lubricity. The various flow patterns are as follows:

Flow pattern S: This pattern occurs characteristically when a billet with uniform flow stress over the cross section is extruded with low friction against the billet and the container wall, including the die. With sufficiently low friction, there will be complete sliding at these interfaces during extrusion. Then the peripheral layers of the billet will flow along the die faces and through the die hole slightly later than the core of the billet. This is easily seen by observing the appearance of the radial lines of the grid pattern for flow type S in Fig. 18.5.

Flow pattern A: This flow pattern occurs for a billet with uniform flow stress over the cross section if there is sticking friction along the die–billet interface,

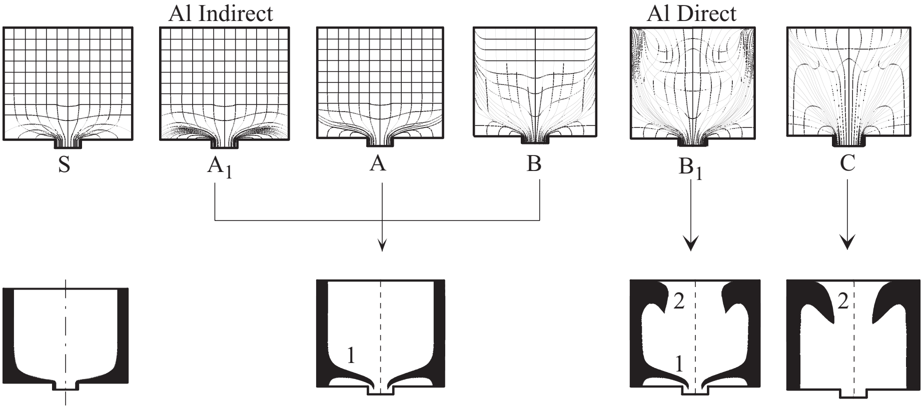

Figure 18.5. Modified classification system with flow patterns A_1 and B_1 added.

but complete sliding at the container–billet interface. Under these circumstances, the material in the corner between die and container will remain unextruded as a dead zone.

Flow pattern B: The flow type develops if there is sticking friction at the die–billet interface, and if friction along the billet–container wall is high enough to reduce sliding of the metal adjacent to the container wall. With such conditions the peripheral layer of the billet will be *retained* along the container wall and in the dead zone corner, while the core of the billet will flow faster. Because of reduced sliding along the container wall, the size of the dead zone will then increase in comparison with that for flow pattern A. This behavior is seen from the appearance of the radial lines of the grid pattern for flow type B in Fig. 18.5.

Flow pattern C: This type of flow occurs as a combined effect of flow stress gradients across the billet section and high friction along the billet–container interface. It characteristically occurs in α and β brasses that are extruded in a container with considerably lower temperature than the billet. Because of cooling effects, the outer peripheral layer of the billet will then have considerably higher flow stress than the core. With a stiff, hard peripheral layer the core will flow most readily, and a large dead zone will develop, which extends from the die to the very rear end of the billet.

When aluminum and aluminum alloys are hot-extruded through flat-faced dies without use of lubrication, in either indirect or direct extrusion, they develop flow patterns that are intermediate types between those proposed by Pearson and Parkins and by Dürrschnabel. Metal flow has more recently been investigated with great precision using grid pattern techniques where the pattern is made by internal pins of indicator alloy inside the billet; see Ch. 12. In this way, deformation-resistant grid patterns have been achieved, which are visible even in heavily deformed regions of the billet, as in the shear zones. This grid pattern technique does not require use of parting agents as in the much-used conventional split billet technique. Because of this, there are no uncertainties about whether the container wall is unlubricated when this technique is used. A special extrusion and removal technique has also been developed that allows partially extruded billets to be removed from the container without plastic deformation during removal; see Fig. 19.2. In this manner, perfect grid patterns have been achieved, which map the frozen deformation condition of the billet when extrusion is stopped; see Fig. 12.4.

In view of the more recent investigations, two new, intermediate flow patterns characterizing indirect and direct extrusion can be added to the classification system proposed by Pearson and Parkins and by Dürrschnabel. It is proposed to term these flow patterns A_1 and B_1; see Fig. 18.5. Pattern A_1 is intermediate between patterns S and A, and pattern B_1 is intermediate between patterns B and C.

Flow pattern B_1: This flow pattern (see Fig. 18.5) is characterized by complete sticking between the billet and the container wall or die. Because of this, the *peripheral skin* – including a *subsurface layer* of the billet – remains at the container wall and is *scraped off* by the advancing ram during the course of extrusion. This material therefore gathers in the rear corner of the billet, where it first flows radially inwards, and thereafter in the extrusion direction. Because of this, the material in the rear end of the billet is subjected to a gradual *predeformation* throughout the extrusion stroke, prior to its arrival into the primary deformation zone above the die hole. Except for this additional flow in the rear end of the billet, the flow in direct extrusion of aluminum does not deviate much from that previously described for flow pattern B. However, an exception is that the shear zone becomes more developed and extends deeper into the rear end of the billet. The shear zone forms between the stationary layer of material at the container wall and in the dead zone and the core of the billet which flows forward past the stationary material, toward the die opening.

Flow pattern A_1: Metal flow in unlubricated indirect extrusion deviates considerably from that in direct extrusion, because of the stationary condition of the billet material inside the container. Deformation occurs as the die is pushed into the billet. Because there is sticking friction between the peripheral layer of the billet and the container wall, this layer is scraped off from the container wall by the advancing die, in a way similar to the scraping by the ram at the rear billet end in direct extrusion. Because of the scraping action of the die against the container wall, no dead zone corresponding to that in direct extrusion forms. However, a thin initial metal layer adjacent to the flat-faced die will remain there during extrusion and will become heavily deformed by the strong metal flow deeper inside the billet material. This layer will be contained in the shear zone, where it is subjected to heavy deformations but will remain unextruded because it is located so close to the die. Moreover, because of the mentioned flow phenomenon in the corner between the die and the container, the radial lines of the grid pattern will show a convex curvature adjacent to the die, instead of concave shape as in direct extrusion.

18.5 Outflow of the Outer Layers and the Skin of the Billet

As explained in the preceding section, different flow types occur in extrusion due to different friction conditions at the interface between the billet and the container wall and die. Because of cooling effects, the outer layers of the billet can have higher flow stress than the interior of the billet. Then there is even stronger retention of the peripheral layer of the billet, and this will make the billet flow according to flow type C.

The tendency of outflow of the peripheral skin of the billet and the subsurface layers below the skin into the extrusion is therefore uniquely determined by the flow pattern, as depicted in Fig. 18.5, where the subsurface layers have been painted black.

18.5.1 Flow Pattern S

When the billet flows according to flow type S, the billet skin and the material below will slide along the container wall and the die. At a certain stage of extrusion, they will start to flow out of the die opening, into the extrusion. Here they will appear on the surface of the extrusion; see Fig. 18.5. Hence, when steady-state conditions have been reached in the extrusion process, the outer skin of the extrusion will originate from the billet skin. In addition, a subsurface layer of given thickness from the as-cast billet will appear as a subsurface layer in the final extrusion. In the extrudate, this layer will have approximately constant thickness when the steady-state condition has been reached.

18.5.2 Flow Patterns A, A_1, and B

Because of partial or complete sticking at the interface between the billet and the die or container wall, some material initially in the front end of the billet will remain stagnant in the front end during extrusion, either in the dead zone adjacent to the die, or in the shear zone.

With some sliding at the container wall, as experienced for flow types A and B, the billet skin – including the subsurface layers below the skin – will flow into the interior of the billet, on top of the stagnant material in the dead zone and in the shear zone; see Fig. 18.5. This material will flow slowly forward until it flows out of the die hole and into the extrusion, where it will appear as a subsurface layer.

Because of the deformation in the shear zone, a thin layer of material is concurrently fed out gradually from the shear zone into the very outer surface layer of the extrusion. This material will cover the sublayer created from the outer layers of the billet and will also generate the new surface skin that is formed on the extrusion. The small region inside the billet that feeds this material forward was shown in Fig. 12.9(b), and can preferably be termed the *slow flowing zone*.

If the initial billet skin *overfolds* on top of the dead zone and flows into the subcutaneous layers of the extrusion, it will appear as an extrusion defect, commonly called *scaling*. Depending on the nature of the initial oxide film on the surface of the billet and an eventual lubrication following the film, the metal layer flowing from the slow flowing zone, appearing on top of the initial billet skin, may behave differently. It can either partially pressure-weld onto the billet skin or, in case of poor welding, be pulled off from the extrudate as a *loose scale*. The process of inward flow of the initial peripheral skin of the billet on top of the dead zone into the extrusion can be compared with the well-known phenomenon of overfolding sometimes taking place in forging; see Fig. 16.10. In forging, the phenomenon is known to cause material defects like laps or cold shuts.

When the overfolding occurs, i.e., whether it occurs early or late during extrusion, depends on two factors. These are the degree of slipping at the container wall, and the size of the flat-faced portion of the die on which the dead zone rests. With increased slipping, i.e., with reduced friction along the billet–container interface, the peripheral layer and the billet skin tend to flow into the extrusion at an earlier stage. The same happens if the die hole is moved closer to the container wall. Then a smaller dead zone forms, and the flow path of the skin and peripheral subsurface layer of the billet, on top of the dead zone and the slow flowing zone, into the extrusion becomes shorter.

In unlubricated indirect extrusion of aluminum, i.e., for flow pattern A_1, there is complete sticking in the boundary layer between the billet and the container wall. The billet skin then sticks to the container and does not flow on top of the material from the dead zone and the slow flowing zone. However, the thin subsurface peripheral layer of the billet will still flow that way and will finally appear right under the surface of the extrusion. If this layer contains *contamination*, it can cause surface quality problems in the extrusion process. If no lubrication is used in the extrusion process, the surface skin of the billet will accumulate in the billet discard and will not flow into the extrusion. This is advantageous in that the billet skin then will be present in the final metal residue, which is discarded after the end of each press cycle.

18.5.3 Flow Pattern B_1

For this flow type, the inward flow of the peripheral billet layer on top of the dead zone and into the profile will occur in the same way as described previously for flow types A_1, A, and B; see Fig. 18.5. Now, however, this flow will be delayed, because the retention of the peripheral layer of the billet is stronger than for the other flow types. Because of sticking friction along the container wall and the die, the skin of the billet will not flow into the extrusion, unless traces of lubricant are present on the billet skin or on the container wall.

Because of the previously mentioned scraping off of the adhering peripheral billet layer as the ram advances down along the container wall, and the packing of this layer radially inwards into the rear end of the billet, this material will tend to flow inwards into the rear end of the billet; see Fig. 18.5. Hence, for this flow type, there will be two concurrently occurring directions of flow[6] of the peripheral layer of the billet:

Direction 1, i.e., the layer flows on top of the dead and the shear zone, into the subsurface layers of the extrusion.
Direction 2, i.e., the layer flows inwards into the rear end of the billet.

In the case of flow in direction 2, the peripheral metal layer that is packed into the rear end of the billet will tend to flow out into the core of the extrusion at a late stage of extrusion.

18.5.4 Flow Pattern C

Because of the large dead zone formed when material flow conforms to flow pattern C, there is no material flow in direction 1 for the outer layer of the billet; see Fig. 18.5. For this flow type, the dead zone then extends backwards along the container wall, up to the very rear end of the billet. The scraping-off action of the ram at the rear end of the billet will then be more pronounced than for flow type B_1. The scraped-off layer will be thicker, and more material will gather in the lump in front of the ram, than for flow type B_1. Because of this, the flow in direction 2 will be stronger, and the peripheral layers of the billet will flow faster in this direction. Thus, the peripheral layer of the billet may appear inside the core of the billet at a rather early stage of extrusion; see Fig. 18.5. In cases of partial sliding at the billet–container interface, the peripheral oxide skin of the billet can flow into the core of the extrusion, at the rear end of the product, following flow direction 2. Here it can cause lamination or delamination close to the center of the extrusion and the occurrence of the defect termed *pipe*, so that the extrusion comes out with a hollow core at the back end. The term the *extrusion defect* is often used to characterize these flow-related defects, which may occur in the rear end of an extrusion.

From the preceding description, it is obvious that for all flow types except S, the presence of lubricant in the interface between the billet and the container is detrimental to the extrusion process, because overfolding of the billet skin into the interior of the billet is likely to result. At a later stage of extrusion, the overfolded skin will then flow out into the extrusion, where it will appear as an extrusion defect.

18.6 Use of Taper to Optimize Upsetting

As previously mentioned, it is important to have right conditions during the upsetting stage in extrusion, to keep air from getting trapped in between the billet and the tooling. If this happens, there is great risk that surface defects like blisters will form; see Fig. 18.3.

Favorable conditions with regard to upsetting are for instance those depicted in Fig. 18.6(a), where upsetting occurs in such a manner that radial flow starts adjacent to the die and then spreads continuously backwards. Then the rear end of the billet

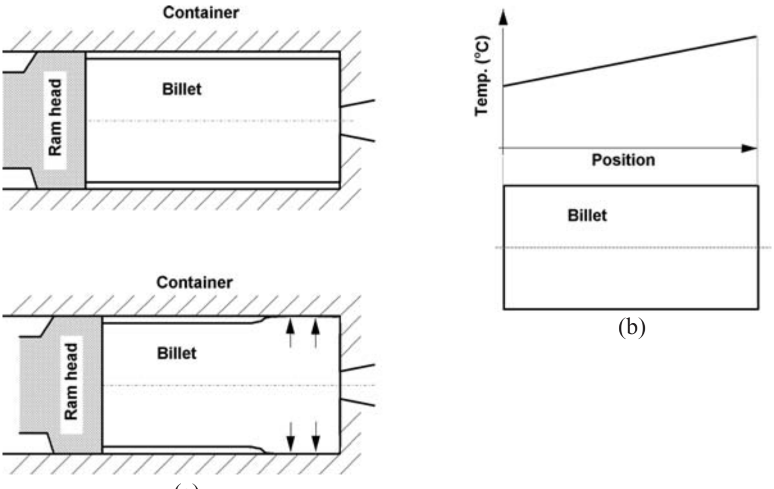

(a) (b)

Figure 18.6. (a) Favorable material flow during upsetting achieved by use of taper. (b) The taper in the billet before upsetting.

adjacent to the ram head will be the last part of the billet to be upset and to fill the container. If upsetting occurs this way, the initial air in the gap between the billet and the container wall will accumulate at the rear end of the billet, from where it can escape. Upsetting of the billet this way is obtained in industrial extrusion if the billet is given a temperature gradient along its length during heating before it is loaded into the container. Such a temperature gradient is in extrusion terminology called *taper*. The taper should preferably be characterized by a temperature drop from front to rear end of the billet of approximately 50°C. When the billet is hottest in the front end, lateral metal flow upon upsetting will start from there. When the billet has expanded and filled the clearance in the front end of the container, the lateral flow will spread backwards in a continuous manner, until the whole air gap between the container and the billet has disappeared.

In case of the opposite taper, filling of the air gap will start from the rear end of the billet. The last space to be filled then is in the corner between the die and the container. Confinement of air will then occur there, and this will be detrimental to the extrusion process. The air stuck at this location will tend to flow out into the subsurface layers of the extrusion, where it can create laminations and/or blistering.

18.7 The Burp Cycle

In addition to applying a billet taper in the forward extrusion process, it is common also to remove eventually confined air from the front of the billet adjacent to the die. This is done after upsetting of the billet, by a slight withdrawal of the billet and the container from the die, so that confined air can escape. This operation is in general extrusion terminology called the *burp cycle*. In many ways, it resembles the way one treats babies after they have been given milk from a feeding bottle to make them sleep comfortably during the night, so that their parents can get a good night's sleep.

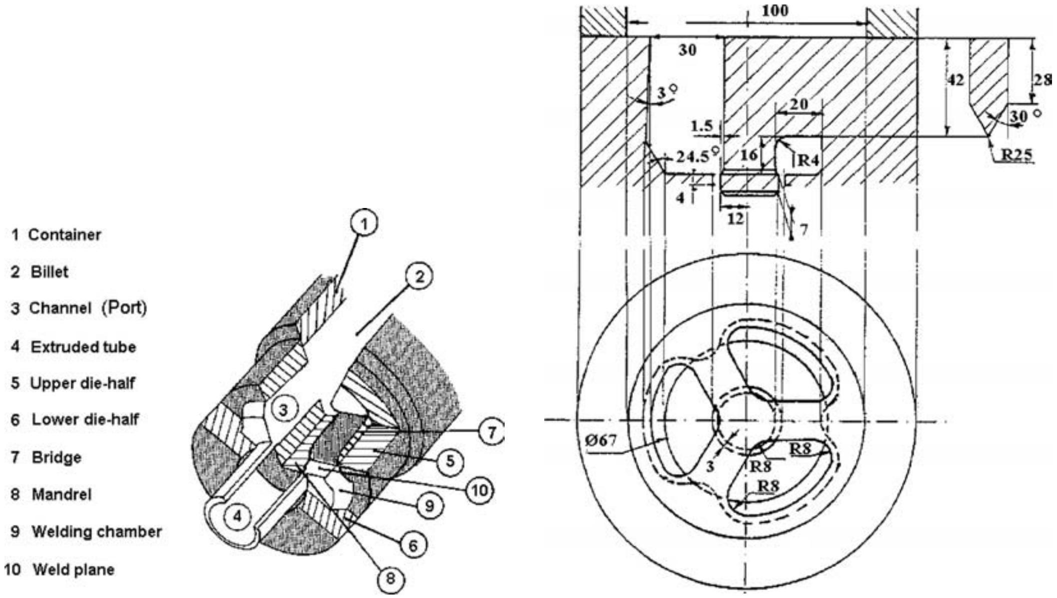

(a) (b)

Figure 18.7. (a) Three-dimensional sketch of a porthole die filled with metal. (b) Machine drawing of a porthole extrusion die. (Courtesy of A. W. Hansen, NTNU.)

18.8 Extrusion of Hollow Profiles Using Porthole Dies

Extrusion of hollow profiles was mentioned briefly in Ch. 2.2.5, and the metal flow in a typical porthole die was shown in Fig. 2.5. In this figure, all tool elements were omitted to ease visualization of the flow in the process. Because of this, it was possible to see that the metal from the billet is split in three different streams by the *die bridges*. When the streams have reached down into the *welding chamber* of the die, they are brought together again, and join into one single metal stream, by *extrusion welding*. In this manner, a hollow profile is created in extrusion.

In Fig. 18.7(a), the extrusion process is shown by means of a perspective sketch. It shows the applied tool elements and the metal inside the die, as well as the extrusion in the space behind the die. In addition, a traditional machine drawing of the extrusion die is shown in Fig. 18.7(b). The three images shown together in Fig. 2.7 and in Fig. 18.7 illustrate the general geometrical complexity of *hollow profile extrusion*. The figure also depicts how the metal streams are pressure-welded together in the welding chamber, so that the metal is transformed into a tube-shaped profile as it exits the die.

Behind each bridge, or *die web*, two separate metal streams join to create the extrusion seam weld. The weld extends in the longitudinal direction along the length of the profile. The welding process that takes place behind each bridge is very efficient. The joining metal streams are pressed tightly together, in hot condition, without the presence of air, because the die is completely filled with metal. A *metallic*

Section category	Section type	Examples
A	Simple bar	
B	Shaped bar	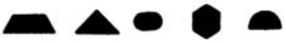
C	Standard sections	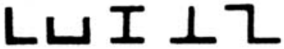
D	Simple solid sections	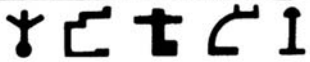
E	Semihollow sections	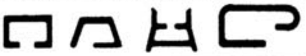
F	Sections with abrupt section transitions and thin walls; wide sections	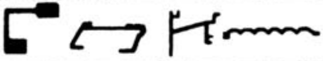
G	Sections with difficult tongues and very narrow inlets	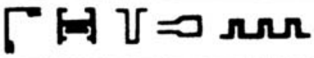
H	Tubes	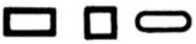
J	Simple hollow sections	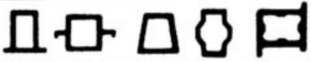
K	Difficult hollow sections; hollow sections with two or more cavities	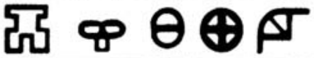
L	Tube sections with external projections	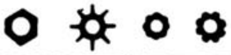
M	Tube shapes with internal projections or K + L	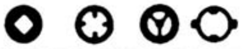
N	Large or wide hollow sections	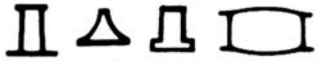

Figure 18.8. Classification system for the geometry of extruded profiles with respect to how difficult they are to extrude.[7] (Reprinted with permission of Carl Hanser Verlag ©, München.)

bond then easily forms across the two metal streams, because there is high temperature concurrently with large plastic deformation of the metal. The mechanism of welding in such a die is classified as *solid pressure welding*, because there is no melting of the metal surfaces that join.

18.9 Classification of Extruded Shapes of Aluminum Profiles

A *classification system* has been established for various shapes of profiles commonly produced in aluminum extrusion. The shapes are classified in groups according to how difficult they are to extrude; see Fig. 18.8. As the figure depicts, profiles of simple shape, as, for instance, round or square cross sections, are easy to extrude, whereas large, wide, hollow profiles are difficult to extrude. It is not only complexity of cross-sectional shape that will make the extrusion process more difficult.

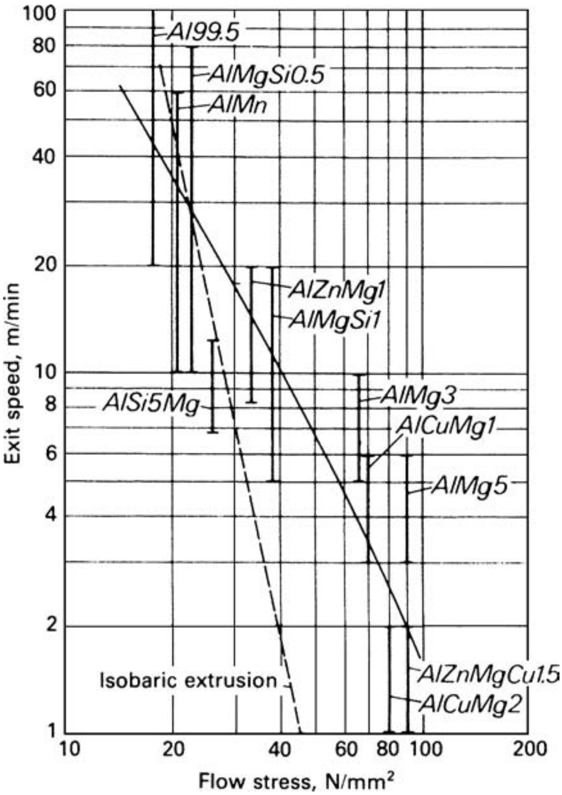

Figure 18.9. Common range of extrusion velocities[8] for some Al alloys. (Reprinted with permission of Giesel-Verlag Gmbh; www.giesel-verlag.de.)

Geometrical details, such as thin walls or webs on the extrusion or sharp transitions from thick to thin wall thickness, also increase the degree of difficulty in extrusion. So does also the transition from massive to hollow profiles.

18.10 Extrudability of Aluminum Alloys

In practice, some alloys are much more difficult to extrude than others. An alloy that can only be extruded at low speed is said to have low *extrudability*. On the other hand, alloys that can be extruded at high speed are considered easy to extrude. Based on industrial experience regarding possible extrusion speeds for different alloys, Fig. 18.9 has been compiled. One important material parameter that determines whether an alloy will be easy or difficult to extrude is its flow stress. Alloys with high flow stress are commonly difficult to extrude, in contrast with alloys with low flow stress; see Fig. 18.9. So on this basis, the most commonly applied extrusion alloys are commonly divided into three classes.[8] Some important alloys within these three classes are

1. Easy-to-extrude alloys: pure Al, AlMg1, AlMn1, AlMgSi0.5
2. Alloys with intermediate extrudability: AlMg 3, AlMgSi1, AlZn4.5Mg1
3. Difficult-to-extrude alloys: AlCuMg2, AlZnMgCu1.5, AlMn 4.5Mg

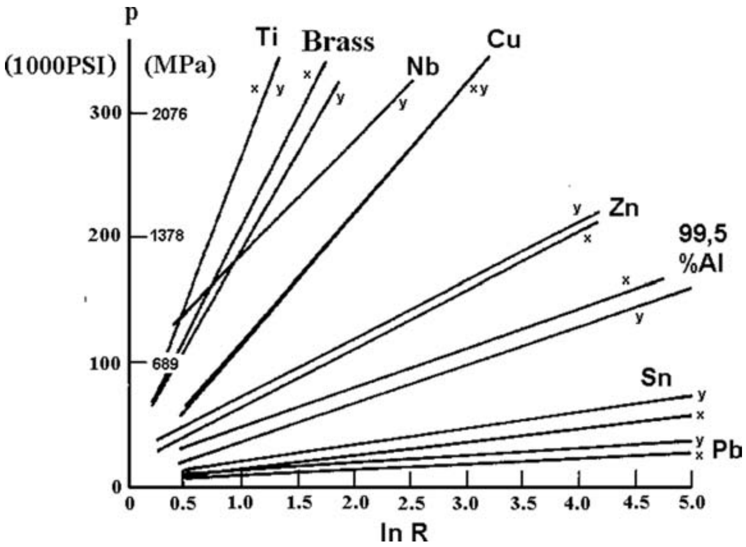

Figure 18.10. Experimentally determined extrusion pressures for different metals and alloys.[9] Here x denotes low (0.17–2.3 mm/s) and y high (33–400 mm/s) extrusion ram velocity.

18.11 Extrusion Force and Pressure[1]

The *average contact pressure* against the extrusion ram in extrusion can be determined from the measured *extrusion force* F by dividing it by the cross-sectional area of the ram head, A_S. Thus the average ram pressure can be determined as

$$p = \frac{F}{A_S} \tag{18-1}$$

Measured pressure data for a number of metals and alloys in forward rod extrusion have been published as graphs; see Fig. 18.10. They reveal that the extrusion pressure is approximately a linear function of the extrusion ratio R in each situation. (For the definition of R, see eq. 5-8.) Because the extrusion force is proportional to the extrusion pressure, the following relationship must exist between the extrusion force and the reduction ratio in extrusion:

$$F = a + b \ln R \tag{18-2}$$

The parameters a and b in this equation can be determined by curve fitting for each material, from the data in Fig. 18.10. In addition, as shown by Fig. 18.10, the extrusion force generally depends on the applied extrusion speed; hence, the constants a and b also depend on the extrusion speed. In hot extrusion of common metals, it is observed that the extrusion force, and the extrusion pressure, will increase strongly as the extrusion speed is increased.

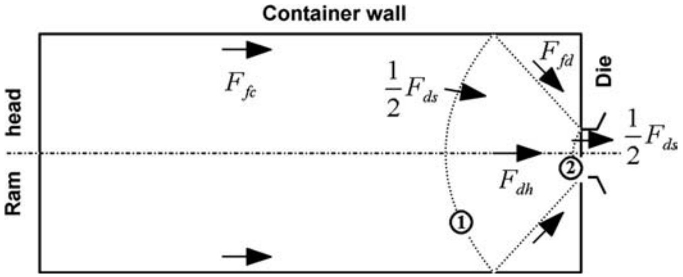

Figure 18.11. The total extrusion force is made up of four parts.

18.11.1 Theoretical Estimate of Extrusion Force and Pressure

The extrusion force and the extrusion pressure can be determined in theoretical analysis by use of (for instance) the slab method, or by an upper bound solution. In such a theoretical analysis, it is assumed that a number of different deformation phenomena in the extrusion process contribute separately to the total energy consumption in the process. The required energy input into the extrusion process and the required extrusion force are then divided into four separate *additive parts* (see Fig. 18.11), as shown by the formula

$$F = F_{fc} + F_{dh} + F_{fd} + F_{ds} \tag{18-3}$$

The first term, F_{fc}, is the force required to overcome the friction force against the container wall when the billet is pushed forward and starts to slide against this wall. The second term, F_{dh}, is the required force to overcome the deformational resistance to deform the metal homogeneously upon flow through the conical primary deformation zone in front of the die; see Fig. 18.11. If one considers a disc-shaped element of material flowing through this cone (see the sketch in Fig. 18.13), the disc is compressed in the circumferential direction and it elongates in the axial direction.

The third term in eq. 18-3, F_{fd}, is the force required to overcome frictional resistance as the extrusion material in the primary deformation zone is sheared against the surrounding dead zone. If extrusion is conducted through a conical die instead, there is no dead zone ahead of the die, but the material will then slide against the die cone itself, and the term then will represent the force required to overcome friction against the die.

Finally, the last term, F_{ds}, is the force required to shear-deform the material as it flows through the velocity discontinuities present at the entrance into the primary deformation zone and at the exit from this zone; see Fig. 18.11. Along these discontinuity lines the material will change its direction of movement.

In the subsequent treatment, it will be shown how the four different load contributions just defined, which together make up the total extrusion force, can be determined by means of theory.

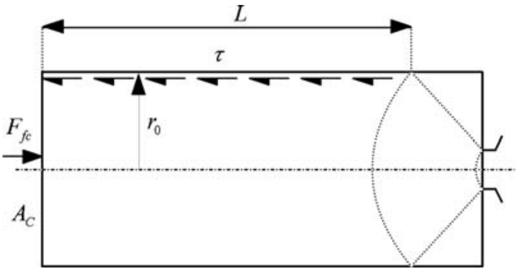

Figure 18.12. Force equilibrium for billet sliding against container wall.

18.11.2 Force Due to Friction against the Container Wall

An expression for the force contribution due to sliding friction against the container wall, F_{fc}, can be determined by considering force equilibrium for a billet of length L inside the container as expressed by eq. 18-4; see Fig. 18.12. The required force must counteract the shear stress τ directed against the sliding movement of the billet against the container wall:

$$F_{fc} = \tau \cdot A_C = \tau \cdot 2\pi r_0 L \tag{18-4}$$

18.11.3 Force Due to Friction against the Dead Zone and Homogeneous Deformation Force in the Primary Deformation Zone

To obtain an equation for the two force components $F_{fd} + F_{dh}$, i.e., the component required to overcome friction against the die or the dead zone, and the component to homogeneously deform the material upon flow through the primary deformation zone, one can apply the theoretical slab method as previously described in Sec. 13.2. When this is done, one usually assumes that the cone angle α of the primary deformation zone is small. Corresponding equations under the assumption of larger angle have been developed elsewhere.[10]

Consider a material element in the form of a slab, sliding through the primary deformation zone ahead of the die, as depicted in Fig. 18.13. The shear stress τ and the normal stress component p_α will act on the conical outer surface of the element; see Fig. 18.13(a). These stresses on the slab element can be decomposed into two components acting in the horizontal and the radial direction, respectively, as done in Fig. 18.13. The decomposed components, when multiplied by the surface areas on which they act, yield the force components shown in Fig. 18.13(b) and (c). By means of these components, a force balance for the whole slab element can be set up, for both the radial and the axial direction:

$$(\sigma_z + d\sigma_z)\,\pi\,(r + dr)^2 - \sigma_z \pi r^2 + F_z + F_z^\tau = 0 \tag{18-5}$$

$$\sigma_r 2\pi r \mathrm{d}z + F_r - F_r^\tau = 0 \tag{18-6}$$

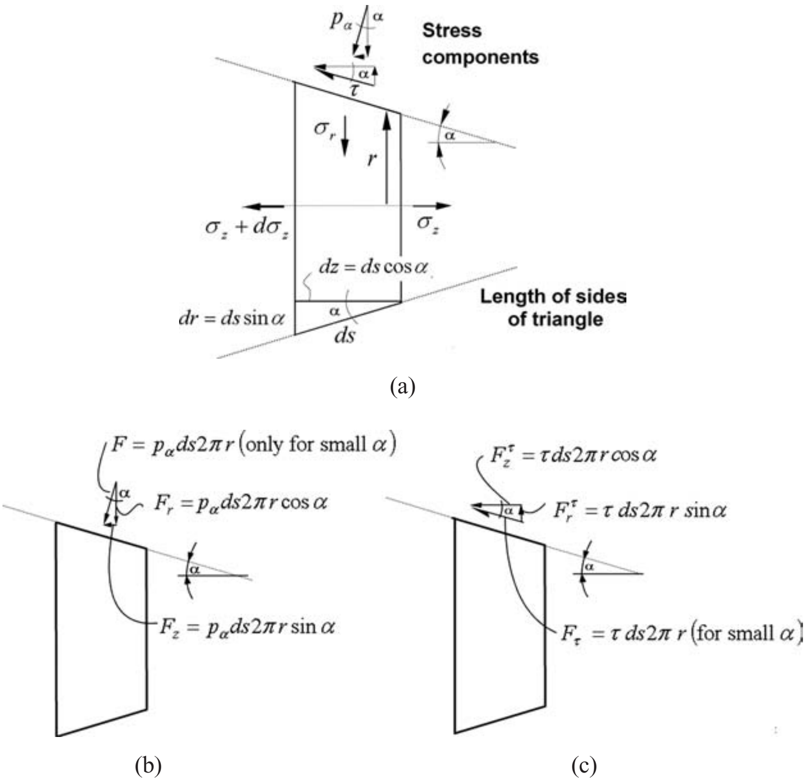
p_α
α
Stress components
τ
σ_r
r
$\sigma_z + d\sigma_z$
σ_z
$dz = ds\cos\alpha$
$dr = ds\sin\alpha$
ds
Length of sides of triangle
(a)
$F = p_\alpha ds 2\pi r$ (only for small α)
$F_r = p_\alpha ds 2\pi r \cos\alpha$
$F_z = p_\alpha ds 2\pi r \sin\alpha$
(b)
$F_z^\tau = \tau ds 2\pi r \cos\alpha$
$F_r^\tau = \tau\, ds 2\pi\, r\, \sin\alpha$
$F_\tau = \tau\, ds 2\pi\, r$ (for small α)
(c)

Figure 18.13. Force equilibrium for slab element sliding through conical converging channel. (a) Stress components. Force components on the channel wall due to (b) normal stress and (c) shear stress.

If the product of the stress and the area it acts on is introduced into these equations [see Fig. 18.13(b,c)], the following expressions are obtained:

$$(\sigma_z + \mathrm{d}\sigma_z)\,\pi\,(r + \mathrm{d}r)^2 - \sigma_z \pi r^2 + p_\alpha\,\mathrm{d}s\,2\pi r\,\sin\alpha + \tau\,\mathrm{d}s\,2\pi r\,\cos\alpha = 0 \tag{18-7}$$

$$\sigma_r\,2\pi r\,\mathrm{d}z + p_\alpha\,\mathrm{d}s\,2\pi r\,\cos\alpha - \tau\mathrm{d}s\,2\pi r\,\sin\alpha = 0 \tag{18-8}$$

Equation (18-8) yields the following result:

$$p_\alpha = \tau\,\tan\alpha - \sigma_r \tag{18-9}$$

The von Mises flow criterion coupled with the Levy–Mises flow rule for axisymmetric conditions (see eq. 13-10) yields the following relationship:

$$\sigma_z - \sigma_r = \bar{\sigma} \tag{18-10}$$

Now σ_r from eq. 18-10 can be inserted in eq. 18-9. Then p_α can be solved for and substituted in eq. 18-7. This yields the following differential equation:

$$r\,\mathrm{d}\sigma_z + 2\,(\tau\,\tan\alpha + \bar{\sigma})\,\mathrm{d}r + 2\,\mathrm{d}r\frac{\tau}{\tan\alpha} = 0 \tag{18-11}$$

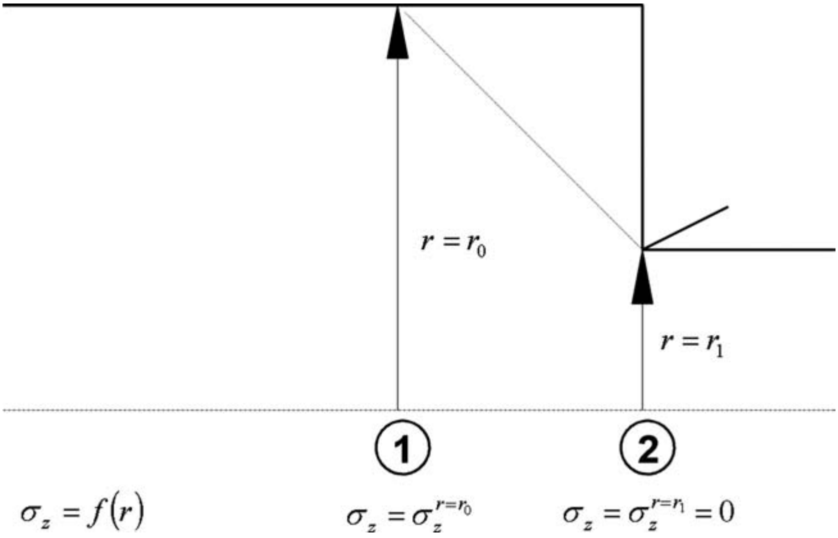
$r = r_0$
$r = r_1$
①
②
$\sigma_z = f(r)$
$\sigma_z = \sigma_z^{r=r_0}$
$\sigma_z = \sigma_z^{r=r_1} = 0$

Figure 18.14. Boundary conditions at the inlet and the outlet from the conical deformation zone.

This equation has the following solution:

$$\sigma_z = -2\left(\tau \tan\alpha + \bar{\sigma} + \frac{\tau}{\tan\alpha}\right)\ln r + C \tag{18-12}$$

The boundary condition at the exit from the deformation cone, i.e., at the die orifice (see Fig. 18.14), is

$$\sigma_z^{r=r_1} = 0$$

This expression, introduced into eq. 18-12, gives the value of the integration constant:

$$C = 2\left(\tau \tan\alpha + \bar{\sigma} + \frac{\tau}{\tan\alpha}\right)$$

C can then be eliminated from eq. 18-12. The resulting equation expresses the general stress distribution in the z-direction in the primary deformation zone:

$$\sigma_z = \left(\tau \tan\alpha + \bar{\sigma} + \frac{\tau}{\tan\alpha}\right)\ln\frac{r_1^2}{r^2} \tag{18-13}$$

By means of this expression, we now can determine the axial stress at the entrance into the deformation cone (see Fig. 18.14)

$$\sigma_z^{r=r_0} = \left(\tau \tan\alpha + \bar{\sigma} + \frac{\tau}{\tan\alpha}\right)\ln\frac{A_1}{A_0}$$

The expression can be rewritten as

$$\sigma_z^{r=r_0} = -\left(\bar{\sigma}\ln\frac{A_0}{A_1} + \frac{\tau}{\sin\alpha\cos\alpha}\ln\frac{A_0}{A_1}\right) \tag{18-14}$$

The force required to extrude the billet through the primary deformation zone can now be determined by multiplying the stress in eq. 18-14 by the cross-sectional area of the billet. In addition, it is reasonable to change the sign to make the extrusion force positive. The stress was initially defined so that the resulting extrusion force has come out negative. The final expression arrived at consists of two parts. The first part quantifies the required force to deform the material homogeneously during flow through the die; the second part is the force required to overcome friction against the die or the dead zone:

$$F_{dh} + F_{fd} = \pi r_0^2 \sigma_z^{r=r_0} = \pi r_0^2 \bar{\sigma} \ln \frac{A_0}{A_1} + \pi r_0^2 \frac{\tau}{\sin\alpha \cos\alpha} \ln \frac{A_0}{A_1} \tag{18-15}$$

The shear stress τ against the die or the dead zone can be described in two fundamentally different ways. If one extrudes through a conical die, in the absence of dead zones, this stress is the friction stress transferred from the billet to the surface of the die cone, expressed as

$$\tau_i = \frac{m}{\sqrt{3}} \bar{\sigma} \tag{18-16}$$

Here m is the Tresca friction factor and $\bar{\sigma}$ the effective flow stress of the extrusion metal.

If extrusion is done through a flat-faced die instead, a dead zone of extrusion metal will appear in front of the die. The interior metal flow in the billet will occur against this dead zone. The shear stress then will equal the maximum shear stress of the billet metal, i.e., the shear stress specified in eq. 18-16, with m set equal to 1. In this case, eq. 18-15 can be expressed as

$$F_{dh} + F_{fd} = \pi r_0^2 \sigma_z^{r=r_0} = \pi r_0^2 \bar{\sigma} \ln \frac{A_0}{A_1} + \pi r_0^2 \frac{\bar{\sigma}}{\sqrt{3} \sin\alpha \cos\alpha} \ln \frac{A_0}{A_1} \tag{18-17}$$

18.11.4 Force Due to Shear Deformation at the Velocity Discontinuities

During extrusion through a conical converging channel, there are two velocity discontinuities, one at the entrance to and one at the exit from the primary deformation zone; see the lines numbered 1 and 2 in Fig. 18.11. The force required to cause shear deformation along these lines, i.e., to maintain the velocity discontinuities, is denoted by the symbol F_{ds}.

Let us assume the flow field through the primary deformation zone to be as defined in Fig. 18.15. Previously (see eq. 13-17) the power consumption during flow through a general velocity discontinuity was expressed as

$$\mathrm{d}\dot{W}_S = k \, \Delta v \, \mathrm{d}A$$

Let us now consider a material particle that flows toward the first velocity discontinuity, Γ_1, so that after passage of the discontinuity it flows along a straight line oriented at an angle θ to the axis of the billet; see Fig. 18.15. The velocity change during passage of the line Γ_1 then will be

$$\Delta v = v_0 \sin\theta$$

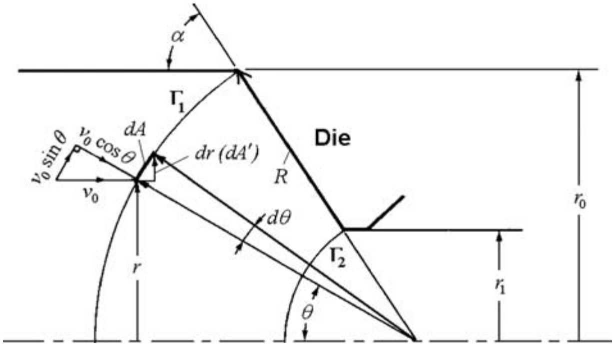

Figure 18.15. Assumed flow field[1] through primary deformation zone. (Reprinted with permission of Prof. Taylan Altan. www.ercnsm.org.)

Let us now first determine the differential $\mathrm{d}A$. Because $R = r_0/\sin\alpha$, one gets

$$r = R\sin\theta \quad \Rightarrow \quad \mathrm{d}r = R\cos\theta\,\mathrm{d}\theta$$

The area obtained upon rotation of $\mathrm{d}r$ (see Fig. 18.15) is $\mathrm{d}A' \approx 2\pi r\,\mathrm{d}r$, so

$$\frac{\mathrm{d}A'}{\mathrm{d}A} = \cos\theta \quad \Rightarrow \quad \mathrm{d}A = \frac{1}{\cos\theta}\cdot 2\pi r\,\mathrm{d}r \quad \Rightarrow \quad \mathrm{d}A = \frac{2\pi}{\cos\theta} r\,\mathrm{d}r$$

$$\mathrm{d}A = \frac{2\pi}{\cos\theta} R\sin\theta \cdot R\,\mathrm{d}\theta \cdot \cos\theta = 2\pi R^2 \sin\theta\,\mathrm{d}\theta$$

The power consumption upon passage of the material particle through the velocity discontinuity can now be expressed as

$$\begin{aligned}
\dot{W}_S &= \int_A k\,\Delta v\,\mathrm{d}A = \int_0^{\alpha} \frac{\bar{\sigma}}{\sqrt{3}} \cdot v_0 \sin\theta \cdot 2\pi R^2 \sin\theta\,\mathrm{d}\theta \\
&= \frac{\bar{\sigma}}{\sqrt{3}} v_0 \cdot 2\pi R^2 \int_0^{\alpha} \sin^2\theta\,\mathrm{d}\theta \\
&= \frac{\bar{\sigma}}{\sqrt{3}} v_0 \cdot 2\pi R^2 \left(-\frac{1}{2}\sin\alpha\,\cos\alpha + \frac{1}{2}\alpha\right) \\
&= \frac{\bar{\sigma}}{\sqrt{3}} \pi v_0 \cdot r_0^2 \left(\frac{\alpha}{\sin^2\alpha} - \frac{\cos\alpha}{\sin\alpha}\right) \\
&= \frac{\bar{\sigma}}{\sqrt{3}} \pi v_0 \cdot r_0^2 \left(\frac{\alpha}{\sin^2\alpha} - \cot\alpha\right) \qquad (18\text{-}18)
\end{aligned}$$

If the energy dissipation upon passage through the second velocity discontinuity Γ_2 is also computed, one actually obtains the same result as for the first velocity discontinuity. Therefore (see Fig. 18.11), the following result is obtained:

$$\frac{1}{2} F_{ds} \cdot v_0 = \frac{\bar{\sigma}}{\sqrt{3}} \pi v_0 \cdot r_0^2 \left(\frac{\alpha}{\sin^2\alpha} - \cot\alpha\right)$$

$$\Rightarrow \quad F_{ds} = \frac{2\bar{\sigma}}{\sqrt{3}} \pi r_0^2 \left(\frac{\alpha}{\sin^2\alpha} - \cot\alpha\right) \qquad (18\text{-}19)$$

18.11.5 Result of the Theoretical Analysis

As shown in the preceding treatment, the extrusion force can be determined as the sum of four force components, determined by use of a force balance, the slab method, and an upper bound solution. The equations obtained this way, when summed, give the following expression for the extrusion force in axisymmetric forward extrusion:

$$\begin{aligned}F &= F_{fd} + F_{fc} + F_{dh} + F_{ds}\\ &= \tau \cdot 2\pi r_0 L + \pi r_0^2 \bar{\sigma} \ln \frac{A_0}{A_1} + \pi r_0^2 \frac{\bar{\sigma}}{\sqrt{3}\sin\alpha\cos\alpha} \ln \frac{A_0}{A_1} + \frac{2\bar{\sigma}}{\sqrt{3}}\pi r_0^2 \left(\frac{\alpha}{\sin^2\alpha} - \cot\alpha\right)\\ &= (F_{fd} + F_{ds}) + A_0\left(\bar{\sigma} + \frac{\bar{\sigma}}{\sqrt{3}\sin\alpha\cos\alpha}\right)\ln R = a' + b' \ln R \qquad \text{(18-20)}\end{aligned}$$

As the equation depicts, the extrusion force obtained in the theoretical analysis depends on the same extrusion parameters as did the force described by the empirical formula given in eq. 18-2. Note that in eq. 18-20 the dependence of extrusion force upon extrusion velocity is included through the effective flow stress term $\bar{\sigma}$. As previously discussed in Ch. 8, the flow stress in warm and hot forming of metals commonly increases with increasing strain rate; hence, the flow stress must increase when the forming velocity is increased.

If one assumes the friction between billet and container wall to be expressed by Tresca friction, the symbol τ in eq. 18-20 can be replaced by the expression specified in eq. 18-16.

Problems

18.1 An aluminum alloy billet is extruded[11] into a round axisymmetric rod of 12 mm diameter, applying a ram velocity of $v_s = 15\ \text{mm s}^{-1}$. The billet geometry is specified in Fig. 18.16(a), and so is the geometry of the extrusion discard left in the container at the end of extrusion.

(a) Determine the extrusion ratio R and the extrusion speed of the resulting rod.

Figure 18.16(b) and (c) show recordings, made during the extrusion experiment, of the extrusion force and the temperature of the rod at the die exit.

(b) Compute the average exit temperature of the rod under the assumption that all heat developed in the process remains in the rod and follows it through the die hole. Comment upon the validity of this assumption on the basis of the temperature recordings given in Fig. 18.16(c).

(c) Write down the theoretical expression for the extrusion force derived in the chapter. Explain the origin of the various terms in the formula, and specify which theoretical methods are used to develop each derived part.

(d) Determine the two force components F_{dh} and F_{fd} for the extrusion process described in Fig. 18.6(a), by means of an upper bound solution. Assume the

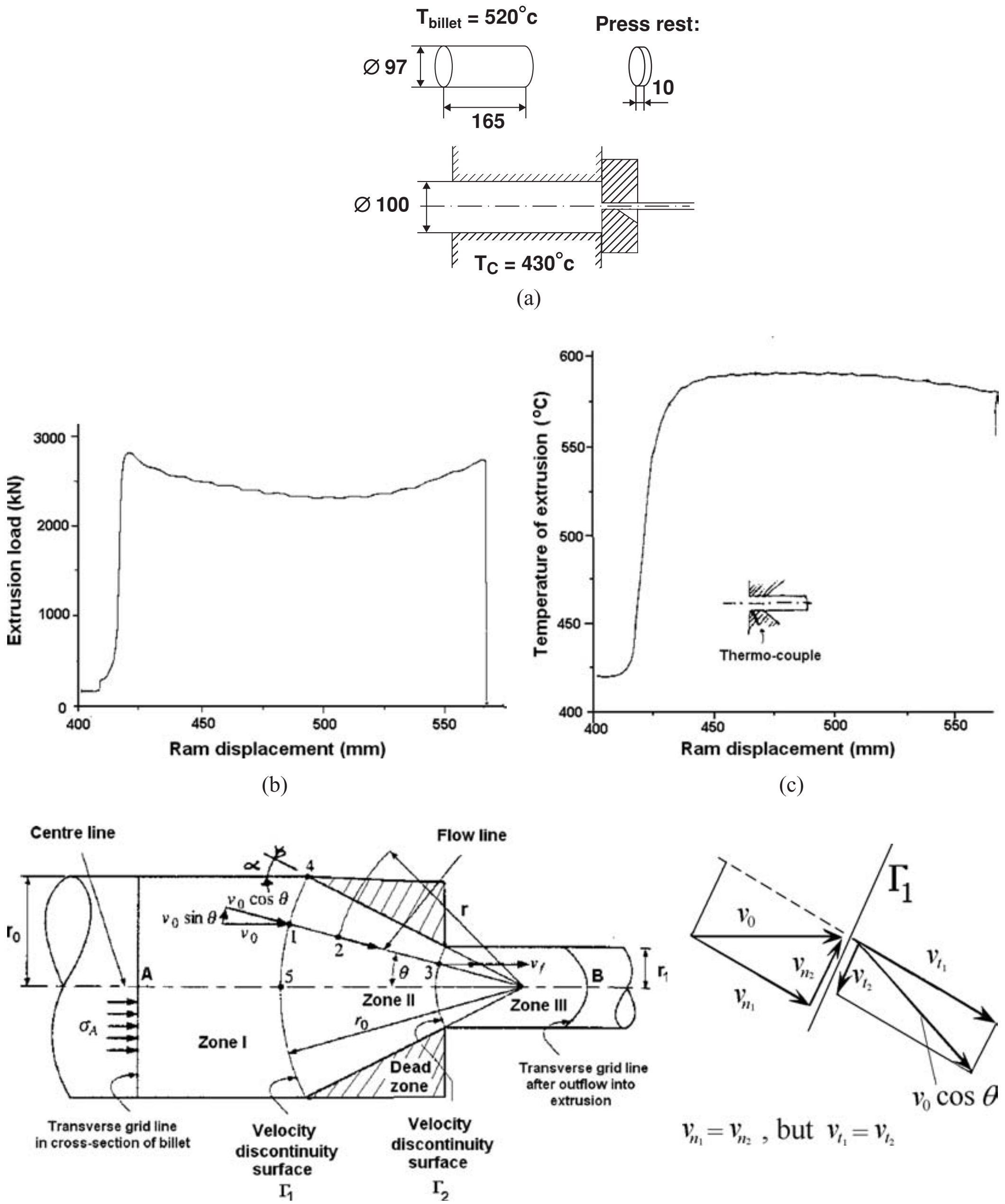

(a)

(b) (c)

(d)

Figure 18.16. (a) The extrusion process (dimensions in millimeters). (b) Load–stroke record during extrusion. (c) Measured temperature on the bearing surface of the die. (d) Schematic representation of the velocity field in the extrusion process. (Courtesy of S. Støren, NTNU.)

velocity field during flow of metal through the conical primary deformation zone ahead of the die to be as defined in Fig. 18.16(d). Assume the cone angle to be $\alpha = 45^\circ$.

Zone I: Constant axial velocity over the cross section of the billet: $v_0 = v_0$.
Zone II: Velocity along a flow line, i.e., along the line connecting points 1, 2, and 3:

$$v_{\mathrm{II}} = v_0 \left(\frac{r_0}{r}\right) \cos\theta$$

Zone III: Constant axial velocity over the cross section of the extruded rod: v_{III}.

For axisymmetric flow in zone II, the following relationships are valid: In a spherical coordinate system, the velocity field is given by

$$v_r = v_r(r, \theta), \qquad v_\theta = v_\varphi = 0$$

The strain-rate components in this coordinate system can then be expressed as

$$\dot{\varepsilon}_r = \frac{\partial v_r}{\partial r}, \qquad \dot{\varepsilon}_\theta = \dot{\varepsilon}_\varphi = \frac{v_r}{r}$$

$$\dot{\varepsilon}_{r\theta} = \frac{1}{2}\frac{1}{r}\frac{dv_r}{d\theta}, \qquad \dot{\varepsilon}_{r\varphi} = \dot{\varepsilon}_{\theta\varphi} = 0$$

The effective strain rate can in general be expressed as

$$\mathrm{d}\dot{\bar{\varepsilon}} = \left(\frac{2}{3}\left[\mathrm{d}\dot{\varepsilon}_x^2 + \mathrm{d}\dot{\varepsilon}_y^2 + \mathrm{d}\dot{\varepsilon}_z^2 + 2\left(\mathrm{d}\dot{\varepsilon}_{xy}^2 + \mathrm{d}\dot{\varepsilon}_{yz}^2 + \mathrm{d}\dot{\varepsilon}_{zx}^2\right)\right]\right)^{1/2}$$

The effective strain rate in polar coordinates with axisymmetric conditions is

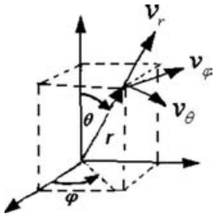

$$\dot{\bar{\varepsilon}} = \sqrt{\frac{2}{3}\left(\dot{\varepsilon}_r^2 + \dot{\varepsilon}_\theta^2 + \dot{\varepsilon}_\varphi^2 + 2\dot{\varepsilon}_{r\theta}^2\right)}$$

NOTES

1. Altan, T., Oh, S.-I., and Gegel, H. L.: "Metal Forming, Fundamentals and Applications," ASM Int., 1983, pp. 189–229.
2. Laue, K., and Stenger, H.: "Strangpressen; Verfahren – Maschinen – Werkzeuge," Aluminium-Verlag, Düsseldorf, 1976.
3. Pearson, E. C., and Parkins, R. N.: "The Extrusion of Metals," 2nd ed., Chapman and Hall, London, 1960.
4. Dürrschnabel, W.: "Der Materialfluss beim Strangpressen von NE-Metallen I, II, III" (in German), Metall, Vol. 22, 1968, pp. 426–437, 995–998, 1215–1219.
5. Valberg, H.: "A modified classification system for metal flow adapted to unlubricated hot extrusion of Al and Al-alloys," Proc. 6th Int. Aluminum Extrusion Technology Sem., 1996, Chicago, Vol. 2, pp. 95–100.

6. Lefstad, M., Reiso, O., and Johnsen, V.: “Flow of the billet surface in aluminium extrusion,” Proc. 5th Int. Aluminum Extrusion Technology Sem., Chicago, 1992. Vol. 2, pp. 503–517.
7. Laue, K.: “Möglichkeiten werkstoffgerechter Gestaltung von Leichtmetallprofilen,” Z. f. Metallkunde, Vol. 54, 1963, pp. 667–671.
8. Akeret, R.: “Untersuchungen über das Strangpressen unter besonderer Berücksichtigung der thermischen Vorgänge, Aluminium,” Vol. 44, 1968, pp. 412–415.
9. Pugh, H. L. D., and Watkins, M. T.: “Experimental Investigation of the Extrusions of Metals,” The Inst. of Prod. Engg., Brighton, England, 1960.
10. Johnson, R. W., and Rowe, G. W.: “Redundant work in drawing cylindrical stock,” J. Inst. Metals, 1968, Vol. 96, p. 105.
11. Støren, S.: Private communication NTNU.

REFERENCES

Bauser, M., Sauer, G., and Siegert, K. (Eds.): “Extrusion,” 2nd ed., ASM Int., Metals Park, Ohio, 2006.

Laue, K., and Stenger, H.: “Extrusion,” ASM Int., Metals Park, Ohio, 1976.

Saha, P. K.: “Aluminium Extrusion Technology,” ASM Int., Metals Park, Ohio, 2000.

Sheppard, T.: “Extrusion of Aluminium Alloys,” Kluwer Academic Publishers, 1999.

19 FEA of Extrusion

Extrusion as a metal forming process has previously been dealt with in Sec. 2.2.5 and Ch. 18. In Ch. 12, commonly used experimental grid pattern techniques were described, and it was shown that such techniques are required in order to be able to describe the deformations occurring in forward and backward extrusion. The treatment showed that metal flow and deformational behavior in the extrusion processes are indeed complex.

It will now be shown how simple axisymmetric aluminum extrusion can be modeled by FEA, with respect to both forward and backward extrusion. A comparison of results obtained by means of simulation models with corresponding results from experimental grid pattern analysis confirms that these simulations describe the real metal flow in extrusion with good accuracy. Finally, the FEM models are used to show some differences in deformation characteristics in forward and backward extrusion.

19.1 Forward Extrusion of Aluminum

19.1.1 Forward Extrusion Divided into Subprocesses

A new concept[1] has been proposed to explain the complex metal flow phenomena taking place in the unlubricated forward extrusion process, as applied for hot extrusion of Al and Al alloys. The concept is based on considering the process to be partitioned into four *subprocesses*. Then, by FEA, it is possible to model and to analyze each of the four different subprocesses by individual FEM models, which each describe particularly well the different deformation phenomena encountered in the forward extrusion process. The concept of division into subprocesses is useful for gaining deeper insight into the mechanics of the process. Analysis can also be done individually for each subprocess to optimize the complete unlubricated extrusion process.

The proposed principle of subdivision is shown in Fig. 19.1. The subprocesses, which together make up forward extrusion, are (1) shearing, (2) scratching, (3) radial compression, and (4) extrusion. In the figure, different DEFORM-2D

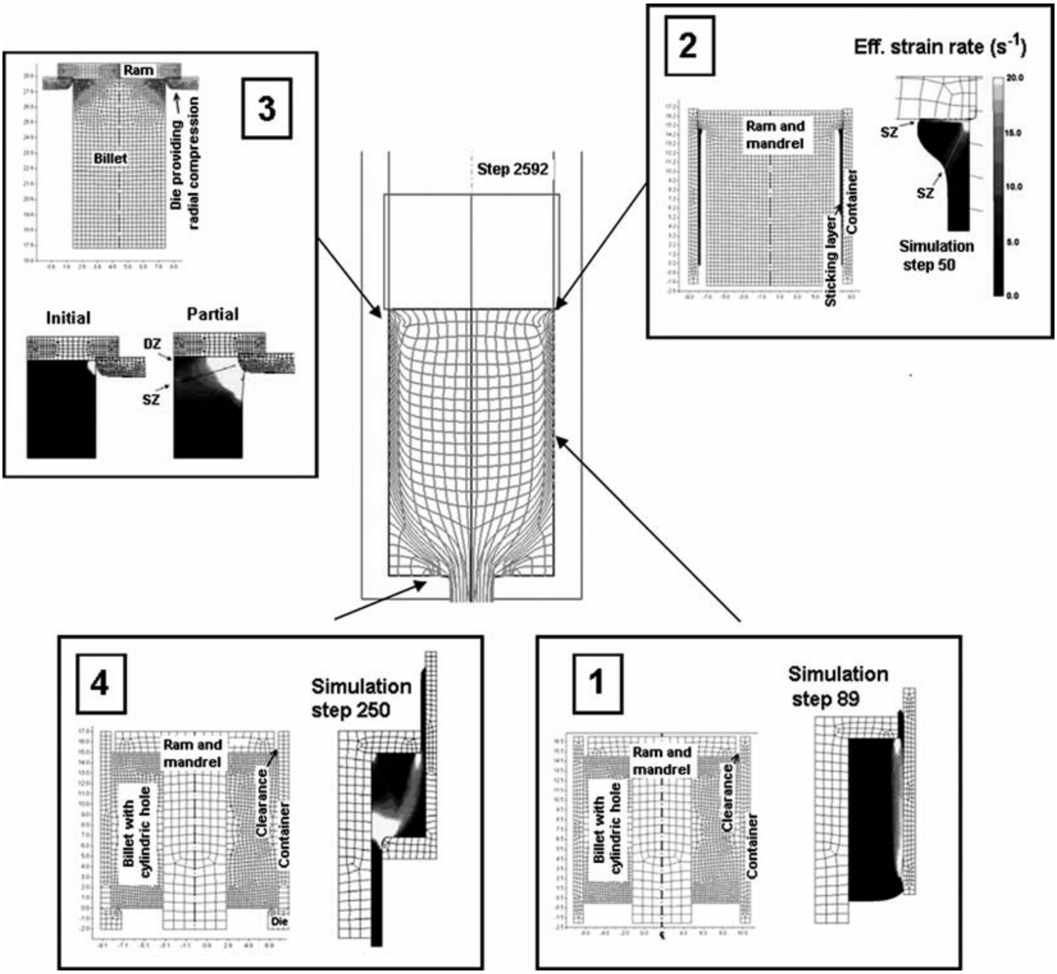

Figure 19.1. Unlubricated forward extrusion divided into four idealized subprocesses.

FEM models that mimic each subprocess are shown in rectangular boxes, with arrows indicating where inside the deforming billet each subprocess takes place.

First there is *shearing*, which takes place in the peripheral layer of the billet during extrusion, adjacent to the container wall. This layer is therefore commonly termed the shear zone and was previously described in connection with Fig. 12.7. The deformation phenomenon here can be considered subprocess 1. In the box 1, in Fig. 19.1, a simple FEM model of this subprocess is shown, where shearing is considered as the only deformation phenomenon present. The idealized shearing process is obtained by use of a hollow cylindrical workpiece, which is pushed forward inside a shell-like container by forward movement of a ram, fitted with a mandrel inside the hollow workpiece. In the simulation, localized shearing in the peripheral layer of the workpiece is then obtained, similar to what takes place in common forward extrusion; see the strain-rate distribution in this simulation model, depicted on the right-hand side in box 1.

Alternatively, shearing can be modeled with concurrent extrusion, as depicted in the box 4 in Fig. 19.1. Then there is also strong localized shear in the peripheral layer of the billet, i.e., in the shear zone, as indicated by high strain rates, visualized by light color in the figure. With extrusion reduction, in addition, the conditions are not altered much from that of the pure shear process, except that the shear zone spreads somewhat deeper into the billet, and a dead zone appears in the corner between the die and the container. The shear zone in front of the die now has a distinctly curved shape, as it extends from the container wall toward the die exit.

Second, there is the *scratching*, or *scraping*, process, considered as subprocess 2. It takes place inside the deforming billet, as the advancing ram head moves down along the container wall. A layer of workpiece material remains at this wall, because of the sticking friction in the boundary layer between the billet and the container wall. A simple FEM model of the process can thus be made as shown in box 2 in Fig. 19.1. Because of the scratching action of the ram head down along the container wall, workpiece material from the sticking layer at the surface of the container wall is scraped off by the advancing ram. This layer is then packed up as a small *lump* in the rear corner of the billet. In this simple model, two intensive shear zones (SZ), or shear bands, are seen to appear inside the lump, as a result of the scratching process.

As the lump builds up in the rear corner of the container, the material initially there is subjected to radial *compression*. Because of the growth of the lump during the course of extrusion, material in the rear end of the billet is forced to flow radially toward the center of the billet. This phenomenon can also be considered as a *pinching* action taking place in the back end of the billet. This process is considered as subprocess 3. The simplest way to mimic it in a FEM model is by use of a special die with approximately the same shape as the lump. This die must be moved inwards at the rear end of the billet, and the billet must remain stationary in the container without being extruded. The simple model of this subprocess is shown in box 3 in Fig. 19.1. During the radial compression, a dead zone is seen to appear in the middle in the rear end of the billet. With further radial inward penetration of the die, imitating the lump, into the billet, the material of the secondary dead zone becomes reactivated and starts to deform again.

Finally, of course, there is *general extrusion* of billet material through the die, considered as subprocess 4. It appears as soon as metal starts to flow through the die hole because of the presence of the extrusion die at the bottom of the container.

To distinguish those four flow phenomena as subprocesses by experimental means is difficult. However, it is easily accomplished using 2D FEM analysis, by means of four simple idealized axisymmetric FEM models. When the models were made, the workpiece material was assumed to consist of the alloy AA 6082. The billet was modeled as rigid–plastic, and the tooling as rigid. To model subprocesses 1 and 4, a clearance was specified between ram and container wall to prevent billet material from accumulating in the back corner between container and ram. In this way, concurrent presence of subprocesses 2 and 3 was avoided. Then, instead, the material at the container wall flowed through the gap between container and ram head.

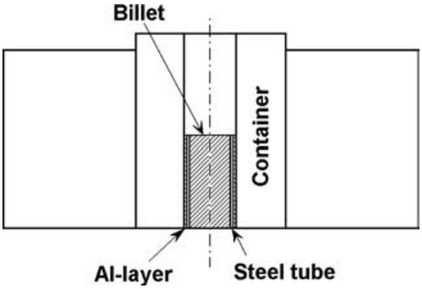

Figure 19.2. Extrusion in steel shell inside the container.

19.1.2 Experimental Study of Metal Flow

Use of experimental grid pattern analysis to map the real deformations taking place in metal forming was explained thoroughly in Ch. 12. There are certain disadvantages connected with the use of scratched grid patterns in the longitudinal section of the workpiece. The new special grid pattern technique applied, based on insertion of contrast material into the workpiece, generally does not have the same drawbacks, and hence yields more accurate results. By insertion of radial and axial contrast pins in the billet, it has been possible to record perfect partially deformed grid patterns for a particular forward laboratory extrusion process; see Fig. 12.4. The pattern consisted of stripes extending in the axial and the radial direction on the midplane of the billet. From the stripes, a complete grid pattern was made for the whole longitudinal section, as shown in Fig. 12.5. Even the pattern inside the final extrusion was obtained in these experiments; see Fig. 12.6(b).

This illustrates the superiority of this method in the precision with which these kinds of grid patterns can be recorded. They are able to reveal the deformations inside the shear zone also, even when large reduction ratios (40 or more), are used. Such experimental grid patterns have been obtained for the alloys AA 6063 and AA 6082. The metal flow was found to be similar for the two alloys; hence, Fig. 12.4 depicts the true metal flow of both alloys. The initial grid pattern is shown in the drawing in Fig. 12.3, and the deformed patterns in Fig. 12.4 represent the frozen version of the grid at each stage of extrusion. A good FEM simulation model of extrusion would then be a model that could mimic this metal flow, i.e., which could reproduce these patterns at the stages at which they were recorded.

To obtain such perfect grid patterns, an experimental problem had to be solved first. Partially extruded billets are commonly removed from the container by pushing them forward in the direction of extrusion, after removal of the die. But during this removal operation the billet residue in the container will tend to deform plastically, because the billet metal sticks to the container wall. To overcome these problems, a special experimental procedure was developed, which allowed removal of the metal residue from the container without post-extrusion deformation.

A steel shell, in the form of a tube of die steel, was inserted into the container of a laboratory extrusion press (see Fig. 19.2) in a special operation, so that a layer of soft Al was obtained in the narrow clearance between the container and the tube. The inner steel tube was then used as the *liner*. After extrusion, the steel shell, with

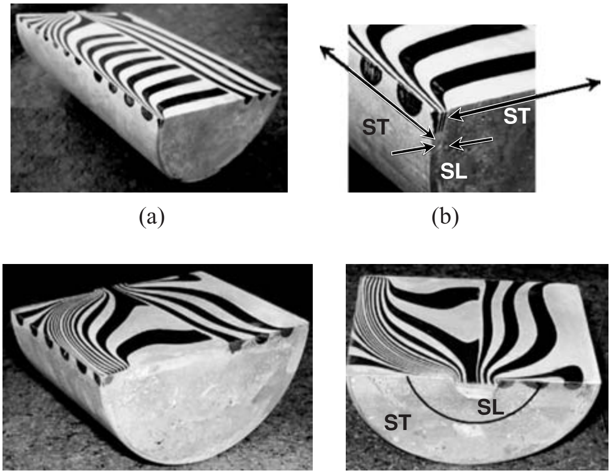

(a) (b)

(c) (d)

Figure 19.3. Appearance of marker pins in the partially extruded material: (a) view from rear corner at early extrusion stage; (b) magnification of (a). Billet residue at late stage of extrusion viewed from (c) back end and (d) front end.

the partially extruded billet inside, was pushed out of the container, with the billet residue inside the tube. The shell was then immersed in liquid nitrogen, and because of the larger thermal contraction of Al than Fe, the billet residue then came loose from the shell without damage.

19.1.3 Boundary Conditions at the Billet–Tooling Interface

In addition to providing information regarding metal flow inside the billet, our experiments[2,3] also yielded information about contact conditions at the interface between billet and tooling, i.e., the tribological conditions along the container wall during the course of extrusion; see Fig. 19.3. The circular ends of the radial contrast pins extending into the peripheral surface of the billet, and the corresponding axial pins in the front and the rear faces of the billet, when compared at initial and final stages of compression, revealed the following: The appearance of the contrast pins along the peripheral cylinder face of the billet did not change at all during extrusion; hence, there must have been sticking friction (ST) between the billet and the container wall over the cylinder face. One exception, however, was that the number of pins in this surface had been reduced, because the billet residue – of course – had become shorter than the initial billet. The pins that initially extended into the rear of this surface had been displaced, so that after partial extrusion they appeared on the rear face of the billet, i.e., they had now established contact with the ram head. This observation shows that there must have been a small zone near the periphery of the ram head that had undergone sliding contact (SL) during extrusion.

Hence, the behavior close the rear edge of the billet, as mentioned before (see Fig. 19.1, box 2), is one where the peripheral surface layer of the billet, which initially adheres to the container wall, is scratched off by the advancing ram and is forced to accumulate as a lump of metal near this edge. When this happens, the initially

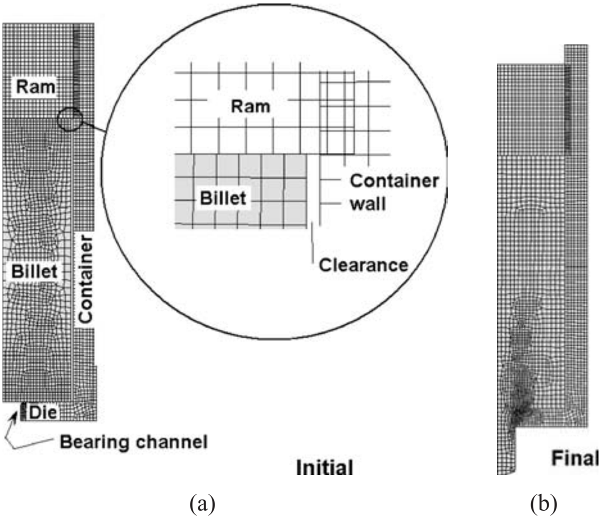

Figure 19.4. FEM model of the upsetting stage of extrusion.

radial pins are forced to flow radially inwards a short distance, along the surface of the ram head.

19.1.4 FEM Model to Reproduce a Particular Extrusion Experiment

To study what controls the metal flow in direct extrusion, a DEFORM-2D FEM model was built.[4] The model was made most possible similar to the axisymmetric extrusion experiment, mentioned in the preceding subsection. The aim was to use the FEM model to compute metal flow, to check whether the simulation would predict the flow as in reality, i.e., as in the perfect grid pattern experiments.

Figures 19.4 and 19.5 show this FEM model of the extrusion process. The die and the container were modeled simplified as one single tool. The billet geometry was the same in experiment and model and so was the inner geometry of the tooling. The container wall was made thinner in the model than in the experiment. The die was modeled with a *parallel bearing*, different from the experimental die, which had no bearing. The bearing is the outlet channel in the die. To reduce the simulation time, the die opening was made larger, with diameter 20 mm, in the model, instead of 12 mm, which was used in the experiment. Hence, whereas the reduction ratio was 39.1 in the experiment, it was 14.1 in the simulation. The applied billet had 150 mm length and 73 mm diameter. The diameter of the shell, which was used as extrusion container, was 75 mm. These dimensions were the same in the simulation model and in the experiment.

The billet was set to be rigid–plastic, and the tooling to be rigid. A nonisothermal model was used, which included thermal exchange between workpiece and tooling. Appropriate thermal data were specified for the die and the workpiece material, and so also were data characterizing the heat transfer between workpiece and die. The initial billet temperature was 480°C, and the container temperature was set

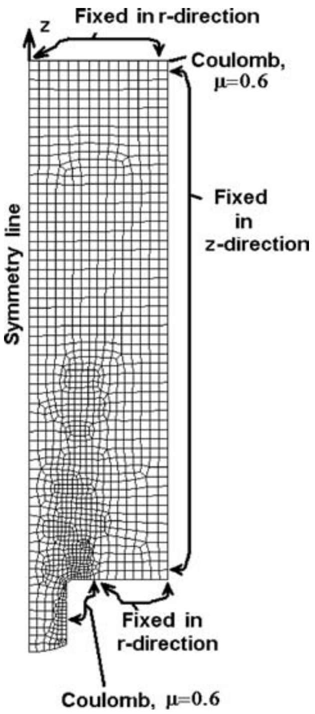

Figure 19.5. FEM model for the extrusion stage.

equal to 450°C in the FEM model, as it was in the experiment. The ram speed was the same in both model and experiment: 5 mm s^{-1}.

A short simulation was first run to reproduce the upsetting phase of the extrusion process, see Fig. 19.4. During upsetting, the boundary conditions at the interface between the billet and the tooling were modeled as Tresca friction with $m = 1$ and no restriction regarding movement of workpiece material along tool interfaces. The short simulation was terminated when contact had been established between the surface nodes of the billet and the tooling.

The end stage of the upsetting simulation was then used as input to create a new simulation, representing the extrusion process itself; see Fig. 19.5. The friction along the boundary interface between the billet and the tooling was now specified as complete sticking friction, i.e., the surface nodes of the billet were fixed against the surface of the tooling, so no sliding occurred for these nodes against the tooling. An exception, however, was made for the corner node of the workpiece in contact with the ram and the container. The same exception was made for the nodes of the workpiece in the outlet portion of the die. These nodes were allowed to slide against the die; see Fig. 19.5. The other nodes of the die, i.e., those close to the corner between die and container wall, however, were specified to be fixed against the die, i.e., they were not allowed to move in either the axial or the radial direction. Hence, the boundary conditions in the model corresponded well to those mapped in the grid pattern experiments.

In a first trial, flow stress data were used as input into the model, in terms of a Zener–Hollomon relation (see eq. 8-10), as obtained from compression testing of the alloy AA 6082 in a Gleeble test machine. The tests were run at different temperatures in the range 400–500°C, for constant strain rates of 0.1, 1.0, and 10 s^{-1} in each test, compressing small cylinders up to the total average strain of 1. The load–stroke curve was recorded in the tests, and true stress–strain curves were derived from them, correcting the data for the effect of friction in the compression test. The flow stress of the AA 6082 alloy was then described by a Zener–Hollomon fit on basis of this experimental data (see Example 8.5):

$$\sigma = \frac{1}{0.0102}\sinh^{-1}\left[\left(\frac{\dot{\varepsilon}\exp\left(\frac{152176.632}{8.314T}\right)}{9.90\times 10^{12}}\right)^{\frac{1}{7.643}}\right] \tag{19-1}$$

After the model had been created, a number of simulations were run to study the effect of various extrusion parameters on the metal flow, using these flow stress data. The input parameters (friction, thermal conditions of billet and container, etc.) were varied within a realistic range, but all simulations yielded more or less the same flow. Hence, the metal flow seemed not to depend significantly on any of these traditional extrusion parameters. The simulation result also deviated from the experiment, especially with regard to the appearance of the shear zone, which was less localized in the simulations than in the experiment.

In a final trial, flow stress data on the workpiece material were changed, because the shear deformations in the shear zone did not localize as much in simulation as in the experiments. Simulation predicted an effective strain rate close to 1 s^{-1} in this shear zone, so the flow stress was decreased for this particular strain rate, while the flow stress for other strain rates was kept unchanged. Now the metal flow was altered significantly, and became much more similar to the experimental flow. Good correspondence was obtained this way when the flow stress was reduced by 20% in the shear zone below the data from the compression test.

Metal flow very close to the experimental flow was then finally obtained, as shown in Fig. 19.6. This was for the same discard lengths as in the experiments; see Fig. 12.4. The conclusion is that there is good overall correspondence between simulated and experimental metal flow, with the exception of the first two stages of extrusion, where there is less forward flow in the core of the billet in simulation than in the experiment.

19.1.5 Simulation Results from the FEM Model of Forward Extrusion

The distribution of the effective strain rate (s^{-1}) inside the billet at a particular stage of extrusion was now determined by the simulation model; see Fig. 12.4 and Fig. 19.7. As this figure depicts, two zones of different deformation characteristics become visible in the interior of the billet. These zones are not readily revealed by the deformed grid pattern itself. In addition to the dead zones in the corner between the die and the container and adjacent to the ram, there is also a tertiary dead zone in the core of the billet. Moreover, in between this dead zone and the secondary dead zone in the billet adjacent to the ram, there is an arrow-shaped secondary

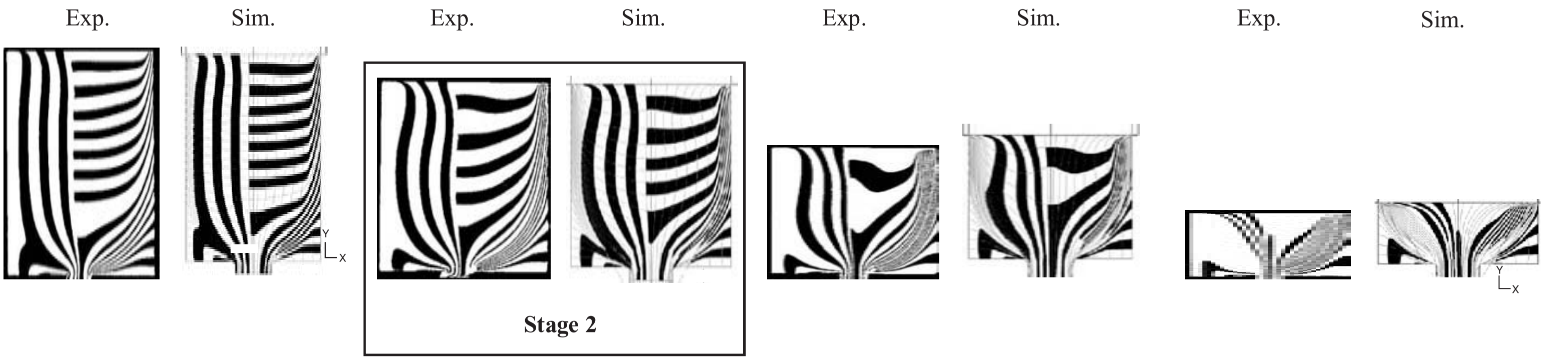

Figure 19.6. Good agreement between the experimental and the FEM-simulated grid pattern.

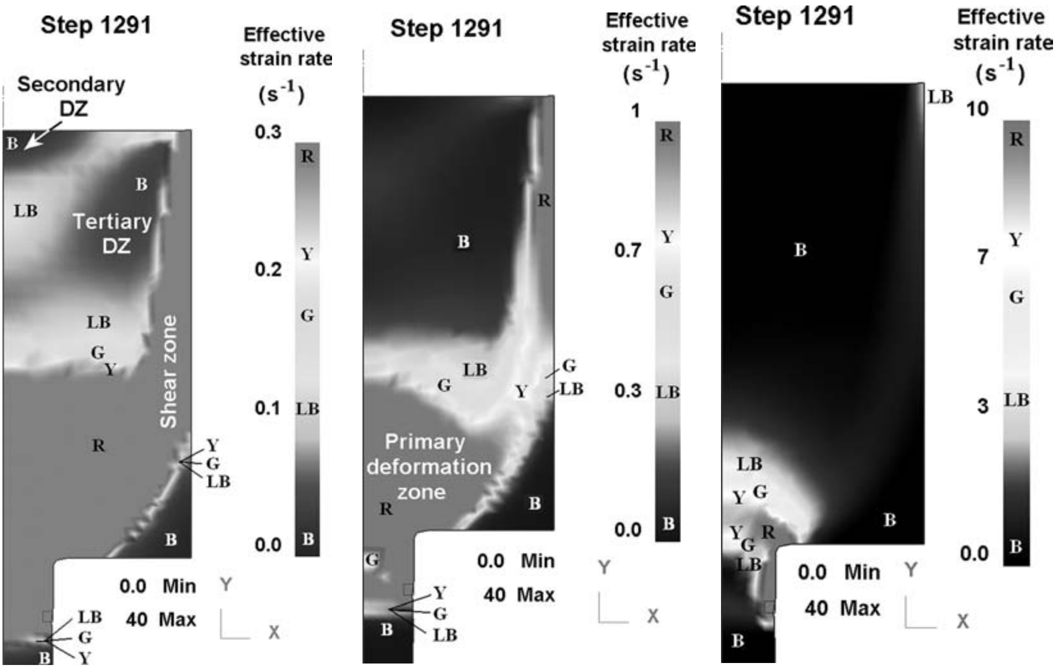

(a) (b) (c)

Figure 19.7. Distribution of the effective strain rate inside the longitudinal section of the partially extruded billet (at stage 2) depicts the presence of an additional shear zone. (a), (b), and (c) are on different strain-rate scales.

shear zone. Effective strain rates subjected to the various parts of the deforming billet, as predicted by DEFORM, are as follows:

Dead zones	$\dot{\bar{\varepsilon}} < 0.05$
Arrow-shaped secondary shear zone	$\dot{\bar{\varepsilon}} \approx 0.1\text{–}0.15$
Primary shear zone	$\dot{\bar{\varepsilon}} \approx 1$
Primary deformation zone	$\dot{\bar{\varepsilon}} \approx 8\text{–}10$
Strain-rate peak over sharp edge of die ($r = 2$ mm)	$\dot{\bar{\varepsilon}} \approx 30$

The deformation, in terms of the effective strain distribution inside the partial extruded billet, was also computed by the simulation model; see Fig. 19.8. This figure reveals that the deformation at stage 2 of the extrusion process, quantified as effective strain, is rather small in the core of the billet ($\bar{\varepsilon} < 1.2$) and considerably larger in the surface layer of the billet ($\bar{\varepsilon} \approx 2$), where the shear zone is present. From there down into the primary deformation zone, the deformation increases. The actual cross section of the extrudate emerging from the die orifice, at this stage of the process, is predicted by the model to have acquired deformations, in terms of effective strain, as high as $\bar{\varepsilon} \approx 3.5$ in the core and $\approx$4.5 in the outer surface layer.

We may conclude, at this point, that by simulation it has been possible to reproduce with good accuracy the evolution of the internal grid pattern, as in the experimental investigation. Thus the actual velocity field inside the billet during extrusion

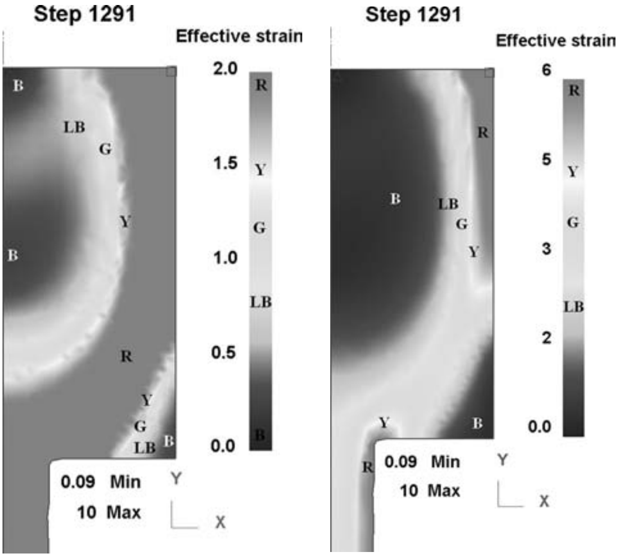

Figure 19.8. Effective strain distribution inside the billet and the rod, on two scales.

must also have been reproduced accurately. The computed strain and strain-rate distributions can therefore be considered reliable to the extent that the FEM program is able to calculate such large strains exactly. To arrive at these results, it has been necessary to reduce the flow stress data in the shear zone by 20%, in relation to the primary data obtained directly from the compression test. This seems to indicate that the flow criterion used in the software should be altered to give lower flow stress in the case of shear deformations than does the currently used criterion.

An overall concluding remark is that the FEA has proved to be useful for the investigation of the nature of the metal flow in forward hot Al extrusion. The study has led to new insight regarding what conditions control the material flow.

19.2 Backward Extrusion of Aluminum

19.2.1 Experimental Study of Metal Flow

A backward extrusion experiment was run in a laboratory extrusion press fitted with a container with 100 mm diameter. A flat-faced die with hole diameter 15.8 mm was used in the experiment. The billet, which consisted of the Al alloy AA 6082, had 95 mm diameter and 250 mm length, and the ram speed was 2 mm s^{-1}. The initial temperatures of the billet and the container were 505°C and 437°C, respectively. The length of the discard at the end of extrusion was 19 mm. The initial grid pattern that was used for the characterization of the metal flow in this case is shown in Fig. 12.6(a). The final deformed grid pattern obtained after removal of the discard is shown on the left-hand side in Fig. 19.10. The emptying diagram made on basis of this experiment has already been presented in Fig. 12.10(c) and (d).

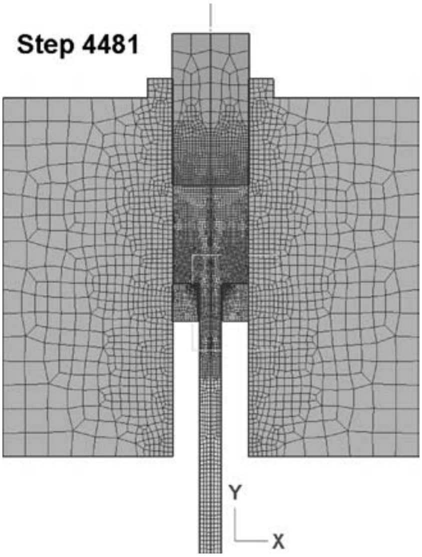

Figure 19.9. FEM simulation model of the indirect extrusion process.

19.2.2 FEM Model

The FEM model imitating the backward extrusion experiment is shown in Fig. 19.9.[5] The die and the container were assumed to be rigid bodies with the same size as in the experiments, with the exception that the diameter of the die hole was increased in the simulation model to 28 mm, to ease simulation. In the experiment, this diameter was 15.8 mm. The radius of curvature from the flat face of the die into the bearing was also increased to 2 mm, though in the experiment it was much smaller. The billet was modeled as rigid–plastic with flow stress given by eq. 19-1.

The nonisothermal FEM model included generation and flow of heat within the die–workpiece system. The process was modeled in two separate simulations, with the upsetting stage as one model, as described in the preceding subsection for forward extrusion. In the first model, the billet was upset until the initial clearance between billet and container had disappeared. The friction in the first model was chosen to be Tresca shear friction with $m = 1$. When the billet had expanded and contact had been established between all surface nodes of the billet and the container wall, the first simulation was stopped.

The last upset step was then used to create the final extrusion simulation. Full sticking was now specified between billet material and tooling, i.e., no movement of the surface nodes of the billet occurred along the container and the die wall. However, exceptions were made for the die face close to the die hole and in the bearing channel, where there was specified Tresca friction with $m = 1$. This model was run to the same stage of extrusion as in the experiment, leaving a metal residue of the same size. Actually, the simulation was run even further, until all the material of the billet had been squeezed out of the die as a rod.

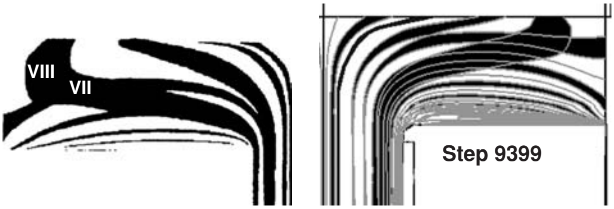

(a) (b)

Figure 19.10. Deformed grid pattern in (a) experiment and (b) simulation.

19.2.3 Simulation Results

When the FEM model of indirect extrusion had been realized, a grid pattern analysis corresponding to the experimental analysis mentioned in Sec. 12.9.1 was performed. When this was done, good agreement was obtained between the final deformed pattern inside the discard in the simulation and in the experiment; see Fig. 19.10. In this figure, the grid pattern of the sectioned metal residue from the experiment is shown on the left-hand side and the corresponding simulation on the right-hand side. The most obvious difference is that deformations in the rear end of the discard are slightly larger in simulation than in experiment. This is seen from the appearance of the vertical contrast stripe closest to the container wall, denoted VII–VIII in Fig. 19.10. In the layer of the discard adjacent to the die, conditions are opposite, i.e., deformations are larger in experiment than in simulation. Taking into account that errors in the simulated metal flow accumulate throughout the extrusion process, the conclusion is, however, that the FEM model mimics the experiment well.

With good correspondence obtained between the evolution of the deformed grid pattern in the experiment and in the simulation, the predicted velocity field inside the billet in the simulation must be close to the experimental field. Simulation predicts the deformation in the shear zones adjacent to the die to be slightly smaller than in reality. A reason for this may be gradual development of anisotropy in the workpiece material during extrusion, so that shear zones soften in comparison with the material model used in the FEM analysis. Alternatively, the difference could be due to use of an inaccurate flow criterion in the simulation code.

To include anisotropy in the model, in order to arrive at more accurate simulation results, might be difficult. A difference between experiment and simulation was also that the die hole was made bigger in the simulation than in the experiment. This difference may account for some of the observed difference in metal flow. The smaller reduction was used in the model to keep the computing time down. With future development of more efficient computers and FEM codes, expectations are that the FEM model can be improved to agree fully with the experiment.

Having yielded good agreement between simulated and experimental metal flow, the simulation model can now provide a lot of results regarding conditions of deformation in the backward extrusion process. The model can for instance be used to create a computer-made emptying diagram for the process, i.e., a pattern

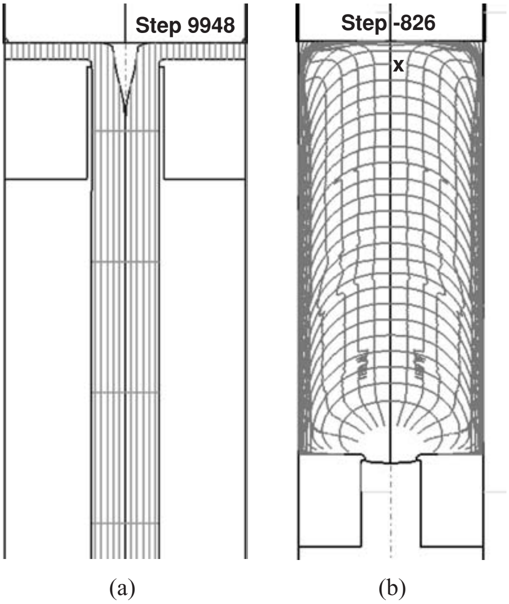

Figure 19.11. Imaginary grid pattern inside the rod (a) at end of extrusion, (b) when traced back to the end of the upsetting stage to create the emptying diagram.

corresponding to those shown in Fig. 12.10, which previously were made manually with much labor. Because the simulation was run further than the experiment [see Fig. 19.11(a)], the emptying diagram can also be obtained for the end phase of extrusion, when the last material residue is squeezed completely out of the die.

To create the emptying diagram in simulation, the longitudinal section of the extruded rod was fitted with a pattern of straight T and L lines; see Fig. 19.11(a). This pattern was then traced backwards to the previous stages of extrusion. Figure 19.11(b) shows this pattern at the end stage of upsetting. (Remember that the use of this methodology was explained in Sec. 12.6.) The computed pattern obtained is similar to the corresponding diagram made manually on the basis of the experiment; see Fig. 12.10(d). A new feature, however, is observed in the new emptying diagram created by the computer. Because the extrusion was run to the end, the emptying diagram extends to the very rear of the upset billet. The emptying diagram depicts that in the rear end of the billet the L-lines of the pattern spread out laterally in a fanlike manner. Hence, the mainly steady-state nature of the process no longer prevails during late extrusion, when the material in the discard is pressed out of the die.

Additional information regarding the flow field ahead of the die can be deduced from the FEM model. The emptying T-line labeled x in Fig. 19.11(b) is the boundary line between material inside the upset billet, which experiences steady-state flow, and material behind, which does not. From the emptying diagram one can see that it is mainly initial material close the rear end of the billet. This material accumulates in the butt toward the end of extrusion, and it also includes a thin layer that extends down along the billet surface to the die. This thin layer is not clearly visible in Fig. 19.11(b), because of the high line density of the obtained pattern.

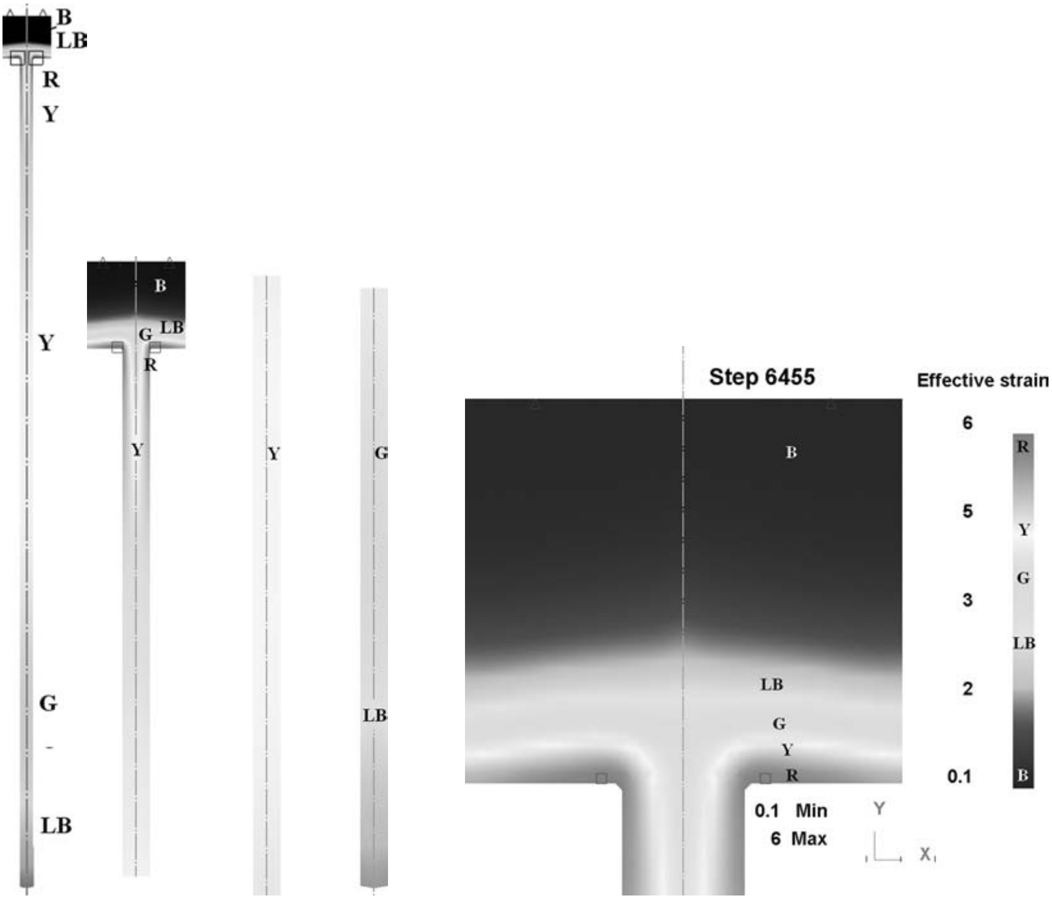

Figure 19.12. Deformation in indirect extrusion in terms of effective strain values predicted by the simulation model.

Another result that can be obtained from the simulation model and is not readily obtained by other means is the deformation inside the partially extruded billet and the rod, at a particular stage of extrusion. The deformation distribution, in terms of the effective strain, is shown in Fig. 19.12. This figure shows that the largest effective strains in the billet are in the layer adjacent to the die. Inside the extruded rod, the outer surface layer is strained much more than is the core, except in the front end of the rod. Also, the effective strain in the surface layer of the rod is predicted to increase along the length of the rod. Another prediction is that the front end of the rod remains rather undeformed, as was also shown to be the case in forward extrusion.

By use of the point-tracking option in DEFORM, Fig. 19.13 was made. A row of points, Pt.8–Pt.22, were added across the rod diameter, behind the die hole, at an arbitrary late stage of extrusion, and another row, P1–P7, across the heavily strained layer adjacent to the die. The simulation program then was used to trace these points back to earlier stages of extrusion, up to the end of the upsetting stage.

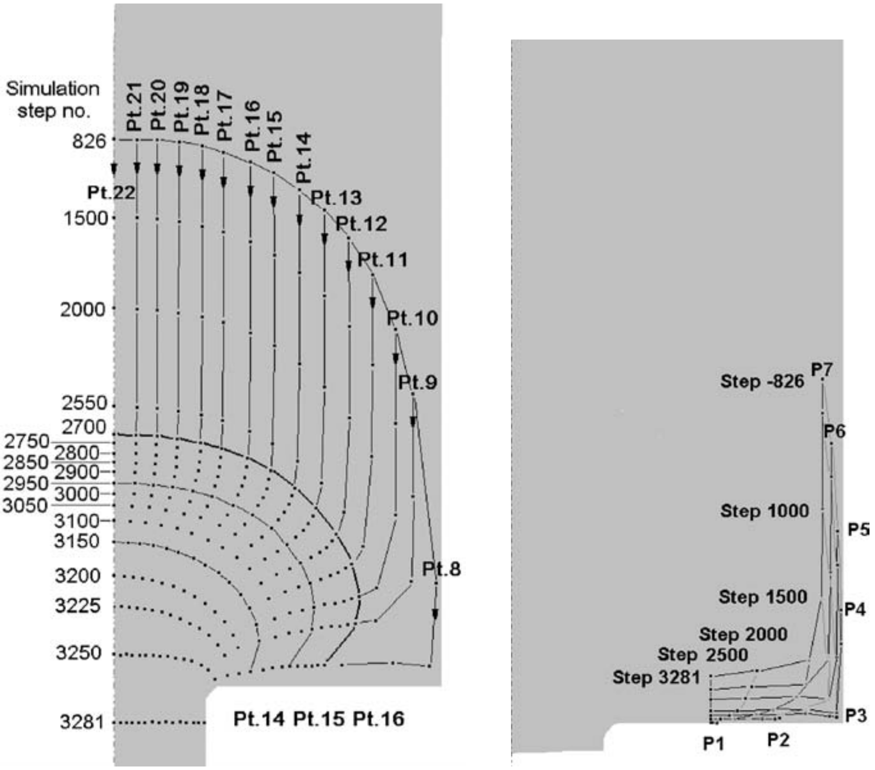

Figure 19.13. FEM-predicted particle paths for material points during flow toward the die and the die exit.

The predicted locations of these points at various stages of extrusion are shown in Fig. 19.13. It is now readily seen that the material point Pt.8, close the surface of the rod, originated from a location close the front end (in the surface layer) of the billet. This point, in relation to a fixed point on the die, first moves toward the die. Then, when it has approached sufficiently close to the die, it starts to move radially inward toward the center of the billet, and slightly backwards away from the die. On approaching sufficiently close to the billet center, it again shifts direction of movement as it enters the main metal stream directed toward the die-hole. From then on, it flows more or less directly toward the die exit and out of the die hole at a high velocity.

Figure 19.14 depicts the strain-rate distribution inside the billet volume as predicted by the simulation model. Note the different scaling of the strain rates in the two pictures in the figure. In Fig. 19.14(a), the scale was selected to depict the presence of a ring-shaped zone of stagnant metal in the corner between the die and the container wall and the presence of the intense shear bands formed between this stagnant zone and the tooling.

We conclude that FEA can be applied successfully to reproduce the hot-extrusion experiments performed with the AA 6082 alloy. With sticking friction

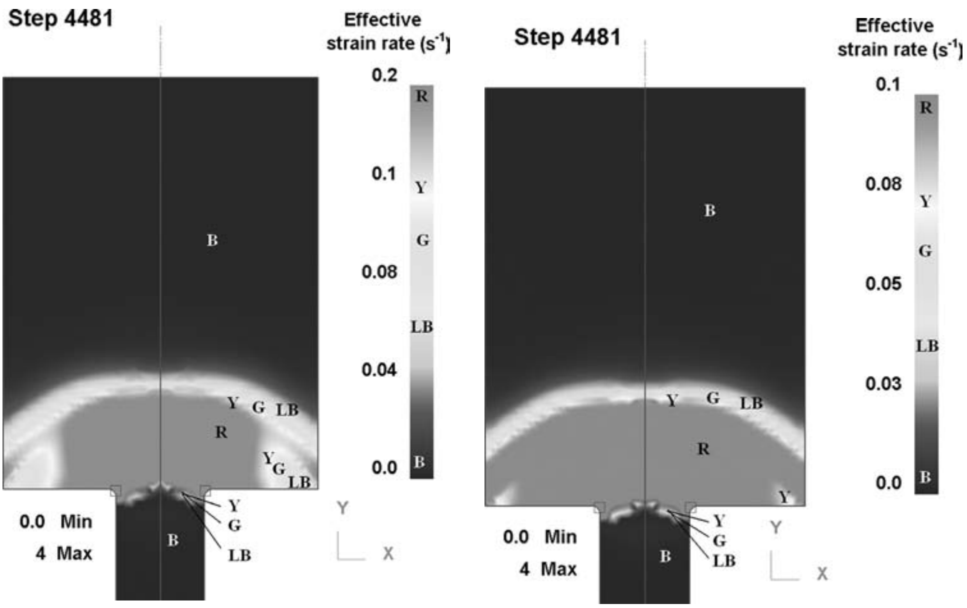

(a) (b)

Figure 19.14. Effective strain-rate distributions inside the billet as predicted by the FEM model.

between billet and tooling, metal flow and deformations similar to those in the experiment were obtained in the simulation. The FEM model predicts the deformations in backward extrusion to be very different from those in forward extrusion. Whereas in forward extrusion, there is dead zone formation ahead of the die as billet material is stowed into the corner between the die and the container, conditions are completely different in backward extrusion.

In backward extrusion, the material initially in the corner between the die and the container is subjected to very large deformation throughout the course of extrusion. Some of this material remains in front of the die throughout the whole extrusion stroke and becomes more and more heavily deformed as extrusion continues. In addition, some of this material flows out of the die, where it appears as the heavily deformed outer surface layer of the rod.

Problem

19.1 Use the available simulation model of the direct extrusion process described in this chapter to obtain the following postprocessing data:

(a) The emptying diagram of the process.

(b) A particle-path diagram for direct extrusion corresponding to the one shown in Fig. 19.13 for indirect extrusion.

NOTES

1. Valberg, H., and Sandbakk, Ø.: "Direct non-lubricated Al-extrusion partitioned into the sub-processes shearing, scratching, radial compression and extrusion," Proc. 6th Int. Conf. on Material Forming, Salerno, Italy, 2003, pp. 307–310.
2. Valberg, H., and Uyyuru, R. K.: "New accurate experimental techniques to quantify metal flow inside workpiece – and along boundary interface of workpiece – in metal forming," Proc. 2nd Int. Conf. on Tribology in Manufacturing Processes, Nyborg, Denmark, 2004, Vol. 2, pp. 453–474.
3. Valberg, H.: "Experimental techniques to characterize large plastic deformations in unlubricated hot aluminium extrusion," Key Engineering Materials, Vol. 367, 2008, pp. 17–24.
4. Valberg, H., and Pohl, C.: "Boundary conditions and metal flow in forward extrusion of aluminium alloys," Conf. Proc. Euromech 435, Valencienne, 2002, pp. 33–45.
5. Valberg, H., and Misiolek, W. Z.: "Plastic deformations in indirect hot extrusion of an aluminium alloy characterised by FEM-analysis with experiment," Proc. 9th Esaform Conf., Glasgow, 2006, pp. 487–490.

REFERENCE

Valberg, H.: "Experimental techniques to characterize large plastic deformations in unlubricated hot aluminium extrusion," Key Engineering Materials, Vol. 367, 2008, pp. 17–24.

20 Rolling

Rolling is the metal forming process by which the largest amount of metal is being worked in the world. In terms of tonnage of metal, this process must therefore be considered the most important one. In Sec. 2.2.4, some important aspects of this forming process were discussed. In this chapter, some additional practical topics important in industrial rolling will be considered. The treatment will be limited to flat rolling; section rolling is outside the scope of this book.

The velocity conditions of the workpiece along the roll surface, through the roll gap, will first be considered. It will be shown that the velocity conditions here depend on whether there is sliding friction or sticking friction between the rolls and the workpiece. In industrial rolling, it is important to be able to estimate the loads acting on the rolls from the workpiece, i.e., to determine the required rolling force. Because of this, a large number of rolling force formulas have been developed over the time. One such simple formula will be considered in this chapter. Afterwards, it will be shown how the strain and strain-rate conditions vary throughout the roll gap, if one assumes homogeneous deformation in the workpiece material during rolling. In that case, a rectangular slab element of material that enters the roll gap should maintain its rectangular shape during passage through the gap. Finally, it will be shown how an approximate estimation of the contact pressure over the roll surface can be deduced by means of the slab method. This expression is valid when there is homogeneous deformation in the roll pass.

20.1 Velocities in the Roll Gap in Flat Rolling

The *contact conditions* along the boundary interface between the roll and the workpiece material can, in principle, be characterized either by sticking friction or by sliding friction. The *velocity conditions* for the material particles on the surface of the workpiece inside the roll gap will be significantly different in the two cases of friction.

Consider a material particle on the workpiece surface, which moves in the direction toward the roll gap with the velocity v_0. If there is sticking friction between the roll and the workpiece material, this particle will immediately, when it establishes

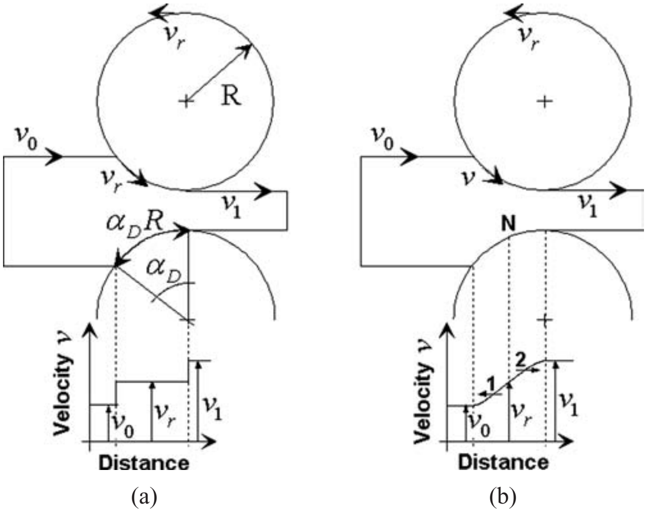

Figure 20.1. Velocity conditions for material particle on the surface of the workpiece upon passage through the roll gap in case of (a) sticking friction and (b) sliding friction.

contact with the roll surface, attain an increased speed equal to the surface speed of the roll, i.e., v_R; see Fig. 20.1(a). At the exit side of the roll gap, in this case, the rolled product must, however, have higher velocity, v_1, than the surface velocity of the roll. The entrance and exit velocities of the workpiece and the rolled product, respectively, then must conform to the conditions

$$v_0 < v_R < v_1 \tag{20-1}$$

This means that a material particle on the surface of the workpiece, which enters into the roll gap at low speed, will be accelerated up to a velocity equal to the surface speed of the roll when it comes in contact with the roll. This speed will also be maintained while the particle passes throughout the roll gap, but when it reaches the exit of the roll gap, it will be accelerated up to an even higher speed, the same speed as that of the rolled product; see Fig. 20.1(a). Hence, the velocity conditions of the workpiece material, in terms of the velocities through the roll gap, will be determined by the surface velocity of the roll and the degree of reduction in the rolling pass. These velocities can be determined by means of the principle of constancy of volume i.e., the volume flowing into the gap during a time increment dt must equal the volume flowing out during the same time:

$$V_0 = v_0\,\mathrm{d}t\,A_0 = v_1\,\mathrm{d}t\,A_1 = V_1 \quad\Rightarrow\quad v_1 = v_0\frac{A_0}{A_1} = v_0\frac{1}{1-r} \tag{20-2}$$

See eq. 5-5 for the definition of the reduction of area in rolling, r.

In the case of sliding friction between roll and workpiece, the velocity conditions at the inlet and outlet side of the roll gap will be the same as if there were sticking friction, but conditions along the boundary interface between the roll and the workpiece will be different. Instead of a steep increase in the velocity of material particles at the entrance into the gap and constant velocity through the gap, there will be a gradual increase in the velocity from the entrance to the outlet of the roll gap, where there is maximum velocity; see the graph in Fig. 20.1(b). The exit velocity from the gap in the case of sliding friction is also described by eq. 20-2. But now there is a position somewhere along the roll and the workpiece interface where the roll speed equals the speed of the material in the roll gap. This position is commonly termed the *neutral point*; it is point N in Fig. 20.1(b). Because the roll gap extends in the direction into the plane of the paper, i.e., it has three-dimensional character; there is in reality a *neutral line* inside the roll gap, which extends across the width of the workpiece. Along this line there are neutral conditions, so that material particles that cross this line possess for an instant the same speed as the roll. Hence, at this instant, there is no sliding against the roll. On each side of the neutral line, however, there is sliding between the material particles on the surface of the workpiece and the surface of the roll. This sliding movement is generally called *slip*.

As indicated in Fig. 20.1(b), in the region between the inlet and the neutral point in the roll gap, the roll surface moves faster than the workpiece surface, so the workpiece material slides backwards in relation to the surface of the roll. Because the material here has lower speed than the surface of the roll, there is *positive slip* on this part of the roll. Frictional shear stresses act in the direction against the sliding movement, so that the friction stresses on the workpiece here must be directed from the inlet toward the neutral point. These shear stresses contribute to pulling the workpiece into the gap. However, in the region between the neutral point and the outlet from the gap, the sliding movement must be directed the opposite way [see Fig. 20.1(b)], and so is the shear stress transferred from the roll to the workpiece. The workpiece material must move faster than the roll surface here, so there is *negative slip*, and the friction stress over this part of the roll opposes the forward movement of the workpiece out of the roll gap.

In Fig. 20.1(b) the backward-sliding movement against the roll at the front side of the roll – i.e., the backward, or positive, slip – has been indicated by an arrow labeled 1, and the corresponding forward or negative slip at the other side of the roll has been indicated by an arrow labeled 2.

20.2 Simple Rolling Load Formula

It is of great importance in industry to be able to predict the *required roll force* in a rolling operation with acceptable accuracy. In the technical literature, a large number of *roll force equations* have therefore been proposed. By means of these equations, it is possible to arrive at an estimate of the required rolling load in flat rolling. A simple equation showing the main effects of important rolling parameters on rolling load will be developed in the forthcoming treatment.

The method used to derive this formula is to consider flat rolling as analogous to plane strain compression; see the schematic sketch in Fig. 20.2. Previously, in

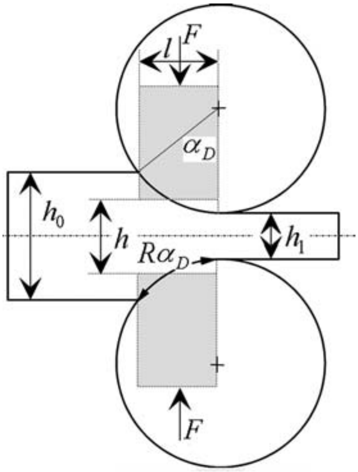

Figure 20.2. Rolling considered as equivalent to plane strain compression to deduce a rolling load formula.

Sec. 13.2.1.1, the following expression was deduced for the compression force in plane strain compression of a specimen with height h and half width l:

$$F = \frac{2\bar{\sigma}}{\sqrt{3}}\left(1 + \frac{ml}{4h}\right) l$$

The formula was developed assuming Tresca friction characterized by a friction factor m, and for a workpiece material of constant flow stress $\bar{\sigma}$. The formula calculates the required compression force for a specimen of one unit breadth, extending into the plane of the paper. For a specimen of breadth B, the corresponding force is

$$F = \frac{2\bar{\sigma}}{\sqrt{3}}\left(1 + \frac{ml}{4h}\right) lB \tag{20-3}$$

In Fig. 20.2, a rolling process is sketched, and a corresponding equivalent compression process is added on top of the sketch, with hatched compression dies. As the figure illustrates, the slab must be compressed down to a thickness equal to half of the final thickness in the rolling process, i.e., to a thickness equal to

$$h = \frac{1}{2}(h_0 + h_1) \tag{20-4}$$

One-half of the workpiece inside the roll gap will then be compressed too much, while the other half is compressed too little. Thus one can assume rolling to be equivalent to plane strain compression down to half the thickness reduction used in the rolling process.

Based upon this analogy, the rolling load in flat rolling, under plane strain conditions, can be expressed by the following formula:

$$F = \frac{2\bar{\sigma}}{\sqrt{3}}\left(1 + \frac{ml}{2(h_0 + h_1)}\right) lB \tag{20-5}$$

In the literature it is sometimes recommended that the *projected length of the arc of roll contact* in this formula, i.e., l, should be replaced by the real length of this arc, i.e., $\alpha_D R$; see Fig. 20.2. This increases the calculated rolling load somewhat, as

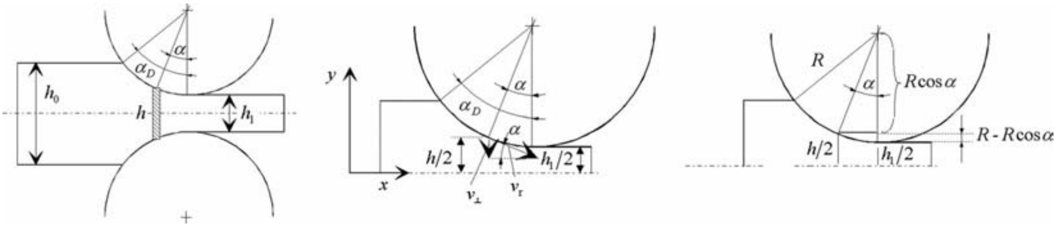

(a) (b) (c)

Figure 20.3. Disc element inside the roll gap, being compressed in homogeneous deformation.

expressed by the following modified rolling load formula:

$$F = \frac{2\bar{\sigma}}{\sqrt{3}}\left(1 + \frac{m\alpha_D R}{2\,(h_0 + h_1)}\right)\alpha_D R B \tag{20-6}$$

As these equations imply, it is generally required that one know the flow stress of the workpiece material, $\bar{\sigma}$, in order to predict the rolling load. In cold rolling, this flow stress, as explained in Ch. 8, mainly depends on the strain imposed on the workpiece material, whereas in hot forming, it mainly depends on the strain rate and the temperature of the workpiece material in the roll gap.

20.3 Strain and Strain Rate in Rolling

If one assumes homogeneous deformations and plane strain conditions in rolling, then the strain and strain rate in the roll gap can easily be determined for flat rolling. Plane strain requires that there be zero breadth increase of the workpiece in the roll gap, an assumption that is often acceptable in plate and sheet rolling processes.

The *through thickness strain* in the workpiece in the roll gap, i.e., the strain in the y-direction [see Fig. 20.3(b)], can be easily calculated by its redefined value using eq. 5-11:

$$\dot{\varepsilon}_y = \ln \frac{h_0}{h} \tag{20-7}$$

This strain increases from zero at the entrance to the roll gap to its maximum value $\varepsilon_{\max}$ at the exit of the gap:

$$\varepsilon_{\max} = \ln \frac{h_0}{h_1} \tag{20-8}$$

In the case of compression (see eq. 7-13), it was shown that the strain rate in the compression direction can be expressed as the ratio between the compression velocity and the height of the workpiece:

$$\dot{\varepsilon}_y = \frac{v_s}{h} \tag{20-9}$$

By means of this formula it is easy to determine the strain rate in the thickness direction of a plate subjected to rolling, if two simplifying assumptions are made. One assumption is that there is homogeneous working of the plate in the roll gap, and the other that there is sticking friction between the roll and the surface of the plate. Deformation in rolling then can be considered to occur as a vertical plane strain compression process for the disc element shown in Fig. 20.3(a). As the disc moves through the roll gap from the inlet to the exit side, it is gradually compressed in the thickness direction.

The whole *contact angle* between roll and plate is denoted by the symbol α_D; the angle between the outlet and an instantaneous position of the disc is denoted by α, as shown in Fig. 20.3(a). If we assume sticking friction between workpiece and roll, then a material point on the workpiece in contact with the roll will have a velocity equal the surface velocity of the roll, i.e., v_R. This velocity can be decomposed into a vertical and a horizontal component. The vertical velocity component, $v_\perp$, will be the velocity at which the disc element is compressed in the vertical direction; see Fig. 20.3(b). Because there are two rolls that compress the plate from both sides, the *strain rate in the thickness direction* of the plate can be expressed as

$$\dot{\varepsilon} = \frac{2v_\perp}{h} = \frac{2v_R \sin\alpha}{h} \tag{20-10}$$

The equality $v_\perp = v_R \sin\alpha$ is obvious when one considers Fig. 20.3(b).

In Fig. 20.3(c), it is shown that the height of the plate inside the roll gap can be expressed by $h = h_1 + 2R(1 - \cos\alpha)$. The strain rate in the vertical thickness direction of the plate can therefore be expressed as

$$\dot{\varepsilon} = \frac{2v_R \sin\alpha}{h} = \frac{2v_R \sin\alpha}{h_1 + 2R(1 - \cos\alpha)} \tag{20-11}$$

From this equation, we can see that the highest and lowest through-thickness strain rates, respectively, are found at the inlet to and at the exit from the roll gap, so that

$$\dot{\varepsilon}_{\text{inlet}} = \frac{2v_R \sin\alpha_D}{h_0} \tag{20-12}$$

$$\dot{\varepsilon}_{\text{exit}} = 0 \tag{20-13}$$

The *mean* through-thickness strain rate of the plate in the roll gap can easily be determined as the average between the minimum and the maximum value,

$$\dot{\varepsilon}_m = \frac{\dot{\varepsilon}_{\text{inlet}} - \dot{\varepsilon}_{\text{outlet}}}{2} = \frac{v_R \sin\alpha_D}{h_0} \tag{20-14}$$

Alternatively, a slightly different mean value can be determined by integration as

$$\dot{\varepsilon}_m = \frac{v_R}{h_0}\left[\frac{2\,(h_0 - h_1)}{R}\right]^{\frac{1}{2}} \tag{20-15}$$

EXAMPLE 20.1: STRAIN-RATE CONDITIONS IN THE ROLL GAP

Problem: A rolling pass is characterized by the following rolling parameters: $h_0 = 5.2\,\text{mm}$, $h_1 = 4.3\,\text{mm}$, $R = 215\,\text{mm}$, $l = 13.9\,\text{mm}$, $v_R = 2.29\,\text{m s}^{-1}$

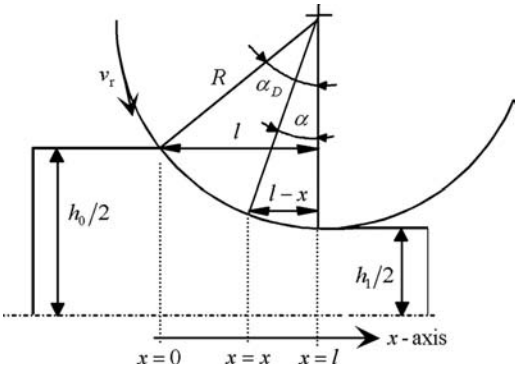

Figure 20.4. Geometrical conditions in rolling.

(a) Compute the strain rate in the thickness direction of the workpiece as a function of the length coordinate throughout the roll gap, and show a plot of the relationship. Assume homogeneous deformation in the rolling process.

(b) Compute the average strain rate of the rolling step, and include this strain-rate value in the graph.

Solution:

(a) Consider a plate subjected to rolling. Assume the angle α to vary from $\alpha = \alpha_D$ to $\alpha = 0^\circ$, as shown in Fig. 20.4. Then the strain-rate variation through the roll gap can be expressed by eq. 20-11. Let us then specify a length axis in the roll gap as depicted in Fig. 20.4. We can now show that the following relationship is valid:

$$\frac{l-x}{R} = \sin\alpha \quad \Rightarrow \quad \alpha = \arcsin\frac{l-x}{R}$$

Equation 20.11 can be transformed to the following expression:

$$\dot{\varepsilon}_y = f(x) = \frac{2v_r\dfrac{l-x}{R}}{h_1 + 2R(1-\cos\left(\arcsin\dfrac{l-x}{R}\right))}$$

This expression can be used in an Excel spreadsheet, for instance, to compute the strain rate for different x-values as follows:

x (mm)	$\dot{\varepsilon}_y$ (s^{-1})
0	56.95
3	47.85
6	36.66
9	23.66
13.9	0

(b) The mean vertical strain rate in the rolling step can be computed either by eq. 20-14 or by eq. 20-15. First, it is required to determine the arc of contact

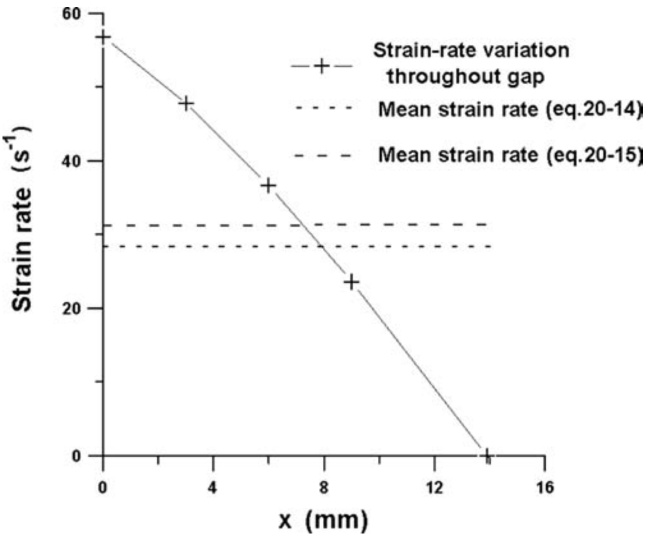

Figure 20.5. Idealized strain-rate conditions in the roll gap.

as follows:

$$h_0 = h_1 + 2R(1 - \cos\alpha_D) \quad \Rightarrow \quad \cos\alpha_D = 1 - \frac{h_0 - h_1}{2R} = 0.9979$$
$$\Rightarrow \quad \alpha_D = 3.71^\circ$$

Equation 20-14 then yields the following mean vertical strain rate:

$$\dot{\bar{\varepsilon}}_m = \frac{v_R \sin\alpha_D}{h_0} = \frac{2.29\,\text{m s}^{-1} \cdot \sin 3.71^\circ}{5.2\,\text{mm}} = \underline{\underline{28.48\,\text{s}^{-1}}}$$

Correspondingly eq. 20-15 yields

$$\dot{\bar{\varepsilon}}_m = \frac{v_R}{h_0}\left[\frac{2\,(h_0 - h_1)}{R}\right]^{\frac{1}{2}} = \frac{2.29\,\text{m s}^{-1}}{5.2\,\text{mm}}\left[\frac{2\,(5.2\,\text{mm} - 4.3\,\text{mm})}{215\,\text{mm}}\right]^{\frac{1}{2}} = \underline{\underline{31.31\,\text{s}^{-1}}}$$

The strain-rate conditions in the roll gap then can be shown in a diagram; see Fig. 20.5.

20.4 Length of the Projected Arc of Contact

The formula for the rolling load, eq. 20-5, which was developed earlier in this chapter, shows that the rolling load depends strongly on the projected length of the arc of contact. In the literature,[1] it is sometimes recommended to replace this length l with the real length of the arc of contact, $R\alpha_D$, which has a somewhat higher value than l, and therefore provides a higher estimate of the rolling load; see eq. 20-6.

Both of these two parameters, the real and the projected length of the arc of contact, are shown in Fig. 20.6. In order to calculate the *projected length of the arc*

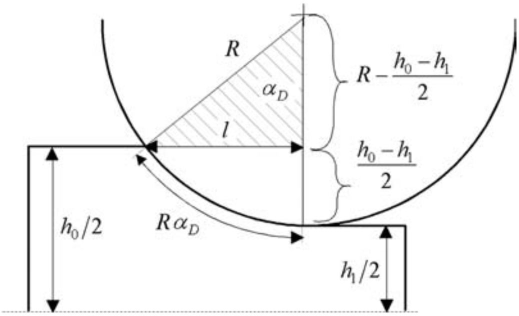

Figure 20.6. Geometrical relationship in rolling.

of contact, the following approximate formula can be used (see Example 20.2):

$$l \approx \sqrt{R(h_0 - h_1)} = \sqrt{R\,\Delta h} \tag{20-16}$$

This relationship is based on the assumption that the roll radius in the actual case is much bigger than the height reduction in the rolling pass.

EXAMPLE 20.2: FORMULA FOR THE PROJECTED LENGTH OF THE ARC OF CONTACT

Problem: Show that the length of the projected arc of contact in a rolling pass approximately equals the square root of the product of the roll radius and the thickness reduction in the rolling step.

Solution: The Pythagorean theorem, used on the hatched triangle in Fig. 20.6, yields the following expression:

$$R^2 = l^2 + \left(R - \frac{\Delta h}{2}\right)^2$$

$$R^2 = l^2 + R^2 - \Delta h R + \frac{\Delta h^2}{4}$$

In rolling, most commonly $\Delta h \ll R$, and the term $\Delta h^2/4$ can therefore be neglected. This yields

$$l^2 = \Delta h R \quad \Rightarrow \quad \underline{\underline{l}} \approx \sqrt{R(h_0 - h_1)} = \underline{\underline{\sqrt{R\,\Delta h}}}$$

20.5 Pressure Distribution over the Arc of Contact of the Roll

Attempts have been made to obtain expressions that accurately predict the *contact pressure* variation over the arc of contact of the roll. A theoretical analysis,[2] based on the slab method (see Fig. 20.7), provides the following pressure distribution:

For the entry zone, i.e., for $0 \le x \le x_n$:

$$\sigma_{x,1} = 2\frac{\bar{\sigma}_a}{h}\left(\frac{x_n x}{R} - \frac{x^2}{2R} - \mu x\right) + \frac{C_1}{h} \tag{20-17}$$

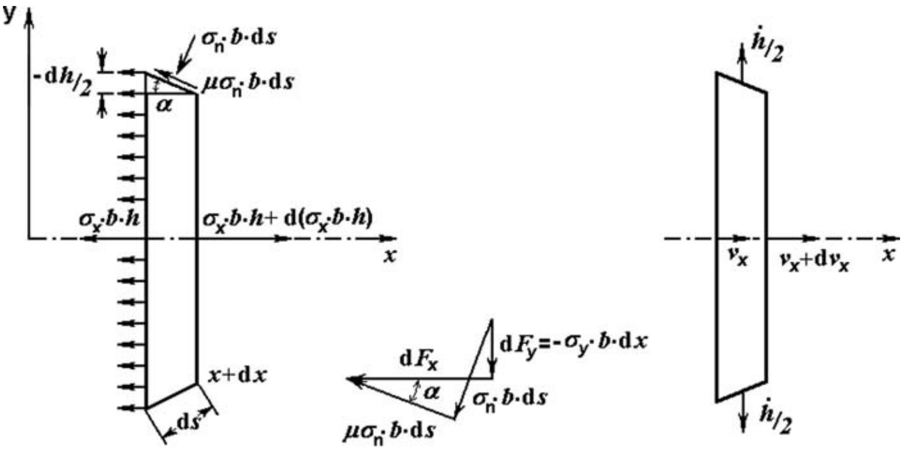

(a) (b) (c)

Figure 20.7. (a) Stresses and (b) forces on a slab element inside the roll gap. (c) Velocity conditions.

For the exit zone, i.e., for $x_n \le x \le x_e$:

$$\sigma_{x,2} = 2\frac{\bar{\sigma}_a}{h}\left(\frac{x_n x}{R} - \frac{x^2}{2R} + \mu x\right) + \frac{C_2}{h} \tag{20-18}$$

Here C_1 and C_2 are constants given by

$$C_1 = 0 \tag{20-19}$$

and

$$C_2 = -2\bar{\sigma}_a\left(\frac{x_n^2}{2R} + \mu x_e\right) \tag{20-20}$$

The neutral plane can be determined from eqs. 20-17 and 20-18 by setting $\sigma_{x,1} = \sigma_{x,2}$. The following result is then obtained:

$$x_n = \frac{x_e}{2}\left(1 + \frac{x_e}{2\mu R}\right) \tag{20-21}$$

When the preceding pressure distribution equations are used to determine the pressure distribution over the roll in strip rolling, good agreement is obtained with corresponding distributions obtained from FEM simulations; see Fig. 21.19.

Problems

20.1 Flat profiles of steel are rolled in a rolling mill. The operation requires many rolling steps where both flat and grooved passes are used. The initial workpiece is a billet with rectangular cross section 150 mm × 300 mm, as shown in the accompanying figure. The same figure shows how the cross section of the workpiece is reduced throughout the rolling stands. During the rolling operation, the temperature of the steel drops because of cooling, and the measured temperature in each rolling step is also specified in the figure. It is desirable that the rolling load be kept below 500 tons to prevent the rolling mill from being overloaded by fatigue.

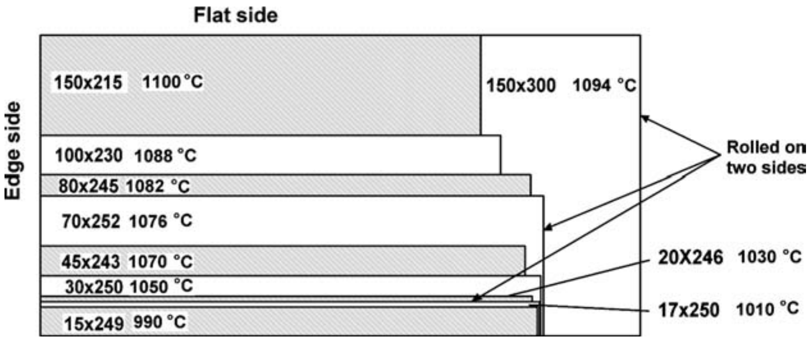

(a) Calculate the required rolling force in rolling stands 4 and 5, assuming that the rolling is always performed in flat passes.
(b) Propose changes in the rolling operation to harmonize the rolling loads.

Given data:

Angle of contact:

$$\alpha = \arccos\left[1 - \frac{1}{2}\left(\frac{h_0 - h_1}{R}\right)\right]$$

Flow stress of steel:

$$\bar{\sigma} = K\bar{\varepsilon}^n\dot{\bar{\varepsilon}}^m \exp\frac{\beta}{T} = 4.2553\bar{\varepsilon}^{0.19}\dot{\bar{\varepsilon}}^{0.128} \exp\left(\frac{4337.4}{T}\right) \qquad \text{(MPa)}$$

Roll radius: $R = 425\,\text{mm}$
Roll velocity: $v_r = 4\,\text{m}\,\text{s}^{-1}$ (on roll periphery)
Friction factor: $m = 0.3$

20.2 Use the slab method to develop the expressions for the pressure distribution given in eqs. 20-17 to 20-20. Hint: Apply Fig. 20.7 when you solve this problem.

NOTES

1. Altan, T., Oh, S.-I., and Gegel, H. L.: "Metal Forming, Fundamentals and Applications," ASM Int., Metals Park, Ohio, 1983, pp. 253–254.
2. Lange, K.: "Handbook of Metal Forming," McGraw-Hill, New York, 1985, pp. 5.12–5.15, 12.5–12.7.

REFERENCES

Lenard, J. G.: "Primer on Flat Rolling," Elsevier, London, 2007.
Roberts, W. L.: "Hot Rolling of Steel," Marcel Dekker, New York, 1983.
Sing, R. V.: "Aluminium – Rolling; Process, Principles and Applications," TMS, 2000.
Tselikov, A.: "Stress and Strain in Metal Rolling," University Press of the Pacific, 2003.

21 FEA of Rolling

Three different cases of metal rolling will be analyzed in this chapter by use of FEA. The simulation results obtained in each case will be examined in order to describe the mechanics of these typical industrial rolling situations. It will be shown that the deformation process is indeed very different in *slab rolling* from what it is in *strip rolling* because of the use of very different thickness-to-width ratios of material in the roll gap. In addition, the effect of the use of a light pass in the slab rolling process is considered. The main rolling parameters used in the three different cases of rolling analyzed here are specified in Table 21.1. The obtained results reveal clearly that the mechanics of rolling are complex. The deformation distribution obtained in the roll gap is found to depend strongly on the parameter Δ (see eq. 5-13), as well as on the reduction taken in the rolling step. Note that, in this chapter, slab rolling is considered as a hot rolling process applied to the alloy AA 3003. Strip rolling, on the other hand, is considered as cold rolling process for an alloy with a flow stress described by $\sigma = 180\varepsilon^{0.1}$. In all cases considered here, plane strain FEM models are used to model the rolling process.

21.1 Hot Rolling of an Aluminum Slab in a Light Pass

To analyze the mechanics of deformation when utilizing a very light rolling pass, the upper half of the FEM model shown in Fig. 21.1 was made. To secure *seizure* of the slab upon entrance into the roll gap, a *manipulator* in the form of a small moving die was placed at the rear end of the slab. In the beginning of the rolling process, the manipulator was moved with low velocity toward the rolls, in order to push the slab into the roll gap.

The rotational velocity of the roll was specified sufficiently high, in relation to the velocity of the die, that when the slab had been pushed sufficient deep into the roll gap, conditions of *unaided entrance* were achieved. The roll now started to pull the slab in the direction of rolling, faster than the movement of the manipulator.

Figure 21.1(a) shows the tool and workpiece configuration at the start of the simulation model. Now the rolls are positioned at one end of the slab and the pushing die at the other end. At this instant, movement into the roll gap of the slab

Table 21.1. *Rolling parameters applied in the present FEM study of rolling*

Case no.	Roll velocity (rad s^{-1})	h_0 (h_1) (mm)	Workpiece (roll) temp. (°C)	Δ	Area red. (%)	Contact length (mm)	Roll diameter (mm)	Friction factor
1	1.5	400 (395)	520 (20)	7.8	1.3	51	700	0.5
2	1.5	400 (350)	520 (20)	3.0	12.5	125	700	0.8
3	5	4.5 (3.9)	20 (20)	0.2	13.3	18	894	0.14

is provided by the manipulator. Figure 21.1(b) depicts a later step of simulation, after seizure has been achieved. Now the rolls feed the slab forward, and the manipulator lags behind. Finally, Fig. 21.1(c) shows the end stage of rolling, when the whole slab has passed through the roll gap and has been rolled down in thickness.

This case is one where the reduction of area is very small, only 1.3%, and hence the parameter Δ is high, 7.8. The appearance of the FEM-predicted plastic zone obtained in this example of rolling is shown in Fig. 21.2 and Fig. 21.3.

21.1.1 Deformations

Figure 21.2(a) and c) shows that there are special end effects when the front and the back end of the slab are rolled. During rolling of the rest of the slab, however, the conditions are of *steady-state* type, i.e., the *effective strain-rate field* is constant and time-independent; see Fig. 21.2(b).

As Fig. 21.2(b) shows, the strain-rate field in the steady-state condition is characterized by a balloon-shaped region of high strain rate. The balloon is depicted by dark gray in Fig. 21.2(b), as it extends down into the slab below each roll, with the region of maximum effective strain rate displaced toward the entrance side of the roll gap. Each high-strain-rate region extends to a depth inside the slab of approximately one-third of the whole slab thickness.

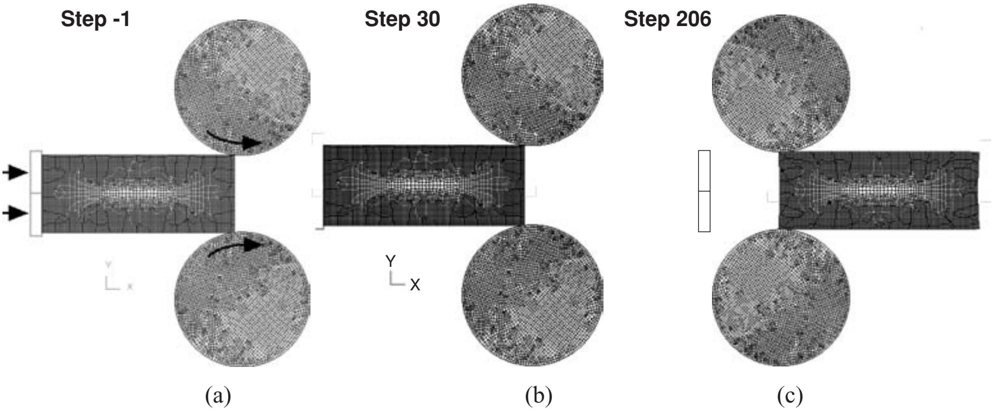

Figure 21.1. FEM model of hot rolling of slab of Al alloy in a light pass.

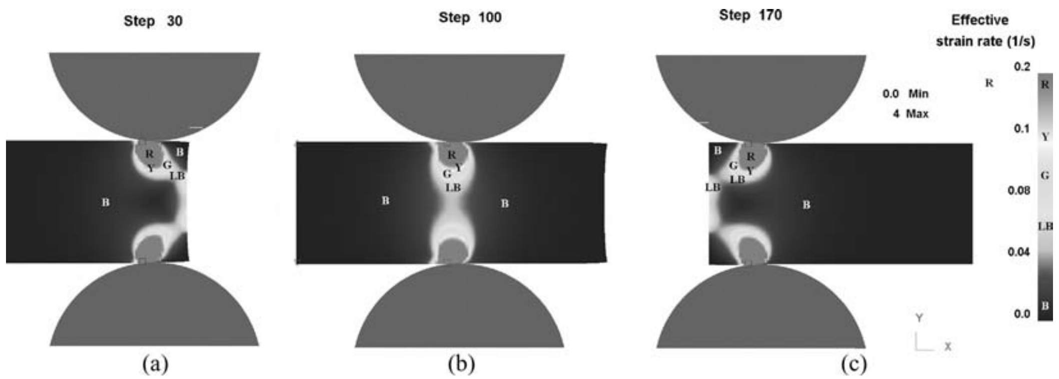

Figure 21.2. Appearance of plastic zone in light-pass hot rolling of slab. Different stages of rolling: (a) entrance, (b) steady state, and (c) exit of slab from the roll gap.

Below the high-strain-rate region, there is a *region with lower strain rate*, which appears in light gray in Fig. 21.2(b), as if the balloon is blown further up, until it encounters the corresponding balloon extending from the other side of the slab.

When rolling is conducted close to the ends of the slab [see Fig. 21.2(a,c)], the conditions deviates from those in the steady-state regime. The balloon-shaped higher-strain-rate region then extends sideways, directed toward the end face of the slab, while there are insignificant deformations in the material in the middle of the roll gap.

The steady-state effective-strain-rate field predicted by the FEM code can be shown alternatively with a different scale, as depicted in Fig. 21.3(a). Then the material subjected to low strain rate also becomes visible. This picture clearly reveals that the plastic zone does not remain only in the roll gap in light-pass slab rolling. In

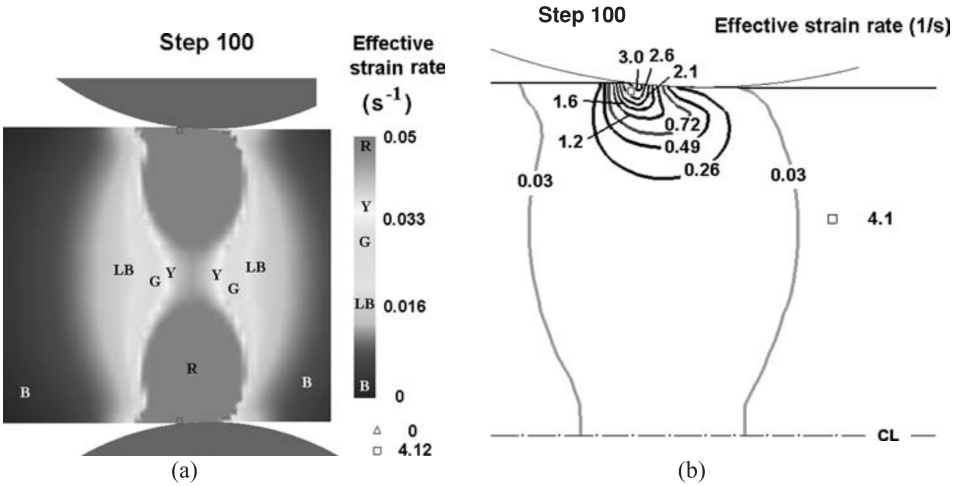

Figure 21.3. (a) Extension of the plastic zone. (b) Levels of effective strain rate depicted by contour lines.

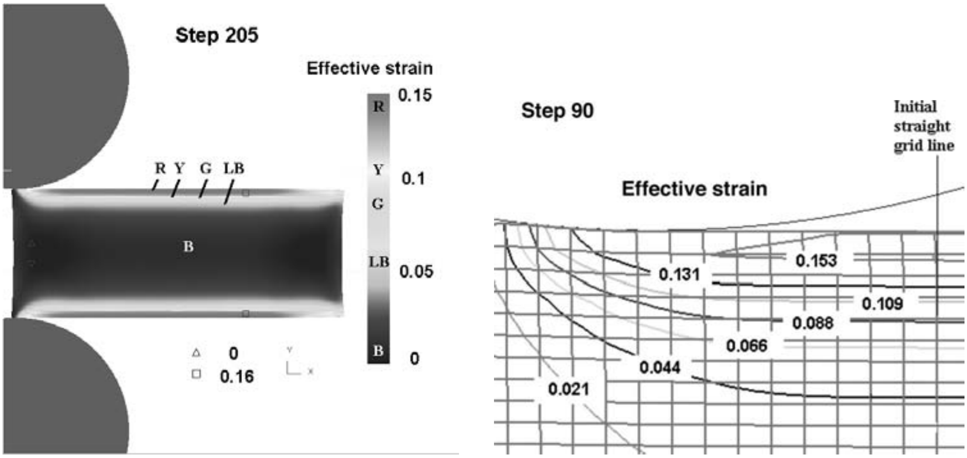

(a) (b)

Figure 21.4. Effective strain distribution inside the slab after rolling, shown by (a) grayscale and (b) contour lines, including the distortions of an internal grid pattern.

fact, it spreads out into a larger volume of the slab, extending on both sides of the roll gap.

Another alternative is to show levels of predicted effective strain rate in the roll gap by means of a contour line plot; see Fig. 21.3(b). One can then see that, whereas on the axis of the slab the effective strain rate is $\approx 0.04\,\mathrm{s}^{-1}$, it is predicted to be as high as $\approx 4\,\mathrm{s}^{-1}$ for the surface material of the slab, which is strained at the maximum rate.

The deformations imposed on the slab material in the roll pass, as depicted by the simulation program quantified as effective strains, are those shown in Fig. 21.4. The figure depicts that there are end effects also on the size of the deformations in terms of the effective strain, in each end of the slab.

The highest effective strain in the slab has the value $\bar{\varepsilon}_{\max} = 0.16$. This strain is experienced in the outer surface layer of the slab. Close to each end of the slab there is less deformation than this. Most of the cross section of the slab is in reality subjected to rather small deformations, $\varepsilon < 0.05$. At the center of the slab, the deformations are even smaller, <0.03. Hence, the midlayer of the slab has been little worked by the rolls.

21.1.2 Grid Pattern Distortions

The plastic deformation imposed on the surface layer of the slab in the case of light-pass slab rolling, as quantified in the preceding subsection, is visually best judged by considering *distortions* obtained in an internal grid pattern inside the slab upon passage through the roll gap. As shown in Fig. 21.4(b), simulation predicts that an initially straight vertical grid line inside the slab will remain straight in the core of the slab but will bend backwards in the most heavily deformed layer close to the slab surface. To illustrate this effect, an initially straight line has been drawn in

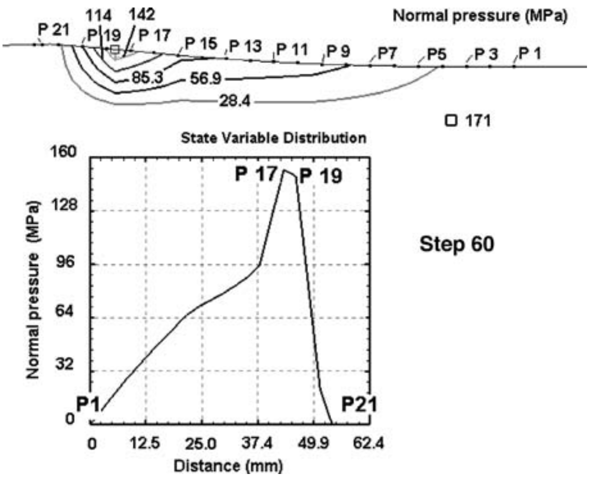

Figure 21.5. FEM-predicted normal pressure distribution over the contact zone against the roll.

Fig. 21.4(b), on top of the deformed grid line. The deformed grid line has become bent. Hence, the net effect of the deformations imposed by the rolls is that the surface layer of the slab is squeezed backwards in relation to the core of the slab. Deformations in the thin outer surface layer are therefore characterized by considerable shear deformations.

21.1.3 Pressure Distribution

The point-tracking option of the FEM code was used to determine the contact stress distribution over the roll–slab interface, to check whether there is a friction-hill distribution of pressure in this rolling operation. As shown previously in Ch. 13, such a distribution is predicted theoretically by the slab method. The results of the analysis are visualized in two different ways in Fig. 21.5. As shown in the figure, the contact pressure is predicted to have a peak value of approximately 170 MPa near the inlet to the roll gap. In the roll gap, the pressure falls off gradually from this peak value, down to zero at the exit. Hence, the computed contact pressure in the rolling operation is very different from the friction-hill distribution predicted in theoretical analysis (see Fig. 13.4), where the maximum pressure should be in the midregion of the roll gap.

21.1.4 Thermal Conditions

Computed thermal conditions in the subsurface layers of the rolls and the slab are shown in Fig. 21.6. For the rolling operation investigated in this simulation model, the prediction is that the roll, initially at room temperature, will cool down the outer surface of the slab from 520°C down to 487°C (Fig. 21.6(a)). The maximum temperature drop on the surface of the slab, hence, is determined to be ~33°C. Behind the roll, however, the heat from the interior of the slab will again quickly heat up the outer surface layer of the slab, upon exit from the roll gap. So in Fig. 21.6(a), for the point P1 on the surface of the slab, which is located rather far behind the rolls, the temperature has risen to 508°C. Note also thermal distribution along the surface

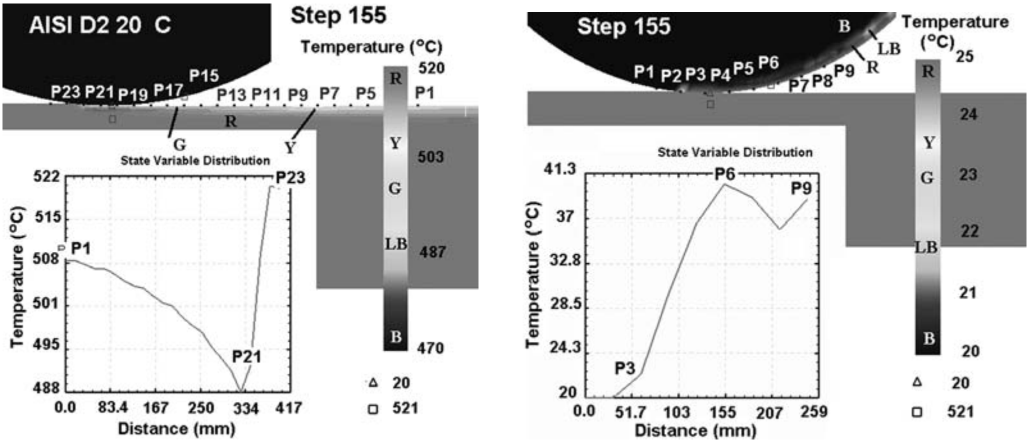

(a) (b)

Figure 21.6. Temperature distribution, obtained from the simulation model, below (a) slab surface and (b) roll surface.

layer of the slab as depicted by the shaded distribution picture at the top of Fig. 21.6(a).

Correspondingly, thermal conditions inside the roll, as computed by the simulation program, at a particular instant of rolling, are visualized in Fig. 21.6(b). The maximum temperature rise on the periphery of the roll gap is predicted to be ≈20°C, i.e., the temperature increases from room temperature at the inlet to ≈40°C at the exit side of the roll gap. The shaded distribution picture at the top of Fig. 21.6(b) also shows that thermal effects shortly after start of rolling, of course, are shallow and limited to the surface layer of the roll.

21.1.5 Damage Parameter and Maximum Principal Stress

The predicted value of the Cockcroft–Latham damage parameter in its distribution over a longitudinal section of the slab is shown in Fig. 21.7 and Fig. 21.8(d).

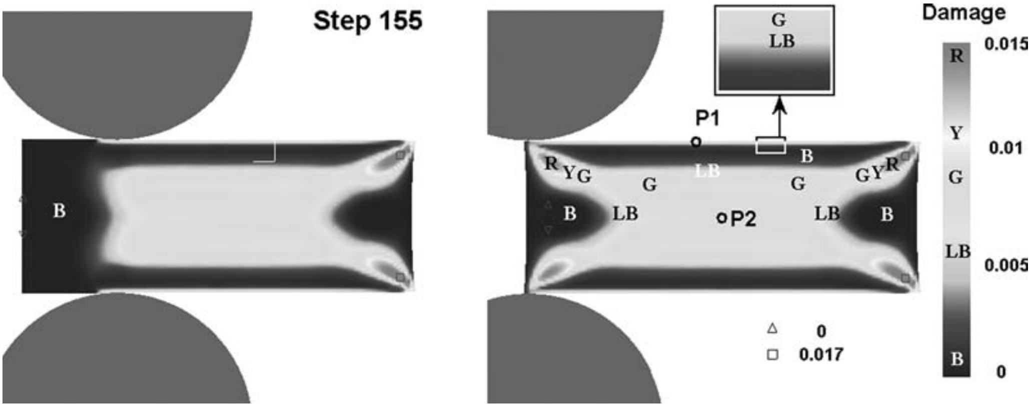

(a) (b)

Figure 21.7. Distribution of the damage parameter inside the slab after (a) three-fourths of the slab has been rolled and (b) end of rolling.

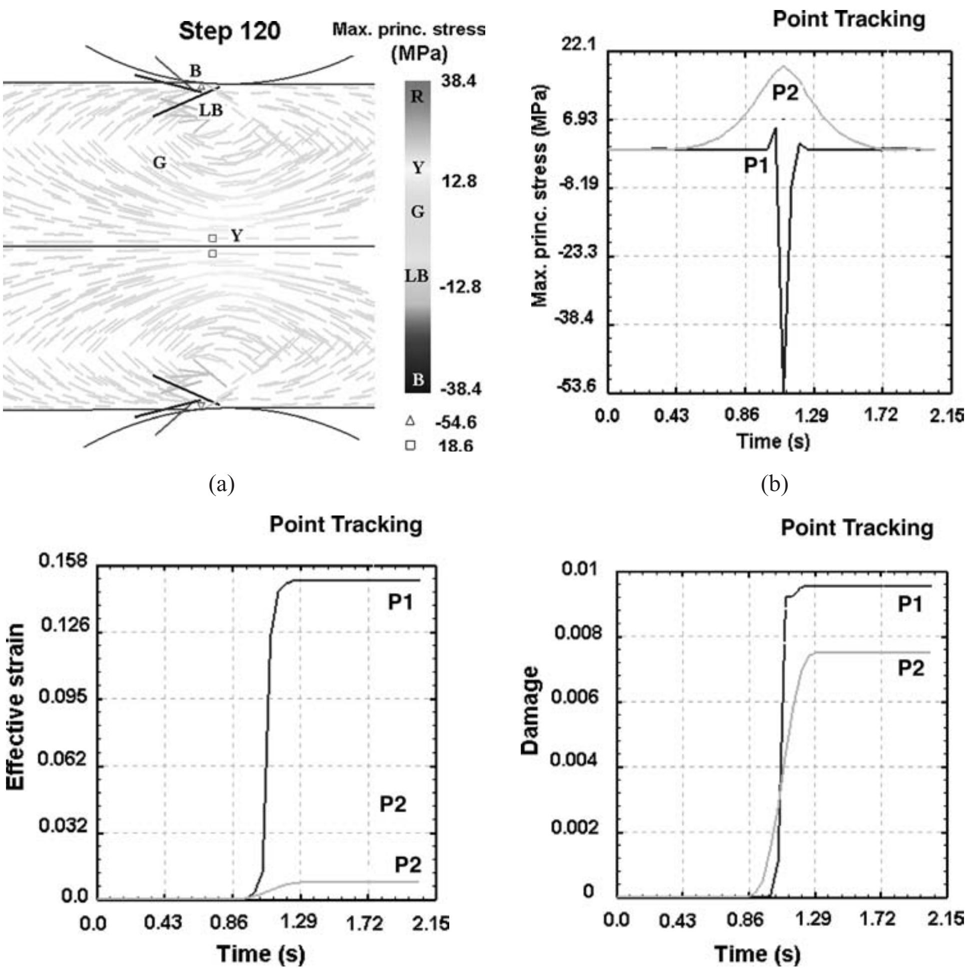

(a) (b)

(c) (d)

Figure 21.8. (a,b) Maximum principal stress distribution inside the slab. Data obtained from point tracking on two material points. (c) Effective strain. (c) Damage parameter.

The latter figure is based on point tracking done for two reference points, one on the surface (P1) of the slab, and another at its center (P2). As Fig. 21.7(b) shows, the highest damage-parameter value is obtained close to the edges of the slab, in the shear-deformed layers in the front and the back end of the slab. Except for this, the parameter is high in the middle of the slab and close to its surface. There is also a rather thick subsurface layer in which the damage parameter is low.

As explained in Sec. 9.3, there are two factors that contribute to the Cockcroft–Latham damage parameter. One is the largest principal stress component, when it is tensile. The other is the effective strain imposed on the material as it is stressed. In Fig. 21.8(a–c), each of these parameters is visualized, including the damage parameter, as computed by the simulation program for the two points considered.

As Fig. 21.8(a) depicts by means of light gray lines, there is high tensile stress in the axial direction of the slab at its center, and this axial stress is also the largest principal stress. The point-tracking result in the diagram in Fig. 21.8(b) shows that P2, at the center of the slab, experiences a gradual increase in tensile stress, up to a peak value, when it appears in the middle of the roll gap, whereafter it drops to zero behind the roll gap. On the other hand, P1, at the surface of the slab, experiences compressive stresses while inside the roll gap. But before entrance and after exit from the roll gap, this point is subjected to low tensile stress.

When one considers the effective strains imposed on the material, Fig. 21.8(c) depicts the same result as that already discussed in connection with Fig. 21.4 – that is, that the material particle on the surface of the slab is subjected to much higher deformation than the particle in the core. This is why the damage parameter reaches higher values for the former than for the latter.

There is no doubt that the mechanical working conditions inside the slab are unfavorable in this rolling operation. The core of the slab is subjected to high tensile stress without being deformed significantly. In the presence of a cast microstructure, with low ductility in the slab, the middle of the slab would therefore be prone to cracking. Concurrently, the surface layer of the slab is subjected to excessive deformations, because this layer is squeezed backwards along the slab.

21.2 Hot Rolling of the Slab in a Pass with Normal Reduction

To illustrate the effect of changing from a light, to a larger draft in slab rolling, the model described in the preceding section was slightly modified. The upper roll in the model was moved to a lower position, before start of simulation, to give a reduction of 12.5% in the rolling pass. This increase in the roll *draft* causes a drop in the parameter Δ from 7.8 to 3.0; see Table 21.1. The change in the rolling conditions as result of this change, as predicted in simulation, will be discussed in forthcoming subsections.

21.2.1 Deformations

Figure 21.9, when compared with Fig. 21.2 and Fig. 21.3, reveals that when the reduction is increased, there is a stronger relative increase in the strain rate in the core of the slab than in its outer surface layer. This is perhaps best seen if one computes the ratio between the highest predicted strain rate near the surface of the slab and the lowest strain rate in the core. When this is done, the values given in Table 21.2 are obtained. From this table, it is clear that this ratio is reduced approximately tenfold when the reduction is increased from 1.3% to 12.5% in the rolling process. Even though the deformation is still inhomogeneous in the roll gap when the normal draft is taken, the inhomogeneity is still considerably less than when the draft was small. This reduced inhomogeneity of deformation because of the increase in the draft is also seen when Fig. 21.4(a) is compared with Fig. 21.10.

One can also consider the inhomogeneity in the rolling processes, by comparison of the effective strain value at the center with the value near the surface of the slab. When considered in the steady-state regime of the rolling process, these values

Table 21.2. *Effective strain rates in the plastic zone in the considered slab rolling processes*

Reduction (%)	$\dot{\varepsilon}_{e,\max}$ (s^{-1}) (surface layer of slab)	$\dot{\varepsilon}_{e,\min}$ (s^{-1}) (core of slab)	$\dot{\varepsilon}_{e,\max}/\dot{\varepsilon}_{e,\min}$
1.3	4.12	0.04	≈100
12.5	7.61	0.6	≈13

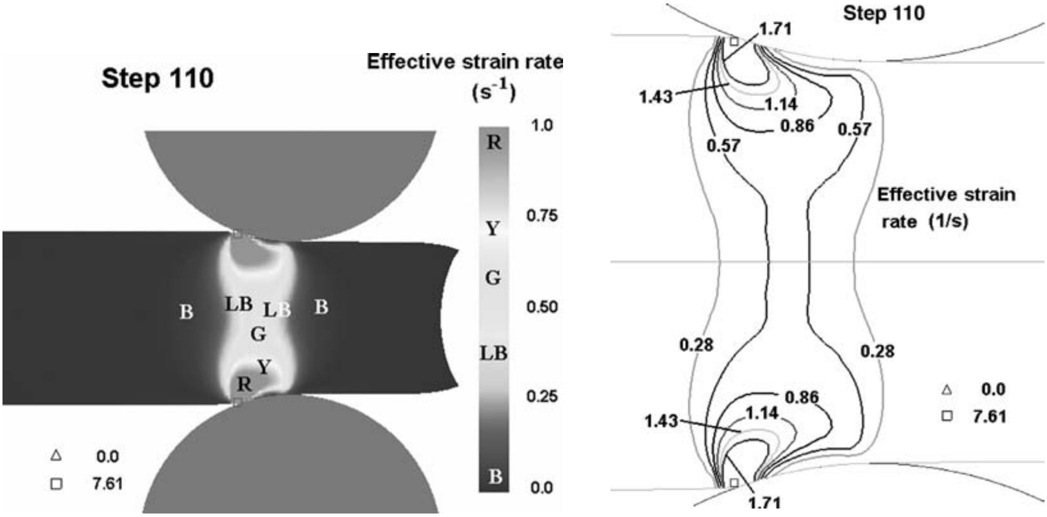

(a) (b)

Figure 21.9. The strain-rate distribution in the roll gap in the normal reduction pass, visualized by (a) grayscale and (b) contour plot.

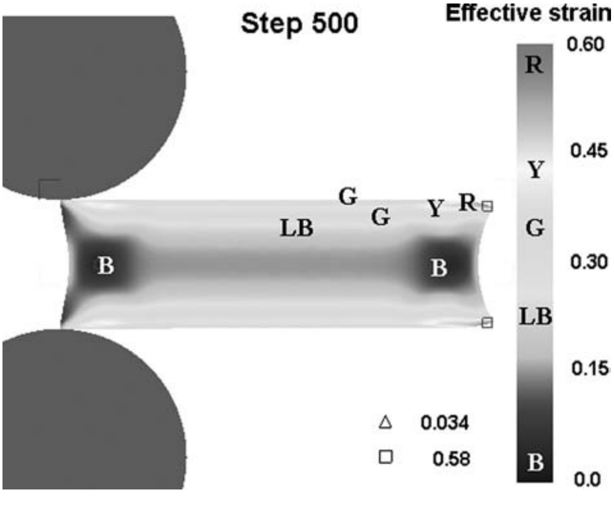

Figure 21.10. Effective strain distribution inside the slab in normal-draft rolling.

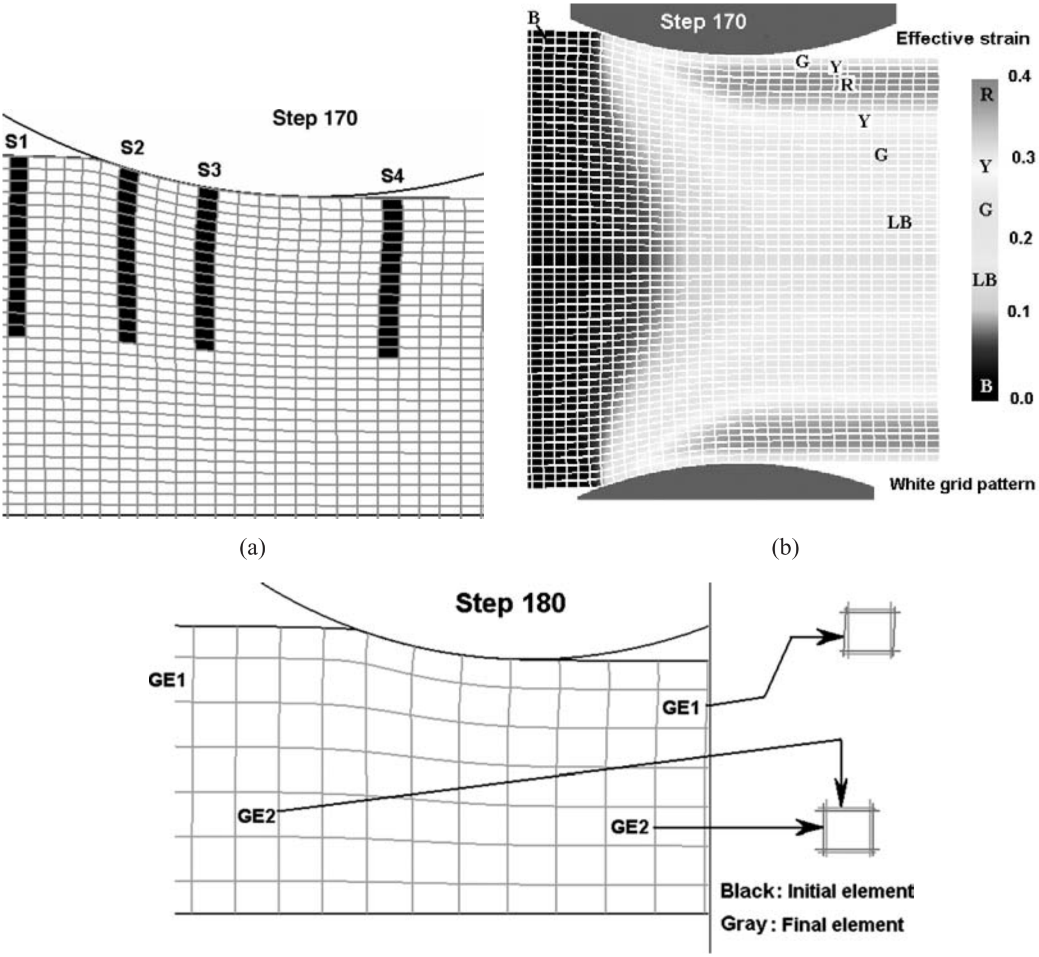

(a) (b)

(c)

Figure 21.11. (a) Predicted deformation of internal grid pattern in normal draft slab rolling. (b) Grid pattern and effective strain distribution superimposed. (c) Change in shape of grid elements upon passage through roll gap.

are ≈0.15 at the center and ≈0.4 on the surface, for the rolling pass performed with the largest draft; see Fig. 21.10 or Fig. 21.11(b). Hence, the effective deformation in the surface layer is two to three times larger than it is in the core of the slab. If the effective strain scale is selected properly, as shown in Fig. 21.11(b), one can see that the simulation program actually predicts the effective strain to be largest in the subsurface layer of the slab.

21.2.2 Grid Pattern Distortions

In Fig. 21.11 are shown some postprocessing results regarding predicted distortions occurring in the internal grid pattern, inside the longitudinal section of the slab, upon passage through the roll gap. Figure 21.11(a) shows that an initially straight vertical stripe S1 inside the slab gradually will attain a bent configuration during

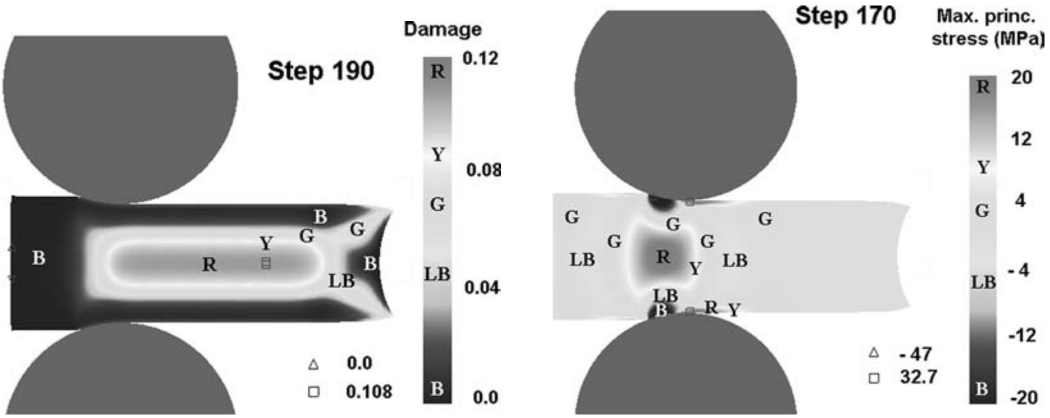

(a) (b)

Figure 21.12. Slab rolling using normal reduction pass: (a) damage parameter and (b) maximum principal stress.

passage through the roll gap. This is realized if one looks at the grid stripes S2–S4, which all initially were straight vertical stripes ahead of the roll gap. At the frozen stage of rolling shown in the figure, however, stripes with increasing number have moved deeper and deeper into the roll gap. On the inlet side of the gap, the stripes start to bend in the rolling direction, close the surface of the slab.

But as the stripe flows deeper into the roll gap, it starts to bend the opposite way near the surface. Hence, the net result after travel through the plastic zone in the roll gap is that the stripe attains a doubly curved shape.

An overlay plot is shown Fig. 21.11(b), where the effective strain distribution inside the roll gap is shown on top of the distorted grid pattern. Finally, in Fig. 21.11(c) is shown the distortion of two specific grid elements upon flow through the roll gap. This graph shows that, while the grid element GE1, located in the high-strain subsurface layer of the rolled slab, has been subjected to a significant amount of shear deformation, a corresponding grid element GE2, in the middle of the slab, has mainly been compressed in the through-thickness direction of the slab.

21.2.3 Damage Parameter and Maximum Principal Stress

In Fig. 21.12 and Fig. 21.13 are shown the FEM-predicted parameters, which could predict material failure during slab rolling in case crack-sensitive materials are rolled. The FEM-predicted Cockcroft–Latham damage parameter in the normal-draft slab rolling pass is shown in Fig. 21.12(a). In this picture, one can see that the highest damage parameter now will be experienced in the core of the slab. Besides, the numerical value of the highest damage parameter in the slab material now will be approximately ten times higher than in the light-draft pass.

When one looks at Fig. 21.13(a) and (b), and compares the level of the largest principal stress in the normal draft with the corresponding parameter in the light

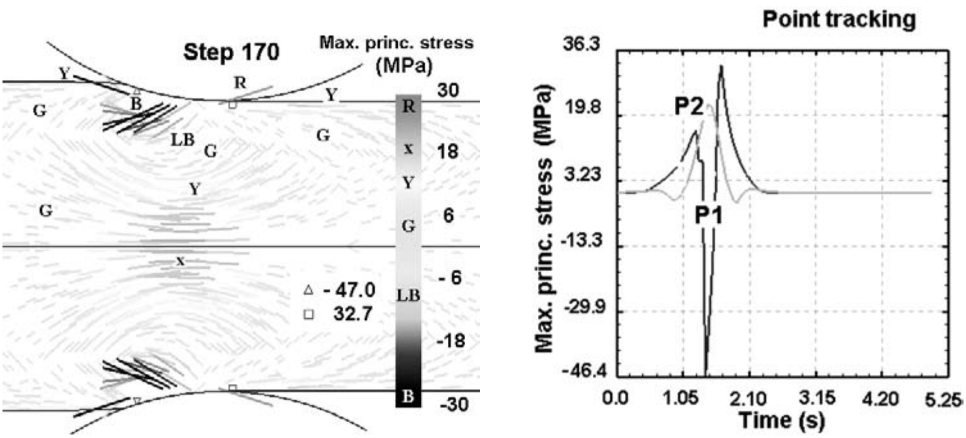

(a) (b)

Figure 21.13. Distribution of maximum principal stress inside slab in the steady-state stage of the normal-draft rolling pass: stresses visualized by (a) line vectors and (b) point-tracking data (point P1 near surface and point P2 near center of slab).

draft [see Fig. 21.8(a) and (b)], two distinct features are seen. One is that the axially oriented largest tensile stress at the center of the plastic zone inside the roll gap, indicated in the figure by darker gray lines at the center of the slab, is not increased much when the reduction is increased tenfold. The increase is to ≈30 MPa, as compared to ≈20 MPa for the light draft. Hence, the large increase in damage factor at the center of the slab in normal-draft rolling is mainly caused by the increased deformation there, quantified by the effective strain value. This can be seen by comparison of Fig. 21.4(a) and Fig. 21.10.

Another feature is that there is a high tensile stress in the slab surface behind the roll gap as the slab material is delivered from the roll gap; see Fig. 21.13. However, because there are no significant plastic deformations in this location, the damage parameter is low in this tensile zone.

21.2.4 Pressure Distribution

In Fig. 21.14, the normal pressure distribution against the roll, along the region of contact, is shown as predicted by the simulation model. As the figure depicts, this pressure distribution does not conform to that predicted theoretically, for instance, by the slab method. In simulation, a high pressure peak is predicted at the inlet side of the roll gap, where the slab surface comes in contact with the roll. This prediction is the same as in the light-draft pass; see Fig. 21.5. There is not much difference in the predicted peak pressure value between the light- and the normal-draft pass.

21.2.5 Thermal Conditions

Cooling and heating effects predicted in simulation between the cold roll and the hot slab were computed in same manner as previously done for the light-draft case

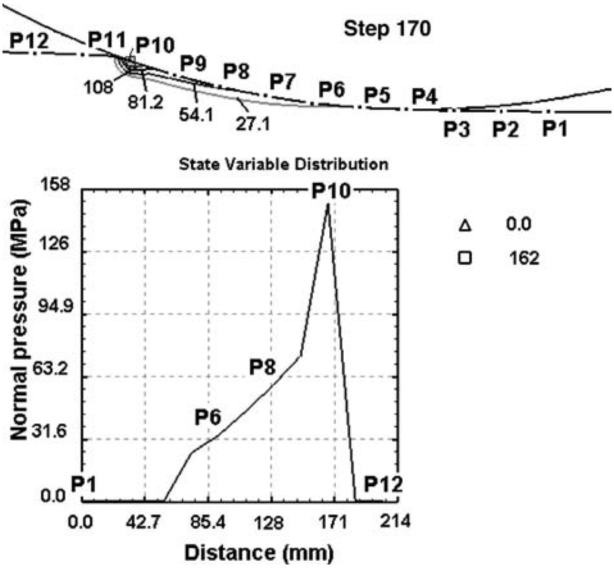

Figure 21.14. Normal pressure distribution over the contact zone of the roll.

of rolling (see Fig. 21.6). Conditions are analogous in these two cases, except that the thermal effects, of course, are stronger when the larger draft is taken. This is because the contact time is increased as the reduction is increased, when the rolling speed is kept constant. The maximum temperature drop in the surface layer of the slab, cooled by the cold roll, is now predicted to be ≈76°C, whereas the temperature rise in the roll is predicted to be ≈50°C. (Remember that in the light draft they were, respectively, ≈33°C and ≈20°C; see Fig. 21.6.)

21.3 Cold Strip Rolling

The characteristics of a cold strip rolling process are now to be examined. Because of symmetry around the longitudinal axis of the strip, only one-half of the process was modeled. The model was set to be isothermal, for thermal effects usually are negligible in cold forming. Figure 21.15 shows the mirrored version of the FEM model of the process, in which a 4.5 mm thick strip was worked down to 3.9 mm

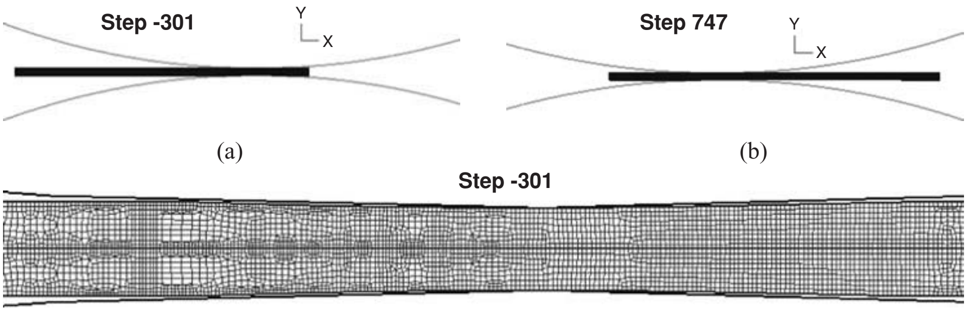

(a) (b)

(c)

Figure 21.15. FEM model of strip rolling: (a) initial state after compression of sheet by the rolls, (b) intermediate stage characterized by steady-state rolling, and (c) magnified version of simulation model showing the applied FEM mesh.

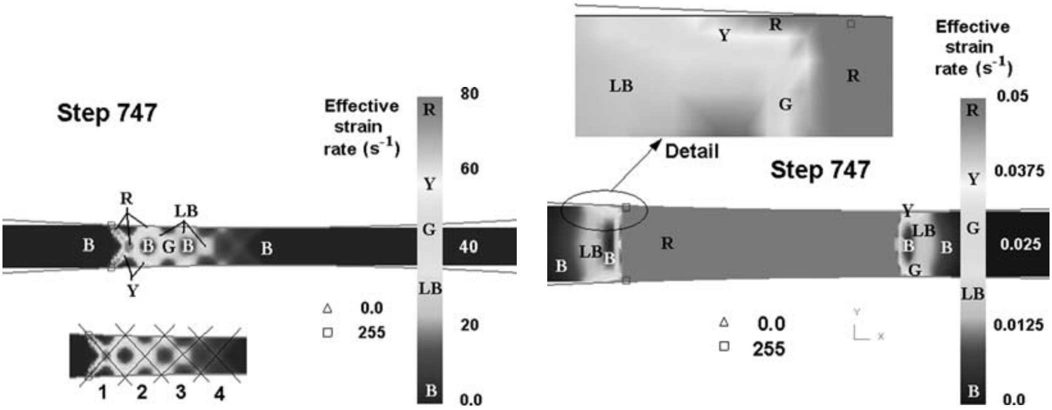

(a) (b)

Figure 21.16. Effective-strain-rate distribution in the roll gap in strip rolling: scale chosen to show (a) high strain rates and (b) low strain rates.

thickness by rolls of 894 mm diameter. The reduction ratio and the parameter Δ in this process were 13.3% and 0.2, respectively; see Table 21.1.

Because a thin strip will bend if it is pushed into the roll gap, a different approach from the previous models was chosen to provide entrance of the strip into the roll gap. The strip was initially taken to be positioned in between the rolls, in a first simulation model, whereafter the rolls were moved down against each other to compress the strip locally to thinner thickness. The last step of this simulation was then used to create a second simulation model. In it, the rolling was provided by rotational movement instead of compression.

A rather short length of strip was considered for the workpiece. But the length was sufficient to achieve steady-state conditions in the strip material before the end of the simulation. The initial and an intermediate stage of the FEM model of the analyzed rolling process are shown in Fig. 21.15(a) and (b). In addition, the initially compressed portion of the strip in the roll gap is shown with larger magnification in Fig. 21.15(c). As this figure depicts, the model had a rather large number of FEM elements across the half thickness of the strip, without being a very big model. Hence, good accuracy was obtained in the simulation model even though the computation time was short.

After the simulation model had been built, the simulation was run. Finally, postprocessing data were obtained by this model, corresponding to those for the slab rolling analysis performed in the previous sections.

21.3.1 Deformations

The effective-strain-rate distribution as computed by the simulation program for the considered strip rolling process is shown in Fig. 21.16. To visualize the variation of this parameter inside the roll gap, two different scales of strain rate are required. In Fig. 21.16(a) is shown the distribution of the high strain rates. As this picture shows, the deformations are quite nonuniform in the roll gap in this forming operation.

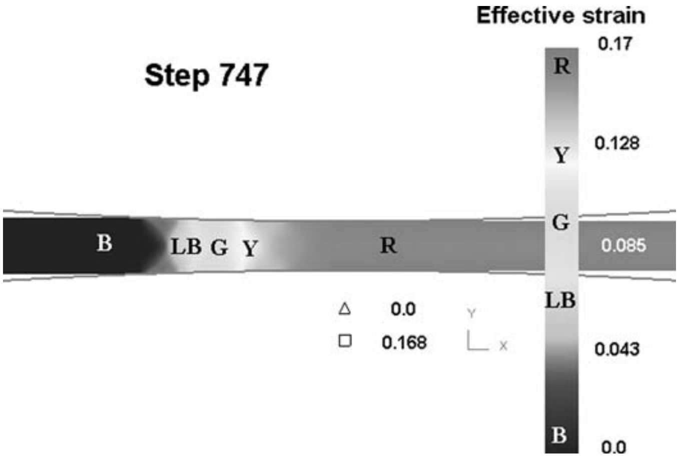

Figure 21.17. Effective strain distribution in the strip during rolling.

Four distinct *deformation crosses* are predicted in the plastic zone inside the roll gap. Each cross has been indicated in the figure by a superposed X. There are also dead zones inside the plastic zone. Close to the surface of the strip, there are four dead zones located between the legs of each deformation cross. In the middle of the strip, there are altogether three dead zones, each located between neighboring deformation crosses. When a scale depicting low strain rates is chosen [see Fig. 21.16(b)], one can see that at the entrance and the exit of the roll gap, special deformation effects are predicted to occur adjacent to the strip surface. The deformations imposed on the surface layer of the strip in these regions, however, are rather small.

In Fig. 21.17, the distribution of the deformation inside the strip, in the roll gap, and on the entrance and the exit sides of the gap is shown as computed by the simulation program in terms of effective strain. This figure shows that the net effect of the passage of the strip through the roll gap is that the material is evenly strained over the whole strip thickness. This occurs in spite of the presence of a number of deformation crosses in the roll gap, which deform the material locally in an inhomogeneous manner. The deformations even out in the final deformed strip upon delivery of it behind the rolls, because the material is fed in a continuous manner through the roll gap from its inlet to its exit. During this passage, the material travels both through the shear bands making up the deformation crosses and through the dead zones between the crosses. The net effect of accumulated deformation, in terms of effective strain, is therefore approximately the same for the whole cross section of the strip, upon exit from the roll gap.

21.3.2 Grid Pattern Distortions

The distortions created in an internal grid pattern in strip rolling, as predicted by the simulation program, are shown in Fig. 21.18. The shape of a vertical row of grid elements, prior to and after rolling, is shown on the right-hand side of this figure. As shown, the total deformation after passage of the strip material through the rolling

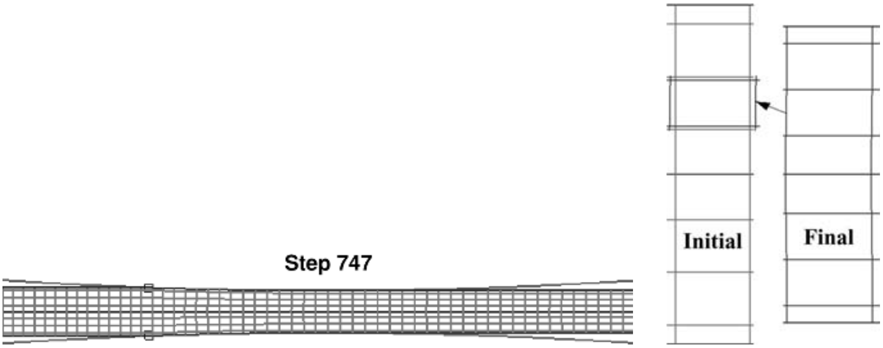

Figure 21.18. Deformations yield distortions in an internal grid pattern.

pass agrees well with predictions regarding the effective strain distribution, namely, that the deformations are uniform over the thickness of the strip. The shape of the deformed grid elements, also confirms this; the grid is mainly compressed in the thickness direction and elongated in the rolling direction.

21.3.3 Pressure Distribution

The FEM-computed distribution of contact stress over the periphery of the roll, in the contact zone between roll and strip, was determined by the FEM program for our particular case of strip rolling, see Fig. 21.19. The distribution is similar the traditional friction-hill distribution as predicted by theory, as, for instance, by the slab method; see Sec. 13.2.1.

One difference, however, is that the FEM-computed distribution curve has a *wavy appearance*, with alternating *high peaks*. In addition, there are *regions with lower pressure – valleys* – between the peak values. Altogether there are four peaks with three valleys in between. The peak values seems to appear in locations on the roll surface where the legs of the deformation crosses are present, i.e., at the places where the shear bands of the deformation crosses extend to the surface of

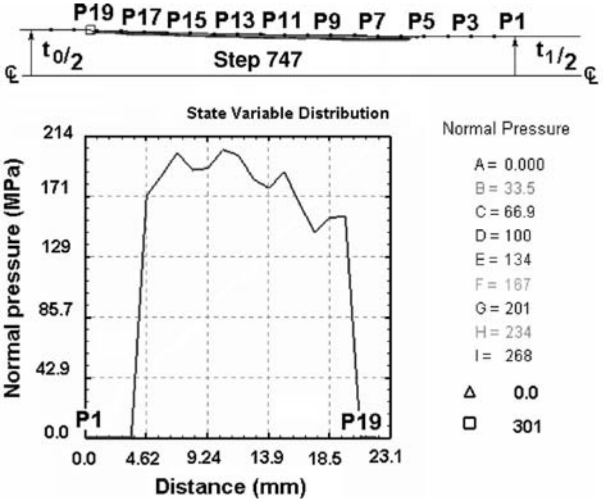

Figure 21.19. Pressure distribution over the roll–strip interface.

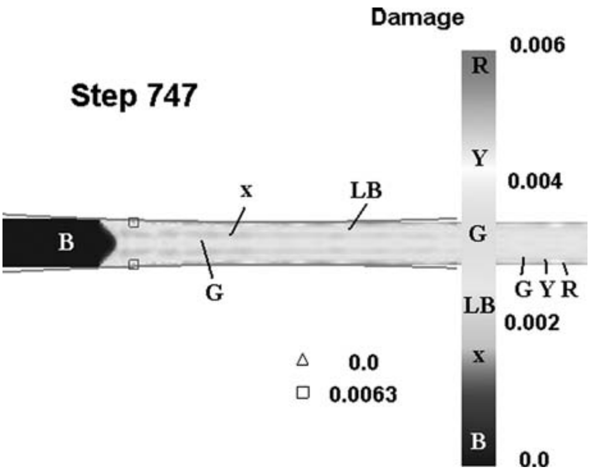

Figure 21.20. Damage distribution predicted in strip rolling.

the workpiece; see Fig. 21.16(a). Likewise, the valleys of the pressure distribution seem to appear adjacent to the workpiece surface at the locations of dead zones. If the pressure distribution given in Fig. 21.19 is compared with the theoretical distribution predicted by eqs. 20-17 to 20-20, good agreement is found between the two (Problem 21.1). This confirms that in the case of strip rolling with roll gap geometry characterized by small Δ (namely, $\Delta = 0.2$), classical theory predicts the contact stress distribution exerted on the roll rather accurately.

21.3.4 Damage Parameter and Maximum Principal Stress

The damage parameter was determined for the actual strip rolling operation, and the obtained results are presented in Fig. 21.20. As this figure shows, the highest damage parameter is obtained in the surface layer of the strip during the rolling operation, but the numerical value of this parameter is much smaller than it was in slab rolling; hence, the risk of cracking should be low. As Fig. 21.21 depicts, there are predicted tensile stress zones in the material before entrance into and after exit from

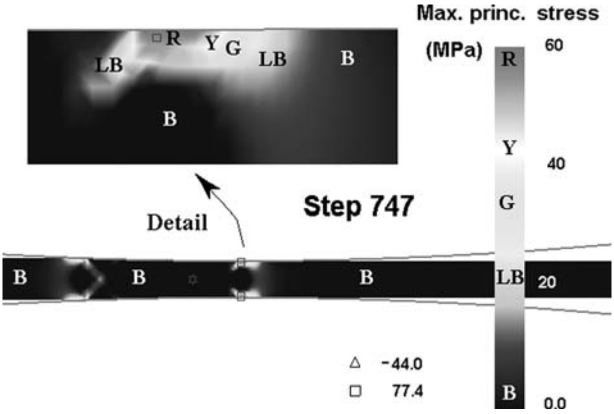

Figure 21.21. Region of high tensile stress close to the surface of the strip, at the entrance to and at the exit from the roll gap.

the roll gap, but they do not contribute significantly to the damage factor, because they appear in regions where the plastic deformation is insignificant.

21.4 Concluding Remarks

The analysis performed here, where three different cases of rolling were considered (namely, a light-reduction pass and a normal-reduction pass in hot slab rolling, and finally a normal-reduction pass in cold strip rolling), shows that the deformations imposed on the workpiece material are very different in the different situations. An important reason the deformations are so different is that the parameter Δ is different in the cases. Whereas in the first case $\Delta = 7.8$, it is reduced by a factor of 2.6 to $\Delta = 3.0$ in the second case, and reduced by a further factor of 15, to $\Delta = 0.2$ in the third case.

In the strip rolling pass, the material is predicted by the FEA to deform homogeneously over the cross section of the strip, so the effective strain imposed on the surface layer approximately equals the effective strain at the center of the strip. This occurs in spite of the presence of multiple deformation crosses in the roll gap, which locally deform the material in a inhomogeneous manner. The reason for this seems to be that the deformations accumulated in the material during flow through the roll gap even out, because all material must flow through a number of deformation crosses and dead zones in the roll gap.

In the two slab rolling passes considered here, however, deformations are predicted to be very nonuniform across the cross section of the rolled slab. The situation is that the surface layer of the slab experiences much larger deformations than does the core. For the normal slab pass conducted with 12.5% area reduction, the effective strain in the core of the slab is predicted to be approximately half that in the surface layer.

In the low-reduction slab pass, where there is only 1.3% area reduction, the surface layer of the slab is predicted to be squeezed backwards in relation to the core of the slab, which is indeed very lightly worked. The surface of the slab is therefore subjected to much higher strains, in the form of shear deformations, than is the core of the slab. It is therefore recommended to avoid use of such light passes, especially in early stages of rolling, while the microstructure still may contain casting defects.

Problem

21.1 The pressure distribution over the roll surface in the roll gap, for the strip rolling process considered in this chapter, was predicted by the FEM model to be as shown by the graph in Fig. 21.19. The data used to create this graph are provided in a separate Excel spreadsheet as pressure values vs. axial distance throughout the roll gap.

(a) The equations presented in Sec. 20.5 express the pressure distribution against the roll, deduced on the basis of theoretical analysis. Use these equations to determine the pressure distribution in this case. For comparison make an overlay plot of the pressure distribution computed by theory and the corresponding results from FEA.

(b) Discuss how well the theoretical pressure distribution agrees with the corresponding distribution obtained in the FEA.

REFERENCE

Bakken, A.: "FEM-modelling as tool for optimisation of cold and hot rolling processes," M.Sc. thesis, Norwegian Institute of Science and Technology (NTNU), 2005 (in Norwegian).

22 Drawing of Wire, Profiles, and Tubes

Wiredrawing was described briefly in Ch. 2.2.6 as a metal forming process in which a wire is reduced in thickness by pulling it through a drawing die shaped as a conical channel. It was also mentioned that drawing can be performed for profiled cross sections also, not only round ones. In addition to this, hollow products like tubes can be manufactured by drawing.

Drawing processes are attractive in that they are cold forming processes, use a stiff die with rather small reduction. Because of this, the forming load on the die is small. Therefore, the dimensional stability is better than if the product were made by alternative processes, like extrusion or rolling. To improve the dimensional accuracy of the cross section of rolled or extruded products, they are sometimes given a final *calibration draw* before final use.

In this chapter, various practical aspects of wiredrawing will first be considered. It will be shown how a thin wire is manufactured by drawing down a thick wire in many steps in a drawing machine. Typical dies used in order to reduce the diameter of the wire will then be described.

It was early figured out that the drawing force is an important parameter in drawing, because higher friction contributes to increase in the required drawing force. A methodology was therefore developed, that allowed friction to be measured directly, using a longitudinally split drawing die. The measuring principle used for this purpose will be described. Finally, it will be shown how a complex drawing force equation can be developed, based on theoretical models, including the slab method and upper bound solutions. The expression for the drawing force obtained this way is useful in that it shows how different drawing parameters affect the required drawing force.

22.1 General about Wiredrawing

The main difference between rod drawing and wiredrawing is that the cross section of the workpiece and, of course, the die, is much larger in rod than in wire; the mechanics are similar. Thick rods are commonly drawn in straight lengths and

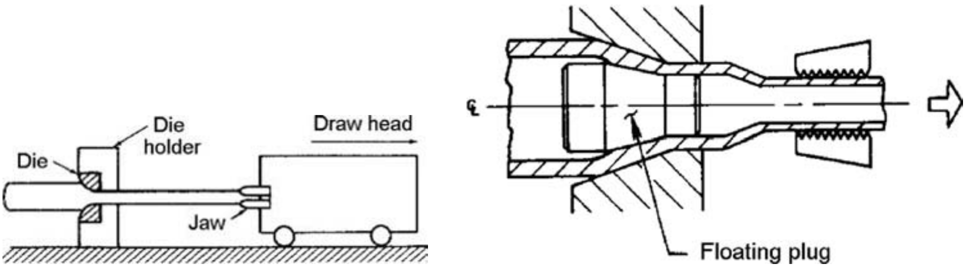

(a) (b)

Figure 22.1. Drawing of (a) thick rod or profile in straight lengths, and (b) tube, using floating internal plug ((a) is reprinted with permission of The McGraw Hill Companies from Dieter, G.: "Mechanical metallurgy," McGraw-Hill, 1986).

therefore require drawing to be performed in one single step at a time. In drawing of thick rods,[1] a gripping device called a *jaw* is used to pull the workpiece through the die; see Fig. 22.1(a). Drawing of profiles differs from rod drawing mainly with regard to the shape of the cross section of the workpiece. In rod drawing the section is circular, whereas in profile drawing it is of complex shape; it can for instance be triangular or rectangular, or of even more complex shape.

Drawing speeds in thick rod and profile drawing are moderate, for each rod or profile has to be pulled in one draw, whereupon the drawing process must be stopped. The next rod or profile has to be threaded into the die and gripped before the start of the next drawing operation. Hence, thick rod and profile drawing are *discontinuous processes*. Thinner rod and profiles, however, can be drawn in a *continuous operation* through a die, whereafter the drawn product is coiled or spooled, the same way as in wiredrawing.

In all drawing processes it is required to *point* the front end of the wire, to allow threading of it into the die, before start of drawing. *Pointing of the end* is done either by machining or by rolling down the cross section of the end piece of the wire. For thin soft wire, pointing can be done manually by pulling the wire while it is bent over the round edge of the handle of pliers.

Tubes can be drawn, following the same principles as for rod and wire.[2] As regards shaping of the inside of a tube, there are three different alternatives: use no internal tooling to shape the inside, use a stationary *mandrel*, or use a *floating plug* inside the tube. Tube drawing with a floating plug is shown in Fig. 22.1(b). In the case of drawing with an internal mandrel, the process is always discontinuous, for the mandrel must be fixed outside the tube, in such a way that it extends throughout the inner hole of the tube. Use of internal tooling, in the form of either a mandrel or a floating plug, is advantageous if good internal dimensional stability is required for the end product.

In wiredrawing, the wire is kept in a coil if thick, and on a spool if thin. Drawing wheels, also called *capstans*, are used to pull the wire through the die. Most commonly the process is run continuously with many drawing steps in succession, and high drawing speeds are used.

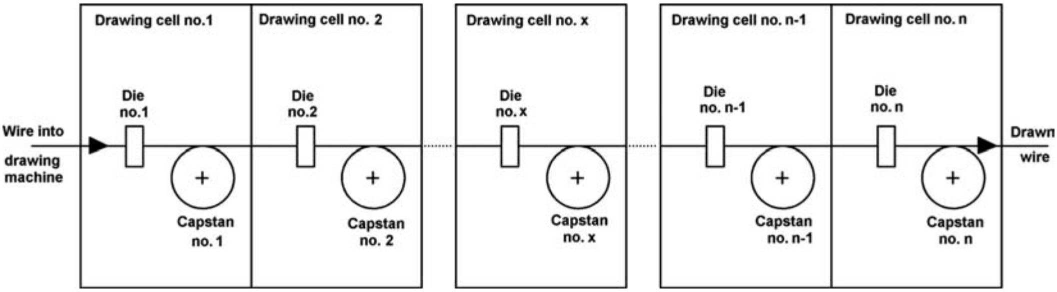

Figure 22.2. Drawing of wire through drawing units placed in sequence.

22.2 Wiredrawing as an Industrial Process

Wiredrawing is an old metal forming technique. It was used, for instance, in ancient Egypt for drawing of gold and silver wires, used in jewelery. The wires were drawn manually through dies made from animal bone.

Modern wiredrawing, however, is a sophisticated production process, where wire is drawn in a continuous operation through many successive dies. The drawing force in each die is provided by a rotating capstan, i.e., a drawing wheel, placed behind that die. To ease drawing, a lubricant is supplied to the wire ahead of the die, for instance, by letting the wire move through a box filled with lubricant. In drawing thin copper wire, it is also common to submerge the whole drawing process, with capstans and dies, in a lubricant bath – to lubricate and to cool the wire – during the drawing operation. Such lubrication is of great importance for the stability of the drawing process. Lubricant enters the interface between the wire and the die, and reduces friction and heat generation. The lubricant also greatly contributes to reduced energy consumption and reduces die wear significantly. For thin wire, the wire is drawn through many dies, or *reduction steps*, perhaps as many as twenty in sequence. As the wire is drawn, it gets thinner and longer, and the wire speed increases correspondingly. A schematic sketch showing drawing in a *continuous drawing machine*, with a number n of *drawing units*, placed in sequence, is shown in Fig. 22.2.

The stock material used in wiredrawing is hot-rolled rod or wire, supplied from a hot-rolling mill, usually in coils. The inlet diameter is commonly 5–15 mm. When wire is manufactured this way in many drawing steps, very thin wire, as for instance 0.4 or 0.1 mm diameter, can be produced at low cost.

Because drawing is performed as a cold-forming process, the material will strain-harden during drawing. Because of this, the ductility of the material will be reduced with additional drawing. So when a small wire dimension has been obtained, it will be difficult to draw it further without *breaks*. It is then required to *soft-anneal* the wire before further drawing. During soft annealing the ductility of the material is restored, and the wire can afterwards be drawn further down. If the wire consists of a material that strain-hardens much, or if the total reduction of the wire in the drawing process is large, it can be necessary to use multiple soft-annealing treatments, with drawing in between.

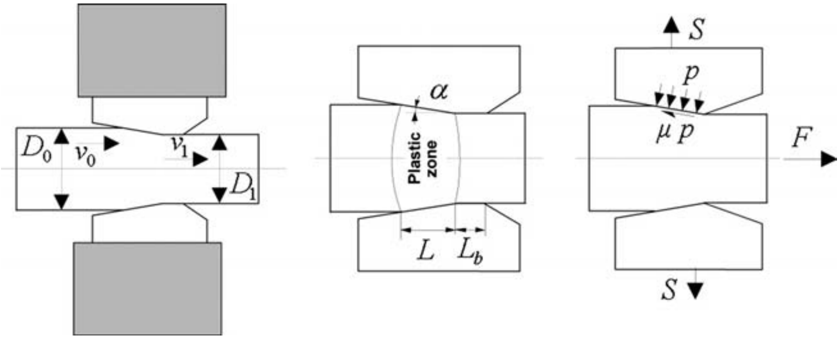

(a) (b) (c)

Figure 22.3. Sketches showing wire passage through the die. Important drawing parameters are shown.

A characteristic wiredrawing die has been sketched in Fig. 22.3(a). This figure shows that the die consists of an *insert* shrink-fitted into an outer steel ring. The die itself is commonly made of a hard metal, such as a *cermet*, or alternatively of *diamond*, both brittle materials. They will perform best if loaded in compression, and this is why they are shrink-fitted into the outer steel ring. Without the compressive stresses provided by this ring, the die material will tend to crack, and eventually fracture. The die life then will be unacceptable, and the wire cannot be drawn economically.

22.3 Drawing Force and Backpull Force in Continuous Wiredrawing

When wire is drawn in continuous processes, it is pulled from a coil, or a spool, under low tension in the first *drawing cell*. Then, in the succeeding drawing cells (see Fig. 22.2), it is pulled off the capstan under low tension. In common wiredrawing terminology this tension is called *backpull*. The load characteristics of the wire, as it moves through a general drawing cell (cell x), are shown in Fig. 22.4. This figure shows the tensile force in the wire as it runs through the drawing machine. Before

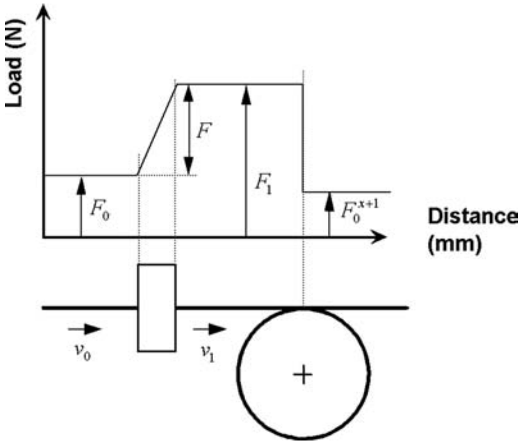

Figure 22.4. Tensile force on the wire in a particular drawing step.

the wire enters the die there is backpull force F_0 on the wire. As the wire is drawn through the die, the drawing force F is exerted on the wire. Because of this, the tensile force in the wire at the outlet side of the die can be expressed as

$$F_1 = F_0 + F \tag{22-1}$$

If drawing is to proceed in a stable manner, it is an absolute requirement that the drawing force must not exceed the breaking force of the wire, F_f, given by the following expression:

$$F_1 = F_0 + F < F_f = R_m A_0 \tag{22-2}$$

In this expression, A_0 is the area of the cross section of the wire, and R_m the tensile strength of the wire in the location behind the die. If the tensile load on the wire equals the fracture load of its material, the wire will be overloaded behind the die and will fracture there.

When the wire is pulled forward by the capstans from one drawing cell to the next, the tensile force must in some or other way be reduced before entrance into the next drawing step. A common way to do this is by letting the capstans rotate with slightly higher surface velocity than the wire. Then friction forces will be transferred from the capstan to the wire in the direction of movement of the wire. When this is done, one says that one runs the drawing machine with *slip of wire* over the capstan. The wire then undergoes a slow backward sliding movement in relation to the capstan surface. In this way, it is possible to reduce the tensile load of the wire to an appropriate level, over the *turns of wire* laid around the capstan. In this manner, the tensile load is lowered on the wire before it enters each drawing step. In the next step, this tensile load will be the backpulling force on the wire ahead of the die. In such drawing machines, it is thus possible, by use of slip over the capstan, to reduce the tensile force on the wire in each drawing step to the appropriate level, before entrance of the wire into the next drawing step. This is done by use of an appropriate number of turns of wire laid around each capstan.

22.4 Geometrical and Mechanical Conditions in a Die

As shown in Fig. 22.3(a), the wire enters the die with speed v_0 and diameter D_0, and leaves it with increased speed v_1 and reduced diameter D_1. The reduction in the drawing step can be determined from the wire dimension into and out of the die, by using eq. 5-5 or eq. 5-6. The velocity out of the die can be computed from the velocity into the die, or vice versa, as was shown for rolling, by the use of eq. 20-2.

To draw the wire through the die, it is required to use a drawing force F. If there is no backpull on the wire in front of the die, this force will also be the force exerted on the wire behind the die.

In Fig. 22.3(a) and (b) is shown a typical industrial wiredrawing die, with a conical converging channel, including a parallel bearing behind. In industrial drawing, it is important to have a parallel bearing to secure constant diameter over the length of the drawn wire. The bearing will contribute somewhat to the necessary drawing force, as there will be friction when the wire is pulled through the bearing.

In theoretical analysis, it is common to analyze the situation when there is no bearing behind the converging channel of the die, as shown in Fig. 22.3(c). This is also the approach chosen in the forthcoming sections, when a formula for the required wiredrawing force is developed. One should, however, be aware that this is not the total drawing force if a die with parallel bearing is used. In that case, an additional force component will be required to overcome the friction when the wire is drawn through the bearing channel.

Whether or not the die has a bearing, the wire material will deform plastically only upon passage through the converging die channel. This means that a distinct region can be identified inside the wire, where there are plastic deformations. This region makes up the *plastic zone* and is shown in the sketch in Fig. 22.3(b). Outside the plastic zone the wire material will be deformed elastically only, as there are no plastic deformations outside this zone. The converging channel of the die has a cone shape with a given cone angle 2α, where α is the half cone die angle; see Fig. 22.3(b). Length measures, such as the cone length L and the length L_b of the die bearing, are also required to describe the drawing geometry of the die completely; see Fig. 22.3(b).

When the wire is pulled through the die, a normal contact pressure p will be exerted by the wire material on the die surface, as shown in Fig. 22.3(c). Because of this pressure, and in addition the sliding of the wire over the surface of the die, a frictional shear stress will exist at the interface between wire and die, as depicted by a shear stress arrow. This shear stress is oriented in the direction opposite to the movement of the wire; see Fig. 22.3(c). In the case of Coulomb friction, the friction shear stress can be expressed as the product of the contact pressure and the coefficient of friction of the interface, i.e., by

$$\tau = \mu p \tag{22-3}$$

Because the friction stress acts opposite to the direction of drawing of the wire, it is clear that the friction stress will contribute to increase the required drawing force in comparison with frictionless drawing. It is therefore also obvious that it is advantageous to use lubrication in wiredrawing to reduce the friction stress on the wire and hence the required drawing force.

22.5 Measurement of Friction Using a Split Die

Consider a drawing experiment, in which a conical die without parallel bearing is used; see Fig. 22.3(c). In addition, assume that the die has been split longitudinally, so it consists of two halves; see the sketch in Fig. 22.5. It is then possible, from a concurrent direct measurement of the die splitting force S and the drawing force F, to determine the coefficient of friction in the actual experiment.[3,4]

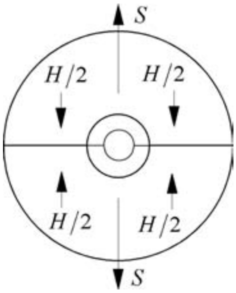

Figure 22.5. Longitudinally split drawing die viewed from the inlet side. The die splitting force and the counterforce are indicated by arrows.

The die-splitting force is transferred from the wire onto half of the die and is denoted by S in Fig. 22.5. It acts in the radial direction of the wire. To determine this force experimentally, it is required to apply a measurable counterforce H on each half of the die. In the beginning of the experiment, the counterforce should exceed the splitting force, so the two halves of the die are kept together. Then the counterforce should gradually be reduced, until one half of the die starts to depart from the other half. At this instant the size of the splitting force equals the applied counterforce while wiredrawing is performed inside the die. The measurement requires a sophisticated experimental setup, but was successfully used by Wistreich[5] to determine the friction in a series of classical wiredrawing experiments.

When this measurement has been conducted, it is possible, by means of a force balance, to develop a set of equations by which the mean normal contact stress and the tangential contact stress transferred through the wire–die interface can be computed; see Example 22.1. The equations obtained this way are

$$\bar{\sigma} = \frac{\dfrac{F}{4\pi} + 4S\cot\alpha}{\cos\alpha\left(1+\cot^2\alpha\right)\cdot\left(D_0^2 - D_1^2\right)} \tag{22-4}$$

$$\bar{\tau} = \frac{\dfrac{F}{4\pi} - 4S\left(\cot^2\alpha - \cot\alpha + 1\right)}{\cos\alpha\,\left(D_0^2 - D_1^2\right)\cdot\left(1+\cot^2\alpha\right)} \tag{22-5}$$

When these contact stresses have been determined in the actual case, the mean coefficient of friction is also easily obtained, by the expression

$$\bar{\mu} = \frac{\tau_i}{\sigma_n} = \frac{\bar{\tau}}{\bar{\sigma}} \tag{22-6}$$

EXAMPLE 22.1: FRICTION FROM SPLIT-DIE WIREDRAWING EXPERIMENT

Problem: Assume that the die-splitting force S and the drawing force F have been measured in a wiredrawing experiment, in a split die with cone angle 2α. Develop the two equations 22-4 and 22-5 for this case.

Solution: The mean stress components transferred from the wire to the die – i.e., the mean contact pressure $\bar{\sigma}$ and the mean shear stress $\bar{\tau}$ – are shown by

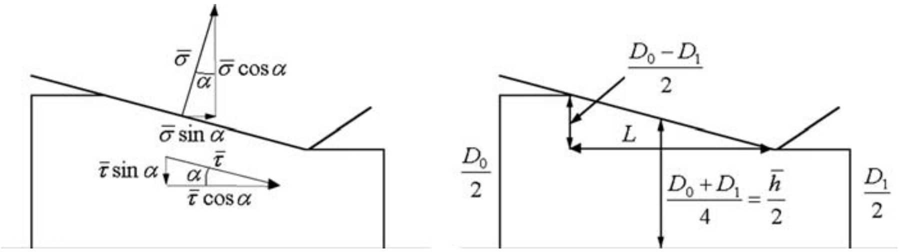

(a) (b)

Figure 22.6. (a) Contact stresses on the die wall decomposed in the axial and the radial direction. (b) Geometrical relations valid in wiredrawing.

arrows in Fig. 22.6(a). To solve the problem, decompose these two stresses into stress components acting in the radial and the axial direction of the wire. Then compute the total mean radial stress $\bar{\sigma}_r$ and the axial stress $\bar{\sigma}_a$ acting on the die:

$$\bar{\sigma}_r = \bar{\sigma}\cos\alpha - \bar{\tau}\sin\alpha$$

$$\bar{\sigma}_a = \bar{\sigma}\sin\alpha + \bar{\tau}\cos\alpha$$

Now consider some geometrical relationships valid in wiredrawing, as shown in Fig. 22.6(b). The radial compressive force on one half of the die, i.e., the die-splitting force, can be expressed as

$$\begin{aligned} S &= \bar{\sigma}_r l \frac{D_0 + D_1}{2} = (\bar{\sigma}\cos\alpha - \bar{\tau}\sin\alpha)\, l \frac{D_0 + D_1}{2} \\ &= \frac{1}{4}\cos\alpha\,(\bar{\sigma}\cot\alpha - \bar{\tau})\cdot\left(D_0^2 - D_1^2\right) \end{aligned} \tag{22-7}$$

The resultant of the axial stress components acting on the die wall yields the following drawing force:

$$\begin{aligned} F &= \bar{\sigma}_a \pi \left(\frac{D_0 + D_1}{2}\right)\left(\frac{l}{\cos\alpha}\right) \\ &= (\bar{\sigma}\sin\alpha + \bar{\tau}\cos\alpha)\pi\left(\frac{D_0 + D_1}{2}\right)\left(\frac{D_0 - D_1}{2}\right)\frac{1}{\tan\alpha}\left(\frac{1}{\cos\alpha}\right) \\ F &= \frac{1}{4}\pi(\bar{\sigma} + \bar{\tau}\cot\alpha)(D_0^2 - D_1^2) \end{aligned} \tag{22-8}$$

When the two forces F and S are known from measurement, the mean contact stresses on the die can be found from these two equations. The final result obtained when this is done is presented in the text as eq. 22-4 and eq. 22-5.

EXAMPLE 22.2: THE REDUCTION AND THE PARAMETER Δ IN WIREDRAWING

Problem: Assume a die with cone angle 2α, and inlet and outlet wire dimensions D_0 and D_1.

(a) Determine an expression for Δ for this wiredrawing die, if deformations are assumed to be localized inside the die cone.

(b) Wire is to be drawn in a die under the following conditions: (1) $2\alpha = 8.02^\circ$, $D_0 = 3.43\,\text{mm}$, and $D_1 = 2.54\,\text{mm}$, and (2) $2\alpha = 15.47^\circ$, $D_0 = 3.01\,\text{mm}$, and $D_1 = 2.54\,\text{mm}$. Calculate the reduction of area and the parameter Δ in the two cases.

Solution:

(a) The parameter Δ was defined in eq. 5-13 as the ratio between the height and the width of the plastic zone. From Fig. 22.6(b), it is seen that it is reasonable to define Δ in wiredrawing as the ratio between the mean diameter of the wire inside the drawing cone, $\bar{D}$, and the length of the same cone, L:

$$\Delta = \frac{h}{L} = \frac{\bar{D}}{L} = \frac{\dfrac{D_0 + D_1}{2}}{\dfrac{D_0 - D_1}{2\tan\alpha}} = \frac{D_0 + D_1}{D_0 - D_1}\tan\alpha$$

(b) The area reduction was defined in eq. 5-5. For wiredrawing, it can be expressed as

$$r = \frac{A_0 - A_1}{A_0} = \frac{\pi\left(\dfrac{D_0}{2}\right)^2 - \pi\left(\dfrac{D_1}{2}\right)^2}{\pi\left(\dfrac{D_0}{2}\right)^2} = \frac{(D_0)^2 - (D_1)^2}{(D_0)^2}$$

$$= 1 - \left(\frac{D_1}{D_0}\right)^2$$

When we insert the given values into these two equations, we get:

Condition 1:

$$r = 1 - \left(\frac{D_1}{D_0}\right)^2 = 1 - \left(\frac{2.54\,\text{mm}}{3.43\,\text{mm}}\right)^2 = \underline{\underline{0.452}}$$

$$\Delta = \frac{D_0 + D_1}{D_0 - D_1}\tan\alpha = \frac{3.43\,\text{mm} + 2.54\,\text{mm}}{3.43\,\text{mm} - 2.54\,\text{mm}}\tan\frac{8.02^\circ}{2} = \underline{\underline{0.945}}$$

Condition 2:

$$r = 1 - \left(\frac{2.54\,\text{mm}}{3.01\,\text{mm}}\right)^2 = \underline{\underline{0.288}}$$

$$\Delta = \frac{3.01\,\text{mm} + 2.54\,\text{mm}}{3.01\,\text{mm} - 2.54\,\text{mm}}\tan\frac{15.47^\circ}{2} = \underline{\underline{3.268}}$$

22.6 Siebel's Drawing Force Equation

An equation that expresses the force required to draw a metal wire through a conical converging die was developed quite early by the German scientist Siebel.[2,6] The equation is useful in that it states how the main process parameters in wiredrawing contribute to the drawing force. The procedure used to develop this equation is analogous to that used when the extrusion force equation is developed; see eq. 18-20.

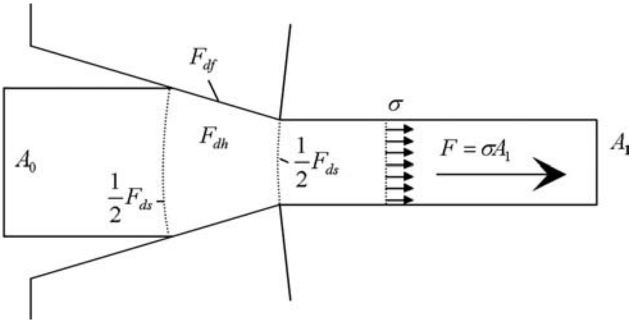

Figure 22.7. Sketch showing the different contributions to the drawing force.

To arrive at an expression for the drawing force in wiredrawing, it is common to split this force into three additive parts:

$$F = F_{dh} + F_{df} + F_{ds} \tag{22-9}$$

As in extrusion, the first force component is denoted by the index *dh*. The abbreviation stands for "die homogeneous" and means the force component on the die required to deform the wire homogeneously upon passage through the die. In addition, there is the second force component labeled *df*, which refers to "die friction." It is the force required to overcome friction when the wire moves through the die. Finally, there is the third force component acting on the die, labeled *ds*, which stands for "die shear." It is the drawing force required to produce shear deformations in the wire material as it flows through the die. The shear is due to inhomogeneous deformation upon passage of the wire through the velocity discontinuities, both at the entrance into and at the exit from the plastic zone inside the die. The origin inside the wire of each of these three components contributing to the drawing force is visualized in the sketch in Fig. 22.7.

Now consider wiredrawing without backpull on the wire, i.e., assume F_0 in eq. 22-1 to be equal to zero. The drawing force on the wire behind the die then will equal $F = F_1$. Hence, the symbol F is used from now on for the drawing force. This force manifests itself as a tension on the wire behind the die. This tension must not exceed the tensile strength of the material, if drawing is to be stable. In the literature, the tensile strength is often denoted R_m, or sometimes σ_{TS}:

$$\sigma = \frac{F}{A_1} < R_m = \sigma_{TS} \tag{22-10}$$

This equation states that if the tension on the wire behind the die is increased to a value equal to the tensile strength of the wire, the wire will fracture, and wiredrawing cannot continue. Most commonly, the material used in wiredrawing will have good ductility. If the wire becomes overloaded during drawing, it will start to neck. The neck will grow and soon develop into a fracture, as in tensile testing. When a wire break occurs this way, further wire processing is impossible. Then the wire must be pointed and rethreaded through the dies in the drawing machine, and wire turns must be laid over the capstans of the die, before the process can be started again.

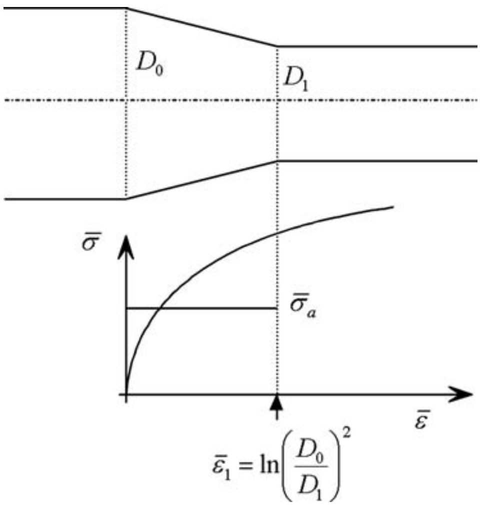

Figure 22.8. Flow stress variation upon flow through the deformation zone for a strain-hardening material.

To arrive at an expression for the drawing force in terms of the three force components defined in eq. 22-9, it is necessary to compute the energy consumed in the wiredrawing process. The drawing force can then be computed from the energy used. Let us consider the required energy consumption in drawing. It consists of three parts, corresponding to those already specified for the drawing force; see eq. 22-9. Now the following equation can be set up:

$$W = W_{dh} + W_{df} + W_{ds} \tag{22-11}$$

22.6.1 Energy Consumption Due to Homogeneous Deformation

The term W_{dh} in eq. 22-11 can be determined easily by means of an upper bound solution, corresponding to the first term in eq. 13–14:

$$W_{dh} = \int_V \bar{\sigma}\bar{\varepsilon}\,\mathrm{d}V = \bar{\sigma}\bar{\varepsilon}V = \bar{\sigma}V\ln\frac{A_0}{A_1} = V\bar{\sigma}_a\ln\frac{A_0}{A_1} \tag{22-12}$$

The expression is valid for a non-strain-hardening rigid–plastic material for which the flow stress remains constant during the drawing operation. However, because wiredrawing normally is started with the wire at room temperature, it is classified as a cold-forming process. The most commonly used wire materials exhibit strain hardening upon drawing. It is therefore common to include the effect of strain hardening on the drawing force, by introducing the mean strain-hardened flow stress value $\bar{\sigma}_a$. For a material that strain-hardens in accordance with the power law, this is done as follows (see Fig. 22.8):

$$\bar{\sigma}_a \cdot \varepsilon = \int_0^{\varepsilon} \bar{\sigma}\,\mathrm{d}\bar{\varepsilon} = \int_0^{\varepsilon} K\bar{\varepsilon}^n \mathrm{d}\bar{\varepsilon} = \frac{K}{n+1}\bar{\varepsilon}^{n+1} \quad \Rightarrow \quad \bar{\sigma}_a = \frac{K}{n+1}\bar{\varepsilon} \tag{22-13}$$

In this equation $\bar{\varepsilon} = \bar{\varepsilon}_1$ is the strain experienced by the material upon passage through the die; see Fig. 22.8. An alternative approach is to determine the mean flow stress, as half the sum of the flow stress values at the inlet, $\bar{\sigma}_i$ and at the

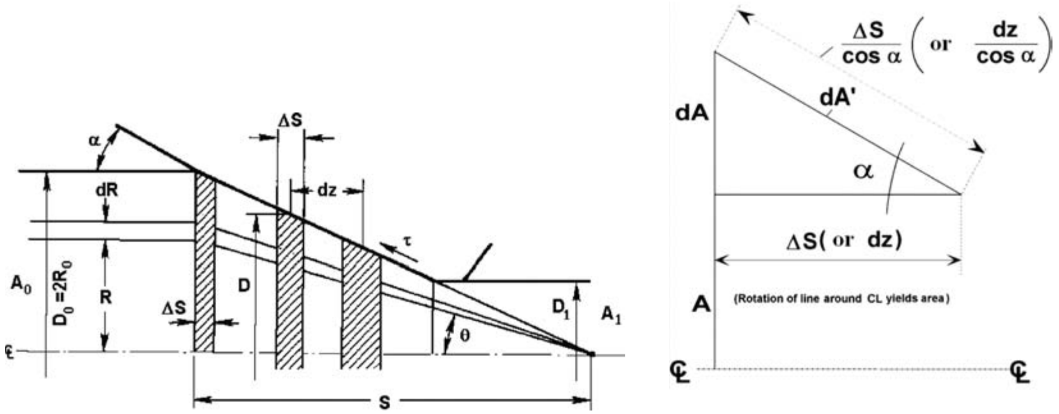
α
ΔS
dR
dz
τ
A₀
D₀ =2R₀
R
ΔS
D
D₁
A₁
θ
S
ΔS / cos α (or dz / cos α)
dA
dA'
α
ΔS(or dz)
A
(Rotation of line around CL yields area)

(a) (b)

Figure 22.9. (a) Flow of disc-shaped element through the plastic zone in a drawing die. (b) Geometrical relationship in the die.[2] ((a) is reprinted with permission of ASM International. All rights reserved. www.asminternational.org.)

outlet, $\bar{\sigma}_o$. When this approach is used, the average flow stress can be expressed by the equation

$$\bar{\sigma}_a = \frac{\bar{\sigma}_i + \bar{\sigma}_o}{2} \tag{22-14}$$

22.6.2 Energy Consumption Due to Friction against the Die

The energy consumption due to sliding friction, during passage of the wire through the die, can be determined by an upper bound solution. Consider a vertical disc of wire material of thickness ΔS, sliding through the deformation cone of the die, as shown in Fig. 22.9(a).

When the disc has advanced into the cone to a location where its mean diameter is D, the contact length of the disc against the die wall will equal $\Delta S/\cos\alpha$. The contact area between the disc and the die then equals $\pi D \Delta S/\cos\alpha$; see the sketch in Fig. 22.9(b). If we assume that the disc element slides the length dz in the drawing direction inside the deformation zone, the sliding length will equal d$z/\cos\alpha$. The energy dissipation will then be

$$\mathrm{d}W_F = \tau_f \cdot (\text{contact area}) \cdot (\text{sliding length}) = \tau_f \cdot \pi D \frac{\Delta S}{\cos\alpha} \cdot \frac{\mathrm{d}z}{\cos\alpha} \tag{22-15}$$

Rewriting this expression gives the following equation:

$$\mathrm{d}W_F = \tau_f \cdot \pi D \frac{\mathrm{d}z}{\cos\alpha} \cdot \frac{\Delta S}{\cos\alpha} = \tau_f \cdot (\text{sliding surface}) \cdot \frac{\text{element thickness}}{\cos\alpha} \tag{22-16}$$

The sliding surface has been visualized in Fig. 22.9(b) as $\mathrm{d}A' = \pi D \,\mathrm{d}z/\cos\alpha$. The component of this sliding surface, directed normal to the wire movement, is

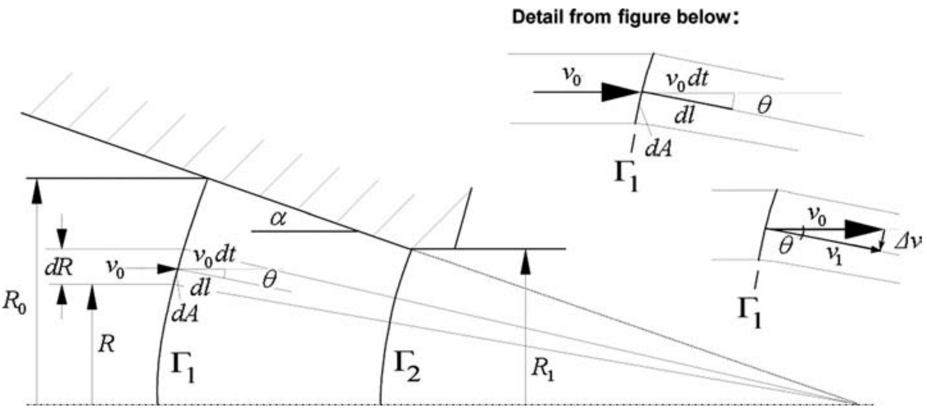

Figure 22.10. Shear deformation of the wire material upon flow through the velocity discontinuity surface Γ_1 at the inlet to the die cone.

shown in the same figure as

$$\mathrm{d}A = \mathrm{d}A' \sin\alpha \quad \Rightarrow \quad \mathrm{d}A' = \frac{\mathrm{d}A}{\sin\alpha}$$

In addition, the following expression is valid: $\Delta S = \Delta V / A$, where ΔV represents a volume element of wire material.

Equation 22-16 now can be rewritten as

$$\mathrm{d}W_F = \tau_f \cdot \pi D \frac{\mathrm{d}z}{\cos\alpha} \cdot \frac{\Delta S}{\cos\alpha} = \tau_f \cdot \mathrm{d}A' \cdot \frac{\Delta V}{A\cos\alpha} = \tau_f \cdot \frac{\mathrm{d}A}{\sin\alpha} \cdot \frac{\Delta V}{A\cos\alpha}$$
$$= \frac{\tau_f \Delta V}{\sin\alpha\cos\alpha} \cdot \frac{\mathrm{d}A}{A}$$

Integration yields

$$W_{df} = \int_{A_1}^{A_0} \frac{\tau_f \Delta V}{\sin\alpha\cos\alpha} \cdot \frac{\mathrm{d}A}{A} = \frac{\tau_f \Delta V}{\sin\alpha\cos\alpha} \int_{A_1}^{A_0} \frac{\mathrm{d}A}{A} = \frac{\tau_f \Delta V}{\sin\alpha\cos\alpha} \ln\frac{A_0}{A_1}$$
$$= \frac{\tau_f \ln\frac{A_0}{A_1}}{\sin\alpha\cos\alpha} \int_0^V \Delta V = \frac{\tau_f \ln\frac{A_0}{A_1} V}{\sin\alpha\cos\alpha}$$

If the angle α is small, the approximations $\sin\alpha \approx \alpha$ (radians) and $\cos\alpha = 1$ are valid. The equation then can be simplified to the following expression:

$$W_{df} = \frac{\tau_f}{\alpha} \ln\frac{A_0}{A_1} V \qquad (22\text{-}17)$$

22.6.3 Energy Consumption Due to Shear at the Velocity Discontinuities

The energy consumption due to shear deformations when the wire material flows through the velocity discontinuity at the inlet to the die cone, i.e., through the boundary surface Γ_1 in Fig. 22.10, can be computed for an area element $\mathrm{d}A$ on the boundary surface. This is done by use of eq. 13-17, in which the velocity difference at the present velocity discontinuity is introduced (see Fig. 22.10):

$$\dot{W}_S = \int_A k \cdot |\Delta v| \mathrm{d}A \quad \Rightarrow \quad \mathrm{d}W_S = k \cdot v_0 \sin\theta \, \mathrm{d}A \, \mathrm{d}t \tag{22-18}$$

This expression can further be developed into

$$\mathrm{d}W_S = k \cdot v_0 \, \mathrm{d}t \cdot \sin\theta \, \mathrm{d}A = k \cdot \frac{\mathrm{d}l}{\cos\theta} \cdot \sin\theta \, \mathrm{d}A = k \tan\theta \, \mathrm{d}l \, \mathrm{d}A = k \tan\theta \, \mathrm{d}V \tag{22-19}$$

The quantities $v_0\mathrm{d}t$ and $\mathrm{d}l$ represent the displacements of the wire into the deformation cone of the die, as shown in Fig. 22.10. Here $\mathrm{d}V$ represents the volume of material flowing through the area element $\mathrm{d}A$ during the time $\mathrm{d}t$.

Assume the wire to be made of a von Mises material having the flow stress $\bar{\sigma}_0$ at the inlet to the die. Then the following substitutions can be made in eq. 22–19:

$$k = \frac{\bar{\sigma}_0}{\sqrt{3}}, \qquad \mathrm{d}V = 2\pi R \, \mathrm{d}R \, \Delta S$$

In the latter expression, ΔS denotes the thickness of a disc of material at the inlet to the die, as shown in Fig. 22.9(a). For small angles α and θ, the following approximations can be made:

$$\tan\theta \approx \theta \approx \frac{R}{S}, \qquad \tan\alpha \approx \alpha \approx \frac{R_0}{S} = \frac{D_0}{2S}$$

In this expression, S denotes the whole length of the deformation cone; see Fig. 22.9(a). Equation 22-19 now can be transformed into the expression

$$\begin{aligned} \Delta W_S &= \int_0^{R_0} k \tan\theta \, \mathrm{d}V = k \int_0^{R_0} \frac{R}{S} 2\pi \, R \mathrm{d}R \Delta S = k \, 2\pi \frac{\Delta S}{S} \int_0^{R_0} R^2 \mathrm{d}R \\ &= k \, 2\pi \frac{\Delta S}{S} \frac{1}{3} R_0^3 = \frac{2}{3} k \frac{R_0}{S} \pi \, R_0^2 \, \Delta S = \frac{2}{3} \frac{\bar{\sigma}_0}{\sqrt{3}} \alpha \, \Delta V \end{aligned} \tag{22-20}$$

Here ΔV represents the material volume flowing through the deformation zone in the time step $\mathrm{d}t$. A total volume of wire material, V, flowing through the velocity discontinuity surface, yields the energy dissipation:

$$W_S^{\Gamma_1} = \Delta W_S \frac{V}{\Delta V} = \frac{2}{3} \frac{\bar{\sigma}_0}{\sqrt{3}} \alpha \, \Delta V \cdot \frac{V}{\Delta V} = \frac{2}{3} \frac{\bar{\sigma}_0}{\sqrt{3}} \alpha V \tag{22-21}$$

A corresponding calculation of energy dissipation can be done for the same volume of material when it flows through the velocity discontinuity line at the exit side of the die, i.e., Γ_2. This energy dissipation is equal to that during flow through the first discontinuity line, except for the effect of strain hardening of the material. On its way through the plastic zone the material has strain-hardened up to a flow stress $\bar{\sigma}_1$. Hence, the total energy dissipation due to shearing when the material volume V flows through the die will be

$$W^{\Gamma_1+\Gamma_2} = W_S = \frac{2}{3\sqrt{3}} \alpha V \left(\bar{\sigma}_0 + \bar{\sigma}_1\right) \tag{22-22}$$

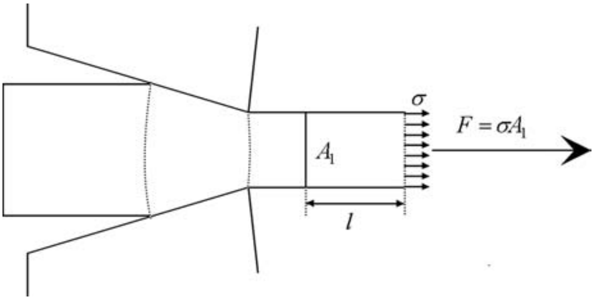

Figure 22.11. Drawing of a piece of wire of length l.

In case of a non-strain-hardening material with constant flow stress $\bar{\sigma}$, the equation takes the form

$$W_S^{\Gamma_1+\Gamma_2} = W_{ds} = \frac{4}{3\sqrt{3}}\alpha V\bar{\sigma} \tag{22-23}$$

22.6.4 The Force Equation in Wiredrawing

In the previous treatment, three different contributions to the energy consumption were calculated. If we sum these contributions, we get the total energy consumed during the wiredrawing process, which can be expressed as

$$W = W_{dh} + W_{df} + W_{ds} = V\bar{\sigma}\ln\frac{A_0}{A_1} + \frac{\tau_f V}{\alpha}\ln\frac{A_0}{A_1} + \frac{4}{3\sqrt{3}}\alpha\bar{\sigma}V \tag{22-24}$$

As depicted in Fig. 22.11, the energy consumption when the length l of wire is pulled through the die can also be expressed:

$$W = Fl = \sigma A_1 l = \sigma V \tag{22-25}$$

Setting the two equations 22-24 and 22-25 equal gives the following expression:

$$W = Fl = \sigma V = V\bar{\sigma}\ln\frac{A_0}{A_1} + \frac{\tau_f V}{\alpha}\ln\frac{A_0}{A_1} + \frac{4}{3\sqrt{3}}\alpha\bar{\sigma}V \tag{22-26}$$

Now the drawing force F, or the axial tension in the wire behind the drawing die, σ, can be determined. The expression obtained for the axial tension in the wire is

$$\sigma = \bar{\sigma}\ln\frac{A_0}{A_1} + \frac{\tau_f}{\alpha}\ln\frac{A_0}{A_1} + \frac{4}{3\sqrt{3}}\alpha\bar{\sigma} \tag{22-27}$$

To arrive at a final equation for the drawing force (the wire tension in drawing), it is required to replace the friction stress term, τ_f in eq. 22-27, by parameters easier to determine. When this is done, there are two options:

(1) Friction obeys the Tresca friction model, and the flow stress of the material conforms to the von Mises flow criterion. In this case, the shear stress against the drawing die can be expressed by eq. 10-8, i.e., by

$$\tau_f = \frac{m\bar{\sigma}}{\sqrt{3}}$$

Substituting τ_f in eq. 22-27 and then solving for the drawing force yields

$$F = \sigma A_1 = \left(\bar{\sigma} \ln \frac{A_0}{A_1} + \frac{m\bar{\sigma}}{\sqrt{3}\alpha} \ln \frac{A_0}{A_1} + \frac{4}{3\sqrt{3}}\alpha\bar{\sigma}\right) A_1 \tag{22-28}$$

(2) Friction obeys the Coulomb friction model, and the flow stress of the material conforms to the Tresca flow criterion. Then the shear stress of the material can be expressed as

$$k = \frac{\bar{\sigma}}{2}$$

This modifies the term calculated in eq. 22-20. Let us also assume the wire material to be rigid–plastic without strain hardening, so the material has constant flow stress $\bar{\sigma}$. Then eq. 22-27 instead can be expressed as

$$\sigma = \bar{\sigma} \ln \frac{A_0}{A_1} + \frac{\tau_f}{\alpha} \ln \frac{A_0}{A_1} + \frac{2}{3}\alpha\bar{\sigma} \tag{22-29}$$

In the case of Coulomb friction, the shear stress against the die wall can be expressed by

$$\tau_f = \mu p = \mu\sigma$$

In this expression, σ is the normal stress transferred from the wire onto the die wall. For small angles α, this stress approximately equals the flow stress of the wire material:

$$\tau_f = \mu\sigma = \mu\bar{\sigma}$$

The tension on the wire due to drawing, and thus the drawing force, then will be given by

$$\sigma = \bar{\sigma} \ln \frac{A_0}{A_1} + \frac{\mu\bar{\sigma}}{\alpha} \ln \frac{A_0}{A_1} + \frac{2}{3}\alpha\bar{\sigma} \tag{22-30}$$

and

$$F = A_1\sigma = A_1\left(\bar{\sigma} \ln \frac{A_0}{A_1} + \frac{\mu\bar{\sigma}}{\alpha} \ln \frac{A_0}{A_1} + \frac{2}{3}\alpha\bar{\sigma}\right) \tag{22-31}$$

The latter equation is commonly called *Siebel's drawing force equation*, after the scientist who first developed it. If the wire material strain-hardens, the flow stress $\bar{\sigma}$ in the equation can be replaced by the mean flow stress of the material in the drawing cone, expressed by eq. 22-13.

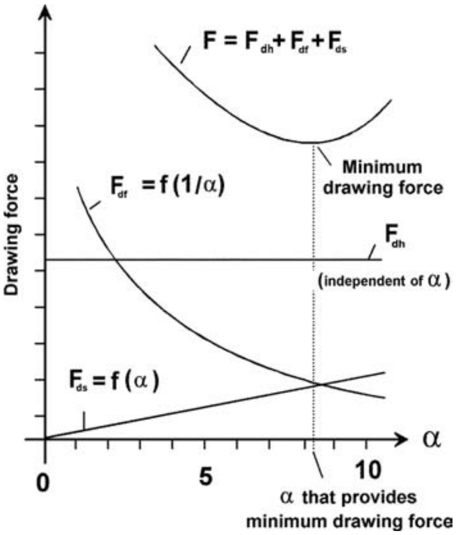

Figure 22.12. Sketch showing variation in each contribution to the drawing force, and in the total drawing force, when the die angle is changed.

22.7 The Optimum Die Angle in Wiredrawing

Siebel's drawing force equation as expressed in eq. 22-31 shows that the drawing force is a function of the applied die angle. The variation in the drawing force upon change of this die angle can be presented graphically as shown in Fig. 22.12. In this diagram, the total drawing force and each force component are plotted as separate graphs.

As the figure depicts, the force component due to homogeneous deformation is independent of the applied die angle, whereas the component due to inhomogeneous deformation increases linearly with increasing angle. Finally, there is the component due to friction, which is inversely proportional to the die angle and hence decreases with increasing die angle.

The sum of the three components is initially high for low values of the angle but drops rapidly when the angle is increased. Then it reaches a minimum value where after it increases when the angle is further increased. In practical cases of wiredrawing, it is therefore advantageous to choose a die angle that provides a force close to the minimum drawing force. This angle is commonly termed the *optimum die angle* in wiredrawing terminology.

The optimum die angle can be determined from Siebel's drawing force equation, by differentiating this expression (eq. 22-31), with respect to the half die cone angle, and then setting the result equal to zero. This procedure provides the following formula:

$$\alpha_{\text{opt.}} = \sqrt{\frac{3}{2}\mu \ln \frac{A_0}{A_1}} \tag{22-32}$$

Experimental drawing force data[7] obtained in copper wiredrawing are shown in Fig. 22.13. As the data show, the optimum half die angle of the drawing cone also

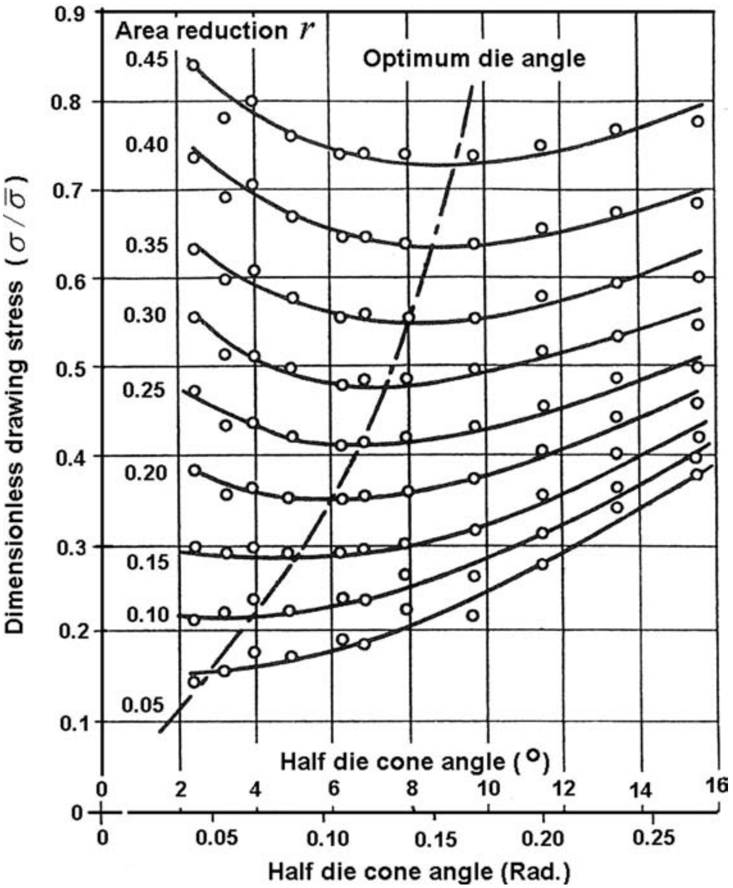

Figure 22.13. Experimental data[5] showing that the optimum die angle in wiredrawing depends on the reduction in the die.

depends on the reduction of area in the die. The optimum angle is 4° at a low reduction 5%, and increases to 10° at a high reduction (40%).

Problems

22.1 Consider wiredrawing with initial wire diameter 2.85 mm and final diameter 2.54 mm. The half die cone angle is 8°. Assume that the numerical values for the die-splitting and the drawing force have been measured as $S = 3670\,\mathrm{N}$ and $F = 627\,\mathrm{N}$.

(a) Calculate the area reduction used in the die and the Δ-parameter.
(b) Calculate the mean contact stress components on the die and the mean coefficient of friction.

22.2 Soft-annealed copper wire of 2.5 mm diameter was drawn down to 2.18 mm diameter wire in a die. The force component due to inhomogeneous deformation was determined to be 30 N. The die had a conical inlet and no parallel bearing. Assume the friction coefficient to be $\mu = 0.05$.

(a) Find the required drawing force for the process by use of Siebel's drawing force equation. Assume the flow stress to be given by $\sigma = 160\varepsilon^{0.3}$ MPa.

(b) Discuss the different components that contribute to the total drawing force.

(c) Determine the optimum die cone angle for this wiredrawing operation.

NOTES

1. Dieter, G.: "Mechanical Metallurgy," McGraw-Hill Book Company, 1987, p. 636.
2. Altan, T., Oh, S.-I., and Gegel, H. L.: "Metal Forming, Fundamentals and Applications," ASM Int., 1983, pp. 277–293.
3. MacLellan, G. D. S.: "A critical survey of wire-drawing theory," J. Iron and Steel Instituta, 1948, pp. 347–356.
4. MacLellan, G. D. S.: "Some friction effects in wiredrawing," J. Institute of Metals, Vol. 81, 1952–53, pp. 1–13.
5. Wistreich J. G.: "Investigation of the mechanics of wire drawing," Proc. Institute of Mechanical Engineers, 169, 1955, pp. 654–665.
6. Lange, Kurt (Ed.): "Handbook of Metal Forming," McGraw-Hill, p. 13.20.
7. Wistreich, J. G.: "The fundamentals of wiredrawing," Metallurgical Rev., Vol. 3, 1958, pp. 97–142.

23 FEA of Wiredrawing

When the author of this book was a small child, Wistreich[1] performed extensive experimental work in which he studied steel and copper wiredrawing. In this connection, he applied longitudinally split dies and measured both the drawing force and the die-splitting force in the drawing operation. From the measured data, he calculated the mean contact stresses on the die wall, by means of the formulas presented in the Sec. 22.5. From the contact stresses, he finally determined the mean coefficient of friction for the various drawing geometries used in his investigation. In the following, more details about Wistreich's copper wiredrawing experiments will be presented. In addition, some of his experiments will be reproduced in FEA to characterize the mechanics of these approximately 50-year-old experiments. As will be shown, the mechanics of wiredrawing are complex and are changed a lot when the drawing geometry is altered by changing the parameter Δ and the reduction of area in the die.

In Wistreich's experiments, the die geometry was varied by varying two parameters: the cone angle and the reduction of area in the die. A large number of experiments were run, and many different die geometries were tested. The die half cone angle was varied from $\approx 3^\circ$ up to $\approx 15.5^\circ$, and the reduction of area correspondingly from 0.05 to 0.45. Nine of Wistreich's experiments were later reproduced by FEA,[2] and an additional case corresponding to normal drawing will be considered here. To visualize the variation in the geometrical conditions in Wistreich's test series, the diagram in Fig. 23.1 has been made. In this diagram, the half cone die angle is plotted vs. reduction of area in each case. Hence, in this diagram, an experiment will appear as a point. The results of Wistreich's experiments[2] that were reproduced by FEA are denoted by S1 to S10 in Fig. 23.1.

As Fig. 23.1 depicts, the geometrical conditions in these experiments vary far beyond those common in industrial wiredrawing. Depending upon the wire material, the half die cone angle in a normal industrial wiredrawing process typically will be 8°, and the reduction of area will lie in the range 0.15–0.20. The experiment denoted S10 in the diagram thus represents a normal industrial drawing geometry and will therefore be subjected to an in-depth analysis using FEM simulation.

Table 23.1. *Wiredrawing operations to be analyzed by FEM simulation*

Case of drawing	Wire dimension (mm)		Reduction of area	Half cone die angle (deg)	Δ	Coefficient of friction
	Inlet	Outlet				
S7	2.65	2.54	0.08	15.5	12.6	0.032
S10 (normal)	2.85	2.54	0.2	8	2.4	0.028
S3	3.43	2.54	0.44	2.3	0.3	0.017

In addition, the two cases denoted S7 and S3 will be analyzed in more detail also, because the deformations in these cases differ considerably from the usual ones.

The drawing parameters in the experiments, other than die angle and reduction, are specified in Wistreich's article[1]; the wire material consisted of electrolytic copper, which prior to the experiments had been drawn down to different thicknesses, whereafter it had been soft-annealed. The inlet wire dimension in each die was always such that, after each experiment, a wire diameter of 2.54 mm was obtained. The wire was lubricated by dipping it in a solution of sodium stearate in methyl alcohol, and was afterwards dried in air. The dies consisted of steel, and the drawing speed was always 1.83 mm min^{-1}. The flow curve of the copper wire was determined by Wistreich by means of tensile testing.

The characteristic drawing conditions in each of the three cases of wiredrawing to be considered here are listed in Table 23.1.

23.1 Drawing with Small Reduction and Large Half Cone Die Angle

To reproduce experiment S7 by FEA, half of the FEM model shown in Fig. 23.2 was built. Figure 23.2(a) depicts the initial state of wiredrawing in the simulation model, and Fig. 23.2(b) the end stage. The wire was initially assumed to be pointed with the same cone shape as that of the die cone, and threaded into the die. In the final stage of simulation, a sufficient length of wire had been drawn through the die to establish steady-state conditions.

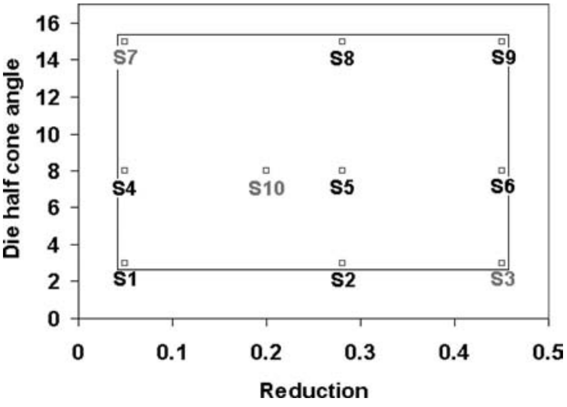

Figure 23.1. Drawing parameters applied in Wistreich's experiments. Experiments S1–S10 have been reproduced in FEA.[2] Experiments S3, S7, and S10 are considered here.

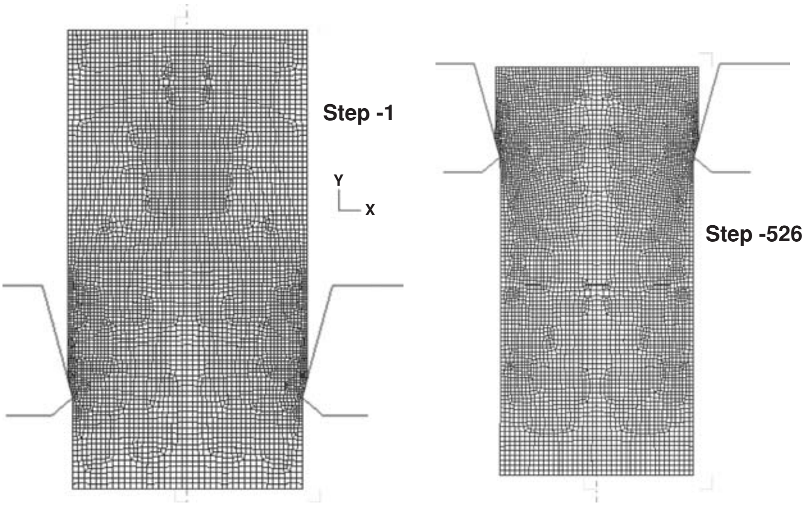

(a) (b)

Figure 23.2. Mirrored FEM model of copper wiredrawing.

The boundary condition at the pointed end of the wire was specified as zero velocity in the axial direction. This means the end remained fixed, while the die was given an upward velocity equal that used in Wistreich's experiment. The flow stress of the material in the FEM model was described by the relationship $\sigma = (125\varepsilon + 360)$ MPa, obtained by fitting to the flow curve given in Wistreich's article. The die was assumed rigid, and the workpiece material ideally rigid–plastic. Thermal effects were neglected in the analysis, i.e., the process was modeled as isothermal. Half of the wire and the die were modeled. When full longitudinal sections of wire and die are shown, they have been created by use of the mirroring option in the FEM program.

23.1.1 Deformations

In the particular case S7 of wiredrawing, the reduction of area of the wire is small, and the half cone angle large. Because of this, the parameter Δ is also large: $\Delta = 12.6$. The appearance of the plastic zone, as predicted by the distribution of the effective strain rate computed by the FEM model, for this case is shown in Fig. 23.3.

There is close resemblance between Fig. 23.3(b), which represents wiredrawing, and Fig. 21.2(b), which represents plane strain rolling, both characterized by use of small reduction in the forming step, and therefore a large Δ. As Fig. 23.3 depicts, the deformation rate in the core of the wire lies in the range $\approx$5–7 s^{-1} and is much lower than the corresponding strain rate toward the surface layer of the wire, which is > 9 s^{-1}. Locally, close to the die surface, it is much higher and the maximum predicted effective strain rate reaches 168–198 s^{-1}.

In this case of wiredrawing, as shown in Fig. 23.3(a) and (b), the high-strain-rate region near the surface of the wire extends into the material ahead of the die

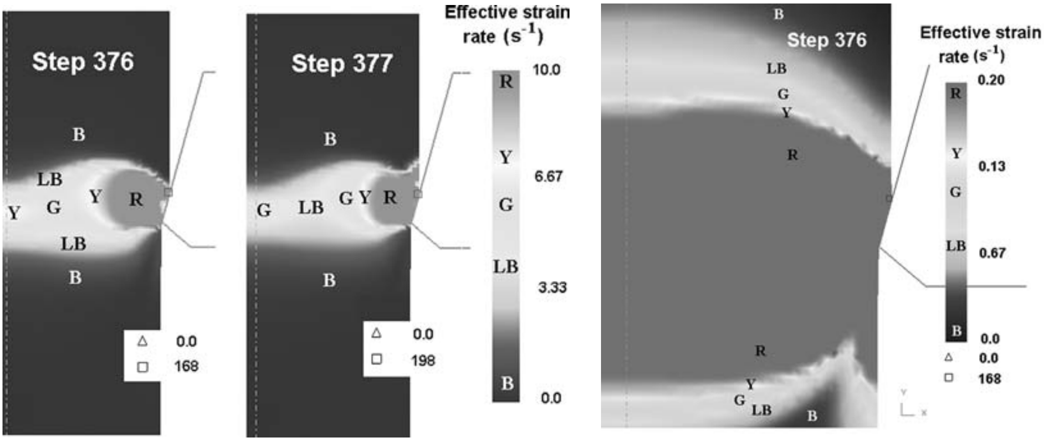

(a) (b) (c)

Figure 23.3. Appearance of the plastic zone in drawing with small reduction and large Δ. (a, b) Effective strain-rate distribution at two different steps of simulation. (c) Strain-rate scale selected so as to reveal low strain rates.

entrance. In this simulation, the surface material of the wire was also predicted to bulge up before entrance into the die. In addition, the strain-rate conditions ahead of the die were not predicted to be stable. Actually, there were fluctuations in the strain rate ahead of the die throughout the course of the simulation. The fluctuation from one step to the next is seen when Fig. 23.3(a) is compared with Fig. 23.3(b). From one step to the next, the high-strain-rate region spreads out ahead of the die, so as to include the surface bulge there.

To depict the strain-rate variations in the plastic zone in more detail in this case, Fig. 23.3(c) and Fig. 23.4 were made. In this figure, the levels of different strain rate are shown by contour lines. Fig. 23.4(a) shows that the simulation program predicts the presence of a small stagnant, or dead, zone (DZ) of wire material, adjacent the conical die face. At each side of this zone shear, bands are predicted to form as high-strain-rate regions surround the stagnant zone.

The periodic fluctuation of the deformations in the bulge of the wire ahead of the die inlet is better visualized in this figure than it was in Fig. 23.3.

In Fig. 23.3(c), a different scaling is used to show the effective strain-rate distribution. Here it is seen that the plastic zone in S7 is not located only in the drawing cone. Instead, the plastic deformations spread out into a large volume of wire material. The wire is in reality subjected to plastic deformations both in front of and behind the die. This seems to be due to the special deformation phenomena predicted in this particular case of drawing, where *bulging* occurs ahead of the die, and *thinning* behind. For details about these phenomena, see Sec. 23.1.3.

The deformations in the workpiece in case S7 of wiredrawing, as depicted in terms of effective strain, are shown in Fig. 23.5(a). The figure shows that the accumulated deformations in the wire are predicted to be very nonuniform over the cross section of the wire. While the surface layer experiences effective strains as

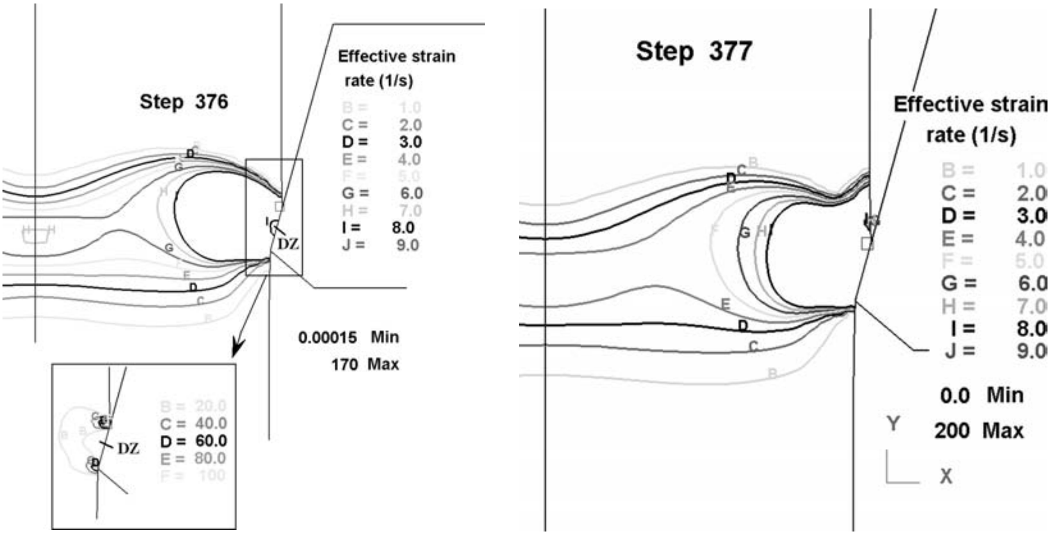

(a) (b)

Figure 23.4. Levels of effective strain rate inside the plastic zone depicted by contour lines in (a) one particular simulation step and (b) the following step.

high as ≈0.45, the strains in the core of the wire are less than one-third of this value (<0.15).

23.1.2 Grid Pattern Distortions

Figure 23.5(b) depicts how the deformations computed in the simulation model manifest themselves in distortions of an internal grid pattern placed on the

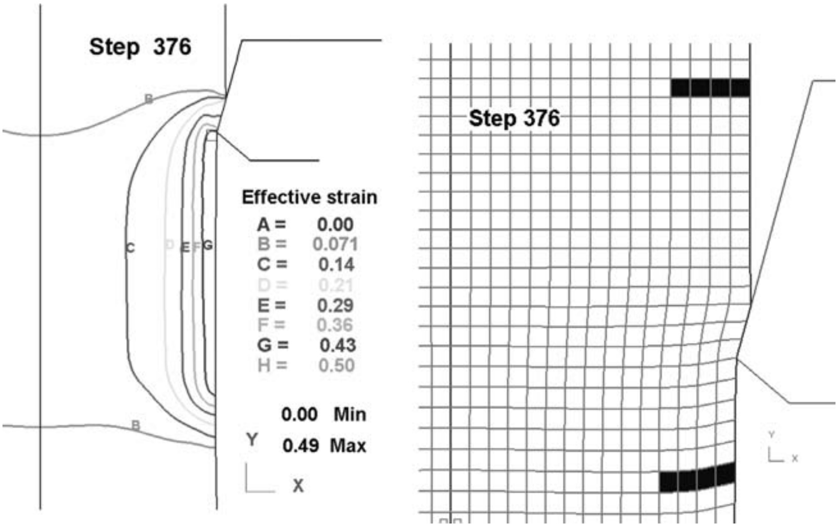

(a) (b)

Figure 23.5. (a) Effective strain-rate distribution inside the wire shown by contour lines. (b) Distortion of an internal grid pattern in the wire.

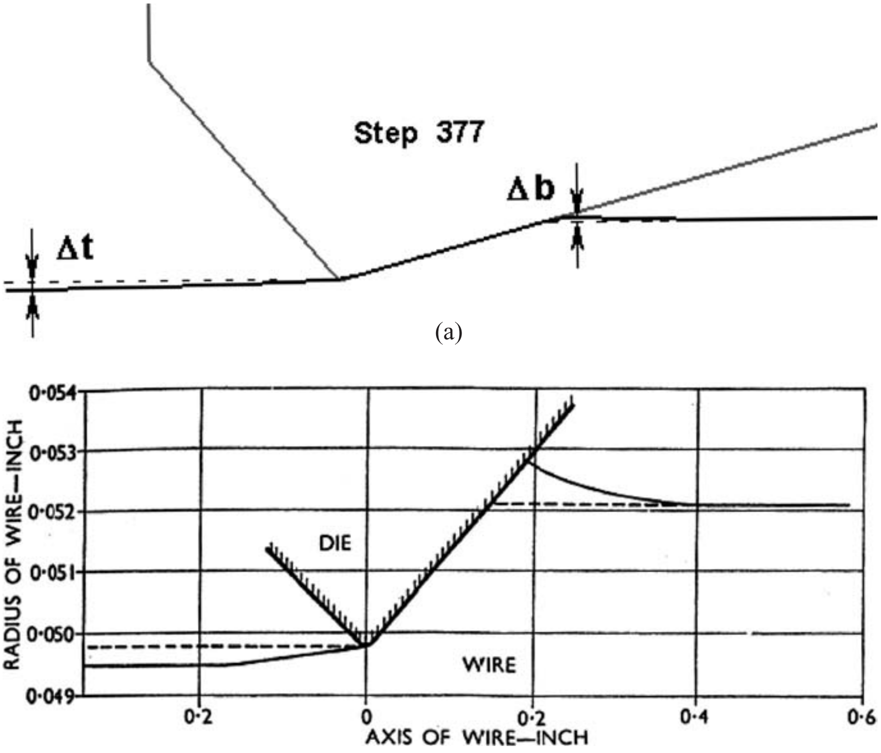

(a)

(b)

Figure 23.6. Bulging and thinning in low-reduction wiredrawing: (a) as predicted in the simulation model and (b) as observed[1] in one of Wistreich's experiments.

midplane of the wire. A row of four elements has been painted black at the inlet side of the die, before entrance into the drawing cone. The corresponding row of elements as it appears behind the outlet of the die (after drawing through the die) is also shown in the same figure. As the figure depicts, the elements near the surface lag behind the rest of the grid elements in the same row. From this, it is clear that the larger deformation in the outer surface layer of the rod is also due to shear deformation, as a result of the outer surface layer of the wire being dragged backwards along the wire in relation to the core.

23.1.3 Bulging and Thinning

In Fig. 23.6(a) are shown the two phenomena of bulging and thinning, as they were predicted to occur in simulation S7. In his article, Wistreich noted that in some experiments performed with similar die geometry to that in the S7 simulation model, bulging did occur ahead of the die, and thinning behind the die. In one experiment, he even measured the geometrical shape of the wire in the bulge ahead of the die and in the thinned part behind the die; see Fig. 23.6(b).

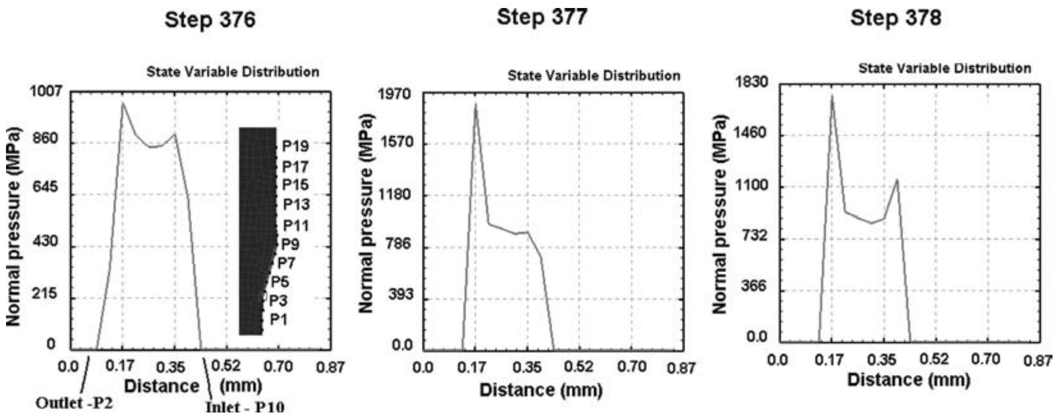

Figure 23.7. Contact pressure distribution over contact zone between wire and die as predicted at different simulation steps in the FEM simulation.

The drawing geometry for which he measured bulging and thinning was one different from that used in the simulation model. Because of this, a direct comparison of the shape of the wire in simulation vs. experiment cannot be made. But at least it was confirmed that bulging and thinning did occur in the S7 FEM simulation model as in Wistreich's experiments.

23.1.4 Die Pressure

The point-tracking option in the FEM program was used to determine the pressure distribution over the contact length between the die and wire inside the drawing cone. The result of the analysis is shown in Fig. 23.7. The stress distribution depends a lot on the simulation step considered. A likely explanation is that this is due to size effects of the grid elements of the FEM mesh. It is also possible that these variations are true, i.e., that they also are present in wiredrawing experiments. They could, for instance, stem from the observed periodic variation in metal flow at the inlet side of the die where the bulge is present. Remember from the preceding description that periodic fluctuations in the strain-rate field were observed here, in connection with the presence of the bulge in this location.

When one considers the FEM-computed contact pressure distributions shown in Fig. 23.7, one must be aware that they represent the mirrored image in relation to the friction hill, as the inlet to the die is on the right-hand side, and the exit on the left-hand side, of the figure. As Fig. 23.7 depicts, a pressure peak is always predicted near the outlet from the die, and the contact pressure in the middle of the die is lower than this peak. The last observation seems reasonable in that there is a stagnant zone of metal adjacent the die cone; see Fig. 23.4. At the inlet side of the die, however, there are considerable fluctuations in pressure from one simulation step to the next. Sometimes a pressure peak is predicted here, sometimes not. A likely explanation is that these pressure variations are caused by variations in the deformation field in

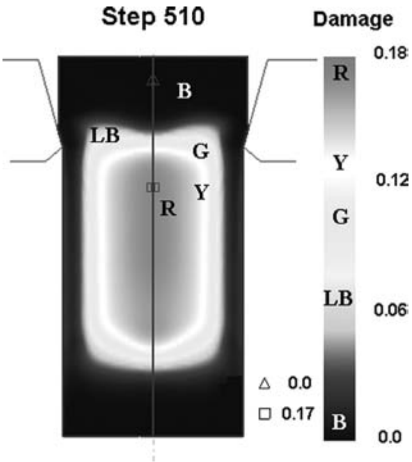

Figure 23.8. Distribution of the damage parameter in the longitudinal section of the wire, shown by grayscale.

the bulge ahead of the die, which in turn generate stepwise fluctuations in the strain rate inside the wire, as already explained in connection with Fig. 23.3 and Fig. 23.4.

23.1.5 Damage Parameter and the Formation of Chevron Cracks

In Fig. 23.8 is shown the FEM-predicted value of the damage parameter, computed according to the Cockcroft–Latham criterion. The figure shows this parameter in terms of the distribution of the parameter along the axial midsection of the drawn wire. A similar representation of the simulated damage parameter is shown in Fig. 23.9, but with a different scaling to visualize predicted variations in the damage parameter at the center of the wire. Here *center burst* or *chevron cracks* are likely to be formed[3] when unfavorable geometrical conditions are used in the drawing process, as in our analysis.

The highest level of the damage parameter is seen to be along the axis of the wire. In Fig. 23.9, the wire and the die have been oriented horizontally, in contrast to the vertical picture shown in Fig. 23.8. The simulation that was run in this case was identical to the previously mentioned simulation model of case S7, except that now a longer length of wire was pulled through the die.

As shown in Fig. 23.9(a), the FEM program predicts periodic variations in the damage factor along the axis of the wire. Because of this, voids can in principle be initiated periodically along this axis, at each maximum of the damage factor. This could explain why chevron cracks tend to appear periodically, with approximately constant distance between them, when wire is drawn through dies with small reduction and large die cone angle.

An attempt was made to find what could cause the variations in the damage factor. It seemed natural to check the simulated effective strain, for this parameter contributes to the damage factor. It was found that this parameter varied in the same manner along the axis of the wire as the damage parameter, i.e., with peak values occurring at fixed intervals; see Fig. 23.9(b). Further investigations into this

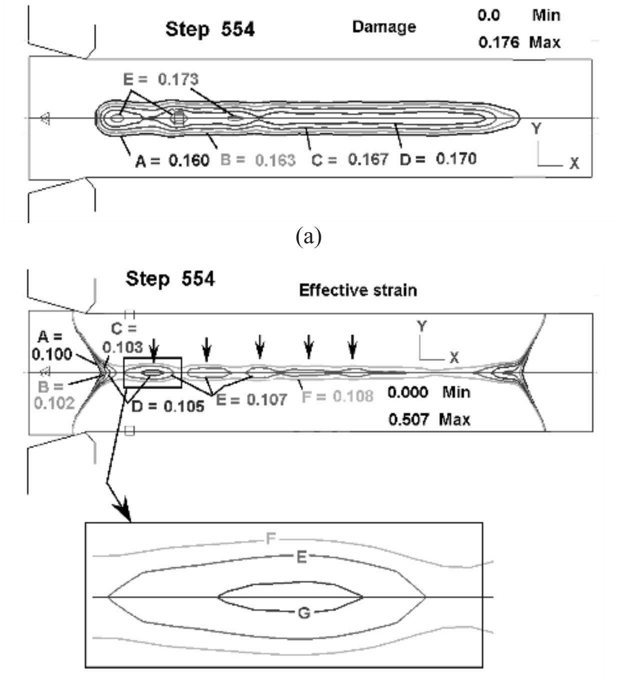

(a)

(b)

Figure 23.9. Distribution of (a) damage parameter and (b) effective strain in the core of the wire.

phenomenon are recommended for better understanding of the mechanism causing the formation of chevron cracks.

Periodic fluctuations in the shape of the plastic zone, and narrowing of this zone from both sides along the axis into a single point, as a proposed by Avitzur[3] as a probable mechanism for generation of the chevron cracks, were not predicted at all in the FEM simulations.

23.1.6 FEM Simulation of the Chevron Cracking Phenomenon

The FEM program applied contains a fracture mechanics module. It allows simulation of crack formation by *deletion of mesh elements*. When this option was used, it was possible to compute and visualize the phenomenon of chevron cracking, as shown in Fig. 23.10(a). Here it is shown that in the beginning of drawing a void was generated on the axis of the wire, but the stress then was not severe enough for this initial defect to start propagating. Later, however, when the second void was generated, conditions were different, so that the void now grew into an arrowhead crack.

As shown in Fig. 23.10(b), initiation of a void and growth of it into a chevron crack are predicted to occur just behind the die, where the principal stress starts to decrease rapidly. This seems to be why the crack propagates just for a while, and then stops. Hence, the defect becomes trapped in the middle of the wire as an internal defect, with the potential to cause breakage in later drawing steps.

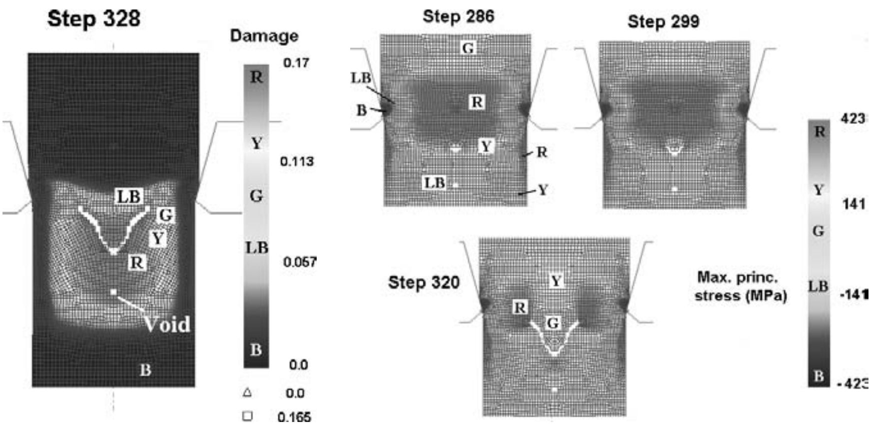

(a) (b)

Figure 23.10. (a) Damage and (b) maximum principal stress in the wire section in the case of chevron cracking.

In Fig. 23.11 is shown the FEM-predicted distribution of the largest principal stress in a defect-free wire pulled through the die. Figure 23.11(a) reveals that there are high tensile stresses in a tulip-shaped region in the middle of the plastic zone, and that there is also a high-tensile-stress zone in the surface layer of the wire, just behind the die, where thinning occurs. The vector plot in Fig. 23.11(b) shows that the highest principal stress acts in the radial, outward-pointing direction in the high-tensile-stress regions of the wire, i.e., both in the core and in the surface layer.

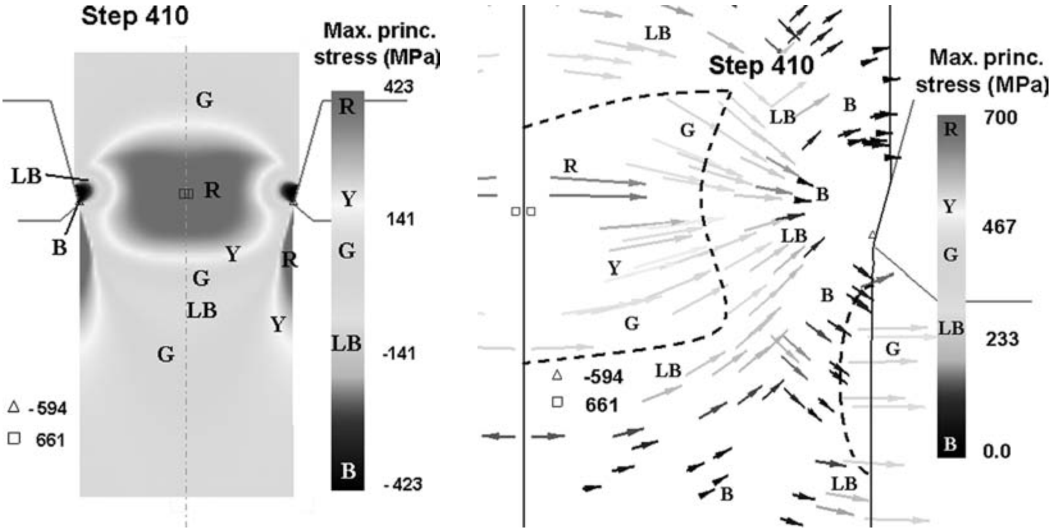

(a) (b)

Figure 23.11. Maximum principal stress conditions in the wire: distribution in a longitudinal section presented (a) and (b) with a grayscale as a vector plot.

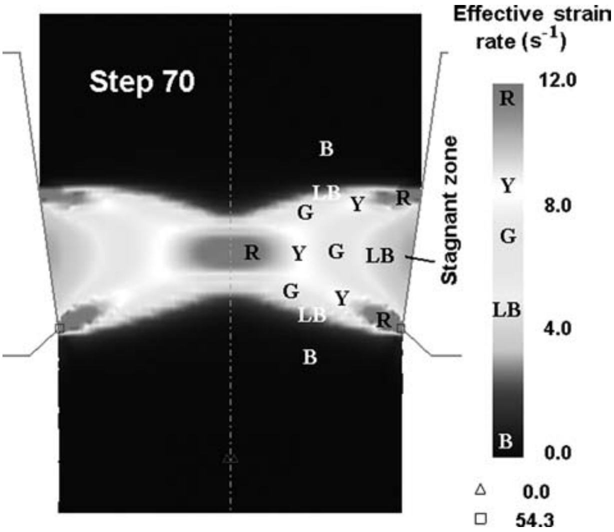

Figure 23.12. Strain-rate distribution in normal wiredrawing visualized by a grayscale.

23.2 Wiredrawing in a Die with Normal Geometry

As mentioned previously, reduction 0.2 and half cone die angle 8° must be considered normal industrial wiredrawing conditions. In Fig. 23.1, this condition is represented by the experiment and the corresponding simulation denoted S10. The parameter Δ in this case was 2.4, much lower than in case S7. A corresponding FEM model to that of S7 was made for this normal die geometry, and simulation results corresponding to those of the first case were obtained by means of the preprocessor. The results will be discussed in the following treatment, and comparison will be made with the first case.

23.2.1 Deformations

Figure 23.12, compared with Fig. 23.3, shows that the plastic zone in normal wiredrawing is completely different from the corresponding zone in the high-Δ case S7. In normal wiredrawing, a distinct deformation cross is predicted in the plastic zone of the wire. Moreover, this zone is predicted to be confined inside the cone of the die; it does not extend out of the cone. Taking into account the axisymmetric nature of the drawing process, i.e., the rotational symmetry, one realizes that what appears like a deformation cross inside the longitudinal section of the wire will, in actual three-dimensional space, have a shape similar to an hourglass. This means that the shear bands consist of two oppositely oriented cones joined at their vertices.

As Fig. 23.12 depicts, there are two high-strain-rate zones toward the surface of the wire, one at the entrance into the die, and another at the outlet side of the drawing cone. Both these zones occur in connection with change of direction of the material flow; see the simulated particle paths depicted in Fig. 23.18. In addition, there is a high-strain-rate region in the middle of the plastic zone.

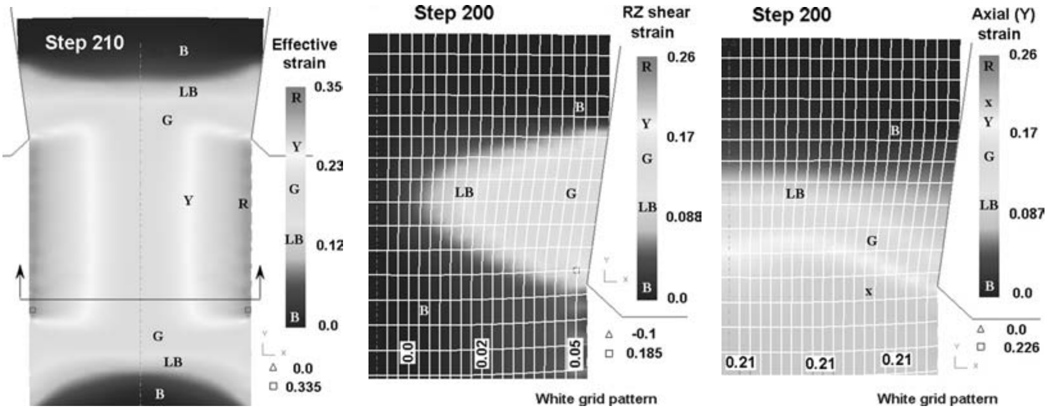

(a) (b) (c)

Figure 23.13. Strain distributions in the longitudinal section of the wire in normal wiredrawing: (a) effective strain, (b) shear strain, and (c) length strain.

There is also a stagnant zone with moderate or low strain rate inside the wire, adjacent to the cone wall of the die. In view of the rotational symmetry of the wiredrawing process, this stagnant zone has a ring shape, and extends circumferentially around the wire. Local deformations in the longitudinal section of the wire, in terms of strain rates, resemble the corresponding pattern obtained in plane strain compression; see Fig. 3.12(b). But the deformation imposed on the material is very different from what it was in plane strain compression. This is because in wiredrawing the material flows through the plastic zone,whereas in plane strain compression the material remains in the deformation zone, as it is squeezed out laterally away from the neutral plane, located in the middle of the plastic zone.

The accumulated effect of the strain rates on the material flowing through the die, in terms of the distributions of different strain components, is shown in Fig. 23.13. Consider first the effective strain distribution shown in Fig. 23.13(a). The front end of the wire initially threaded through the die is not drawn and does not deform at all. Behind is the pointed conical part of the wire, which was initially placed inside the die cone. This part of the wire is subjected to increasing effective strains along its length, for obvious reasons: Material initially deeper inside the cone has traveled a shorter distance through the plastic zone than has material less deep inside the cone.

Finally, there is the steady-state situation experienced by material initially located ahead of the die. During the course of the simulation, this material flows the whole way through the plastic zone. In Fig. 23.13(a) this material has been marked by a line with two arrows. As the figure depicts, the FEM simulation predicts inhomogeneous deformation over the cross section of the wire, with larger deformation in the outer surface layer of the wire than in the core. But if we compare with the S7 case of drawing with especially high Δ [see Fig. 23.5(a)], we see that in normal wiredrawing there is much less difference in effective strain between the core and

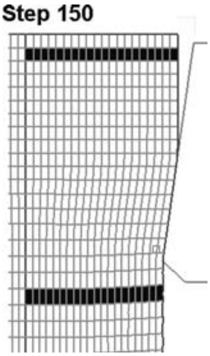

Figure 23.14. Distortions of internal grid pattern in normal wiredrawing.

the surface of the wire than in the S7 case. Hence, we can state that the deformations in normal wiredrawing are much more uniform over the cross section of the wire than if drawing is conducted with very high Δ.

In Fig. 23.13(b) is shown the shear strain component of deformation. The material close the die wall is subjected to much shear deformation when it flows past the shear band at the inlet to the die, but during passage down along the cone wall there is no additional shear straining, instead the shear strain remains constant. However, when this material flows across the second shear band, near the outlet from the die, shear deformation is inverted, and the shear strain value is reduced again. This behavior is visualized well by the internal grid pattern overlaid on the shear strain distribution in the figure. In Fig. 23.13(b), resulting shear strain values behind the die outlet are not well visualized by the scale; hence, they have also been shown as numerical labels. As shown by these numbers, the outer surface layer of the wire material has been deformed up to a shear strain of ≈ 0.05. The shear strain value is highest at the surface, and decreases toward the core of the wire, so that in the middle of the wire there is predicted zero shear strain.

The length, or axial, strain of the wire material drawn through the die is shown in Fig. 23.13(c). As this figure depicts, the axial strain at the outlet of the die is predicted to be uniform over the cross section of the wire.

23.2.2 Grid Pattern Distortions

The FEM-predicted distortions of an internal grid pattern inside the middle of the wire is shown in Fig. 23.13(b) and (c), and also in Fig. 23.14. The black-painted row of grid elements ahead of the die represents the undeformed state, and should be compared with the corresponding row behind the die, in which the elements have flowed through the plastic zone and have been deformed. It is seen that the elements are stretched out upon passage through the plastic zone, and that they become elongated in the length direction of the wire. If sufficiently far from the axis of the wire, they will also shear-deform. Because of this, an initially straight radial line inside the wire, ahead of the die, remains straight only in the central region after drawing. Away from the center this line has curvature. The net result of

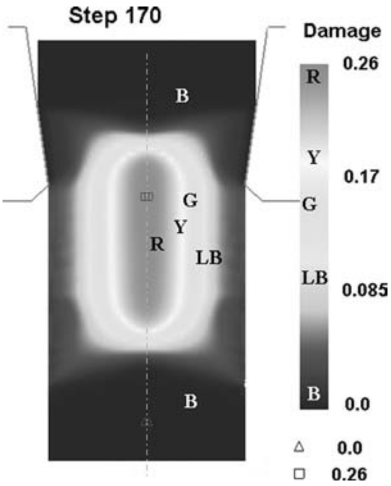

Figure 23.15. Distribution of the damage parameter inside the wire.

deformation during passage of the wire material through the die is that the surface layer lags behind the core of the wire.

23.2.3 Damage Parameter

The FEM-predicted Cockcroft–Latham damage parameter in normal wiredrawing is shown in Fig. 23.15. When this figure is compared with Fig. 23.8, it is seen that the distributions are rather similar in normal wiredrawing and in S7 with low reduction and high Δ. One difference, however, is that in normal wiredrawing the damage factor is predicted to be higher at the center of the wire than in S7.

The largest principal stress in normal wiredrawing is shown in Fig. 23.16 for comparison with the case of low reduction in Fig. 23.11. The distributions are not very different in the two cases. But there is one exception, namely, that in normal wiredrawing three high-strain regions are predicted inside the wire, instead of only two such regions in the low-reduction case. In both cases, there is one high-tensile-stress region in the middle of the plastic zone, and also one right behind the die, adjacent to the surface of the wire. In normal wiredrawing, there is in addition predicted a high-tensile-stress region right ahead of the die, just below the surface of the wire. This is the location where a bulge was formed when wiredrawing was conducted with low reduction.

23.2.4 Contact Pressure

The contact pressure distribution against the die in normal wiredrawing was obtained the same way as previously shown in Fig. 23.7 for drawing with low reduction and high Δ. The pressure distribution in normal wiredrawing was predicted to have one peak value close to the inlet, and one close to the outlet from the die; see Fig. 23.17. The peak values occurred at the same positions in the die cone as where the internal shear bands start on the surface of the wire, i.e., at the place where the

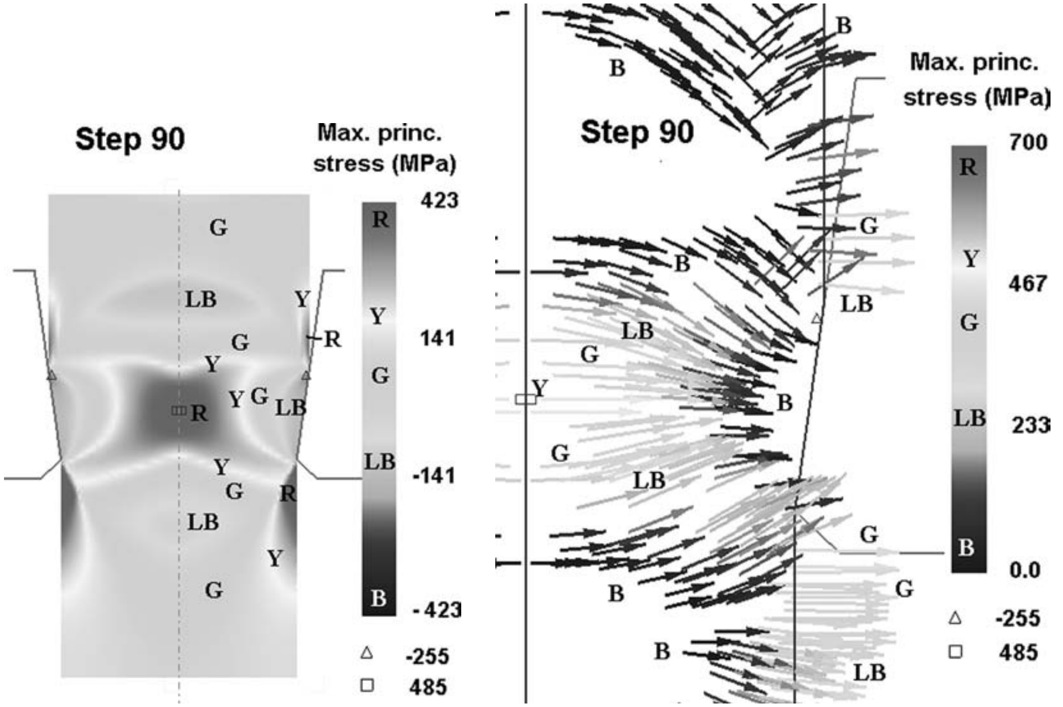

(a) (b)

Figure 23.16. (a) Distribution, inside the longitudinal section of the wire, of the maximum principal stress. (b) Stress directions visualized by vectors.

direction of material flow is changed when the wire material flows into and out of the die cone.

23.2.5 Particle Paths and Velocity Field

Particle velocities for the material that flows through the plastic zone in normal wiredrawing were determined by the simulation program. This was done by means

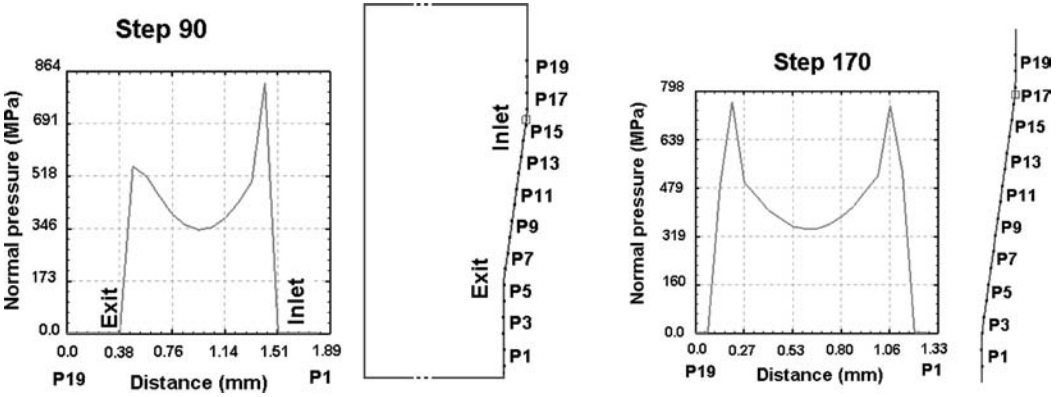

Figure 23.17. Pressure distribution over the wire–die interface predicted in FEM simulation.

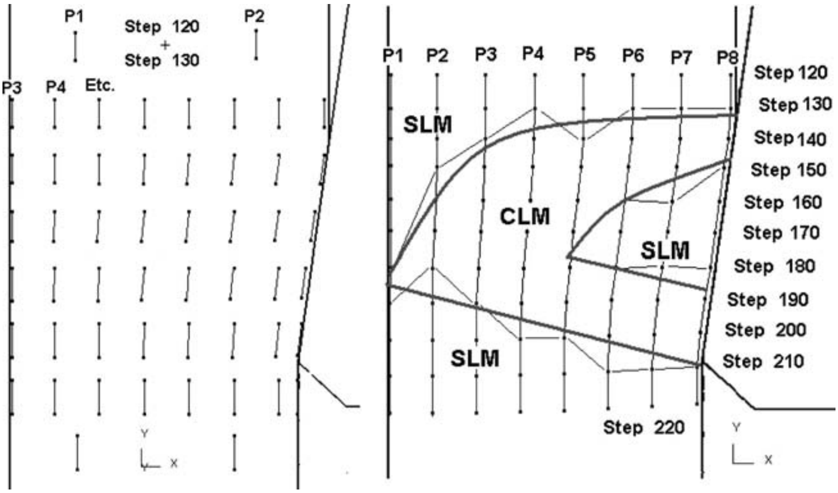

(a) (b)

Figure 23.18. Different representations of particle paths inside the plastic zone as computed in simulation.

of the point-tracking option in the software. Many material points were specified in the wire material inside the die at a certain stage of drawing, in such a manner that many horizontal rows of points were obtained inside the drawing cone; see Fig. 23.18(a).

The positions of the same points at a later instant of drawing were also recorded and added to the first picture. Lines were then drawn between the two positions of the same material point, as shown in Fig. 23.18(a). Hence, this figure depicts by the lengths of the resulting lines the velocity distribution of the particles in the material. From the figure, it is seen how the particle velocities of the wire material increase as it flows through the die.

Figure 23.18(b) correspondingly shows the particle paths of a single row of material points distributed across the diameter of the wire, initially located ahead of the die, and finally appearing as a row of particles across the wire behind the die. The broken line was drawn to distinguish between straight- and curved-line particle movement. Straight-line movement (SLM) is of course predicted to occur in the region ahead of the die and behind the die. In addition there is a zone adjacent the die cone where the material particle movement is also in straight lines. This is in the region where a stagnant zone is predicted to occur; see Fig. 23.12. In between these regions, the particle paths are curved (CLM), as the material moves through the shear bands of the deformation cross inside the plastic zone.

23.3 Wiredrawing with Large Reduction and Small Die Angle

A FEM model corresponding to the experiment denoted S3 in Fig. 23.1 was made, to see what deformation conditions are predicted for this rather extreme die geometry. In Figs. 23.19 and 23.20 are shown some postprocessing data from this simulation. These data are to be discussed in detail by the reader of this book; see

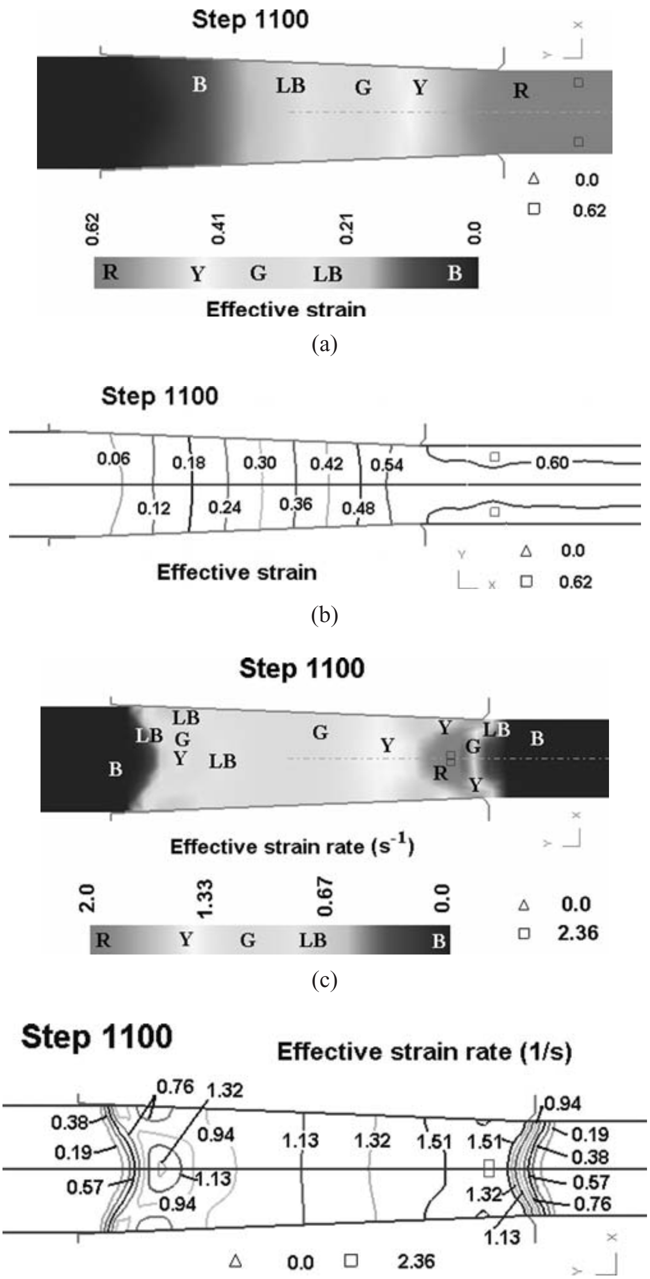

(a)

(b)

(c)

(d)

Figure 23.19. Postprocessing results from simulation S3: (a, b) effective strain; (c, d) effective strain rate.

Problem 23.1. Here only one result that can be deduced from Fig. 23.19(a) and (b) will be considered.

From Fig. 23.19(a), it may appear as if FEM simulation in this case predicts constant effective strain values, i.e., uniform deformation, over the thickness of the

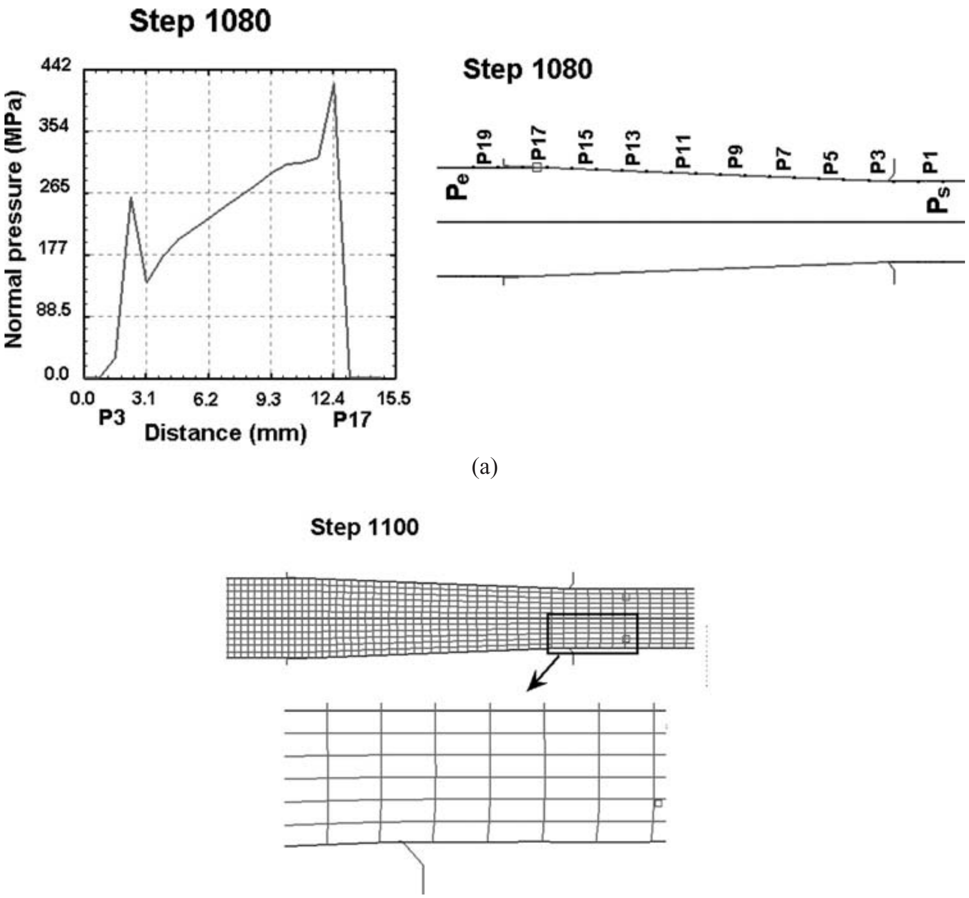

(a)

(b)

Figure 23.20. More postprocessing results from simulation S3.

drawn wire. However, if one visualizes the effective strain distribution by means of contour lines and selects an appropriate scaling [see Fig. 23.19(b)], one actually can see that the outer surface layer of the wire is predicted to deform slightly more than does the core. However, the difference is small. Hence, when applying a die with small cone angle and high reduction, as in case S3, the deformation inside the drawn wire can be considered homogeneous, i.e., all parts of the wire will deform approximately the same amount.

23.4 Concluding Remarks

From the preceding treatment, it is clear that the average height-to-width ratio of the wire contained in the die cone in wiredrawing (i.e., the parameter Δ) used in the drawing process has a profound influence on how the wire material deforms. The main results from this analysis are summarized in Fig. 23.21. Inside the parameter window shown in this figure three different regions can be identified:

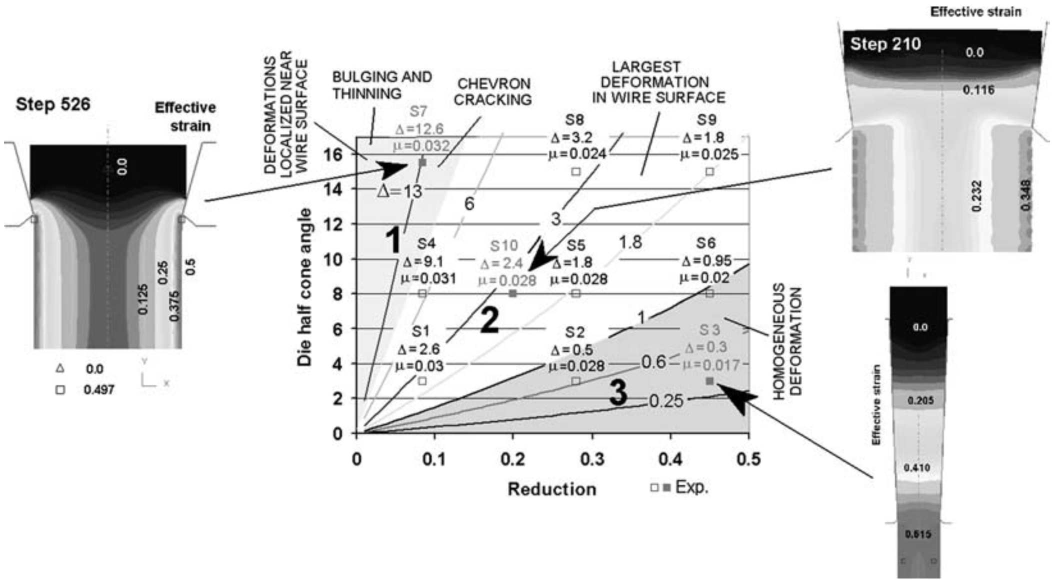

Figure 23.21. S1–S10 are wiredrawing geometries investigated by Wistreich, later reproduced in FEM simulation.

Region 1

Wiredrawing with small reduction in the die and large die cone angle falls within region 1. This is the high-Δ region of drawing (Δ > 9), which preferably should be avoided, because of the occurrence of a number of negative deformation phenomena when drawing is conducted in steep-cone-angle dies, especially when a small reduction is used.

Under these circumstances, the plastic deformations will localize in the outer layers of the wire, while the core will experience only minor plastic deformations. In addition, for this drawing geometry, the wire material will tend to bulge up in front of the die and to thin behind it. Especially the latter phenomenon is disadvantageous in that it precludes obtaining a stable wire dimension after the drawing process. The third negative effect is that the core of the wire will be subjected to high tensile stresses, in fact, in three directions perpendicular to each other. There is therefore a risk that chevron cracks will form in the middle of the wire.

Region 2

This is the intermediate-Δ region (9 >Δ> 1), where wiredrawing can be performed with good stability. Here such phenomena as chevron cracking, bulging, thinning, and highly localized deformation in the surface layer of the wire will be avoided. The larger the Δ-parameter inside this region, the more nonuniform will be the deformation over the thickness of the wire. Use of a die geometry that provides low Δ within this region is advantageous in that the deformations in the wire then will be more homogeneous. However, there are also unfavorable effects when the lowest possible Δ is chosen. The drawing force will become excessive; it will be larger than the ideal minimum drawing force at the optimum die angle (see Fig. 22.13). Use of a

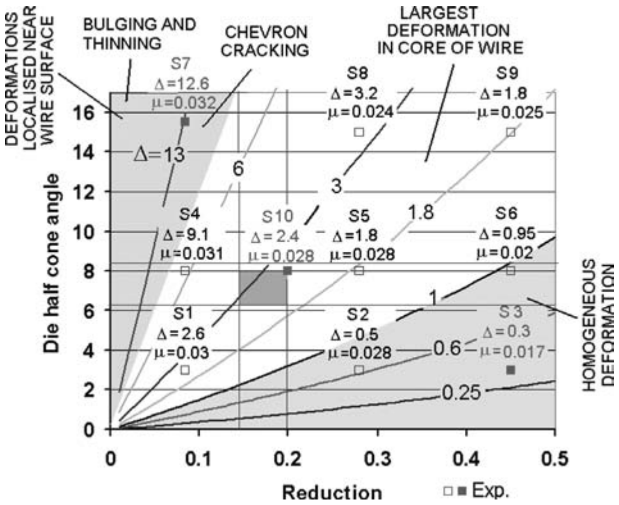

Figure 23.22. Normal drawing parameters commonly applied in industrial wiredrawing are contained in the shaded rectangle.

small reduction should also be avoided, because this of course gives low productivity per wiredrawing die. Hence, the recommendable die angle and reduction, which are commonly applied in industry, are those specified within the shaded rectangle in Fig. 23.22.

Region 3

Wiredrawing through dies with small die angle, or somewhat larger die angle combined with larger reduction, falls within region 3 in the diagram in Fig. 23.21. When such geometrical conditions are used, Δ is low. Because excessive drawing force is then experienced, these conditions are not recommendable for industrial purposes. However, wiredrawing within this region does, as shown, provide very homogeneous deformation inside the wire. Drawing within this region can therefore be beneficial if one wants to bring the wire up to large homogeneous strain values, for instance, for later mechanical testing of the material at high deformation.

Problems

23.1 Discuss the information contained in the postprocessing data from simulation S3 shown in Fig. 23.19 and Fig. 23.20, as was done in this chapter for the two other wiredrawing simulations, S7 and S10. Compare also the conditions in S3 with corresponding conditions in S7 and S10.

23.2 Rerun the simulation of the normal wiredrawing case with higher friction than that determined in Wistreich's experiments: Set the coefficient of friction equal to $m = 0.2$ and then to $m = 0.4$.

a) Present the corresponding postprocessing data as was done in case S10.
b) Discuss what effect increasing friction has on the conditions in this wiredrawing operation.

23.3 Use simulation models S7 and S10 to compute the smallest principal stress in the wire. Show the data as stress distributions inside the longitudinal section of the wire. Consider also the maximum principal stress distribution for the two cases presented in Fig. 23.11 and Fig. 23.16.

a) Discuss the stress conditions in the center of the wire in these two cases.
b) Try to find a good explanation why chevron cracks are likely to form in case S7, while they are not in case S10.

NOTES

1. Wistreich, J. G.: "Investigation of the mechanics of wire drawing," Proc. Inst. Mechanical Engineers, Vol. 169, 1955, pp. 654–665.
2. Valberg, H., and Wanheim, T.: "FE-analysis as a tool for the investigation of the mechanics of wire-drawing," Int. J. Materials and Product Technology, Vol. 13, 1998, No. 3–6, pp. 234–265.
3. Avitzur, B.: "Study of flow through conical converging dies," in "Metal Forming," A. L. Hoffmanner (Ed.), Plenum Press, New York, 1971, pp. 1–46.

24 Sheet-Metal Forming

As pointed out previously in Ch. 2, sheet-metal forming differs a lot from bulk-metal forming in that the stress condition in a sheet-metal forming operation usually is characterized by tensile stress, whereas most commonly in bulk-metal forming there is compressive stress. Because of this, necking and fracturing of the workpiece material is a much larger problem in sheet-metal forming than in bulk-metal forming. A useful tool for optimization of sheet-metal forming processes, so that they can be conducted without problems due to necking or fracture, is *circle grid analysis*. The principles applied in circle grid analysis will therefore be described in this chapter. After this, some technological test methods applied in order to test the formability of sheet metals will be described: plane strain stretching, biaxial stretching, and the Erichsen test.

The principles used when forming-limit diagrams (FLDs) are made will be explained. It will also be shown how such diagrams and circle grid analysis can be used in order to optimize the deformation conditions in a typical industrial sheet-metal forming operation.

Elastic springback is a phenomenon of great importance in sheet-metal forming. Commonly the cross section of the sheet does not become fully plasticized in such processes. In bending, the midlayer of the sheet will deform elastically only, and will therefore cause elastic springback in the material when the forming load is removed.

Sheet metals used for forming are commonly anisotropic, i.e., they have different properties in different directions. In the forthcoming sections, it will be shown how such anisotropy can be described and quantified by measurements performed on sheet-metal specimens deformed in technological tests. Finally, the phenomenon of springback in sheet metals will be discussed in more depth. It will be shown how different material and process parameters affect the amount of springback occurring in bending operations.

24.1 Circle Grid Analysis

The deformations that the workpiece is subjected to in sheet-metal forming can be quantified by means of circles on the surface of a sheet-metal specimen. Such circles

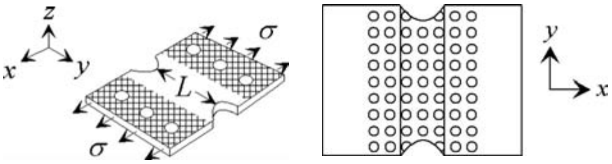

(a) (b)

Figure 24.1. Specimen for tensile testing of sheet metal under plane strain deformation, viewed (a) in 3D configuration and (b) from top side, with pattern of circles placed on the surface.

can be placed on the sheet before forming, by either printing or etching. When the specimen deforms, the circles will deform with the material and will visualize the deformations imposed on the sheet. From the shape of the circles after forming, the deformations can be quantified in terms of the normal strain components. This is demonstrated in the following example, which particularly deals with stretching in plane strain.

EXAMPLE 24.1: CIRCLE GRID ANALYSIS

Problem: A special tensile test specimen can be made from sheet metal, so that during the course of the test the specimen will deform in plane strain; see the sketch presented in Fig. 24.1. When this is done, the test specimen will elongate in the direction of stretching, i.e., in the *x*-direction, without changing its dimension in the width direction, i.e., the *y*-direction.

(a) Explain where the deformations will take place in the specimen.
(b) Show how the deformations can be quantified by circle grid analysis.

Solution:

(a) The test rig that stretches the specimen grips the specimen's ends, i.e., the portion of the specimen shown hatched in Fig. 24.1. Highest tension will then be present in the midregion of the specimen, where on purpose it has been narrowed down in width. Because of this, the deformations will localize in this narrow part of the specimen. The deformations here will be plane strain deformations, because the rigid ends of the specimen will hinder the midregion of the specimen from contracting in the width direction. Hence, the deformations will be characterized by elongation in the direction of stretching, while the width of the specimen is not changed significantly, i.e., the dimension L is maintained constant, so that $\varepsilon_y = 0$.
(b) When circle grid analysis is used to analyze the deformations in sheet-metal forming, a pattern of circles is placed on the surface of the specimen; see Fig. 24.1(b). The pattern is stretched with the sheet metal during the test, and the circles deform and thus characterize the deformations in the specimen. From the shape change of the circles during the deformation, the principal strain components and their directions can be determined. In plane strain stretching (see Fig. 24.2), a circle with initial diameter a will be stretched into an ellipse upon deformation. During the test, the shortest axis will remain constant ($b = d$), while the longest axis a gradually will

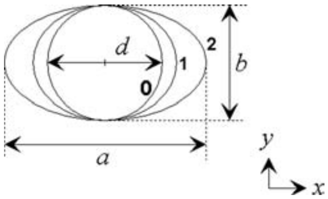

Figure 24.2. Plane strain deformation of a circle on the surface of a sheet-metal specimen.

increase in length. Hence, the circle shown in Fig. 24.2 represents the initial state (condition 0), whereas the smallest ellipse represents an intermediate stage of deformation of the sheet (condition 1). Finally, the largest ellipse (condition 2) represents the end stage of forming. When the lengths of the axes of the ellipsis, i.e., the lengths a and b, are known at a particular stage of forming, two of the principal strains in the sheet can easily be computed, for they coincide with the directions of the axes. The third principal strain can be computed from the thickness change of the sheet metal. The strains can be calculated either as nominal or as true strains. Here, let us calculate the nominal strains. In case of true strains, the strain definition specified in eq. 4-13 will apply instead. The nominal strains are

$$e_1 = e_x = \frac{a-d}{d} \tag{24-1}$$

$$e_2 = e_y = \frac{b-d}{d} = 0 \tag{24-2}$$

$$e_3 = e_z = \frac{t-t_0}{t_0} < 0 \tag{24-3}$$

The first two of these strains occur in the plane of the sheet metal, and the third, i.e., the thickness strain, acts in the direction orthogonal to the sheet. The symbols t_0 and t denote the sheet thickness before and after stretching.

In the case of deformations where the straining of the sheet metal deviates from plane strain deformation, the smaller axes of the ellipses will also change length during the course of deformation, so that the mean strain will be different from zero, i.e., $e_2 \neq 0$. The formulas 24-1 to 24-3, however, are general, and are valid then also. In complex deformations, the axes of the principal strains in the plane of the sheet may change their direction during the course of deformation. To determine the actual conditions of straining in that case, it is required to record the shape of the circle as it deforms into an ellipse at many stages during the course of deformation.

24.2 Technological Tests Used in Sheet-Metal Forming

Plane strain stretching, as described in Example 24.1, is one among many common technological test methods that are applied for the study of the behavior of sheet metals during forming. Especially important are technological tests used for

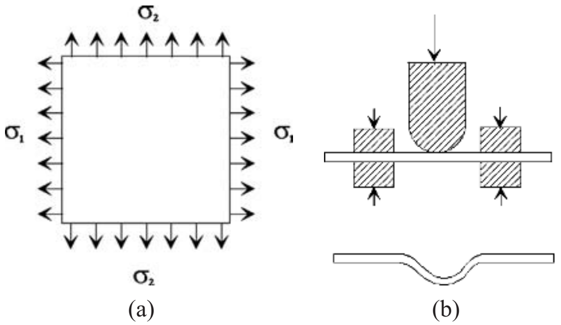

Figure 24.3. Examples of technological test methods applied in sheet-metal forming: (a) biaxial stretching (principle) and (b) the Erichsen test.

measuring the formability of a sheet. They are to be described in Sec. 24.4. In the forthcoming treatment, two quite common variants of specialized tests, used in connection with sheet-metal forming, will be described. These tests are biaxial stretching and the Erichsen test.

24.2.1 Biaxial Stretching

The principle of *biaxial testing* is illustrated by the sketch shown in Fig. 24.3(a). In this test, a piece of sheet metal of initially square or rectangular shape is stretched in two perpendicular directions in the plane of the sheet. The stresses applied in the two directions, σ_1 and σ_2, may be equal, or may differ. If they are equal, the test method is generally called *balanced biaxial testing*. In sheet-metal forming processes, the conditions in particular places in the sheet metal could be of biaxial nature. This is illustrated in Fig. 24.4(b), where balanced biaxial stretching (BBS) takes place, when a product similar to a square loaf pan but in addition with a round depression in the bottom is formed by means of deep drawing.

24.2.2 The Erichsen Test

This test method is a so-called *simulative test*, as it mimics industrial deep drawing; see Fig. 24.3(b). The test is usually run on small sheet-metal blanks, which are shaped into cups; the size is generally much smaller than that used in industrial deep drawing. The punch head used in this test commonly has hemispherical shape. When it is pressed down into the sheet to create the cup, the bottom portion of the cup will of course also be hemispherical. Thus the bottom of the cup will be formed under balanced biaxial conditions. The deformations taking place then will be *out of the plane* of the sheet specimen. Deformations in the sheet-metal specimen in this test are therefore significantly different from those experienced in the biaxial test depicted in Fig. 24.3(a). Another difference is that the sheet-metal specimen will have *tool contact* during a large part of the test. Forming will therefore be influenced by interfacial friction forces transferred from the punch head to the sheet metal specimen during the course of forming. The general biaxial test described in Fig. 24.3(a), in contrast, is commonly performed without any contact between tool and sheet at all in the midregion of the specimen.

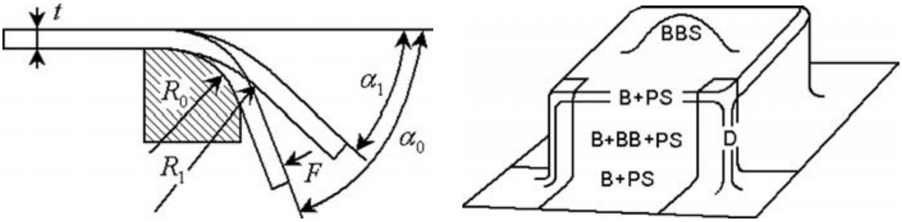

(a) (b)

Figure 24.4. Sheet-metal forming processes: (a) bending with elastic springback upon unloading, and (b) deep drawing of cup with rectangular bottom.

24.3 Types of Deformation in Sheet-Metal Forming

Deformations occurring in industrial sheet-metal forming processes may be highly complex. Strain and stress conditions during the course of forming may vary a lot from one location to another on the sheet. Varying conditions can also occur in one location on the sheet throughout the course of forming.

For instance, consider the local generic deformation modes occurring in sheet-metal forming by bending or deep drawing; see Fig. 24.4. During the bending operation the blank is formed without significant tensile stress in the direction along the plane of the sheet. To obtain the intended bending radius on the bent specimen, it is bent against a die with a chosen radius of curvature, R_0, as shown in Fig. 24.4(a). Then the neutral plane will be located approximately at the midthickness of the sheet, where the strain and stress in the direction along the sheet are zero; see Fig. 24.5.

On each side of the neutral plane the stresses will be of different sign: the stress is tensile on the outer side of the bend, and compressive on the inner side. The compressive stress increases in magnitude with increasing distance from the neutral

Figure 24.5. Stress distribution over the thickness of the bent sheet in loaded condition.

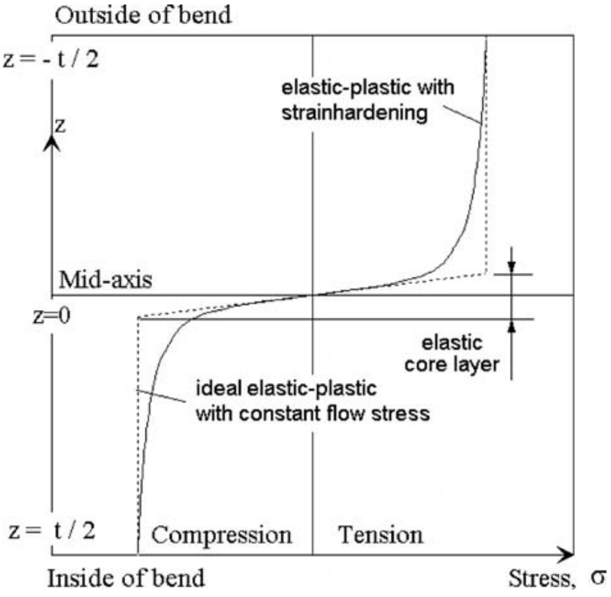

axis of the bend, toward the surface of the sheet. The highest compressive stress is hence on the inner surface of the bend. On the outer side of the bend, the stress distribution is the same as on the inside; however, the sign of the stress is opposite.

The stress near the neutral plane is low, so there must be a thin layer of material approximately in the middle of the specimen that remains in elastic state, while the layers on both sides of this *elastic layer* deform plastically.

Hence, on the outside half of the sheet there is axial stretching of the fibers, and on the inside half there is compression; see Fig. 24.5. Because of the elastic layer in the bend, the specimen will not maintain its shape (i.e., the bending angle α_0) when the bending force F is removed; instead, it will unbend a small amount (see Fig. 24.4). This phenomenon is generally called *springback*. After release of the bending load, the final geometry of the bend will be characterized by the angle α_1, being less than α_0. For the bending angles α_0 and α_1, the geometry of the bend is characterized by the bend radii R_0 and R_1.

When a sheet-metal blank is stretch-formed into a curved configuration (see Fig. 2.10), in contrast to bending, the sheet may be subjected to tensile stresses over its whole thickness. Then the whole cross section deforms plastically, and the deformations are completely different from those in bending. The amount of springback is also reduced significantly in stretching or stretch-bending from what is experienced in pure bending processes.

In deep drawing [see Fig. 2.8(b) and Fig. 24.4(b)], cups with round or square, or more generally rectangular, shape of the bottom are made. The deformations imposed on the sheet are then strongly dependent on the shape of the bottom of the cup – round, square, or rectangular. Round cups are commonly made from a round blank. If an isotropic sheet-metal material is used, the process is then axisymmetric.

What happens in deep drawing is that the outer flange of the blank is compressed between the die and the blankholder as it is pulled inwards by the punch head. During this action, the circumference of the flange is reduced as the sheet in the flange thickens. When the material is pulled over the radius of the die to become the sidewall of the cup, the flange becomes bent over the radius of the die. The material forming the sidewalls of the cup is subjected to deformation different from that of the flange. This material is subjected to stretching. When it has been pulled down into the cup wall, it will thereafter elongate in plane strain upon further stretching.

Let us consider deep drawing of a cup with a rectangular bottom, with a hemispherical protrusion in the middle of the bottom, as shown in Fig. 24.4(b). During forming of this shape the deformations are more complex than in the processes previously mentioned. Many different kinds of deformation modes are present when this component is shaped. In Fig. 24.4(b), letters have been used to denote the conditions of deformation when different parts of this cup are formed. The protrusion in the bottom of the cup is formed in a deformation mode close to balanced biaxial stretching. The label BBS has therefore been assigned to the protrusion.

The rounded edges between the bottom and the wall of the cup are first subjected to bending (B) and thereafter to plane strain stretching (PS) upon further forming. The plane walls of the cup are first subjected to bending, when the flange of the blank is drawn over the radius of the die. Then they are bent back again into a plane shape when they are pulled off from the rounded edges of the die. Hence, the material in these walls is first bent, and thereafter subjected to backward bending (BB). Upon further drawing, the cup walls are stretched in plane strain mode. Finally, there is the material of the edges located between adjacent cup walls. They experience a quite different deformation mode, called drawing, denoted by D in Fig. 24.4(b).

24.4 FLD Diagram in Sheet-Metal Forming

The purpose of sheet-metal forming is to give the blank, as shown, for instance, in Fig. 2.8(b) to Fig. 2.11, a bent or hollow shape by bending, stretching, or drawing it over or onto the surface of a rigid forming die.

In deep drawing, for instance, the rigid die that the sheet must conform to is the punch. The bottom die and the upper blankholder die are additional tooling required to transform the blank into the appropriate shape. During the transformation the sheet metal must be subjected to high stresses in order to change its shape by plastic deformation. Sometimes these stresses become excessive, so that the sheet material in a critical region will start to neck and develop fracture. When necking begins, the situation is most commonly considered critical, because fracture then soon will occur upon further forming, or during use of the finished component. Because of this, the formation of a beginning neck in sheet-metal forming is usually considered unacceptable.

Hence, in sheet-metal forming there are limits to how intricate and deep sheet components can be manufacture from a particular blank in one single forming step. If forming is performed in multiple steps, more intricate shapes can usually be achieved, but even in this case, there are limits regarding what shapes can be made without risking fracture. Experimentally it is observed that the acceptable amount of straining of sheet metal depends strongly on the straining mode in the specimen.

A diagram[1,2] can be made that depicts this connection; it is commonly called a *forming limit diagram* (FLD). A specific sheet material of given thickness, in a particular metallurgical state, can be described by a FLD; see Fig. 24.6. If the thickness or the metallurgical state of the material of the sheet is changed, the bounding lines (i.e., the lines 1, 2, and 3 in Fig. 24.6(b)) in the FLD will also change.

There are also other limiting phenomena in sheet-metal forming than the possible necking (1) followed by fracture of the sheet. One such phenomenon is, for instance, the formation of wrinkles on the shaped component, in regions where it is required to obtain a smoothly curved surface. Another limiting phenomenon is the eventual development of shear fracture in the sheet-metal blank during the forming operation. Such defects can occur in the case of supercritical shear deformations in the forming operation. Limiting lines for these two phenomena, shear fracture (2) and wrinkling (3), are included in the FLD shown in Fig. 24.6(b). The region bounded by the three limiting lines for necking followed by tensile fracture, shear fracture, and wrinkling, i.e., the hatched area in Fig. 24.6(b),

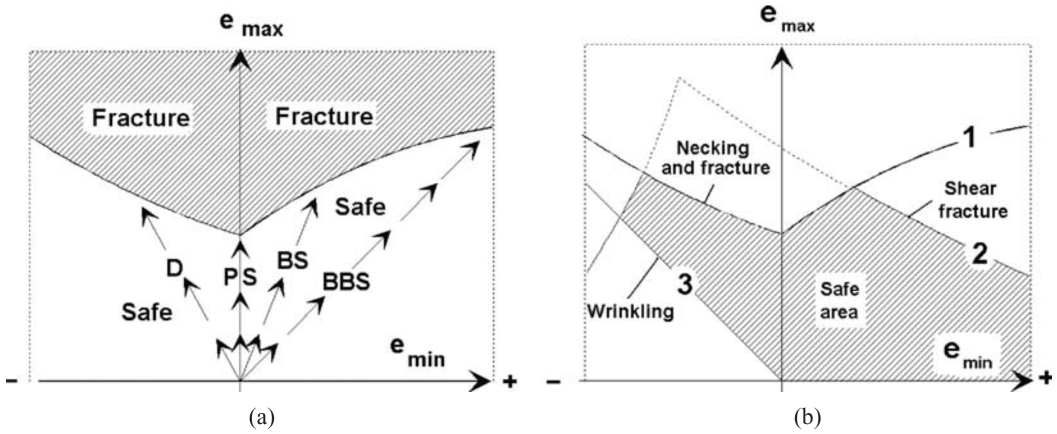

Figure 24.6. (a) Characteristic FLD for sheet metal. (b) FLD where limiting lines for formation of shear fracture (2) and wrinkles (3) also have been included.

represents safe allowable deformations for the blank, which provide defect-free formed components.

24.5 Isotropy vs. Anisotropy

Semifinished flat metallic products are provided as plate, sheet, strip, or foil. *Plate* is a flat product of thickness greater than 6 mm; sheet and strip have thickness less than 6 mm. *Strip* refers to products of breadth not greater than 600 mm; *sheet*, to those of greater breadth. *Foil* comprises the thinnest flat products, which can be as thin as 0.008 mm. Flat metallic products are commonly produced in rolling processes, from an initial cast workpiece. The cast workpiece is most commonly *isotropic*, i.e., has the same mechanical properties in three orthogonal directions. During rolling the metal usually develops a *directionally oriented microstructure* and becomes *anisotropic*. This means that rolled plate, sheet, and strip, as well as foil, most commonly have different mechanical properties in different directions inside the material, i.e., they are anisotropic. In certain sheet-metal forming operations such anisotropic properties are favorable, as, for instance, in deep drawing, in which formability of the sheet metal often can be improved through an increased degree of anisotropy; see Fig. 24.11.

A rolled sheet's direction-dependent deformation properties, i.e., its anisotropy, can be determined by uniaxial tensile testing of the sheet. It can be quantified by a *factor of anisotropy*, commonly denoted by the symbol R. This parameter is defined as the ratio between the plastic strain values obtained in the width and the thickness direction of an uniaxial tensile test specimen made from the sheet (see Fig. 24.7), i.e.,

$$R = \frac{\varepsilon_w}{\varepsilon_t} = \frac{\ln(w_1/w_0)}{\ln(t_1/t_0)} \tag{24-4}$$

In this equation, index 0 refers to dimensions before the tensile test, and index 1 after the test. The parameter R is also equal to the ratio between the flow stresses of

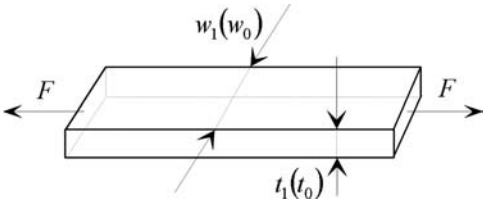

Figure 24.7. A sheet-metal specimen contracts both in the width and in the thickness direction upon stretching.

the material, measured in the same two directions. One can see from the definition of the factor of anisotropy that when this factor has the value 1, the strains of the material in the thickness and width directions are equal, so in that case the material is isotropic. If the R-value is different from 1, the material is anisotropic. There are two kind of anisotropic materials, characterized, respectively, by R larger than 1 or less than 1. In the first case, the material tends to contract more in the width direction than in the thickness direction. This is favorable, for instance, in deep drawing. The higher the R-value of a material is above 1, the less thinning will be experienced when the material is deep-drawn. Materials with low R-value, on the other hand, have low formability in deep-drawing applications.

The anisotropy parameter R will also depend on the orientation of the material in the sheet with respect to the direction of rolling. To fully quantify the anisotropy of a sheet material, it is therefore necessary to stretch a number of specimens, cut out in different directions from the sheet.

It is a common practice to take out tensile specimens from three different directions, namely, the directions oriented at 45° and 90° to the direction of rolling, and the direction of rolling itself. Figure 24.8(a) shows such samples in a sheet. All specimens are made with the full thickness of the material. After testing three anisotropy values are obtained, one for each direction inside the sheet material, respectively. These values are computed by use of eq. 24-4, and are commonly denoted R_0, R_{45}, and R_{90}. When the three R-values have been obtained, two new *compounded* R-values are calculated:

$$\bar{R} = \frac{R_{0^\circ} + R_{90^\circ} + 2R_{45^\circ}}{4} \tag{24-5}$$

$$\Delta R = \frac{R_{0^\circ} + R_{90^\circ} - 2R_{45^\circ}}{2} \tag{24-6}$$

The first parameter is commonly called the *normal anisotropy*, and the latter the *planar anisotropy*, of the sheet metal. Figure 24.8(b) illustrates how R can vary as the orientation of a tensile test specimen is changed in relation to the direction of rolling. The figure also illustrates that the normal anisotropy in reality is a mean value, taking into account all directions inside the sheet material. Likewise, the figure depicts that the planar anisotropy quantifies the degree of variation in R when all directions of the material are taken into account. It is common to determine the normal and the planar anisotropy for a sheet material at a certain degree of deformation of the test specimens, for example, at 12% nominal strain.

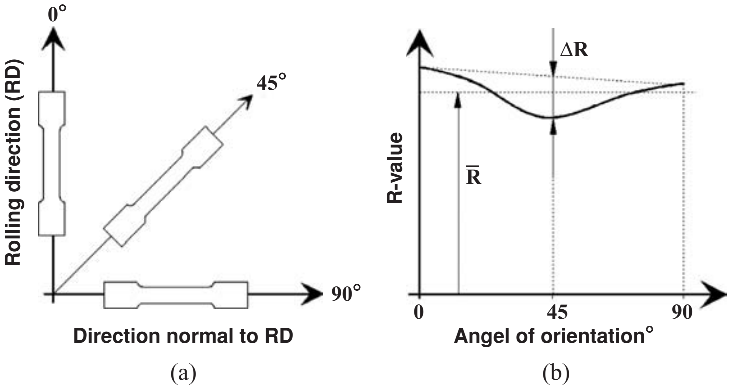

Figure 24.8. (a) Specimen directions to determine the anisotropy in sheet metal. (b) Typical variation of R with orientation in rolled sheet, showing the normal and the planar anisotropy values.

24.6 The Limiting Draw Ratio in Deep Drawing

In deep drawing of round cups, it is necessary to use a *blankholder* die, as was shown in Fig. 2.8(b). The blankholder die exerts a compressive force on the flange of the blank during deep drawing. When compressed this way between the blankholder and the deep-drawing die, the flange will not wrinkle. The compression pressure between the blankholder and the sheet is commonly adjusted to an optimum level, so it does not become excessive but is still kept sufficiently high to avoid *buckling* or *wrinkling* of the flange.

If the blankholder pressure is kept at the optimum level and if the diameter of the blank is increased gradually, one will find a *critical blank size* that can be drawn into a cup without breakdown of the material due to fracture. If the blank size is increased more, a full draw of the blank to cup shape is impossible for the sheet material used, because the stress in the cup wall then will exceed the tensile stress of the material. It will then develop necking which soon leads to fracture.

Hence, it is obvious that sheet metals with good formability in deep drawing are materials that allow drawing of the highest possible cups. Therefore, a commonly used measure in deep drawing to quantify the formability of the sheet metal is the *limiting draw ratio* of the metal, commonly abbreviated LDR, or denoted $\beta_{\max}$. The LDR is determined experimentally in a tool arrangement for deep drawing of small, round cups. The diameter of the punch is D_s, and blanks with gradually increased size are deep-drawn, so the whole flange is pulled down to become the cup wall under optimum blankholder pressure. In this way, a critical drawable blank size $D_{\max}$ can be determined for the particular sheet metal tested. The LDR is then computed using the following definition; the inner diameter of the cup is approximately equal to the outer diameter of the punch ($D_i \approx D_s$):

$$\mathrm{LDR} = \beta_{\max} = \frac{D_{\max}}{D_s} \approx \frac{D_{\max}}{D_i} \tag{24-7}$$

From this explanation, it should be obvious that the higher the LDR of a sheet metal, the better it should perform in deep drawing, and thus the higher cups can be manufactured from the material in one single draw without fracture.

24.7 Parameter to Characterize Formability in Stretch Forming

A sheet metal that performs well in deep drawing does not necessarily also perform well in other sheet-metal forming operations, as, for instance, in stretch forming. The stretch-forming operation (see Fig. 2.10) is characterized by high tensile stresses imposed on the material by jaws holding the periphery of the sheet as the sheet is bent and drawn over the die. Because of the high tensile stresses imposed on the material in this operation, the stress condition of the sheet will be similar to that in tensile testing. For materials with flow stress that conforms to a power law, it was shown in Example 7.3 that the strain at start of necking equals the strain-hardening exponent n of the material. This implies that the higher the strain hardening exponent is for a material, the more it can be deformed by stretching before necking (and fracture) occurs. This is also demonstrated in Sec. 9.2. The strain-hardening exponent of the material is therefore a parameter that should preferably be high to secure good formability in sheet metals used in stretch-forming applications. A material with high n allows deeper components to be made by stretch forming than one with low n. The formability in stretch forming is not significantly influenced by the anisotropy of the material, quantified either by its normal or by its planar anisotropy value.

24.8 $\bar{R}$ as a Formability Parameter in Deep Drawing

In deep drawing of round cups, experiments show that the formability of a sheet metal is increased in general if the normal anisotropy of the metal is made higher.[3] This can be seen from experimental data presented in Fig. 24.10 and Fig. 24.11. It happens because the stress condition in the flange (B and B') and the stress condition in the cup wall (A and A') are different; see Fig. 24.9.

In the flange, there are compressive stresses in the circumferential direction and tension in the radial direction. However, in the cup wall, there is biaxial tension. Moreover, as shown in Fig. 24.9, the yield locus for an anisotropic material has an elongated elliptical shape, instead of the less elongated shape for an isotropic material. It is therefore advantageous to increase the anisotropy of the sheet metal, because this allows cups with higher walls to be deep-drawn.

It is therefore obvious that on making a material more and more anisotropic, i.e., on increasing the value of $\bar{R}$, the flow stress of the material in the flange will decrease, while the flow stress of the material in the cup wall will increase. Hence, an increased $\bar{R}$ will strengthen the cup wall, while pulling the flange inward becomes easier. But, as shown in Fig. 24.10(a), experiments show that there is no significant improvement in formability in terms of increased cup height in deep drawing if the strain-hardening exponent n of the material is increased, as it is in stretch forming.

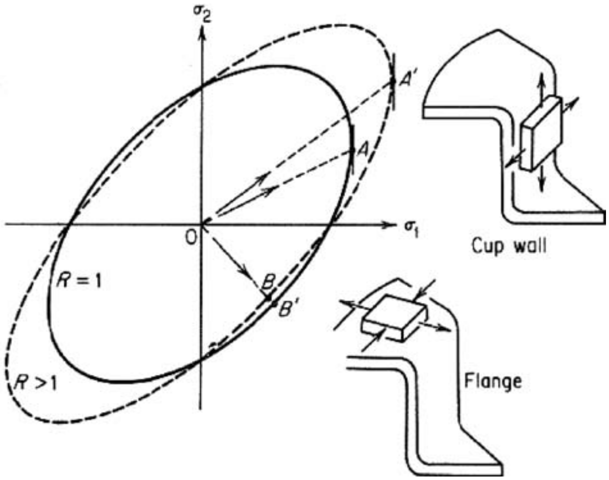

Figure 24.9. High $\bar{R}$ is advantageous in deep drawing, because increasing $\bar{R}$ above 1 softens the flange while the cup wall becomes stronger. (Reprinted with permission of The McGraw Hill Companies from Dieter, G.: "Mechanical metallurgy," McGraw-Hill, 1986.)

It has been shown that different metals have different ability to develop high normal anisotropy $\bar{R}$. High $\bar{R}$ can be obtained[3] for steel alloys, and especially for titanium alloys. Because of this, these metals perform better in deep drawing than, for instance, Cu and Al alloys and brass; see Fig. 24.11.

24.9 Earing in Deep Drawing

When sheet metal is deep-drawn into round cups, the cups will develop so-called *earing* if the sheet metal is anisotropic. Earing means that the final cup height is not even around its periphery; instead, the edge of the cup has a wavy appearance, so that four ear-shaped elongations appear around the circumference of the cup wall. This is because the anisotropic material being deep-drawn has different ability to

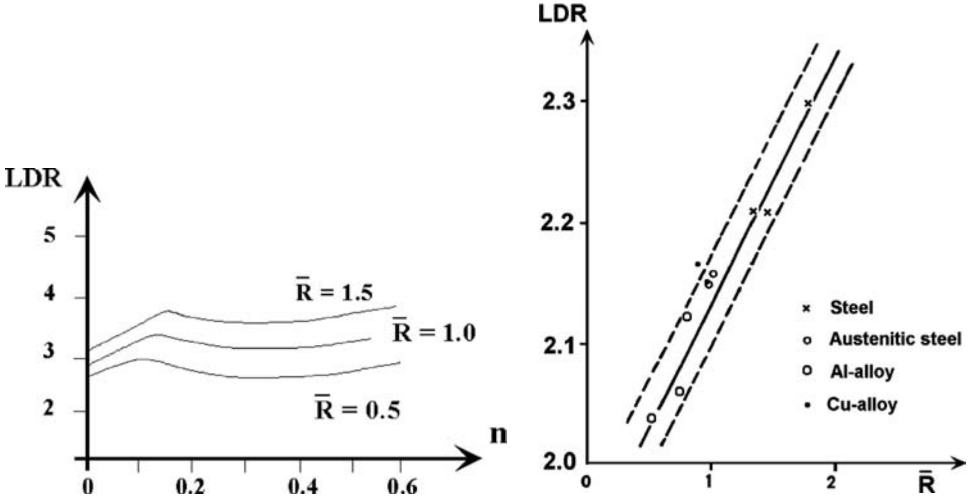

Figure 24.10. Formability in deep drawing is improved if the $\bar{R}$-value of the sheet-metal is increased,[4] but there is no corresponding improvement if the strain-hardening exponent is increased. (Reprinted with permission of Swerea IVF AB.)

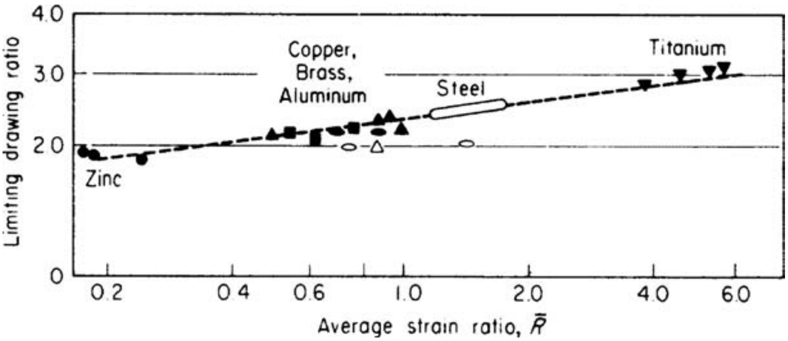

Figure 24.11. R-value and achievable LDR for some metals.[5]

stretch and elongate in the different directions in relation to the rolling direction of the sheet. A cup with earing is shown at the upper left in Fig. 24.12. As this figure depicts, the height of the cup varies continuously around its circumference, from the minimum h_d between ears, to the maximum h_e at each ear. The degree of earing in deep drawing of round cups is commonly quantified by the following formula:

$$\Delta h = \frac{h_e - h_d}{0.5(h_e + h_d)} \times 100\% \tag{24-8}$$

Experimentally it has been shown that the tendency to earing in deep drawing of round cups increases significantly when the numerical value of the planar anisotropy, ΔR, of the sheet metal is increased; see Fig. 24.12. Earing in deep drawing is considered undesirable for two reasons. One reason is that when it is present, it is required to cut away some material to produce a final cup with an even edge. Because of this, the material yield is reduced from when earing is absent. Another reason is that when high ears form, they will also tend to wrinkle, and when the ears are pulled through the gap between the punch and the die, there will be excessive die wear. The die life is therefore reduced in deep-drawing operations if there is much earing.

24.10 Springback in Sheet-Metal Forming

The springback phenomenon in bending of sheet or plate specimens was explained in Sec. 24.3. As shown in Fig. 24.4(a), the bending angle of the specimen is less after unloading of the bending force than before. Because of this [see Fig. 24.4(a)], the final radius of curvature of the bend is also larger after unloading than it was before, i.e., $R_1 > R_0$.

We can denote the axial length of the bend, i.e., the *bend allowance*, by the symbol B; see Fig. 24.13. This length will approximately be the same before and after bending; hence, the following approximation is valid:

$$B = \left(R_0 + \frac{t}{2}\right)\alpha_0 = \left(R_1 + \frac{t}{2}\right)\alpha_1 \tag{24-9}$$

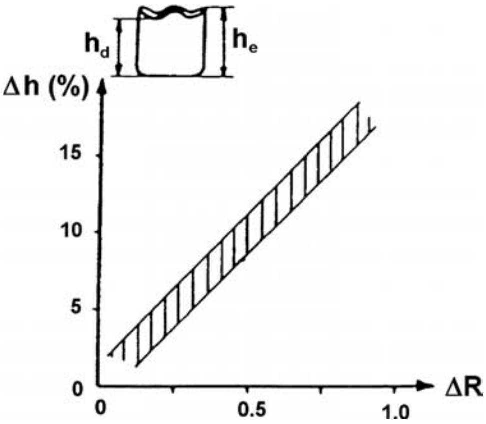

Figure 24.12. The degree of earing increases with increasing planar anisotropy of sheet metals.

In bending, a parameter called the *springback ratio* is commonly defined:

$$K_s = \frac{\alpha_1}{\alpha_0} \tag{24-10}$$

Combination of the preceding two equations gives the following expression for the springback ratio:

$$K_s = \frac{\alpha_1}{\alpha_0} = \frac{R_0 + \dfrac{t}{2}}{R_1 + \dfrac{t}{2}} = \frac{\dfrac{R_0}{t} + \dfrac{1}{2}}{\dfrac{R_1}{t} + \dfrac{1}{2}} \tag{24-11}$$

As we see from eq. 24-11, the springback ratio depends on the ratio between the radius of curvature of the bent sheet or plate and its thickness. Experimental springback data gathered for the case of bending are available in the literature[6] for different materials, as graphs of the function $K_s = f(R_1/t)$; see Fig. 24.14.

For sheet materials of some aluminum, nickel, titanium, and steel alloys, experimental springback data[7,8] in bending have been fitted with the following relationship:

$$\frac{R_0}{R_1} = 4\left(\frac{R_0\sigma}{Et}\right)^3 - 3\left(\frac{R_0\sigma}{Et}\right) + 1 \tag{24-12}$$

Springback in bending thus can be estimated either from eq. 24-12 or from eq. 24-11, with values of the springback ratio obtained from the graphs in Fig. 24.14.

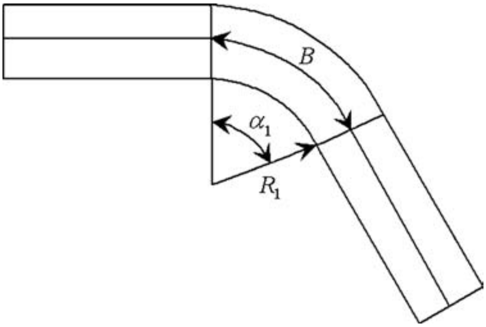

Figure 24.13. Final geometry in the bend after release of the bending force.

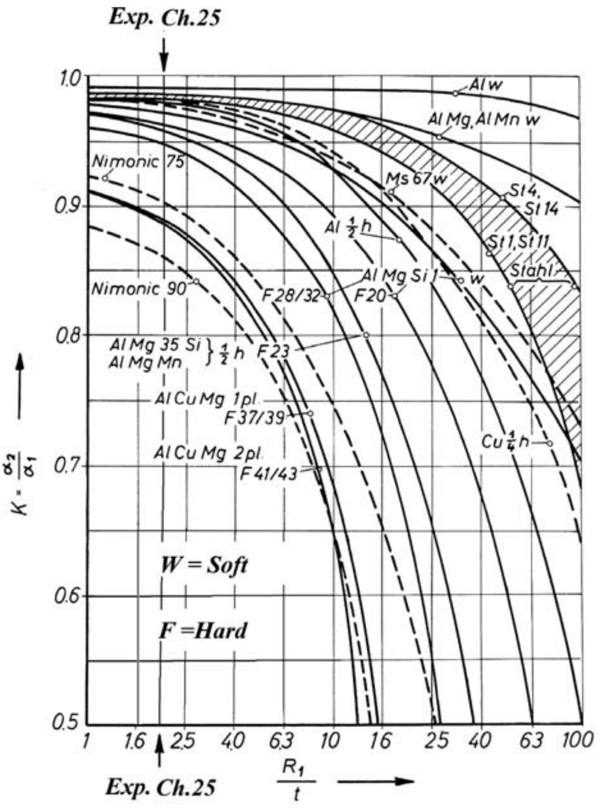

Figure 24.14. Experimental springback-ratio data for some sheet materials. (Reprinted with permission of Carl Hanser Verlag © München.)

In industrial bending, the phenomenon of springback is of great importance. This is because over time there will be considerable variation in the main mechanical properties, as, for instance, the flow stress of the material in a particular industrial bending operation. Variation in mechanical properties of the material used can, for instance, stem from variations in the chemistry of the incoming material, or in processing conditions in the rolling process when the sheet metal is fabricated. This variation has great effect on the amount of springback obtained in the bending operation. Hence, there will be shape variations in the bent components over time, which will be difficult to predict, and also to correct for.

Because of the variation in the springback, it is difficult to obtain accurate shape of bent components, in terms of a final constant bending angle, α_1, if no special precautions are taken. This angle may therefore vary considerably for the same component when it is produced over some time under apparently identical conditions.

There are some ways to compensate for springback in bending. To a large extent, excessive springback can be eliminated[9] by use of one of the following compensation methods:

(1) *Overbend* the component slightly; i.e., use a bending die that bends the component to a somewhat too large bending angle. Then the bent component will spring back to the correct shape when the bending force is released.

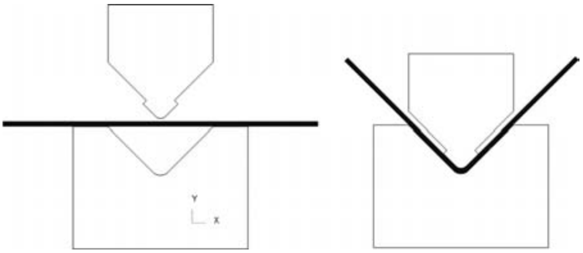

Figure 24.15. Coining of the bend to eliminate springback.

(2) Use a bending die that *coins*, i.e., plasticizes, the cross section of the specimen locally in the bend, in the end stage of the bending process; see Fig. 24.15.

(3) *Stretch-bend* the component so that the whole cross section of the sheet is shaped under tension during bending.

When method (2) is applied, the mechanics of the bending operation will change toward the end, so it becomes similar to forging, in which springback is not a big problem.

Problems

Stage	α (deg)	Width (mm)	Length (mm)	Thickness (mm)
Initial		12.7	50	0.275
After test	0	11.4	59	
	45	11.6	59	
	90	11.4	59	

24.1 To measure the anisotropy of a particular sheet material, tensile test specimens were taken out of it at angles of 0°, 45°, and 90° to the rolling direction. The samples were stretched up to 18% nominal strain without any tendency of necking. Prior to and after testing, the geometric parameters in the accompanying table were measured from the thinned region of the samples.

(a) Determine the thickness of the specimens after the end of testing: $t_{\alpha=0^\circ}$, $t_{\alpha=45^\circ}$, $t_{\alpha=90^\circ}$.

(b) Find the factor of anisotropy for the specimens in the three directions: $R_{\alpha=0^\circ}$, $R_{\alpha=45^\circ}$, and $R_{\alpha=90^\circ}$.

(c) Determine the normal anisotropy and the planar anisotropy of the sheet.

(d) Would you expect the sheet material to have better formability in deep drawing than a similar isotropic material?

(e) The following material parameters can be determined in tensile testing: $\bar{R}$, ΔR, K, n. How will these parameters affect the formability and required forming load in the following sheet-metal forming operations:

- (i) Deep drawing
- (ii) Stretch forming

24.2 Describe as briefly as possible, but completely, how the normal anisotropy and the planar anisotropy of a rolled plate are determined.

24.3 The anisotropic properties of a plate are determined to be $\Delta R = 0.2$ and $\overline{R} = 2.2$. A round cup of 300 mm diameter is to be produced from this plate by means of deep drawing.

- (a) Determine the height of the highest possible cup that can be made from this plate in a single deep drawing operation. Assume that the wall-thickness of the cup remains constant and equal to the thickness of the plate over the whole cup wall.
- (b) Specify the maximum cup height that can be made, as a fraction of the inner diameter of the cup. Discuss the validity of the assumption made.
- (c) Determine the height of the ears obtained on the resulting cup.

NOTES

1. Keeler, S. P.: "Rating the formability of sheet metal," Metals Progress, Oct. 1966, pp. 148–153.
2. Goodwin, G. M.: "Application of strain analysis to sheet metal problems in press shop," Metallurgica Italiana, Vol. 60, 1968, pp. 767–774.
3. Dieter, G.: "Mechanical Metallurgy," McGraw-Hill, 1986.
4. Weidemann, C.: "Determination of the deep drawability of materials," Expert Conference, Lerum, Sweden, 14–15 Sept., 1972, Jernkontoret, Stockholm.
5. Atkinson, M.: "Assessing normal anisotropic plasticity of sheet metals," Sheet Metal Industries, Vol. 44, 1967, pp. 167–178.
6. Oehler, G.: "Biegen," Hanser, München, 1963 (in German).
7. Gardiner, F. J.: "The springback of metals," Trans. ASME, Vol. 79, 1957, pp. 1–9.
8. Queener, C. A., and De Angelis, R. J.: "Elastic springback and residual stresses in sheet metal formed by bending," ASM Trans. Quarterly, Vol. 61, 1968, pp. 757–768.
9. Kalpakjian, S., and Schmid, S. R.: "Manufacturing Processes for Engineering Materials," 5th ed., Prentice-Hall, 2008, p. 410.

REFERENCES

Boljanovic, V.: "Sheet Metal Forming Processes and Design," Industrial Press, New York, 2004.

Hu, J., Marciniak, Z., and Duncan, J.: "Mechanics of Sheet Metal Forming," 2nd ed., Butterworth-Heinemann, 2002.

Oehler, G.: "Bending," Hanser Verlag, München, 1963.

Szumera, J.: "The Metal Stamping Process: Your Product from Concept to Customer," Industrial Press, New York, 2002.

Index

accumulation of outer layer of billet in discard, 322
adaptive remeshing, 223
adhesion of lubricant to workpiece, 146
advantage and disadvantage of backward extrusion, 24, 324
allotropic behavior of steel, 118
analogy, between stress and strain, 62, 66
anisotropy
  factor of, 442
  measurement, 443
  normal, 443
  planar, 443
  in sheet-metal, 442
  in worked metals, 7
area reduction, 77
aspect ratio in
  cylinder compression, 81
  plain strain compression, 35
asperity, 141
  plastification, 142
atoms, packing of, 3
austenite, 118
average
  length strain, 78
  pressure in frictionless compression, 81
axi-symmetric FEM model, 225

back-pull in wiredrawing, 398
backward cup extrusion
  effective strain rate distribution, 286
  effective strain distribution, 288
  FEA of process, 285–301
balanced biaxial stretching, 438
barreling of cylinder in compression, 108
bearing in wiredrawing dies, 399
bend allowance, 447
bending, 28
  of sheet-metal, 439
biaxial stretching, 438
billet, 22
  removal without deformation, 350
blank holder, 27, 444
blanking, 30
  conventional, 30
  fine, 30
blister defect, 323, 331
bloom, 22
bottleneck in forming, 12
boundary
  film lubrication, 146, 147–149
  lubrication, 146
boundary conditions in FEA, 224
breakdown of material, 127
  due to cracking, 134
breakdown of
  cast microstructure, 4
  lubricant film, 13
Bridgman's
  assumptions in necking analysis, 243
  correction factor in tensile testing, 105
  theoretical analysis of, 104
buckling, 19
  in deep-drawing, 444
bulging in
  cylinder compression, 108
  wire drawing, 417, 418
bulk metal forming, 9, 18
burp cycle, 332

calibration draw, 395
capstan, 396
casting
  defect formation, 5
  material loss, 5
cast iron, 3
cavity filling, 268
cementite flakes 2, 3
center bursts, 421
center zone in plain strain compression, 41
cermets, 398

  material model, 115
chevron cracks, 421
  growth in FEA, 423
circle grid analysis, 435, 436
  to determine strains, 68
classification system
  extrudability of Al-alloys, 335
  extrusion processes, 10
  metal forming, 9, 18
  shapes of Al-profiles, 334
  shapes of forgings, 271, 272
  subdivision metal forming processes, 10
  types of metal flow in extrusion, 326
clay, deformation of, 1
  deformation mechanism, 3
clean cut in shearing, 30
cleaning, of surfaces, 144
closed die forging, 20–21
  die filling in, 302
  example of laboratory process, 302
  FEA of, 302–316
  optimized process, 279
Cockroft-Latham failure criterion, 134
coefficient of friction, 142
cogging, 20
coiling of wire, 396
cold drawing of wire, 27
cold forming
  cold working by wiredrawing, 27
  to gain high strength, 7
  temperature range of, 118
  vs. hot forming, 34
complex strain path in sheet-metal forming, 437
compression
  axial, 87
  homogeneous slab, 87
  retarded stroke for constant strain rate, 108
compression testing, advantages over tensile testing, 95
compressive stress
  on inside of bend, 439
  in wiredrawing die, 398
cone angle in wiredrawing, 400
confinement of air in extrusion material, 332
constancy of volume, 63
  deviation from rule of, 64
constitutive equation
  definition, 115
  in cold forming, 118
  general expression, 117
  in hot forming, 122
  including microstructural mechanisms, 122
  metals in general, 115–118
contact angle in rolling, 370
contact area
  apparent area, 141
  in compression, 107
  real area, 141
contact conditions between
  billet and container, in extrusion, 351
  roll and workpiece, in rolling, 365
contact mechanisms, workpiece-die, 143
contact pressure against die as process parameter, 14
contact pressure against die in
  cylinder compression, 230–233
  deep drawing, 27
  from the slab method, 373
  light slab rolling, 380
  normal slab rolling, 387
  normal wiredrawing, 427
  strip rolling, 391
  wiredrawing, 400
contact zone against
  die in closed-die forging, 302–305
contamination
  as subsurface defect in extrusion, 330
  of surfaces, 144
continuous casting, 22
continuum
  mechanics, 2
  medium, 2
converging channel of wiredrawing die, 399
conversion coating, 300
cooling
  effects, 159, 162
  of plate against die, 163–164
copper wiredrawing, 414
Coulomb friction
  model, 140–142
  validity of model, 142
cracking, 127
  due to lamination, 8
  in cylinder bulge, 134, 136
  in shear, 136
  transverse cracking in extrusion, 134
critical blank size in deep-drawing, 444
crystals, aggregate of, 3
cup forming by deep drawing, 27
curve fitting
  applied for the flow stress, 118
  determination of constants, 119
cutting, 10
cylinder compression
  basic mechanics of test method, 106
  compression velocity, 106
  deformation in corner of bulge, 252
  deformations in compression test, 253–254
  dies applied in test, 106
  experimental set-up, 106
  FEA of test, 229
  flow curve in test, 107
  with friction, 108
  friction effects, 199
  friction measurement using pins, 153–154
  frictionless compression, 1
  homogeneous compression, 107, 251

  principal stress in frictionless case, 210
  reduced friction in test, 109
  strain rate field in frictionless case, 210
  as technological test, 93, 95
  velocity field in frictionless case, 209

damage parameter in
  light slab rolling pass, 381
  normal slab rolling pass, 386
  normal wiredrawing from FEA, 427
  plain strain compression, 47
  small reduction, large cone angle wiredrawing, 421
  strip rolling pass, 392
  wiredrawing, 421
damage parameter, critical value, 134
dead zone in
  backward cup extrusion, 286
  cylinder compression, 109
  extrusion, 183, 322
  plain strain compression, 41
  strip rolling, 390
deep drawing, 27
  applied tooling, 27
  fracture in, 28
  of rectangular cup, 440
  of round cup, 440
  of sheet-metal, 439
  wrinkling, 28
defects
  avoid defects because of economy, 14
  blisters in extrusion, 323
  of critical size, 130
  in forging, 279
  hot tearing in Al-extrusion, 159
DEFORM®-code, 223
  FEM-approach used, 224
deformation
  comparison of compression and tension, 59
  over edge of plain strain compression die, 44
  effect of varying clearance in shearing, 260–263
  elastic, 1
  energy, 160
  fluctuations in wiredrawing, 417
  homogeneity in cylinder compression, 108
  homogeneity in extrusion seam, 238
  of inhomogeneous nature, 2
  macroscopic, 2
  mapping of, 2
  mechanism of, 4
  microscopic, 3
  multiplication of deformation crosses, 46
  near punch in backward cup extrusion, 296
  patterns in wiredrawing, 431
  of permanent character, 116
  plastic, 1
  simple measure of total deformation, 77
deformation analysis, 40–46
deformation characteristics of extruded rod, 192
deformation cross in
  normal wiredrawing, 424
  plain strain compression, 44
  strip rolling, 390
  cylinder compression, 253
deformation from
  deformed grid pattern, 182
  effective strain distribution, 43
  effective strain rate distribution, 43
  grid pattern in backward extrusion, 290–292
  strain rate distribution in wiredrawing, 425
  velocity field, 85–87
deformation in
  backward cup extrusion, 286
  deep-drawing, 440
  extruded rod from grid pattern, 192–195
  extruded rod, 361
  extrusion, 24
  extrusion billet from strain rate, 362
  front end of extruded rod, 322
  hot closed die forging, 310–314
  light pass slab rolling, 377, 379
  neck from circle pattern, 247
  necking section, 243
  neck in tensile test, 103
  normal pass slab rolling, 383
  plain strain compression test, 40–46
  shearing, 30, 259
  sheet-metal forming, 438
  strip rolling, 389
  wiredrawing, low reduction – large angle, 416
  wiredrawing, normal drawing geometry, 425
degree of reduction, 79
deletion of FEM-mesh to model cracking, 422
Δ-parameter, 81
  in plain strain compression, 36
  in rolling, 376
  in strip rolling, 393
  in wiredrawing, 403, 414
  in Wistreich's wiredrawing experiments, 414
diamond in wiredrawing die, 398
die bridge in extrusion, 333
die cavity, 20
die filling in closed-die forging, 277, 302
die geometry, characteristic parameters, 400
die-life, influenced by fatigue, 142
die orifice, 23
dies
  in metal forming, 13
  wear of, 13
die splitting force in
  strip drawing, 149
  wiredrawing, 401, 414
diffuse necking, 131
dimensional stability in drawing, 395
direct contact between surfaces, 144
directionally oriented microstructure, 442

discard
  in extrusion, 321, 323
  removal of, 324
dislocation, 3
  density, 3
  movement, 3
dislocation networks in cold and hot forming, 122
displacement components, 86
division processes, shearing, 30
draft in rolling, 383
drawing
  as continuous process, 396
  as discontinuous process, 396
  of strip, 64
  unit in wiredrawing machine, 397
  wheel, 396
drawing cell in drawing machine, 398
drawing conditions in normal wiredrawing, 424
ductility, 128
  increase through metal working, 7

earing
  factors influencing earing, 447
  phenomenon in deep-drawing, 446
ease of working, 128
economy in metal forming, 14
edges for cutting, 30
effective strain distribution, plain strain compression, 43
effective strain rate distribution, plain strain compression, 43
elastic
  layer in bend, 440
  zone, 191
elastic deformation
  of dies, 53
  in tensile test, 102
elasticity theory, 53
elastic-plastic
  materials, 116
emissivity, 164
emptying diagram
  in backward cup extrusion, 296
  concept, 195
  in extrusion made by FEA, 359
emptying line
  longitudinal, 199
  transverse, 197
energy consumption
  definition of, 69
  in extrusion, 325
  friction energy, 406
  for homogeneous deformation, 405
  for inhomogeneous deformation, 407–409
  total in wiredrawing, 405, 409
energy dissipation, 69
entrance into roll gap, 376
equation to find friction in split die experiment, 401
Erichsen-test, 438
Eulerian description, 222
eutectic phases, as contamination in extrusion, 324
excessive stresses in sheet-metal forming, 441
experiments to validate FEM analysis, 35
explicit FEM-method, 222
exponent of strain hardening, 118
extrudability of
  Al, 25
  Al-alloys, 335
extrudate, 320
extruded profiles, 23
extrusion, 23–26, 320
  advantage of direct over indirect, 24
  backward process, 23
  billet, 23
  classification of processes, 10
  complex hollow profile extrusion, 25
  container, 23
  of copper and brass, 24
  defect, 331
  direct process, 23
  division into subprocesses, 326, 347
  flow of outer layer of billet, 24
  force, 337
  force against container wall, 338
  forward process, 23
  friction force, 341
  homogeneous deformation force, 341
  hot extrusion of Al, 322
  hot lubricated, 25
  indirect process, 23
  inhomogeneous deformation force, 342
  limitations in backward extrusion, 24
  of light metals, 24
  load in backward extrusion, 325
  metal flow in direct and indirect process, 24
  in multi-hole dies, 24
  peripheral billet layer, 24
  practice in forward extrusion, 323
  pressure, 337
  pressure welding, 25
  punch, 23
  ram, 23
  residue, 321, 323
  seam welds, 26
  shell extrusion, 24
  of steel, 25
  tooling in porthole die extrusion, 25
  total force, 337, 343
  welding, 26
  welding, FEM-model of, 233–238
  welding chamber, 25

failure
  criteria, 134
  catastrophic, 130

FEA
  correction of flow curve, 245–246
  to determine thermal effects, 168–173
  in general, 220
  general importance in metal forming, 221
  graphical presentation of results, 229
  results as parameter distribution, 229
FEM-codes
  development of, 221
  to model metal forming, 223
FEM model, 2D
  backward Al-extrusion, 358–362
  backward cup extrusion, 285–301
  cylinder compression, 136, 200–201, 229–233, 250–253
  extrusion welding, 237–238, 333
  forward Al-extrusion, 352–357
  forward extrusion, subprocesses, 347–349
  plain strain compression, 225, 226
  shearing, deformations in sheared layer, 257–263
  shearing, to find K and n, 264–265
  slab rolling pass, 376–393
  tensile test, formability consideration, 130–131
  tensile testing, risk of cracking, 135–136
  tensile testing, stress conditions in neck, 243–246
  wiredrawing, 415–431
FEM model, 3D
  closed-die forging, 302–316
  cylinder compression, 253
  extrusion welding, 233–237
  plain strain compression, 37–50
  tensile testing, necking, 247
FEM-modeling, in general, 220
FEM-solver, 224
ferrite, 2, 118
finished product, 13
finishing die, 274
finite difference method, 204
finite element analysis (FEA), 34
  validation of, 35
finite element method (FEM), 34
finite elements, 221
flash, 21
  formation of, 4
flash gap, 277
  characteristic geometrical conditions, 281
  common designs, 281
  design rules in closed-die forging, 280
flash less forging, 20
flat rolling, 22
flat-faced die, in extrusion, 322
FLD-diagram, 130, 441
flow criteria, the von Mises and Tresca criterion, 111
flow criterion, correctness of, 38
flow curve, 116
  determination in cold forming, 107
  determination curve in hot forming, 107
  from tensile test, 102
  true and nominal curve, 103
flow direction of outer layer of billet in extrusion, 331
flow formulation, 222
flow patterns in extrusion, 326–328
flow rule of Lévy-Mises, 73
flow stress
  of Al-alloys in bending experiments,
  in cold, warm, and hot forming, 115, 116
  from compression test, 107
  of copper wire, 117, 416
  general function, 118
  to get right metal flow in Al-extrusion, 353
  mean value of in wiredrawing, 405
  parameter influence, 116
  as process parameter, 14
  from shearing test, 263–265
  temperature dependence, 117
  variation due to microstructure, 118
flow types in extrusion, 190
foil, 442
folds, 279
force
  on the roll, 367
  total force in wiredrawing, 399
forgeability, 269
  of different metals, 270
forging
  as a requirement, 7
  avoiding unsound grain flow, 8
  as nonstationary process, 85
  deformation in hot closed die forging, 310–314
  design of multistep series, 274–276
  design principles, 276
  design to avoid defects, 280
  to improve fatigue resistance, 8
  mass distribution principle in, 276
  optimum temperature, 269
  stock, 274
  typical multi-step forging sequence, 275
forgings
  complexity of, 271
  shapes difficulty to forge, 272
formability, 127
  to avoid defect formation, 14
  improvements in deep-drawing, 442
  limits, 441
  of metals in deep-drawing, 446
  parameter in deep-drawing, 445
  parameter in stretch forming, 445
forming under
  compressive stress, 9, 18
  tensile stress, 9, 18

fracture, 127
  elongation, 94, 103
  in forgings due to defects, 280
  in shear, 138
  strain, 94, 103
free forming, 19
friction
  in backward cup extrusion, 300
  Causing load increase in bending, 216
  determination in plain strain compression, 37
  dry friction, 144–145
  effects in metal forming, 139
  effects on flow curve from compression, 254
  energy dissipation, 162
  factor, 143
  force, 141
  force as process parameter, 14
  heating, 161
  hill, 208
  influence on forming load, 139
  measurement in forming, 149–155
  measurement in wiredrawing, 400
  measurement using pins, 152
  shear stress, 142
  shear stress in wiredrawing, 400
  from surface ring pattern, 199
friction coefficient, 142
  value, boundary film lubrication, 148
  value, hydrodynamic lubrication, 147
frictionless compression, average pressure vs. Δ, 81
friction models, 140
  comparison of models, 143
  implementation of in FEM-codes, 229
full separation of contact surfaces, 144
fusion welding, 26

general extrusion, part of extrusion process, 349
generic deformation modes in sheet-metal forming, 439
Gleeble simulator, 96
  testing, 35
  working principle of simulator, 96
grain
  boundaries, 2
  as crystals, 3
  flow in forgings, 8
graphical tools in FEM analysis, 224
grid pattern analysis
  in compression experiment, 249
  deformation of grid elements, 41
  in extrusion welding, 237
  in FEA of compression, 250
  in shearing experiment, 259
grid pattern distortions in
  backward Al-extrusion, 359
  light slab rolling pass, 379
  normal slab rolling pass, 385
  normal wiredrawing, 426
  strip rolling pass, 390
  wiredrawing, small reduction, large cone angle, 418
grid pattern technique, 2, 181
  advantage of pattern from pins, 184
  appearance of grid, 182
  in backward extrusion of Al cup, 290–292, 357
  contrast materials, 184
  deformed pattern in extrudate, 183, 188
  identification of grid elements, 186, 189
  intrinsic pattern, 184
  making pattern from contrast pins, 184, 185
  notation to identify grid lines, 186
  parting agent to avoid welding, 182
  perfect deformed pattern in Al-extrusion, 187
  in plain strain compression, 36
  scratched patterns, 181

hardness testing
  contact pressure, 82
  indenter, 93
  test method, 93
heat
  capacity, 160
  effects, 159
  transfer coefficient, 163
height strain, 80
height-to-diameter-ratio, in cylinder compression, 80
Hensel-Spittel constitutive equation, 118
high-strain-rate zone in
  normal wiredrawing, 424
  plain strain compression, 45
  rolling, 377
  wiredrawing, 416
hollow
  extrusion dies, 25
  profile extrusion, 333
homogeneous deformation in cylinder compression, 109
Hooke’s law, 73, 115
hot forming
  temperature range of, 118
  vs. cold forming, 34
hot tearing, 159
  mechanism in Al-extrusion, 178
hottest spot in Al-extrusion die, 178
hydra-wedge for multistep compression, 98
hydrostatic extrusion, 322

ideal work method, 204
impact extrusion, 21
  backward method, 21
  forward method, 21
implicit FEM-method, 222
inclusions, of MnS, 7
incremental strain from velocity field, 85

index notation for stress tensor, 55
inferior properties due to lamination, 8
ingot, 19
inhomogeneous deformation in
  cylinder compression, 109
  light slab rolling pass, 379
  normal slab rolling pass, 383
  normal wiredrawing from FEA, 425
  strip rolling pass, 390
inserts, used in wiredrawing dies, 398
instability, 18
  causing necking, 131
  criterion for start of necking, 104
  in high slender cylinder compression, 95
  in tensile testing, 103
integrity of materials, 128
interface between die and workpiece, 13
intrinsic ductility, 128
inverse modeling, 37
  determine flow curve in tensile testing, 246
  determine friction in backward cup extrusion, 299–301
inverse parameter identification to
  determine friction, 37
  get right localized shear, 37
inverse segregation in extrusion billet, 324
inward compression, part of extrusion process, 349
isothermal FEM model, 225
isotropic materials, 63
isotropy of sheet-metal, 442

joining
  of metal streams in extrusion, 25
  processes, 9

Lagrangian description, 222
lamination, 8
  in extrusion, 321
laps, 279
largest principal stress in normal wiredrawing, 427
layered appearance, 8
length
  strain, transformed to reduction of area, 79
Lévy-Mises flow rule, 73
limiting draw ratio, LDR in deep-drawing, 444
load-stroke curve
  cylinder compression, 107
  extrusion, 325
  forging, 277
  optimized curve in closed-die forging, 315
localized necking, 94, 131
logs of Al, 24
loss of material, 4
low-cycle fatigue of dies, 142
lubricant, 13
  thick lubricant film through wedge effect, 147
  viscosity of, 147
lubricated extrusion, 322
lubrication
  boundary film, 147
  boundary films in, 148
  in drawing, 397
  in forging, 271
  glass in extrusion, 25
  hydrodynamic, 146–147
  mechanisms, 144
Ludvig's law, 119

machines, used in metal forming, 13
machining
  material removal, 6
macro etching, 8
malleability, 128, 269
manufacturing
  cheapest process, 7
  classification system, 9
  comparison of processes, 4
  methods, 1
  of rod and wire, 26
mass production, 6
material
  failure in forming, 127
  flow phenomena in wiredrawing, 431
  inhomogeneity on micro-scale, 3
  loss, 4
  loss reduction in forging, 314
  models implemented in FEA, 227
  removal, 4
matte surface, hydrodynamic lubrication, 146
maximum principal stress to explain chevron cracking, 423
mean through thickness strain rate in rolling, 370
measurement techniques applied in Al-extrusion, 175
mechanical properties
  improved by forming, 4
  of a material, 103
  of finished product, 15
mechanical working to gain high strength, 7
mechanism of chevron crack formation, 422
metal flow analysis, 181
metal flow in
  direct compared to indirect extrusion, 195
  Al-extrusion from FEA, 354
  extrusion, 326–328
  in FEA, validated experimentally, 354
  idealized 2D extrusion welding, 235
  unlubricated direct extrusion, 189–191
metal forming
  characteristics of, 4
  classification system, 9
  definition of, 1
  overview of processes, 10
  requirements for sound process economy, 13
  simulator, 93
  stable process, requirement, 7, 13

metal removal
  processes, 9
  by shearing, 30
metallic bond formed in extrusion welding, 334
mixed lubrication, 149
modeling techniques
  description of methods, 220
  goal for performing engineering analysis, 219
model material, 181
Mohr's circle, 56
  sign convention, 57
  for strains, 62
multistep
  forming, 19, 98
  wiredrawing, 398

near net shaping, 20
neck
  average axial stress in, 105
  as defect in sheet metal forming, 103
  formation, 18
  growth in tensile testing, 102
  radius of curvature in, 105
  tri-axial stress state in, 104
necking
  failure in sheet-metal forming, 130, 441
  FEM model of, 130
  instability in, 94
  localized, 131
  in tensile testing, 94, 102, 130
neutral plane in
  bending, 439
  plane strain compression, 34
neutral point in rolling, 367
node in FEM-mesh, 221
nominal strain from
  circle grid analysis, 437
  tensile test, 102
nominal stress from tensile test, 101
nonstationary processes, 84
normal stress, definition of, 53
Northon-Hoff constitutive equation, 118
numerical modeling, 220

open die forging, 19–20
optimum die cone angle in wiredrawing, 411
origin inside billet of surface layer of rod, 195
outer billet layer, outflow of in extrusion, 329–331
out of the plane stretching, 438
overfolding, 279
  in extrusion, 329
overloading of tools, 53
oxide layer, 144
oxide layer on
  Al, 145
  Al, oxide effect on emissivity, 165
  Cu, 145

particle paths, 85
  in wiredrawing, 429
pearlite, 2
peripheral billet skin, flow of in extrusion, 328
physical
  in big WUMSI simulator, 98
  metal forming simulation, 35
  modeling, 37, 96–101
  modeling techniques, 220
  simulation, 92, 96
pinching, part of extrusion process, 349
pin measurement of friction, 149
pipe, defect in extrusion, 181, 331
plain strain compression
  applied to sheet metals, 109
  average contact pressure in, 111
  effective strain in, 111
  effective stress in, 111
  inside channel-shaped die, 95
  maintain ideal conditions 35, 109, 111
  mechanics of ideal test, 110
  relative contact pressure in, 82
  technological test, 34, 93, 95
  test to mimic rolling, 109
  thermal effects in test, 227
  thickness strain in, 111
  with overhanging platens, 96
plain strain
  tensile test, 436
  FEM model, 225
plastic
  constraint in plain strain compression, 110
  straining, 4
  yield, 70, 116
plasticity theory, 53
plastic zone, 12
  geometrical shape of, 81
  in backward cup extrusion, 286
  in normal wiredrawing, 424
  in wiredrawing, 400, 416
plastification, 4, 53
  of forming dies, 142
plate material, 442
pointing of wire or rod before drawing, 396
point-tracking, in FEA to trace metal flow, 361
polymers
  deformation mechanism, 3
  deformation of, 1
porthole die extrusion, 25, 333
postprocessing results in plain strain compression, 40–50
postextrusion deformation, avoiding phenomenon, 351

postprocessing, 224
power law
  cold forming, 119
  hot forming, 122
power of deformation, 70
Prandtl-Reuss equations, 222
precision forging, 20
predeformation of back end of billet, 193, 328
preforming in forging, 274
preform optimization in closed-die forging, 314
preprocessing, 224
prescribed circumference of extruded profile, 24
pressure
  through boundary interface, 141
  distribution against die in wiredrawing, 420
  pad, 321
  peak in friction hill in wiredrawing, 420
  peak in friction hill in rolling, 380
  welding, 26
  welding in extrusion, 334
  welding onto the die, 13
primary
  dead zone in extrusion, 191, 356
  deformation zone (extrusion), 190, 322, 356
  shear zone in extrusion, 356
principal strains from circle grid analysis, 437
principal stress
  definition of, 55
  distribution of parameter in neck, 243
  largest value in light slab rolling pass, 382
  largest value in normal slab rolling pass, 386
  in plain strain compression, 48
problem areas, in forming, 12
process parameters, 14
  importance of, 14
  in metal forming, 14
product in forming, 13
production processes
  characteristics of, 6
  select the best process, 6
production in low numbers, 6
productivity, high level of, 13
profile drawing, 396
projected length of arc of contact, 368, 372
punch load, friction effects in backward cup extrusion, 296
pure shear in torsion test, 111
pyrometry, 159, 164

radial compression, part of the extrusion process, 349
radiation of heat, 159
Ramberg-Osgoods equation, 119
recovery, 122
recrystalization, 7, 122
redefined strain in compression, 80
reduction ratio
  definition of, 77
  in extrusion, 79
reduction in
  percent, 79
  wiredrawing, 399, 403
remeshing, 223
  to get good FEM mesh, 223
removal of material, 4
results of FEM-analysis, 224
retention of peripheral layer of billet, 191, 327
rigid-plastic materials, 116
rigid zone, 42
ring compression test, 149–152
  measurement technique, 149
  ring proportions, 151
riser, in casting, 5
rod, drawing of, 27, 395
roll
  force equation, 367
  forging, 275
  gap, 366
rolling
  force, 367
  problem areas, 12
  processes, 22–23
  schedule, 23
roughening rolling mill, 22

sawing to make workpiece, 7
scaling defect in extrusion, 330
scalping operation in extrusion, 324
scraping of ram against container, 193
scraping
  of ram head against container wall, 328
  part of extrusion process, 349
scratching
  at rear end of container, 351
  part of extrusion process, 349
secondary
  dead zone, 191
  deformation zone, 190, 322
  shear zone, in extrusion, 356
section rolling, 22
security components, 6, 302
seizure of workpiece in rolling, 376
selection of forward or backward extrusion method, 324
semifinished products, 22
shape change, permanent type, 53
shaping methods, 1
shear
  band formation in plain strain compression, 42
  cracking, 136
  cross in cylinder compression, 136
  flow stress, 71, 143
  fracture in sheet-metal forming, 441

shear (*cont.*)
  layer of moderate shear, 42
  localization, 138
  strain in wiredrawing, 426
  zone in Al-extrusion, 183, 191
shearing, 10, 30
  part of extrusion process, 348
  as technological test, 257
  FEM model of process, 257
  to make workpiece, 7
shear stress
  at an interface, as process parameter, 14
  definition of, 53
  maximum value of, 56
  positive or negative stress, 55
sheet material, 442
sheet metal forming, 9, 18, 27–29
shiny surface appearance in thin-film lubrication, 146
shut lap, 280
Siebel's drawing force equation, 403
simulation, 224
simulative tests in sheet-metal forming, 438
slab, 22
slab method, 205
  applied in cylinder compression, 209–212
  applied in extrusion, 338
  applied in plain strain compression, 205
  applied in rolling, 373
  die pressure in cylinder compression, 212
  die pressure in plane strain compression, 208
  the force balance, 207
  force in cylinder compression, 212
  force in plane strain compression, 208
  general assumptions, 206
slab rolling, 376
  description normal pass, 383
sliding
  contact zone at rear end of billet, 351
  against die, plane strain compression, 161
  friction, 145
slip
  in rolling, 367
  of wire against capstan, 399
slip line field method, 204
slow flowing zone in extrusion, 329
slug in backward cup extrusion, 285
soft annealed condition, formability of material in, 131
soft annealing, 27
  in wiredrawing production, 397
  of workpiece in backward cup extrusion, 285
softening, strain-induced, 136
solid formulation, 222
spinning, 29
  tooling in, 29
split billet technique, 182
split die principle, to measure friction, 400
springback
  because of elasticity, 440
  compensation by coning of bend, 450
  compensation by overbending, 449
  compensation by stretch bending, 450
  compensation methods, 449
  phenomenon of, 447
  prediction in FEA, 227
  ratio, definition of, 448
  ratio, experimental data for metals, 448
  reduced by stretch forming, 29, 440
  why difficult to predict, 449
stable drawing as requirement, 399
stagnant zone in
  cylinder compression, 109
  plain strain compression, 41, 45
  in wiredrawing, 425
static remeshing, 223
stationary processes, 84
steel
  C-Mn-steels, 2
  of high strength, 7
sticking, 143
  between billet and container, 351
  friction, 145
stock material in wiredrawing, 397
straight line particle movement in wiredrawing, 429
strain
  additive nature of true strain, 59
  conditions in rolling, 369
  definition of, 58
  deviatoric, 66
  effective value of, 67
  engineering shear strain, 61
  finding direction of principal strain, 62
  hydrostatic, 66
  increment, 58
  logarithmic, 58
  maximum shear strain, 62
  mean strain, 66
  natural, 58
  nominal, 58
  normal strain definition, 61
  plane strain state, 60
  principal value of, 62
  as process parameter, 14
  shear strain definition, 61
  transformation from true to nominal value, 59
  true strain, 58
  true strain in the neck, 105
  volume strain, 63
strain and strain rate from velocity field, 88
strain hardening, 116
  as parameter influencing necking, 131
  exponent, 118

strain-induced softening, 136
straining to improve mechanical properties, 4
strain rate
  conditions in rolling, 370
  constant value in plain strain compression, 36
  definition, 67
  effective value in frictionless compression, 107
  effective value of, 67
  as process parameter, 14
  as tensor, 67
  sensitivity, 118
  from velocity field, 86
strength coefficient, 118
stress
  bi-axial, 56
  components, 55
  definition of, 53
  deviator, 65
  effective value of, 67
  finding principal stress, 56
  general state of, 55
  homogeneous, 54
  hydrostatic, 65
  mean (normal) stress, 65
  nominal, 54
  plane, 56
  positive or negative stress, 55
  states in technological tests, 111
  tensor, 55
  transformation, 54
  transformation by Mohr's circle, 56
  true, 54
stress, strain, strain rate, compared by effective value, 67
stretch forming, 28
strip
  drawing, 149
  material, 442
  rolling, 376
  rolling as cold working process, 388
subsurface
  lamination, 321
  layer of billet, flow of, 328
subsurface sliding, 143
surface appearance, speckled, 149
surface expansion
  in backward cup extrusion, 297–299
  in closed-die forging, 316
surface layer of billet, 24
surface quality
  in extrusion, 322
  friction influence, 139
  importance of, 13
surface ring pattern
  in backward cup extrusion, 299
  in plain strain compression, 36
  technique, 199–201
surface
  appearance, boundary film lubrication, 148
  contamination of, 144
  created in metal forming, 13
  finish, 13
  quality, 13
  skin of billet, outflow of in extrusion, 329–331
Swift's equation, 119

T4-condition, formability of material, 131
taper, used in extrusion, 332
technological tests, 92
  description of test methods, 93
  mechanics of tests, 92
  in sheet-metal forming, 437
temperature
  conditions in extrusion, 175
  determined indirectly by microstructure, 176
  generation in metal forming, 160
  at hot spot inside extrusion die, 173
  in the die bearing in extrusion, 172
  measurement, 164–167
  as process parameter, 14
  sensitivity, 118
  at surface of Al-profile, 176
tensile cracking, FEA study of tensile test, 134
tensile strength, 103
tensile stress cracking, 134
  FEA of for compression test, 136
tensile stress zone
  in normal wiredrawing, 427
  on outside of bend, 439
  behind roll gap in normal slab rolling, 387
  in strip rolling, 392
tensile testing
  to find flow curve, 94
  mechanics of test method, 101
  as technological test, 93, 94
tensor
  to describe strains, 62
  notation, 55
theoretical methods in metal forming, 204
thermal
  effects, 159–164
  gradients in forging dies, 167
  response of thermocouple, 165
thermal conditions in
  Al-extrusion, 171–176
  light slab rolling pass, 380
  normal slab rolling pass, 387
  nonstationary forging, 167–169
  stationary processes, 169–175
  wire drawing, 170–171
thermally coupled FEM models, 226

thermocouple, 159, 165
  with short thermal response time, 165
thermomechanical treatment, 7
thick-film lubrication, 146
thin film lubrication, 148
thinning
  in sheet metal forming, 28
  3D-DEPORM®, 224
  of wire behind drawing die, 417, 418
torsion testing
  deformation without shape change, 96
  to determine flow stress and ductility, 96
  as technological test, 93, 96
transformation of microstructure in steel, 118
transient, thermal, 164
Tresca friction model, 140
  description of, 142–144
  mathematical expression, 143
Tresca yield criterion, 71
trimming
  of flash, 4, 21
  by shearing, 30
true strain from tensile test, 102
true stress
  best stress definition, 54
  from tensile test, 101
tube drawing, 396
  using floating plug, 396
  using internal mandrel, 396
tube extrusion, 25
turns of wire over capstan, 399
2D-DEFORM®, 223
types of metal flow in Al extrusion, 190

uniform
  deformation in tensile test, 102
  energy method, 204
unlubricated extrusion, 321
upper bound method, 213
  in cylinder compression, 216
  friction sliding energy, 214
  homogeneous deformation energy, 214
  inhomogeneous deformation power, 214
  power consumed in velocity discontinuity, 215
  power consumption, 213, 342
  in wiredrawing, 406
upsetting
  optimization of process, 331
  of the extrusion billet, 323

validation of
  forging load in closed die forging, 309
  friction in plain strain compression, 39
  metal flow in plain strain compression, 39
velocity
  in backward cup extrusion, 292
  components, 86
  conditions in wiredrawing, 399
  discontinuities in wiredrawing, 407
  discontinuity in extrusion, 341
  discontinuity lines, 214
  field, 84
  field in normal wiredrawing, 428
  requirement to velocity field, 87
velocity
  of material particle through roll gap, 365
visualization in FEA, 225
Voce's equations, 119
volume constancy, 63
von Mises yield criterion, 71

Wanheim and Bay's friction model, 140
warm forming, temperature range of, 118
weak
  layers (z-direction lamination), 8
  planes, 8
wear of dies, 13
  influence of friction, 139
web of extrusion die, 333
welding chamber in extrusion, 333
weld joint of thermocouple, 165
wire breaks, 26, 397
  avoiding breaks in drawing, 399, 404
wiredrawing, 26–27, 395
  bearing channel, 26
  as calibration process, 27
  capstan used in, 26
  as cold-forming process, 397
  as continuous process, 26
  converging die channel, 26
  experiments of Wistreich, 414
  force, 404
  force from Siebel's equation, 410
  as industrial process, 397, 399
  machines, 397
  parameters in industrial process, 414
  spooling of the wire, 27
  tension on the wire, 410
Wistreich's experiments, drawing parameters used, 414
workability, 127, 269
  of Al-alloys in extrusion, 335
  judged from tensile test, 94
working
  of metal, 19
  of microstructure, 7
working conditions, unfavorable in rolling, 383
workpiece, 1
  final stage, 13
  initial stage, 12

wrinkling, 19
  in deep-drawing, 444
  in sheet-metal forming, 441
wrought products, 13
WUMSI simulator, working principle, 98

X-ray inspection, 130

yield criterion, 70
  graphical representation of, 71
  shear stress criterion, 71
  Tresca or von Mises, 71
yield stress, 103

Zener-Hollomon constitutive equation, 122